

KATHOLIEKE UNIVERSITEIT LEUVEN
FACULTEIT TOEGEPASTE WETENSCHAPPEN
DEPARTEMENT ELEKTROTECHNIEK
Kasteelpark Arenberg 10, 3001 Leuven (Heverlee)

EQUALIZATION AND ECHO CANCELLATION IN DMT–BASED SYSTEMS

Jury:
Prof. dr. ir. P. Verbaeten, voorzitter
Prof. dr. ir. M. Moonen, promotor
Prof. dr. ir. B. Preneel
Prof. dr. ir. M. Steyaert
Prof. dr. ir. L. Vandendorpe (U.C.L.)
Prof. dr. ir. B. De Moor
Prof. dr. ir. G. Leus (T.U.Delft)
Prof. dr. ir. H. Van hamme

Proefschrift voorgedragen tot
het behalen van het doctoraat
in de toegepaste wetenschappen

door

Geert YSEBAERT

U.D.C. 621.376 April 2004

© Katholieke Universiteit Leuven – Faculteit Toegepaste Wetenschappen
Arenbergkasteel, B-3001 Heverlee (Belgium)

Alle rechten voorbehouden. Niets uit deze uitgave mag vermenigvuldigd en/of openbaar gemaakt worden door middel van druk, fotocopie, microfilm, elektronisch of op welke andere wijze ook zonder voorafgaande schriftelijke toestemming van de uitgever.

All rights reserved. No part of the publication may be reproduced in any form by print, photoprint, microfilm or any other means without written permission from the publisher.

D/2004/7515/13

ISBN 90-5682-475-9

Voorwoord

Bij de aanvang van dit doctoraatswerk had ik slechts een vaag vermoeden van wat doctoreren juist inhield. Gaandeweg werd het begrip 'doctoraat' concreter en groeide het vertrouwen, wat uiteindelijk geleid heeft tot het proefschrift dat nu voor u ligt. Bij het beëindigen van dit werk is het tijd om een aantal mensen te bedanken.

Als eerste in de rij zou ik Prof. Marc Moonen willen bedanken, de promotor van dit doctoraat. Dankzij Marc kende mijn onderzoekswerk een vliegende start. Door zijn uitstekende en uitermate persoonlijke begeleiding slaagde ik erin om dit doctoraat tot een goed einde te brengen, mijn oprechte dank hiervoor.

Verder gaat mijn dank uit naar alle leden van de jury. Ik besef dat het heel wat inspanning vergt om een dergelijk werk in een vrij korte tijdspanne na te lezen en te beoordelen. In het bijzonder dank ik de leden van het leescomité: Prof. Luc Vandendorpe (U.C.L.) for his flexibility when I was fixing my PhD defense and for his constructive remarks, Prof. Bart Preneel en Prof. Michiel Steyaert voor hun constructieve suggesties m.b.t. het proefschrift. Prof. Bart De Moor en Prof. Geert Leus (T.U. Delft) wil ik speciaal bedanken voor hun interesse in mijn onderzoek, voor de verhelderende discussies en voor het zetelen in de jury. Prof. Hugo Van hamme dank ik voor zijn onmiddellijke bereidheid om in laatste instantie mijn jury te vervolledigen. Prof. Pierre Verbaeten ben ik dankbaar voor het opnemen van het voorzitterschap van de jury.

I would like to express my gratitude to Prof. Richard Johnson, Jr. for inviting us to his research group at the Cornell University, USA. It was an enriching experience to share our research ideas with him and with his assistants. I will keep in mind the post-research activities like the BBQ, 'sherade', pasta-evening,... that he organized during our relatively short stay. Special thanks to Rick, Andy and John for their hospitality. In addition, I would like to thank Prof. Brian Evans (University of Texas at Austin, USA) and his assistants Ming and Milos for sharing their expertise in the field of DSL communications.

I would like to show my appreciation to Fabio Pisoni and his colleagues from

ST Microelectronics. I will never forget our fruitful collaboration and especially the typical Italian 'Colomba' cake that Fabio gave us for Easter.

De eerste jaren van mijn doctoraat werden gekenmerkt door een verrijkende en stimulerende samenwerking met Alcatel. Hierbij wil ik in het bijzonder de volgende personen bedanken: Katleen Van Acker, Piet Vandaele, Thierry Pollet, Luc De Clercq, Jan Verlinden, Danny Van Bruyssel, Peter Reusens en Mark Van Bladel.

Het IWT wens ik te danken voor de financiering van dit onderzoek.

Bij deze gelegenheid wil ik ook mijn bureaugenoten Gert, Koen en Toon bedanken voor de aangename werksfeer. Talrijke discussies en sociale activiteiten zorgden voor een leuke werkplek. Ook de overige leden van SISTA, met in het bijzonder de leden van de DSP-club Geert, Simon, Ann, Narendra, Hilde, Imad, Raphael, Olivier, Geert, Koen en Thomas wil ik danken voor hun directe en indirecte hulp bij het totstandkomen van dit doctoraat.

Tot slot wil ik mijn ouders, Inge, Riet, Kim en de familie Schoevaerts bedanken voor hun rotsvast vertrouwen. Een heel speciaal woordje van dank gaat uit naar Ilse voor haar goede zorgen en haar onvoorwaardelijke steun.

Geert Ysebaert, April 2004.

Abstract

Digital subscriber line (DSL) is a technology to provide broadband communications over the existing twisted pair telephone network. The signals received by a DSL modem are typically corrupted by channel induced noise, background noise, radio frequeny interference (RFI) and undesired echo. In this thesis we focus on the design of digital signal processing algorithms to improve the bit rate and/or the loop reach of current and future DSL systems. Furthermore, in the proposed algorithms we aim at keeping the hardware cost as low as possible.

The transmission format of many DSL systems is based on discrete multitone modulation (DMT). To combat channel induced noise, DMT-based receivers perform an *equalization* step by means of a time domain equalizer (TEQ) and a one-tap frequency domain equalizer (FEQ) per used tone. Despite the variety of TEQ design methods presented in the literature, we show that almost all designs can be formulated as the maximization of a product of generalized Rayleigh quotients. This unified framework allows us to highlight the subtle differences between the different design methods. Special attention is paid to minimum mean square error (MMSE) TEQ design with three distinct unit-energy constraints. We illustrate that the resulting TEQs have equal performance and can be obtained from a single iterative initialization method.

The modem structure can also be extended with *receiver windowing* to reduce the sensitivity to narrowband RFI. We show how to design a TEQ in combination with a time domain window in order to maximize the achievable bit rate. Simulations indicate that equalizer taps can be exchanged for additional windowing coefficients, resulting in substantial complexity savings. The design procedure also allows to design an equalizer and a window for small groups of tones or for each tone separately (per tone equalization).

Besides equalization and receiver windowing, we also investigate structures that effectively cancel undesired echo. In a first step, we enhance existing mixed time/frequency domain *echo cancelers* by adding double talk cancellation and by minimizing the complexity, independent of the misalignment between trans-

mitted echo symbols and received far end symbols. In a second step, an alternative structure is proposed, where less transmit power is required to update the echo canceler coefficients.

Finally, we propose an efficient method for fast initialization of a receiver structure based on an equalizer and an echo canceler for each tone separately (per tone equalization and echo cancellation). We show that the computational complexity and memory requirements can be substantially reduced compared to existing methods.

Korte Inhoud

Digitale lijnen naar de abonnee (*digital subscriber lines* of DSL) laten breedbandcommunicatie toe over het bestaande, getwiste paren telefoonnetwerk. De signalen, ontvangen door een DSL modem, worden typisch aangetast door ruis t.g.v. het kanaal, achtergrondruis, radiofrequentie-interferentie (RFI) en ongewenste echo. In dit proefschrift focuseren we ons op het ontwerp van digitale signaalverwerkingsalgoritmen om de bitsnelheid en de reikwijdte van bestaande en toekomstige DSL systemen te verbeteren. Verder is ons doel om de hardware kost van de voorgestelde algoritmes zo laag mogelijk te houden.

Het zendschema van vele DSL-systemen is gebaseerd op discrete multitoonmodulatie (*discrete multitone modulation* of DMT). Om ruis t.g.v. het telefoonkanaal tegen te gaan, voeren DMT-ontvangers een egalisatie-stap uit d.m.v. een tijdsdomein egalisatiefilter (*time domain equalizer* of TEQ) en een 1-taps frequentiedomein egalisatiefilter (*frequency domain equalizer* of FEQ) per gebruikte toon. Ondanks de verscheidenheid aan TEQ-ontwerpmethodes die verschenen zijn in de literatuur, tonen we aan dat bijna alle ontwerpstrategieën geformuleerd kunnen worden als een maximisatie van een product van veralgemeende Rayleigh quotiënten. Dit veralgemeend kader laat ons toe om de subtiele verschillen tussen de verschillende ontwerpmethodes toe te lichten. Speciale aandacht wordt besteed aan het TEQ-ontwerp, waarbij de gemiddelde kwadratische fout geminimiseerd (*minimum mean square error* of MMSE) wordt in de aanwezigheid van drie verschillende eenheidsenergiebeperkingen. We tonen aan dat de resulterende TEQs een gelijke performantie vertonen en verkregen kunnen worden via eenzelfde, iteratieve initialisatiemethode.

De modemstructuur kan eveneens uitgebreid worden met een vensterfunctie om de gevoeligheid voor smalbandige RFI te reduceren. We geven aan hoe een TEQ en een vensterfunctie (in het tijdsdomein) gezamenlijk ontworpen kunnen worden om de haalbare bitsnelheid te maximiseren. Simulaties tonen aan dat egalisatiefiltertaps uitgewisseld kunnen worden voor vensterfunctiecoëfficiënten, resulterend in aanzienlijke complexiteitsbesparingen. De ontwerpprocedure laat ook toe om een egalisatiefilter en een vensterfunctie te ontwerpen voor kleine toongroepen of voor elke toon afzonderlijk (per-toon egalisatie).

Naast egalisatie en vensterfuncties bestuderen we ook structuren om echo te onderdrukken. In een eerste stap verbeteren we bestaande tijds- en frequentiedomein echo-onderdrukkers door dubbelspraakonderdrukking toe te voegen en door de complexiteit ervan te minimiseren, op een wijze die onafhankelijk is van de alignering tussen de verzonden echo-symbolen en de ontvangen symbolen die afkomstig zijn van de andere zijde van de telefoonlijn. In een tweede stap stellen we een alternatieve echo-onderdrukkingsstructuur voor waar minder vermogen moet worden uitgezonden om de coëfficiënten van de echo-onderdrukker aan te passen.

Ten slotte stellen we een efficiënte methode voor om een ontvanger die gebaseerd is op egalisatie en echo-onderdrukking per toon te initialiseren (per-toon egalisatie en echo-onderdrukking). Er wordt aangetoond in de thesis dat de rekenkundige complexiteit en de geheugenvereisten aanzienlijk gereduceerd kunnen worden in vergelijking met reeds bestaande werkwijzen.

Glossary

Mathematical Notation

$\mathbb{N}$	the set of natural numbers
$\mathbb{Z}$	the set of integer numbers
$\mathbb{Q}$	the set of rational numbers
$\mathbb{R}$	the set of real numbers
$\mathbb{C}$	the set of complex numbers
$\mathbb{R}^M$	set of real M–dimensional vectors
$\mathbb{R}^{L \times M}$	set of real $L \times M$–dimensional matrices
$\mathbb{C}^M$	set of complex M–dimensional vectors
$\mathbb{C}^{L \times M}$	set of complex $L \times M$–dimensional matrices
a	scalar a
$\mathbf{a}$	(column) vector $\mathbf{a}$
A	(column) vector $A \in \mathbb{C}$ with frequency domain samples, discrete Fourier transform of $\mathbf{a}$
$\mathbf{A}$	matrix $\mathbf{A}$
$\mathbf{a}[m]$	m–th element of vector $\mathbf{a}$
$\mathbf{A}[l, m]$	element on the l–th row and the m–th column of matrix $\mathbf{A}$
$\mathbf{A}[l : m, :]$	rows l up to m of matrix $\mathbf{A}$
$\mathbf{A}[:, l : m]$	columns l up to m of matrix $\mathbf{A}$
$\mathbf{A}^T$	transpose of matrix $\mathbf{A}$
$\mathbf{A}^*$	complex conjugate of matrix $\mathbf{A}$
$\mathbf{A}^H = (\mathbf{A}^*)^T$	Hermitian transpose of matrix $\mathbf{A}$
$\mathbf{A}^{-1}$	inverse of matrix $\mathbf{A}$
$\mathbf{A}^{1/2}$	Cholesky factor of $\mathbf{A}$
$\mathbf{A}^\dagger$	pseudo–inverse of matrix $\mathbf{A}$
$\lvert\mathbf{A}\rvert$	determinant of matrix $\mathbf{A}$
$\mathrm{tr}\{\mathbf{A}\}$	trace of matrix $\mathbf{A}$
$\mathrm{diag}\{\mathbf{a}\}$	square diagonal matrix with vector $\mathbf{a}$ as diagonal
$\mathcal{R}e\{\mathbf{a}\}$	real part of $\mathbf{a} \in \mathbb{C}$
$\mathcal{I}m\{\mathbf{a}\}$	imaginary part of $\mathbf{a} \in \mathbb{C}$
$\hat{\mathbf{a}}$	estimate of $\mathbf{a}$

$\|\|\mathbf{a}\|\|_2$	2–norm of $\mathbf{a}$
$\mathbf{a}_{N\downarrow}$	$\mathbf{a}$ N–fold downsampled
$\mathbf{a}_{N\uparrow}$	$\mathbf{a}$ N–fold upsampled
$\lfloor a \rfloor$	largest integer smaller than or equal to $a \in \mathbb{R}$
$\|a\|$	absolute value of a
$a \ll b$	a is much smaller than b
$a \gg b$	a is much larger than b
$a \approx b$	a is approximately equal to b
$\mathbf{a} \star \mathbf{b}$	linear convolution of $\mathbf{a}$ and $\mathbf{b}$
$\mathbf{A} \odot \mathbf{B}$	component wise multiplication of $\mathbf{A}$ and $\mathbf{B}$
$\mathcal{E}\{\cdot\}$	statistical expectation operator
σ_a	standard deviation of a
$\nabla_{\mathbf{a}} J$	gradient of J with respect to $\mathbf{a}$

Fixed Symbols

J	cost function
L	channel order (= length of the channel impulse response - 1)
N	(I)DFT size
T	number of (P)TEQ taps
T_E	number of echo canceler taps
b	number of bits
f	frequency domain variable
i	tone or subcarrier index
j	$\sqrt{-1}$
k	block time index or symbol index
l	discrete time index or sample index
r	bit rate in bits per second
z	z–domain variable
$\mathbf{b}$	target impulse response (TIR)
$\mathbf{c}$	effective channel $\mathbf{c} = \mathbf{h} \star \mathbf{w}$
$\mathbf{e}_p$	canonical vector: all zero vector except for a one at the p-th position
$\mathbf{g}$	gradient of J, $\mathbf{g} = \nabla J$
$\mathbf{h}$	channel impulse response (CIR)
$\mathbf{v}$	PTEQ equalizer taps based on difference terms
$\mathbf{w}$	P(TEQ) equalizer taps
$\mathbf{w}_E$	echo canceler taps in the time domain
$\mathbf{n}^k$	additive noise samples at symbol period k
$\mathbf{u}^k$	transmitted echo time domain samples at symbol period k
$\mathbf{x}^k$	transmitted far–end time domain samples at symbol period k

$\mathbf{y}^k$	received time domain samples at symbol period k
U^k	frequency domain vector of transmitted, QAM–modulated echo symbols at symbol period k
U_i^k	QAM symbol of U^k for tone i
X^k	frequency domain vector of transmitted, QAM–modulated far–end symbols at symbol period k
X_i^k	QAM symbol of X^k for tone i
$\hat{X}_i^k$	FEQ or PTEQ output for tone i at symbol period k
$\mathbf{H}$	channel matrix
$\mathbf{H}_{win}$	channel matrix with 'windowed' part of the channel
$\mathbf{H}_{wall}$	channel matrix with 'walled' part of the channel
σ_n^2	noise power
σ_x^2	power of transmitted far–end signal
σ_u^2	power of transmitted echo signal
Γ	SNR gap
γ_m	system margin
γ_c	coding gain
ϵ	exponential weighting factor, $0 < \epsilon \leqslant 1$
κ	subsampling factor
λ	eigenvalue of a square matrix
μ	adaptive filter step size
ν	cyclic prefix length
σ	singular value of a matrix
D_i	one–tap FEQ for tone i
F_s	sampling frequency
T_s	sampling interval
N_u	number of used tones
$\mathcal{S}$	set of used tones
$\mathcal{F}_N$	N–point DFT matrix,
$\mathcal{I}_N$	N–point IDFT matrix, $\mathcal{I}_N = \frac{1}{N}\mathcal{F}_N^H$
$\mathbf{I}_P$	$P \times P$ identity matrix
$\mathbf{0}$	zero vector or zero matrix
$\mathbf{0}_P$	$P \times P$ zero matrix
$\mathbf{0}_{P\times Q}$	$P \times Q$ zero matrix
$\mathbf{R}_{xx}$	auto-correlation matrix corresponding to vector $\mathbf{x}$
$\mathbf{R}_{xy}$	cross-correlation matrix between $\mathbf{x}$ and $\mathbf{y}$

Acronyms and Abbreviations

ADC	Analog–to–Digital Converter
ADSL	Asymmetric DSL
ANSI	American National Standards Institute
APA	Affine Projection Algorithm

ARPA	Advanced Research Projects Agency
AWGN	Additive White Gaussian Noise
BM-TEQ	Bit rate Maximizing TEQ
BM-Win	Bit rate Maximizing Window
BM-WinTEQ	Bit rate Maximizing Window and TEQ
bps	bits per second
CDC	Circulant Decomposition Canceler
CES	Circular Echo Synthesis
cf.	`confer`: compare with
CIR	Channel Impulse Response
CLEC	Competitive Local Exchange Carrier
CO	Central Office
CP	Cyclic Prefix
CSA	Carrier Serving Area
DAB	Digital Audio Broadcasting
DAC	Digital–to–Analog Converter
DFT	Discrete Fourier Transform
DMT	Discrete Multitone
DSL	Digital Subscriber Line
DSLAM	Digital Subscriber Line Access Multiplexer
DSP	Digital Signal Processor
DTC	Double Talk Cancellation
DVB	Digital Video Broadcasting
EC	Echo Canceling
e.g.	`exempli gratia`: for example
et al.	`et alii`: and others
ETSI	European Telecommunications Standards Institute
FDAF	Frequency Domain Adaptive Filter
FDD	Frequency Division Duplexing
FEQ	Frequency domain EQualizer
FEXT	Far–End CrossTalk
FFT	Fast Fourier Transform
FIR	Finite Impulse Response filter
FTTH	Fiber To The Home
HAM	amateur radio
HDSL	High data rate DSL
HDTV	High Definition Television
HFC	Hybrid Fiber Coax
ICI	Inter–Carrier–Interference
IDFT	Inverse Discrete Fourier Transform
i.e.	`id est`: that is
IFFT	Inverse Fast Fourier Transform
IIR	Infinite Impulse Response filter
ILEC	Incumbent Local Exchange Carrier
ISDN	Integrated Services Digital Network

ISP	Internet Service Provider
ISI	Inter–Symbol–Interference
ITF-EC	Improved Time Frequency Domain EC
ITU	International Telecommunication Union
LAN	Local Area Network
LMS	Least Mean Square adaptive filter
MC	Multicarrier
MIMO	Multi–Input Multi–Output system
MMSE	Minimum Mean Square Error
MSE	Mean Square Error
NEXT	Near–End CrossTalk
NLMS	Normalized Least Mean Square adaptive filter
OFDM	Orthogonal Frequency Division Multiplexing
PAPR	Peak-to-Average Power Ratio
PC	Personal Computer
PCM	Pulse Code Modulation
PGA	Programmable Gain Amplifier
POTS	Plain Old Telephone Service
P/S	Parallel–to–Serial converter
PSD	Power Spectral Density
PSTN	Public Switched Telephone Network
PTEQ	Per Tone EQualization
PTEC	Per Tone Echo Cancellation
QAM	Quadrature Amplitude Modulation
READSL	Range Extended ADSL
RFI	Radio Frequency Interference
RLS	Recursive Least Squares adaptive filter
RS	Reed-Solomon
RT	Remote Terminal
SAGE	Semi-Automatic Ground Environment
SDSL	Symmetric DSL
SISO	Single–Input Single–Output system
SNR	Signal–to–Noise Ratio
S/P	Serial–to–Parallel converter
SR	Square-Root
SSNR	Shortening SNR
SVD	Singular Value Decomposition
TEQ	Time domain EQualizer
TIR	Target Impulse Response
UTP	Unshielded Twisted Pair
VDSL	Very high bit rate DSL
vs.	versus
w.l.o.g.	without loss of generality
ZF	Zero Forcing
@	at

Contents

Voorwoord **i**

Abstract **iii**

Korte Inhoud **v**

Glossary **vii**

Contents **xiii**

Dutch summary **xxi**

1 Introduction **1**

1.1 Past, present and future communications 2

1.1.1 A brief history of wireline communications 2

1.1.2 Present and future broadband communications 5

1.2 Characteristics of the DSL environment 8

1.2.1 Multicarrier modulation 8

1.2.2 Channel induced interference 10

1.2.3 External noise 12

1.3 Outline of the thesis and contributions 16

1.3.1 Motivation 16

1.3.2 Thesis overview and contributions 17
1.4 Conclusions 20

2 Basic concepts and notation **21**
2.1 Capacity of a transmission medium 22
2.2 Discrete multitone modulation (DMT) 23
2.2.1 Block transmission with cyclic prefix 23
2.2.2 Transmitter and receiver structure 28
2.2.3 Receiver windowing 32
2.2.4 Bit loading 34
2.3 Data model 37
2.3.1 Basic data model, symmetric setup 38
2.3.2 Data model with echo 39
2.3.3 Data model for TEQ and receiver windowing 42
2.4 Conclusions 43

3 Equalizer design: a unified approach **45**
3.1 Common formulation 46
3.2 Single equalizer design with one Rayleigh quotient 48
3.2.1 Minimum mean square error (MMSE) 49
3.2.2 Maximum shortening SNR (MSSNR) 58
3.2.3 Multicarrier equalization by restoration of redundancy (MERRY) 60
3.2.4 Minimum-ISI (Min-ISI) 61
3.2.5 Minimum delay spread (MDS) 62
3.2.6 Carrier nulling algorithm (CNA) 63
3.3 Single equalizer design with multiple Rayleigh quotients 64
3.3.1 Maximum geometric SNR (MGSNR) method 64

3.3.2 Maximum Bit Rate (MBR) method 66
3.3.3 Near optimal TEQ design method (NO-TEQ) 67
3.3.4 Bit rate maximizing TEQ (BM-TEQ) 67
3.4 Multiple equalizer design with a single Rayleigh quotient per tone 69
3.4.1 Per tone equalization (PTEQ) 69
3.5 Exceptions to the common formulation 73
3.5.1 Improved and iterative bit rate maximizing TEQ design 73
3.5.2 Channel shortening by sum-squared auto-correlation minimization (SAM) 73
3.6 Simulation results 73
3.6.1 Comparison of TEQ design algorithms 75
3.6.2 Bit rate performance of TEQ design methods for different loops 79
3.6.3 Iterative initialization for MMSE TEQ design with unit-energy constraints 81
3.7 Conclusions 81

4 Bit rate maximizing joint window and equalizer design 85
4.1 Notation and bit rate expression 87
4.1.1 Notation 87
4.1.2 Bit rate expression 87
4.1.3 Constrained versus unconstrained MMSE FEQ 89
4.2 Bit rate maximizing equalizer and window design 90
4.2.1 Single TEQ and window design (BM-WinTEQ) 90
4.2.2 Per group equalizer and window design (BM-PGWinTEQ) 93
4.2.3 Per tone equalizer and window design (PTEQ) 94
4.3 Special cases 96
4.3.1 Equalizer-only design 96

4.3.2 Window-only design 97
4.3.3 Other variants 100
4.4 Complexity and memory requirements 101
4.5 Simulation results 104
4.5.1 Performance of BM-Win 104
4.5.2 Performance of BM-WinTEQ and BM-FWinTEQ . . . 106
4.6 Conclusions 111

5 Mixed time/frequency domain echo cancellation 117
5.1 Time domain echo canceling (TD-EC) 119
5.1.1 Symmetric rate TD-EC 119
5.1.2 Multi-rate TD-EC 122
5.1.3 Complexity 125
5.2 Circular echo synthesis (CES) 126
5.2.1 Symmetric rate CES-based EC 126
5.2.2 Multi-rate CES-based EC 129
5.2.3 Complexity 131
5.3 Double talk cancellation (DTC) 132
5.3.1 Double talk cancellation for TD-EC 133
5.3.2 Double talk cancellation for CES-based EC 135
5.3.3 Complexity 136
5.4 Improved time/frequency domain echo canceling (ITF-EC) . . 136
5.4.1 Motivation 137
5.4.2 Symmetric rate ITF-EC 139
5.4.3 Multi-rate ITF-EC 142
5.4.4 Complexity 143
5.5 Circulant decomposition canceler (CDC) 146

5.5.1 Motivation 146
5.5.2 Symmetric rate CDC 147
5.5.3 Multi-rate CDC 151
5.5.4 CDC combined with PTEQ and DTC 156
5.5.5 Complexity 158
5.6 Simulation results 160
5.6.1 Double talk cancellation 160
5.6.2 Performance of ITF-EC 162
5.6.3 Performance of CDC 168
5.7 Conclusions 171

6 Split SR-RLS for per tone equalizer and per tone echo canceler initialization 173

6.1 Standard adaptive filtering algorithms 174
6.1.1 Introduction 174
6.1.2 Normalized least mean square (NLMS) 176
6.1.3 Square-root recursive least square (SR-RLS) 177
6.2 Split SR-RLS with reduced complexity 179
6.2.1 Algorithm outline 179
6.2.2 Convergence 180
6.3 RLS-LMS for PTEQ initialization 182
6.3.1 PTEQ revisited 182
6.3.2 NLMS-based PTEQ initialization 183
6.3.3 SR-RLS-based PTEQ initialization 184
6.3.4 RLS-LMS-based PTEQ initialization 184
6.3.5 Complexity 189
6.4 Split SR-RLS for PTEQ/PTEC initialization 193

6.4.1 Joint per tone echo cancellation and per tone equalization 193
6.4.2 NLMS-based PTEQ/PTEC initialization 195
6.4.3 SR-RLS-based PTEQ/PTEC initialization 195
6.4.4 Split SR-RLS-based PTEQ/PTEC initialization 197
6.4.5 Complexity 198
6.4.6 Similar applications 200
6.5 Simulation results 201
6.5.1 PTEQ initialization 201
6.5.2 Joint PTEQ/PTEC initialization 204
6.6 Conclusions 206

7 Conclusions and further research **211**
7.1 Conclusions 211
7.2 Further research 214

Bibliography **217**

Appendices **229**
A Basic linear algebra definitions 229
A.1 Structured matrices 229
A.2 Subspace related definitions 232
A.3 Matrix decompositions 232
A.4 Iterative eigensolvers 235
A.5 Differentiation with respect to a parameter vector . . . 236
B Appendix to Chapter 3 238
B.1 MMSE TEQ design with unit-norm constraint on TEQ 238
B.2 MMSE TEQ design with unit-tap constraint on TEQ . 239
B.3 MMSE TEQ design with unit-energy constraints 239

B.4 The unconstrained MMSE PTEQ 243
C Appendix to Chapter 4 247
C.1 SNR for TEQ filtering combined with windowing 247
C.2 Gradient and Hessian of the BM-WinTEQ cost function 247
C.3 Efficient computation of the correlation matrices 251
D Appendix to Chapter 5 254
D.1 Convergence in the mean ITF-EC 254
D.2 Circulant and skew-circulant decomposition 256
D.3 Convergence in the mean CDC 257
E Appendix to Chapter 6 260
E.1 Convergence in the mean split SR-RLS 260
E.2 Upper bound for the step size of split SR-RLS 261

List of publications **263**

Curriculum vitae **267**

Egalisatie en echo-onderdrukking in DMT-gebaseerde systemen

Nederlandse samenvatting

Hoofdstuk 1: Inleiding

Breedband communicatie

Met de komst van het Internet is de vraag naar breedband communicatie enorm toegenomen. Ondanks uitgebreid onderzoek naar datacompressie vereisen de huidige multimedia toepassingen nog steeds een hoge bitsnelheid om het te transporteren over een communicatienetwerk. Verschillende technologieën laten breedband communicatie van de netwerkzijde naar de gebruikerszijde toe, zoals b.v. kabelmodems, draadloze systemen en digitale lijnen naar de abonnee (E: digital subscriber lines of DSL). In deze thesis gaat de aandacht uit naar DSL-gebaseerde systemen.

DSL maakt het mogelijk om van het bestaande, getwiste paren telefoonnetwerk, dat oorspronkelijk diende voor smalbandige, analoge telefonie (E: plain old telephone service of POTS), een toegangsweg te maken tot breedbandige communicatie, zie **Fig. 1.1**. Het DSL-netwerkmodel gaat uit van de veronderstelling dat glasvezel steeds verder doordringt in het netwerk naar de gebruiker toe. M.a.w. DSL-technologie biedt een oplossing om de 'laatste mijl' te overbruggen tussen de netwerkzijde en de gebruikerszijde.

DSL kent verschillende varianten, maar de meest bekende DSL-vorm is zeker ADSL (E: asymmetric DSL of ADSL). ADSL laat asymmetrische bitsnelheden toe van 8 Mbps naar de abonnee en van 640 kbps naar het netwerk. Deze snelheden breiden de capaciteit van traditionele spraakband modems uit met een factor 100 of meer zonder de noodzaak om de huidige bekabeling te

vernieuwen. In tegenstelling tot de traditionele spraakbandmodems zorgt het ADSL-frequentieplan (zie **Fig. 1.2**) er bovendien voor dat de bestaande telefoniediensten (POTS of ISDN) gelijktijdig met ADSL kunnen aangeboden worden, cf. **Fig. 1.3**.

Karakteristieken van de DSL-omgeving

De meeste DSL-systemen maken gebruik van discrete multitoon modulatie (E: discrete multi tone modulation of DMT), zie Subsectie 1.2.1. DMT is een modulatieschema waarbij de beschikbare frequentieband opgedeeld wordt in verschillende smalle banden of tonen. Elke toon wordt dan in kwadratuur en in amplitude (E: quadrature amplitude modulation of QAM) gemoduleerd, waarbij modulatie en demodulatie uitgevoerd worden d.m.v. een discrete (inverse) Fourier transformatie (E: discrete Fourier transform of DFT). In tegenstelling tot de eerste, analoge multidrager-modulatieschema's, maakt DMT gebruik van een digitaal uitvoerbaar modulatieschema, waarbij de verschillende deelbanden sinc-vormig zijn en met elkaar overlappen. Verder zorgt de snelle Fourier transformatie (E: fast Fourier transform of FFT) voor een efficiënte implementatie van het DMT-modulatieschema.

Eén van de voordelen van DMT is de flexibele wijze waarop bits toegekend kunnen worden aan de verschillende tonen (E: bit loading). De QAM-constellatiegrootte voor een bepaalde toon is afhankelijk van de signaal-ruisverhouding (E: signal-to-noise ratio of SNR) op die toon, die gemeten wordt tijdens de initialisatiefase. Dit concept wordt geïllustreerd door **Fig. 1.4**. Het is duidelijk dat tonen met een hoge SNR meer bits kunnen doorsturen dan tonen met een lage SNR, voor een gegeven bitfoutkans. Deze techniek maakt het mogelijk om bitsnelheden te behalen in de buurt van de kanaalcapaciteit.

De telefoonlijn waarover het DSL-signaal propageert, heeft een tijdsdispersief karakter, i.e. de kanaalimpulsresponsie is uitgesmeerd in de tijd, zie Subsectie 1.2.2. Hierdoor zullen opéénvolgende, verstuurde DMT-symbolen bij ontvangst met elkaar interfereren. Zonder aangepaste signaalverwerking in de ontvanger zal dit leiden tot inter-symbool-interferentie (E: inter-symbol-interference of ISI). Bovendien kan de wiskundige orthogonaliteit van aangrenzende tonen verloren gaan, wat resulteert in ongewenste inter-drager-interferentie (E: inter-carrier-interference of ICI). In deze thesis gaan we o.a. na hoe deze ISI en ICI gereduceerd kunnen worden a.d.h.v. egalisatie-algoritmes.

Verschillende oorzaken liggen aan de basis van het tijdsdispersief karakter van het kanaal. Signalen die uitgestuurd worden over de telefoonlijn ondergaan zowel een frequentie-afhankelijke kanaalverzwakking als een frequentie-afhankelijke voortplantingssnelheid. Zowel de lijnlengte, draaddiameter als het type draad zorgen ervoor dat de reikwijdte van ADSL beperkt blijft tot telefoonlijnen van ongeveer 3.7 km. Verder worden DSL-signalen ook beïnvloed door vertakkingen (E: bridged taps) van de telefoonlijn, zie **Fig. 1.5**. Een

vertakking zorgt ervoor dat het verstuurde signaal opgesplitst wordt in twee componenten. Eén component zal reflecteren aan het open uiteinde van de ongebruikte vertakking en zal zich uit fase opnieuw toevoegen aan de tweede component. Afhankelijk van de plaats en de lengte van de vertakking kunnen beide componenten destructief interfereren, wat leidt tot een reductie in de kanaalcapaciteit.

De verscheidenheid aan telefoonlijnen zorgde ervoor dat een aantal testlijnen gedefinieerd werden in de DSL-standaarden. De signaalverwerkingsalgoritmen die ontwikkeld zullen worden in dit proefschrift zullen dan ook uitgetest worden op deze gestandaardiseerde lijnen.

Stoorbronnen in de DSL-omgeving

Naast interferentie veroorzaakt door de telefoonlijn zelf, is een DSL-systeem ook onderhevig aan allerlei externe ruisbronnen, zie Subsectie 1.2.3. Men kan de volgende ruisbronnen onderscheiden: achtergrondruis, overspraak, echo, radiofrequentie-interferentie en impulsruis.

Achtergrondruis is de ruis die veroorzaakt wordt door de thermische agitatie van de elektronen in de koperdraden. Deze ruis zal gemodelleerd worden als additieve, witte, Gaussiaanse ruis (E: additive white Gaussian noise of AWGN).

Aangezien een telefoonkabel bestaat uit een bundel van verschillende getwiste paren, zal er elektromagnetische koppeling ontstaan tussen de paren onderling. Deze koppeling wordt *overspraak* (E: crosstalk) genoemd, zie **Fig. 1.6**. Wanneer de overspraak afkomstig is van signalen die zich in tegengestelde richting voortplanten, spreekt men van overspraak van een nabije zender (E: near-end crosstalk of NEXT). Overspraak veroorzaakt door signalen die zich in dezelfde richting verplaatsen, noemt men overspraak van een verre zender (E: far-end crosstalk of FEXT). Overspraak leidt in vele gevallen tot een degradatie van de DSL-performantie, aangezien het overspraakniveau vaak hoger ligt dan het niveau van de achtergrondruis, zie **Fig. 1.7**.

Om bidirectionele communicatie mogelijk te maken over één telefoonlijn worden de zend- en ontvangzijde van een modem gekoppeld aan de lijn d.m.v. een hybriede. Een perfecte hybriede zorgt voor een ontkoppeling van de verstuurde en de ontvangen signalen. In de praktijk echter zal de hybriede niet perfect aangepast zijn aan de telefoonlijn, waardoor het verzonden signaal gedeeltelijk terug naar de ontvangzijde zal gereflecteerd worden, zie **Fig. 1.6**. Deze ongewenste reflectie wordt *echo* genoemd.

In de praktijk gedraagt elke telefoonlijn zich als een antenne die energie uitstraalt en opvangt. Radio-signalen afkomstig van draadloze zenders zullen opgepikt worden door de koperen telefoonlijnen. Aangezien de gebruikte RFI-frequenties overlappen met de ADSL-frequentieband, resulteert dit in *radio frequentie interferentie* (E: radio frequency interference of RFI).

Impulsruis is ruis veroorzaakt door het sporadisch schakelen van elektronische apparaten in de buurt van telefoonlijnen. Impulsruis is typisch kortstondig, maar heeft een energie-inhoud die vele malen hoger kan zijn dan het ontvangen DSL-signaal. Deze ruisvorm wordt typisch bestreden d.m.v. bitcodering.

Thesisoverzicht en bijdragen

De toenemende vraag naar breedband communicatie leidde tot de ontwikkeling van verscheidene DSL-systemen. Ondanks de recente ontplooiing van ADSL in verschillende landen, zijn wij van mening dat de DSL-technologie nog een toekomst heeft van vele jaren om de 'laatste mijl' naar de gebruiker te overbruggen. Ondanks het grote succes van DSL, moet men rekening houden met een aantal beperkingen. Aangezien de signaalverzwakking toeneemt met de lijnlengte, komen mensen, die zich te ver van de telefooncentrale (E: central office of CO) bevinden, niet in aanmerking voor ADSL. Daarom wordt er in dit proefschrift aandacht besteed aan *geavanceerde digitale signaalverwerkingsalgoritmen* om de reikwijdte van bestaande DSL-systemen te vergroten. Een andere mogelijkheid bestaat erin om de ruismarge te vergroten zonder de reikwijdte aan te passen, wat leidt tot een verhoogde robuustheid van de modem. Verder zullen de voorgestelde algoritmen ontworpen worden met het oog op het reduceren van de rekenkundige complexiteit, geheugenvereiste en/of uitgestuurd vermogen.

In **Hoofdstuk 2** zullen eerst de basisprincipes van DMT-transmissie wiskundig uitgelegd worden. In dit hoofdstuk zal ook het gebruikte datamodel geïntroduceerd worden.

Om interferentie veroorzaakt door het transmissiekanaal te reduceren, kan men gebruik maken van een cyclische prefix (E: cyclic prefix of CP) in combinatie met egalisatietechnieken. In DMT-systemen wordt elk verstuurd symbool voorzien van een CP. Indien de kanaalimpulsresponsie korter is dan de lengte van de CP plus één, kan de ontvanger de kanaaleffecten verwijderen a.d.h.v. een 1-tap frequentiedomein egalisator (E: frequency domain equalizer of FEQ) per toon. In ADSL echter overschrijdt de lengte van de kanaalimpulsresponsie de duur van de CP, waardoor ISI en ICI ontstaat. Een oplossing hiervoor is het toevoegen van een extra tijdsdomein filter (E: time domain equalizer of TEQ) aan de ontvangzijde vóór om het kanaal te verkorten. Een alternatief egalisatieschema bestaat uit het uitvoeren van de TEQ-FEQ combinatie per toon ná de demodulatie en wordt per-toon egalisatie (E: per tone equalization of PTEQ) genoemd. In **Hoofdstuk 3** wordt er een wiskundig kader ontwikkeld, waarin (bijna) alle bestaande egalisatie-ontwerpmethodes geformuleerd kunnen worden. Deze gemeenschappelijke formulering is gebaseerd op een product van veralgemeende Rayleigh quotiënten en laat toe om de subtiele verschillen tussen verschillende methodes te verduidelijken.

Hoofdstuk 3 besteedt ook extra aandacht aan MMSE (E: minimum mean square error) TEQ-ontwerp. We tonen aan dat MMSE TEQ-ontwerp met drie

verschillende eenheidsenergie-beperkingen resulteert in: a) TEQ-coëfficiënten met een gelijke performantie, b) een éénvoudig, iteratief initialisatieschema op basis van de power-methode of inverse iteraties en c) een geometrische interpretatie.

RFI kan bestreden worden door het toevoegen van een vensterfunctie aan de ontvanger. **Hoofdstuk 4** behandelt het ontwerp van de coëfficiënten voor de egalisator en voor de vensterfunctie met het oog op het maximiseren van de bereikbare bitsnelheid. De resulterende ontvanger zal dan minder gevoelig zijn aan RFI en ruis veroorzaakt door het kanaal.

Wanneer de frequentiebanden voor upstream (van de gebruiker naar het netwerk) en downstream (van het netwerk naar de gebruiker) transmissie geheel of gedeeltelijk overlappen, ontstaat er ongewenste echo. Daarom onderzoeken we in **Hoofdstuk 5** verschillende schema's om echo te verwijderen aan de ontvanger. Traditioneel wordt echo volledig onderdrukt in het tijdsdomein. DMT-gebaseerde systemen laten echter een meer efficiënte wijze van echo-onderdrukking toe, waarbij de echo gedeeltelijk onderdrukt wordt in het tijdsdomein en gedeeltelijk in het frequentiedomein. In dit hoofdstuk tonen we aan hoe bestaande gemengde tijds-/frequentiedomein echo-onderdrukkingschema's uitgebreid kunnen worden met dubbelspraakonderdrukking (E: double talk cancellation of DTC) om het tracking gedrag te verbeteren. Verder stellen we een echo-onderdrukkingsschema voor, waarbij de complexiteit geminimaliseerd kan worden onafhankelijk van de alignering tussen de verzonden echo-symbolen en de ontvangen symbolen afkomstig van de andere zijde. Tenslotte stellen we een echo-onderdrukker voor, gebaseerd op een circulante ontbinding van verzonden echo-symbolen (E: circulant decomposition canceler of CDC), waarbij minder vermogen dient verstuurd te worden in vergelijking met bestaande systemen om de echo-onderdrukker te laten convergeren.

In **Hoofdstuk 6** bespreken we een efficiënte methode voor de initialisatie van de PTEQ enerzijds en de initialisatie van de PTEQ gecombineerd met per-toon echo-onderdrukking (E: per tone echo cancellation of PTEC) anderzijds. Het voorgestelde initialisatieschema is gebaseerd op gesplitste recursieve kleinstekwadraten (E: split recursive least square of split RLS) adaptieve filtering, waarbij de rekenkundige complexiteit en geheugenvereisten aanzienlijk gereduceerd worden in vergelijking met een volledige RLS.

Tenslotte worden de finale conclusies en suggesties voor verder onderzoek gegeven in **Hoofdstuk 7**.

Hoofdstuk 2: Basisconcepten en notatie

In dit hoofdstuk worden de basisbegrippen rond DSL-communicatie uitgelegd. Na een korte uiteenzetting van Shannons capaciteitsformules in Sectie 2.1, zal discrete multitoon modulatie besproken worden in Sectie 2.2. Tenslotte komt het datamodel, dat voortdurend gebruikt zal worden in deze thesis, uitgebreid aan bod in Sectie 2.3.

Capaciteit van een transmissie-medium

Aangezien de meeste DSL-systemen trachten om de haalbare bitsnelheid over een getwist koperpaar te maximiseren, is het belangrijk om de capaciteit van het gebruikte transmissie-medium te kennen. Shannon leidde reeds in de jaren '40 een bovengrens af voor het aantal bits dat over een vlak AWGN kanaal kan doorgestuurd worden, zie (2.1). Deze formule kan uitgebreid worden wanneer de datatransmissie plaatsvindt over meerdere, parallelle subkanalen, zie (2.2). Om met een eindige complexiteit bits te versturen aan een vooraf vastgelegde bitfoutkans zal men in de praktijk echter gebruik maken van een SNR-kloof (E: SNR gap). Deze SNR-kloof reduceert het aantal te versturen bits en is afhankelijk van het gebruikte modulatieschema, de codering en de voorziene ruismarge, zie (2.4).

Discrete multitoon modulatie

In de vorige sectie werd een vlak AWGN-kanaal verondersteld zonder ISI. In praktische DSL-systemen is het kanaal echter tijdsdispersief met ISI tot gevolg. Om het tijdsdispersief karakter aan te pakken kan het kanaal opgedeeld worden in een groot aantal smalle subkanalen. Wanneer elk subkanaal voldoende smalbandig is en mits toevoeging van een cyclische prefix zal elk subkanaal bij benadering vlak en AWGN zijn, met weinig of geen ISI. Dit wordt *multitoon* transmissie genoemd.

Om de verdeling in smalle subkanalen mogelijk te maken wordt een bloktransmissieschema toegepast, waarbij de verstuurde monsters (E: samples) gegroepeerd in blokken van lengte s, met s veel groter dan de orde L van het kanaal, zie (2.8). Hierbij omvat het kanaal alle filters aan de zend- en ontvangzijde plus de karakteristieken van het gebruikte koperpaar, zie **Fig. 2.1**. Om ISI tussen opeenvolgende blokken of symbolen te compenseren wordt er een *cyclische prefix* (CP) voorzien in elk verstuurd symbool. Hierbij worden de laatste ν monsters van een symbool herhaald aan het begin van dit symbool, zie **Fig. 2.2** en (2.12). Aan de ontvanger worden enkel de laatste N monsters per symbool verder verwerkt, zie (2.13).

Afhankelijk van de orde van het kanaal kunnen twee gevallen onderscheiden worden:

1. als $L \leq \nu$ is het symbool verzonden op tijdstip k onafhankelijk van het symbool verzonden op tijdstip $k-1$, m.a.w. het systeem is vrij van ISI.

De resulterende kanaalmatrix $\mathbf{C}$ is daarenboven *circulant* en kan gediagonaliseerd worden d.m.v. een DFT en IDFT, zie (2.16). De diagonaalelementen omvatten de frequentieresponsie van het kanaal, waardoor we een transmissieschema krijgen dat ontkoppeld of wiskundig orthogonaal is in het frequentiedomein, zie (2.17). Anders gezegd: het tijdsdispersief kanaal is geconverteerd in N parallelle, smalbandige subkanalen of tonen, vandaar de naam *discrete multitoon modulatie*.

2. als $L > \nu$ zijn symbolen die verstuurd zijn op verschillende tijdstippen niet meer onafhankelijk van elkaar en ontstaat er ongewenste ISI en ICI, zie (2.19).

De zender- en ontvangerstructuur in **Fig. 2.3** en in **Fig. 2.5** weerspiegelen de zojuist besproken DMT-principes. Aan de zendzijde wordt het DMT-communicatieschema gerealiseerd d.m.v. een IDFT, die efficiënt uitgevoerd kan worden m.b.v. het FFT-algoritme. Elke IDFT-ingang of toon wordt QAM-gemoduleerd, waarbij de QAM-constellatiegrootte afhangt van de SNR aan de ontvanger op die frequentie. De QAM-symbolen X_i^k worden vervolgens gespiegeld, volgens (2.21), om na de IDFT een reële uitgang te bekomen. Na toevoeging van de CP en een parallel-naar-serieel conversie worden de monsters op de lijn gezet. Aan de ontvanger gebeuren de inverse operaties. De amplitude- en fasedistortie van de ontvangen QAM-symbolen t.g.v. het kanaal worden opgeheven d.m.v. een *1-tap frequentiedomein egalisator per toon* (E: frequency domain equalizer of FEQ). Na de FEQ's volgt een beslissing om de verstuurde symbolen te reconstrueren. Wanneer de kanaalorde groter is dan de lengte van de CP wordt er eveneens een *T-taps egalisator* toegevoegd in het tijdsdomein (E: time domain equalizer of TEQ) om het kanaal te verkorten tot de CP-lengte.

Door het brede frequentiespectrum dat voorzien is voor DSL-systemen, zullen bepaalde frequenties die gebruikt worden voor smalbandige radio-communicatie (RFI) overlappen met de DSL-frequentieband. Het bloktransmissieschema van DSL-systemen heeft als gevolg dat het spectrum van de ongewenste RFI geconvolueerd wordt met een sinc-functie. Wanneer de RFI-frequentie niet exact past op het DMT-grid zullen de meeste tonen sterk aangetast worden. Om de frequentieselectiviteit van de DFT-operatie te verhogen kan er een vensterfunctie (E: windowing) toegepast worden op de symbolen aan de ontvanger. Hierbij worden de laatste μ monsters van de CP en de laatste μ monsters van het eigenlijke symbool vermenigvuldigd met respectievelijk $\mathbf{d}_h$ en $\mathbf{d}_t$. De eerste μ monsters worden teruggevouwen en opgeteld bij de laatste μ monsters om de DMT-orthogonaliteit te bewaren. **Fig. 2.6** illustreert hoe windowing aan de ontvanger de spectrale lek reduceert.

Datamodel

In Sectie 2.3 wordt het datamodel en de bijhorende notatie uitgelegd. Subsectie 2.3.1 behandelt het basis datamodel waarbij de IDFT aan de zendzijde

en de DFT aan de ontvangzijde even groot zijn. Het datamodel beschouwt drie opeenvolgende symbolen om de ISI en ICI correct te modelleren. Subsectie 2.3.2 beschrijft hoe echo kan toegevoegd worden aan het basis datamodel. Afhankelijk van de grootte van de DFT en de IDFT verkrijgen we een model met interpolatie of decimatie van het echo-signaal. Tenslotte wordt het basis datamodel uitgebreid in Subsectie 2.3.3 om windowing wiskundig te kunnen beschrijven.

Hoofdstuk 3: Egalisatie: een veralgemeende benadering

Zoals uitgelegd in Hoofdstuk 2 bestaat de egalisatie in DMT-gebaseerde modems uit een combinatie van een TEQ en FEQ's. TEQ-ontwerp werd reeds uitvoerig bestudeerd in de literatuur, waarbij het ultieme doel bestaat uit de maximalisatie van de haalbare bitsnelheid. De bijdragen van dit hoofdstuk zijn:

- het opstellen van een gemeenschappelijk wiskundig kader, waarin de verschillende bestaande egalisator-ontwerpmethodes kunnen uitgedrukt worden. Deze veralgemeende aanpak zal onderlinge verschillen tussen de methodes verduidelijken.
- er zal aangetoond worden dat MMSE TEQ-ontwerp met drie verschillende eenheidsenergie-beperkingen resulteert in: a) TEQ-coëfficiënten met eenzelfde performantie in termen van bitsnelheid, b) een éénvoudig, iteratief initialisatieschema op basis van de power-methode of inverse iteraties en c) een geometrische interpretatie.

Gemeenschappelijke formulering

Ondanks de verscheidenheid aan egalisator-ontwerpmethodes kunnen bijna alle algoritmes herleid worden tot een *maximalisatie van een product van M veralgemeende Rayleigh quotiënten*, zie (3.1). Deze kostfunctie is niet-lineair met eventueel lokale optima en vereist niet-lineaire optimalisatie-technieken. Met $M = 1$ wordt de kostfunctie echter gereduceerd tot een veralgemeend eigenwaardenprobleem, zie (3.2), waarvoor er een unieke oplossing bestaat. Een tweede speciaal geval bekomt men met $M = 1$ en wanneer er een aparte egalisator ontworpen wordt voor elke gebruikte toon i, zie (3.7). Het resultaat is een bank van egalisatoren die de oplossing zijn van een veralgemeend eigenwaardeprobleem per toon. In Subsecties 3.2, 3.3 en 3.4 wordt aangetoond hoe verschillende ontwerpmethodes geformuleerd kunnen worden als (3.2), (3.1) of (3.7).

Eén Rayleigh quotiënt voor een enkelvoudige egalisator

Wanneer de kanaalorde groter is dan de lengte van de CP wordt een T-taps TEQ toegevoegd aan de ontvanger om het transmissiekanaal te verkorten. Hoe-

wel kanaalverkorting niet noodzakelijk leidt tot de maximalisatie van de bitsnelheid, zijn toch vele TEQ-ontwerpmethodes gebaseerd op dit idee. Subsecties 3.2.1-3.2.6 tonen aan hoe de MMSE, MSSNR, MERRY, Min-ISI, MDS en CNA TEQ-ontwerpen berekend kunnen worden op basis van één veralgemeend Rayleigh quotiënt met de bijhorende **A** en **B** matrices, cf. (3.2).

Van alle methodes gaat de meeste aandacht uit naar MMSE TEQ-ontwerp, zie Subsectie 3.2.1. Bij deze methode moet de convolutie van de TEQ **w** met het kanaal **h** zo nauwkeurig mogelijk een doelimpulsresponsie **b** (E: target impulse response of TIR) met $\nu + 1$ taps benaderen, zie **Fig. 3.1**. Om de nuloplossing te vermijden kunnen verschillende beperkingen op **w** en **b** opgelegd worden. Afhankelijk van de beperking krijgt men een ander veralgemeend eigenwaardeprobleem. We tonen aan dat MMSE TEQ-ontwerp met *drie verschillende eenheidsenergie-beperkingen* aanleiding geeft tot TEQ-oplossingen die op een schaalfactor na identiek zijn. Aangezien deze schaling opgevangen wordt door de FEQ's, zullen deze oplossingen bijgevolg resulteren in *identieke bitsnelheden*. De TEQ's kunnen berekend worden als de meest dominante eigenvector van de matrix **Q** in (3.30) via een iteratieve procedure gebaseerd op de *power-methode* of *inverse iteraties*, zie (3.32) en (3.33). Met behulp van een geometrische interpretatie tonen we aan dat MMSE TEQ-ontwerp met eenheidsenergie-beperkingen neerkomt op het bepalen van de *kleinste principale hoek (en de bijhorende principale vectoren) tussen de deelruimtes omspannen door de verstuurde en de ontvangen signaalvectoren*. Bovendien blijkt dat de eigenwaarden van **Q** steeds kleiner of gelijk zijn aan één, wat gebruikt kan worden om de convergentie van de 'inverse iteratie'-methode te versnellen. Ondanks zijn eenvoud is MMSE TEQ-ontwerp niet gelijkwaardig met de maximalisatie van de bitsnelheid. Bovendien is de performantie vaak sterk afhankelijk van de keuze van de synchronisatievertraging.

Meerdere Rayleigh quotiënten voor een enkelvoudige egalisator

De TEQ-methodes die gebaseerd zijn op de optimalisatie van één veralgemeend Rayleigh quotiënt zijn in het algemeen niet equivalent met de maximalisatie van de bitsnelheid. TEQ-methodes die bitsnelheid-optimalisatie nastreven, zoals MGSNR, MBR, NO-TEQ en BM-TEQ, hebben meestal een product van meerdere veralgemeende Rayleigh quotiënten als kostfunctie, zie Subsecties 3.3.1-3.3.4. Deze kostfuncties geven elk aanleiding tot een niet-lineaire optimalisatie met eventueel lokale optima. Ondanks de verschillende ontwerpmethodes bestaat er slechts één TEQ-ontwerp dat effectief de bitsnelheid maximiseert, nl. de BM-TEQ. De overige methodes gaan uit vrij veel veronderstellingen, met suboptimale performantie tot gevolg.

Meerdere Rayleigh quotiënten voor meerdere egalisatoren

In Secties 3.2 en 3.3 werden TEQ-ontwerpmethodes behandeld, waarbij een enkelvoudige TEQ alle tonen gezamenlijk egaliseert. Om een niet-lineaire op-

timalisatie te vermijden en bitsnelheid-optimalisatie mogelijk te maken, kan men het egalisator-ontwerp ontkoppelen per toon. Het gevolg is een bank van egalisatoren, waarbij elke egalisator geoptimaliseerd wordt voor elke toon afzonderlijk. Deze egalisatie-vorm komt neer op de maximalisatie van één veralgemeend Rayleigh quotiënt per gebruikte toon, zoals b.v. voor de per-toon-egalisatoren (E: per tone equalization of PTEQ) in Subsectie 3.4.1. Hierbij wordt TEQ-FEQ egalisatie-structuur herleid tot één T-taps PTEQ per toon. De resulterende PTEQ-structuur is weergegeven in **Fig. 3.4**, waarbij elke toon een lineaire combinatie maakt van de DFT-uitgang voor die toon en $T-1$ reële verschiltermen. Aangezien de PTEQ een veralgemening is van de TEQ, zal de PTEQ-performantie steeds een bovengrens vormen voor de performantie van de TEQ.

Uitzonderingen op de gemeenschappelijke formulering

Zoals bij elke veralgemeende benadering zijn er ook hier een aantal uitzonderingen op de gemeenschappelijke formulering van (3.1). Deze zijn beschreven in Sectie 3.5 en omvatten o.a. een verbetering van de MGSNR TEQ-ontwerpmethode en kanaalverkorting d.m.v. SAM.

Simulatieresultaten en conclusies

Fig. 3.5 toont de acht gestandaardiseerde CSA (E: carrier serving area) testkanalen, waarop de TEQ-methodes getest zullen worden. **Fig. 3.6** illustreert de grillige performantie van MMSE TEQ's met verschillende beperkingen t.o.v. de synchronisatievertraging voor downstreamtransmissie. Vooral de eenheidsnorm-beperking op $\mathbf{w}$ leidt tot een onaanvaardbaar lage performantie. **Fig. 3.7** vergelijkt de onderlinge performantie tussen verschillende TEQ-ontwerpmethodes. Zoals verwacht leveren de BM-TEQ en de PTEQ de hoogste bitsnelheid die haalbaar zijn met respectievelijk een enkelvoudige TEQ en een per-toon-filterbank. Gelijkaardige conclusies zijn geldig wanneer de performantie bekeken wordt voor de verschillende testkanalen, zie **Fig. 3.11** en **Fig. 3.12**. De iteratieve initialisatie van de MMSE TEQ met eenheidsenergie-beperking(en) wordt geïllustreerd in **Fig. 3.13**. Dankzij de kennis van de bovengrens voor de grootste eigenwaarde van $\mathbf{Q}$ leiden inverse iteraties tot een aanzienlijk snellere convergentie dan de power-methode.

Hoofdstuk 4: Gemeenschappelijk ontwerp van vensterfuncties en egalisatoren voor maximalisatie van de bitsnelheid

De ontvanger in DMT-gebaseerde DSL-systemen ervaart typisch twee soorten ruis: ISI/ICI veroorzaakt door het kanaal zelf en externe ruis zoals b.v. RFI. Om de totale ruis te reduceren worden verschillende werkwijzen gevolgd in de literatuur:

1. egalisator-ontwerp: de toevoeging van een T-taps TEQ of PTEQ aan de

ontvanger reduceert ISI en ICI.

2. vensterfunctie-ontwerp: wanneer de kanaalorde beperkt blijft tot $\nu - \mu$ taps blijven er nog μ monsters van de CP van de ontvangen symbolen over om een vensterfunctie (E: windowing) toe te passen. Vensterfuncties laten toe om de DFT-zijlobben te reduceren, waardoor de gevoeligheid aan RFI afneemt.
3. PTEQ-ontwerp met een vaste vensterfunctie: met de combinatie van een egalisator per toon en een vensterfunctie tracht men de bitsnelheid te maximiseren, ten koste van een aanzienlijke geheugenvereiste.

De bijdragen van dit hoofdstuk zijn:

- het opstellen van een algemeen wiskundig kader voor het gemeenschappelijk ontwerp van een *optimaal venster en een optimale TEQ (BM-WinTEQ) met als doel de maximalisatie van de bitsnelheid*,
- het ontwerp van meerdere BM-WinTEQ's voor toongroepen,
- het aantonen hoe bestaande TEQ- en vensterfunctie-ontwerpen als speciale gevallen van het resulterend wiskundig kader naar boven komen.

Notatie en uitdrukking voor de bitsnelheid

In Sectie 4.1 wordt het data model en de notatie uitgelegd om tot de BM-WinTEQ uit **Fig. 4.1** te komen. Alvorens de BM-WinTEQ af te leiden wordt er vertrokken van Shannons uitdrukking voor de bitsnelheid, zie (4.4), waarbij de SNR voor toon i gegeven wordt door (4.8). De SNR wordt opgesteld aan de FEQ-uitgang zodat de signaal- en ruiscomponent gemakkelijk gescheiden kunnen worden. Om tot deze eenvoudige SNR-uitdrukking te komen werden 'zero forcing' (ZF) FEQ's verondersteld. In de praktijk kan elke FEQ-definitie toegepast worden, maar enkel ZF FEQ's geven geen aanleiding tot een afwijking (E: bias) van de signaalcomponent α_i t.o.v. het verstuurde symbool X_i^k. Indien $\alpha_i \neq 1$ moet het beslissingsblok (E: slicer) aan de FEQ-uitgang geschaald worden om tot beslissingen te komen die de vooropgestelde bitfoutkans niet verhogen. Deze schaling is vaak ongewenst en maakt de SNR-uitdrukking complexer, cf. (4.14).

Egalisator- en vensterfunctie-ontwerp voor bitsnelheid-maximalisatie

In Sectie 4.2 wordt de gemeenschappelijke optimalisatie van een enkelvoudige TEQ en een vensterfunctie uitgelegd. Simulaties tonen aan dat de TEQ, die traditioneel gebruikt werd voor de onderdrukking van ISI en ICI, ook geschikt is als notch-filter tegen RFI. Vensterfuncties, daarentegen, kunnen bijdragen tot de egalisatie door de spectrale karakteristieken van de demodulerende DFT te verbeteren. Sectie 4.2 beschrijft in eerste instantie hoe de uitdrukking voor de bitsnelheid kan geschreven worden in termen van de TEQ en venstercoëfficiënten enerzijds en de signaalstatistieken anderzijds. De resulterende kostfunctie, cf. (4.30), is een niet-lineaire functie zonder beperkingen die m.b.v. MATLAB® kan opgelost worden.

Wanneer het aantal gebruikte tonen opgedeeld wordt in kleinere toongroepen en wanneer een egalisator en een vensterfunctie berekend worden voor elke toongroep, dan spreken we van *per groep windowing en tijdsdomein egalisatie voor de maximalisatie van de bitsnelheid (BM-PGWinTEQ)*. De bijhorende kostfunctie wordt gegeven door (4.33). In Subsectie 4.2.3 tonen we aan dat BM-PGWinTEQ voor toongroepen van één toon equivalent is met een MMSE PTEQ van $\mu + T$ taps, waarbij de afwijking van de signaalcomponent (E: bias) verwijderd wordt door het toevoegen van ZF FEQ's. M.a.w. een vensterfunctie per toon kan effectief opgenomen worden in de PTEQ-operatie door het aantal PTEQ-taps te verhogen van T naar $T + \mu$, cf. (4.40).

Speciale gevallen

Het algemeen wiskundig kader van Sectie 4.2 laat toe om een aantal speciale gevallen af te leiden. Wanneer enkel een TEQ zonder vensterfunctie vereist is, verkrijgt men de *BM-TEQ* kostfunctie in (4.43). Verder resulteert het optimaliseren van de BM-TEQ-kostfunctie per toon in een *T-taps MMSE PTEQ met beperking*. Wanneer egalisatie niet in rekening gebracht wordt, verkrijgt men de kostfunctie voor een *vensterfunctie die de bitsnelheid maximiseert (BM-Win)*, cf. (4.58). Een vensterfunctie per toon resulteert opnieuw in een ($\mu + 1$-taps) *MMSE PTEQ met beperking*, cf. (4.64). Andere varianten zijn natuurlijk ook mogelijk, zoals b.v. een *BM-TEQ gevolgd door een vast venster (BM-FWinTEQ)*.

Complexiteit en geheugenvereiste

De rekenkundige complexiteit tijdens datatransmissie en de geheugenvereiste voor de verschillende ontwerpmethodes is weergegeven in respectievelijk **Tabel 4.1** en **Tabel 4.2**. Hieruit kan men de volgende besluiten trekken:

- De extra complexiteit voor het toevoegen van een vensterfunctie bij een enkelvoudige TEQ is verwaarloosbaar.
- De TEQ-complexiteit tijdens datatransmissie is hoger dan die van de PTEQ, maar een PTEQ vereist wel meer geheugen.
- Toongroepering zorgt voor een verhoogde performantie t.o.v. een enkelvoudige TEQ in combinatie met een enkelvoudig venster, maar de rekenkundige complexiteit en de geheugenvereiste nemen eveneens toe.
- Een TEQ per toongroep in combinatie met een enkelvoudig venster leidt tot dezelfde complexiteit als een TEQ per toongroep in combinatie met een venster per toongroep.

Simulatieresultaten en conclusies

Sectie 4.5 bevat de simulatieresultaten voor dit hoofdstuk. Ondanks het gebruik van niet-lineaire kostfuncties werden er geen problemen met lokale optima vastgesteld, i.e. alle lokale optima resulteerden in een performantie die consistent

en vermoedelijk optimaal is. We hebben echter geen sluitend bewijs om deze observatie te kunnen veralgemenen. **Fig. 4.2** vergelijkt de SNR van het BM-Win-ontwerp met een bestaand venster-ontwerp voor een scenario met zes RF-stoorders. Het is duidelijk dat het toepassen van een vensterfunctie de spectrale lek reduceert en dus de bitsnelheid aanzienlijk verbetert. **Fig. 4.4** veralgemeent de bovenstaande resultaten voor verschillende testkanalen. De gemiddelde bitsnelheidswinst is ongeveer 180 kbps in vergelijking met een niet-geoptimaliseerd vast venster. **Fig. 4.5** illustreert de haalbare bitsnelheid met een BM-WinTEQ-ontwerp t.o.v. het aantal TEQ- en vensterfunctie-coëfficiënten. Met deze figuren tonen we aan dat, voor eenzelfde performantie, een aantal egalisator-coëfficiënten kunnen uitgewisseld worden voor vensterfunctie-coëfficiënten, wat leidt tot aanzienlijke complexiteitsbesparingen. **Fig. 4.8** en **Fig. 4.9** tonen aan dat wanneer aan bestaande TEQ-ontwerpen een vast venster toegevoegd wordt, men een verbeterde performantie verkrijgt. M.a.w. korte vensterfuncties helpen de egalisator bij het oplossen van het egalisatie-probleem. **Fig. 4.11** en **Fig. 4.13** illustreren dat de egalisator op zijn beurt als notch-filter kan helpen bij het oplossen van het RFI-probleem.

Hoofdstuk 5: Gemengde tijds-/frequentiedomein echo-onderdrukking

Echo-onderdrukking (E: echo canceling of EC) is noodzakelijk wanneer up- en downstream (gedeeltelijk) overlappende frequentiebanden toegewezen krijgen om zo hogere bitsnelheden te halen. EC laat toe om het bereik, de bitsnelheid en/of de ruismarge van bestaande ADSL-systemen te verhogen. Het principe van EC werkt als volgt: de echo wordt nagebootst en verwijderd van het ontvangen signaal in het tijdsdomein of gedeeltelijke in het tijds- en het frequentiedomein. Het echo-pad, vereist voor de echo-nabootsing, wordt geschat a.d.h.v. een adaptieffilter-algoritme. De bijdragen van dit hoofdstuk zijn:

- *Dubbelspraak-onderdrukking (E: double talk cancellation of DTC):* tijdens duplex-transmissie zal het signaal afkomstig van de andere zijde van de lijn het adaptieffilter-algoritme verstoren, met trage convergentie en tracking tot gevolg. Bestaande EC-algoritmes zullen daarom uitgebreid worden met DTC om het 'verre-eind'-signaal te onderdrukken.
- *Verbeterde tijds- en frequentiedomein EC (E: improved time-frequency domain echo canceling of ITF-EC):* een EC-schema zal ontworpen worden, waarbij de rekenkundige complexiteit geminimaliseerd kan worden onafhankelijk van de aligning tussen de verzonden echo-symbolen en de ontvangen symbolen afkomstig van de andere zijde.
- *EC gebaseerd op een circulante ontbinding van de verzonden echo-symbolen (E: circulant decomposition canceler of CDC):* dit EC-schema vereist minder vermogen om het echo-pad te schatten in vergelijking met bestaande systemen.

Tijdsdomein EC (TD-EC)

Traditioneel wordt EC volledig in het tijdsdomein uitgevoerd, i.e. de echo wordt in het tijdsdomein zowel gemodelleerd als verwijderd uit het ontvangen signaal. Sectie 5.1 geeft een overzicht van tijdsdomein EC-schema's voor DMT-gebaseerde systemen. Initieel wordt een symmetrische modemarchitectuur verondersteld (met gelijke IDFT- en DFT-grootte), cf. Subsectie 5.1.1 en **Fig. 5.2** De wiskundige beschrijving voor symmetrische TD-EC wordt gegeven door (5.4) en het echo-pad wordt geschat d.m.v. het blok-LMS-algoritme (E: least mean square) in (5.6). Uitbreidingen naar asymmetrische modems (met een factor κ tussen IDFT- en DFT-grootte) worden afgeleid in Subsectie 5.1.2. Wanneer het echo-pad bandbegrensd is tot $\kappa N/2\gamma$ tonen verkrijgt men een complexiteitsreductie met (ruwweg) een factor $\kappa\gamma$ t.o.v. symmetrische modems.

Circulaire echo-synthese (CES)

Zoals beschreven in Sectie 5.2 kan EC in DMT-gebaseerde systemen efficiënter gebeuren d.m.v. tijds-/frequentiedomein EC. Subsectie 5.2.1 beschrijft deze vorm van EC voor een symmetrische modem. De echo wordt gedeeltelijk in het tijds- en gedeeltelijk in het frequentiedomein gemodelleerd en verwijderd, cf. (5.17) en (5.20). Het tijdsdomein gedeelte maakt hiertoe de nodige correcties op de ontvangen echo zodat de residuele echo periodisch lijkt (E: circular echo synthesis of CES). De schatting van het echo-pad gebeurt volledig in het frequentiedomein m.b.v. een efficiënt 1-tap LMS-algoritme per toon. De tijdsdomein filtercoëfficiënten worden dan eenvoudig bekomen d.m.v. een IDFT die infrequent kan uitgevoerd worden, zie (5.21). De complexiteit van tijds-/frequentiedomein EC wordt hoofdzakelijk gedomineerd door het tijdsdomein gedeelte (CES). In vergelijking met TD-EC wint men een factor twee in complexiteit. Uitbreidingen naar asymmetrische modems worden afgeleid in Subsectie 5.2.2 en geven (net als bij TD-EC) aanleiding tot extra complexiteitsreducties.

Dubbelspraakonderdrukking

Door temperatuursvariaties van de lijn en van de front-end filters zal het echo-pad traag variëren over de tijd. Om deze variaties te kunnen volgen worden adaptieve algoritmes, zoals LMS, gebruikt om het echo-pad te schatten. Wanneer tijdens het adaptatieproces van de EC signalen ontvangen worden afkomstig van de andere zijde van de lijn (situatie van dubbelspraak), zal het echo-pad foutief geschat worden. Om dit te vermijden beschrijft Sectie 5.3 hoe DTC toegevoegd kan worden aan bestaande EC-schema's. Het DTC-principe is vrij eenvoudig: het oorspronkelijke, frequentiedomein foutsignaal voor het adaptatie-proces wordt vervangen door een geschaalde versie (door inverse FEQ's) van het verschilsignaal over de 'slicer', zie **Fig. 5.7**. De extra DTC-complexiteit is verwaarloosbaar t.o.v. de complexiteit van de EC zelf.

Verbeterde tijds- en frequentiedomein EC (ITF-EC)

Door het toepassen van een alternatieve alignering Δ tussen verzonden en ontvangen echo-symbolen kan de CES-complexiteit extra gereduceerd worden met een factor twee. O.w.v. de propagatievertraging van het kanaal kan deze alignering slechts aan één zijde van de lijn gekozen worden. De alignering aan de andere zijde ligt dan automatisch vast en zal in het algemeen asynchroon zijn. Sectie 5.4 beschrijft een alternatieve manier om de tweevoudige complexiteitswinst te verwezenlijken, onafhankelijk van de gekozen alignering. Op die manier kan de complexiteit van de EC aan *beide zijden* van de telefoonlijn geminimaliseerd worden. Subsectie 5.4.2 beschrijft de EC-structuur voor symmetrische modem, terwijl asymmetrische modem-structuren in Subsectie 5.4.3 aan bod komen.

EC gebaseerd op een circulante ontbinding van de verzonden echo-symbolen (CDC)

Het echo-filter van CES-gebaseerde EC-schema's wordt aangepast in het frequentiedomein d.m.v. een 1-tap LMS-procedure per toon. Hierbij worden de verzonden frequentiedomein echo-symbolen U^k gebruikt als 'aanpassingsrichting'. Aangezien de elementen van U^k toegewezen zijn aan de up- of downstreamrichting zullen bepaalde modes in U^k niet geëxciteerd worden. De bijhorende frequentiedomein echo-filtercoëfficiënten zullen bijgevolg niet aangepast worden, wat uiteindelijk resulteert in een foutieve schatting van het echo-pad. Dit effect kan vermeden worden door extra vermogen te versturen op ongebruikte tonen, wat echter ongewenst is. Sectie 5.5 beschrijft een alternatief tijds- en frequentiedomein EC-schema voor symmetrische en asymmetrische modems, waarbij geen extra vermogen moet verstuurd worden. Het resulterende schema krijgt de naam CDC aangezien de echo-filtering gebaseerd is op een opsplitsing van een Toeplitz-matrix in een circulante en een skew-circulante matrix. Deze ontbinding kan efficiënt uitgevoerd worden m.b.v. DFTs en IDFTs, resulterend in (5.67). De echo-filter-aanpassing gebeurt eveneens d.m.v. een 1-tap LMS per toon en een aantal infrequente transformaties, cf. (5.73) en (5.74). In Subsectie 5.5.4 wordt aangetoond hoe het nieuwe schema eenvoudig gecombineerd kan worden met DTC en PTEQ. Tenslotte laat de complexiteitsstudie in 5.5.5 zien dat de rekenkundige complexiteit van CDC vergelijkbaar is met die van CES-gebaseerde EC-systemen.

Simulatieresultaten en conclusies

Sectie 5.6 bevat de simulatieresultaten voor dit hoofdstuk. **Fig. 5.19** illustreert hoe de LMS-excessfout gereduceerd wordt door gebruik te maken van DTC. **Fig. 5.22** en **Fig. 5.29** tonen aan dat de convergentie van ITF-EC en CDC vergelijkbaar is met CES-gebaseerde EC-schema's.

Hoofdstuk 6: Gesplitste SR-RLS voor de initialisatie van de per toon egalisator en de per toon echo-onderdrukker

Naast egalisatie per toon (PTEQ) is het ook mogelijk om EC uit te voeren per toon (PTEC). Waar het vorige hoofdstuk egalisatie en EC behandelde als twee aparte problemen, laat de combinatie PTEQ/PTEC toe om de SNR per toon te optimaliseren voor een gegeven aantal egalisator- en EC-taps. De optimale PTEQ's en PTEC's zijn de oplossing van een MMSE-probleem per toon. Directe MMSE-initialisatie van deze structuur resulteert in een te hoge complexiteit. Daarom zal de aandacht in dit hoofdstuk gericht zijn op:

- het ontwikkelen van een aangepast initialisatieschema voor de 'per toon'-algoritmes,
- de efficiënte initialisatie van de PTEQ's (zonder PTEC's) op basis van trainingsymbolen,
- de gecombineerde initialisatie van de PTEQ's en de PTEC's, eveneens op basis van trainingsymbolen.

Standaard adaptieve filteralgoritmes

Sectie 6.1 geeft een overzicht van verschillende, bestaande adaptieve filteralgoritmes om een MMSE-probleem (benaderend) iteratief op te lossen. Hierbij wordt uitgegaan van de probleemstelling in (6.1) waarbij de coëfficiënten $\mathbf{w}$ een lineaire combinatie maken van de ingangsvector $\mathbf{z}^k$, zonder de aanwezigheid van extra signaalstructuur in $\mathbf{z}^k$. Subsecties 6.1.2 en 6.1.3 behandelen achtereenvolgens het genormaliseerd LMS-algoritme (NLMS) en het SR-RLS-algoritme (E: square-root recursive least square).

Afhankelijk van de eigenwaardespreiding van de autocorrelatiematrix van het ingangssignaal kan NLMS aanleiding geven tot trage convergentie. SR-RLS convergeert over het algemeen veel sneller dan NLMS ten koste van een aanzienlijke toename van de rekenkundige complexiteit. I.p.v. de ingangsvector te gebruiken om de filtercoëfficiënten aan te passen (cf. NLMS), wordt deze vector eerst getransformeerd met de inverse van de autocorrelatiematrix. De resulterende Kalmanvector wordt dan gebruikt in de adaptatie, waardoor de eigenwaardespreiding volledig verdwijnt en waardoor de convergentie optimaal is.

Gesplitste SR-RLS met gereduceerde complexiteit

Om de rekenkundige complexiteit van een volledig SR-RLS te verlichten zonder al te veel in te boeten aan convergentie kan een gesplitste versie van SR-RLS toegepast worden, zie Sectie 6.2. Na een opdeling van de ingangsvector in twee of meer groepen wordt er per groep een SR-RLS-probleem uitgewerkt. Deze methode breidt het bestaande gesplitste QR-RLS algoritme uit met inverse aanpassing. Het resulterende algoritme wordt beschreven in **Tabel 6.2**. Voor

twee ingangsgroepen kan men bewijzen dat het algoritme convergeert en dat de nieuwe adaptatierichting erin slaagt om de eigenwaardespreiding te reduceren, wat resulteert in een convergentiesnelheid tussen SR-RLS en NLMS. Het voorgestelde algoritme kan de complexiteit en de geheugenvereiste aanzienlijk reduceren, zoals b.v. bij de PTEQ- en de PTEQ/PTEC-initialisatie.

RLS-LMS voor PTEQ-initialisatie

In Sectie 6.3 wordt het gesplitste SR-RLS afgestemd op de initialisatie van de PTEQ-coëfficiënten. Een T-taps PTEQ-structuur maakt per toon een lineaire combinatie van één toonafhankelijke, complexe ingang met $T-1$ toononafhankelijke en reële verschiltermen. De eigenwaardespreiding van de autocorrelatiematrix van het PTEQ-ingangssignaal is enorm groot, waardoor NLMS-convergentie te traag is. Wanneer SR-RLS wordt toegepast, geven de verschiltermen aanleiding tot een toononafhankelijke, reële $(T-1)\times(T-1)$ benedendriehoeksmatrix en een $1\times T$ complexe, toonafhankelijke rij, zie **Fig. 6.3**. De rekenkundige complexiteit en de geheugenvereiste zijn hiermee evenredig.

Om de hoge rekenkundige kost van het toonafhankelijke gedeelte verder te verlagen kan het gesplitste SR-RLS-algoritme toegepast worden, waarbij de ingangsvector opgedeeld wordt in de toononafhankelijke en de toonafhankelijke ingangen. Het toepassen van SR-RLS op de toonafhankelijke ingang (i.e. de DFT-uitgang) komt neer op een LMS-stap op die ingang. M.a.w. het gesplitste SR-RLS-algoritme reduceert zich tot een combinatie van SR-RLS en LMS, vandaar de naam RLS-LMS. Uit **Fig. 6.4** en **Fig. 6.5** blijkt duidelijk de gereduceerde complexiteit en geheugenvereiste per toon t.o.v. een volledige SR-RLS.

Gesplitste SR-RLS voor PTEQ/PTEC-initialisatie

In Sectie 6.3 wordt het gesplitste SR-RLS toegepast op de gecombineerde PTEQ/PTEC-initialisatie. Deze structuur met een T-taps PTEQ en een T_E-taps PTEC bevat (voor symmetrische modems) twee toonafhankelijke, complexe ingangen en $T+T_E-2$ toononafhankelijke, reële ingangen, i.e. verschiltermen. Ook hier geeft een volledige SR-RLS aanleiding tot een hoge complexiteit en een aanzienlijke geheugenvereiste. Uit **Fig. 6.6** blijkt de complexiteitswinst en het gereduceerd geheugengebruik van het gesplitste SR-RLS-algoritme t.o.v. een volledige SR-RLS.

Simulatieresultaten en conclusies

Sectie 6.5 bevat de simulatieresultaten voor dit hoofdstuk. **Fig. 6.7** illustreert de typische convergentiecurves van RLS-LMS t.o.v. NLMS en SR-RLS voor de initialisatie van de PTEQ-coëfficiënten. Uit 6.14 blijkt dat RLS-LMS ongeveer 4.4 keer trager convergeert dan SR-RLS, met slechts een fractie van de complexiteit. **Fig. 6.12** en **Fig. 6.13** tonen de convergentiecurves voor de gemeenschappelijke initialisatie van de PTEQ's en PTEC's. Ook hier is de

convergentie voldoende snel in vergelijking met het aantal beschikbare trainingsymbolen in ADSL.

Hoofdstuk 7: Besluiten en verder onderzoek

Besluiten

In dit proefschrift werden geavanceerde, digitale signaalverwerkingsalgoritmen bestudeerd om de bitsnelheid, reikwijdte en/of ruismarge van bestaande DSL-systemen te verbeteren. Meer bepaald werd er aandacht besteed aan egalisatie en echo-onderdrukkingsschema's.

In DSL de egalisatie wordt traditioneel uitgevoerd d.m.v. een TEQ/FEQ-combinatie. In **Hoofdstuk 3** werd er een algemeen wiskundig kader, waarin (bijna) alle bestaande egalisatie-ontwerpmethodes geformuleerd kunnen worden. De basis van dit wiskundig kader is de maximalisatie van een product van veralgemeende Rayleigh quotiënten. Speciale gevallen van dit kader leidde tot verschillende egalisatie-mogelijkheden. De meeste TEQ-algoritmes kunnen herleid worden tot de maximalisatie van één enkel veralgemeend Rayleigh quotiënt. Deze methodes geven elk aanleiding tot een eenvoudig, convex optimalisatieprobleem, maar zijn niet equivalent met de maximalisatie van de bitsnelheid. Voor bitsnelheid-maximalisatie met een enkelvoudige TEQ bestaat de kostfunctie uit een *product* van veralgemeende Rayleigh quotiënten. Simulaties toonden aan dat van alle TEQ-methodes enkel de BM-TEQ effectief de bitsnelheid maximiseert. Wanneer een hogere geheugenkost aanvaardbaar is, kan deze laatste eigenschap ook bereikt worden door de TEQ/FEQ-structuur te vervangen door een egalisatie per toon (PTEQ), waarbij er een veralgemeend Rayleigh quotiënt geoptimaliseerd moet worden per toon.

In **Hoofdstuk 3** werd ook aangetoond dat MMSE TEQ-ontwerp met drie verschillende eenheidsenergie-beperkingen resulteert in een gelijke performantie. De uiteindelijke TEQ's kunnen eenvoudigweg berekend worden d.m.v. een iteratief algoritme gebaseerd op de power-methode of inverse iteraties. Een geometrische interpretatie toonde aan dat MMSE TEQ-ontwerp met eenheidsenergie-beperkingen nauw gerelateerd is met de principale hoeken tussen de deelruimtes omspannen door de verzonden en ontvangen signalen.

In **Hoofdstuk 4** werd de combinatie van een TEQ en een vensterfunctie aan de ontvanger bestudeerd, met als doel het maximiseren van de bitsnelheid. De resulterende ontvangerstructuur is geschikt voor een gecombineerde egalisatie en RFI-onderdrukking. We toonden aan dat het ontwerp van een enkelvoudige TEQ en een tijdsdomein venster (BM-WinTEQ) resulteert in een niet-lineaire kostfunctie, waarbij simulaties aangeven dat lokale optima quasi geen performantieverlies opleveren. Het BM-WinTEQ-ontwerp kan verder uitgebreid worden door een apart venster en een aparte egalisator te ontwerpen voor kleinere

toongroepen. Bovendien wordt er verduidelijkt hoe bestaande ontwerpmethodes, zoals b.v. de BM-TEQ en de PTEQ, als speciale gevallen opduiken in het voorgestelde ontwerpkader. Simulaties tonen aan dat een combinatie van een TEQ en een venster kan leiden tot een gereduceerde complexiteit.

Hoofdstuk 5 behandelde echo-onderdrukking voor DMT-gebaseerde DSL-modems. Na een bespreking van de in de literatuur beschreven TD-EC en CES-gebaseerde EC werd dubbelspraakonderdrukking (DTC) behandeld. Simulaties toonden aan dat DTC grotere stapgroottes mogelijk maakt in het adaptatieproces van de EC, wat toelaat om tijdsvariaties van het echopad beter op te vangen. In tweede instantie werd er een methode (ITF-EC) voorgesteld om de complexiteit van CES-gebaseerde systemen te minimaliseren, onafhankelijk van de alignering tussen verzonden en ontvangen echo-symbolen. Tenslotte werd er een alternatief tijds- en frequentiedomein EC-schema (CDC) bestudeerd, waarbij minder vermogen dient uitgestuurd te worden voor de EC-adaptatie in vergelijking met bestaande schema's.

In **Hoofdstuk 6** werd er aandacht besteed aan de initialisatie van de PTEQ en de gecombineerde PTEQ/PTEC. Aangezien een directe MMSE-initialisatie rekenkundig complex is, werd een recursieve initialisatie op basis van trainingsymbolen bestudeerd. Het voorgestelde initialisatieschema bestaat uit een gesplitst SR-RLS-algoritme, waarbij twee (of meer) SR-RLS-problemen moeten opgelost worden op twee (of meer) verschillende delen van de ingangsvectoren. De ingangen van de PTEQ en de gecombineerde PTEQ/PTEC kunnen opgesplitst worden in een toononafhankelijk en een toonafhankelijk deel. Het toononafhankelijk deel resulteert in de adaptatie van een benedendriehoeksmatrix die gemeenschappelijk is voor alle tonen. De toonafhankelijke ingangen zijn typisch kleiner in aantal en de verwerking ervan resulteert in een bijna verwaarloosbare kost. Simulaties toonden aan dat het voorgestelde algoritme de rekenkundige complexiteit reduceert t.o.v. een volledig SR-RLS-algoritme, terwijl de convergentie aanvaardbaar snel blijft.

Verder onderzoek

Uitgebreide simulaties toonden aan dat de lokale optima van de niet-lineaire BM-TEQ- en BM-WinTEQ-kostfuncties resulteren in quasi optimale performantie. Verder onderzoek is nodig om deze observatie te staven en eventueel te bewijzen, zodat de BM-TEQ en BM-WinTEQ effectief als praktische ontwerpmethodes kunnen gebruikt worden.

Naast de PTEQ/PTEC-initialisatie kan het gesplitste SR-RLS-algoritme gebruikt worden in een aantal andere ADSL-toepassingen. Deze toepassingen werden vermeld in Subsection 6.4.6, maar werden nog niet verder onderzocht.

Door de relatief lage rekenkundige complexiteit komen RLS-LMS en het gesplitste SR-RLS-algoritme in aanmerking voor implementatie in hardware. Om

die reden is een theoretisch onderzoek naar de niet-lineaire effecten t.g.v. eindige woordlengte noodzakelijk.

In dit proefschrift werden de DSL-modems beschouwd als een systeem van enkelvoudige gebruikers. Een andere mogelijkheid bestaat erin om alle DSL-modems die gegroepeerd zijn in een kabelbundel gezamenlijk te behandelen. Deze nieuwe benadering laat o.a. toe om onderlinge overspraak te reduceren en/of volledig te onderdrukken, zodat opnieuw hogere bitsnelheden over het bestaande telefoonnetwerk behaald kunnen worden.

Naast overspraak afkomstig van systemen met eenzelfde transmissieschema wordt de performantie van DSL-modems ook gelimiteerd door overspraak van 'vreemde' systemen met frequenties die overlappen met de DSL-frequentieband. Verder onderzoek is noodzakelijk om ook dit probleem efficiënt op te lossen.

Chapter 1

Introduction

WITH the invention of the Internet a new era is entered where the delivery of information in video and multimedia formats plays a crucial role. Despite many research efforts in data compression, typical Internet applications still demand high bit rates. In an attempt to meet these requests a lot of effort has been spent over many years in developing new modem technologies. Therefore, an overview of past, present and future communications will be given in Section 1.1.

One of the recent modem technologies is digital subscriber line (DSL). DSL is able to convert existing twisted-pair telephone lines into access paths for high-speed data communications. At present, the most well-known type of DSL certainly is *asymmetric digital subscriber line (ADSL)*. ADSL can transmit up to 8 Mbps to a subscriber and 640 kbps or more in both directions [47]. Such rates expand existing access capacity of traditional voice band modems by a factor of 100 or more without new cabling. Consequently, ADSL enables service providers to enter new markets such as video-on-demand, distant learning, teleworking, corporate local area networks (LAN), etc.

To deliver high bit rates towards the customer, DSL modem design depends on advanced digital signal processing. In Section 1.2 we will discuss the discrete multitone transmission format as adopted by several DSL standards. In addition, several loop and noise characteristics of the DSL environment will be highlighted. In this thesis several algorithms will be presented to mitigate some of these DSL impairments. A chapter by chapter overview and a summary of the contributions of this thesis will be given in Section 1.3. This chapter ends with some concluding remarks in Section 1.4.

1.1 Past, present and future communications

Although high speed access is nowadays almost self-evident to everybody, this has certainly not been the case in the early days of communications. In Subsection 1.1.1 a brief overview of the communications history is given, starting from the beginning of the previous century up till present. In addition, the origin of some important signal processing concepts, which will be used extensively throughout this thesis, will be clarified. Afterwards, Subsection 1.1.2 discusses different means for broadband access today and in the future. Whereas many alternatives exist to deliver data to the customer, this section will focus on *wireline* communications in particular.

1.1.1 A brief history of wireline communications

Communications before the mid-1940s: the first low-speed efforts

With the invention of electricity the door was opened for the development of a variety of applications. At the end of the nineteenth century, one of these applications focused on the development of *telegraph* services (Samuel Morse 1844) [111]. The most important innovation of the telegraph was its ability to transmit information without a physical movement of goods or people. After telegraph lines were spanned overland over much of Europe and America, engineers found ways to connect continents by means of *transoceanic cables*. By this, long distance information transportation was born, be it at speeds on the order of only a *few words per minute* [123].

One of the major difficulties encountered in submarine telegraphy was the *attenuation* and *dispersion* of signals passing through long cables. Transmission speeds were severely limited by the nonlinear phase characteristic of the telephone line. These problems inspired researchers to investigate the characteristics of such a transmission system. A conceptual revolution was presented by William Thompson in 1854, where he decoupled the signal (the transmitted pulse) from the medium (the telephone cable) [23]. His work formed the theoretical basis for subsequent work in communications and signal processing.

By the mid-1870s several electricians began to investigate harmonic telegraphy, where different tones were used to transmit many telegraph signals simultaneously. Alexander Graham Bell realized that if a telegraph line could carry several musical tones, it would also be able to convey human speech. This insight led to the revolutionary invention of the *telephone* in 1876 [127]. To counteract line losses and signal distortion, amplifiers and inductive loading were introduced in the telephone loop. At the end of the twentieth century loading coils appeared to be one of the major limiting factors to provide broadband communications over certain loops of the old telephone network.

At the beginning of the 20th century, researchers (e.g. Nyquist) started to investigate methods to overcome the nonlinear phase characteristics of the telephone line. From these studies, fundamental concepts, like *equalizing* lines with phase distortion, were introduced.

Communications mid-1940s till mid-1960s

As the second half of the 20th century progressed, people became more accustomed to having home and public telephones available for use. Military and commercial interests in data processing systems during the second World War and the post-war period led to a new impulse to use telephone lines for digital data transmission. In 1948, two amazing developments laid the foundation for subsequent developments in digital data communication: the *invention of the transistor* (Shockley, Bardeen and Brattain) [128] and the publication of *Shannon's revolutionary paper*: 'A Mathematical Theory of Communication' [109]. The former led in the early 1950s to the development of digital computers where transistors replaced vacuum tubes to produce more reliable computers. The latter resulted in a derivation of the capacity limits for transmission of information over a communication channel.

In 1949, the United States started with the development of the Semi-Automatic Ground Environment (SAGE) system, a new air defense system to protect the United States from long-range bombers and other weapons [37]. The SAGE system transmitted information from geographically dispersed radars over telephone lines and gathered it at a central location. The system used *modems* to transmit data over ordinary analog telephone lines at speeds of 1200 bits per second (bps). The use of telephone lines to communicate from computer to computer introduced the basis for today's modem technology.

Communications mid-1960s till the 1970s

By the mid-1960s, numerous modulation techniques had been proposed for obtaining higher data rates. During this period, some theoretical work appeared on the design of higher order signal constellations, like *quadrature amplitude modulation (QAM)*. At that time, these multilevel structures did not find immediate application due to extensive inter-symbol-interference (ISI). From then, it was clear that channel amplitude and delay distortion were the major impairments to be focused on. Two methods were taken into consideration to overcome these impairments. One was the use of a *multicarrier system* [148]; the other was the application of an *'automatic' equalizer* to cancel ISI [149]. In this thesis it will become clear that these techniques, which led to an increase in data rates to 9600 bps by the late 1960s, are still used in present modem technology.

During the same period, developments in fiber technology and the invention of

the laser enabled scientists to use *fiber optics* to carry a telephone conversation [23]. Researchers showed that glass fiber appeared to be a low-loss ($<$ 20 dB/km) and high bandwidth transmission medium suitable for communication at very high rates. From the mid-1970s installation of fiber cables in the field started to replace the ancient copper telephone wires.

In 1966, the Defense Advanced Research Projects Agency (ARPA or DARPA) of the United States initiated a program to connect computing sites at universities across the country. The resulting *ARPANET* served as a testbed for new networking technologies and is considered to be the precursor of the Internet [116]. The development of the ARPANET introduced a technology capable of interconnecting networks at almost indefinite expansion. As a consequence, the demand for information at high data rates increased tremendously.

Communications in the 1980s and the 1990s: towards higher speeds

At the end of the seventies and the beginning of the eighties, research was focused on improving the flexibility of communication systems, e.g. by means of the *TCP/IP protocol* (Vinton Cerf 1978). Experiments demonstrated how radio, telephone and satellite networks could interact for joint networking. In addition, the commercialization of Internet technology started.

Till the seventies, *voice band modems* were operating over the existing telephone network at data rates of 9600 bps, using a bandwidth of 2400 Hz (16-point signal constellations). An increase in bandwidth to 3600 Hz, higher constellation sizes and advances in digital signal processing and coding led to bit rates beyond 9600 bps. Paradyne was one of the first companies that built a 14.4 kbps modem, based on 64-point QAM modulation with a bit error probability of 10^{-5} [95]. A number of V.series standards (V.34, V.90, etc.) followed for modem operation over the public switched telephone network (PSTN). Around 1993, V.34 modems were able to transmit at 33 600 bps, while in 1996 V.90 modems allowed rates up to 56 kbps in the downstream direction (from the network to the customer) [119]. Modems operating at 56 kbps could only achieve their rates when a digital connection based on pulse code modulation (PCM) existed from the digital source to the network end of the subscriber's line. In addition, advances in data compression prior to the transceiver were able to increase the above mentioned data rates at the expense of a higher impact of transmission errors.

In the meantime, the first preliminary DSL (digital subscriber line) technology was conceived, namely *ISDN (integrated services digital network)*. On a single wire pair, ISDN modems applied two binary one quaternary (2B1Q) encoding to create the familiar 2B+D basic ISDN channels with an aggregate bit rate of 160 kbps using a bandwidth of 80 kHz [97]. ISDN transmission can be viewed as a form of DSL, with one important difference: ISDN integrates voice and

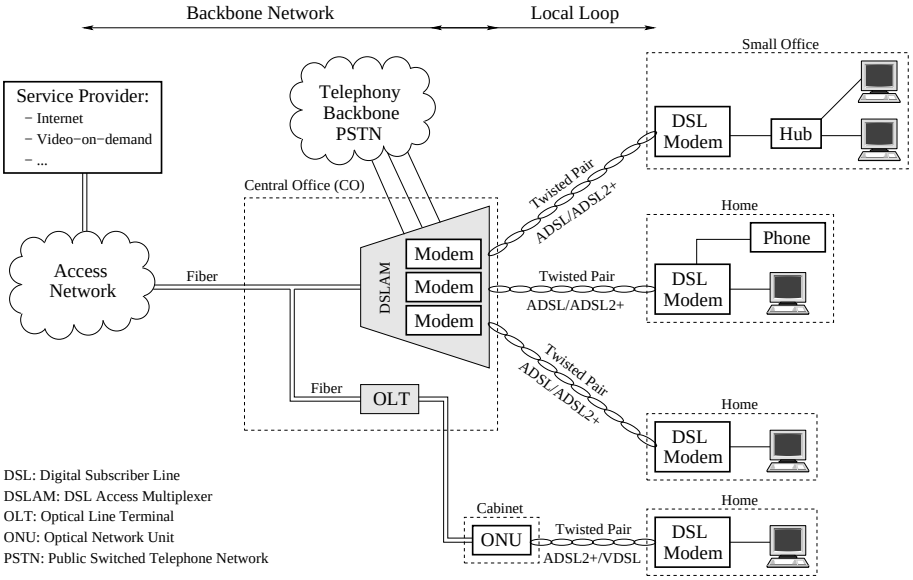

Figure 1.1: xDSL network architecture.

data communications on the phone network, while DSL transmits voice and data on separate networks. In 1983 and 1987 ISDN trials began in Japan and in the United States respectively.

True broadband access started with the deployment of *asymmetric DSL (ADSL)*. ADSL technology was developed in the BellCore laboratories in 1987 and the first field trials started in 1995. The performance of current and future DSL systems can exceed that of voice band modems by a factor of one hundred or more. Thereby, many transmission techniques employed by DSLs found their origin in voice band modem technology.

1.1.2 Present and future broadband communications

At present, many technologies (and the corresponding companies) are competing to deliver broadband services to the customer. Present and (near) future developments will leave the customer three choices: DSL, cable access or wireless access. In the following, each of these access methods will be discussed briefly.

Digital subscriber lines (DSL)

A general DSL network architecture is depicted in **Fig. 1.1**. As can be seen in the figure, DSL operates over twisted pairs and the DSL network model assumes

that fiber is progressively evolving towards the customer. At the central office (CO), a DSL access multiplexer (DSLAM) is used to multiplex the different data signals onto the fiber. Alternatively, the fiber could extend to a cabinet outside the CO, but closer to the subscriber. The ability to move the fiber into these remote locations (along with extended loop reach technologies) enables service provisioning to customers who would otherwise be beyond the reach of DSL systems. Hence, DSL technology provides a solution to bridge the 'last mile' between the network end and the customer.

DSL comes in different flavours: ADSL, ADSL2, ADSL2+, HDSL, SDSL, VDSL, etc.; hence the more general name xDSL. **Table 1.1** summarizes the differences between each of these technologies. Note that the bit rates highly depend on the length of the twisted pair: higher bit rates are only offered on relatively short loops due to signal attenuation caused by the telephone line. Since line attenuation increases with line length and frequency, short loops are able to exploit a broader frequency spectrum and hence enable higher data rates.

Currently, operators are investing in DSL technology for three reasons. First, the deployment of fiber to the home (FTTH) is too costly, since new fiber cables have to upgrade the old ancient telephone network. Secondly, the deregulation of the communication market put an end to the monopolies of the incumbent local exchange carriers (ILECs) and opened the competition with other competitive local exchange carriers (CLECs). Thirdly, operators face the competition with other means for broadband communication like e.g. cable modem services.

Cable modems

Cable modem technology uses the coax, which is used for TV distribution, for broadband services. The technology allows downstream speeds up to 40 Mbps in a 6-MHz cable channel. Upstream speeds can be configured to be 320 kbps up to 10 Mbps [36][119]. Similar to DSL, cable modem systems are based on a hybrid fiber coax (HFC) network. Whereas the cable network was originally designed for unidirectional TV transmission, cable companies have to upgrade their network to bidirectional coax for broadband data transmission. As opposed to DSL, the cable medium is *shared* among several users. Drawbacks of a shared medium are that bandwidth can not be guaranteed and that each user can listen to all the other signals on the line, in contrast to telephone wires, which are physically secure. Finally, recent studies have shown that the DSL market is rapidly growing and is beating the cable market as a means for broadband access [62].

Wireless access

Digital wireless services today are mainly narrowband. In the near future, emerging third-generation wireless networks will compete with cable and DSL

TABLE 1.1
Copper access technologies [12][56][119][120].

Type	Meaning	Bit rate	Mode and Applications
ISDN	Integrated Services Digital Network	160 kbps	2B+D service on a single wire pair up to 5.5 km: voice and data
HDSL	High-data-rate DSL	1.544 Mbps	T1 service[a] over two twisted pairs up to 3.7 km: WAN[b], LAN[c] access, server access
SDSL	Symmetric or Single line DSL	1.544 Mbps	same service as HDSL but over one twisted pair and premises access for symmetric services possible
ADSL	Asymmetric DSL	6 Mbps down[d], 640 kbps up[e]	services over one twisted pair up to 3.7 km: Internet access, video on demand, remote LAN access
ADSL2	Second generation ADSL	6 Mbps down, 640 kbps up	same services as first generation ADSL but over lines up to 3.9 km
ADSL2+	Second generation ADSL with extended bandwidth	15 Mbps down, 1.5 Mbps up	same services as first generation ADSL but over lines up to 1.8 km
VDSL	Very High Data Rate DSL	13 to 52 Mbps down, 1.5 to 2.3 Mbps up	same services as ADSL but over shorter loops (up to 1.2 km) plus HDTV[f]

[a] transmission system especially used in North America
[b] wide area network
[c] local area network
[d] downstream: transmission direction from the network to the customer
[e] upstream: transmission direction from the customer to the network
[f] high-definition television

for broadband access in the local loop. Wireless networks have the advantage that they can reach out more easily to rural homes and others who are currently not served by DSL or cable. Recently, field trials started in Japan to conquer the broadband market [26]. Unfortunately, wireless deployment lags behind DSL and cable alternatives and, as such, still has to prove its added value.

1.2 Characteristics of the DSL environment

In this section the main signal and noise characteristics of a DSL system will be discussed. In Subsection 1.2.1 the discrete multitone transmission format will be explained. The different noise sources present in a DSL environment will be treated in Subsection 1.2.2 and Subsection 1.2.3.

1.2.1 Multicarrier modulation

During the last decades extensive research has been done to provide broadband communication to and from the customer premises. To cope with the time dispersive transmission character of wireline and wireless communication, multicarrier (MC) modulation offers a viable solution. Starting in the 1960s, the first MC systems were conceived and implemented [24][103], albeit only in analog form. Here, several low rate information channels, occupying disjoint frequency bands, were multiplexed to one wideband 'multicarrier' signal. The realization of this frequency division multiplexing was effectively implemented by means of expensive subcarrier oscillators and coherent demodulators. It was not until 1971 that a widespread interest was created due to an all digital implementation based on the cost-effective fast Fourier transform (FFT) algorithm [148]. Nowadays, MC systems are included in digital audio/video broadcasting (DAB/DVB) [60][61], in wireless local area networks such as IEEE802.11a [93] and HIPERLAN2 [59] and in wireline communication over twisted pairs such as in ADSL, ADSL2, ADSL2+ and soon also in VDSL [17][46][63][68].

At present, the transmission format as presented in [148] is more commonly known as discrete multitone (DMT) or orthogonal frequency division multiplexing (OFDM). DMT divides the available bandwidth into several parallel frequency bins or tones, see **Fig. 1.2**. Each tone is then quadrature amplitude modulated (QAM), where modulation and demodulation can efficiently be executed by means of an inverse fast Fourier transform (IFFT) and a fast Fourier transform (FFT) respectively. As opposed to analog MC systems, an FFT-based implementation allows substantial overlap between subchannels, leading to high bandwidth efficiency.

The frequency plan designed for ADSL, ADSL2 and ADSL2+ creates three information channels: a high speed downstream channel, a medium speed upstream channel and a plain old telephone service (POTS) or integrated services digital network (ISDN) channel, see **Fig. 1.2**. These three channels are separated in frequency by means of digital and analog front end filters in the modem. A specific filter excluded from the modem circuitry, the so-called POTS/ISDN-splitter, is designed to separate the POTS/ISDN channel from the DSL frequency band such that POTS and ISDN can operate independently from the digital modem, see **Fig. 1.3**. Hence, the modem can be active

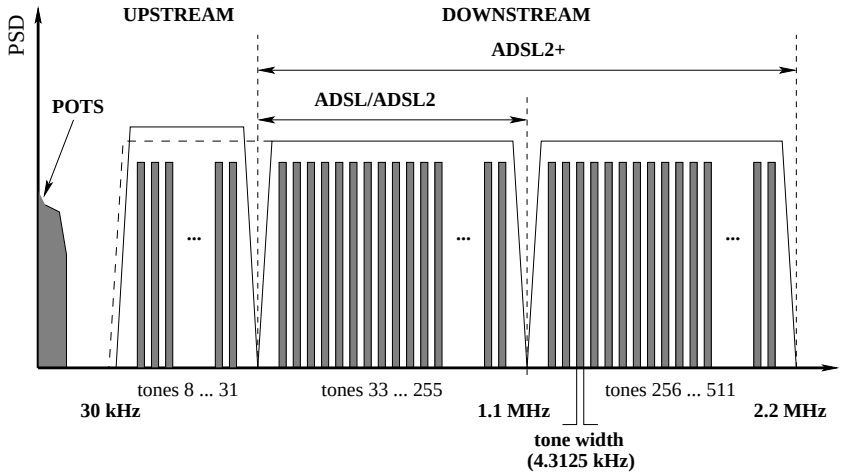

Figure 1.2: ADSL/ADSL2/ADSL2+ frequency plan.

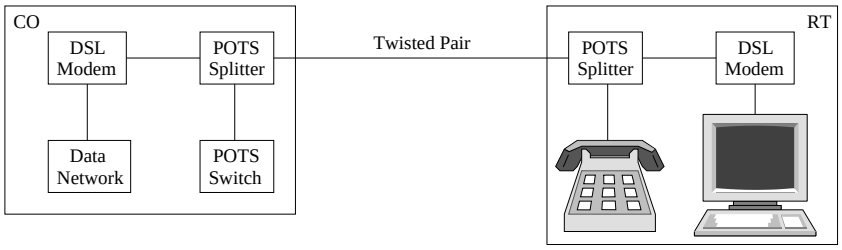

Figure 1.3: DSL configuration to guarantee uninterrupted POTS (or ISDN).

even when POTS/ISDN is in use and uninterrupted POTS/ISDN supply is guaranteed even if the DSL modem fails.

One of the advantages of DMT is the flexible way of loading bits onto the different tones. The QAM constellation size for a particular tone will be determined by the available signal-to-noise ratio (SNR) on that tone, which is measured during the initialization phase of the modem. **Fig. 1.4** illustrates this concept. The first drawing represents the theoretical maximum bit loading of 15 bits per tone. The third drawing shows how the bits are mapped onto the different tones, based on the SNR measurement, as given in the second drawing. Clearly, tones with high SNR are able to carry more bits for a predetermined bit error rate than tones with low SNR. In the most severe case tones with an SNR below a certain threshold will be switched off. As DMT enables efficient bit loading, the modem can operate at bit rates near the channel capacity. Adaptive bit loading is one of the major differences between DMT and OFDM.

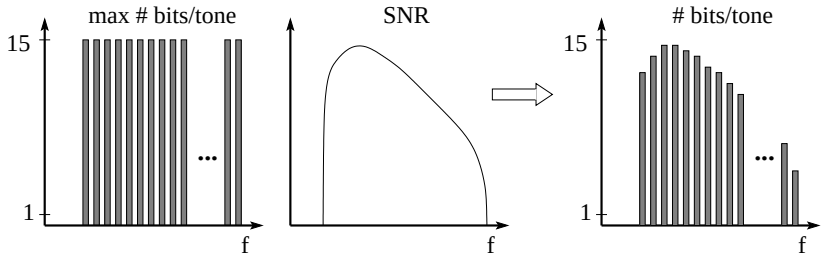

Figure 1.4: Bit loading in DMT-based systems.

A drawback of DMT- and OFDM-based systems is the peak-to-average power ratio (PAPR) of the transmitted signal. The transmitted time-domain MC signal is in fact a sum of sines with different phases and frequencies. Through the use of the central limit theorem, the probability density function of the multichannel signal approaches a Gaussian distribution. As a consequence, high amplitude peaks may occur with a certain probability when the signals from the different tones add constructively. Compared to the average signal power, the instantaneous power of these peaks is high, and consequently, so is the PAPR. A high PAPR is undesirable, as it requires a large dynamic range of the digital-to-analog converter (DAC) and analog-to-digital converter (ADC). Hence, to keep the quantization noise at an acceptable level, a large precision is required. In addition, power amplifiers have to be highly linear to avoid saturation or clipping, which introduces additional noise. Fortunately efficient techniques exist to counteract these PAPR problems [48][50][89][125].

1.2.2 Channel induced interference

In DSL the impulse response of the overall transmission channel is time dispersive, e.g. a typical ADSL channel can be modeled as a finite impulse response (FIR) filter with more than 300 taps at 2.2 MHz. Without appropriate signal processing, the received DMT symbols will be distorted by *inter-symbol-interference (ISI)*. In addition, orthogonality between neighbouring tones will be lost, resulting in undesired *inter-carrier-interference (ICI)*. In this thesis some *equalizer algorithms* will be discussed to reduce the ISI and ICI levels. This subsection covers some of the loop characteristics that cause the channel to be time dispersive.

Line propagation

Unshielded twisted pair (UTP) is undoubtedly the most common transmission system for more than 100 years. It comprises two copper wires, which are separately insulated and twisted around each other to reduce crosstalk. The use of this type of cable was originally designed for the transmission of voice

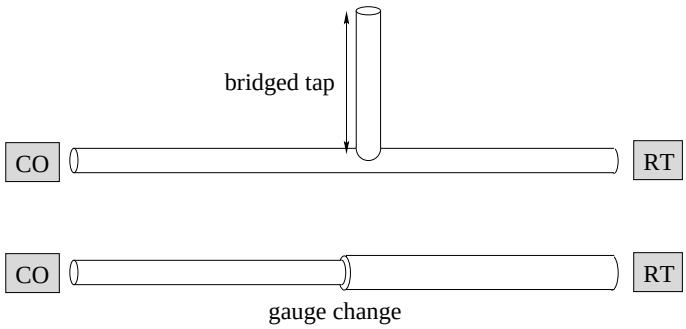

Figure 1.5: A bridged tap and a change in wire gauge.

only. However, twisted pairs can also be used for digital data transmission under certain restrictions:

- Propagation loss occurs due to the attenuating character of the line, where the highest frequencies experience the most attenuation. As attenuation increases with loop length, customers connected to CO with very long telephone lines can not subscribe to DSL services.
- Apart from signal attenuation, different frequencies travel with different velocities, resulting in dispersion of the received signal.

Extensive research is still ongoing to extend the loop reach of currently deployed ADSL systems, see e.g. [94] for techniques used in range extended ADSL (READSL).

Bridged taps

A bridged tap originates from the method of cabling for telephone lines. A twisted pair coming from the CO side can terminate in several different locations, see **Fig. 1.5**. The telephone company may assign this pair to any subscriber near these terminal locations. Once a customer disconnects, the twisted pair is available for another customer at any of the terminals. DSL signals are affected by bridged taps in the sense that signals traveling towards the customer will be reflected by the end of the bridged tap. The reflected signal will be out of phase and mixed with the original signal. Especially short bridged taps, near the customers end can be very harmful.

Wire gauge

In DSL the diameter of the copper wire is often expressed in American wire gauge (AWG) [119], e.g. 26 AWG=0.404 mm and 24 AWG=0.511 mm. To

avoid excessive loop resistance, long telephone loops often consist of different wire dimensions along the line, see **Fig. 1.5**. Splicing one wire gauge to a different wire gauge causes undesired signal reflections due to an impedance mismatch between the line sections. Hence, the exact loop topology has to be taken into account when computing the transfer function of the line.

In the DSL standards, several test loops have been defined to evaluate the performance of DSL modems [63]. The test loops have various lengths and consist of several wire gauge changes and bridged taps. The algorithms proposed in this thesis will be tested on some of these standardized loops.

1.2.3 External noise

Apart from channel induced interference, as treated in the previous section, the DSL environment is subjected to several other noise sources, which couple into the telephone line. The most common sources are discussed in this subsection.

Background noise

All DSL systems experience a noise floor due to the thermal agitation of electrons in the copper wire, i.e. the so-called background or thermal noise. This noise source can be modeled as additive, white and Gaussian (AWGN). The background noise level is often determined by a reasonable value (-140 dBm/Hz) for the analog-to-digital converter (ADC) quantization noise, rather than the actual thermal limit of -173 dBm/Hz at room temperature [120].

Crosstalk

Telephone cables are bundled into binder groups of several twisted pairs. Pairs within a binder group experience electromagnetic coupling or crosstalk from neighbouring pairs. Two types of crosstalk can be distinguished: *near-end crosstalk (NEXT)* and *far-end crosstalk (FEXT)*, see **Fig. 1.6**. NEXT is caused by signals traveling in opposite directions on different twisted pairs. FEXT between twisted pairs occurs due to signals traveling in the same direction. When crosstalk originates from a system using the same transmission technology, it is called self-NEXT or self-FEXT. Crosstalk from a system with a different technology, e.g. with a different symbol rate, with a different transmission format, etc., is referred to as alien crosstalk. **Fig. 1.7** shows different crosstalk spectra as experienced by a downstream ADSL receiver. Crosstalk can severely degrade the DSL performance when it can not be eliminated.

NEXT and FEXT levels increase with frequency according to $\sim f^{3/2}$ and $\sim f^2$ respectively [120]. Self-NEXT can be reduced by assigning different frequency bands to the two transmission directions. Self-FEXT, on the other hand, can

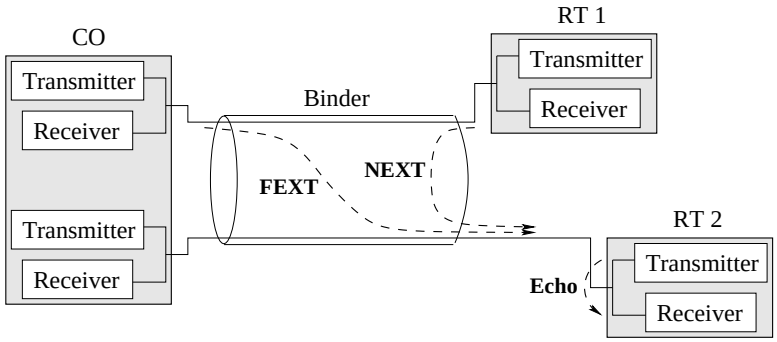

Figure 1.6: NEXT, FEXT and echo impairments in a DSL environment.

not be avoided and plays a crucial role in ADSL and VDSL. At present, the mitigation of crosstalk is a highly active research area. Some researchers exploit the cyclostationarity of the crosstalk noise [1][99][145]. Others assume some coordination between the different twisted pairs within one binder and treat it as a multiple-input, multiple-output system [18][21][22][51][169].

Echo

To allow bidirectional communication over one twisted pair, the transmit and receive side of a modem have to be coupled to the telephone line by a hybrid. The hybrid decouples transmit signals from receive signals when the hybrid impedance is exactly matched to the telephone line. In practice, however, the hybrid can not be exactly balanced for all loops and hence transmit signals are reflected back to the receiver and *echo* occurs, see **Fig. 1.6**.

Since the far-end signal is attenuated by the telephone line, the echo signal is typically much stronger than the desired far-end signal, leading to a severe SNR degradation. To avoid undesired echo, the ADSL standard allows two duplexing methods: *frequency division duplexing (FDD)* and *echo canceling (EC)* [33][63][86]. In an FDD setup, the two directions of transmission are separated by assigning different frequency bins to up- and downstream. Steep front end filters and a small frequency gap of unused tones between up- and downstream bands are required to extract the desired far-end signal from the overall received signal.

As opposed to FDD systems, EC systems allow a smaller frequency gap or even overlapping up- and downstream frequency bands, see **Fig. 1.2**. The expensive analog front end filters of the FDD system are replaced by filters with relaxed specifications and the resulting echo is then removed by an *echo canceler*. The principle of echo canceling is illustrated in **Fig. 1.8**. Since echo is a filtered version of the transmitted signal, an echo canceler adaptively estimates the echo

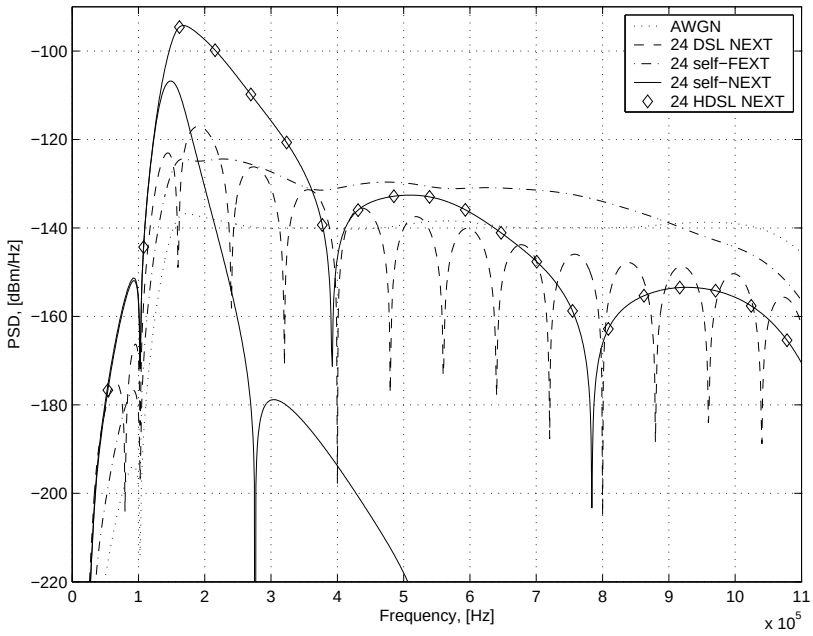

Figure 1.7: Power spectral density (PSD) of different crosstalk sources (each with 24 disturbers) as experienced by a downstream ADSL receiver.

path and generates a replica of the filtered echo transmit signal. The replica is subtracted from the received signal to obtain the desired echo-free signal. Echo cancellation duplexing is able to use the available bandwidth more efficiently than FDD systems, resulting in improved performance and/or extended loop reach. In this thesis, several echo canceling structures will be treated in more detail.

Some drawbacks of EC systems include the increased sensitivity to self-NEXT and the high dynamic range of the received signal. Self-NEXT behaves like echo from a different user but can not be compensated since there is typically no coordination assumed between users. In ADSL, self-NEXT will be limited since the frequencies where NEXT occurs are low and have weak crosstalk coupling. In an FDD system, self-NEXT is almost completely removed in the same way as echo by the front end filters. Allowing echo at the receiver will also lead to high dynamic ranges of the received signal. The far end signal, attenuated by the telephone line, has to compete with the echo signal, which only shows little attenuation. This will limit the values of the programmable gain amplifiers (PGA) that are set to maximize the signal levels at the analog-to-digital converter (ADC). Limited PGA values will increase the digital noise floor. These drawbacks can be partially mitigated by carefully designing the

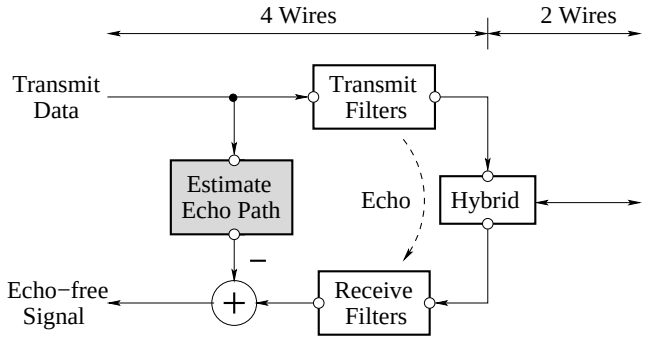

Figure 1.8: Principles of echo canceling.

EC system. An adjacent FDD system with no overlap and no frequency gap between up- and downstream tends to be a good compromise.

Radio frequency interference (RFI)

Each telephone line acts as an antenna that emits and receives energy. Radio frequency signals from wireless transmitters impinge on the copper telephone lines, resulting in *radio frequency interference (RFI)* [121]. RFI is usually narrowband and some frequencies may overlap with the DSL frequency bands. The most harmful radio noise for DSL applications originates from AM radio broadcasts and amateur radio transmissions (HAM). Especially downstream ADSL, downstream ADSL2+ and VDSL are affected by RFI.

RFI from AM transmitters arises from commercial radio stations and can be characterized as a stationary noise source. HAM noise is typically non-stationary since operators continuously switch carrier frequency and the carrier is switched off when no information is transmitted. Since AM and HAM RFI levels rise above the crosstalk and background noise, they can not be neglected in the receiver design. DMT-based systems are very sensitive to RFI [40][139]. Due to the sinc shaped filter characteristics of the discrete Fourier transform (DFT) demodulator, a narrowband RFI with high power will affect many of the received tones, leading to a substantial SNR degradation. In this thesis, some methods will be presented to mitigate RFI.

Impulse noise

Impulse noise is caused from sporadic switching of electronic devices in the vicinity of telephone lines, e.g. switching on a computer, on and off switching of a refrigerator, ringing of phones, etc. Whereas RF noise is narrowband in frequency, impulse noise is narrow in time. The noise level associated with these short impulses appear enormous to a receiver in comparison to received

DSL signal levels [67][119][120].

Many applications enabled by DSL involve real time signal processing, e.g. digital video. These applications can not use network level error control procedures to correct for bit errors. ADSL modems therefore incorporate forward error correction that dramatically reduces errors caused by impulse noise. Error correction on a symbol-by-symbol basis also reduces errors caused by continuous noise coupled into a line.

1.3 Outline of the thesis and contributions

This section starts with a motivation of the DSL research that will be presented in this thesis. Then an outline of the thesis and the corresponding contributions will be given.

1.3.1 Motivation

In the seventies, telecommunications was mainly analog and voice-oriented, as discussed in Subsection 1.1.1. In the early nineties, Internet and its associated digital applications started to enter the mass-consumer market, thereby inducing a strong demand for broadband communications. From that point in time, DSL technologies started to 'conquer the world'. Although ADSL deployment has already started a few years ago, we believe that DSL technologies in general will still face the future for many years to bridge the last mile to the customer.

Despite its worldwide success to deliver broadband services to the customers, DSL has some limitations. Since signal attenuation increases with distance, DSL has a limited loop reach, typically on the order of 3600 m for homeowners [26]. Hence, people living at large distance from the CO can not subscribe to DSL services. Since the signal attenuation for a specific loop is unavoidable, we will focus in this thesis on *the design of advanced digital signal processing algorithms, such as equalization, RFI mitigation and echo cancellation* as a means to improve the loop reach of existing DSL systems. An increase of the loop reach for a fixed data rate will expand the addressable DSL market. Alternatively, one can state that, for the same loop reach, the noise margin will improve. A higher noise margin leads to increased robustness of the modem, since more noise can be tolerated by the receiver before exceeding a predetermined bit error rate.

Furthermore, in the proposed algorithms we aim at *reducing the computational cost, memory requirements and/or the transmitted power*. Savings in computational cost and memory requirements are important to keep the hardware cost as low as possible. A reduction of the transmitted power leads to less egress or

crosstalk to other systems that use the same frequency band.

Finally, we would like to mention that in this thesis we will especially focus on transceiver design within the limits of the ADSL and the VDSL standard. Nevertheless, the proposed algorithms can in general be applied to other DMT-based or OFDM-based systems as well.

1.3.2 Thesis overview and contributions

This thesis consists of seven chapters. A chapter by chapter overview will be given in this subsection. In addition, the contributions associated with each chapter will be listed.

In **Chapter 2** the basic concepts of DMT transmission will be explained mathematically. In particular, we will focus on Shannon's bit rate equation, since this performance measure will be used extensively in subsequent chapters. Furthermore, the notation and the data model that will be used throughout this thesis will be introduced.

In **Chapter 3** a mathematical framework will be presented to unify existing equalizer design methods that have appeared in literature. It will be shown that almost all designs can be formulated as the maximization of a product of generalized Rayleigh quotients. By means of this unified framework it will be possible to clarify the subtle differences between the different design approaches and to compare their performance with a common performance measure.

The results of this chapter are partially incorporated in a two-part manuscript that has been written in collaboration with two other research groups, i.e. BARD (Prof. C.R. Johnson, Jr.) at the Cornell University (USA) and ESPL (Prof. B.L. Evans) at the Texas University (USA):

- R.K. Martin, K. Vanbleu, M. Ding, G. Ysebaert, M. Milosevic, B.L. Evans, M. Moonen and C.R. Johnson, Jr. Multicarrier equalization: Unification and evaluation. Part I: Optimal designs. Internal Report ESAT-SISTA/TR 03-51, K.U.Leuven, Belgium. Submitted to *IEEE Trans. on Signal Proc.*, December 2003.

- R.K. Martin, K. Vanbleu, M. Ding, G. Ysebaert, M. Milosevic, B.L. Evans, M. Moonen and C.R. Johnson, Jr. Multicarrier equalization: Unification and evaluation. Part II: Complexity reduction, adaptation, and performance evaluation. Internal Report ESAT-SISTA/TR 03-52, K.U.Leuven, Belgium. Submitted to *IEEE Trans. on Signal Proc.*, December 2003.

Besides the general equalization framework, **Chapter 3** will pay special attention to the MMSE TEQ design criterion. We will show that MMSE TEQ

design with three distinct unit-energy constraints results in essentially identical TEQs with exactly the same bit rate performance. Moreover, an iterative initialization method, based on the power method or inverse iterations, will be devised. In addition, the mathematical derivations will be interpreted geometrically in terms of the principal angles of the signal subspaces involved. This research has resulted in the following publication:

- G. Ysebaert, K. Van Acker, M. Moonen and B. De Moor. Constraints in channel shortening equalizer design for DMT-based systems. *Signal Processing*, 83(3):641–648, March 2003.

In **Chapter 4** equalization is extended with receiver windowing to reduce the high spectral sidelobes of the demodulating DFT filters. We will show how to design a single equalizer in combination with a single window taper in order to maximize the achievable bit rate. The resulting receiver will be less sensitive to narrowband RFI and channel induced interference. Moreover, equalizer taps can be exchanged for additional windowing coefficients, leading to substantial complexity savings. The resulting bit rate maximizing framework will be extended to design an equalizer and a window for smaller groups of tones or even for each tone separately, which is more commonly known as per tone equalization. Finally, some special design cases within this framework will be addressed. The outcome of this chapter has resulted in the following publications:

- G. Ysebaert, K. Vanbleu, G. Cuypers and M. Moonen. Joint window and time domain equalizer design for bit rate maximization in DMT-receivers. To appear in *IEEE Trans. on Signal Proc.*, 2004.
- G. Ysebaert, K. Vanbleu, G. Cuypers and M. Moonen. ADSL per-tone/per-group optimal equalizer and windowing design. In *Proc. of the Asilomar Conf. on Signals, Systems and Computers*, Pacific Grove, California, November 2002.
- G. Ysebaert, K. Vanbleu, G. Cuypers and M. Moonen. Bit rate maximizing window and equalizer design for DMT-systems. Internal Report ESAT-SISTA/TR 04-11a, K.U.Leuven, Belgium. Submitted to *European Signal Proc. Conf. (EUSIPCO)*, January 2004.

In **Chapter 5** we will investigate different echo canceling structures, where the echo is partly canceled in the time domain and partly in the frequency domain. After a brief review of existing methods, the tracking behaviour of the echo canceler will be enhanced by adding double talk cancellation (DTC). Then, we propose a modification to the existing mixed time/frequency echo cancelers in order to minimize the complexity independent of the misalignment

between transmitted echo symbols and received far end symbols. The resulting scheme is referred to as improved time/frequency domain echo canceling (ITF-EC). Finally, we propose an alternative echo canceling structure, named circulant decomposition canceler (CDC), that requires less transmit power for convergence than existing methods. We will show how the CDC scheme can easily be extended with DTC and per tone equalization. Publications related to this chapter are:

- G. Ysebaert, K. Vanbleu, G. Cuypers, M. Moonen and J. Verlinden. Echo cancellation for discrete multitone frame-asynchronous ADSL transceivers. Internal Report ESAT-SISTA/TR 02-186, K.U.Leuven, Belgium. Submitted to *IEEE Trans. on Commun.*, December 2002.

- G. Ysebaert, F. Pisoni, M. Bonaventura, R. Hug, and M. Moonen. Echo cancellation in DMT-receivers: Circulant decomposition canceler. To appear in *IEEE Trans. on Signal Proc.*, 2004.

- G. Ysebaert, K. Vanbleu, G. Cuypers, M. Moonen and K. Van Acker. Double talk cancellation in echo cancelled DMT-systems. In *Proc. of Signal Processing Symposium (SPS)*, pages 169–172, Leuven, Belgium, March 2002.

- G. Ysebaert, K. Vanbleu, G. Cuypers, M. Moonen and K. Van Acker. Double talk cancellation in echo cancelled DMT-systems. In *Proc. European Signal Proc. Conf. (EUSIPCO)*, volume II, pages 381–384, Toulouse, France, September 2002.

- G. Ysebaert, K. Vanbleu, G. Cuypers, M. Moonen and J. Verlinden. Echo cancellation for discrete multitone frame-asynchronous ADSL transmission. In *Proc. IEEE Int. Conf. on Commun. (ICC)*, volume 4, pages 2421–2425, Anchorage, Alaska, May 2003.

- G. Ysebaert, F. Pisoni, M. Bonaventura, R. Hug and M. Moonen. Circulant decomposition canceler for echo cancellation in DMT-based receivers. To appear in *Proc. IEEE Int. Conf. on Commun. (ICC)*, Paris, France, June 2004.

In **Chapter 6** we will focus on the recursive initialization of the per tone equalizers on the one hand and of the combined per tone equalizers and per tone echo cancelers on the other hand. The initialization will be based on a combination of square-root recursive least square (SR-RLS) adaptive filtering and split RLS. By this, the computational complexity and memory requirements will be substantially reduced compared to full SR-RLS. This recursive initialization procedure has resulted in the following publications:

- G. Ysebaert, K. Vanbleu, G. Cuypers, M. Moonen and T. Pollet. Combined RLS-LMS initialization for per tone equalizers in DMT-receivers. *IEEE Trans. on Signal Proc.*, 51(7):1916–1927, July 2003.
- G. Ysebaert, K. Vanbleu, G. Cuypers and M. Moonen. Split SR-RLS for the joint initialization of the per-tone equalizers and per-tone echo cancelers in DMT-based receivers. To appear in *EURASIP Journal on Applied Signal Processing, Special Issue on Multicarrier Communications and Signal Processing*, 2004.
- G. Ysebaert, M. Moonen and T. Pollet. Combined RLS-LMS initialization for per tone equalizers in DMT-receivers. In *Proc. IEEE Int. Conf. on Acoustics, Speech and Signal Proc. (ICASSP)*, volume III, pages 2537–2540, Orlando, Florida, May 2002.

In **Chapter 7** the final conclusions are presented and some topics for further research are listed.

Apart from the main contributions listed above, we have also co-authored a few other publications in the DSL domain. For a list of all the publications we refer to the end of this thesis.

1.4 Conclusions

In this chapter we explained that DSL is a technology to deliver broadband communications over the existing twisted pair telephone network. We showed that the data rates in DSL depend on many factors: bridged taps, echo, crosstalk, RFI, line length, etc. Since the signal attenuation becomes more severe with increasing loop length, some customers are excluded to subscribe on DSL services. Advanced signal processing algorithms are able to improve the loop reach and/or the data rates of existing DSL systems. Therefore, in the remainder of this dissertation, we will focus on designing algorithms to improve equalization, RFI mitigation and echo cancellation.

Chapter 2

Basic concepts and notation

SOME basic DSL concepts will be discussed in this chapter and the necessary signal processing tools, which facilitate the understanding of the rest of this text, will be presented. In Section 2.1 we start with a review of the capacity formulas for a transmission medium, as originally proposed by Shannon. Since we are especially interested in designing algorithms that maximize the data rate for a given bit error rate, the capacity formulas will give an insight in the performance of the algorithms, presented in the remainder of this thesis.

In Section 2.2 discrete multitone modulation (DMT) is explained, which is a special form of multicarrier modulation to approximate the capacity of the channel. DMT uses block transmission with the addition of a cyclic prefix (CP), as discussed in Subsection 2.2.1. The resulting transmitter and receiver structure are given in Subsection 2.2.2. In some DSL applications, the receiver is provided with windowing. The concept of receiver windowing as a means to improve the spectral containment of the DFT-based receiver is discussed in Subsection 2.2.3. Since bit loading is a key feature of DMT, the principles of bit loading are explained in Subsection 2.2.4. In addition, some existing bit loading algorithms are presented.

Based on the DMT principles, the data model, which will be frequently used in this thesis, is presented in Section 2.3. Since we will focus on signal enhancement in DSL receivers, we are especially interested in the signals arriving at the receive side of the modem. In Subsection 2.3.1 the effects of the far end channel and the external noise sources on the far end receive signal is explained mathematically. In Subsection 2.3.2 the received echo component is added to the data model. Depending on the modem structure we will make a distinction between interpolated and decimated echo signals. The basic data model is extended in Subsection 2.3.3 to incorporate windowing at the receiver.

Finally, conclusions are drawn in Section 2.4. Since most signal processing techniques presented in this thesis will be described by vector and matrix operations, a brief review of some basic linear algebra definitions and matrix decompositions can be found in Appendix A.

2.1 Capacity of a transmission medium

The theoretical upper bound on the data rate that can be reliably transmitted over a transmission medium is called the *capacity* of the medium. In the late 1940s, Claude Shannon developed his mathematical theory of information that provides us with some fundamental boundaries to the performance of a communication system. According to Shannon's theory [109][115], the maximum number of bits that can be transmitted over a flat AWGN channel (i.e. with no ISI), H, is given by

$$b = \log_2(1 + \text{SNR}), \quad \text{with} \quad \text{SNR} = \frac{\sigma_x^2 |H|^2}{\sigma_n^2}, \tag{2.1}$$

where σ_x^2 is the transmitted signal power, σ_n^2 is the received noise power and SNR is the ratio of the received signal power to the received noise power. Note that the maximum data rate, expressed in bits per second, can easily be computed by multiplying (2.1) with the symbol rate F_s. When the transmission takes place over N parallel and independent subchannels, (2.1) has to be computed for each subchannel i and the result has to be summed

$$b = \sum_{i=0}^{N-1} b_i = \sum_{i=0}^{N-1} \log_2(1 + \text{SNR}_i), \quad \text{with} \quad \text{SNR}_i = \frac{\sigma_{x,i}^2 |H_i|^2}{\sigma_{n,i}^2}, \tag{2.2}$$

where the subscript i denotes the subchannel dependencies. In practice, infinite transceiver complexity is required to obtain this maximum number of bits at low bit error probabilities, P_e. Most practical coding and modulation schemes are characterized by a gap that quantifies the loss in SNR with respect to the capacity at a given fixed P_e, such that

$$b = \sum_{i=0}^{N-1} b_i = \sum_{i=0}^{N-1} \log_2\left(1 + \frac{\text{SNR}_i}{\Gamma_i}\right), \quad \text{with} \quad \text{SNR}_i = \frac{\sigma_{x,i}^2 |H_i|^2}{\sigma_{n,i}^2}, \tag{2.3}$$

where Γ_i represents the gap for subchannel i. The smaller the gap, the better the line code. Hence, any realistic system transmits at a data rate below the theoretical capacity of the channel.

Quadrature amplitude modulation (QAM), as used in DSL systems, achieves a gap of 9.8 dB at $P_e = 10^{-7}$ [119][120]. The gap can be reduced by making use of efficient coding techniques. In practical systems an additional noise margin

has to be foreseen to make the system robust against noise fluctuations. By this, the gap is increased again and can be computed as

$$\Gamma_i = 9.8 - \gamma_{c,i} + \gamma_{m,i}, \tag{2.4}$$

where $\gamma_{c,i}$ and $\gamma_{m,i}$ are the coding gain and noise margin for subchannel i respectively. Typical values for DSL are $\gamma_{c,i} = 3...4$ dB and $\gamma_{m,i} = 6$ dB [29].

2.2 Discrete multitone modulation (DMT)

Whereas the theory in Section 2.1 assumes that the channel is AWGN and free of ISI, this is not the case in a practical DSL system. To mitigate severe ISI, Shannon proposed in his mathematical theory of communication [109] to partition the available channel into a large number of narrowband AWGN subchannels. Typically, these subchannels are separated in frequency, hence the name *multitone* transmission. If each subchannel has sufficiently narrow bandwidth and if a cyclic prefix is applied, then each subchannel has little or no ISI and approximates an AWGN channel. By this, equation (2.3) can still be applied to compute the attainable bit rate. This will be discussed in more detail in the following subsection. A nice overview related to the insertion of transmit-redundancy can be found in [104][105][147].

2.2.1 Block transmission with cyclic prefix

Discrete-time equivalent transmission

Before we explain DMT transmission, we will first create the link between a physical continuous-time channel and its discrete-time equivalent. Consider the setup in **Fig. 2.1**, where a baseband sequence x_l with sampling rate $F_s = 1/T_s$ is transmitted through the real valued baseband continuous-time channel impulse response $h(t)$. The channel $h(t)$ typically consists of a transmit filter $h_{tr}(t)$, the actual twisted pair $h_{tw}(t)$ and the receive filters $h_{re}(t)$, i.e. $h(t) = h_{tr}(t) \star h_{tw}(t) \star h_{re}(t)$, where $\star$ denotes a linear convolution. The overall received signal can then be written as

$$y(t) = \sum_{l=-\infty}^{+\infty} x_l h(t - lT_s) + n(t), \tag{2.5}$$

where $n(t)$ is additive Gaussian noise filtered by the front end filters, $h_{re}(t)$, at the receiver. When $y(t)$ is sampled at instants $t = lT_s$, the received discrete-time samples, y_l, are given by

$$y_l = \sum_{m=0}^{L} h_m x_{l-m} + n_l, \tag{2.6}$$

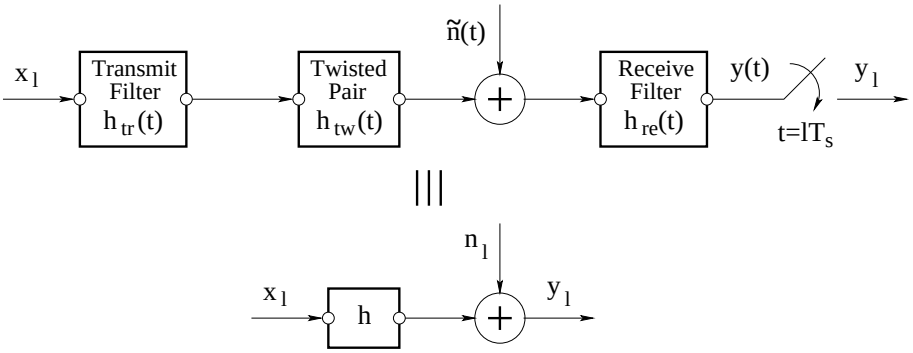

Figure 2.1: Discrete-time equivalent of a continuous-time DSL communication system.

where $h_m = h(mT_s)$ and where the overall channel is modeled as a finite impulse response (FIR) filter of order L.

Block transmission

Assume we group the transmitted samples, x_l, into *blocks or symbols* of length $s \gg L$, where the kth transmitted and received symbol are defined as

$$\bar{\mathbf{x}}^k = [x_{ks}\ x_{ks+1}\ \ldots\ x_{(k+1)s-1}]^T, \qquad \bar{\mathbf{y}}^k = [y_{ks}\ y_{ks+1}\ \ldots\ y_{(k+1)s-1}]^T, \quad (2.7)$$

where we tacitly assume that the channel has a zero group delay. Based on (2.6), we can write

$$\bar{\mathbf{y}}^k = \mathbf{H}_0\bar{\mathbf{x}}^k + \mathbf{H}_1\bar{\mathbf{x}}^{k-1} + \bar{\mathbf{n}}^k, \quad (2.8)$$

where $\bar{\mathbf{n}}^k$ is the corresponding noise vector. The real valued, $s \times s$ Toeplitz matrices $\mathbf{H}_0$ and $\mathbf{H}_1$ are given by

$$\mathbf{H}_0 = \begin{bmatrix} h_0 & 0 & & \ldots & \ldots & 0 \\ h_1 & h_0 & 0 & \ldots & \ldots & 0 \\ \vdots & \ddots & \ddots & & & \vdots \\ & & & & & \\ h_L & & & & & \vdots \\ \vdots & \ddots & & \ddots & \ddots & 0 \\ 0 & \ldots & h_L & \ldots & h_1 & h_0 \end{bmatrix}, \quad (2.9)$$

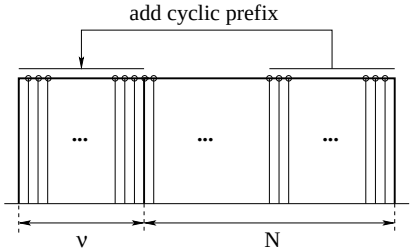

Figure 2.2: The addition of a cyclic prefix of length ν in front of the original symbol of length N.

$$\mathbf{H}_1 = \begin{bmatrix} 0 & \dots & h_L & \dots & h_1 \\ \vdots & \ddots & & \ddots & \vdots \\ \vdots & & & & h_L \\ \vdots & & & \ddots & \vdots \\ 0 & \dots & \dots & \dots & 0 \end{bmatrix}. \tag{2.10}$$

From (2.8), we can clearly see that due to the dispersive character of the channel, ISI occurs between successive symbols. As a consequence, $\bar{\mathbf{y}}^k$ depends on both $\bar{\mathbf{x}}^k$ and $\bar{\mathbf{x}}^{k-1}$.

To mitigate ISI, a *cyclic prefix* (CP) [98] of length ν can be introduced in each transmitted block, by repeating the last ν samples of a symbol at the beginning of that symbol, see **Fig. 2.2**. Starting with the vectors $\mathbf{x}^k \in \mathbb{R}^N$ and $\mathbf{x}^{k-1} \in \mathbb{R}^N$, we create $\bar{\mathbf{x}}^k = \mathbf{P}_N \mathbf{x}^k \in \mathbb{R}^s$ and $\bar{\mathbf{x}}^{k-1} = \mathbf{P}_N \mathbf{x}^k \in \mathbb{R}^s$, with

$$\mathbf{P}_N = \left[\begin{array}{c|c} \mathbf{0}_{\nu\times(N-\nu)} & \mathbf{I}_\nu \\ \hline \multicolumn{2}{c}{\mathbf{I}_N} \end{array}\right], \tag{2.11}$$

where $\mathbf{P}_N \in \mathbb{R}^{s\times N}$, with $s = N + \nu$. Equation (2.8) can now be modified to

$$\bar{\mathbf{y}}^k = \mathbf{H}_0 \mathbf{P}_N \mathbf{x}^k + \mathbf{H}_1 \mathbf{P}_N \mathbf{x}^{k-1} + \bar{\mathbf{n}}^k. \tag{2.12}$$

At the receiver, the first ν samples of $\bar{\mathbf{y}}^k$ are discarded, by multiplying $\bar{\mathbf{y}}^k$ by the receive matrix $\mathbf{Q} = [\mathbf{0}_{N\times\nu} \mid \mathbf{I}_N]$. The resulting block transmission scheme can now be summarized as

$$\breve{\mathbf{y}}^k = \mathbf{Q}\bar{\mathbf{y}}^k = \mathbf{Q}\mathbf{H}_0 \mathbf{P}_N \mathbf{x}^k + \mathbf{Q}\mathbf{H}_1 \mathbf{P}_N \mathbf{x}^{k-1} + \breve{\mathbf{n}}^k, \tag{2.13}$$

with $\breve{\mathbf{y}}^k \in \mathbb{R}^N$ and where the noise vector $\breve{\mathbf{n}}^k \in \mathbb{R}^N$ only holds the last entries of $\bar{\mathbf{n}}^k$, i.e. $\breve{\mathbf{n}}^k = \mathbf{Q}\bar{\mathbf{n}}^k$.

ISI-free transmission due to the cyclic prefix

Based on (2.13), two special cases can be considered: $L \leqslant \nu$ and $L > \nu$.

1. When the *channel order L, is less or equal than the CP length ν,* the received symbol is independent of the transmitted symbol at time $k-1$, i.e. $\mathbf{Q}\mathbf{H}_1\mathbf{P}_N\mathbf{x}^{k-1} = \mathbf{0}$. Hence, the insertion of a CP by $\mathbf{P}_N$ and discarding the first ν samples at the receiver by $\mathbf{Q}$ results in an ISI-free system, given by

$$\breve{\mathbf{y}}^k = \mathbf{Q}\mathbf{H}_0\mathbf{P}_N\mathbf{x}^k + \breve{\mathbf{n}}^k, \tag{2.14}$$

where $\mathbf{C} = \mathbf{Q}\mathbf{H}_0\mathbf{P}_N$ is a *circulant* matrix. Hence, the linear convolutive channel of (2.8) is converted to a circular one in (2.14) without ISI. The circulant matrix $\mathbf{C} \in \mathbb{R}^{N\times N}$

$$\mathbf{C} = \begin{bmatrix} h_0 & 0 & \dots & 0 & h_L & \dots & h_1 \\ h_1 & h_0 & & & & \ddots & \vdots \\ \vdots & \ddots & \ddots & & & & h_L \\ h_L & & & & & & 0 \\ 0 & h_L & & & & & \\ \vdots & \ddots & \ddots & & \ddots & \ddots & \vdots \\ 0 & \dots & 0 & h_L & \dots & h_1 & h_0 \end{bmatrix}, \tag{2.15}$$

can be diagonalized by pre- and post-multiplication with the N-point DFT and IDFT matrices (cf. Appendix A) [53], i.e.

$$\mathcal{F}_N\mathbf{C}\mathcal{I}_N = \mathrm{diag}\{[H_0 \ \dots \ H_{N-1}]^T\}, \tag{2.16}$$

where $[H_0 \ \dots \ H_{N-1}]^T$ is the frequency response of the channel, i.e. $[H_0 \ \dots \ H_{N-1}]^T = \mathcal{F}_N\mathbf{C}[:,1]$. This property holds since the eigenvectors of a circulant matrix are given by the columns of a DFT matrix. When the transmitted symbols are generated in the frequency domain, i.e. $\mathbf{x}^k = \mathcal{I}_N[X_0^k \ \dots \ X_{N-1}^k]^T$, and the received symbols are converted to the frequency domain, i.e. $[Y_0^k \ \dots \ Y_{N-1}^k]^T = \mathcal{F}_N\breve{\mathbf{y}}^k$, we obtain the very simple input-output relationship

$$\begin{bmatrix} Y_0^k \\ \vdots \\ Y_{N-1}^k \end{bmatrix} = \begin{bmatrix} H_0 & \dots & 0 \\ \vdots & \ddots & \vdots \\ 0 & \dots & H_{N-1} \end{bmatrix} \begin{bmatrix} X_0^k \\ \vdots \\ X_{N-1}^k \end{bmatrix} + \begin{bmatrix} N_0^k \\ \vdots \\ N_{N-1}^k \end{bmatrix}, \tag{2.17}$$

where $[N_0^k \ \dots \ N_{N-1}^k]^T = \mathcal{F}_N\breve{\mathbf{n}}^k$. Each received frequency domain symbol on subchannel i, denoted by Y_i^k, is simply a scaled version of the transmitted frequency domain symbol X_i^k plus Gaussian white noise, for $i = 0, \dots, N-1$. Moreover, every subchannel i can be processed independently of the other subchannels $j \neq i$.

To summarize: when $L \leqslant \nu$, block transmission with CP has converted a time dispersive channel into N parallel, narrowband, flat subchannels or

tones each having a channel gain H_i and additive white Gaussian noise $N_i^k,\ i = 0, \ldots, N-1$, hence the term *discrete multitone transmission (DMT)* [148].

Due to the DMT technique, the capacity formulas of (2.2) and (2.3), which were derived for ISI-free channels, can be applied. However, the insertion of the CP introduces a reduction with a factor $N/(N+\nu)$ of the attainable bit rate, which is eventually given by

$$r = \frac{F_s}{N+\nu} \sum_i \log_2(1 + \frac{\text{SNR}_i}{\Gamma_i}), \quad \text{with} \quad \text{SNR}_i = \frac{\sigma_{x,i}^2 |H_i|^2}{\sigma_{n,i}^2}, \tag{2.18}$$

where r is expressed in bits per second and $\sigma_{x,i}^2 = \mathcal{E}\{|X_i^k|^2\}$ and $\sigma_{n,i}^2 = \mathcal{E}\{|N_i^k|^2\}$.

2. When the *channel order L, is larger than the CP length ν*, additional interference arises [100][108]. Starting from (2.13) and applying the DMT transmission techniques, the received frequency domain symbols in the noiseless case are obtained by

$$\begin{bmatrix} Y_0^k \\ \vdots \\ Y_{N-1}^k \end{bmatrix} = \mathcal{F}_N \mathbf{Q}\mathbf{H}_0 \mathbf{P}_N \mathcal{I}_N \begin{bmatrix} X_0^k \\ \vdots \\ X_{N-1}^k \end{bmatrix} + \mathcal{F}_N \mathbf{Q}\mathbf{H}_1 \mathbf{P}_N \mathcal{I}_N \begin{bmatrix} X_0^{k-1} \\ \vdots \\ X_{N-1}^{k-1} \end{bmatrix}. \tag{2.19}$$

The second term does not vanish since $\mathbf{Q}\mathbf{H}_1$ is not equal to zero when $L > \nu$. Moreover, $\mathbf{Q}\mathbf{H}_0\mathbf{P}_N$ does not produce a circulant matrix any more. When looking at a particular tone i, we have

$$\begin{aligned} Y_i^k &= \mathcal{F}_N[i,:]\mathbf{Q}\mathbf{H}_0\mathbf{P}_N\mathcal{I}_N[:,i]X_i^k + \sum_{j\neq i} \mathcal{F}_N[i,:]\mathbf{Q}\mathbf{H}_0\mathbf{P}_N\mathcal{I}_N[:,j]X_j^k + \\ &\quad \sum_j \mathcal{F}_N[i,:]\mathbf{Q}\mathbf{H}_1\mathbf{P}_N\mathcal{I}_N[:,j]X_j^{k-1}. \end{aligned} \tag{2.20}$$

We can distinguish three contributions:

- The first term represents the desired signal component since it shows how the transmitted frequency domain symbol at symbol period k on tone i is transformed to the receiver. Note that $\mathcal{F}_N[i,:]\mathbf{Q}\mathbf{H}_0\mathbf{P}_N\mathcal{I}_N[:,i]$ is in general not equal to H_i, which is an important observation when designing an equalizer for the received frequency domain symbols. The last two terms represent unwanted contributions.
- In the second term, the interference originates from tones other than tone i and from the symbol transmitted during the same symbol period k. This type of interference is referred to as *inter-carrier-interference (ICI)*.
- The third term includes interference from one symbol period into another symbol period. This type of interference is the so-called *inter-symbol-interference (ISI)*.

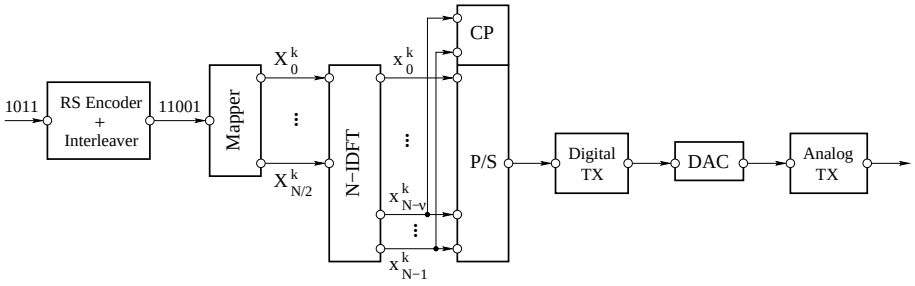

Figure 2.3: Block diagram of a DMT transmitter.

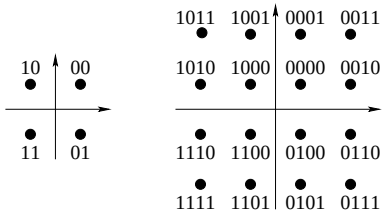

Figure 2.4: M-QAM constellations with M=4 and M=16.

2.2.2 Transmitter and receiver structure

After the brief review of DMT in the previous subsection, the basic structure of a DMT transmitter and receiver can be explained in more detail [29][150].

Transmitter

The DMT transmitter is based on the derivation in (2.14)-(2.16), where we showed how an appropriate construction of the transmitted signal, i.e. $\bar{\mathbf{x}}^k = \mathbf{P}_N \mathcal{I}_N [X_0^k \ \ldots \ X_{N-1}^k]^T$, leads to a tone by tone communication system. This is reflected in **Fig. 2.3**, where a block diagram of a DMT transmitter is depicted. The following operations can be distinguished:

- The incoming, serial bit stream is first Reed-Solomon (RS) encoded, interleaved and divided into $\frac{N}{2}+1$ parallel bit streams. Each single stream is assigned to a certain tone and mapped onto a complex valued M-QAM constellation point, where $M = 2^{b_i}$ typically ranges from 2^1 to 2^{15} [63]. In **Fig. 2.4** an example is given for 4-QAM and 16-QAM constellations. The constellation size and hence the number of bits b_i transmitted on a certain tone can differ from tone to tone, depending on the SNR of the tone. A higher SNR allows more bits to be transmitted and vice versa. At symbol period k and per tone i one complex valued constellation point is assigned to $X_i^k,\ i = 0, \ldots, N-1$.

- Before performing an N-point IDFT $\mathcal{I}_N$, which is cheaply implemented by means of the inverse fast Fourier transform (IFFT) [101], the symbols X_i^k are arranged to have a real valued IDFT output, i.e.

$$X_i^k = (X_{N-i}^k)^* \quad \text{for} \quad i = 1, \ldots, N-1. \tag{2.21}$$

  The subsymbol X_0^k, which corresponds to the DC value, is always put to zero in order to avoid the DC notch of the twisted-pair transformer coupling [119]. Furthermore, (2.21) dictates that $X_{N/2}^k$ has to be strictly real valued. The output of the IDFT modulation results in a time domain symbol $\mathbf{x}^k$ of N samples.

- A guard period of ν samples is added in front of the symbol $\mathbf{x}^k$ to obtain the digital time domain symbol that is effectively transmitted, i.e. $\bar{\mathbf{x}}^k = \mathbf{P}_N \mathbf{x}^k$.

- The resulting time domain symbols are first parallel-to-serial (P/S) converted. Then, the serial data stream is sent through the digital front end filters, the digital-to-analog converter (DAC) and the analog front end filters before transmission over the telephone line.

It is clear that DMT-based systems are very attractive since they exploit efficient frequency division multiplexing to transport a serial bit stream over several carriers within the usable frequency band of the channel.

Remark 2.1 One of the drawbacks of a DMT transmitter is that the transmitted waveforms exhibit a Gaussian-like amplitude distribution. When all the transmitted sine waves add in phase, high amplitudes may be reached, resulting in high peak-to-average power ratios (PAPR). Because of the high dynamic range of these signals, DMT transmitters require very linear and expensive output amplifiers. To overcome this problem, power backoff may be applied with loss in power efficiency. Signals will occasionally clip against the nonlinearities of the power amplifier, leading to nonlinear distortion and out-of-band radiation. Various methods have been proposed to reduce the PAPR, including the use of pilot tones, the exploitation of unused tones and various coding techniques, see [15][85][89][124] and references therein. □

Receiver

In **Fig. 2.5**, the DMT receiver operations are shown. In the receiver, the reverse operations are implemented, which are given by (2.19).

- The received analog signal is first converted to a digital signal by means of an analog-to-digital converter (ADC).

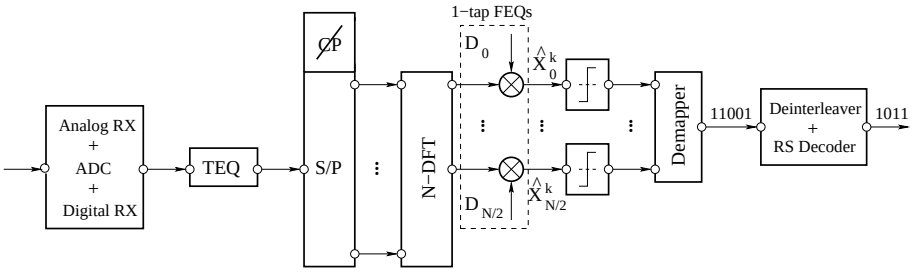

Figure 2.5: Block diagram of a DMT receiver.

- Ignoring the TEQ and FEQ blocks, the digital signal is serial-to-parallel (S/P) converted, the CP is discarded and an N-point FFT demodulation $\mathcal{F}_N$ is performed. At symbol period k, this results in the frequency domain symbols $Y_i^k,\ i = 0, \ldots, N-1$.
- When the channel order L is shorter than the length of the CP ν, it is clear from (2.17) that every transmitted subsymbol X_i^k will just be scaled and phase rotated due to the channel, i.e. $Y_i^k = H_i X_i^k + N_i$. Consequently, a *1-tap (complex valued) frequency domain equalizer (FEQ)* D_i for each used tone i is able to effectively invert the channel.
- A decision device makes decisions on the noisy constellation points, which are given by the FEQ outputs

$$\begin{bmatrix} \hat{X}_0^k \\ \vdots \\ \hat{X}_{N/2}^k \end{bmatrix} = \begin{bmatrix} D_0 & \ldots & 0 \\ \vdots & \ddots & \vdots \\ 0 & \ldots & D_{N/2} \end{bmatrix} \begin{bmatrix} Y_0^k \\ \vdots \\ Y_{N/2}^k \end{bmatrix}. \tag{2.22}$$

  The demapper recovers the transmitted bits by mapping the QAM constellation points on the corresponding bits, cf. **Fig. 2.4**.
- Following the demapper, the output bit stream is deinterleaved and the Reed-Solomon codewords are decoded to obtain an estimate of the transmitted bit stream.

Up till now we have assumed that the channel order L fits within the CP length. However, in an ADSL system, the channel impulse response is often quite long. This is partly due to the long line lengths (the longer the line, the longer the impulse response) and partly due to the impulse response of the analog and digital front end filters [150]. To cope with long channel impulse responses, two paths can be followed:

- The CP length could be increased. However, a longer CP leads to extra overhead and reduced data rates (cf. (2.18)). Therefore a short CP is desirable.

- Based on (2.20), a time dispersive channel exceeding the CP length leads to severe ISI and ICI. To avoid interference in the presence of a short CP and a long channel impulse response, a short finite impulse response (FIR) filter with T taps could be included in the receive path to *shorten* the overall channel. This additional filter is called a *time domain equalizer (TEQ)*[29][119].

The ADSL standard has opted for a short CP and hence a TEQ has typically to be used at the receiver, where the TEQ is designed during modem initialization. Optimal TEQ design appears to be a difficult problem and many algorithms have appeared in the literature. An overview of existing and new TEQ design methods will be given in Chapter 3 and Chapter 4.

VDSL has a similar CP duration as ADSL, but operates on shorter lines. Moreover, VDSL's need for front end filters is drastically reduced, thereby leading to much shorter overall channels. The short channel impulse responses in VDSL makes a TEQ unnecessary [150].

Example 2.1 In *upstream ADSL* the tone spacing is 4.3125 kHz. The ADSL standard allows to use the frequency band between 25.875 kHz and 138 kHz [63]. Hence, a minimum symbol length of $N = 64$ $(= 2 * 138/4.3125)$ samples is required. The CP overhead is determined to be 1/16th of the symbol length, i.e. $\nu = 4$. With the upstream sample frequency equal to $F_s = N * 4312.5 = 276$ kHz, the CP duration is 14.5 μsec. The symbol rate is given by $F_s/(N+\nu) = 4$ kHz. The channel impulse response length sampled at $F_s = 276$ kHz is typically on the order of N, which is significantly longer than the CP. △

Example 2.2 *Downstream ADSL* uses the same tone spacing of 4.3125 kHz and symbol rate of 4 kHz as in upstream. The downstream frequency band is limited to 1.104 kHz and as such a minimum symbol length of $N = 512$ has to be used [63]. The CP consists of $\nu = 32$ samples with a sample frequency equal to $F_s = N * 4312.5 = 2.208$ MHz. Also downstream channels are typically much longer than the CP length. △

Example 2.3 *ADSL2+* doubles the maximum frequency used for downstream data transmission from 1.1 MHz to 2.2 MHz. Thus, the symbol length N, the CP ν and the sampling frequency F_s are doubled as well. △

Example 2.4 To maintain interoperability with the current ADSL standard, upcoming DMT VDSL modems use the same tone spacing of 4.3125 kHz as ADSL. Support of 2048 tones is considered as default, but the number of tones can be as large as 4096, leading to $N = 8192$. According to different frequency plans, the available bandwidth can go up to 17.66 MHz, resulting in $F_s =$

35.328 MHz [120]. The CP has a length of 640 samples and the VDSL channel impulse response lengths are almost always much less than the 18 μsec cyclic extension. Thus, a TEQ is not required in VDSL and subchannels can be treated independently. $\triangle$

2.2.3 Receiver windowing

Compared to traditional voice band modems, one of the major changes towards higher bit rates is the extension of the bandwidth from 4 kHz to 1.104 MHz for ADSL, to 2.208 MHz for ADSL2+ and to 17.66 MHz for VDSL. Consequently, the increased spectrum occupied by high speed DSL modems overlaps with the bands used for radio communications, leading to narrow band RFI.

Since the DFT at the DSL receiver will only consider a rectangular frame of N samples, the reception of narrow band RFI will extend out on all carriers due to the bad spectral containment of the DFT. This can easily be seen as follows. Let $\breve{\mathbf{n}}^k = [n_{ks+\nu}\ n_{ks+1}\ \ldots\ n_{(k+1)s-1}]^T$ be equal to the noise vector at symbol period k observed at the receiver. The N-point DFT output for tone i is then obtained as

$$N_i = \mathcal{F}_N[i,:]\breve{\mathbf{n}}^k = [1\ e^{-j\frac{2\pi i}{N}}\ \ldots\ e^{-j\frac{2\pi i(N-1)}{N}}]\breve{\mathbf{n}}^k, \tag{2.23}$$

where we multiplied $\breve{\mathbf{n}}^k$ with the i-th DFT row. The variance of N_i is given by

$$\begin{aligned}
\sigma^2_{n,i} = \mathcal{E}\{|N_i|^2\} &= \mathcal{F}_N[i,:]\mathcal{E}\{\breve{\mathbf{n}}^k(\breve{\mathbf{n}}^k)^T\}\mathcal{F}_N[i,:]^H, &(2.24)\\
&= N\sum_{l=-(N-1)}^{N+1}\left(1-\frac{|l|}{N}\right)\mathbf{r}_n[l]e^{-j\frac{2\pi l}{N}}, &(2.25)\\
&= P_n(\omega)\star N^2\frac{\sin^2(N\omega/2)}{(N\omega/2)^2}\bigg|_{\omega=\frac{2\pi i}{N}}, &(2.26)
\end{aligned}$$

where $\mathbf{r}_n[l]$ and $P_n(\omega)$ denote the l-th auto-correlation coefficient and the power spectral density (PSD) of the sequence $\breve{\mathbf{n}}^k$ respectively. From (2.26), we can clearly see that the DFT operation results in a convolution with a sinc, which has very high sidelobes, see **Fig. 2.6**. If we consider one interferer, modeled in the frequency domain as a single impulse with unit amplitude at ω_{rfi}, (2.26) reduces to

$$\sigma^2_{n,i} = N^2\frac{\sin^2(N(\frac{2\pi i}{N}-\omega_{rfi})/2)}{(N(\frac{2\pi i}{N}-\omega_{rfi})/2)^2}. \tag{2.27}$$

According to (2.27), the RFI only affects a single tone when the RFI frequency coincides with the DMT grid. When the RFI frequency is located in between the grid, all tones are severely disturbed.

To improve the frequency selectivity of the DFT, Spruyt et al. proposed to use a time domain window in front of the DFT [118]. The window function

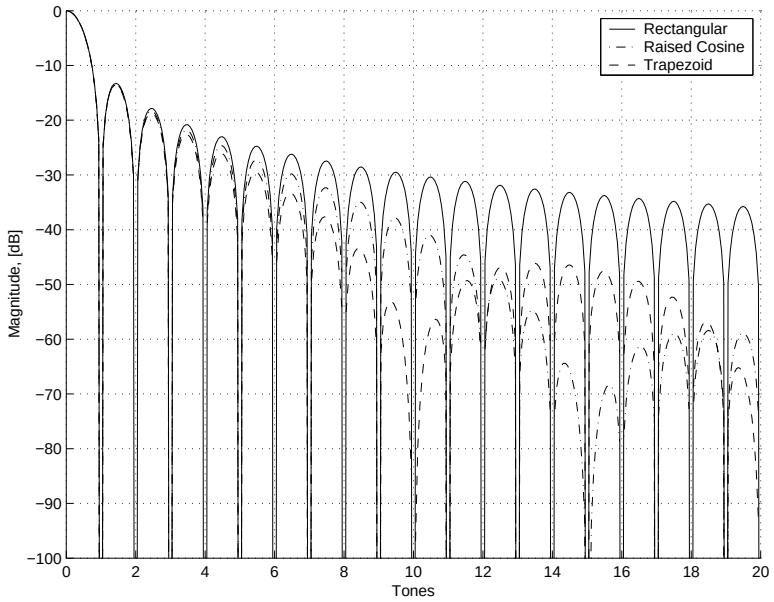

Figure 2.6: DFT sidelobes and the effect of windowing on the DFT sidelobes.

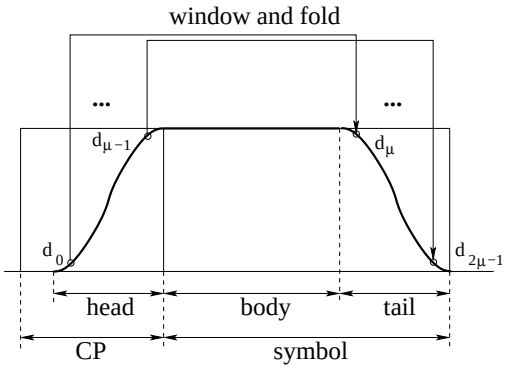

Figure 2.7: Window and fold operation on a DMT symbol.

extends beyond the N samples of the symbol but within the CP of the symbol, see **Fig. 2.7**. The window consists of a head, a body and a tail. The last μ samples of the CP are multiplied with the head of the window function $\mathbf{d}_h = [d_0 \dots d_{\mu-1}]^T$, e.g. with a raised cosine shape. The last μ samples of the actual symbol are multiplied with the tail of the window $\mathbf{d}_t = [d_\mu \dots d_{2\mu-1}]^T$. The body is kept equal to unity. Before taking the DFT, the first μ samples are folded back to the last μ samples to obtain a symbol of length N. To

maintain the DMT orthogonality the head and the tail are designed to be complementary, i.e. $d_l + d_{l+\mu} = 1$, for $l = 0, \ldots, \mu - 1$. Due to the CP of the DMT symbols, the window-and-fold operation is equivalent to the use of a conventional rectangular window in the noiseless case. It should be remarked that the part of the prefix used for windowing can overlap with the part of the prefix used to cope with ISI. In theory, this destroys the DMT orthogonality, but in Chapter 4 we will show how to design the window function in order to deal with this effect.

Note that windowing will help to obtain high spectral containment in general, cf. **Fig. 2.6**, not only for RFI. Receiver windowing reduces spectral leakage from crosstalk signals, narrowband interference and often even ICI, thereby improving the system's performance. Receiver windowing is not commonly used in ADSL but will be adopted in the DMT-based VDSL standard. Also for ADSL, the use of windowing functions is important in order to improve performance, as will be shown in Chapter 4.

2.2.4 Bit loading

An important aspect of DMT is the fact that it uses an optimized frequency division allocation of energy and bits to maximize the achievable data rates that can be transmitted over bandlimited channels. Every used tone can transmit a different number of bits and energy depending on the available SNR on this tone and the desired bit error rate. During startup of the modem, the receiver measures the quality of the signals received on each tone. The receiver computes the optimal bit and energy distribution over the tones and reports this information to the transmitter [63]. Bit loading has some important advantages:

- Due to line conditions that differ from user to user, the modem is able to adapt itself to different line characteristics in order to maximize the transmitted data rate. The information and spectral distribution is tailored to the channel attenuation and noise characteristics. Typically, the more attenuated higher frequencies carry less information than the lower frequencies. The optimal solution to this problem is referred to as *single user water filling*.

- Multiple DSL lines in a binder can alter their transmit spectra to reduce the overall crosstalk in the binder. This allows multiple DSL lines in a binder to enhance the spectral compatibility. The optimal solution to obtain the best spectra remains an unsolved problem in information theory today. However, *iterative water filling* can be close to optimum [169].

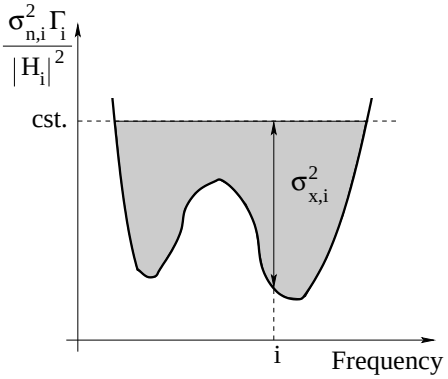

Figure 2.8: Graphical representation of the water filling solution.

Single user water filling and bit loading

Optimal line adaptation requires that the number of bits that can be transmitted over a certain line is maximized with respect to the transmitted power on each tone. The power $\sigma_{x,i}^2$ on each tone can be varied subject to an overall power constraint P. If we assume that ISI is perfectly cancelled, we have

$$\max_{\sigma_{x,i}^2} \sum_i \log_2 \left(1 + \frac{\sigma_{x,i}^2 |H_i|^2}{\sigma_{n,i}^2 \Gamma_i}\right), \quad \text{subject to} \quad \sum_i \sigma_{x,i}^2 = P. \tag{2.28}$$

Using Lagrange multipliers, the power allocation problem can be written as

$$\max_{\sigma_{x,i}^2} \sum_i \log_2 \left(1 + \frac{\sigma_{x,i}^2 |H_i|^2}{\sigma_{n,i}^2 \Gamma_i}\right) + \lambda \left(\sum_i \sigma_{x,i}^2 - P\right). \tag{2.29}$$

Setting the derivative with respect to $\sigma_{x,i}^2$ equal to zero for each tone yields

$$\frac{1}{\ln 2} \frac{\sigma_{n,i}^2 \Gamma_i}{(\sigma_{n,i}^2 \Gamma_i + \sigma_{x,i}^2 |H_i|^2)} \frac{|H_i|^2}{\sigma_{n,i}^2 \Gamma_i} + \lambda = 0. \tag{2.30}$$

Taking the power constraint into account, the optimum transmit powers satisfy

$$\sigma_{x,i}^2 + \frac{\sigma_{n,i}^2 \Gamma_i}{|H_i|^2} = \text{constant}. \tag{2.31}$$

When $\Gamma_i = 1$, the solution of (2.31) comes down to a *water filling optimization*, where water is poured into the inverse of the 'channel-to-noise ratio' curve up to a certain level [71], see **Fig. 2.8**. The maximum level is determined by the overall power constraint and the areas below this level correspond to the optimal power distribution over the set of used tones. When $\Gamma_i \neq 1$ but equal for all the tones, the solution of (2.31) is also based on water filling, but now

over a scaled version of the 'channel-to-noise ratio' curve. Once the $\sigma_{x,i}^2$'s are known, the corresponding number of bits per tone can be allocated, hence the name *bit loading*. Clearly, tones with high $|H_i|^2/\sigma_{n,i}^2$ values will receive a larger amount of power and bits to be transmitted.

Since each modem only measures the channel and noise characteristics on its own line, the water filling procedure is performed independently across all DSL lines in a binder. Therefore, this type of water filling is simply called *single user water filling*.

In the literature, many loading algorithms have appeared. Without going into detail, different approaches can be distinguished [119]:

- One can maximize the number of bits per symbol subject to an overall power constraint [71]. The optimal solution is obtained by water filling, where the bit distribution b_i results in *non-integer* b_i values.
- Some authors are interested in *power minimization* for a fixed bit rate instead of bit rate maximization. The solution is again given by the water filling solution except that the maximum water level is now determined by the desired bit rate instead of an overall power constraint.
- Algorithms exist to compute bit allocations with *integer* b_i values [30][73]. Chow et al. suggest to compute the (suboptimal) bit distribution by rounding the bit loading obtained by an approximate water filling method and by adjusting the subchannel powers accordingly [30]. Optimum discrete loading is the solution of a greedy optimization. The basic concept is that each additional bit to be transmitted is placed on the tone that would require the least incremental power for its transport [16][19][20][58].

Example 2.5 In the G.DMT ADSL standard [63], bit loading is allowed subject to a power spectral density constraint. The standard defines spectral masks for upstream and downstream transmission since operators are concerned with the effects of emission from ADSL modems on other transmission systems or electronic devices. The spectral masks are nominally flat in the passband region but a limited gain scaling g_i per carrier is allowed for integer bit loading. The values of g_i are equal to zero or set within a range of 0.19 to 1.33 (=-14.5 dB to +2.5 dB). △

Iterative water filling

A new challenge for next generation DSL systems is to take into account the multi-user aspects of a DSL transmission environment [18][120]. Since several DSL systems share the same binder cable, the high transmit energy on one line may cause severe crosstalk interference on neighbouring lines. At present,

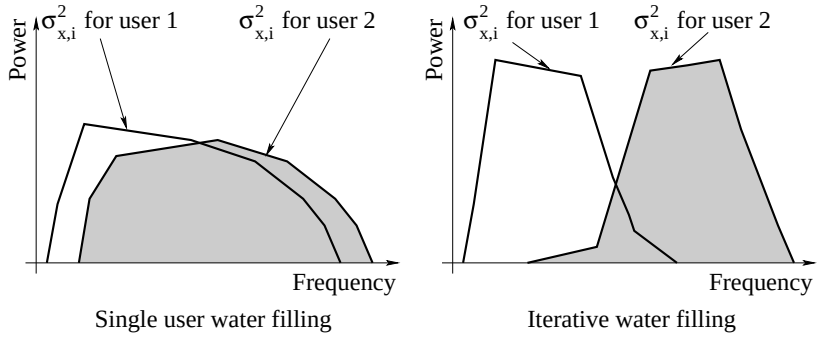

Figure 2.9: Transmit spectra for two users after single user water filling and iterative water filling respectively.

each DSL modem operates independently without considering its own crosstalk emission. Since crosstalk is handled as additional noise, the performance of the whole binder will be strongly limited.

Iterative water filling enables DSL transceivers to automatically optimize their transmit spectra with respect to the channel while limiting the harm to other DSL systems [169], see **Fig. 2.9**. The iterative water filling procedure works as follows: with a fixed total power constraint for each user, the first user updates its power allocation by deriving a single user water filling spectrum while regarding all other user's crosstalk as additive noise. Then, single user water filling is successively applied to the second user, the third user, etc., then applied again to the first user, second user, etc., until convergence. The resulting spectrum allocation is in general much better than the allocation obtained with the current single user water filling.

2.3 Data model

In this section, the data model and corresponding notation that will be used throughout this thesis will be given. Since the symbol rate at the transmit and receive side of a DMT-based system is equal, larger (smaller) DFT sizes will result in higher (lower) sampling rates. Depending on the IDFT and DFT sizes at the transmitter and receiver respectively, the transmission system can either be a single rate or a multi-rate system. In Subsection 2.3.1, we will first introduce the basic data model with equal transmit IDFT and receive DFT size. When echo is present in the system (cf. Chapter 5 and Chapter 6), the modem can have a multi-rate structure. Hence, interpolated and decimated modem structures are discussed in Subsection 2.3.2. In Chapter 4, optimal receiver windowing combined with equalization will be treated. Therefore,

the basic data model extended with equalization and windowing is given in Subsection 2.3.3. The different data models are mostly based on [129] and [136].

2.3.1 Basic data model, symmetric setup

In this subsection, we will introduce the basic data model where the transmit IDFT and receive DFT size are both equal to N. Consequently, the sampling rate at both sides is equal and given by F_s. When the CP is of length ν, the DMT-symbols have length $s = N+\nu$ and are transmitted at a rate $F_s/(N+\nu)$. In Subsection 2.2.1, we started from a data model with two successive symbols, thereby assuming that the channel had a zero group delay. When the group delay is non-zero, the data model in (2.13) can be generalized using three successive symbols to model the ISI and ICI correctly.

The samples obtained at the receiver can be described as

$$\begin{aligned}
\underbrace{\begin{bmatrix} y^k_{-T+1} \\ \vdots \\ y^k_{N-1} \end{bmatrix}}_{\mathbf{y}^k} &= \underbrace{\left[\begin{array}{c|ccc|c} & \boxed{\mathbf{h}} & 0 & \cdots & \\ \mathbf{0}_{(1)} & & \ddots & \ddots & \mathbf{0}_{(2)} \\ & 0 & \cdots & \boxed{\mathbf{h}} & \end{array}\right]\begin{bmatrix} \mathbf{P}_N\mathcal{I}_N & \mathbf{0} & \mathbf{0} \\ \mathbf{0} & \mathbf{P}_N\mathcal{I}_N & \mathbf{0} \\ \mathbf{0} & \mathbf{0} & \mathbf{P}_N\mathcal{I}_N \end{bmatrix}}_{\mathbf{H}} \cdot \\
&\quad \underbrace{\begin{bmatrix} X^{k-1}_{0:N-1} \\ X^{k}_{0:N-1} \\ X^{k+1}_{0:N-1} \end{bmatrix}}_{\mathbf{X}^k} + \underbrace{\begin{bmatrix} n^k_{-T+1} \\ \vdots \\ n^k_{N-1} \end{bmatrix}}_{\mathbf{n}^k}, \\
&= \mathbf{H}_{N+i}X^k_i + \bar{\mathbf{H}}\bar{\mathbf{X}}^k + \mathbf{n}^k, \qquad (2.32)
\end{aligned}$$

where

- the superscript k and the index i denote the symbol period and the tone index respectively, T is the equalizer length,
- $y^k_l = y((ks+l+\nu)T_s)$ and $n^k_l = n((ks+l+\nu)T_s), l = -T+1, \ldots, N-1$, with $y(t)$ given by (2.5),
- $\mathbf{h}$ is the FIR channel impulse response of length N with its coefficients in reverse order,
- $X^k_{0:N-1} = [X^k_0 \ldots X^k_i \ldots X^k_{N-1}]^T$ is the transmitted QAM frequency domain symbol of length N, transmitted at time k such that the IDFT output is real valued, i.e. $X^k_i = (X^k_{N-i})^*$ for $i = 1, \ldots, N-1$,
- X^k_i denotes the symbol of interest, $\mathbf{H}_{N+i}$ denotes the $(N+i+1)$-th column of $\mathbf{H}$, i.e. $\mathbf{H}_{N+i} = \mathbf{H}[:, N+i+1]$, $\bar{\mathbf{H}}$ is equal to $\mathbf{H}$ without its $(N+i+1)$-th column, $\bar{\mathbf{X}}^k$ is obtained by omitting X^k_i from $\mathbf{X}^k$,

- $\mathbf{n}^k$ is the additive channel noise,
- the frequency domain symbols are transformed to the time domain, by means of $\mathcal{I}_N$, and the CP is added by $\mathbf{P}_N$ defined in (2.11).

Typical DSL channels, which include the transmit filters, the receive filters and the actual loop, can be modeled as FIR channels with a length that is limited to the duration of one symbol. Thus, sampled at the sampling rate F_s, $\mathbf{h}$ is completely determined by N samples. When the group delay of the channel is equal to Δ_1, $\mathbf{h}$ is given by

$$\mathbf{h} \quad = \quad [h_L \ \ldots \ h_1 \ h_0 \ h_{-1} \ \ldots \ h_{-\Delta_1}], \tag{2.33}$$

with $\Delta_1 + L + 1 = N$. The delay Δ_1 is computed by determining the $\nu + 1$ successive samples $[h_\nu \ \ldots \ h_0]$ with maximum energy. Since Δ_1 is only a rough estimate of the group delay, the receiver has the flexibility to choose a decision delay δ_1 relative to Δ_1 to maximize the performance. Hence, δ_1 is a design parameter. The matrices $\mathbf{0}_{(1)}$ and $\mathbf{0}_{(2)}$ are zero matrices of size $(N + T - 1) \times (2\nu - T + \Delta_1 + \delta_1 + 2)$ and $(N + T - 1) \times (N + \nu - \Delta_1 - \delta_1)$ respectively and take into account the overall delay $\Delta_1 + \delta_1$. Clearly, when $T > 2\nu + \Delta_1 + \delta_1 + 2$ an additional symbol $X^{k-2}_{0:N-1}$ has to be included in the model.

2.3.2 Data model with echo

Symmetric setup

When echo is present in the system, the echo can be modeled in the same way as the far end signal. The resulting model will be used in Chapter 5 and Chapter 6. We first assume a symmetric DSL setup with equal DFT/IDFT size N for up- and downstream. The received echo signal is modeled as a linear convolution of $\mathbf{h}_E$ with cyclic prefixed echo reference symbols. The overall received signal is then given by

$$\underbrace{\begin{bmatrix} y^k_{-T+1} \\ \vdots \\ y^k_{N-1} \end{bmatrix}}_{\mathbf{y}^k} = \underbrace{\left[\begin{array}{c|ccc|c} \mathbf{0}_{(1)} & \boxed{\mathbf{h}} & 0 & \cdots & \\ & \ddots & \ddots & & \mathbf{0}_{(2)} \\ & 0 & \cdots & \boxed{\mathbf{h}} & \end{array}\right]}_{\mathbf{H}} \hat{\mathbf{P}}_N \hat{\mathcal{I}}_N \underbrace{\begin{bmatrix} X^{k-1}_{0:N-1} \\ X^{k}_{0:N-1} \\ X^{k+1}_{0:N-1} \end{bmatrix}}_{\mathbf{X}^k} +$$

$$\underbrace{\left[\begin{array}{c|ccc|c} \mathbf{0}_{(3)} & \boxed{\mathbf{h}_E} & 0 & \cdots & \\ & \ddots & \ddots & & \mathbf{0}_{(4)} \\ & 0 & \cdots & \boxed{\mathbf{h}_E} & \end{array}\right]}_{\mathbf{H}_E} \hat{\mathbf{P}}_N \hat{\mathcal{I}}_N \underbrace{\begin{bmatrix} U^{k-1}_{0:N-1} \\ U^{k}_{0:N-1} \\ U^{k+1}_{0:N-1} \end{bmatrix}}_{\mathbf{U}^k} +$$

$$\underbrace{\begin{bmatrix} n_{-T+1} \\ \vdots \\ n_{N-1} \end{bmatrix}}_{\mathbf{n}^k},$$

$$= \mathbf{H}_{N+i} X_i^k + \bar{\mathbf{H}} \bar{\mathbf{X}}^k + \mathbf{H}_E \mathbf{U}^k + \mathbf{n}^k, \tag{2.34}$$

where

- $\mathbf{h}_E$ is the FIR echo channel impulse response of length N with its coefficients in reverse order,
- $\hat{\mathbf{P}}_N$ and $\hat{\mathcal{I}}_N$ are block diagonal matrices, i.e. $\hat{\mathbf{P}}_N = \text{diag}\{\mathbf{P}_N, \mathbf{P}_N, \mathbf{P}_N\}$ and $\hat{\mathcal{I}}_N = \text{diag}\{\mathcal{I}_N, \mathcal{I}_N, \mathcal{I}_N\}$,
- $U_{0:N-1}^k = [U_0^k \dots U_i^k \dots U_{N-1}^k]^T$ is the transmitted, QAM modulated echo frequency domain symbol of length N, transmitted at time k with $U_i^k = (U_{N-i}^k)^*$ for $i = 1, \dots, N-1$,
- X_i^k is the (far end) symbol of interest.

Furthermore, the definitions of Subsection 2.3.1 still apply. The group delay Δ_2 of the echo channel is obtained in a similar way as Δ_1. Again one can determine a delay δ_2 relative to Δ_2. Here, δ_2 represents the misalignment between the received far end and echo symbols (see Chapter 5), since both symbols will arrive at different time instants at the receiver. The matrices $\mathbf{0}_{(1)}$, $\mathbf{0}_{(2)}$, $\mathbf{0}_{(3)}$ and $\mathbf{0}_{(4)}$ are zero matrices of size $(N+T-1) \times (2\nu - T + \Delta_1 + \delta_1 + 2)$, $(N+T-1) \times (N + \nu - \Delta_1 - \delta_1)$, $(N+T-1) \times (2\nu - T + \Delta_2 + \delta_2 + 2)$ and $(N+T-1) \times (N + \nu - \Delta_2 - \delta_2)$ respectively.

When echo canceling is applied, $\mathbf{h}_E$ will be estimated and convolved with the echo reference symbols to emulate the received echo. The input to the echo canceler is then given by

$$\mathbf{u}^k = [\mathbf{0}_{(5)} | \mathbf{I}_{N+T_E-1} | \mathbf{0}_{(6)}] \hat{\mathbf{P}}_N \hat{\mathcal{I}}_N \mathbf{U}^k, \tag{2.35}$$

where T_E corresponds to the number of echo canceler taps and $\mathbf{0}_{(5)}$, $\mathbf{0}_{(6)}$ are zero matrices of size $(N+T_E-1) \times (N+2\nu-T_E+\delta_3+1)$ and $(N+T_E-1) \times (N+\nu-\delta_3)$ respectively. Since the echo canceler tries to model the true echo channel $\mathbf{h}_E$ (of length N) with $T_E \leqslant N$ taps, the delay δ_3 is introduced to determine the samples of the echo channel that will be modeled.

Interpolated setup

In ADSL, the upstream and downstream data rates are asymmetric, leading to different sampling rates for each direction. In the *RT modem*, for instance,

the transmit IDFT (size N) is κ times smaller than the receive DFT (size κN). Note that we assume here that the far end IDFT (at CO) has equal size as the receive DFT (at RT). As a consequence, the echo signal is transmitted at a low sampling rate and received at a high rate. To take into account this multi-rate system, the echo signal needs to be interpolated. The data model with interpolated echo is given by

$$\underbrace{\begin{bmatrix} y^k_{-T+1} \\ \vdots \\ y^k_{\kappa N-1} \end{bmatrix}}_{\mathbf{y}^k} = \underbrace{\left[\begin{array}{c|ccc|c} \mathbf{0}_{(1)} & \boxed{\mathbf{h}} & 0 & \cdots & \\ & \ddots & \ddots & & \mathbf{0}_{(2)} \\ & 0 & \cdots & \boxed{\mathbf{h}} & \end{array}\right] \hat{\mathbf{P}}_{\kappa N} \hat{\mathcal{I}}_{\kappa N}}_{\mathbf{H}} \underbrace{\begin{bmatrix} X^{k-1}_{0:\kappa N-1} \\ X^{k}_{0:\kappa N-1} \\ X^{k+1}_{0:\kappa N-1} \end{bmatrix}}_{\mathbf{X}^k} +$$

$$\underbrace{\left[\begin{array}{c|ccc|c} \mathbf{0}_{(3)} & \boxed{\mathbf{h}_E} & 0 & \cdots & \\ & \ddots & \ddots & & \mathbf{0}_{(4)} \\ & 0 & \cdots & \boxed{\mathbf{h}_E} & \end{array}\right] \hat{\mathbf{P}}^{\text{int}}_{N} \hat{\mathcal{I}}_{N}}_{\mathbf{H}^{\text{int}}_E} \underbrace{\begin{bmatrix} U^{k-1}_{0:N-1} \\ U^{k}_{0:N-1} \\ U^{k+1}_{0:N-1} \end{bmatrix}}_{\mathbf{U}^k} +$$

$$\underbrace{\begin{bmatrix} n_{-T+1} \\ \vdots \\ n_{\kappa N-1} \end{bmatrix}}_{\mathbf{n}^k}, \tag{2.36}$$

where the received symbol is now of length $\kappa N + T - 1$ and where the echo channel $\mathbf{h}_E$, and hence also Δ_2, are at receiver rate (high rate). The matrix $\hat{\mathbf{P}}^{\text{int}}_N$ performs the cyclic prefixing together with the upsampling to receiver rate and is given by

$$\hat{\mathbf{P}}^{\text{int}}_N = \mathbf{I}_{3\kappa N}[:, 1:\kappa:3\kappa N]\text{diag}\{\mathbf{P}_N, \mathbf{P}_N, \mathbf{P}_N\}, \tag{2.37}$$

where $\mathbf{I}_{3\kappa N}$ is the unity matrix of size $3\kappa N \times 3\kappa N$ and where $\mathbf{P}_N$ adds the CP of length ν at low rate. The matrices $\mathbf{0}_{(1)}$, $\mathbf{0}_{(2)}$, $\mathbf{0}_{(3)}$ and $\mathbf{0}_{(4)}$ are now of size $(\kappa N + T - 1) \times (2\kappa\nu - T + \Delta_1 + \delta_1 + 2)$, $(\kappa N + T - 1) \times (\kappa N + \kappa\nu - \Delta_1 - \delta_1)$, $(\kappa N + T - 1) \times (2\kappa\nu - T + \Delta_2 + \delta_2 + 2)$ and $(\kappa N + T - 1) \times (\kappa N + \kappa\nu - \Delta_2 - \delta_2)$ respectively. Note that the echo channel will act as an interpolation filter. Since this interpolation filter is not perfect, the received echo signal will be replicated over the entire receive bandwidth.

Decimated setup

When the transmit IDFT (size κN) is κ times larger than the receive DFT (size N), the echo signal will be decimated. This is typically the case in the ADSL *CO modem*, where the downstream bandwidth in the transmit direction is κ times larger than the upstream bandwidth in the receive direction. Again

we assume that the far end IDFT (at RT) has equal size as the receive DFT (at CO).

The data model with decimated echo can be written as

$$\underbrace{\begin{bmatrix} y^k_{-T+1} \\ \vdots \\ y^k_{N-1} \end{bmatrix}}_{\mathbf{y}^k} = \underbrace{\left[\begin{array}{c|ccc|c} \mathbf{0}_{(1)} & \boxed{\mathbf{h}} & 0 & \cdots & \\ & \ddots & \ddots & & \mathbf{0}_{(2)} \\ & 0 & \cdots & \boxed{\mathbf{h}} & \end{array}\right] \hat{\mathbf{P}}_N \hat{\mathcal{I}}_N}_{\mathbf{H}} \underbrace{\begin{bmatrix} X^{k-1}_{0:N-1} \\ X^k_{0:N-1} \\ X^{k+1}_{0:N-1} \end{bmatrix}}_{\mathbf{X}^k} +$$

$$\underbrace{\mathbf{D}\left[\begin{array}{c|ccc|c} \mathbf{0}_{(3)} & \boxed{\mathbf{h}_E} & 0 & \cdots & \\ & \ddots & \ddots & & \mathbf{0}_{(4)} \\ & 0 & \cdots & \boxed{\mathbf{h}_E} & \end{array}\right] \hat{\mathbf{P}}_{\kappa N} \hat{\mathcal{I}}_{\kappa N}}_{\mathbf{H}^{\text{dec}}_E} \underbrace{\begin{bmatrix} U^{k-1}_{0:\kappa N-1} \\ U^k_{0:\kappa N-1} \\ U^{k+1}_{0:\kappa N-1} \end{bmatrix}}_{\mathbf{U}^k} +$$

$$\underbrace{\begin{bmatrix} n_{-T+1} \\ \vdots \\ n_{N-1} \end{bmatrix}}_{\mathbf{n}^k}, \tag{2.38}$$

where the received symbol is now of length $N+T-1$ at low rate and where the echo channel $\mathbf{h}_E$, and hence also Δ_2, are at echo transmit rate (high rate). The matrix $\mathbf{D}$ performs the decimation at the receiver

$$\mathbf{D} = \mathbf{I}_{3\kappa N}[1:\kappa:3\kappa N, :], \tag{2.39}$$

where $\mathbf{I}_{3\kappa N}$ is the unity matrix of size $3\kappa N \times 3\kappa N$. The matrices $\mathbf{0}_{(1)}$, $\mathbf{0}_{(2)}$, $\mathbf{0}_{(3)}$ and $\mathbf{0}_{(4)}$ are now of size $(N+T-1)\times(2\nu-T+\Delta_1+\delta_1+2)$, $(N+T-1)\times(N+\nu-\Delta_1-\delta_1)$, $(\kappa N+\kappa T-\kappa)\times(2\kappa\nu-\kappa T+\Delta_2+\delta_2+\kappa+1)$ and $(\kappa N+\kappa T-\kappa)\times(\kappa N+\kappa\nu-\Delta_2-\delta_2)$ respectively. Note that the echo channel will act as an imperfect decimation filter, resulting in an aliased echo signal at the receiver.

2.3.3 Data model for TEQ and receiver windowing

When TEQ and windowing is applied at the receiver, a $N+\mu+T-1$ length vector of received samples is required, where μ and T are the window and equalizer length respectively. Therefore, the basic data model of (2.32) has to be extended as follows

$$\underbrace{\begin{bmatrix} y^k_{-\mu-T+1} \\ \vdots \\ y^k_{N-1} \end{bmatrix}}_{\mathbf{y}^{ext,k}} = \underbrace{\left[\begin{array}{c|ccc|c} \mathbf{0}_{(1)} & \boxed{\mathbf{h}} & 0 & \cdots & \\ & \ddots & \ddots & & \mathbf{0}_{(2)} \\ & 0 & \cdots & \boxed{\mathbf{h}} & \end{array}\right] \hat{\mathbf{P}}_N \hat{\mathcal{I}}_N}_{\mathbf{H}^{ext}} \underbrace{\begin{bmatrix} X^{k-1}_{0:N-1} \\ X^k_{0:N-1} \\ X^{k+1}_{0:N-1} \end{bmatrix}}_{\mathbf{X}^k} +$$

$$\underbrace{\begin{bmatrix} n^k_{-\mu-T+1} \\ \vdots \\ n^k_{N-1} \end{bmatrix}}_{\mathbf{n}^{ext,k}},$$

$$= \mathbf{H}^{ext}_{N+i} X^k_i + \bar{\mathbf{H}}^{ext} \bar{\mathbf{X}}^k + \mathbf{n}^{ext,k}, \tag{2.40}$$

where similar definitions hold as for (2.32) and where the echo component is not explicitly modeled. The matrices $\mathbf{0}_{(1)}$ and $\mathbf{0}_{(2)}$ are now zero matrices of size $(N+\mu+T-1)\times(2\nu-\mu-T+\Delta_1+\delta_1+2)$ and $(N+\mu+T-1)\times(N+\nu-\Delta_1-\delta_1)$ respectively.

Define $\mathbf{Y}^{ext,k}$ as a Toeplitz matrix (of size $(N+\mu)\times T$) of received samples

$$\mathbf{Y}^{ext,k} = \begin{bmatrix} y^k_{-\mu} & \cdots & y^k_{-\mu-T+1} \\ \vdots & \ddots & \vdots \\ y^k_{N-1} & \cdots & y^k_{N-T} \end{bmatrix}, \tag{2.41}$$

and $\mathbf{Y}^k$ as the N last rows of $\mathbf{Y}^{ext,k}$. When $\mathbf{w} = [w_0 \ \ldots \ w_{T-1}]^T$ denotes a TEQ of T taps, convolution with a TEQ can now easily be represented by $\mathbf{Y}^{ext,k}\mathbf{w}$. Receiver windowing, as discussed in Subsection 2.2.3, multiplies the last μ samples of the CP with a window function $\mathbf{d} = [d_0 \ \ldots \ d_{\mu-1}]^T$ and adds them to the last μ samples of the incoming DMT symbol, which are multiplied by $1-\mathbf{d}$ (fold operation). These window and fold operations are equivalent to the multiplication of the received samples with a matrix $\mathbf{\Omega}$ of size $N\times(N+\mu)$

$$\mathbf{\Omega} = \begin{bmatrix} \mathbf{0}_{(N-\mu)\times\mu} & \mathbf{I}_{N-\mu} & \mathbf{0}_{(N-\mu)\times\mu} \\ \mathrm{diag}(\mathbf{d}) & \mathbf{0}_{\mu\times(N-\mu)} & \mathbf{I}_\mu - \mathrm{diag}(\mathbf{d}) \end{bmatrix}, \tag{2.42}$$

$$= \underbrace{\begin{bmatrix} \mathbf{0} & \mathbf{I}_{N-\mu} & \mathbf{0} \\ \mathbf{0} & \mathbf{0} & \mathbf{I}_\mu \end{bmatrix}}_{\mathbf{\Omega}_1} + \underbrace{\begin{bmatrix} \mathbf{0} & \mathbf{0} & \mathbf{0} \\ \mathrm{diag}(\mathbf{d}) & \mathbf{0} & -\mathrm{diag}(\mathbf{d}) \end{bmatrix}}_{\mathbf{\Omega}_2}, \tag{2.43}$$

where $\mathrm{diag}(\mathbf{d})$ represents a diagonal matrix with the elements of $\mathbf{d}$ on its diagonal. The time domain vector of length N at time k that is fed to the N-point DFT after windowing and TEQ filtering is now the result of the product $\mathbf{\Omega}\mathbf{Y}^{ext,k}\mathbf{w}$. Windowing without TEQ filtering is represented by $\mathbf{\Omega}\mathbf{Y}^{ext,k}[:,1]$, while TEQ filtering without windowing is given by $\mathbf{Y}^k\mathbf{w} = \mathbf{\Omega}_1\mathbf{Y}^{ext,k}\mathbf{w}$.

2.4 Conclusions

In this chapter we introduced the basic concepts and notation that will be used throughout this thesis. Starting from Shannon's capacity formulas for AWGN channels in Section 2.1, we explained in Section 2.2 how DMT modulation

is able to convert an ISI channel into a large number of narrowband AWGN subchannels. As a result, DMT is able to approximate Shannon's capacity and is therefore adopted in many DSL standards.

As discussed in Subsection 2.2.1, DMT uses a DFT-based block transmission scheme where a CP is added to mitigate ISI. When the channel order is shorter than the CP, every subchannel or tone is scaled and rotated in phase due to the channel. This can easily be compensated by a one tap FEQ to perform a complex scalar multiplication per tone. When the channel order exceeds the CP, a TEQ filter is required to shorten the channel. This is reflected in the transmitter and receiver structure given in Subsection 2.2.2. In Subsection 2.2.3 we briefly explained how the addition of windowing at the receiver is able to improve the spectral containment of the demodulating DFT. In Subsection 2.2.4 the principles of bit loading were given. Bit loading is an important aspect of DMT to optimally allocate power and bits per tone in order to maximize the achievable data rate.

Finally, the data model that will be used throughout this thesis was given in Section 2.3. After introducing the basic data model for a DSL transmission system, the data model was extended in Subsection 2.3.2 to model echo noise and in Subsection 2.3.3 to add equalization and receiver windowing.

Chapter 3

Equalizer design: a unified approach

IN DMT modulation, an elegant equalization method relies on inserting a CP in between the transmitted symbols [16][98]. When the order of the channel impulse response is confined to the CP length, perfect equalization is achieved by means of a bank of *one-tap frequency domain equalizers (FEQ)*. However, when the time span of the channel impulse response is longer than the CP, which is e.g. the case for ADSL modems, an additional *time domain equalizer (TEQ)* can be introduced before DFT demodulation to shorten the channel. This TEQ-FEQ equalization structure was discussed in Chapter 2.

The intriguing problems encountered in TEQ design are mainly due to the demodulating DFT. Since the TEQ is in front of the DFT, all frequency bins are equalized in the same way and the TEQ output can not be compared directly with the desired signal. Moreover, the bad spectral containment of the demodulating DFT imposes a difficult interference structure [100] and may lead to noise enhancement combined with 'noise pick-up' from out-of-band noise.

In the DSL context, the ultimate goal of TEQ design is to maximize the bit rate of the communication system. TEQ design has inspired many researchers since true bit rate optimization leads to a highly non-linear optimization problem. Hence, simplified procedures are resorted to. Alternatively, one could consider a bank of TEQ equalizers, one for each subcarrier or tone. This type of equalizers is referred to as per tone equalizers (PTEQ). Although the equalizer design could also be generalized to the multiple-input, multiple-output (MIMO) case as in the wireless context [2][14][74][75], we will restrict ourselves to the single-input, single-output (SISO) transmission model.

This chapter presents an overview of the different equalizer design algorithms.

Two main contributions are included in this chapter:

- The goal of this chapter is to provide a *unified mathematical framework* and a *unified notation* for different equalizer designs, including a *unified evaluation* in terms of performance. Despite the variety of equalizer algorithms, almost all approaches have a common formulation: *the maximization of a product of generalized Rayleigh quotients*. This will be discussed in Section 3.1. Sections 3.2, 3.3 and 3.4 show how many equalizer algorithms are in fact special cases of the common formulation. Exceptions to the common formulation are treated in Section 3.5 and simulation results and conclusions are given in Sections 3.6 and 3.7 respectively.
- In Subsection 3.2.1 the Minimum Mean Square Error (MMSE) TEQ design criterion is reviewed as a special case of the common formulation. Although this criterion does not optimize bit rate, it is often used in practice. MMSE TEQ design requires a non-triviality constraint to avoid the trivial all-zero solution. In Subsection 3.2.1 we show that the MMSE TEQ solutions for a unit-energy constraint on the received signal, a unit-energy constraint on the signal of interest and both constraints together are equal (up to a scale factor). As a consequence, the achieved bit rates will be the same. In addition, we provide a geometrical interpretation and we devise a single iterative procedure for these unit-energy MMSE designs.

3.1 Common formulation

There are many ways of designing a DMT equalizer, depending on how the optimization problem is posed. However, despite the variety of algorithms and structures, almost all of the algorithms fit into a common formulation: the maximization of a product of generalized Rayleigh quotients, given by

$$\mathbf{w}_{opt} = \arg\max_{\mathbf{w}} \prod_{i=1}^{M} \frac{\mathbf{w}^T \mathbf{B}_i \mathbf{w}}{\mathbf{w}^T \mathbf{A}_i \mathbf{w}}, \tag{3.1}$$

where $\mathbf{w}$ is the T-taps equalizer and the $T \times T$ matrices $\mathbf{A}_i$, $\mathbf{B}_i$ are design specific. This general cost function is non-linear and requires non-linear optimization techniques, like gradient descent, iterative (quasi-)Newton algorithms, simplex algorithms, etc. The difficulty is that there can be many locally optimal solutions that are not necessarily globally optimal. Interesting to note is that $\mathbf{w}_{opt}$ *in (3.1) is determined up to a scale factor*: a scaling of the equalizer will not alter the value of the generalized Rayleigh quotients. This is in correspondence with the performance in terms of bit rate, which is also scale invariant, since any scaling of $\mathbf{w}_{opt}$ will be compensated for by the one tap FEQs.

Example 3.1 TEQ algorithms that require to solve a problem like (3.1) are the geometric SNR (GSNR) method [6], the MBR method [10], Milosevic's TEQ [88], and the BM-TEQ method [144]. These algorithms will be briefly reviewed in Section 3.3. △

In general, the optimal solution of (3.1) is not given in closed form and therefore difficult to obtain. However, for the special case $M = 1$ one has

$$\mathbf{w}_{opt} = \arg\max_{\mathbf{w}} \frac{\mathbf{w}^T\mathbf{B}\mathbf{w}}{\mathbf{w}^T\mathbf{A}\mathbf{w}}. \tag{3.2}$$

Alternatively, one could minimize the inverse of the ratio in (3.2) to obtain the same solution, i.e.

$$\mathbf{w}_{opt} = \arg\min_{\mathbf{w}} \frac{\mathbf{w}^T\mathbf{A}\mathbf{w}}{\mathbf{w}^T\mathbf{B}\mathbf{w}}. \tag{3.3}$$

Whereas (3.1) requires non-linear optimization techniques to find the solution, (3.2) is much easier to solve. The problem in (3.2) is equivalent to the constrained optimization problem

$$\mathbf{w}_{opt} = \arg\max_{\mathbf{w}} \mathbf{w}^T\mathbf{B}\mathbf{w} \;\text{ subject to }\; \mathbf{w}^T\mathbf{A}\mathbf{w} = 1, \tag{3.4}$$

which is in fact a generalized eigenvalue problem (cf. Appendix A) of the form

$$\mathbf{B}\mathbf{w} = \lambda\mathbf{A}\mathbf{w}. \tag{3.5}$$

Here, one is interested in finding the generalized eigenvector of the matrix pair $(\mathbf{B}, \mathbf{A})$ corresponding to the largest generalized eigenvalue λ [53]. If $\mathbf{A}$ is invertible, the problem can be posed as an ordinary eigenvalue problem to find the 'largest' eigenvector of $\mathbf{A}^{-1}\mathbf{B}$. Alternatively, when $\mathbf{B}$ is invertible, the 'smallest' eigenvector of $\mathbf{B}^{-1}\mathbf{A}$ gives the desired solution. When $\mathbf{A}$ is symmetric and positive definite, another approach is to form the Cholesky decomposition $\mathbf{A} = \mathbf{A}^{T/2}\mathbf{A}^{1/2}$ (cf. Appendix A). With $\mathbf{v} = \mathbf{A}^{1/2}\mathbf{w}$, (3.5) reduces to

$$\underbrace{\mathbf{A}^{-T/2}\mathbf{B}\mathbf{A}^{-1/2}}_{\mathbf{C}}\mathbf{v} = \lambda\mathbf{v}, \tag{3.6}$$

where the eigenvector $\mathbf{v}_{opt}$ of $\mathbf{C}$ associated with the largest eigenvalue is computed. The equalizer is finally obtained as $\mathbf{w}_{opt} = \mathbf{A}^{-1/2}\mathbf{v}$. The problem in (3.6) requires $\mathbf{A}$ to be invertible. In some cases, $\mathbf{A}$ or $\mathbf{B}$ is the identity matrix, such that (3.5) leads to a traditional eigenvalue problem.

Since the problem in (3.2) can be formulated as finding the eigenvector belonging to the largest or smallest eigenvalue of an ordinary eigenvalue problem, efficient solution techniques can be applied, such as the power method, or inverse iteration, see Appendix A.4 for more details.

Example 3.2 Examples of TEQ designs of the form of (3.2) or (3.3) include the Minimum Mean Squared Error (MMSE) design [5][44], the Maximum Shortening SNR (MSSNR) design [83], the MSSNR with a symmetric TEQ constraint (Sym-MSSNR) [80], the Minimum Inter-Symbol-Interference (Min-ISI) design [10], the Minimum Delay Spread (MDS) design [106], and the Carrier Nulling Algorithm (CNA) [41]. △

A second special case of (3.1) appears when $M = 1$ and a separate equalizer $\mathbf{w}_i$ is designed for each used tone i, i.e.

$$\mathbf{w}_{i,opt} = \arg\max_{\mathbf{w}_i} \frac{\mathbf{w}_i^T \mathbf{B}_i \mathbf{w}_i}{\mathbf{w}_i^T \mathbf{A}_i \mathbf{w}_i} \quad \text{for} \quad i \in \mathcal{S}, \tag{3.7}$$

where $\mathcal{S}$ is the set of used tones and the matrices $\mathbf{A}_i$ and $\mathbf{B}_i$ are now tone dependent. This problem formulation is attractive since this bank of equalizers can effectively be optimized for each tone separately. For this equalizer flexibility an improved performance is expected with respect to (3.1). In addition, (3.7) is equivalent to solving a generalized eigenvalue problem per used tone, thereby circumventing the non-convex optimization problem of (3.2).

Example 3.3 Examples of the equalizer design method in (3.7) are the per tone equalizer (PTEQ) [129][135][136] and the TEQ filter banks (TEQ-FB) according to [88] and [144]. △

With the introduction of the common framework of (3.1) the goal is to show how almost all of the TEQ designs require similar solution techniques. The common framework also shows how the designs differ in terms of e.g. the number of Rayleigh quotients M and the choices of the matrices $\mathbf{A}_i, \mathbf{B}_i$. This allows for an increased understanding why the behaviour of the various designs can be distinctly different. The next four sections deal with the cases $M = 1$ for a single equalizer, $M > 1$ for a single equalizer, $M = 1$ for multiple equalizers and exceptions to the common rule, respectively. The various designs will be explained in detail and the similarities and differences will be expounded upon.

3.2 Single equalizer design with one Rayleigh quotient

In DMT transceivers a T-taps TEQ is typically used to *shorten* the effective channel impulse response. Although the underlying idea of channel shortening is not necessarily related to bit rate optimization, many researchers have devised single TEQ designs based on this idea. For more than a decade now, this

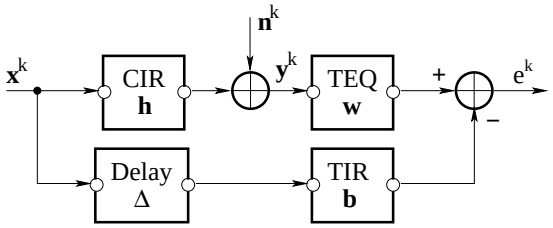

Figure 3.1: Block diagram used for MMSE channel shortening.

research has lead to an overwhelming number of publications and interestingly enough it appears that several design methods can be reformulated as the maximization of a single Rayleigh quotient, cf. (3.1) with $M = 1$. In this section these methods will be treated in more detail and advantages and disadvantages of each method will be discussed. In our survey, we will especially focus on MMSE TEQ design with unit-energy constraints for which some interesting properties will be derived.

3.2.1 Minimum mean square error (MMSE)

In the 1970s, Falconer et al. [44] introduced an MMSE method to shorten the impulse response of a communication channel for maximum likelihood (ML) receivers. Their objective was to design a filter prior to the Viterbi algorithm; a well known algorithm frequently used for ML data sequence estimation [71]. Since the complexity of the Viterbi algorithm increases exponentially with the length of the channel, this pre-filtering attempted to reduce the length of the overall channel to save complexity.

In the early nineties, Chow et al. [28] provided another dimension to the MMSE channel shortening problem by designing the 'pre-filter' for the purpose of time domain equalization in multicarrier systems. In [28], a finite and infinite length TEQ is computed to shorten the channel impulse response (CIR) to a $(\nu+1)$-taps target impulse response (TIR), where ν is the CP length. Here, we will mainly focus on the finite length case.

The idea behind MMSE TEQ design is depicted in **Fig. 3.1**. Define $\mathbf{x}^k = [x_l \ \ldots \ x_{l-\nu}]^T$ as a vector of $\nu+1$ consecutively transmitted time domain samples and $\mathbf{y}^k = [y_l \ \ldots \ y_{l-T+1}]^T$ as a vector of T received samples, where l is the sample index. The transmitted signal $\mathbf{x}^k$ is passed through the CIR $\mathbf{h}$ and is equalized by a T-taps TEQ $\mathbf{w} = [w_0 \ \ldots \ w_{T-1}]^T$. The equalizer output is compared with a delayed version of the input signal filtered by a $(\nu+1)$-taps TIR $\mathbf{b} = [b_0 \ \ldots \ b_\nu]^T$. The delay Δ is the decision delay and is given by $\Delta_1+\delta_1$, cf. Section 2.3.1. The difference e^k is then minimized in mean square sense with respect to the unknowns $\mathbf{w}$ and $\mathbf{b}$, i.e. the cost function can be expressed as

$$J(\mathbf{w},\mathbf{b}) = \mathcal{E}\{(e^k)^2\} = \mathcal{E}\{(\mathbf{w}^T\mathbf{y}^k - \mathbf{b}^T\mathbf{x}^{k-\Delta})^2\}, \quad (3.8)$$
$$= \mathbf{w}^T\mathbf{R}_{yy}\mathbf{w} + \mathbf{b}^T\mathbf{R}_{xx}\mathbf{b} - 2\mathbf{b}^T\mathbf{R}_{yx}(\Delta)^T\mathbf{w}, \quad (3.9)$$

where $\mathbf{R}_{xx} = \mathcal{E}\{\mathbf{x}^k(\mathbf{x}^k)^T\}$, $\mathbf{R}_{yy} = \mathcal{E}\{\mathbf{y}^k(\mathbf{y}^k)^T\}$ are the autocorrelation matrices of $\mathbf{x}^k$ and $\mathbf{y}^k$ respectively and $\mathbf{R}_{yx}(\Delta) = \mathbf{R}_{xy}^T(\Delta) = \mathcal{E}\{\mathbf{y}^k(\mathbf{x}^{k-\Delta})^T\}$ is the corresponding cross-correlation matrix which is a function of the delay parameter Δ. For the sake of compact notation we will use $\mathbf{R}_{yx}$ instead of $\mathbf{R}_{yx}(\Delta)$. The delay Δ is a design parameter and hence (3.9) should be solved for various Δ values to find the optimal solution. The trivial all zero solution for $\mathbf{w}$ and $\mathbf{b}$ can be avoided by adding a constraint [5][28][119][129][140][159], e.g. a unit-norm constraint $\mathbf{w}^T\mathbf{w} = 1$, $\mathbf{b}^T\mathbf{b} = 1$; a unit-tap constraint $\mathbf{e}_p^T\mathbf{w} = 1$, $\mathbf{e}_p^T\mathbf{b} = 1$; a unit-energy constraint $\mathbf{b}^T\mathbf{R}_{xx}\mathbf{b} = 1$, $\mathbf{w}^T\mathbf{R}_{yy}\mathbf{w} = 1$, etc., where $\mathbf{e}_p$ is the canonical vector with a 1 in the p-th position and zero elsewhere.

MMSE TEQ design is very popular since the cost function is quadratic and has a unique minimum. However, MMSE channel shortening is not equivalent to bit rate maximization, as desired in DSL. The impact of ICI generated by the demodulating DFT, for instance, is not taken into account. Therefore, the TEQ performance in terms of bit rate may be very unpredictable. Nevertheless, the MMSE optimization problem with various constraints can be cast into the general problem formulation of (3.2) with different $\mathbf{A}$ and $\mathbf{B}$ matrices depending on the constraint. This will be shown in the following subsections.

Unit-norm constraint on TEQ

Minimizing (3.9) subject to $\mathbf{w}^T\mathbf{w} = 1$ is equivalent to solving (3.2) with

$$\boxed{\begin{aligned} \mathbf{A} &= \mathbf{R}_{yy} - \mathbf{R}_{yx}\mathbf{R}_{xx}^{-1}\mathbf{R}_{xy}, \quad (3.10)\\ \mathbf{B} &= \mathbf{I}_T, \quad (3.11)\end{aligned}}$$

which can easily be shown using Lagrange multipliers, see Appendix B.1 for a proof. This problem definition is more commonly known as an eigenvalue problem where the optimal TEQ can be found as the eigenvector corresponding to the smallest eigenvalue of $\mathbf{A}$.

In [129][141][159], the unsatisfactory performance of MMSE TEQ design with $\mathbf{w}^T\mathbf{w} = 1$ was reported. Van Kerckhove et al. [141] showed that under this constraint the TEQ typically boosts 'out of band' noise, which leaks into the band of interest due to the bad spectral containment of the demodulating DFT. In order to concentrate the TEQ energy into the desired passband region, virtual (i.e. mathematical) noise can be injected into the stopband [141], using a modified $\mathbf{A}$ matrix:

$$\mathbf{A} = (\mathbf{R}_{yy} + \mu\mathbf{D}) - \mathbf{R}_{yx}\mathbf{R}_{xx}^{-1}\mathbf{R}_{xy}, \quad (3.12)$$

where μ controls the virtual noise level. The matrix $\mathbf{D}$ augments the noise level in the undesired frequency band, i.e.

$$\mathbf{D} = \frac{1}{N}\mathcal{F}_N[a:b,1:T]^H\mathcal{F}_N[a:b,1:T], \tag{3.13}$$

with $[a : b]$ a set of tones in the stopband. Consequently, the virtual noise forces the TEQ to suppress the corresponding frequencies and, as such, lowers the undesired enhancement of the actual channel noise. Note that the noise is virtual in the sense that it is present during TEQ design, but not during the filtering of the received signal.

Unit-norm constraint on TIR

A similar derivation can be made for MMSE TEQ design with $\mathbf{b}^T\mathbf{b} = 1$. When (3.2) is reformulated with $\mathbf{b}$ as unknown variables (instead of $\mathbf{w}$), one has to solve (3.2) with

$$\boxed{\begin{aligned} \mathbf{A} &= \mathbf{R}_{xx} - \mathbf{R}_{xy}\mathbf{R}_{yy}^{-1}\mathbf{R}_{yx}, \qquad (3.14)\\ \mathbf{B} &= \mathbf{I}_{\nu+1}, \qquad (3.15)\end{aligned}}$$

which can be proven similarly to Appendix B.1. After calculating the optimal $\mathbf{b}$, the TEQ can easily be retrieved by setting the gradient $\nabla_{\mathbf{w}}J$ equal to zero:

$$\begin{aligned} \nabla_{\mathbf{w}}J &= \mathbf{R}_{yy}\mathbf{w} - \mathbf{R}_{yx}\mathbf{b} = \mathbf{0}, \qquad (3.16)\\ \Rightarrow \mathbf{w}_{opt} &= \mathbf{R}_{yy}^{-1}\mathbf{R}_{yx}\mathbf{b}_{opt}. \qquad (3.17)\end{aligned}$$

Unit-tap constraint on TEQ

MMSE TEQ design with $\mathbf{e}_p^T\mathbf{w} = 1$ can be solved with (3.2) and

$$\boxed{\begin{aligned} \mathbf{A} &= \mathbf{R}_{yy} - \mathbf{R}_{yx}\mathbf{R}_{xx}^{-1}\mathbf{R}_{xy}, \qquad (3.18)\\ \mathbf{B} &= \mathbf{e}_p\mathbf{e}_p^T. \qquad (3.19)\end{aligned}}$$

A proof is given in Appendix B.2. From the eigenvalue problem in (3.5), it is easy to see that the optimal TEQ can be written in closed form as

$$\mathbf{w}_{opt} = \frac{\mathbf{A}^{-1}\mathbf{e}_p}{\mathbf{e}_p^T\mathbf{A}^{-1}\mathbf{e}_p}. \tag{3.20}$$

Unit-tap constraint on TIR

For a unit-tap constraint on $\mathbf{b}$, i.e. $\mathbf{e}_p^T\mathbf{b} = 1$, the same approach as for a unit-norm constraint on the TIR is used. Again, (3.2) can be reformulated with $\mathbf{b}$ as unknown variables (instead of $\mathbf{w}$) and

$$\boxed{\begin{aligned} \mathbf{A} &= \mathbf{R}_{xx} - \mathbf{R}_{xy}\mathbf{R}_{yy}^{-1}\mathbf{R}_{yx}, \\ \mathbf{B} &= \mathbf{e}_p\mathbf{e}_p^T, \end{aligned}} \quad \begin{matrix} (3.21) \\ (3.22) \end{matrix}$$

which can be proven similarly to Appendix B.2. Solving (3.2) with (3.21) and (3.22) leads to a closed form solution for $\mathbf{b}$

$$\mathbf{b}_{opt} = \frac{\mathbf{A}^{-1}\mathbf{e}_p}{\mathbf{e}_p^T\mathbf{A}^{-1}\mathbf{e}_p}. \tag{3.23}$$

From the optimal TIR, the TEQ can be obtained with (3.17).

Unit-energy constraints on TEQ and TIR

Here, we will investigate MMSE TEQ design subject to intuitively appealing unit-energy constraints and prove a number of interesting properties of the solution vectors. Consider the following cases

- case 1: $\min_{\mathbf{w}_1,\mathbf{b}_1} J(\mathbf{w}_1,\mathbf{b}_1)$ subject to $\mathbf{b}_1^T\mathbf{R}_{xx}\mathbf{b}_1 = 1$,
- case 2: $\min_{\mathbf{w}_2,\mathbf{b}_2} J(\mathbf{w}_2,\mathbf{b}_2)$ subject to $\mathbf{w}_2^T\mathbf{R}_{yy}\mathbf{w}_2 = 1$,
- case 3: $\min_{\mathbf{w}_3,\mathbf{b}_3} J(\mathbf{w}_3,\mathbf{b}_3)$ subject to $\mathbf{w}_3^T\mathbf{R}_{yy}\mathbf{w}_3 = 1$ and $\mathbf{b}_3^T\mathbf{R}_{xx}\mathbf{b}_3 = 1$,

where $J(\mathbf{w},\mathbf{b})$ is defined in (3.9). In Appendix B.3 the following remarkable properties for the optimal solutions are demonstrated:

$$\begin{aligned} \mathbf{w}_{1,opt} &= \sigma\mathbf{w}_{2,opt}, && (3.24)\\ \mathbf{b}_{1,opt} &= \sigma^{-1}\mathbf{b}_{2,opt}, && (3.25)\\ \mathbf{w}_{2,opt} &= \mathbf{w}_{3,opt}, && (3.26)\\ \mathbf{b}_{1,opt} &= \mathbf{b}_{3,opt}, && (3.27)\\ J_{min}(\mathbf{w}_{1,opt},\mathbf{b}_{1,opt}) &= J_{min}(\mathbf{w}_{2,opt},\mathbf{b}_{2,opt}) \leqslant J_{min}(\mathbf{w}_{3,opt},\mathbf{b}_{3,opt}), && (3.28) \end{aligned}$$

where σ is a scale factor and J_{min} denotes the MMSE value. Remarkably, *the three cases lead to the same TEQ coefficients up to a scale factor*. Hence, the performance in terms of achievable bit rates will be equal since the difference in scaling will be compensated for by the one tap FEQs. By this, we also illustrate that $\mathbf{w}_{3,opt}$ is not inferior to the two other solutions, despite its higher MMSE value.

In Appendix B.3 it is also shown that the unit-energy solutions $\mathbf{w}_{1,opt} = \sigma\mathbf{w}_{2,opt} = \sigma\mathbf{w}_{3,opt}$ can be obtained (up to a scalar) by taking the most dominant eigenvector of one and the same matrix, i.e. $\mathbf{Q} = \mathbf{R}_{yy}^{-1}\mathbf{R}_{yx}\mathbf{R}_{xx}^{-1}\mathbf{R}_{xy}$, or equivalently by solving (3.2) with

$$\boxed{\begin{aligned} \mathbf{A} &= \mathbf{I}_T, \qquad (3.29)\\ \mathbf{B} &= \mathbf{Q} = \mathbf{R}_{yy}^{-1}\mathbf{R}_{yx}\mathbf{R}_{xx}^{-1}\mathbf{R}_{xy}. \qquad (3.30) \end{aligned}}$$

This will lead to a unified iterative procedure to obtain the TEQ coefficients for the three cases.

Iterative procedure for MMSE TEQ with unit-energy constraints

To find the most dominant eigenvector of $\mathbf{Q}$, a simple iterative eigensolver could be used, see Appendix A.4. As the scaling factor between $\mathbf{w}_{1,opt}$ and $\mathbf{w}_{2,opt}$ is irrelevant in view of the obtained performance, the solution we actually select might as well be normalized, i.e. $\mathbf{w}_{opt} = \frac{\mathbf{w}_{1,opt}}{\|\mathbf{w}_{1,opt}\|} = \frac{\mathbf{w}_{2,opt}}{\|\mathbf{w}_{2,opt}\|}$. First, consider the *power method* to find the MMSE TEQ with a unit-energy constraint:

$$\begin{aligned} &\mathbf{w}^0 = \mathbf{w}_{init},\\ &\mathbf{Q} = \mathbf{R}_{yy}^{-1}\mathbf{R}_{yx}\mathbf{R}_{xx}^{-1}\mathbf{R}_{xy} = \underbrace{(\mathbf{R}_{yy}^{-1}\mathbf{R}_{yx})}_{\mathbf{Q}_1} \cdot \underbrace{(\mathbf{R}_{xx}^{-1}\mathbf{R}_{xy})}_{\mathbf{Q}_2},\\ &\text{for} \quad k = 1, 2, \ldots, N_{iter}\\ &\qquad \mathbf{w}^k = \mathbf{Q}\mathbf{w}^{k-1},\\ &\qquad \mathbf{w}^k = \mathbf{w}^k / \sqrt{(\mathbf{w}^k)^T\mathbf{w}^k},\\ &\text{end}\\ &\mathbf{w}_{opt} = \mathbf{w}^{N_{iter}}. \end{aligned} \qquad (3.31)$$

A similar procedure may be set up for the computation of $\mathbf{b}_{1,opt}$ and $\mathbf{b}_{2,opt}$, based on the matrix $\mathbf{R}_{xx}^{-1}\mathbf{R}_{yx}^T\mathbf{R}_{yy}^{-1}\mathbf{R}_{yx} = \mathbf{Q}_2\mathbf{Q}_1$. Consequently, the two procedures may then be combined as follows

$$\begin{aligned} &\mathbf{w}^0 = \mathbf{w}_{init},\\ &\mathbf{Q}_1 = \mathbf{R}_{yy}^{-1}\mathbf{R}_{yx},\\ &\mathbf{Q}_2 = \mathbf{R}_{xx}^{-1}\mathbf{R}_{xy},\\ &\text{for} \quad k = 1, 2, \ldots, N_{iter}\\ &\qquad \mathbf{b}^k = \mathbf{Q}_2\mathbf{w}^{k-1},\\ &\qquad \mathbf{w}^k = \mathbf{Q}_1\mathbf{b}^k,\\ &\qquad \mathbf{w}^k = \mathbf{w}^k / \sqrt{(\mathbf{w}^k)^T\mathbf{w}^k},\\ &\text{end}\\ &\mathbf{w}_{opt} = \mathbf{w}^{N_{iter}},\\ &\mathbf{b}_{opt} = \mathbf{b}^{N_{iter}}. \end{aligned} \qquad (3.32)$$

Since $\mathbf{R}_{xx}$ and $\mathbf{R}_{yy}$ are Toeplitz, inexpensive matrix inversion algorithms can be used, e.g. the Trench algorithm which has a quadratic complexity instead of a cubic complexity [53]. Moreover, if chip memory is limited, $\mathbf{R}_{yy}^{-1}$ (size $T \times T$) and $\mathbf{R}_{xx}^{-1}$ (size $(\nu+1) \times (\nu+1)$) do not have to be stored since they could be

recomputed (implicitly[1]) in every iteration. Of course computational complexity will increase leading to a trade-off of memory versus complexity. Finally, if the transmitted signal is assumed to be white, $\mathbf{R}_{xx}$ could be approximated by the identity matrix, thereby avoiding the computation of $\mathbf{R}_{xx}^{-1}$.

One of the drawbacks of the power method is that it can exhibit slow convergence when the largest and second largest eigenvalue are almost equal in magnitude. When a good estimate μ of the most dominant eigenvalue is available, applying *inverse iterations* might be more beneficial. Inverse iteration is in fact equivalent to the power method applied to $(\mathbf{Q} - \mu\mathbf{I}_T)^{-1}$, leading to

$$\begin{array}{l} \mathbf{w}^0 = \mathbf{w}_{init}, \\ \tilde{\mathbf{Q}} = \mathbf{R}_{yy}^{-1}\mathbf{R}_{yx}\mathbf{R}_{xx}^{-1}\mathbf{R}_{xy} - \mu\mathbf{I}_T, \\ \text{for} \quad k = 1, 2, \ldots, N_{iter} \\ \qquad \text{solve}\{\tilde{\mathbf{Q}}\mathbf{v}^k = \mathbf{w}^{k-1}\}, \\ \qquad \mathbf{w}^k = \mathbf{v}^k / \sqrt{(\mathbf{v}^k)^T\mathbf{v}^k}, \\ \text{end} \\ \mathbf{w}_{opt} = \mathbf{w}^{N_{iter}}. \end{array} \tag{3.33}$$

In the next section we will show that the eigenvalues of $\mathbf{Q}$ are upper bounded by one, such that $\mu = 1$ is an excellent choice to speed up convergence.

Geometrical interpretation of MMSE design with unit-energy constraints

MMSE TEQ design with unit-energy constraints gives rise to a nice geometrical interpretation based on the original data matrices of input and output samples. Let us define $\mathbf{X} \in \mathbb{R}^{M\times(\nu+1)}$ and $\mathbf{Y} \in \mathbb{R}^{M\times T}$ to be Toeplitz matrices, where each row corresponds to a set of consecutive (scaled[2]) input samples, $\frac{1}{\sqrt{M}}(\mathbf{x}^{k-\Delta})^T$, and (scaled) output samples, $\frac{1}{\sqrt{M}}(\mathbf{y}^k)^T$, respectively, where M represents the number of realizations of $\mathbf{x}^{k-\Delta}$ and $\mathbf{y}^k$. Now, one may rewrite[3] (3.9) as

$$\min_{\mathbf{w},\mathbf{b}} J(\mathbf{w},\mathbf{b}) = \min_{\mathbf{w},\mathbf{b}} \mathcal{E}\{((\mathbf{y}^k)^T\mathbf{w} - (\mathbf{x}^{k-\Delta})^T\mathbf{b})^2\}, \tag{3.34}$$

$$= \min_{\mathbf{w},\mathbf{b}} \mathbf{w}^T\mathbf{R}_{yy}\mathbf{w} + \mathbf{b}^T\mathbf{R}_{xx}\mathbf{b} - 2\mathbf{b}^T\mathbf{R}_{xy}\mathbf{w}, \tag{3.35}$$

$$\approx \min_{\mathbf{w},\mathbf{b}} \mathbf{w}^T\mathbf{Y}^T\mathbf{Y}\mathbf{w} + \mathbf{b}^T\mathbf{X}^T\mathbf{X}\mathbf{b} - 2\mathbf{b}^T\mathbf{X}^T\mathbf{Y}\mathbf{w}, \tag{3.36}$$

$$= \min_{\mathbf{w},\mathbf{b}} \|\mathbf{Y}\mathbf{w} - \mathbf{X}\mathbf{b}\|_2^2, . \tag{3.37}$$

[1] Instead of computing $\mathbf{b}^k = \mathbf{Q}_2\mathbf{w}^{k-1}$ and $\mathbf{w}^k = \mathbf{Q}_1\mathbf{b}^k$ in every iteration, it is less expensive to solve the sets of linear equations: $\mathbf{R}_{xx}\mathbf{b}^k = \mathbf{R}_{xy}\mathbf{w}^{k-1}$ and $\mathbf{R}_{yy}\mathbf{w}^i = \mathbf{R}_{yx}\mathbf{b}^k$.

[2] The scaling factor $\frac{1}{\sqrt{M}}$ is introduced to simplify the mathematical equations, but does not affect the generality of this discussion.

[3] It is assumed that input and output processes are ergodic and that M is sufficiently large such that correlation matrices can be replaced by the corresponding time averages.

This optimization problem indicates that we look for an exact intersection between the subspace, range($\mathbf{X}$) (see Appendix A), spanned by the columns of $\mathbf{X}$ and the subspace, range($\mathbf{Y}$), spanned by the columns of $\mathbf{Y}$. If there is no exact intersection, we try to find the closest one with respect to one or two unit-energy constraints, i.e $\mathbf{w}^T\mathbf{Y}^T\mathbf{Y}\mathbf{w} = 1$ and/or $\mathbf{b}^T\mathbf{X}^T\mathbf{X}\mathbf{b} = 1$. In other words, we look for a linear combination, $\mathbf{w}$ and $\mathbf{b}$, of resp. $\mathbf{Y}$ and $\mathbf{X}$ such that the distance between the resulting vectors, $\mathbf{Y}\mathbf{w}$ and $\mathbf{X}\mathbf{b}$, is as small as possible, taking into account *unit-norm* constraints on these vectors.

1. In case 1, given that $\mathbf{X}\mathbf{b}_1$ has unit-norm, i.e.

$$\|\mathbf{X}\mathbf{b}_1\|_2^2 = \mathbf{b}_1^T\mathbf{X}^T\mathbf{X}\mathbf{b}_1 = 1, \tag{3.38}$$

the minimal distance between $\mathbf{Y}\mathbf{w}_1$ and $\mathbf{X}\mathbf{b}_1$ is obtained by an orthogonal projection of $\mathbf{X}\mathbf{b}_1$ onto range($\mathbf{Y}$), as illustrated in **Fig. 3.2**. Mathematically, this corresponds to

$$\mathbf{Y}\mathbf{w}_1 = \underbrace{\mathbf{Y}(\mathbf{Y}^T\mathbf{Y})^{-1}\mathbf{Y}^T}_{\perp \text{ projection matrix}}\mathbf{X}\mathbf{b}_1. \tag{3.39}$$

To express (3.39) in terms of covariance matrices, define the QR-factorization of $\mathbf{Y}$ as $\mathbf{Y} = \mathbf{Q}\mathbf{R}$ [53]. After left multiplying (3.39) with $\mathbf{Q}^T$, one obtains

$$\begin{aligned} \mathbf{R}\mathbf{w}_1 &= \mathbf{R}(\mathbf{R}^T\mathbf{R})^{-1}\mathbf{Y}^T\mathbf{X}\mathbf{b}_1, & (3.40)\\ &\approx \mathbf{R}_{yy}^{1/2}\mathbf{R}_{yy}^{-1}\mathbf{R}_{yx}\mathbf{b}_1 = \mathbf{R}_{yy}^{1/2}\mathbf{w}_1, & (3.41) \end{aligned}$$

where we used the fact that $\mathbf{R}_{yy} = \mathbf{R}_{yy}^{T/2}\mathbf{R}_{yy}^{1/2} \approx \mathbf{Y}^T\mathbf{Y} = \mathbf{R}^T\mathbf{R}$. Hence, the data driven problem is turned into a covariance driven problem [43]. From **Fig. 3.2**, it can easily be seen that the distance d between the vectors $\mathbf{X}\mathbf{b}_1$ and $\mathbf{Y}\mathbf{w}_1$ corresponds to $\sin(\theta)$, with θ the angle between the two vectors. In addition, the norm of vector $\mathbf{Y}\mathbf{w}_1$ is $\|\mathbf{Y}\mathbf{w}_1\|_2^2 = \cos^2(\theta)$. The MSE can now be expressed as

$$J(\mathbf{w}_1, \mathbf{b}_1) = \|\mathbf{X}\mathbf{b}_1 - \mathbf{Y}\mathbf{w}_1\|_2^2 = d^2 = \sin^2(\theta). \tag{3.42}$$

Hence, the optimal solution is found for the smallest angle, i.e.

$$J_{min}(\mathbf{w}_{1,opt}, \mathbf{b}_{1,opt}) = \sin^2(\theta_{min}). \tag{3.43}$$

Likewise, we showed in Appendix B.3 that

$$J_{min}(\mathbf{w}_{1,opt}, \mathbf{b}_{1,opt}) = 1 - \lambda_{max}, \tag{3.44}$$

where λ_{max} is equal to the most dominant eigenvalue of $\mathbf{P}^T\mathbf{P}$ with $\mathbf{P} = \mathbf{R}_{yy}^{-T/2}\mathbf{R}_{yx}\mathbf{R}_{xx}^{-1/2}$. From (3.42) and (3.44), we learn that $0 \leqslant \lambda_{max} \leqslant 1$ and

$$\lambda_{max} = 1 - \sin^2(\theta_{min}) = \cos^2(\theta_{min}). \tag{3.45}$$

Case 1:

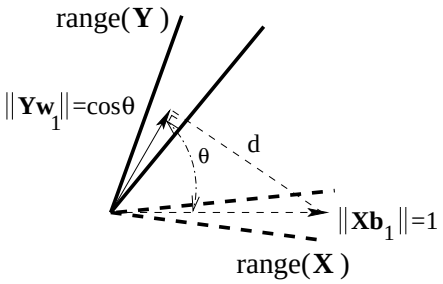

$d=\sin\theta$

$J=d^2=\sin^2\theta$

$\mathbf{b}_1^T\mathbf{X}^T\mathbf{X}\mathbf{b}_1=1$

$\mathbf{Y}\mathbf{w}_1=\mathbf{Y}(\mathbf{Y}^T\mathbf{Y})^{-1}\mathbf{Y}^T\mathbf{X}\mathbf{b}_1$

Case 2:

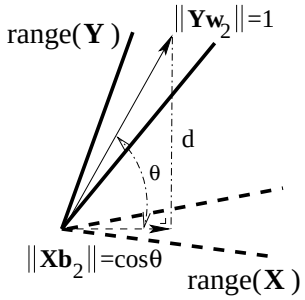

$d=\sin\theta$

$J=d^2=\sin^2\theta$

$\mathbf{X}\mathbf{b}_2=\mathbf{X}(\mathbf{X}^T\mathbf{X})^{-1}\mathbf{X}^T\mathbf{Y}\mathbf{w}_2$

$\mathbf{w}_2^T\mathbf{Y}^T\mathbf{Y}\mathbf{w}_2=1$

Case 3:

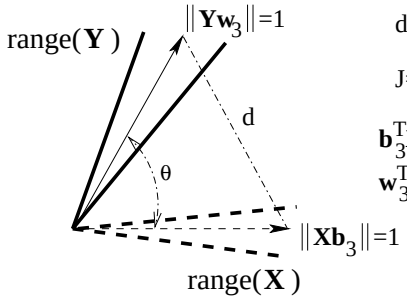

$d=2(\sin\frac{\theta}{2})$

$J=d^2=2(1-\cos\theta)$

$\mathbf{b}_3^T\mathbf{X}^T\mathbf{X}\mathbf{b}_3=1$

$\mathbf{w}_3^T\mathbf{Y}^T\mathbf{Y}\mathbf{w}_3=1$

Figure 3.2: Geometrical interpretation of MMSE TEQ design with three different unit-energy constraints.

To summarize: the MMSE TEQ and TIR with a unit-energy constraint on the TIR can be found as the vectors $\mathbf{w}_1$ and $\mathbf{b}_1$ that minimize the angle between the vectors $\mathbf{Yw}_1$ and $\mathbf{Xb}_1$ given that $\mathbf{Xb}_1$ has unit-norm.

2. The same reasoning can be applied for case 2 (see **Fig. 3.2**), but now with a unit-norm constraint on $\mathbf{Yw}_2$. Similar to (3.39) and (3.42), one may write

$$\mathbf{Xb}_2 = \underbrace{\mathbf{X}(\mathbf{X}^T\mathbf{X})^{-1}\mathbf{X}^T}_{\perp \text{ projection matrix}} \mathbf{Yw}_2, \tag{3.46}$$

and

$$\begin{aligned} J_{min}(\mathbf{w}_{2,opt}, \mathbf{b}_{2,opt}) &= \min_{\mathbf{w}_2,\mathbf{b}_2} \|\mathbf{Xb}_2 - \mathbf{Yw}_2\|_2^2, & (3.47)\\ &= d_{min}^2 = \sin^2(\theta_{min}), & (3.48) \end{aligned}$$

where θ_{min} is the smallest angle between the vectors $\mathbf{Xb}_2$ and $\mathbf{Yw}_2$, given that $\mathbf{Yw}_2$ has unit-norm.

3. In the third case, an orthogonal projection is no longer possible, since the two constraints require that $\mathbf{Yw}_3$ and $\mathbf{Xb}_3$ both have unit-norm. (However, notice that if there is an exact intersection, the optimization procedure will find it.) One can still find a solution which comes down to computing the principal angles between range($\mathbf{X}$) and range($\mathbf{Y}$) [53]. The solution vectors $\mathbf{Yw}_3$ and $\mathbf{Xb}_3$ determine the principal directions of range($\mathbf{X}$) and range($\mathbf{Y}$) belonging to the smallest principal angle. This is equivalent to performing a *canonical correlation analysis* [42] between the subspaces spanned by $\mathbf{X}$ and $\mathbf{Y}$. From **Fig. 3.2**, one sees that the MMSE is given by

$$\begin{aligned} J_{min}(\mathbf{w}_{3,opt}, \mathbf{b}_{3,opt}) &= \min_{\mathbf{w}_3,\mathbf{b}_3} \|\mathbf{Xb}_3 - \mathbf{Yw}_3\|_2^2, & (3.49)\\ &= d_{min}^2 = 2(1 - \cos(\theta_{min})), & (3.50) \end{aligned}$$

where θ_{min} is the smallest angle between the vectors $\mathbf{Xb}_2$ and $\mathbf{Yw}_2$, given that $\mathbf{Yw}_3$ and $\mathbf{Xb}_3$ have unit-norm. Likewise, we showed in Appendix B.3 that

$$J_{min}(\mathbf{w}_{3,opt}, \mathbf{b}_{3,opt}) = 2(1 - \sigma_{max}), \tag{3.51}$$

where σ_{max} is equal to the largest singular value of $\mathbf{P}$. Hence, according to (3.50) and (3.51), the largest singular value of $\mathbf{P}$ is equal to the cosine of the smallest principal angle between the subspaces spanned by $\mathbf{X}$ and $\mathbf{Y}$. As a consequence, the *eigenvalues of* $\mathbf{Q}$ *are smaller than one*, since the singular values of $\mathbf{P}$ squared are equal to the eigenvalues of $\mathbf{P}^T\mathbf{P}$ and $\mathbf{Q}$. This observation can be used to accelerate the inverse iteration method of (3.33).

Final comments

MMSE TEQ design has been extensively studied in the literature [5][28][44][69] [72][129][141]. Chow's basic results of [28] were further explored in [5] with emphasis on unit-tap and unit-norm constraints. The authors of [5] have shown that a unit-norm constraint results in a lower MMSE than a unit-tap constraint. Given this fact, they conclude that the unit-norm constraint solution results in better performance. However, the MMSE performance measure is not directly related to bit rate maximization and hence it is difficult to predict which constraint is preferable. A similar observation holds when considering unit-energy constraints. We showed that MMSE TEQ design with different unit-energy constraints leads to the same TEQ (up to a scale factor) and hence the same bit rate although the obtained MMSE values may be different. Also the problems encountered when mis-constraining a homogeneous least-squares (HLS) problem, as described in [153], are not valid for the problem definition in (3.37), where the MMSE cost function was approximated with the corresponding HLS joint TEQ-TIR design. Yeredor et al. explain in [153] how the constraint or the HLS cost function should be modified to obtain a non-trivial, consistent, ML estimate of the unknown parameter vector. Even when (3.37) would be modified in that sense, bit rate maximization is not guaranteed.

In an attempt to improve the performance of the MMSE shortening algorithm, Van Acker et al. modified the cost function with frequency weighting to disregard explicitly unused frequency bins [129][130][131]. Although the authors report some performance improvement, this approach is still not maximizing the achievable bit rate. In general, the drawback of non bit rate maximizing TEQ designs is that performance is often unpredictable. Moreover, the obtained bit rate is typically a non-smooth function of Δ which prevents choosing the delay parameter in an optimal way.

3.2.2 Maximum shortening SNR (MSSNR)

In 1996, Melsa et al. proposed the maximum shortening signal-to-noise ratio (MSSNR) method to solve the TEQ design problem [83]. The MSSNR-approach is based on shortening the CIR to minimize ISI. Let us define $\mathbf{H}_{win}$ and $\mathbf{H}_{wall}$ as

$$\mathbf{H}_{win} = \begin{bmatrix} h_{\Delta} & \dots & h_{\Delta-T+1} \\ \vdots & \ddots & \vdots \\ h_{\Delta+\nu} & \dots & h_{\Delta+\nu-T+1} \end{bmatrix}, \tag{3.52}$$

$$\mathbf{H}_{wall,1} = \begin{bmatrix} h_0 & 0 & \dots & 0 \\ \vdots & \ddots & & \vdots \\ h_{\Delta-1} & \dots & & h_{\Delta-T} \end{bmatrix}, \tag{3.53}$$

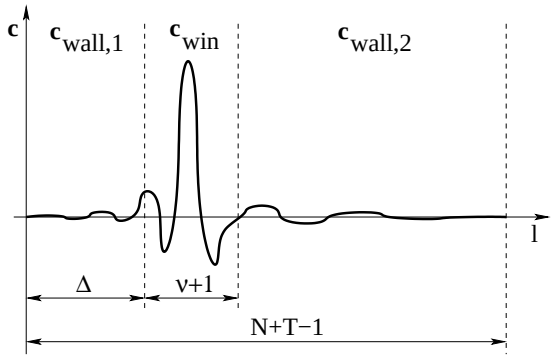

Figure 3.3: Window and wall parts of the effective channel $\mathbf{c} = \mathbf{h} \star \mathbf{w}$.

$$\mathbf{H}_{wall,2} = \begin{bmatrix} h_{\Delta+\nu+1} & \dots & h_{\Delta+\nu-T+2} \\ \vdots & \ddots & \vdots \\ 0 & \dots \; 0 & h_{N-1} \end{bmatrix}, \tag{3.54}$$

$$\mathbf{H}_{wall} = [\mathbf{H}_{wall,1}^T \;\; \mathbf{H}_{wall,2}^T]^T. \tag{3.55}$$

Let the effective channel be equal to $\mathbf{c} = \mathbf{h} \star \mathbf{w}$. The MSSNR technique attempts to *minimize* the energy *outside* a window of $\nu + 1$ consecutive samples of $\mathbf{c}$ (called the 'wall'), while constraining the energy in the remainder of $\mathbf{c}$ to one [27][83], i.e.

$$\min_{\mathbf{w}} \mathbf{w}^T \mathbf{H}_{wall}^T \mathbf{H}_{wall} \mathbf{w} \quad \text{subject to} \quad \mathbf{w}^T \mathbf{H}_{win}^T \mathbf{H}_{win} \mathbf{w} = 1. \tag{3.56}$$

This is depicted in **Fig. 3.3**. When $\mathbf{H}_{win}^T \mathbf{H}_{win}$ has a non-zero null-space, i.e. when $\mathbf{H}_{win}$ has more columns than rows ($T > \nu + 1$), solving (3.56) becomes rather complicated [83].

Alternatively, one could *maximize* the windowed energy, while constraining the wall energy, as suggested in [154] and later on in [107]. Since $\mathbf{H}_{wall}^T \mathbf{H}_{wall}$ is always positive definite in the ADSL context ($N \geqslant \nu + 1 + T$), the latter approach is preferred and comes down to solving (3.2) with

$$\boxed{\begin{aligned} \mathbf{A} &= \mathbf{H}_{wall}^T \mathbf{H}_{wall}, \\ \mathbf{B} &= \mathbf{H}_{win}^T \mathbf{H}_{win}. \end{aligned}} \tag{3.57, 3.58}$$

In addition, one can prove that maximizing 'window to wall energy' provides the same TEQ solution as maximizing 'overall channel energy to wall energy' [31][77].

The MSSNR approach tacitly assumes that the input signal is white, since all frequencies are treated in the same way. Furthermore, noise is clearly ignored

such that the MSSNR TEQ may be referred to as a zero-forcing (ZF) TEQ solution. In [39], it was shown that *in the absence of noise the MSSNR approach is in fact equivalent to the MMSE TEQ solution given that the input signal is white*. An extension of the MSSNR method to the noisy case was presented in [80], where a noise correlation matrix was added to $\mathbf{A}$, i.e.

$$\boxed{\begin{aligned}\mathbf{A} &= \sigma_x^2 \mathbf{H}_{wall}^T \mathbf{H}_{wall} + \mathbf{R}_{nn}, \quad (3.59)\\ \mathbf{B} &= \mathbf{H}_{win}^T \mathbf{H}_{win}, \quad (3.60)\end{aligned}}$$

where $\mathbf{R}_{nn}$ is the noise correlation matrix and σ_x^2 is the power of the transmitted signal. Recently, Martin et al. showed that the *infinite length TEQ* solution for the MSSNR problem defined by (3.57) and (3.58) is always symmetric or skew-symmetric [80][79]. Oddly enough, the *finite* length MSSNR TEQ is more often symmetric than skew-symmetric. With this in mind, the design complexity can be reduced substantially by forcing a perfectly symmetric TEQ. This can be done easily by rewriting $\mathbf{w}^T\mathbf{A}\mathbf{w}$ (with $\mathbf{A}$ defined in (3.57) or (3.59)) as

$$\begin{bmatrix}\mathbf{v}^T & \mathbf{v}^T\mathbf{J}\end{bmatrix}\begin{bmatrix}\mathbf{A}_{11} & \mathbf{A}_{12}\\ \mathbf{A}_{21} & \mathbf{A}_{22}\end{bmatrix}\begin{bmatrix}\mathbf{v}\\ \mathbf{J}\mathbf{v}\end{bmatrix} = \mathbf{v}^T\left[\mathbf{A}_{11} + \mathbf{J}\mathbf{A}_{21} + \mathbf{A}_{12}\mathbf{J} + \mathbf{J}\mathbf{A}_{22}\mathbf{J}\right]\mathbf{v}, \quad (3.61)$$

where $\mathbf{J}$ is a square matrix with ones on the anti-diagonal and where the final TEQ coefficients are given by $\mathbf{w} = [\mathbf{v}^T\ \mathbf{v}^T\mathbf{J}]^T$ with $\mathbf{v}$ half the size of $\mathbf{w}$. Similar definitions hold for $\mathbf{B} = \mathbf{H}_{win}^T\mathbf{H}_{win}$. Again, the desired symmetric TEQ is obtained via (3.2) with

$$\boxed{\begin{aligned}\mathbf{A} &= \mathbf{A}_{11} + \mathbf{J}\mathbf{A}_{21} + \mathbf{A}_{12}\mathbf{J} + \mathbf{J}\mathbf{A}_{22}\mathbf{J}, \quad (3.62)\\ \mathbf{B} &= \mathbf{B}_{11} + \mathbf{J}\mathbf{B}_{21} + \mathbf{B}_{12}\mathbf{J} + \mathbf{J}\mathbf{B}_{22}\mathbf{J}. \quad (3.63)\end{aligned}}$$

3.2.3 Multicarrier equalization by restoration of redundancy (MERRY)

In [78], a *blind* channel-shortening algorithm was presented, which forces the last sample of the equalized CP and the last sample of the equalized symbol to be equal, i.e.

$$\mathbf{w}_{opt} = \arg\min_{\mathbf{w}} \mathcal{E}\left\{\left|[y_{-1}^k \ldots y_{-T}^k]\mathbf{w} - [y_{N-1}^k \ldots y_{N-T}^k]\mathbf{w}\right|^2\right\}, \quad (3.64)$$

where y_l^k are the received samples at symbol period k (see Subsection 2.3.1). An additional constraint, e.g. $\mathbf{w}^T\mathbf{w} = 1$, has to avoid the trivial all zero TEQ. The method is blind in the sense that no knowledge of the transmitted symbols

nor channel information is required to find the solution. From (3.64), it is obvious that MERRY attempts to shorten the channel to ν taps instead of $\nu+1$. MERRY TEQ design can be reformulated as a single Rayleigh quotient optimization (cf. (3.2)) with

$$\boxed{\begin{array}{rcl}\mathbf{A} & = & \mathbf{R}_{\Delta y \Delta y}, \\ \mathbf{B} & = & \mathbf{I}_T,\end{array}} \qquad \begin{array}{l}(3.65)\\(3.66)\end{array}$$

with $\mathbf{R}_{\Delta y \Delta y} = \mathcal{E}\{\Delta y^k (\Delta y^k)^T\}$ and $\Delta y^k = [y^k_{-1} - y^k_{N-1} \ \ldots \ y^k_{-T} - y^k_{N-T}]^T$, which can be proven in a similar way as Appendix B.1.

3.2.4 Minimum-ISI (Min-ISI)

A generalization of the MSSNR method was given in [9][10][11], commonly referred to as the minimum-ISI (Min-ISI) method. To describe the Min-ISI TEQ, Arslan et al. define the SNR for tone i as

$$\mathrm{SNR}_i = \frac{\sigma^2_{x,i} \left|C_{signal,i}\right|^2}{\sigma^2_{n,i} \left|C_{noise,i}\right|^2 + \sigma^2_{x,i} \left|C_{ISI,i}\right|^2}, \tag{3.67}$$

where $\sigma^2_{x,i}$, $\sigma^2_{n,i}$, $C_{signal,i}$, $C_{noise,i}$ and $C_{ISI,i}$ are the transmitted signal power, channel noise power, signal path gain, noise path gain and ISI path gain for the i-th subchannel. The different path gains are defined as

$$\begin{aligned} C_{signal,i} &= \mathcal{F}_N[i,:]\mathrm{diag}\{\mathbf{g}\}\mathbf{H}\mathbf{w}, && (3.68)\\ C_{ISI,i} &= \mathcal{F}_N[i,:](\mathbf{I}_N - \mathrm{diag}\{\mathbf{g}\})\mathbf{H}\mathbf{w} = \mathcal{F}_N[i,:]\mathbf{D}\mathbf{H}\mathbf{w}, && (3.69)\\ C_{noise,i} &= \mathcal{F}_N[i,:][\mathbf{w}^T \ \ \mathbf{0}_{1\times(N-T)}]^T, && (3.70)\end{aligned}$$

where the vector $\mathbf{g} \in \mathbb{R}^N$ and the channel matrix $\mathbf{H} \in \mathbb{R}^{N\times T}$ are given by

$$\begin{aligned} \mathbf{g}[l] &= \begin{cases} 1 & \Delta \le l \le \Delta + \nu \\ 0 & \text{otherwise} \end{cases} && (3.71)\\ \mathbf{H} &= [\mathbf{H}^T_{wall,1} \ \ \mathbf{H}^T_{win} \ \ \mathbf{H}^T_{wall,2}], && (3.72)\end{aligned}$$

with $\mathbf{H}_{win}$, $\mathbf{H}_{wall,1}$ and $\mathbf{H}_{wall,2}$ from (3.52), (3.53) and (3.54) respectively. According to (3.67), three contributions may be distinguished:

- the desired signal after the TEQ originating from the windowed part of the overall channel,
- the ISI noise after the TEQ originating from the walled part of the overall channel and

- the channel noise after TEQ filtering.

When the ISI term of (3.67) is forced to zero for each tone i, the highest achievable SNR is obtained. As a consequence, the authors of [11] propose to minimize the overall ISI, which is estimated as a sum of the subchannel ISI terms. The problem now comes down to solving (3.2) with

$$\boxed{\begin{aligned} \mathbf{A} &= \mathbf{w}^T\mathbf{H}^T\mathbf{D}^T\left(\sum_{i\in\mathcal{S}}\mathcal{F}_N[i,:]\sigma_{x,i}^2\mathcal{F}_N[i,:]^H\right)\mathbf{DHw}, \quad (3.73)\\ \mathbf{B} &= \mathbf{H}^T\mathbf{H}, \quad (3.74)\end{aligned}}$$

where $\mathcal{S}$ denotes the set of used tones and matrix $\mathbf{B}$ acts as a constraint to prevent the trivial all zero TEQ solution. In [10], channel noise was taken into account by modifying (3.73) and (3.74) to

$$\boxed{\begin{aligned} \mathbf{A} &= \mathbf{w}^T\mathbf{H}^T\mathbf{D}^T\left(\sum_{i\in\mathcal{S}}\mathcal{F}_N[i,:]\frac{\sigma_{x,i}^2}{\sigma_{n,i}^2}\mathcal{F}_N[i,:]^H\right)\mathbf{DHw}, \quad (3.75)\\ \mathbf{B} &= \mathbf{H}^T\mathbf{H}. \quad (3.76)\end{aligned}}$$

When comparing (3.57) and (3.58) with (3.75) and (3.76), one can observe that the ISI-noise is now shaped in the frequency domain. Henceforth, the Min-ISI method can be considered as a generalization of the MSSNR method [83]. In fact, both methods would be equivalent if the signal to noise power ratio were constant over all subchannels and if all subchannels were used.

Although the idea behind the Min-ISI method seems attractive, the method is still suboptimal in terms of bit rate performance. When the SNR definition in (3.67) is compared with (2.20), one observes that the ICI noise term is neglected in the denominator of (3.67). In addition, according to (2.20), the signal and ISI definitions of (3.67) are only correct when the overall channel would be perfectly limited to $\nu + 1$ samples. When the the channel is longer, the head and the tail of the effective channel will also contribute to the useful signal component, which may lead to a Min-ISI TEQ with quite unpredictable bit rate behaviour.

3.2.5 Minimum delay spread (MDS)

Another TEQ design approach was presented in [106] by Schur et al. who state that the parts of $\mathbf{c} = \mathbf{h} \star \mathbf{w}$ exceeding the cyclic prefix length cause ISI and ICI depending on the distance to the prefix and its energy, see also [100]. Starting

from the following delay spread definition for $\mathbf{c}$

$$D = \sqrt{\frac{1}{E}\sum_{l=0}^{N+T-2}(l-\bar{l})^2\,|\mathbf{c}[l]|^2}, \tag{3.77}$$

with

$$E = \sum_{l=0}^{N+T-2}|\mathbf{c}[l]|^2, \qquad \bar{l} = \frac{1}{E}\sum_{l=0}^{N+T-2} l\,|\mathbf{c}[l]|^2\,, \tag{3.78}$$

the authors propose to minimize D^2. In matrix notation, this results in a problem definition similar to (3.2) with

$$\boxed{\begin{aligned}\mathbf{A} &= \mathbf{H}^T\mathbf{Q}\mathbf{H}, \\ \mathbf{B} &= \mathbf{H}^T\mathbf{H},\end{aligned}} \tag{3.79}$$
$$\tag{3.80}$$

where $\mathbf{Q} = \text{diag}\{[(0-\bar{l})^2 \quad \ldots \quad (N+T-2-\bar{l})^2]^T\}$ is a diagonal weighting matrix.

As seen from (3.77), the MDS TEQ does not exploit the cyclic prefix redundancy. As a result, the MDS TEQ attempts to shorten the effective channel to a single impulse. Since MDS TEQ design is quite similar to MSSNR TEQ design, all the advantages and drawbacks mentioned in Subsection 3.2.2 also apply here.

3.2.6 Carrier nulling algorithm (CNA)

In [41], the authors propose a *blind* method to combat channel dispersion in a DMT/OFDM-system based on the minimization of the average DFT-output energy of null-carriers. In a typical DMT/OFDM-system the transmitted signal has a finite spectrum, resulting in frequency bins that carry zero information, the so-called null-carriers. At the receiver, a TEQ is designed such that the received symbols at the null-carriers are forced to zero, minimizing the cost function

$$J = \sum_{i\in\bar{\mathcal{S}}}\mathcal{E}\left\{|\mathcal{F}_N[i,:]\mathbf{Y}^k\mathbf{w}|^2\right\}, \tag{3.81}$$

where $\bar{\mathcal{S}}$ represents the set of null-carriers and $\mathbf{Y}^k$ is defined in Subsection 2.3.3. An additional constraint, e.g. $\mathbf{w}^T\mathbf{w}$ has to avoid the all zero solution. Again, this TEQ-design can be cast into the problem formulation of (3.2) with

$$\boxed{\begin{aligned}\mathbf{A} &= \sum_{i\in\bar{\mathcal{S}}}\mathcal{E}\left\{(\mathbf{Y}^k)^T\mathcal{F}_N[i,:]^H\mathcal{F}_N[i,:]\mathbf{Y}^k\right\}, \\ \mathbf{B} &= \mathbf{I}_T.\end{aligned}} \tag{3.82}$$
$$\tag{3.83}$$

Although the authors presented a low complex, adaptive minimization procedure for (3.81) and the algorithm is blind, the CNA-criterion only considers unused carriers without paying attention to the carriers of interest. This will not necessarily lead to channel shortening, nor equalization of the useful carriers. De Courville et al. claim that their algorithm leads to shortening to a single spike [41]. Hence, it may not be the most desirable criterion and the performance may be very unpredictable.

3.3 Single equalizer design with multiple Rayleigh quotients

Despite the fact that the most popular design methods to find a single TEQ are based on the optimization of a *single* Rayleigh quotient, cf. (3.2), they are in general not optimal in the sense of bit rate maximization. For this reason, several attempts have been made in the literature to design a TEQ that effectively maximizes bit rate. Whereas all of these bit rate maximizing design methods are different in nature, they can be described in a common way as a product of multiple Rayleigh quotients, as in (3.1), and hence lead to a non-linear optimization problem. Although there exists only one true bit rate maximizing solution, the different approximations involved in each method still have led to a variety of designs, which will be reviewed in this section.

3.3.1 Maximum geometric SNR (MGSNR) method

The first TEQ design for bit rate maximization was presented by Al-Dhahir et al. in [3][4][6][7], where the equalizer design method is based on *maximizing the geometric SNR (GSNR)*. Starting from the expression for the total number of bits transmitted per DMT symbol (see also (2.3)), one has

$$b_{DMT} = \sum_{i\in\mathcal{S}} \log_2\left(1+\frac{\mathrm{SNR}_i}{\Gamma_i}\right) = \log_2 \prod_{i\in\mathcal{S}}\left(1+\frac{\mathrm{SNR}_i}{\Gamma_i}\right), \tag{3.84}$$

where $\mathcal{S}$ is the set of used tones, SNR_i is the SNR for tone i and $\Gamma = \Gamma_i$ is the SNR gap, which is assumed to be equal for all tones. The GSNR is defined as

$$\mathrm{SNR}_{geom}(\mathbf{w}) \quad = \quad \Gamma \cdot \left(\left[\prod_{i\in\mathcal{S}}\left(1+\frac{\mathrm{SNR}_i}{\Gamma}\right)\right]^{\frac{1}{N_u}} - 1\right), \tag{3.85}$$

such that (3.84) reduces to

$$b_{GSNR}(\mathbf{w}) = N_u \log_2\left(1+\frac{\mathrm{SNR}_{geom}}{\Gamma}\right), \tag{3.86}$$

where N_u is the number of used tones, i.e. the number of tones in $\mathcal{S}$. As the logarithmic function is monotonically increasing, (3.86) indicates that maximizing the bit rate of a DMT system is equivalent to the maximization of the GSNR. Under the high SNR assumption made in [6], (3.85) is approximately equal to the more commonly known geometric average of the SNRs, i.e.

$$\mathrm{SNR}_{geom}(\mathbf{w}) \approx \left(\prod_{i\in\mathcal{S}} \mathrm{SNR}_i\right)^{\frac{1}{N_u}}. \tag{3.87}$$

Let $B_i = \mathcal{F}_N[i,:][\mathbf{b}^T\ \mathbf{0}_{1\times(N-\nu-1)}]^T$, $W_i = \mathcal{F}_N[i,:][\mathbf{w}^T\ \mathbf{0}_{1\times(N-T)}]^T$ and $H_i = \mathcal{F}_N[i,:]\mathbf{h}$ be the i-th frequency domain coefficients of the TIR, the TEQ and the channel respectively, then Al-Dhahir et al. model the subchannel SNR as

$$\mathrm{SNR}_i(\mathbf{w},\mathbf{b}) = \frac{\sigma_{x,i}^2|H_i|^2}{\sigma_{n,i}^2} = \frac{\sigma_{x,i}^2|H_i|^2|W_i|^2}{\sigma_{n,i}^2|W_i|^2} \approx \frac{\sigma_{x,i}^2|B_i|^2}{\sigma_{n,i}^2|W_i|^2}, \tag{3.88}$$

where $\sigma_{x,i}^2$ and $\sigma_{n,i}^2$ are the transmitted signal power and received noise power for tone i respectively and $B_i \approx H_i W_i$. Note that (3.88) does not include the effects of ISI, ICI and noise leakage due to the DFT-based demodulator at the receiver. When equal signal power is assumed on all tones, i.e. $\sigma_{x,i}^2 = \sigma_x^2$, then (3.87) can be modified to

$$\mathrm{SNR}_{geom}(\mathbf{w},\mathbf{b}) \approx \sigma_x^2 \left(\prod_{i\in\mathcal{S}} \frac{|B_i|^2}{\sigma_{n,i}^2|W_i|^2}\right)^{\frac{1}{N_u}}. \tag{3.89}$$

Furthermore, when the noise at the output of the equalizer is assumed to be independent of $\mathbf{b}$, maximizing (3.89) is approximately equivalent to maximizing

$$J(\mathbf{b}) = \frac{1}{N_u}\sum_{i\in\mathcal{S}} \ln|B_i|^2 \tag{3.90}$$

$$= \frac{1}{N_u}\sum_{i\in\mathcal{S}} \ln\left(\mathbf{b}^T\mathbf{Q}_i\mathbf{b}\right), \tag{3.91}$$

with $\mathbf{Q}_i = \mathcal{F}_N[i,1:\nu+1]^H\mathcal{F}_N[i,1:\nu+1]$. To prevent the all zero solution, a non-triviality constraint, e.g. $\mathbf{b}^T\mathbf{b} = 1$, has to be added. Hence, the solution of (3.91) can be found by solving (3.1) for the unknowns $\mathbf{b}$, with $i \in \mathcal{S}$ and with

$$\boxed{\begin{aligned} \mathbf{A}_i &= \mathbf{I}_{\nu+1}, && (3.92)\\ \mathbf{B}_i &= \mathbf{Q}_i. && (3.93) \end{aligned}}$$

Once the optimal $\mathbf{b}$ is found, the corresponding MGSNR TEQ $\mathbf{w}$ can be computed from (3.17). The authors of [6] mention that an additional constraint

could be added to prevent $\mathbf{b}$ from converging to a single spike, e.g. the MSE given by (3.9) at the solution needs to be less than some maximum value MSE_{max}. An iterative GSNR maximization method was presented in [70].

Although the MGSNR method has the aim to maximize bit rate, the large number of approximations and assumptions made in the derivation lead to a *suboptimal* solution. Therefore, other authors have attempted to construct more accurate cost functions for improved performance.

3.3.2 Maximum Bit Rate (MBR) method

In [9][10], Arslan et al. introduced the Maximum Bit Rate (MBR) TEQ as an alternative to the MGSNR TEQ to maximize the throughput of a DMT system. The MBR method follows the subchannel SNR definition of (3.67), leading to

$$\mathrm{SNR}_i(\mathbf{w}) = \frac{\mathbf{w}^T\tilde{\mathbf{B}}_i\mathbf{w}}{\mathbf{w}^T\tilde{\mathbf{A}}_i\mathbf{w}}, \tag{3.94}$$

with

$$\tilde{\mathbf{A}}_i = \sigma_{n,i}^2\mathcal{F}_N[i,1:T]^H\mathcal{F}_N[i,1:T] + \sigma_{x,i}^2\mathbf{H}^T\mathbf{D}^T\mathcal{F}_N[i,:]^H\mathcal{F}_N[i,:]\mathbf{DH}, \tag{3.95}$$

$$\tilde{\mathbf{B}}_i = \sigma_{x,i}^2\mathbf{H}^T\mathrm{diag}\{\mathbf{g}\}\mathcal{F}_N[i,1:T]^H\mathcal{F}_N[i,1:T]\mathrm{diag}\{\mathbf{g}\}\mathbf{H}, \tag{3.96}$$

where $\mathbf{D}$, $\mathbf{g}$ and $\mathbf{H}$ are given by (3.69), (3.71) and (3.72) respectively. With (3.84) and (3.94), the total number of bits per DMT symbol can be modeled as the log of a product of generalized Rayleigh quotients, i.e.

$$b_{MBR}(\mathbf{w}) = \sum_{i\in\mathcal{S}}\log_2\left(1+\frac{\mathbf{w}^T\tilde{\mathbf{B}}_i\mathbf{w}}{\mathbf{w}^T\Gamma_i\tilde{\mathbf{A}}_i\mathbf{w}}\right) = \log_2\prod_{i\in\mathcal{S}}\frac{\mathbf{w}^T\mathbf{B}_i\mathbf{w}}{\mathbf{w}^T\mathbf{A}_i\mathbf{w}}, \tag{3.97}$$

with

$$\boxed{\begin{aligned}\mathbf{A}_i &= \Gamma_i\tilde{\mathbf{A}}_i, \qquad (3.98)\\ \mathbf{B}_i &= \Gamma_i\tilde{\mathbf{A}}_i + \tilde{\mathbf{B}}_i. \qquad (3.99)\end{aligned}}$$

Since the log is a monotonically increasing function, it is clear that the MBR TEQ can be obtained from (3.1) with $i \in \mathcal{S}$ and $\mathbf{A}_i$ and $\mathbf{B}_i$ as in (3.98) and (3.99).

As opposed to the SNR model for the MGSNR TEQ in (3.88), the SNR model for the MBR TEQ does not ignore ISI-induced noise. However, DFT leakage is completely neglected in (3.94) and as such the MBR TEQ is still *suboptimal*.

3.3.3 Near optimal TEQ design method (NO-TEQ)

Milosevic et al. [87][88] improved on the MBR method by forming a more rigorous model of the subchannel SNR. On top of the traditional channel noise, the authors also introduce a digital noise floor (DNF) due to rounding effects of the TEQ coefficients. Milosevic et al. show that the SNR can be written in the form of (3.94), but with different $\tilde{\mathbf{A}}_i$ and $\tilde{\mathbf{B}}_i$ matrices, i.e.

$$\begin{aligned}\tilde{\mathbf{A}}_i &= 2\sigma_{x,i}^2 \left(\mathbf{H}_{wall,1}^T \mathbf{Q}_{i,1} \mathbf{Q}_{i,1}^H \mathbf{H}_{wall,1} + \mathbf{H}_{wall,2}^T \mathbf{Q}_{i,2} \mathbf{Q}_{i,2}^H \mathbf{H}_{wall,2}\right) + \\ &\quad \mathbf{Q}_{n,i} \mathbf{R}_{nn} \mathbf{Q}_{n,i}^H + \sigma_{DNF}^2 \mathbf{I}_T, \qquad (3.100)\\ \tilde{\mathbf{B}}_i &= \sigma_{x,i}^2 \mathbf{H}^T \mathbf{Q}_{x,i} \mathbf{Q}_{x,i}^H \mathbf{H}, \qquad (3.101)\end{aligned}$$

where $\mathbf{H}_{wall,1}$, $\mathbf{H}_{wall,2}$ and $\mathbf{H}$ are as in (3.53), (3.54) and (3.72) resp.; $\mathbf{Q}_{i,1}$, $\mathbf{Q}_{i,2}$ and $\mathbf{Q}_{n,i}$ are Hankel matrices made from the elements in the i-th row of the DFT matrix; $\mathbf{Q}_{x,i}$ is a circular Hankel matrix constructed from the i-th row of the DFT matrix; $\mathbf{R}_{nn}$ is the noise covariance matrix and σ_{DNF}^2 is the power of the noise due to digital rounding of the TEQ coefficients. See [87][88] for full definitions. With the definitions in (3.100) and (3.101), a similar derivation can be made as in (3.97), (3.98) and (3.99) to arrive at the problem definition of (3.1).

Some approximations have been made in defining the SNR model:

- it is assumed that *all* carriers are excited with *equal* power,
- an additional unit-norm constraint on the TEQ is added for easy incorporation of the DNF into the definition of (3.100),
- the desired signal component, given by $\mathbf{w}^T \tilde{\mathbf{B}}_i \mathbf{w}$, is expressed as a circular convolution of the transmitted signal and the channel, which is, according to (2.20), only true if the channel can be perfectly shortened to the cyclic prefix length plus one,
- since the overall noise for tone i is modeled as the total received signal power for tone i minus the desired signal component for this tone, it is clear that the resulting noise component, given by $\mathbf{w}^T \tilde{\mathbf{A}}_i \mathbf{w}$, is also not perfectly accurate.

These approximations are minor compared with the MGSNR TEQ and the MBR TEQ and as such this method leads to improved performance, be it that it is still *suboptimal*, theoretically [87][88].

3.3.4 Bit rate maximizing TEQ (BM-TEQ)

In [143][144], Vanbleu et al. offer a TEQ solution that truly maximizes the achievable bit rate. The resulting TEQ is referred to as the bit rate maximizing

TEQ (BM-TEQ) and it is based on an exact SNR definition. To facilitate the SNR expression, the SNR is expressed at the FEQ output. When D_i is the FEQ for tone i, the FEQ output for tone i can be written as

$$D_i \underbrace{\mathcal{F}_N[i,:]\mathbf{Y}^k\mathbf{w}}_{\text{FEQ input } Y^k_{w,i}} = D_i\mathbf{Y}_i^{sl,k}\mathbf{w} = \alpha_i X_i^k + E_i^k, \tag{3.102}$$

where X_i^k is the symbol of interest transmitted at symbol period k, α_i is a scale factor, $\mathbf{Y}^k$ is a Toeplitz matrix with received samples, defined in Subsection 2.3.3, $\mathbf{Y}_i^{sl,k} = \mathcal{F}_N[i,:]\mathbf{Y}^k$ represents the i-th row of a sliding DFT on the received signal and E_i^k is the overall noise contribution on tone i (including channel noise and ISI+ICI according to (2.20)). When the FEQ is a *constrained (unbiased) MMSE* equalizer, which in case of a one-tap equalizer is equal to a zero forcing (ZF) equalizer, α_i equals 1. Hence, the ZF FEQ, defined as

$$D_i(\mathbf{w}) = \frac{\mathcal{E}\{|X_i^k|^2\}}{\mathcal{E}\{Y_{w,i}^k(X_i^k)^*\}} = \frac{\mathcal{E}\{|X_i^k|^2\}}{\mathcal{E}\{(X_i^k)^*\mathbf{Y}_i^{sl,k}\}\mathbf{w}}, \tag{3.103}$$

gives an unbiased desired signal part at the FEQ output. Without bias, the SNR on tone i can easily be obtained by

$$\mathrm{SNR}_i(\mathbf{w}) = \frac{\text{energy in (desired signal}_i)}{\text{energy in (received signal}_i - \text{desired signal}_i)}, \tag{3.104}$$

$$= \frac{\mathcal{E}\{|X_i^k|^2\}}{\mathcal{E}\{|E_i^k|^2\}} = \frac{\mathcal{E}\{|X_i^k|^2\}}{\mathcal{E}\{|D_iY_{w,i}^k - X_i^k|^2\}}. \tag{3.105}$$

Given the expression for the total number of bits transmitted per DMT symbol, as in (3.84) with SNR_i given by (3.105), Vanbleu et al. show that the BM-TEQ cost function can be written as

$$b_{DMT}(\mathbf{w}) = \sum_{i\in\mathcal{S}} \log_2\left(\frac{\mathbf{w}^T\mathbf{A}_i\mathbf{w}}{\mathbf{w}^T\mathbf{B}_i\mathbf{w}}\right), \tag{3.106}$$

where $\mathbf{A}_i$ and $\mathbf{B}_i$ are independent of $\mathbf{w}$, given by

$$\mathbf{A}_i = \Gamma_i\sigma_{x,i}^2\mathbf{R}_{YY,i} + (1-\Gamma_i)\mathbf{r}_{XY,i}^H\mathbf{r}_{XY,i}, \tag{3.107}$$

$$\mathbf{B}_i = \Gamma_i(\sigma_{x,i}^2\mathbf{R}_{YY,i} - \mathbf{r}_{XY,i}^H\mathbf{r}_{XY,i}), \tag{3.108}$$

with

$$\sigma_{x,i}^2 = \mathcal{E}\{|X_i^k|^2\},\ \mathbf{R}_{YY,i} = \mathcal{E}\{(\mathbf{Y}_i^{sl,k})^H\mathbf{Y}_i^{sl,k}\},\ \mathbf{r}_{XY,i} = \mathcal{E}\{(X_i^k)^*\mathbf{Y}_i^{sl,k}\}. \tag{3.109}$$

Due to the logarithm, computing the BM-TEQ from (3.106) is equivalent to solving (3.1) with $i \in \mathcal{S}$ and with the $\mathbf{A}_i$ and $\mathbf{B}_i$ matrices according to (3.107) and (3.108). Note that although channel shortening is the original underlying idea for using a TEQ, the BM-TEQ criterion does not explicitly impose channel shortening any more. Hence, one could also allow for a complex valued TEQ.

3.4 Multiple equalizer design with a single Rayleigh quotient per tone

In Sections 3.2 and 3.3, we presented TEQ designs that could be restated as the maximization of a single generalized Rayleigh quotient or a product of generalized Rayleigh quotients respectively. Whereas in the previous sections the outcome was a single TEQ to equalize all frequency bins together in some optimal way, the idea in this section is to *decouple the equalizer design*: each data carrying subchannel or tone receives an equalizer, designed to maximize the bit rate on this subchannel. Consequently, when every subchannel carries the maximum number of bits, then the overall bit rate of the DMT system is maximized as well. In terms of the common formulation (3.1), this means that a single generalized Rayleigh quotient has to be maximized per subchannel, resulting in the problem definition of (3.7) for each used tone.

Based on the methods in Section 3.3, a large variety of equalizer designs could be devised, which obey the criterion in (3.7). When each of the previous design methods is applied to design an equalizer for each tone separately, a new class of equalizers is obtained, see e.g. [87][88][135][136]. Since most of these designs are just a generalization of existing methods, we will only focus on one particular type of equalization, namely the per tone equalizers (PTEQ), as presented in [129][135][136].

3.4.1 Per tone equalization (PTEQ)

The idea of the per tone equalizers (PTEQ) was originally proposed by Van Acker et al. in [135]. The derivation starts from the same SNR expression for tone i as in (3.105). Since the bit rate of a DMT system needs to be maximized for a given bit error rate, it is sufficient to maximize the SNR and hence the number of achievable bits for each tone separately. In order to maximize the SNR per tone, Van Acker et al. propose to minimize the denominator of (3.105) for each used tone $i \in \mathcal{S}$

$$\mathbf{w}_{opt,i} = \arg\min_{\mathbf{w}_i} \mathcal{E}\{|\mathcal{F}_N[i,:]\mathbf{Y}^k \underbrace{\mathbf{w}D_i}_{\mathbf{w}_i} - X_i^k|^2\}, \tag{3.110}$$

where X_i^k is the symbol of interest, $\mathcal{F}_N[i,:]\mathbf{Y}^k\mathbf{w}D_i$ denotes the FEQ output for tone i and the one tap FEQ D_i is incorporated into the tone dependent T-taps equalizer $\mathbf{w}_i$. By applying the associativity of the matrix product, the FEQ output becomes

$$\hat{X}_i^k = \mathcal{F}_N[i,:](\mathbf{Y}^k\mathbf{w}_i) = (\mathcal{F}_N[i,:]\mathbf{Y}^k)\mathbf{w}_i, \tag{3.111}$$

$$= \mathrm{row}_i(\mathcal{F}_N\mathbf{Y}^k)\mathbf{w}_i, \tag{3.112}$$

where $\hat{X}_i^k$ is an estimate of the transmitted symbol for tone i. Since $\mathbf{Y}^k$ is a Toeplitz matrix, defined in Subsection 2.3.3, (3.112) implies that the FEQ output can be seen as a linear combination (by $\mathbf{w}_i$) of a sliding DFT on tone i, applied to the unequalized, received signal $\mathbf{y}^k$, i.e.

$$\hat{X}_i^k = \mathrm{row}_i(\mathcal{F}_N \mathbf{Y}^k)\mathbf{w}_i = \bar{\mathbf{w}}_i^T \underbrace{\begin{bmatrix} \boxed{\mathcal{F}_N[i,:]} & \dots & 0 \\ & \ddots & \ddots \\ 0 & \dots & \boxed{\mathcal{F}_N[i,:]} \end{bmatrix}}_{\mathbf{F}_i} \mathbf{y}^k, \qquad (3.113)$$

where $\mathbf{y}^k$ is given by (2.32) and where $\bar{\mathbf{w}}_i = [w_{i,T-1} \ \dots \ w_{i,0}]^T$ denotes the PTEQ equalizer coefficients in reverse order. To avoid the need for T consecutive DFT operations per symbol in (3.113), the Toeplitz structure of $\mathbf{Y}^k$ can be exploited:

$$\mathcal{F}_N[i,:]\mathbf{Y}^k[:,l+1] = \alpha^i \mathcal{F}_N[i,:]\mathbf{Y}^k[:,l] + \underbrace{(y_{-l}^k - y_{N-l}^k)}_{\Delta y_l^k}, \quad l = 1, \dots, T-1, \qquad (3.114)$$

with $\alpha = e^{-j2\pi/N}$. In other words, the DFT of a column of $\mathbf{Y}^k$ can be derived from the DFT of the previous column plus a real valued difference term. Applying (3.114) recursively, it is easy to verify that (3.113) can be replaced by

$$\hat{X}_i^k = \bar{\mathbf{w}}_i^T \mathbf{F}_i \mathbf{y}^k = \bar{\mathbf{w}}_i^T \begin{bmatrix} 1 & \alpha^i & \dots & \alpha^{i(T-1)} \\ & \ddots & & \vdots \\ & & 1 & \alpha^i \\ 0 & & & 1 \end{bmatrix} \left[\begin{array}{c|c|c} \mathbf{I}_{T-1} & \mathbf{0} & -\mathbf{I}_{T-1} \\ \hline \mathbf{0} & \multicolumn{2}{c}{\mathcal{F}_N[i,:]} \end{array}\right] \mathbf{y}^k. \qquad (3.115)$$

This relation indicates that $\hat{X}_i^k$ can also be obtained as a linear combination of the unequalized i-th DFT output Y_i^k with $T-1$ difference terms

$$\hat{X}_i^k = \bar{\mathbf{v}}_i^T \left[\begin{array}{c|c|c} \mathbf{I}_{T-1} & \mathbf{0} & -\mathbf{I}_{T-1} \\ \hline \mathbf{0} & \multicolumn{2}{c}{\mathcal{F}_N[i,:]} \end{array}\right] \mathbf{y}^k, \qquad (3.116)$$

$$= \bar{\mathbf{v}}_i^T \underbrace{\begin{bmatrix} \Delta y_{T-1}^k & \dots & \Delta y_1^k & Y_i^k \end{bmatrix}}_{\mathbf{z}_i^k}, \qquad (3.117)$$

where $\bar{\mathbf{v}}_i = [v_{i,T-1} \ \dots \ v_{i,0}]^T$ are modified PTEQ coefficients for tone i, leading to the structure in **Fig. 3.4**. The coefficients $\bar{\mathbf{v}}_i$ are related to the original coefficients $\bar{\mathbf{w}}_i$ by

$$\bar{\mathbf{v}}_i = \begin{bmatrix} 1 & \alpha^i & \dots & \alpha^{i(T-1)} \\ & \ddots & & \vdots \\ & & 1 & \alpha^i \\ 0 & & & 1 \end{bmatrix}^T \bar{\mathbf{w}}_i, \qquad (3.118)$$

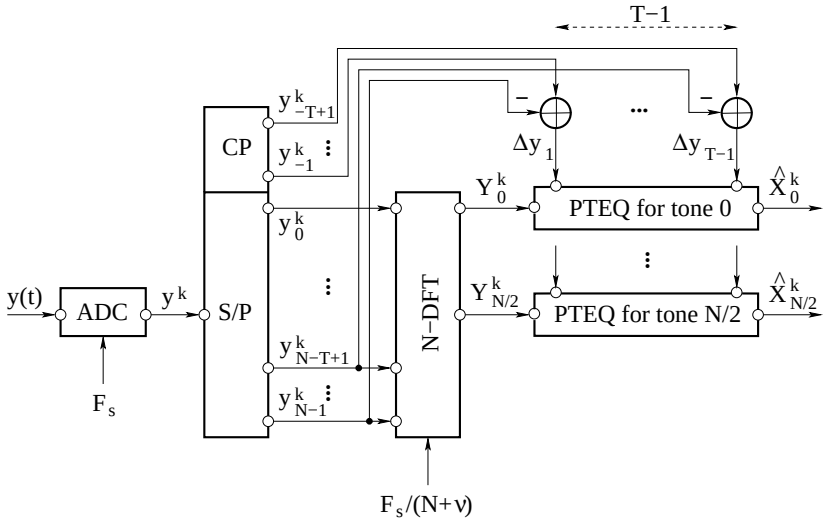

Figure 3.4: Graphical representation of the per tone equalizers.

which can also be written in terms of a very simple recursion [135][136]:

$$v_{i,l} = \alpha^i v_{i,l+1} + w_{i,l}, \quad l = 0, \ldots, T-2, \tag{3.119}$$

$$v_{i,T-1} = w_{i,T-1}. \tag{3.120}$$

From (3.110) and (3.117), it is clear that to find the optimal $\bar{\mathbf{v}}_i$ for each subchannel, it suffices to solve an unconstrained, linear MMSE cost function for each tone $i \in \mathcal{S}$

$$\bar{\mathbf{v}}_{opt,i} = \arg\min_{\bar{\mathbf{v}}_i} \mathcal{E}\left\{\left|\bar{\mathbf{v}}_i^T \mathbf{z}_i^k - X_i^k\right|^2\right\}, \tag{3.121}$$

where $\bar{\mathbf{v}}_i$ is obtained directly without first computing $\bar{\mathbf{w}}_i$. The MMSE solution, given by

$$\bar{\mathbf{v}}_{opt,i} = \left(\mathcal{E}\{(\mathbf{z}_i^k)^*(\mathbf{z}_i^k)^T\}\right)^{-1} \mathcal{E}\{(\mathbf{z}_i^k)^* X_i^k\}, \tag{3.122}$$

can be found based on an estimate of the channel and the overall noise spectrum [129][136]. Alternatively, the PTEQ coefficients could be initialized recursively, as will be discussed in Chapter 6.

The unconstrained MMSE equalizer in (3.121) will in general be *biased* (see Appendix B.4 for a proof) and this bias becomes more important for low SNRs. An unbiased MMSE equalizer gives an unbiased desired signal part at the equalizer output, resulting in minimum probability of error. Therefore, it is desirable to compute an unbiased solution, which can be obtained from a *constrained* MMSE optimization problem (see Appendix B.4)

$$\bar{\mathbf{v}}_{opt,i} = \arg\min_{\bar{\mathbf{v}}_i} \mathcal{E}\left\{\left|\bar{\mathbf{v}}_i^T \mathbf{z}_i^k - X_i^k\right|^2\right\},$$

$$\text{subject to} \quad \bar{\mathbf{v}}_i^T \mathcal{E}\left\{\mathbf{z}_i^k (X_i^k)^*\right\} = \mathcal{E}\left\{X_i^k (X_i^k)^*\right\}. \quad (3.123)$$

It is easy to show that the optimal, unbiased PTEQ coefficients are now given by

$$\bar{\mathbf{v}}_{opt,i} = D_i \left(\mathcal{E}\{(\mathbf{z}_i^k)^* (\mathbf{z}_i^k)^T\}\right)^{-1} \mathcal{E}\{(\mathbf{z}_i^k)^* X_i^k\}, \quad (3.124)$$

where the complex scalar D_i compensates for the bias

$$D_i = \frac{\mathcal{E}\{|X_i^k|^2\}}{\mathcal{E}\{(X_i^k)^* (\mathbf{z}_i^k)^T\}(\mathcal{E}\{(\mathbf{z}_i^k)^* (\mathbf{z}_i^k)^T\})^{-1}\mathcal{E}\{(\mathbf{z}_i^k)^* X_i^k\}}. \quad (3.125)$$

Hence, the constrained (unbiased) MMSE solution of (3.124) is equal to the biased Wiener solution in (3.122) scaled by an additional one tap FEQ D_i to remove the bias.

The optimization problem in (3.123) can also be restated as the maximization of a generalized Rayleigh quotient, cf. (3.7), with

$$\boxed{\begin{aligned} \mathbf{A}_i &= \mathcal{E}\{(\mathbf{z}_i^k)^* (\mathbf{z}_i^k)^T\}, && (3.126) \\ \mathbf{B}_i &= \mathcal{E}\{(\mathbf{z}_i^k)^* X_i^k\}\mathcal{E}\{(X_i^k)^* (\mathbf{z}_i^k)^T\}. && (3.127) \end{aligned}}$$

See Appendix B.4 for a short proof. Since (3.7) is scale invariant, the solution might be biased and again an additional one tap FEQ per used tone has to remove the bias.

Since per tone equalization enables to design an equalizer for each tone separately, its performance should be as good as and in most cases even better than a single TEQ, which equalizes all tones in a common way. Moreover, the PTEQ enables bit rate maximization at roughly the same cost as TEQ filtering during data transmission, as shown in [129][136]. The drawback is that more memory is required to store all the PTEQ coefficients for every tone.

Whereas the PTEQ is derived from a TEQ per tone, Vanbleu et al. provide an alternative derivation based on an infinite-impulse response (IIR) channel model. In [142], it is shown that in order to have perfect equalization in the presence of a general IIR channel, additional PTEQ inputs are required. On top of the difference terms of the received signal, as in (3.117), also difference terms of the transmitted signal have to be used, leading to a more general PTEQ structure. These extra difference terms are obtained by feeding back decisions on the symbol estimates or by exploiting information in pilot and unused tones.

3.5 Exceptions to the common formulation

In the previous sections, we showed how many TEQ algorithms can be written as a product of generalized Rayleigh quotients or as a special case of this product. In this section, some TEQ design methods are addressed that do not fit in the common framework of Section 3.1.

3.5.1 Improved and iterative bit rate maximizing TEQ design

Henkel and Kessler describe in [55] one of the first attempts to improve upon the MGSNR TEQ, presented in Subsection 3.3.1. They present a subchannel SNR model that includes ISI as well as the DFT leakage effect on the channel noise. However, ICI is neglected and the SNR updating algorithm assumes that all carriers are excited. Based on this approximate subchannel SNR model, non-linear optimization techniques are required to optimize the bit rate. Contrary to most other TEQ designs, the frequency response of the TEQ, rather than the time-domain version $\mathbf{w}$, is optimized. As a result, the subchannel SNR updating algorithm renders the method outside of the general framework (3.1).

3.5.2 Channel shortening by sum-squared auto-correlation minimization (SAM)

A recent algorithm meant for blind, adaptive channel shortening was proposed in [13]. The method, which minimizes a sum of squared auto-correlations of TEQ outputs, leads to a cost function that is fourth-order in $\mathbf{w}$ and hence multi-modal. The resulting channel shortening criterion is based on a *sum* rather than a *product* of Rayleigh quotients and as such does not fit into the formulation of (3.1).

3.6 Simulation results

To evaluate the performance of the different TEQ design methods, we consider simulations for the eight carrier serving area (CSA) reference loops. The CSA loops are defined by standardization bodies and their configuration is shown in **Fig. 3.5**. Note that some of these loops have bridged taps and multiple gauge changes, which make the channel more difficult to equalize. The overall channel model includes the analog and digital front end filters from the transmit and receive side, the POTS splitters and the actual transmission loop characteristics. The PSD of the channel noise consists of AWGN of -140 dBm/Hz

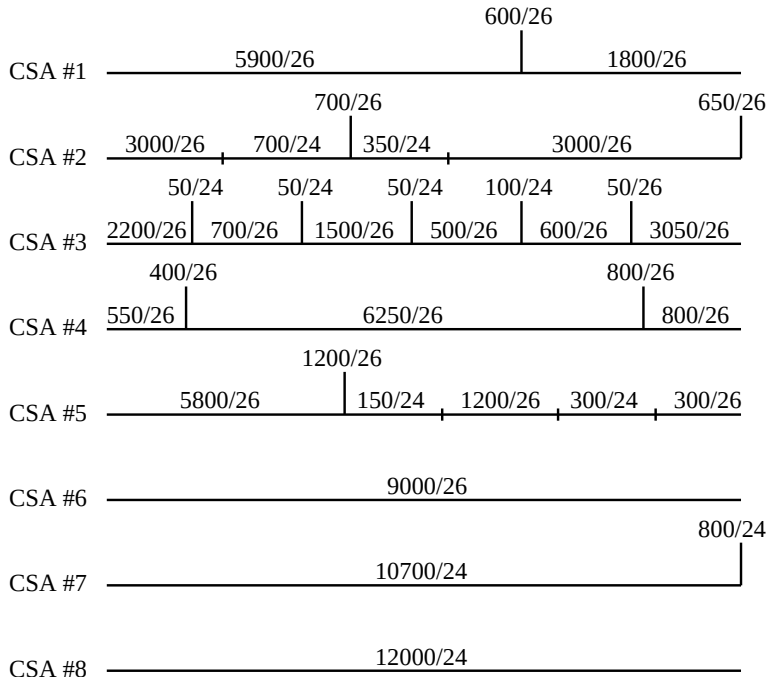

Figure 3.5: Configuration of the 8 CSA reference loops. For every loop segment, the loop length (in foot) and the wire size (in American wire gauge) are given.

and NEXT of 24 DSL disturbers shaped by the receiver front end filters. In addition, residual echo noise, ADC and DAC noise are also included.

The parameters used for simulation are typical for an ADSL environment. More specifically, for downstream simulations the transmit IDFT and receive DFT size N is equal to 512, the cyclic prefix ν is 32 and the sampling rate F_s at the transmitter and receiver is 2.208 MHz. The transmit signal power equals -40 dBm/Hz and is equally distributed over all used subchannels (tones 38 to 255). For upstream simulations we used a 512-point transmit IDFT and a 128-point receive DFT. The upstream tones that carry data are 7 to 29 with a transmit signal power of -38 dBm/Hz. Since the duration of the channel impulse response is typically limited to the duration of one DMT symbol, it is modeled with 512 samples at 2.208 MHz. The carrier spacing for up- and downstream transmission is equal to 4.3125 kHz and hence the symbol rate is $4.3125 \cdot N/(N+\nu) = 4.0588$ kHz.

As performance measure the achievable bit rate is computed, given by

$$r = \frac{F_s}{N+\nu} \sum_{i \in \mathcal{S}} \log_2 \left(1 + \frac{\mathrm{SNR}_i}{\Gamma} \right) \tag{3.128}$$

where Γ is the SNR gap equal to $9.8+6-3 = 12.8$ dB for a bit error probability $P_e = 10^{-7}$. This corresponds to a system margin of $\gamma_m = 6$ dB and a coding gain of $\gamma_c = 3$ dB. The SNR gap is assumed to be equal for all the tones. The SNR for tone i is obtained according to (3.105).

3.6.1 Comparison of TEQ design algorithms

Downstream

In **Fig. 3.6** the performance of the MMSE TEQ algorithm with different constraints is illustrated for the downstream CSA #4 loop. The bit rate is plotted as a function of the decision delay δ_1, which is a design parameter. For a definition of δ_1, we refer to Subsection 2.3.1. The MMSE TEQ has $T = 16$ taps and is subjected to the following constraints: a unit-energy constraint (UEC) $\mathbf{b}^T\mathbf{R}_{xx}\mathbf{b} = 1$, a unit-norm constraint (UNC) $\mathbf{w}^T\mathbf{w} = 1$, a unit-tap constraint (UTC) on the TIR, i.e. $\mathbf{e}_1^T\mathbf{b} = 1$ and a unit-tap constraint (UTC) on the TEQ, i.e. $\mathbf{e}_1^T\mathbf{w} = 1$. Since MMSE TEQ design with unit-energy constraints lead to the same TEQ (up to a scale factor) and hence the same bit rate, only the bit rate for one UEC is depicted. As a benchmark, the performance of the BM-TEQ is given as well. The MMSE channel shortening combined with a particular constraint has no direct relation with the achievable bit rate of the system. Hence, it is difficult to predict a priori which constraint will be the best for this channel. Although the MMSE TEQ cost function does not optimize capacity, it still results in a TEQ with an acceptably large bit rate, as can be seen from the figure. In addition, the figure also shows that the bit rate is a non-smooth function of δ_1, unlike in the BM-TEQ case. This makes an optimal choice for δ_1 very difficult and a search over several delays may be required of find the best performance. Note that MMSE TEQ design with $\mathbf{w}^T\mathbf{w} = 1$ results in unacceptably low performance for most decision delays. An explanation for this behaviour was given in Subsection 3.2.1 and in [129][141].

Fig. 3.7 compares the performance of different equalizer design methods using the same simulation parameters as in the previous figure. More specifically, the bit rate is given for the constrained (unbiased) MMSE PTEQ, the BM-TEQ, the NO-TEQ, the MGSNR TEQ, the MBR TEQ, the MMSE TEQ with $\mathbf{e}_1^T\mathbf{b} = 1$, the Min. ISI TEQ and the MDS TEQ. As expected, the PTEQ provides an upper bound on performance. When considering single TEQ designs, the BM-TEQ outperforms all other designs. Despite the assumptions in the NO-TEQ design procedure, the achieved bit rate is close to optimal. When non-linear optimization techniques have to be avoided, MMSE is the preferred TEQ design criterion. Also observe that the MDS TEQ achieves very low bit rates, since the TEQ attempts to shorten the channel to a single impulse, without exploiting the guard band duration.

In **Fig. 3.8** the SNR for the different TEQ designs ($T = 16$) is shown for a

fixed delay $\delta_1 = 0$. From the figure it is clear that only tones 38 to 255 carry information. Observe that most TEQ methods exhibit equalization difficulties near the lowest band edge. This behaviour is caused by two effects:

- the lowest tones are located near the cut-off frequencies of the front end filters, resulting in more ISI and ICI that has to be compensated;
- the frequencies in the stop band (tones below 38) experience more DSL NEXT and DFT demodulation at the receiver will lead to noise leakage in the band of interest. Since the DFT is computed after TEQ filtering, the TEQ has to suppress this noise to obtain high bit rates.

Hence, optimal TEQ design has to take these two effects into account.

Upstream

In **Fig. 3.9** the bit rate as a function of the decision delay δ_1 (at high rate) is depicted for different equalizer design methods with $T = 40$ and the upstream CSA #4 reference loop. The bit rate was evaluated for the constrained (unbiased) MMSE PTEQ, the BM-TEQ, the MMSE TEQ with UEC $\mathbf{b}^T\mathbf{R}_{xx}\mathbf{b} = 1$, the MMSE TEQ with UNC $\mathbf{w}^T\mathbf{w} = 1$, the MMSE TEQ with UTC $\mathbf{e}_1^T\mathbf{b} = 1$, the MSSNR TEQ according to (3.59) and (3.60) and the MDS TEQ design method. The BM-TEQ outperforms all other single TEQ algorithms, while it approaches the PTEQ performance. Whereas the BM-TEQ bit rate is a smooth function of the decision delay, the other TEQ methods exhibit a rather unpredictable behaviour. Note that MMSE TEQ design with UNC on $\mathbf{w}$ performs again much worse than MMSE TEQs with other constraints.

In **Fig. 3.10** the SNR for the different equalizer designs ($T = 40$) is shown for a fixed delay $\delta_1 = 80$. Only tones 7 to 29 carry information. It is clear that the lowest tones are the most difficult to equalize. Remark that equalization for upstream is more difficult than for downstream and more equalizer taps are required.

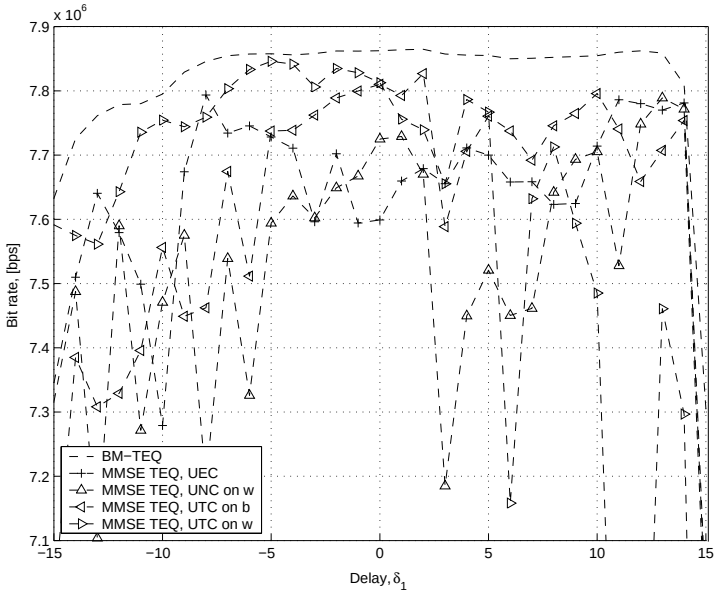

Figure 3.6: Bit rate as a function of the decision delay δ_1 to compare the MMSE TEQ design method with different constraints for the downstream CSA #4 loop with $T = 16$.

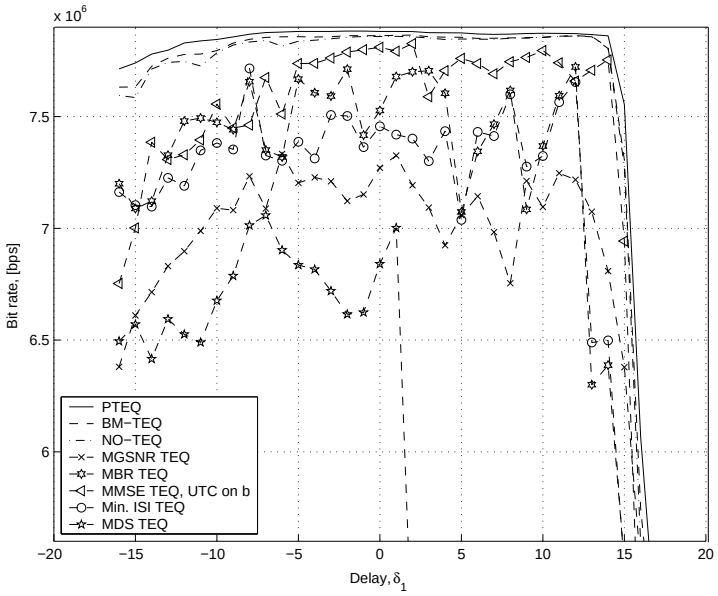

Figure 3.7: Bit rate as a function of the decision delay δ_1 to compare different equalizer design methods for the downstream CSA #4 loop with $T = 16$.

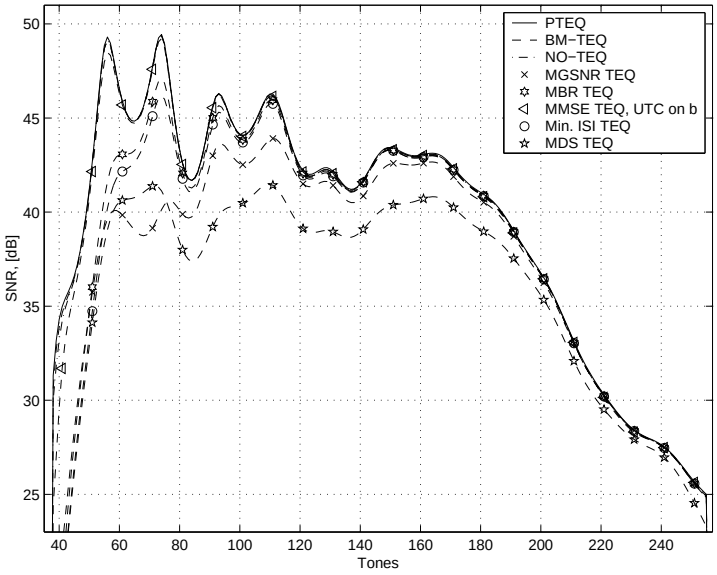

Figure 3.8: SNR for the downstream CSA #4 loop with $T = 16$ and $\delta_1 = 0$ for different equalizer design methods.

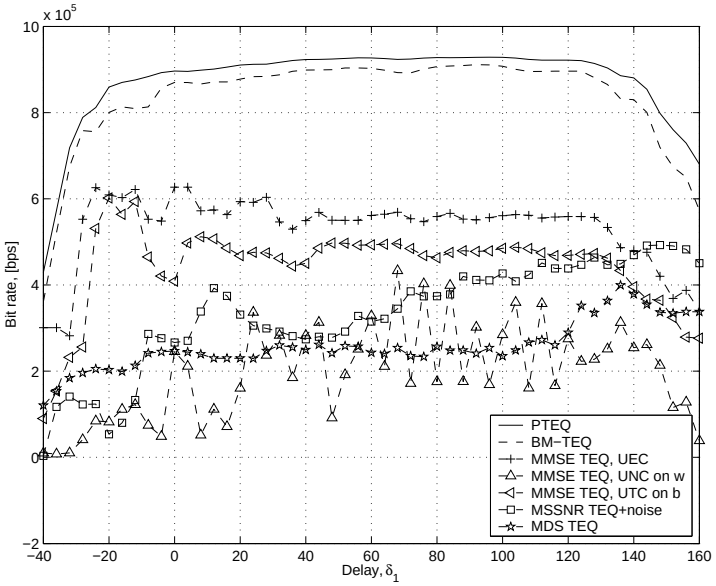

Figure 3.9: Bit rate as a function of the decision delay δ_1 to compare different equalizer design methods for the upstream CSA #4 loop with $T = 40$.

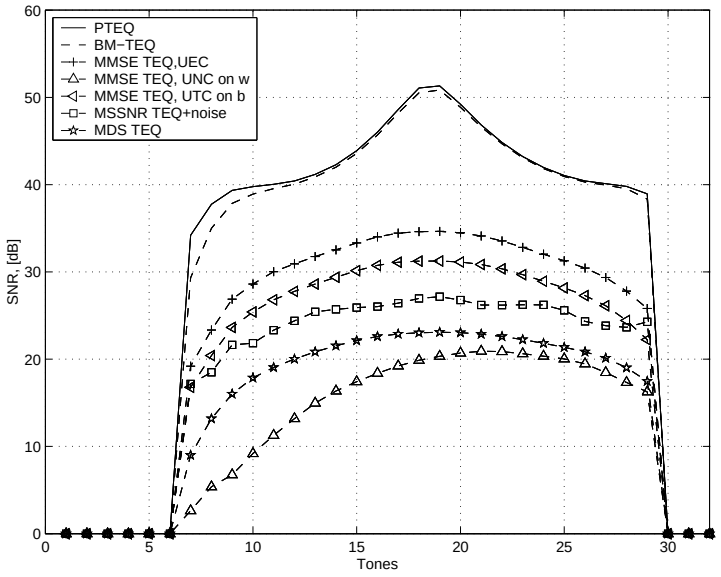

Figure 3.10: SNR for the upstream CSA #4 loop with $T = 40$ and $\delta_1 = 80$ for different equalizer design methods.

3.6.2 Bit rate performance of TEQ design methods for different loops

To generalize the results of the previous subsection, the design methods were tested for the 8 downstream CSA channels. The results for methods based on a single generalized Rayleigh quotient and for bit rate maximizing design methods are depicted in **Fig. 3.11** and **Fig. 3.12** respectively. More specifically, **Fig. 3.11** contains the bit rates (from left to right) for the MMSE TEQ with UEC $\mathbf{b}^T\mathbf{R}_{xx}\mathbf{b} = 1$, the MMSE TEQ with UNC $\mathbf{w}^T\mathbf{w} = 1$, the MMSE TEQ with UTC $\mathbf{e}_1^T\mathbf{b} = 1$, the MSSNR TEQ according to (3.59) and (3.60), the Min. ISI TEQ, the MERRY TEQ and the MDS TEQ. In **Fig. 3.11** the bit rates (from left to right) for the MGSNR TEQ, the MBR TEQ, the NO-TEQ, the BM-TEQ and the PTEQ are given. Delay optimization has been applied by running all methods over a large range of delays, i.e. $\delta_1 = -16, -15, \ldots, 40$. The maximum bit rate over this delay range is depicted.

Referring to **Fig. 3.11**, the bit rates achieved with MMSE TEQ are for all loops sufficiently high. It is also noticed that MDS is not the best measure for TEQ design since it performs consistently worse than the other methods. From **Fig. 3.11**, one can see that the PTEQ, as a more general equalizer structure, outperforms all other methods. Observe again that the performance difference between the BM-TEQ and the PTEQ is very small.

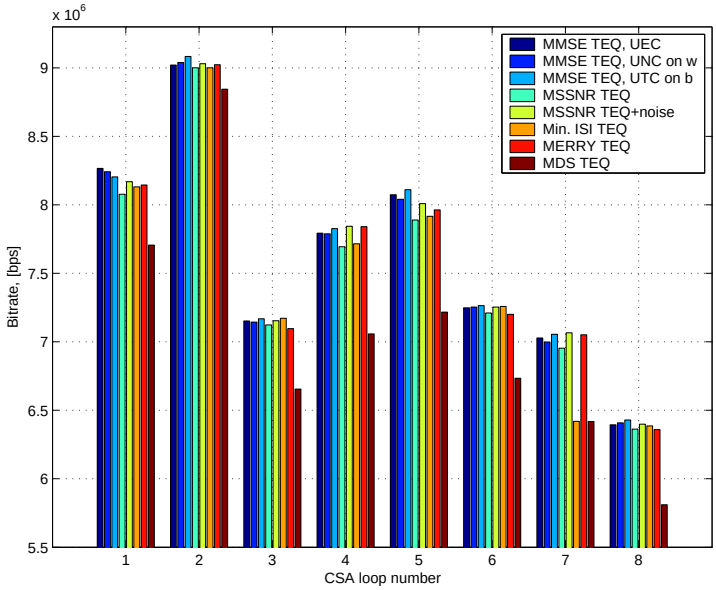

Figure 3.11: Bit rate performance of the TEQ methods based on a single generalized Rayleigh quotient for the 8 downstream CSA loops with $T = 16$ and δ_1 optimized over the range $-16, -15, \ldots, 40$.

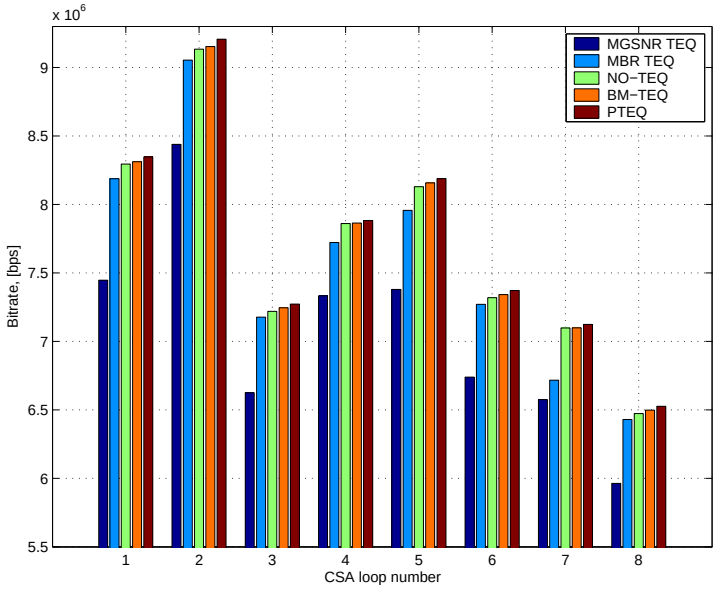

Figure 3.12: Bit rate performance of the equalizer methods that attempt to maximize the bit rate for the 8 downstream CSA loops with $T = 16$ and δ_1 optimized over the range $-16, -15, \ldots, 40$.

3.6.3 Iterative initialization for MMSE TEQ design with unit-energy constraints

Fig. 3.13 depicts the iterative initialization of the MMSE TEQ with UEC for the CSA #2, CSA #4, CSA #6 and CSA #8 reference loops. As discussed in Subsection 3.2.1 the MMSE TEQ with UEC can be found as the eigenvector of $\mathbf{Q}$ corresponding to the largest eigenvalue, with $\mathbf{Q}$ given in (3.30). The most dominant eigenvector can be computed iteratively using the power method or the inverse iteration procedure, cf. (3.31) and (3.33) respectively. In **Fig. 3.13** the bit rate as a function of the number of iterations is plotted. The full line corresponds to initialization with the power method, while the dashed line represents the inverse iteration procedure. Both methods were initialized with $\mathbf{w}_{init} = [0 \ldots 0 \ 1]^T$. The simulation was performed with $T = 16$ for $\delta_1 = -8$. The figure shows that for the power method initial convergence is fast, but eventually slows down since the largest eigenvalue of $\mathbf{Q}$ is not dominant compared to the second largest eigenvalue. This behaviour is observed for each loop.

The knowledge that the largest eigenvalue of $\mathbf{Q}$ is upper bounded by one (cf. Subsection 3.2.1) was used to apply the inverse iteration method of (3.33) with $\mu = 1$. From the figure it is clear that with the inverse iteration method convergence is much faster and the optimal solution is achieved after roughly 10 iterations. The fast convergence is, however, at the cost of a higher computational complexity per iteration, i.e. in the order of $\mathcal{O}(T^3)$ per iteration for (3.33) compared to $\mathcal{O}(T^2)$ per iteration for (3.31).[4]

3.7 Conclusions

In this chapter we presented an overview of existing design methods to tackle the equalization problem in multicarrier systems where the time span of the channel impulse response is longer than the cyclic prefix duration. We have shown how the majority of these techniques can be cast into a common formulation based on a product of generalized Rayleigh quotients. This common formulation had as a goal to provide a unified notational framework and to clarify the subtle differences between the different design methods.

Based on the common formulation, three categories were distinguished, each leading to a different design strategy. First, we showed that single generalized Rayleigh quotients led to suboptimal (in the sense of bit rate maximization) single TEQ designs. Secondly, the more difficult case with a product of multiple

[4]To obtain a clear idea of the complexity of both algorithms, word lengths should be investigated and 'bit true' simulations have to be performed. In addition, the amount of memory, the number of memory accesses and the number of gates effectively required for the computations have to be determined. This is, however, beyond the scope of this text.

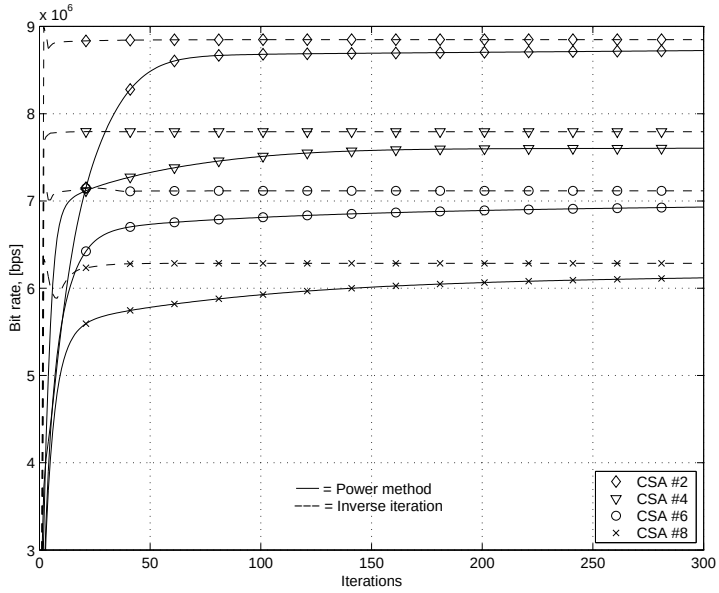

Figure 3.13: Iterative initialization (power method and inverse iteration) of the MMSE TEQ design with unit-energy constraints for the downstream CSA #2, CSA #4, CSA #6 and CSA #8 reference loops with $T = 16$ and $\delta_1 = -8$.

generalized Rayleigh quotients was treated. This case is required for optimal single TEQ design, requiring non-linear optimization techniques to obtain the desired solution. Finally, optimizing a single Rayleigh quotient for each tone separately resulted in the so-called per tone equalization, which is a generalization of the single TEQ case. Of course, an entire class of intermediate designs could be devised based on multiple TEQ designs for subgroups of tones. We also addressed some special TEQ design methods that fall out of the scope of the common framework.

Furthermore, we paid special attention to MMSE TEQ design with three distinct energy constraints: a unit-energy constraint on the target signal, a unit-energy constraint on the equalized signal and both the first and the second constraint together. We showed that all the TEQ solutions are essentially identical (up to a scale factor) and hence yield the same performance in terms of achievable bit rate. The mathematical derivation revealed that a common iterative method, based on the power method or the inverse iteration procedure, could be applied to obtain the solutions for all three cases. A geometrical interpretation was provided to give an insight in the different constraints and a relation was established between MMSE TEQ design subjected to unit-energy constraints and the principal angles between the subspaces spanned by the transmitted and received signal respectively.

The MMSE design criterion is widely used in industry for TEQ design in ADSL modems. However, simulation results showed that the bit rate obtained by MMSE channel shortening is not optimal and very sensitive to the decision delay and the constraint. In this chapter, we showed that the TEQ with the highest performance is obtained by the BM-TEQ design criterion. In addition, it was observed that the BM-TEQ bit rate is flat as a function of the decision delay. Alternatively, per tone equalization could be implemented in DSL modems to achieve optimal performance, at the cost of extra memory requirements.

Chapter 4

Bit rate maximizing joint window and equalizer design

IN DMT-based DSL systems, the noise experienced by the receiver can be separated into two main classes: *channel induced interference* and *external noise*. Channel induced noise emerges when the channel impulse response order is not confined to the cyclic prefix length. If the channel exceeds the cyclic prefix duration, the signal after the receive DFT will be distorted by inter-symbol-interference (ISI) and inter-carrier-interference (ICI), as explained in Subsection 2.2.1.

Apart from this channel induced interference, DMT transmission is also impaired by noise sources such as additive white noise, narrowband radio frequency interference (RFI) (emerging from AM broadcast and HAM radio [40]) and crosstalk. Due to the block based transmission, the signal at the receiver is effectively windowed in time by a rectangular window, leading to sinc shaped sidelobes of the DFT filters. Hence, narrowband interference results in strongly correlated noise between subcarriers. As a result of the bad spectral containment of the sinc shaped filters, the distortion due to the RFIs will be spread over many DMT carriers, cf. Subsection 2.2.3.

To minimize the overall received interference and noise, several paths are followed:

1. *Equalizer design*: to tackle the *channel induced interference*, a T-taps time domain equalizer (TEQ) is usually inserted at the receiver before

the removal of the prefix, such that the combined effect of channel and TEQ is sufficiently short, see Chapter 3.

2. *Window design*: if the channel order is limited to $\nu - \mu$ samples, additional receiver windowing [118] can be applied, using μ redundant samples from the cyclic prefix to construct a window which affects only the (external) noise component in the received signal, leaving the data component unchanged. As discussed in Subsection 2.2.3, receiver windowing is then able to improve the poor spectral containment of the DFT basis functions to mitigate RFI, while preserving the DMT transmission orthogonality, which is required for ISI/ICI free transmission. In [66][102] research is focused on how to apply and design a *fixed* or *adaptive* window to reduce the receiver sensitivity to RFI, without considering the equalization problem. However, the presented algorithms are suboptimal in the sense that the resulting window functions do not necessarily optimize bit rate.

3. *Window incorporated per tone equalizer design*: here, an equalizer is designed and implemented for each tone separately in the presence of a fixed window [38][92][139] or an adaptive window [139] to optimize the bit rate. Since this per tone approach requires a high memory usage to store all the equalizer coefficients, research towards single TEQ design is still relevant.

The goals of this chapter are:

- to provide a general framework, where a combined window and TEQ will be designed to maximize the bit rate for a given number of TEQ and window taps. The outcome will be referred to as the *bit rate maximizing window and TEQ (BM-WinTEQ)*. The derivation of the BM-WinTEQ is presented in Section 4.2,

- to illustrate how the BM-WinTEQ can be used in a *'per group'* scheme, where a TEQ and window is optimally designed per group of used tones,

- to demonstrate the relation with existing designs, which appear as *special cases* of the resulting framework. Special cases are treated in Section 4.3, including: optimal TEQ design without windowing [143][144], optimal TEQ design in the presence of a fixed window, optimal window design without TEQ, ...

Complexity issues, simulations and conclusions can be found in Sections 4.4, 4.5 and 4.6 respectively.

4.1 Notation and bit rate expression

4.1.1 Notation

The data model and notation used in this chapter can be found in Subsection 2.3.3. Recall that D_i is the 1-tap (complex) frequency domain equalizer (FEQ) for tone i, $\mathbf{w} = [w_0 \ \dots \ w_{T-1}]^T$ denotes a TEQ of T taps and $\mathbf{d} = [d_0 \ \dots \ d_{\mu-1}]^T$ are the μ window coefficients, $\mathbf{Y}^{ext,k}$ is a Toeplitz matrix (of size $(N+\mu) \times T$) of received time domain samples:

$$\mathbf{Y}^{ext,k} = \begin{bmatrix} y^k_{-\mu} & \cdots & y^k_{-\mu-T+1} \\ \vdots & \ddots & \vdots \\ y^k_{N-1} & \cdots & y^k_{N-T} \end{bmatrix}, \tag{4.1}$$

where it is tacitly assumed that $\mathbf{Y}^{ext,k}$ depends on the decision delay δ_1, which is a design parameter. The first column of $\mathbf{Y}^{ext,k}$ and the last N rows are denoted as $\tilde{\mathbf{y}}^k$ and $\mathbf{Y}^k$ respectively. The elements of the first row and the first column of $\mathbf{Y}^{ext,k}$ are represented by $\mathbf{y}^{ext,k} = [y^k_{-\mu-T+1} \ \dots \ y^k_{N-1}]^T$, while $\mathbf{y}^k$ contains the last $N+T-1$ elements of $\mathbf{y}^{ext,k}$, see also formula (2.40).

Using the above definitions, a convolution of the received sequence with a TEQ can now easily be written as $\mathbf{Y}^{ext,k}\mathbf{w}$. The window and fold operations for receiver windowing, as discussed in Subsection 2.2.3, are equivalent to a multiplication of the received samples with the $N \times (N+\mu)$ matrix $\mathbf{\Omega}$:

$$\mathbf{\Omega} = \begin{bmatrix} \mathbf{0} & \mathbf{I}_{N-\mu} & \mathbf{0} \\ \mathrm{diag}(\mathbf{d}) & \mathbf{0} & \mathbf{I}_\mu - \mathrm{diag}(\mathbf{d}) \end{bmatrix}, \tag{4.2}$$

$$= \underbrace{\begin{bmatrix} \mathbf{0} & \mathbf{I}_{N-\mu} & \mathbf{0} \\ \mathbf{0} & \mathbf{0} & \mathbf{I}_\mu \end{bmatrix}}_{\mathbf{\Omega}_1} + \underbrace{\begin{bmatrix} \mathbf{0} & \mathbf{0} & \mathbf{0} \\ \mathrm{diag}(\mathbf{d}) & \mathbf{0} & -\mathrm{diag}(\mathbf{d}) \end{bmatrix}}_{\mathbf{\Omega}_2}. \tag{4.3}$$

The time domain vector that is fed to the N-point DFT after TEQ filtering and windowing is now the result of the product $\mathbf{\Omega}\mathbf{Y}^{ext,k}\mathbf{w}$. The corresponding receiver structure is shown in **Fig. 4.1**. Windowing without TEQ filtering is represented by $\mathbf{\Omega}\tilde{\mathbf{y}}^k = \mathbf{\Omega}\mathbf{Y}^{ext,k}[1,:]$, while TEQ filtering without windowing is denoted as $\mathbf{Y}^k\mathbf{w} = \mathbf{\Omega}_1\mathbf{Y}^{ext,k}\mathbf{w}$. Observe in **Fig. 4.1** that TEQ filtering is executed at the sample rate, while the windowing operations are performed at the $(N+\nu)$-fold lower symbol rate.

4.1.2 Bit rate expression

In the derivation of a bit rate maximizing window and TEQ design cost function, we start from the bit rate expression[1] as in (2.3), where the total number

[1] To keep mathematics tractable, we do not consider integer bit loading.

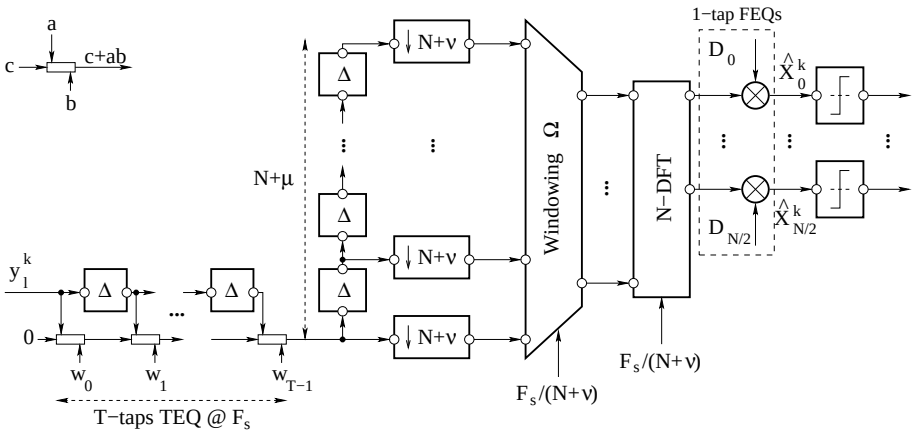

Figure 4.1: Block diagram of a DMT receiver with TEQ filtering followed by windowing operations.

of bits transmitted in one DMT symbol is given by

$$b_{DMT} = \sum_{i \in \mathcal{S}} \log_2 \left(1 + \frac{\mathrm{SNR}_i}{\Gamma_i} \right), \tag{4.4}$$

where SNR_i represents the SNR on tone i, $\mathcal{S}$ is the set of used tones and Γ_i is the SNR gap between the actual SNR_i and the SNR required to achieve Shannon capacity, see also Section 2.1. Similar to the derivation of the BM-TEQ in Subsection 3.3.4, the SNR on tone i can be written in a simple form as:

$$\mathrm{SNR}_i \quad = \quad \frac{\text{energy in (desired signal}_i\text{)}}{\text{energy in (received signal}_i - \text{desired signal}_i\text{)}}, \tag{4.5}$$

where the overall noise contribution is determined by the received signal components that are not related to the desired signal. When a *constrained minimum mean square error (MMSE)* FEQ is used, an unbiased desired signal part at the FEQ output is obtained. Hence, the numerator in (4.5) is given by the average energy of the transmitted symbol on tone i, i.e. $\mathcal{E}\{|X_i^k|^2\}$ [143][144].

Since the FEQ *input* for tone i after windowing ($\mathbf{d}$) and TEQ filtering ($\mathbf{w}$) is given by

$$Y_{dw,i}^k = \mathcal{F}_N[i,:]\mathbf{\Omega}\mathbf{Y}^{ext,k}\mathbf{w}, \tag{4.6}$$

the overall received signal, i.e. the FEQ *output* for tone i can be decomposed as follows

$$D_i Y_{dw,i}^k = X_i^k + E_i^k, \tag{4.7}$$

where D_i is the constrained MMSE FEQ for tone i and E_i^k denotes the residual ISI/ICI and channel noise at the i-th FEQ output. The denominator in (4.5) is then easily obtained as the mean square error (MSE), $\mathcal{E}\{|E_i^k|^2\}$, where *all* noise sources are taken into account. Finally, the SNR_i in (4.5) is equal to

$$\boxed{\text{SNR}_i = \frac{\mathcal{E}\{|X_i^k|^2\}}{\mathcal{E}\{|E_i^k|^2\}} = \frac{\mathcal{E}\{|X_i^k|^2\}}{\mathcal{E}\{|D_i Y_{dw,i}^k - X_i^k|^2\}}.} \tag{4.8}$$

4.1.3 Constrained versus unconstrained MMSE FEQ

In practice, several design criteria for the FEQ could be used. Therefore, let us first define the FEQ output for tone i in a more general form

$$D_i Y_{dw,i}^k = \alpha_i X_i^k + E_i^k, \tag{4.9}$$

where α_i is a scale factor. It can easily be proven that the traditional *unconstrained* MMSE FEQ, given by the Wiener solution

$$D_{uncon,i} = \arg\min_{D_i} \mathcal{E}\{|D_i Y_{dw,i}^k - X_i^k|^2\} = \frac{\mathcal{E}\{Y_{dw,i}^{k^*} X_i^k\}}{\mathcal{E}\{|Y_{dw,i}^k|^2\}}, \tag{4.10}$$

results in a biased desired signal part at the FEQ output, i.e. $\mathcal{E}\{D_{uncon,i} Y_{dw,i}^k - X_i^k | X_i^k\} \neq 0$ or equivalently $\alpha_i \neq 1$. The undesired bias can be estimated and removed by adding a constraint to the MMSE criterion of (4.10), i.e.

$$D_{con,i} = \arg\min_{D_i} \mathcal{E}\{|D_i Y_{dw,i}^k - X_i^k|^2\} \quad \text{s.t.} \quad \mathcal{E}\{D_i Y_{dw,i}^k (X_i^k)^*\} = \mathcal{E}\{|X_i^k|^2\}, \tag{4.11}$$

leading to the so-called *constrained* MMSE equalizer. In other words, the *constrained* MMSE FEQ results in an *unbiased* desired signal part at the FEQ output.

In the case of a one-tap equalizer, the *zero forcing*[2] (ZF) and constrained MMSE criterion yield exactly the same solution. Whereas a multi-taps ZF equalizer may cause noise enhancement and hence a lower SNR [71], a single-tap ZF equalizer scales both the desired and noise components in the same way and hence leaves the SNR unaltered. The ZF FEQ for tone i is defined as

$$\boxed{D_i \;=\; \frac{\mathcal{E}\{|X_i^k|^2\}}{\mathcal{E}\{Y_{dw,i}^k (X_i^k)^*\}}.} \tag{4.12}$$

Observe that the ZF FEQ is not merely equal to the inverse of the ith frequency component of the overall channel, as suggested by (2.17). Clearly, the TEQ and windowing operations have to be taken into account as well.

[2]The ZF criterion forces the residual error to zero under the assumption that noise and ISI/ICI are absent.

The assumption of using constrained MMSE FEQs, given by (4.12), is only required to obtain a simple SNR definition for (4.5). In practice, any other FEQ definition may be applied, as long as the SNR is redefined accordingly. More specifically, assume that the unconstrained MMSE FEQs are used. From (4.9), it is clear that the correct SNR for tone i can be obtained as

$$\mathrm{SNR}_i = \frac{\mathcal{E}\{|\alpha_i X_i^k|^2\}}{\mathcal{E}\{|E_i^k|^2\}} = \frac{\mathcal{E}\{|\alpha_i X_i^k|^2\}}{\mathcal{E}\{|D_{uncon,i} Y_{dw,i}^k - \alpha_i X_i^k|^2\}}, \tag{4.13}$$

$$= \frac{\mathcal{E}\{|X_i^k|^2\}}{\mathcal{E}\{|\beta_i D_{uncon,i} Y_{dw,i}^k - X_i^k|^2\}}, \tag{4.14}$$

with $\beta_i = 1/\alpha_i \neq 1$. Note that for tones with high SNR, the residual interference plus noise is almost negligible, resulting in $D_{uncon,i} \approx D_{con,i}$ and hence $\beta_i \approx \alpha_i \approx 1$. For low SNR, however, the definition of (4.14) implies that the decision device at the FEQ output first scales the FEQ output with β_i before taking decisions. Stated differently, an unconstrained MMSE receiver exhibits a higher bit error rate than a constrained (unbiased) MMSE receiver, unless its decision regions are scaled to compensate for the bias [34]. Since this additional scaling leads to an increased complexity of the decision device (for the same bit error rate), the unbiased approach with constrained MMSE FEQs and with a simple SNR expression (cf. (4.8)) is preferred. Hence, constrained MMSE FEQs (or ZF FEQs) will be assumed in the remainder of this chapter.

In the following sections, we will explicitly define (4.12) and (4.8) for three different designs:

1. bit rate maximizing combined equalizer and window design,
2. bit rate maximizing equalizer-only design,
3. bit rate maximizing window-only design.

The last two cases are in fact special cases of the first one.

4.2 Bit rate maximizing equalizer and window design

4.2.1 Single TEQ and window design (BM-WinTEQ)

In this subsection, we will discuss the joint optimization of a single TEQ combined with a time domain window in order to maximize the overall bit rate. Traditionally, equalization in ADSL is performed by a TEQ-FEQ combination

only [5][6][10][83][144]. On the other hand, receiver windowing and FEQ (without TEQ) is commonly applied in DMT-based VDSL to reduce the susceptibility of the receiver to narrow band interference [118][119]. Since windowing reduces the sidelobe level of the demodulating DFT, it can also help the ADSL equalizer in reducing the ICI. Alternatively, a VDSL receiver may benefit from an additional TEQ to notch out RFI frequencies.

The window and fold operations of (4.3) assume that the last μ samples of the part of $\mathbf{y}^k$ corresponding to the CP are effectively ISI-free to preserve the DMT-orthogonality, see also Subsection 2.2.3. By incorporating windowing into a joint bit rate maximizing window and TEQ design, this assumption can be omitted since then the overall optimal combination of TEQ and window taper will be obtained.

Starting from the definitions in (4.6) and (4.3), the FEQ input can be modified to

$$\begin{aligned} Y_{dw,i}^k &= \mathcal{F}_N[i,:](\mathbf{\Omega}_1 + \mathbf{\Omega}_2)\mathbf{Y}^{ext,k}\mathbf{w}, && (4.15)\\ &= \mathcal{F}_N[i,:]\mathbf{Y}^k\mathbf{w} + \mathcal{F}_N[i,:]\mathbf{\Omega}_2\mathbf{Y}^{ext,k}\mathbf{w}, && (4.16)\\ &= \mathbf{Y}_i^{sl,k}\mathbf{w} + \mathbf{d}_i^T\Delta\mathbf{Y}^{ext,k}\mathbf{w}, && (4.17) \end{aligned}$$

where $\mathbf{Y}_i^{sl,k} = \mathcal{F}_N[i,:]\mathbf{Y}^k$ represents the i-th row of the sliding FFT[3] of the received signal vector and where the vector $\mathbf{d}_i$ denotes the frequency modulated windowing coefficients, i.e.

$$\begin{aligned} \mathbf{d}_i^T &= [d_{i,0} \ \dots \ d_{i,\mu-1}], && (4.18)\\ &= \mathcal{F}_N[i, N{-}\mu{+}1{:}N]\mathrm{diag}\{\mathbf{d}\} = \mathbf{d}^T\mathbf{D}_{\mathcal{F},i}, && (4.19) \end{aligned}$$

with $\mathbf{D}_{\mathcal{F},i} = \mathrm{diag}\{\mathcal{F}_N[i, N{-}\mu{+}1{:}N]\}$. The $\mu \times T$ matrix $\Delta\mathbf{Y}^{ext,k}$ is given by

$$\begin{aligned} \Delta\mathbf{Y}^{ext,k} &= \left[\ \mathbf{I}_\mu \ \middle|\ \mathbf{0}_{\mu\times(N-\mu)} \ \middle|\ -\mathbf{I}_\mu\ \right]\mathbf{Y}^{ext,k}, && (4.20)\\ &= \begin{bmatrix} \Delta y_\mu^k & \dots & \Delta y_{\mu+T-1}^k \\ \vdots & \ddots & \vdots \\ \Delta y_1^k & \dots & \Delta y_T^k \end{bmatrix}, && (4.21) \end{aligned}$$

where $\Delta\mathbf{Y}^{ext,k}$ is again a Toeplitz matrix. Furthermore, with $\Delta\mathbf{y}^{ext,k}$ defined as a vector of $\mu + T - 1$ difference terms

$$\Delta\mathbf{y}^{ext,k} = [\Delta y_{\mu+T-1}^k \ \dots \ \Delta y_1^k]^T, \qquad (4.22)$$

the second term in (4.17) can be written as

$$\mathbf{d}_i^T\Delta\mathbf{Y}^{ext,k}\mathbf{w} = (\Delta\mathbf{y}^{ext,k})^T\mathbf{\Omega}_i\mathbf{w} = (\Delta\mathbf{y}^{ext,k})^T\mathbf{W}_i\mathbf{d}. \qquad (4.23)$$

[3]Apparently, one needs to compute T DFTs, i.e. one DFT for each column of $\mathbf{Y}^k$. However, due to the Toeplitz structure of $\mathbf{Y}^k$, this can be calculated efficiently by means of a sliding FFT [45].

Here $\mathbf{\Omega}_i$ and $\mathbf{W}_i$ tone dependent matrices of size $(\mu+T-1)\times T$ and $(\mu+T-1)\times\mu$ respectively

$$\mathbf{\Omega}_i = \begin{bmatrix} \mathbf{0} & & \mathbf{d}_i \\ & \iddots & \\ \mathbf{d}_i & & \mathbf{0} \end{bmatrix}, \qquad \mathbf{W}_i = \begin{bmatrix} \bar{\mathbf{w}} & & \mathbf{0} \\ & \bar{\mathbf{w}} & \\ \mathbf{0} & & \bar{\mathbf{w}} \end{bmatrix} \mathbf{D}_{\mathcal{F},i}, \quad (4.24)$$

where $\bar{\mathbf{w}}$ contains the TEQ coefficients in reversed order, i.e. $\bar{\mathbf{w}} = [w_{T-1} \dots w_0]^T$. Furthermore, define for each tone i the signal statistics at the receiver as

$$\begin{aligned} \sigma_{x,i}^2 &= \mathcal{E}\{|X_i^k|^2\}, & \mathbf{r}_{X\Delta,i} &= \mathcal{E}\{(X_i^k)^*(\Delta\mathbf{y}^{ext,k})^T\}, \\ \mathbf{r}_{XY,i} &= \mathcal{E}\{(X_i^k)^*\mathbf{Y}_i^{sl,k}\}, & \mathbf{R}_{YY,i} &= \mathcal{E}\{(\mathbf{Y}_i^{sl,k})^H\mathbf{Y}_i^{sl,k}\}, \\ \mathbf{R}_{Y\Delta,i} &= \mathcal{E}\{(\mathbf{Y}_i^{sl,k})^H(\Delta\mathbf{y}^{ext,k})^T\}, & \mathbf{R}_{\Delta\Delta} &= \mathcal{E}\{\Delta\mathbf{y}^{ext,k}(\Delta\mathbf{y}^{ext,k})^T\}. \end{aligned} \quad (4.25)$$

With these definitions the definitions of SNR_i and D_i can be expressed as a function of signal statistics on the one hand and the unknown TEQ and window coefficients on the other hand. When combining (4.12), (4.17), (4.23) and (4.25), one obtains

$$D_i = \frac{\mathcal{E}\{|X_i^k|^2\}}{\mathcal{E}\{Y_{dw,i}^k(X_i^k)^*\}}, \quad (4.26)$$

$$= \frac{\sigma_{x,i}^2}{\mathbf{r}_{XY,i}\mathbf{w} + \mathbf{r}_{X\Delta,i}\mathbf{\Omega}_i\mathbf{w}}. \quad (4.27)$$

Expression (4.8) for the SNR with the ZF FEQs of (4.27) can be written compactly as

$$\mathrm{SNR}_i = \frac{1}{\rho_i^{-2}(\mathbf{d},\mathbf{w}) - 1}, \quad (4.28)$$

with $\rho_i^2(\mathbf{d},\mathbf{w})$ a tone dependent, normalized correlation function, depending on the window and TEQ coefficients, i.e.

$$\rho_i^2(\mathbf{d},\mathbf{w}) = \frac{|\mathcal{E}\{Y_{dw,i}^k(X_i^k)^*\}|^2}{\mathcal{E}\{|Y_{dw,i}^k|^2\}\mathcal{E}\{|X_i^k|^2\}}, \quad (4.29)$$

$$= \frac{|\mathbf{r}_{XY,i}\mathbf{w} + \mathbf{r}_{X\Delta,i}\mathbf{\Omega}_i\mathbf{w}|^2}{\left(\mathbf{w}^T(\mathbf{R}_{YY,i} + \mathbf{R}_{Y\Delta,i}\mathbf{\Omega}_i + \mathbf{\Omega}_i^H\mathbf{R}_{Y\Delta,i}^H + \mathbf{\Omega}_i^H\mathbf{R}_{\Delta\Delta}\mathbf{\Omega}_i)\mathbf{w}\right)\sigma_{x,i}^2}.$$

The proof is straightforward and is given in Appendix C.1. Combining (4.4) and (4.28), the BM-WinTEQ is the solution of

$$\arg\max_{\mathbf{d},\mathbf{w}} b_{DMT} = \arg\max_{\mathbf{d},\mathbf{w}} \sum_{i\in\mathcal{S}} \log_2\left(1+\frac{1}{\Gamma_i(\rho_i^{-2}(\mathbf{d},\mathbf{w})-1)}\right). \quad (4.30)$$

The cost function of (4.30) is an *unconstrained, non-linear cost function* and calls for non-linear optimization techniques. The solution of (4.30) can be obtained by, e.g. the MATLAB® optimization toolbox, which provides a wide set of non-linear optimization routines [126]. Since the knowledge of the gradient and Hessian is often required, expressions for the gradient and Hessian of (4.30) are derived in Appendix C.2.

At first sight, (4.30) requires the computation and storage of the statistical quantities in (4.25). In Appendix C.3, it is shown how the storage can be reduced by deriving $\mathbf{r}_{XY,i}$, $\mathbf{R}_{YY,i}$ and $\mathbf{R}_{Y\Delta,i}$ from $\mathbf{r}_{X\Delta,i}$, $\mathbf{R}_{\Delta\Delta}$ (which is tone independent) and

$$r_{XY,i} = \mathcal{E}\{(X_i^k)^* Y_i\}, \qquad \mathbf{r}_{Y\Delta,i} = \mathcal{E}\{Y_i^k(\Delta\mathbf{y}^{ext,k})^T\}, \quad (4.31)$$

where $r_{XY,i}$ is the first element of $\mathbf{r}_{XY,i}$, $\mathbf{r}_{Y\Delta,i}$ is the first row of $\mathbf{R}_{Y\Delta,i}$ and

$$Y_i^k = \mathcal{F}_N[i,:][y_0^k \ \ldots \ y_{N-1}^k]^T. \quad (4.32)$$

4.2.2 Per group equalizer and window design (BM-PG-WinTEQ)

In (4.30), all tones carrying data are taken into account for the computation of a single TEQ and a single window. Whereas a single TEQ and a single window treat all tones in the same way, bit rate improvements are possible by dividing the available tones into smaller groups. With tone grouping, each group can optimize a separate equalizer and window function, hence the term *bit rate maximizing per group windowing and time domain equalization (BM-PGWinTEQ)*.

When considering N_g tone groups, the overall number of bits that can be transmitted in one DMT symbol is given by

$$b_{DMT}(\mathbf{d}_g,\mathbf{w}_g,g=0,\ldots,N_g-1) = \sum_{g=0}^{N_g-1}\sum_{i\in\mathcal{S}_g}\log_2\left(1+\frac{1}{\Gamma_i(\rho_i^{-2}(\mathbf{d}_g,\mathbf{w}_g)-1)}\right), \quad (4.33)$$

where $\mathbf{d}_g$, $\mathbf{w}_g$ and $\mathcal{S}_g$ are the windowing coefficients, the TEQ coefficients and the set of used tones for tone group g respectively. Since bits are non-negative quantities, maximizing the second summation in (4.33) for each group separately, leads to the overall maximum bit rate.

The idea of tone grouping was first introduced in [132] as a reduced complexity scheme for the PTEQ, where a PTEQ is computed for a group of tones based on the information of the center tone of the group only. The remaining tones in the group receive a PTEQ corresponding to the equivalent TEQ of the center tone. This solution is not necessarily bit rate maximizing and as such suboptimal, especially for large tone groups. Here, we extend the tone grouping idea in two ways:

1. a window is added per tone group, next to the equalizer,
2. the per group coefficients are not only based on the center tone but accommodates the information of all the tones in the group for effective bit rate maximization.

4.2.3 Per tone equalizer and window design (PTEQ)

A special case of the per group approach occurs when an equalizer and a window function are designed for each individual tone. In this case, maximizing the overall bit rate is equivalent to maximizing each term in the summation of (4.4) separately. Since the $\log_2$ is a monotonically increasing function, the maximization of a single term in (4.4) is equivalent to the maximization of its argument. Hence, the cost function for a single tone reduces to

$$\arg \max_{\mathbf{d}_i, \mathbf{w}_i} \mathrm{SNR}_i \quad \forall i \in \mathcal{S}. \tag{4.34}$$

When a ZF FEQ is used, the SNR for tone i is defined by (4.8). Since the numerator of (4.8) is always positive and independent of the equalizer and window coefficients, one might as well minimize the denominator of SNR_i:

$$\arg \min_{\mathbf{d}_i, \mathbf{w}_i} \mathcal{E}\{|D_i Y_{dw,i}^k - X_i^k|^2\}, \quad \forall i \in \mathcal{S}. \tag{4.35}$$

Next, we will show that the solution for this problem effectively corresponds to the *constrained (unbiased) MMSE PTEQ* with $\mu + T$ taps for each tone i. In other words, *the window process can efficiently be incorporated in the PTEQ operation after increasing the number of PTEQ coefficients from T to $\mu + T$.*

Starting from the FEQ input for tone i given by (4.17) and combining it with (4.23), one has

$$Y_{dw,i}^k = \mathbf{Y}_i^{sl,k}\mathbf{w} + (\Delta \mathbf{y}^{ext,k})^T \mathbf{\Omega}_i \mathbf{w}. \tag{4.36}$$

As $\mathbf{Y}_i^{sl,k}$ is equal to $\mathcal{F}_N[i,:]\mathbf{Y}^k = \mathrm{row}_i\{\mathcal{F}_N \mathbf{Y}^k\}$, the first term involves the computation of T DFTs on the incoming time domain samples. Since $\mathbf{Y}^k$ has a Toeplitz structure, this computation can be done in terms of one full

DFT and the $T-1$ difference terms $\Delta y_1^k, \ldots, \Delta y_{T-1}^k$ (see Subsection 3.4.1 or Appendix C.3), i.e.

$$\mathbf{Y}_i^{sl,k}\mathbf{w} = \bar{\mathbf{w}}^T \underbrace{\begin{bmatrix} 1 & \alpha^i & \ldots & \alpha^{i(T-1)} \\ & \ddots & & \vdots \\ & & 1 & \alpha^i \\ 0 & & & 1 \end{bmatrix}}_{\mathbf{Q}} \left[\begin{array}{c|c|c} \mathbf{I}_{T-1} & \mathbf{0} & -\mathbf{I}_{T-1} \\ \hline \mathbf{0} & \multicolumn{2}{c}{\mathcal{F}_N[i,:]} \end{array}\right] \mathbf{y}^k, \quad (4.37)$$

$$= \bar{\mathbf{w}}^T \mathbf{Q} \left[(\Delta\mathbf{y}^k)^T \;\; Y_i^k\right]^T, \quad (4.38)$$

with $\alpha = e^{-j2\pi/N}$, $Y_i^k = \mathcal{F}_N[i,:][y_0^k \;\ldots\; y_{N-1}^k]^T$ and where $\bar{\mathbf{w}}$ denotes the TEQ with coefficients in reversed order. When the joint windowing and TEQ operation in $\mathbf{\Omega}_i\mathbf{w}$ is replaced by one tone dependent vector of unknowns, it is easy to see that the second term in (4.36) comprises a linear combination of the difference terms $\Delta y_1^k, \ldots, \Delta y_{\mu+T-1}^k$. Hence, the overall FEQ input in (4.36) can be written in general as a linear combination of the DFT output for tone i, Y_i^k, and the $\mu+T-1$ real valued difference term of $\Delta\mathbf{y}^{ext,k}$, i.e.

$$Y_{dw,i}^k = \bar{\mathbf{v}}_i^T \left[(\Delta\mathbf{y}^{ext,k})^T \;\; Y_i^k\right]^T, \quad (4.39)$$

where $\bar{\mathbf{v}}_i = [v_{i,\mu+T-1} \;\ldots\; v_{i,0}]^T$ are now the overall unknown coefficients. After applying (4.39), expression (4.35) can be modified to

$$\arg\min_{\mathbf{v}_i} \mathcal{E}\left\{\left| D_i\bar{\mathbf{v}}_i^T \left[(\Delta\mathbf{y}^{ext,k})^T \;\; Y_i^k\right]^T - X_i^k \right|^2\right\}, \quad \forall i \in \mathcal{S}, \quad (4.40)$$

with D_i still given by (4.12), i.e. $D_i\bar{\mathbf{v}}_i$ corresponds to the *constrained (unbiased) MMSE* solution of a $T+\mu$-taps PTEQ design problem. In Chapter 6 the initialization of the constrained MMSE PTEQ will be treated in more detail.

When D_i is fixed to one, the solution of (4.40) reduces to the design of an *unconstrained (biased) MMSE PTEQ* of $\mu+T$ taps, which was first addressed in [139]. As discussed in Subsection 3.4.1, the unconstrained MMSE PTEQ is obtained by the Wiener solution of (4.40) with $D_i = 1$, while the constrained MMSE PTEQ is simply a scaled (unbiased) version of this solution. As a consequence, by applying the correct SNR definition ((4.8) or (4.14) for the unbiased and biased solution respectively) both the constrained and unconstrained MMSE PTEQ lead to the *same maximum bit rate*.

In practice, however, the constrained (unbiased) MMSE PTEQ is preferred due to its simple decision rule at the receiver output for tone i. Hence, in contrast to [139], an extra FEQ at the PTEQ output is required to obtain the *unbiased* solution. Although the per tone consistently leads to improved performance, the required memory to store the unknown coefficients has increased to $N_u(\mu+T)$. Hence, single TEQ and single window designs still remain very important.

4.3 Special cases

The general framework introduced in Section 4.2 allows us to derive some special cases. In the previous section, our main focus was to optimize the combined windowing-equalization problem. By omitting either the windowing part or either the equalization part, the bit rate maximizing cost function can be drastically reduced in complexity. Therefore, equalizer-only and windowing-only designs will be discussed in this section.

4.3.1 Equalizer-only design

A single TEQ (BM-TEQ)

Based on (4.30), a single TEQ to maximize the bit rate can be designed, without receiver windowing, i.e. $\mathbf{d} = \mathbf{0}$. The FEQ input for tone i (cf. (4.17)) is now only a TEQ filtered version of the received samples, given by

$$Y_{w,i}^k = \mathcal{F}_N[i,:]\mathbf{\Omega}_1\mathbf{Y}^{ext,k}\mathbf{w} = \mathbf{Y}_i^{sl,k}\mathbf{w}. \tag{4.41}$$

Also, the ZF FEQ for tone i in (4.12) is adapted accordingly, i.e.

$$D_i = \frac{\mathcal{E}\{|X_i^k|^2\}}{\mathcal{E}\{Y_{w,i}^k(X_i^k)^*\}} = \frac{\sigma_{x,i}^2}{\mathbf{r}_{XY,i}\mathbf{w}}. \tag{4.42}$$

With the data model presented in (2.40) it is again observed that the ZF FEQ is not equal to the inverse of the ith frequency component of the channel convolved with the TEQ. Although the latter is an assumption that is often made in literature, it only holds when the channel is perfectly shortened to the CP length. Plugging (4.41) and (4.42) into (4.4) and (4.8), the bit rate maximizing TEQ (BM-TEQ) cost function is obtained:

$$\arg\max_{\mathbf{w}} b_{DMT}(\mathbf{w}) = \arg\max_{\mathbf{w}} \sum_{i\in\mathcal{S}} \log_2\left(\frac{\mathbf{w}^T\mathbf{A}_i\mathbf{w}}{\mathbf{w}^T\mathbf{B}_i\mathbf{w}}\right), \tag{4.43}$$

where $\mathbf{A}_i$ and $\mathbf{B}_i$ are independent of $\mathbf{w}$, i.e.

$$\mathbf{A}_i = \Gamma_i\sigma_{x,i}^2\mathbf{R}_{YY,i} + (1-\Gamma_i)\mathbf{r}_{XY,i}^H\mathbf{r}_{XY,i}, \tag{4.44}$$

$$\mathbf{B}_i = \Gamma_i\left(\sigma_{x,i}^2\mathbf{R}_{YY,i} - \mathbf{r}_{XY,i}^H\mathbf{r}_{XY,i}\right). \tag{4.45}$$

Although channel shortening is the original underlying idea for using a TEQ, the BM-TEQ criterion (4.43) does not explicitly impose channel shortening any more. The single TEQ design criterion (4.43), derived here as a special case of (4.30), is exactly the same criterion as presented in Subsection 3.3.4 and [143][144]. Although the BM-TEQ is optimizing the bit rate, simulations will show that the addition of a window may reduce equalization complexity for a similar bit rate performance.

Per tone equalization (PTEQ)

When the per group approach of (4.33) is applied to calculate an equalizer for each tone $i \in \mathcal{S}$ without windowing, the design criterion is reduced to the maximization of (4.43) for each tone separately, i.e.

$$\arg\max_{\mathbf{w}_i} \log_2 \left(\frac{\mathbf{w}_i^T \mathbf{A}_i \mathbf{w}_i}{\mathbf{w}_i^T \mathbf{B}_i \mathbf{w}_i} \right), \quad \forall i \in \mathcal{S}, \tag{4.46}$$

$$= \arg\max_{\mathbf{w}_i} \left(1 + \frac{\mathbf{w}_i^T \mathbf{r}_{XY,i}^H \mathbf{r}_{XY,i} \mathbf{w}_i}{\mathbf{w}_i^T \left(\Gamma_i(\sigma_{x,i}^2 \mathbf{R}_{YY,i} - \mathbf{r}_{XY,i}^H \mathbf{r}_{XY,i}) \right) \mathbf{w}_i} \right), \quad \forall i \in \mathcal{S}, \tag{4.47}$$

$$= \arg\min_{\mathbf{w}_i} \left(\frac{\mathbf{w}_i^T \left(\Gamma_i(\sigma_{x,i}^2 \mathbf{R}_{YY,i} - \mathbf{r}_{XY,i}^H \mathbf{r}_{XY,i}) \right) \mathbf{w}_i}{\mathbf{w}_i^T \mathbf{r}_{XY,i}^H \mathbf{r}_{XY,i} \mathbf{w}_i} \right), \quad \forall i \in \mathcal{S}, \tag{4.48}$$

$$= \arg\min_{\mathbf{w}_i} \left(\frac{\mathbf{w}_i^T \mathbf{R}_{YY,i} \mathbf{w}_i}{\mathbf{w}_i^T \mathbf{r}_{XY,i}^H \mathbf{r}_{XY,i} \mathbf{w}_i} \right), \quad \forall i \in \mathcal{S}. \tag{4.49}$$

The minimization of (4.49) is equivalent to a generalized eigenvalue problem, where the solution is given by the generalized eigenvector corresponding to the maximum generalized eigenvalue λ of

$$\boxed{\mathbf{r}_{XY,i}^H \mathbf{r}_{XY,i} \mathbf{w}_i = \lambda \mathbf{R}_{YY,i} \mathbf{w}_i, \quad \forall i \in \mathcal{S},} \tag{4.50}$$

Since the matrix $\mathbf{r}_{XY,i}^H \mathbf{r}_{XY,i}$ is positive semi-definite with rank one and $\mathbf{R}_{YY,i}$ is in general positive definite, only one generalized eigenvalue is strictly positive whereas the other generalized eigenvalues are equal to zero. As shown in [143], the solution of (4.50) and the corresponding generalized eigenvalue are given by

$$\mathbf{w}_{opt,i} = (\mathbf{R}_{YY,i})^{-1} \mathbf{r}_{XY,i}^H, \tag{4.51}$$

$$\lambda_{max,i} = \mathbf{r}_{XY,i} (\mathbf{R}_{YY,i})^{-1} \mathbf{r}_{XY,i}^H. \tag{4.52}$$

Note that (4.51) is equal to the T-taps *unconstrained (biased) MMSE PTEQ* and is in fact the Wiener solution of (4.35) with $D_i = 1$ and $Y_{dw,i}^k = \mathbf{Y}_i^{sl,k} \mathbf{w}$. Finally, the solution of (4.50) is determined up to a scale factor. Therefore, the ZF FEQ succeeding the PTEQ output is determined to obtain an unbiased symbol estimator.

4.3.2 Window-only design

In this subsection, it is assumed that the DMT-system has a *channel impulse response that is strictly shorter than* $\nu - \mu + 1$ *samples*[4] (or perfectly shortened to

[4] This assumption is only made to make the mathematical derivation as simple as possible. The results of this subsection can easily be extended to the case where the channel is not perfectly short.

that length), as e.g. in an asynchronous Zipper VDSL system [84][112][113][114]. Furthermore, assume that μ-taps windowing is added to obtain high spectral containment in order to mitigate RFI from radio amateurs and/or AM broadcast. Under these conditions, the equalization problem reduces to a simple scaling per frequency (FEQ) since the linear convolution is turned into a circular one due to the cyclic prefix. The design of the bit rate maximizing windowing coefficients, on the other hand, is less straightforward. In this subsection, we will investigate the design of a single window and the design of a window for each tone separately. Similar derivations are possible when the assumption on the channel order is not strictly met, but these will not be given here.

A single window (BM-Win)

Since no explicit time domain equalization is considered, the TEQ is given by $\mathbf{w} = [1\ 0\ \ldots\ 0]^T$. Referring to (4.15), the FEQ input for tone i after windowing can then be written as

$$\underbrace{\mathcal{F}_N[i,:]\mathbf{\Omega}\mathbf{Y}^{ext,k}[1\ 0\ \ldots\ 0]^T}_{Y_{d,i}^k} = \mathcal{F}_N[i,:](\mathbf{\Omega}_1+\mathbf{\Omega}_2)\tilde{\mathbf{y}}^k, \quad (4.53)$$

$$= \mathcal{F}_N[i,:]\mathbf{\Omega}_1\tilde{\mathbf{y}}^k + \mathbf{d}^T\mathbf{D}_{\mathcal{F},i}\Delta\tilde{\mathbf{y}}^k, \quad (4.54)$$

$$= Y_i^k + \mathbf{d}_i^T\Delta\tilde{\mathbf{y}}^k, \quad (4.55)$$

where $\mathbf{\Omega}$, $\mathbf{d}_i$ and Y_i^k are defined in (4.3), (4.19) and (4.32) respectively and where $\Delta\tilde{\mathbf{y}}^k = [\Delta y_\mu^k\ \ldots\ \Delta y_1^k]^T$. Equation (4.55) indicates that the windowed FEQ input for tone i is equal to the unwindowed FEQ input for tone i plus a correction based on a linear combination of tone independent, real valued difference terms $\Delta\tilde{\mathbf{y}}^k$ and frequency modulated windowing coefficients $\mathbf{d}_i$. When the channel impulse response is strictly limited to $\nu-\mu+1$ samples, the last μ samples of the part of $\tilde{\mathbf{y}}^k$ corresponding to the CP are free of inter-symbol-interference (assuming there is appropriate synchronization). As a result, $\Delta\tilde{\mathbf{y}}^k$ is zero in the noiseless case. In other words, due to the symmetry of the window function and the folding operation, the window only acts on the external noise without destroying the DMT signal orthogonality.

Since $\Delta\tilde{\mathbf{y}}^k$ only contains external noise information, which is uncorrelated with the transmitted symbol, the ZF FEQ of (4.12) will be independent of the window function and will be equal to the ZF FEQ of the unwindowed case, i.e.

$$D_i = \frac{\mathcal{E}\{|X_i^k|^2\}}{\mathcal{E}\{Y_{d,i}^k(X_i^k)^*\}} = \frac{\mathcal{E}\{|X_i^k|^2\}}{\mathcal{E}\{Y_i^k(X_i^k)^*\} + \mathbf{d}_i^T\underbrace{\mathcal{E}\{\Delta\tilde{\mathbf{y}}^k(X_i^k)^*\}}_{=\mathbf{0}}} = \frac{\sigma_{x,i}^2}{r_{XY,i}}, \quad (4.56)$$

where $Y_{d,i}^k$ was defined in (4.55) and $r_{XY,i}$ is given by (4.31). Since the channel is confined to the duration of the CP, the resulting ZF FEQ is simply the inverse of the channel frequency domain coefficient for tone i.

Similar to (4.8), the SNR for tone i can be obtained as

$$\mathrm{SNR}_i = \frac{\mathcal{E}\{|X_i^k|^2\}}{\mathcal{E}\{|D_i Y_{d,i}^k - X_i^k|^2\}} = \frac{\sigma_{x,i}^2}{\mathcal{E}\{|D_i Y_i^k + D_i(\Delta\tilde{\mathbf{y}}^k)^T\mathbf{d}_i - X_i^k|^2\}}. \quad (4.57)$$

When combining (4.4) with (4.57), one obtains the cost function to design a single, *bit rate maximizing window (BM-Win)*, i.e.

$$\arg\max_{\mathbf{d}} b_{DMT}(\mathbf{d}) = \arg\max_{\mathbf{d}} \sum_{i\in\mathcal{S}} \log_2\left(1 + \frac{\sigma_{x,i}^2}{\Gamma_i g_i(\mathbf{d})}\right), \quad (4.58)$$

with $g_i(\mathbf{d}) = \mathbf{d}^T\mathbf{A}_i\mathbf{d} + 2\mathbf{b}_i^T\mathbf{d} + c_i$, where $\mathbf{A}_i$, $\mathbf{b}_i$ and c_i are independent of $\mathbf{d}$, given by

$$\mathbf{A}_i = |D_i|^2\mathbf{D}_{\mathcal{F},i}^*\mathcal{E}\{\Delta\tilde{\mathbf{y}}^k(\Delta\tilde{\mathbf{y}}^k)^T\}\mathbf{D}_{\mathcal{F},i}, \quad (4.59)$$

$$\mathbf{b}_i = \mathcal{R}e\{D_i\mathbf{D}_{\mathcal{F},i}\mathcal{E}\{(D_i Y_i^k)^*\Delta\tilde{\mathbf{y}}^k\}\}, \quad (4.60)$$

$$c_i = \mathcal{E}\{|D_i Y_i^k - X_i^k|^2\}, \quad (4.61)$$

where $\mathcal{E}\{(X_i^k)^*\Delta\tilde{\mathbf{y}}^k\} = \mathbf{0}$ was again applied and where $\mathcal{R}e\{\cdot\}$ takes the real part of its argument. Once more, the cost function in (4.58) is non-linear and hence non-linear optimization techniques are needed to find the optimal solution.

BM-Win design could be combined with an optimization of the transmission bandwidth, similar to [7], such that only tones with high SNR are incorporated in the cost function of (4.58). Under high SNR conditions, the value 'one' can be neglected in each term of (4.58), leading to

$$\arg\min_{\mathbf{d}} \sum_{i\in\mathcal{S}} \log_2\left(g_i(\mathbf{d})\right) = \arg\min_{\mathbf{d}} \sum_{i\in\mathcal{S}} \log_2\left(\mathcal{E}\{|D_i Y_i^k + D_i(\Delta\tilde{\mathbf{y}}^k)^T\mathbf{d}_i - X_i^k|^2\}\right), \quad (4.62)$$

which clearly corresponds to the minimization of a *product* of squared errors at the FEQ output. In [102], an alternative cost function for window design is formulated, based on a *sum* (or a weighted sum) of squared errors at the FEQ input (using the same assumptions for the channel), i.e.

$$\mathbf{d}_{\mathrm{Red}} = \arg\min_{\mathbf{d}} \sum_{i\in\mathcal{S}} \mathcal{E}\{|Y_i^k + (\Delta\tilde{\mathbf{y}}^k)^T\mathbf{d}_i - X_i^k/D_i|^2\}. \quad (4.63)$$

As opposed to (4.58) and (4.62), this cost function has no direct relation with bit rate optimization and hence results in suboptimal windowing. However, it is a convex cost function (hence easier to optimize) and then (4.58) may serve as an upper bound on the performance that can be achieved.

Per tone windowing (PTEQ)

Similar to the BM-PGWinTEQ, one can perform *bit rate maximizing per group windowing (BM-PGWin)*, where (4.58) is now used to design a μ-taps optimal window for each group of tones. Again, when a window is designed for each tone separately, one effectively ends up with the design of a *constrained (unbiased) MMSE PTEQ*. Maximizing (4.58) for one tone is equivalent to minimizing $g_i(\mathbf{d}_i) = \mathcal{E}\{|E_i^k|^2\}$, leading to

$$\arg\min_{\mathbf{d}_i} g_i(\mathbf{d}_i) = \arg\min_{\mathbf{d}_i} \mathcal{E}\left\{\left| D_i \underbrace{\begin{bmatrix}\mathbf{d}_i^T & 1\end{bmatrix}}_{\bar{\mathbf{v}}_i^T} \begin{bmatrix}\Delta\tilde{\mathbf{y}}^k \\ Y_i^k\end{bmatrix} - X_i^k \right|^2\right\}, \quad \forall i \in \mathcal{S}, \tag{4.64}$$

with $\bar{\mathbf{v}}_i = [v_{i,\mu} \ \ldots \ v_{i,0}]^T$. Observe the similarities between (4.64) and (4.40), where (4.64) takes only the last μ difference terms of $\Delta\mathbf{y}^{ext,k}$ into account. Also here, $D_i\bar{\mathbf{v}}_i$ corresponds to the *constrained (unbiased) MMSE* PTEQ when a ZF FEQ is used, see also Subsection 4.2.3. Due to the definition of $\bar{\mathbf{v}}_i$ in (4.64), the expression for the ZF FEQ of (4.56) is slightly modified to

$$D_i = \frac{\mathcal{E}\{|X_i^k|^2\}}{\bar{\mathbf{v}}_i^T \mathcal{E}\left\{[(\Delta\tilde{\mathbf{y}}^k)^T \ \ Y_i^k]^T (X_i^k)^*\right\}} = \frac{\sigma_{x,i}^2}{v_{i,0} r_{XY,i}}, \tag{4.65}$$

where $\mathcal{E}\{(X_i^k)^*\Delta\tilde{\mathbf{y}}^k\} = \mathbf{0}$ still holds. Apparently, an extra degree of freedom has been gained in (4.64) with the design of $\mu + 1$ unknowns, whereas the starting point was a μ-taps window per tone. However, the ZF FEQ of (4.65) effectively acts as a constraint and ensures that a scaling of the received signal component Y_i^k by the PTEQ is reversed such that $v_{i,0}$ has in fact no effect.

4.3.3 Other variants

In the previous subsections, several special cases were treated. Of course, many other variants can be devised. One case that has been given special attention in literature is referred to as window incorporated per tone equalizer design [38][92][139]. In these papers, per tone equalizer design is considered in the presence of a *fixed* window. In a single TEQ scenario, a cost function can be derived, similar to (4.43), to design a BM-TEQ when it is followed by a windowed DFT with a fixed window, cf. **Fig. 4.1**. The resulting solution, which we will refer to as *BM-FWinTEQ*, could then be used as an upper bound on performance when existing TEQ design algorithms are followed by a windowed DFT instead of an ordinary DFT.

4.4 Complexity and memory requirements

In this section, complexity figures for equalization and/or windowing *during data transmission* are presented. To compute these figures, the number of *real* multiplications and *real* additions per symbol are counted. A multiplication of 2 complex valued scalars is counted as 4 real multiplications. Likewise, a multiplication of a real number with a complex number is counted as 2 real multiplications. An addition of 2 complex numbers is counted as 2 real additions.

The complexity figures are given in **Table 4.1**. Note that the PTEQ is assumed to be complex valued[5], whereas the TEQ or the TEQ per tone group is always considered to be real valued. As opposed to [136], it is assumed that additional ZF FEQs remove the bias of the unconstrained MMSE PTEQ. When considering TEQs for tone groups, a T-taps TEQ $\bar{\mathbf{w}}_g$ for a particular tone group is converted to the corresponding PTEQ $\bar{\mathbf{v}}_i$ for each tone in that tone group by the following recursion, cf. (3.119) and (3.120), i.e.

$$\begin{cases} v_{i,T-1} = w_{g,T-1}, \\ v_{i,l} = v_{i,l+1}\alpha^i + w_{g,l}, \quad l = T-2, \ldots, 0, \ i \in \mathcal{S}_g, \end{cases} \tag{4.66}$$

with $\alpha = e^{-j2\pi/N}$. By this, the sliding DFT operation is implicitly computed by means of difference terms [136]. For the combination of a single TEQ and a single window, we rely on (4.7), where the TEQ filtering is followed by a windowed DFT. Each method in **Table 4.1** requires also the computation of one DFT, which is not explicitly mentioned in the table.

The memory requirements to store the window and/or equalizer coefficients for the different methods are presented in **Table 4.2**. The required memory is expressed in the number of places to store real valued parameters. Each method requires the storage of complex valued FEQ coefficients and as such $2N_u$ real coefficients need to be stored, where N_u represents the number of tones that effectively carry data. Furthermore, since a PTEQ of T taps is assumed to be complex valued, $2N_uT$ storage places are foreseen.

Example 4.1 As a numerical example of the complexity and memory requirements for the different windowing and equalizer designs, consider a downstream scenario with $N = 512$, $T = 8$ equalizer taps, $\mu = 10$ windowing coefficients and $N_u = 220$ used tones. When tone grouping is used, consider $N_g = 22$ tone groups with each 10 tones. Furthermore, the symbol rate is 4.0588 kHz. The resulting complexity values, expressed in operations per second, and memory requirements are given in **Table 4.3**. △

[5]With the procedure in (4.50) it is also possible to design a real valued PTEQ. However, this case is not considered to stay in accordance with [136].

Based on **Table 4.3**, the following conclusions can be drawn:

- Since μ is typically much smaller than N, the extra complexity and memory requirements for adding a single window on top of a single TEQ is almost negligible.
- Since $N_u < N/2$ (e.g. the frequency band reserved for POTS is never used), a single TEQ often leads to a higher processing complexity during data transmission than a PTEQ. The memory of the PTEQ, however, is much higher than the memory required for a TEQ.
- Tone grouping may increase the achievable performance compared to single TEQ and/or single window design, but will also increase the computational complexity and the required memory. Tone grouping requires the conversion of the TEQ to the corresponding PTEQ coefficients for each tone (cf. (4.66) and (4.66)), resulting in extra computations. Alternatively, one could store the PTEQ coefficients for each tone directly, thereby avoiding conversion calculations at the cost of an enlarged memory size. Hence, a trade-off has to be made.
- A TEQ per tone group in combination with a single window leads to the same complexity as a TEQ per tone group in combination with a window per tone group. This is due to the fact that a window in the time domain can be transformed into a tone dependent equalizer, which has to be done for each used tone. Of course, a TEQ per tone group in combination with a window per tone group consumes more memory.
- Since per tone equalization with T taps in combination with a per tone window of μ taps leads to an overall PTEQ with $\mu+T$ taps, the complexity figures are similar to an ordinary PTEQ with an increased number of taps.

TABLE 4.1
Complexity during data transmission for different windowing and equalizer designs.

		# multiplications	# additions
single TEQ	TEQ	NT	$N(T-1)$
	FEQ	$4N_u$	$2N_u$
TEQ per tone group	TEQ conv.	$N_u(4T-6)$	$N_u(2T-3)$
	diff. terms	0	$T-1$
	recursion	$2N_u(T+1)$	$2N_uT$
	FEQ	$4N_u$	$2N_u$
PTEQ [136]	diff. terms	0	$T-1$
	PTEQ	$2N_u(T+1)$	$2N_uT$
	FEQ	$4N_u$	$2N_u$
single TEQ+ single window	TEQ	$(N+\mu)T$	$(N+\mu)(T-1)$
	windowing	2μ	μ
	FEQ	$4N_u$	$2N_u$
TEQ per tone group+fixed window	TEQ conv.	$N_u(4T-6)$	$N_u(2T-3)$
	diff. terms	0	$\mu+T-1$
	recursion	$2N_u(T+1)$	$2N_uT$
	$\mathbf{d}_i$	$2\mu N_u$	0
	$\Delta\mathbf{Y}^{ext,k}\mathbf{w}_g$	μTN_g	$\mu(T-1)N_g$
	$\mathbf{d}_i^T\Delta\mathbf{Y}^{ext,k}\mathbf{w}_g$	$2\mu N_u$	$2(\mu-1)N_u$
	sum	0	$2N_u$
	FEQ	$4N_u$	$2N_u$
TEQ+window per tone group		idem	idem
PTEQ+per tone window	diff. terms	0	$\mu+T-1$
	PTEQ	$2N_u(T+\mu+1)$	$2N_u(T+\mu)$
	FEQ	$4N_u$	$2N_u$

TABLE 4.2
Memory requirements to store the unknown coefficients for different windowing and equalizer designs.

	memory
single TEQ	$T+2N_u$
TEQ per tone group	N_gT+2N_u
PTEQ [136]	$2N_uT+2N_u$
single TEQ+single window	$T+\mu+2N_u$
TEQ per tone group+fixed window	$N_gT+\mu+2N_u$
TEQ+window per tone group	$N_g(T+\mu)+2N_u$
PTEQ+per tone window	$2N_u(T+\mu)+2N_u$

TABLE 4.3
Numerical example of the complexity and memory requirements for different windowing and equalizer designs with $N = 512$, $N_u = 220$, $N_g = 22$, $T = 8$ and $\mu = 10$.

	memory	# multiplications	# additions
single TEQ	448	$20.2 \cdot 10^6$	$16.3 \cdot 10^6$
TEQ per tone group	616	$42.8 \cdot 10^6$	$27.7 \cdot 10^6$
PTEQ [136]	3960	$19.6 \cdot 10^6$	$16.1 \cdot 10^6$
single TEQ+ single window	458	$20.6 \cdot 10^6$	$16.7 \cdot 10^6$
TEQ per tone group+fixed window	626	$85.7 \cdot 10^6$	$51.9 \cdot 10^6$
TEQ+window per tone group	836	$85.7 \cdot 10^6$	$51.9 \cdot 10^6$
PTEQ+per tone window	8360	$37.5 \cdot 10^6$	$34.0 \cdot 10^6$

4.5 Simulation results

To show the performance of the bit rate maximizing window and/or equalizer designs, we consider a downstream ADSL setup with the parameters given in Section 3.6. The channel noise consists of 24 DSL near-end crosstalk (NEXT) disturbers and additive white Gaussian noise (AWGN) of -140 dBm/Hz. The data carrying tones are 37 to 255 and it is assumed that the upstream echo is perfectly cancelled.

4.5.1 Performance of BM-Win

In this subsection the sensitivity of DMT modulation to RFI is investigated. **Fig. 4.2** compares the SNR of the BM-Win design with the window design of Redfern [102] for a downstream CSA #4 loop. The decision delay is fixed and equal to $\delta_1 = 0$. Six narrowband interferers, which are modeled as pure sinusoids, are added with frequencies 541, 650, 680, 760, 790, 840 kHz. The channel was forced to be of length $\nu - \mu + 1$ ($\nu = 32$, $\mu = 10$) by shortening it with an MMSE TEQ ($T = 16$) and by zeroing the resulting channel taps outside this length. The BM-Win solution is obtained by using a steepest descent search direction for the non-linear cost function in (4.58). In these simulations, no problems with local optima were encountered, i.e. the solution found by the steepest descent method always caused the performance to be consistent. However, we do not have a theoretical proof to show whether the

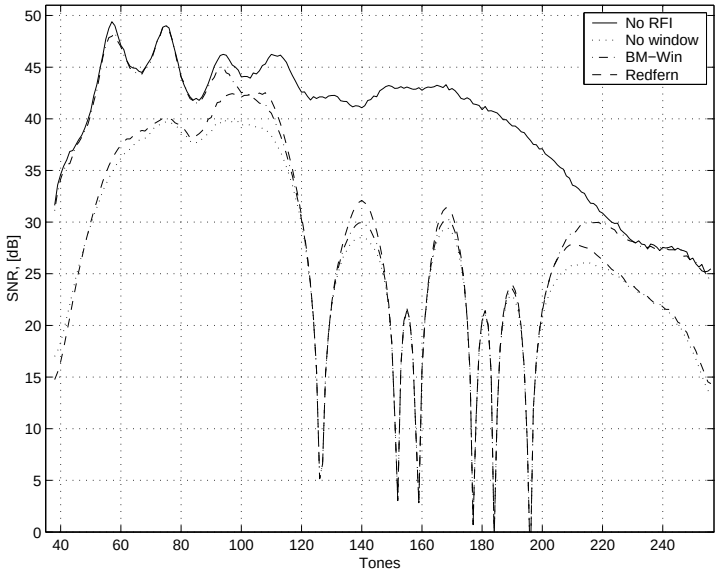

Figure 4.2: SNR for the downstream CSA #4 loop when windowing is applied, with $\mu = 10$ and $\delta_1 = 0$.

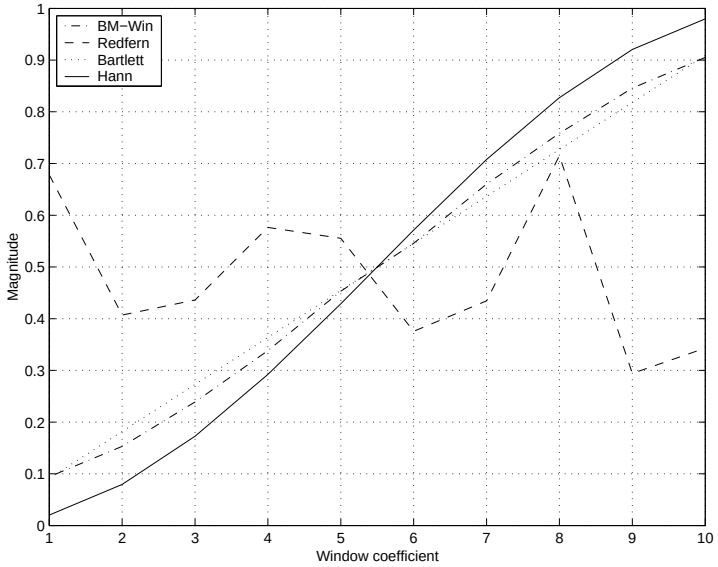

Figure 4.3: Different window tapers for the downstream CSA #4, with $\mu = 10$ and $\delta_1 = 0$.

solution effectively corresponds to the global optimum. The figure also shows the SNR when no windowing is applied and the SNR when no RFIs are present. One can clearly see that a DMT-based receiver is very sensitive to narrowband interferers due to the bad spectral containment of the demodulating DFT. Observe that windowing effectively avoids that all tones are being affected by the interferers. Since the window design method of [102] is not related to bit rate optimization, the BM-Win design leads to higher SNRs and hence a substantial bit rate increase.

To obtain further insight in the shape of the window taper obtained with the BM-Win design procedure, **Fig. 4.3** compares the BM-Win with the window of [102] for the same downstream CSA #4 loop. In addition, the *fixed* Hann and Barlett windows are depicted as well. The fixed Hann window is defined as

$$u_l = \frac{1}{2}\left(1 - \cos\frac{\pi(l+1)}{\mu+1}\right), \quad l = 0, \ldots, \mu-1, \tag{4.67}$$

while the Bartlett window is given by

$$u_l = \frac{l+1}{\mu+1}, \quad l = 0, \ldots, \mu-1. \tag{4.68}$$

Note that the BM-Win has a smooth shape and lies in between the Bartlett and Hann window functions.

Fig. 4.4 evaluates the BM-Win design method for the 8 downstream CSA channels of **Fig. 3.5**. In addition, the figure shows how the bit rate of the BM-Win compares with the fixed Hann and Bartlett windows. More specifically, **Fig. 4.4** contains the bit rates (from left to right) for the unwindowed system, the window design of [102], the fixed Hann window, the fixed Bartlett window and the BM-Win. Note that the BM-Win design always outperforms the other methods. The difference in bit rate between the BM-Win and a fixed window is approximately 180 kbps.

4.5.2 Performance of BM-WinTEQ and BM-FWinTEQ

Equalization without RFI

Whereas the channel was assumed to be perfectly short in Subsection 4.5.1, the channel in this subsection will be shortened by a TEQ and residual ISI and ICI will be taken into account. In **Fig. 4.5**, the bit rate is depicted as a function of the number of BM-WinTEQ coefficients for a $T1.601\#7$ downstream loop with AWGN of -140 dBm/Hz and 24 DSL NEXT disturbers. Note that the curve for $T = 1$ represents the windowing-only case, since for $T = 1$ no time domain equalization is performed in practice: a TEQ with one tap causes a simple scaling of the time domain samples, which is perfectly compensated

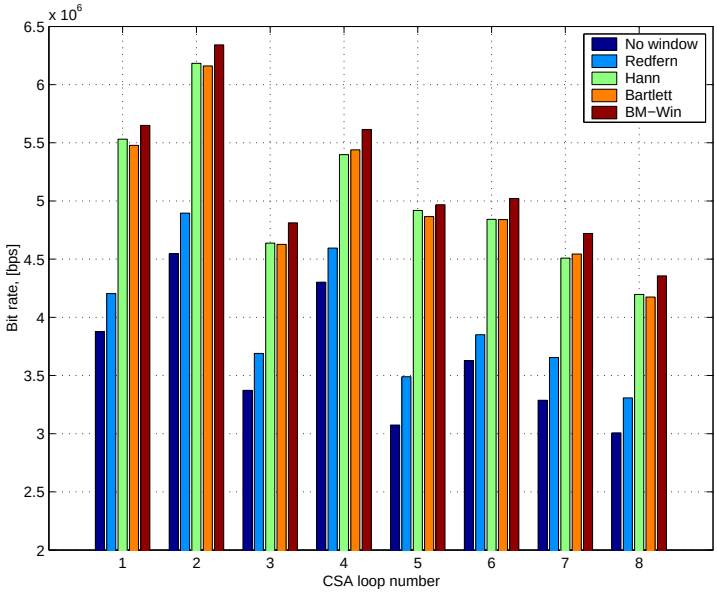

Figure 4.4: Bit rate performance of different windowing methods for the 8 downstream CSA loops with $\mu = 10$ and $\delta_1 = 0$.

by the FEQs in the frequency domain. On the other hand, the curve with $\mu = 0$ shows the performance for the BM-TEQ without windowing. The BM-WinTEQ is calculated by means of (4.30) using the MATLAB® optimization toolbox with the gradient and Hessian definitions of Appendix C.2. Since the BM-WinTEQ cost function is non-linear, 10 different random initializations were used to obtain the results. Although the initializations were completely random, the optimization procedure did not have problems with local optima: different local optima all resulted in close to optimal performance. Again, no theoretical proof is available to generalize this observation. From **Fig. 4.5**, one can clearly see that BM-TEQ taps ($\mu = 0$) can be traded for window taps to obtain the same performance. e.g. a BM-WinTEQ with $T = 3$ and $\mu = 8$ attains the same performance as a single BM-TEQ with $T = 7$, although the former has a much lower complexity, cf. **Table 4.1**.

In **Fig. 4.6**, the optimally computed window of **Fig. 4.5** is replaced by a *fixed* Hann window, defined in (4.67). Hence, only the TEQ coefficients of a BM-FWinTEQ need to be determined, where the TEQ design procedure takes the presence of the fixed Hann window into account. Observe that the use of a fixed window only leads to slightly lower performance.

To illustrate the effect of receiver windowing, **Fig. 4.7** shows the DFT sidelobe behaviour as a function of the tones. Three different cases are considered: no

windowing, a fixed Hann window and the window after BM-WinTEQ initialization with $T = 10$ and $\mu = 10$. Clearly, the addition of a window at the receiver leads to lower sidelobes and the performance of the optimized BM-WinTEQ window exhibits a higher sidelobe attenuation than a traditional Hann window.

Inspired by the previous results, we compare the performance of several TEQ design methods, where the original DFT, which succeeds the TEQ, is replaced by a *windowed DFT* with a *fixed* Hann window. Again, the $T1.601\#7$ loop is considered, with 24 DSL NEXT disturbers and AWGN. In **Fig. 4.8** and **Fig. 4.9**, the achieved bit rate as a function of the number of TEQ taps and windowing coefficients is depicted for the following TEQ methods: MMSE-based TEQ with unit-energy, unit-norm and unit-tap constraint, the maximum shortening SNR (MSSNR) TEQ, the generalized MSSNR TEQ, the min-ISI TEQ, the minimum delay spread (MDS) TEQ and the maximum bit rate (MBR) TEQ, see Chapter 3 for more details on each of these methods. In addition, **Fig. 4.10** repeats the results of the previous figures for a fixed window length of $\mu = 10$ to obtain a better view on the performance differences.

Observe that many TEQ algorithms can benefit from a short window and that the performance comes close to the maximum bit rate, upperbounded by the BM-WinTEQ. Also note that windowing-only (without a TEQ) already improves the bit rates substantially. Hence, the addition of a window effectively helps the TEQ to solve the equalization problem by lowering the sidelobes of the demodulating DFT.

Equalization and RFI mitigation

In the previous simulations only the effect of windowing on the equalization problem was considered. Here, several narrowband RFIs will be added to demonstrate the joint effect of TEQ and receiver windowing on equalization and RFI mitigation. In **Fig. 4.11** the SNR of the BM-TEQ, the BM-WinTEQ and the BM-FWinTEQ are compared for a downstream CSA #4 loop, with $T = 16$ and $\mu = 10$. For the BM-FWinTEQ a fixed Hann window is used. The decision delay is fixed and equal to $\delta_1 = 0$. Two narrowband interferers at 680 kHz and 840 kHz are present during the design of the BM-TEQ, the BM-WinTEQ and the BM-FWinTEQ. After TEQ and window initialization a third RFI at 541 kHz is switched on, which is similar to the behaviour of radio amateurs that discontinuously transmit information. The bit rates achieved by the BM-TEQ, the BM-FWinTEQ and the BM-WinTEQ are respectively equal to 6.06 Mbps, 6.47 Mbps and 6.83 Mbps. From the figure it is clear that windowing helps to improve the SNR and hence also the bit rate. Also note that the BM-TEQ without windowing is able to partially mitigate the RFIs at 680 kHz and 840 kHz and that most of its SNR is lost on the lowest tones due to the interferer at 541 kHz. To explain this behaviour, **Fig. 4.12** shows the DFT of the different TEQ filters. When RFIs are present during training, the

TEQ is able to place a notch on these RFI frequencies before they arrive at the demodulating DFT. Hence, the spreading of the RFI noise power over all the frequency bins is greatly reduced.

In **Fig. 4.13**, the bit rate performance for the eight downstream CSA loops of **Fig. 3.5** is investigated. The same scenario is used as in the previous simulation. For each loop 7 different TEQ designs are applied and each TEQ method is optimized over a delay range $[\Delta_1 - 8 : 4 : \Delta_1 + 16]$, where Δ_1 is defined in Subsection 2.3.1. For each loop, 14 bars are depicted, where each group of 2 bars represents one particular TEQ method. The left bar of such a group shows the performance when the TEQ ($T = 16$) is followed by a traditional DFT ($\mu = 0$); the right bar shows the performance for the same TEQ followed by a windowed DFT with a fixed Hann window ($\mu = 10$). From left to right, one can distinguish the following TEQ methods: the MSSNR TEQ, the Min. ISI TEQ, the MDS TEQ, the MBR TEQ, the MMSE TEQ with unit-energy constraint, the BM-FWinTEQ and the BM-WinTEQ. The BM-FWinTEQ takes the fixed window into account when designing the TEQ taps, while the BM-WinTEQ designs a window and TEQ adjusted to the 680 kHz and 840 kHz RFIs.

The following conclusions can be drawn:

- A TEQ followed by a windowed DFT with a rather short window outperforms the corresponding TEQ followed by an unwindowed DFT.
- Since the MSSNR and MDS methods do not take channel noise into account they have difficulties to cope with RFIs.
- From all the TEQ methods with a convex cost function, the MMSE method has the best performance.
- The BM-WinTEQ or the BM-FWinTEQ outperforms all other designs. However, note that the BM-WinTEQ does not necessarily achieve the best performance, since its coefficients are not trained on the 541 kHz RFI that is switched on after initialization.

Finally, **Fig. 4.14** depicts the window tapers of the BM-WinTEQs for the CSA #4, CSA #6 and CSA #8 loops. The windows are the outcome of the previous simulation. As a reference, the fixed Hann window is depicted as well. Observe that for CSA #4 the initial window coefficients are close to zero. Hence, whenever a window is required that is shorter than μ to optimize the bit rate, the BM-WinTEQ criterion will automatically find this window. Also note that the window tapers can be quite different for different loops and its shape may show a large deviation compared to the fixed Hann window.

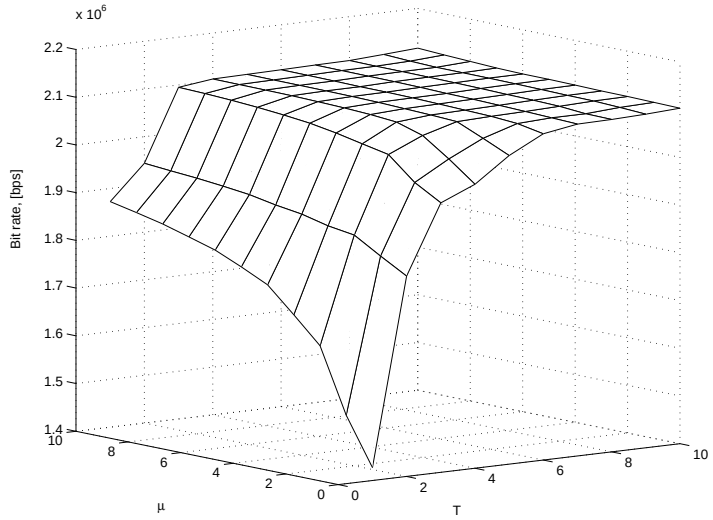

Figure 4.5: Bit rate as a function of the number of TEQ taps T and windowing coefficients μ (BM-WinTEQ) for a $T1.601\#7$ downstream channel in the presence of 24 DSL NEXT disturbers.

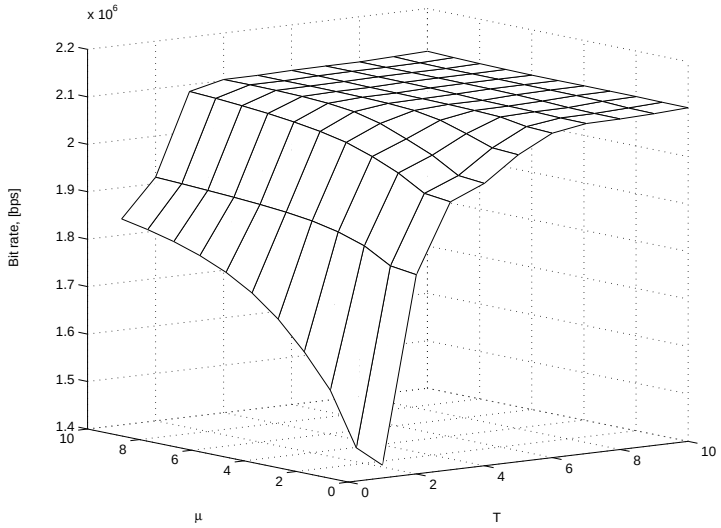

Figure 4.6: Bit rate as a function of the number of BM-FWinTEQ taps T and windowing coefficients μ for a $T1.601\#7$ downstream channel in the presence of 24 DSL NEXT disturbers. The TEQ is followed by a windowed DFT, where the window taper consists of a fixed Hann window.

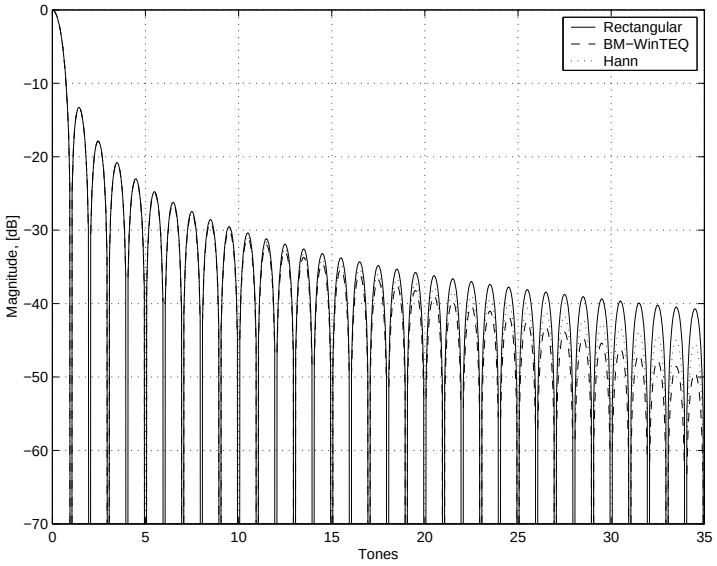

Figure 4.7: DFT sidelobes and the effect of windowing for a fixed Hann window and for the window obtained after BM-WinTEQ initialization.

4.6 Conclusions

In this chapter, we presented a general framework for the *combined* optimization of a TEQ and a window taper (BM-WinTEQ) in order to maximize the achievable bit rate in DMT-based modems. The resulting cost function is non-linear and based on the traditional bit rate expression. Since the bit rate computation requires the knowledge of the SNR for each used tone, a simple SNR definition was derived by using the ZF criterion for the FEQs. We showed that a ZF FEQ (which is equivalent to a constrained MMSE FEQ) for each tone is preferred as it leads to an unbiased desired signal component at the FEQ output and hence a simple decision rule at the receiver.

Furthermore, some special design cases of the bit rate maximizing framework were addressed: a per group design (BM-PGWinTEQ), where a separate equalizer-window pair is computed for groups of tones; an equalizer-only design, which resulted in the BM-TEQ of [144]; a window-only design (BM-Win) and an equalizer design in the presence of a *fixed* (suboptimal) window (BM-FWinTEQ). We linked the BM-PGWinTEQ for a single tone to the constrained (unbiased) MMSE PTEQ, where the per tone window operation is completely absorbed by extra taps in the equalizer. In addition, it was pointed out that the unconstrained MMSE PTEQ, as presented in [136], is biased and that the bias can be removed by adding a constraint in the MMSE criterion. We showed that the constrained and unconstrained MMSE PTEQ solutions,

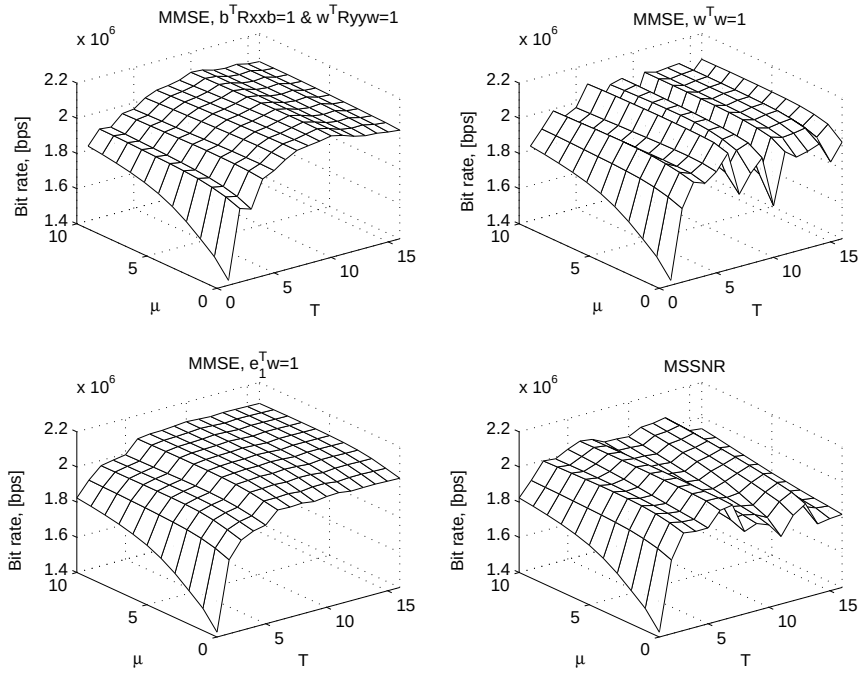

Figure 4.8: Bit rate as a function of the number of TEQ taps T and windowing coefficients μ for a $T1.601\#7$ downstream channel in the presence of 24 DSL NEXT disturbers. The performance of the MMSE and the MSSNR TEQ design method followed by a fixed Hann window is depicted.

remarkably, only differ by a simple scaling and hence lead to the same bit rate, provided that the SNR definition (and hence also the decision rule) is modified to incorporate this scaling. Alternatively, a ZF FEQ succeeding the PTEQ could also remove the bias.

Simulations showed that the BM-FWinTEQ and the BM-WinTEQ outperform all existing TEQ design methods, which were followed by a windowed DFT (instead of an unwindowed DFT) to make a fair comparison. Current ADSL receivers only contain a TEQ followed by an unwindowed DFT and a bank of 1-tap FEQs. Since windowing can contribute to solve the equalization and the RF problem by lowering the sidelobes of the demodulating DFT, a good design practice is to add receiver windowing between TEQ filtering and DFT demodulation. Alternatively, a complexity reduced receiver can be obtained by interchanging the taps of a traditional TEQ for some windowing coefficients. In VDSL modems, only receiver windowing is typically applied since the channel is in general confined to the cyclic prefix. Here, the addition of a TEQ could improve the performance by suppressing the RFIs that are present during TEQ training.

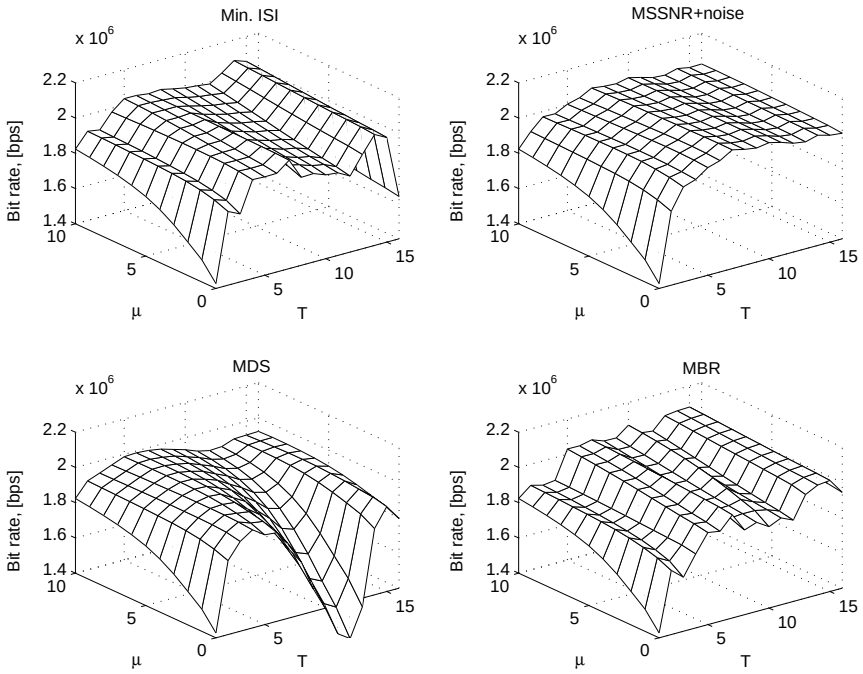

Figure 4.9: Bit rate as a function of the number of TEQ taps T and windowing coefficients μ for a $T1.601\#7$ downstream channel in the presence of 24 DSL NEXT disturbers. The performance of the Min-ISI, the generalized MSSNR, the MDS and the MBR TEQ design method followed by a fixed Hann window is depicted.

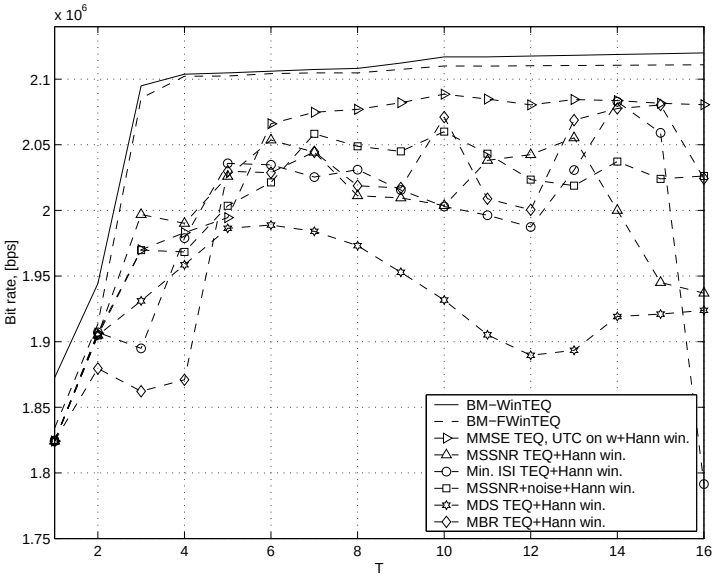

Figure 4.10: Bit rate as a function of the number of TEQ taps T with a fixed window length $\mu = 10$ for a $T1.601\#7$ downstream channel in the presence of 24 DSL NEXT disturbers. The BM-WinTEQ is compared with other TEQ methods that are followed by a fixed Hann window.

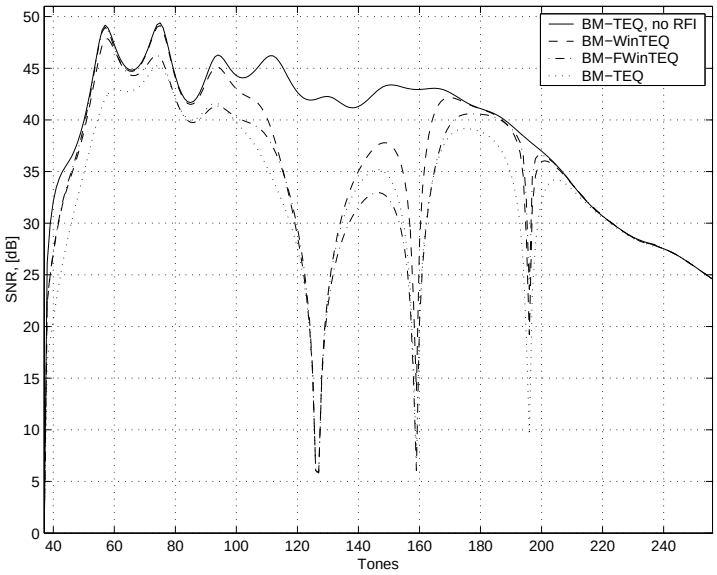

Figure 4.11: SNR for the downstream CSA #4 loop when the BM-WinTEQ and the BM-FWinTEQ are applied, with $\mu = 10$, $T = 16$ and $\delta_1 = 0$.

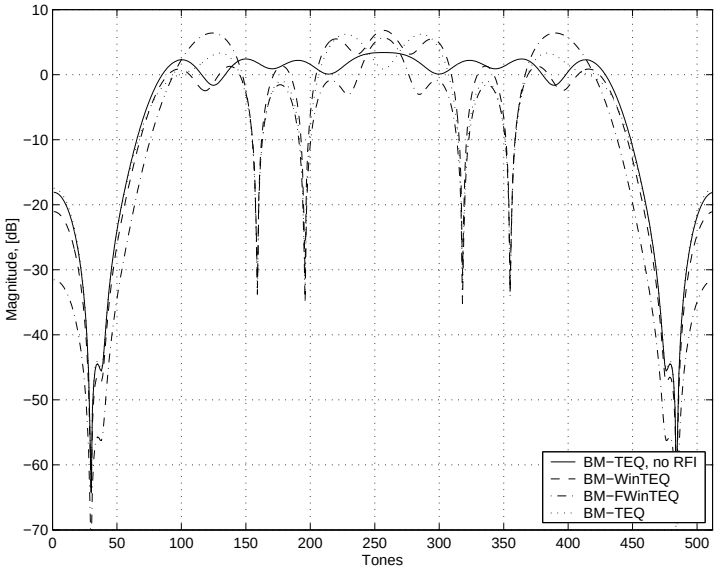

Figure 4.12: DFT of the TEQs obtained with the BM-TEQ, BM-FWinTEQ and BM-WinTEQ design procedures for the downstream CSA #4 loop with $\mu = 10$, $T = 16$ and $\delta_1 = 0$.

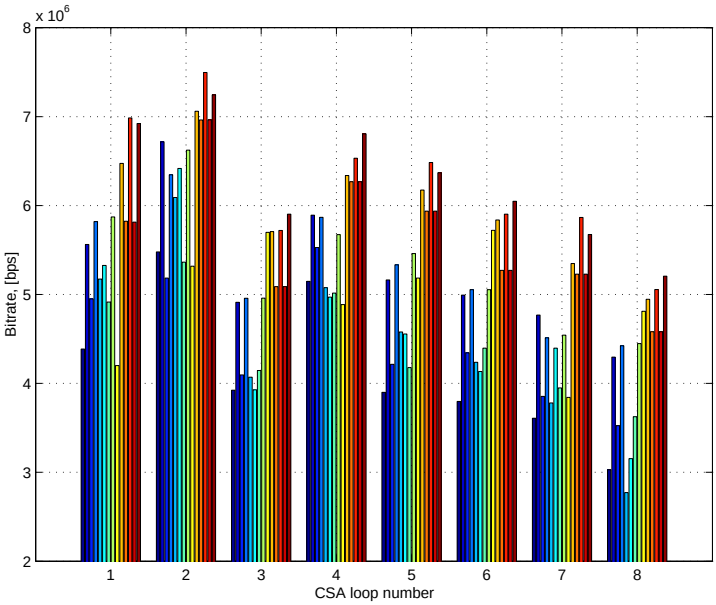

Figure 4.13: Bit rate for the CSA #1-CSA #8 loops with for each loop, from left to right the MSSNR (2x), Min. ISI (2x), MDS (2x), MBR (2x), MMSE (2x), BM-FWinTEQ (2x) and BM-WinTEQ (2x).

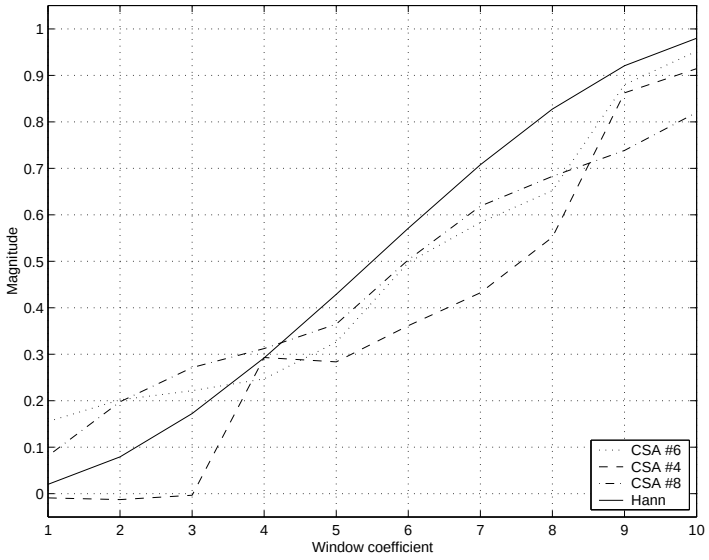

Figure 4.14: Window functions ($\mu = 10$) for the different CSA loops.

Chapter 5

Mixed time/frequency domain echo cancellation

THE ADSL transmission format divides the available bandwidth into N subchannels or tones, which are assigned to the up- or downstream transmission direction. As transmission in both directions takes place over the same loop, the transmitter and receiver at one end of the loop have to be coupled to the line by means of a *hybrid*. A perfectly balanced hybrid prevents leakage of transmitted signals into the receiver. However, a fixed hybrid can not be exactly balanced for all loops and hence leakage or *echo* occurs, see also Chapter 1.

The existing ADSL standard allows two duplexing methods to avoid undesired echo at the receiver: frequency division duplexing (FDD) and echo canceling (EC) [33][63][86]. In FDD, the two directions of transmission are separated by assigning different frequency bins to up- and downstream. Steep front end filters and a small frequency gap of unused tones between up- and downstream bands are required to prevent the transmitted signals to leak into the receive side of the modem.

In EC systems, the expensive analog front end filters of the FDD system are replaced by filters with relaxed specifications and an additional echo canceler. As opposed to FDD systems, EC systems allow for a smaller frequency gap or even overlapping frequency bands. As a result, the transmitted signal causes echo in the overall received signal. This echo is then removed by the echo canceler [90][119][129]. Hence, the expensive analog front end filters of the FDD system are replaced by the DSP cost of echo cancellation. If properly designed, *EC can improve the reach, bit rate and/or noise margin* of an ADSL system.

Several echo cancellation structures for DMT transceivers have been studied in literature [32][57][119][129][137]. A straightforward implementation of an echo canceler emulates the echo in the time domain and subtracts it from the received signal. Typically, a *time domain* least mean square (LMS) adaptive procedure is then used to estimate the echo impulse response [54][90]. Time domain echo canceling (TD-EC) will be discussed in Section 5.1.

In Section 5.2 the more efficient *mixed time/frequency domain echo canceler*, as proposed in [32] and [57], will be reviewed. In [32], the *echo emulation* is still performed in the time domain, but the *updating* process is shifted to the frequency domain. In [57], Ho et al. also move the echo emulation partly to the frequency domain, while the remaining time domain signal processing is only used to remove the 'non-circular' echo component caused by the head and the tail of the echo channel. This is commonly referred to as *circular echo synthesis* (CES). The remaining echo can then be cancelled efficiently in the frequency domain by a complex valued one-tap frequency domain echo canceler per subcarrier.

In an ADSL system, the echo and far end symbols arrive at the receiver with a different propagation delay. As a consequence, the symbol boundaries of the echo and far end symbols at the receiver do not necessarily coincide, i.e. the echo and far end symbols are *misaligned*. The choice of a specific misalignment can reduce the EC complexity. In [65] and [129], the authors determine the optimal misalignment that results in a *minimal* time domain CES complexity. In Section 5.2, this will be discussed in more detail.

The contributions of this chapter can be summarized as follows:

- *Double talk cancellation (DTC)*: When the far end signal is not silenced, as is e.g. the case during duplex transmission ('double talk'), the adaptive update process for TD-EC and CES-based EC may exhibit a large excess mean square error (MSE). A large MSE often leads to slow convergence and/or inferior tracking behaviour. In Section 5.3 we present a practical way to cancel the far end signal during the EC update at a very low computational cost, resulting in improved convergence.

- *Improved time-frequency domain echo canceling (ITF-EC)*: In [65] and [129] the time domain CES complexity is minimized by selecting a specific misalignment between the echo and far end symbols at the receiver. However, once the misalignment has been defined at one end of the loop, the misalignment at the other side of the loop is fixed and determined by the propagation delay of the far end channel. This imposed misalignment does not lead in general to minimal CES complexity in the second modem as well, unless an extra DFT-IDFT pair is added.

  In Section 5.4 we present a modified EC scheme to *minimize the CES complexity without imposing a specific temporal misalignment*. The re-

sulting structure will be referred to as improved time-frequency domain echo canceling (ITF-EC) and will lead to a lower overall EC complexity at both sides of the loop. Also here, DTC is straightforwardly incorporated into the EC structure.

- *Circulant decomposition canceler (CDC)*: In both [32] and [57], the echo filter is adapted in the frequency domain by means of a single-tap LMS procedure per tone, using the transmitted echo frequency domain symbols as 'update direction'. Since not all frequency bins carry data in ADSL, some of the modes of the echo reference signal are not excited, leaving the corresponding echo filter coefficients unaltered. This effect was also observed in [32], where the authors proposed to transmit dummy data with a reduced power level on extra tones to circumvent this problem.

  In Section 5.5 we investigate a new EC structure that does not require such extra transmit power on unused tones for EC updating purposes. This structure will be referred to as the Circulant Decomposition Canceler (CDC)[1]. We will show that the proposed method has a complexity and convergence behaviour comparable to existing EC schemes.

Finally, simulation results and conclusions can be found in Sections 5.6 and 5.7 respectively.

5.1 Time domain echo canceling (TD-EC)

In this section the traditional time domain echo canceling is considered. In Subsection 5.1.1 it is first assumed that the transmit part and the receive part in the modem have equal IDFT/DFT size and equal sampling rates. Multi-rate setups will be treated in Subsection 5.1.2 and the computational complexity will be discussed in Subsection 5.1.3.

5.1.1 Symmetric rate TD-EC

First, assume a symmetric ADSL setup with equal DFT/IDFT size N for up- and downstream. Since the duration of one symbol, consisting of $N + \nu$ samples, is equal in both directions, the sampling rate F_s is also the same. The received echo is modeled as a linear convolution of a finite impulse response (FIR) echo channel, $\mathbf{h}_E$, with cyclically prefixed echo reference symbols $\mathbf{u}^k = [u_0^k \quad \dots \quad u_j^k \dots \quad u_{N-1}^k]^T = \mathcal{I}_N U_{0:N-1}^k$, see also Subsection 2.3.2 for notation.

[1] The CDC structure was developed jointly with F. Pisoni from ST Microelecronics (formerly Alcatel Microelectronics).

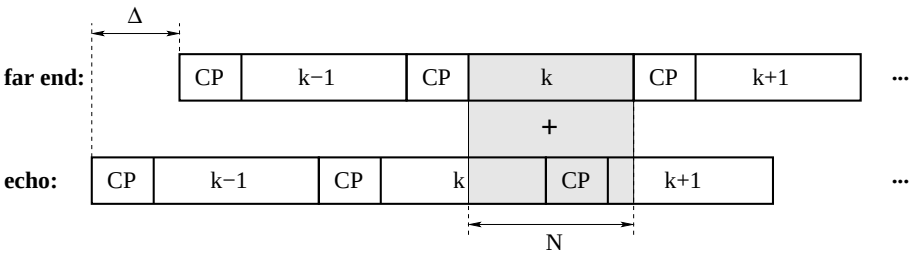

Figure 5.1: Frame asynchronous transmission with misaligned echo and far end symbols, as seen by the receiver.

The overall echo channel contains the contributions of the analog and digital front end filters, hybrid circuitry and the time domain equalizer (TEQ) commonly used in DSL systems to shorten the far end channel, cf. Chapter 3. In a typical ADSL environment, the duration of the overall echo channel is limited to the duration of one DMT symbol. In other words, the echo impulse response contains at most N taps sampled at the sampling rate F_s. Henceforth, the echo channel is assumed to be of length N or zero padded to that length.

Let $\mathbf{y}^k$ be the vector of N received samples at symbol period k as seen by the receive DFT prior to EC, i.e.

$$\mathbf{y}^k = \mathbf{y}_E^k + \mathbf{n}^k, \tag{5.1}$$

where $\mathbf{n}^k$ now contains the received far end signal plus additive Gaussian noise and $\mathbf{y}_E^k$ denotes the received echo. Here, two distinct cases can be considered, namely the *frame-synchronous* and the *frame-asynchronous* operation:

- In the frame-synchronous operation, the symbol boundaries of the echo and far end symbols at the receiver are *aligned* in time.
- In the frame-asynchronous operation, the symbol boundaries are *misaligned* in time.

Example 5.1 To illustrate the concepts of *frame-synchronous* and *frame-asynchronous* transmission, consider an ideal echo channel $\mathbf{h}_E = [1\ 0\ \ldots\ 0]^T$. Hence, the transmitted echo symbols arrive undelayed and without attenuation at the receiver. In addition, assume that the far end channel is a simple delay, i.e. $\mathbf{h} = [0\ \ldots\ 0\ 1\ 0\ \ldots\ 0]^T$. The receiver will synchronize to the symbol boundaries of the desired far end signal. **Fig. 5.1** shows the resulting received vector when no additional channel noise is present. Clearly, the echo symbol as seen by the receive DFT is misaligned with respect to the received far end symbol. As a result, the part of the received echo symbol corresponding to the cyclic prefix can cause echo anywhere in the received far end symbol. Hence,

the echo of this cyclic prefix has to be computed, while in a frame-synchronous modem, these samples are discarded before demodulation. △

When the echo symbols are misaligned with respect to $\mathbf{y}^k$ by a delay Δ, the received echo $\mathbf{y}_E^k$ can be written as a function of samples u_j^k originating from three consecutive echo reference symbols $\mathbf{u}^{k-1}$, $\mathbf{u}^k$ and $\mathbf{u}^{k+1}$, i.e.

$$\mathbf{y}_E^k = \mathbf{U}^{k-1,k,k+1}\mathbf{h}_E, \tag{5.2}$$

where $\mathbf{U}^{k-1,k,k+1}$ is an $N \times N$ Toeplitz matrix defined as

$$\mathbf{U}^{k-1,k,k+1} = \tag{5.3}$$

	sym. k			CP k			sym. $k-1$		
sym. k	u_Δ^k	$\dots$	u_0^k	u_{N-1}^k	$\dots$	$u_{N-\nu}^k$	u_{N-1}^{k-1}	$\dots$	$u_{\Delta+\nu+1}^{k-1}$
	$\vdots$	$\ddots$						$\ddots$	$\vdots$
CP $k+1$	u_{N-1}^k								u_{N-1}^{k-1}
	$u_{N-\nu}^{k+1}$								$u_{N-\nu}^k$
	$\vdots$								$\vdots$
	u_{N-1}^{k+1}								u_{N-1}^k
sym. $k+1$	u_0^{k+1}								u_0^k
	$\vdots$	$\ddots$						$\ddots$	$\vdots$
	$u_{\Delta-\nu-1}^{k+1}$	$\dots$	u_0^{k+1}	u_{N-1}^{k+1}	$\dots$	$u_{N-\nu}^{k+1}$	u_{N-1}^k	$\dots$	u_Δ^k

In a transmission system, one side of the loop can select a specific misalignment, Δ. Once Δ has been defined at one end, the misalignment at the other side of the loop is fixed and determined by the propagation delay of the far end channel. In the frame-asynchronous mode Δ is different from zero, while in the frame-synchronous operation, Δ is equal to zero and $\mathbf{U}^{k-1,k,k+1}$ is completely determined by the samples of the symbols $\mathbf{u}^{k-1}$ and $\mathbf{u}^k$.

The traditional form of echo canceling is *time domain echo canceling (TD-EC)* [25][54]. The echo path, $\mathbf{h}_E$, is modeled by means of an FIR filter $\mathbf{w}_E$ with T_E taps. The echo canceler first estimates the echo path and then generates a replica of the echo to subtract it from the received time domain signal. Adaptive signal processing is required to obtain adequate echo emulation since the echo channel is in general unknown and (slowly) time-varying. The echo canceled received symbol of length N is described by

$$\mathbf{e}^k = \mathbf{y}^k - \underbrace{\mathbf{U}^{k-1,k,k+1}\mathbf{M}\mathbf{w}_E^k}_{\hat{\mathbf{y}}_E^k}, \tag{5.4}$$

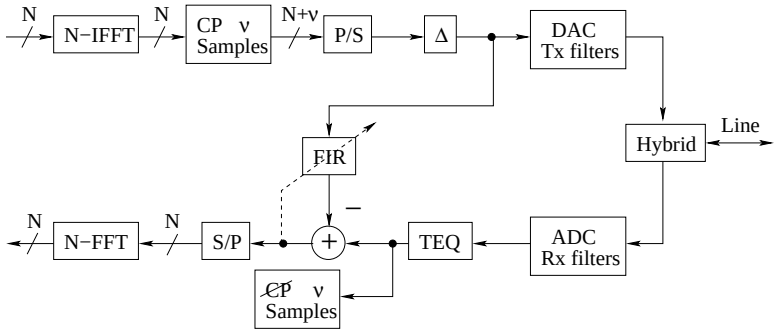

Figure 5.2: Symmetric rate TD-EC.

where the echo emulation, $\hat{\mathbf{y}}_E^k$, is represented by a matrix-vector product of $\mathbf{U}^{k-1,k,k+1}$ with the echo canceler taps at time k. The $N \times T_E$ matrix $\mathbf{M} = [\mathbf{0}_{T_E \times \delta} \;\; \mathbf{I}_{T_E} \;\; \mathbf{0}_{T_E \times (N-T_E-\delta)}]^T$ is used to select T_E columns of $\mathbf{U}^{k-1,k,k+1}$, where δ is the echo transmission delay. The parameter δ can be obtained by localizing the T_E most energetic taps of $\mathbf{h}_E$. Since $\mathbf{h}_E$ will be measured during the startup phase of the modem, determining δ does not form a practical problem. The echo cancelled DMT symbol $\mathbf{e}^k$ in the frequency domain is obtained as

$$E^k = \mathcal{F}_N \mathbf{e}^k = \mathcal{F}_N(\mathbf{y}^k - \mathbf{U}^{k-1,k,k+1}\mathbf{M}\mathbf{w}_E^k), \tag{5.5}$$

where $\mathcal{F}_N$ represents the N-point DFT matrix. After perfect echo cancellation, E^k contains only far end and channel noise contributions. Remark that the vector E^k is subsequently processed by the one tap frequency domain equalizers or FEQs (not displayed in (5.5)), which are commonly used in ADSL to remove the remaining phase and magnitude distortion of the far end channel.

To initialize or to update the echo filter estimate, a straightforward adaptive implementation based on *block Least Mean Square (LMS)* can be used [54], i.e.

$$\mathbf{w}_E^{k+1} \leftarrow \mathbf{w}_E^k + \mu \mathbf{M}^T (\mathbf{U}^{k-1,k,k+1})^T \mathbf{e}^k, \tag{5.6}$$

where μ is the step size. The resulting structure for symmetric rate TD-EC is shown in **Fig. 5.2**. In ADSL, TD-EC as in (5.4) is computationally expensive. With $N = 512$, $T_E = 256$ and a symbol rate of 4 kHz, symmetric rate TD-EC requires $N \cdot T_E \cdot 4 \cdot 10^3 = 524 \cdot 10^6$ multiplications per second. Therefore, the following sections will focus on how to reduce this complexity.

5.1.2 Multi-rate TD-EC

In the previous subsection, it was assumed that the transmit and receive path in the modem work at a unique sampling rate. Due to the asymmetric character of

ADSL, the previous assumption is not necessarily satisfied. In an ADSL system, the Remote Terminal (RT) typically has a (upstream) transmit bandwidth and sampling rate that is κ times smaller than the (downstream) receive bandwidth and sampling rate. As a result the transmit IDFT will be a factor κ smaller than the receive DFT. At Central Office (CO) the opposite is true. When properly designed, echo cancellation can benefit from this multi-rate structure and a distinction can be made between a decimated and an interpolated setup.

Example 5.2 In ADSL (over POTS), the standard allows to use the frequency band 25.875 kHz-138 kHz for upstream transmission, while 25.875 kHz-1.104 MHz is foreseen for downstream transmission [63]. With a carrier spacing of 4.3125 kHz at least 32 tones are required for upstream and 256 for downstream. Since the tones are complex conjugate symmetric the minimum (I)DFT size for up- and downstream transmission are respectively equal to 64 and 512. Hence, the CO modem typically contains a 512-point transmit IDFT and a 64-point receive DFT, while the opposite is true for the RT modem. Note that some vendors prefer to use an oversampled IDFT for a cheaper implementation of the front end filters. △

TD-EC with decimation at the output (CO)

Assume a system where the transmit IDFT is κ times larger than the N-point DFT in the receive path. When the bandwidth of the transmitted echo signal is a factor κ larger than the receive bandwidth, the echo signal will be decimated at the receiver and aliasing occurs due to non-ideal anti-aliasing front end filters. Typically, this is the case at CO. Apart from modeling the echo channel, the echo canceler has to include the aliasing effects as well. To do so, the emulated echo can be decimated at the output of the echo canceler by computing only every κth sample, which is represented mathematically by the $N \times \kappa N$ downsampling matrix $\mathbf{D} = \mathbf{I}_{\kappa N}[1:\kappa:\kappa N,:]$. Similar to (5.4) and (5.6), the echo canceled symbol and the block LMS update in time domain are given by

$$\mathbf{e}^k = \mathbf{y}^k - \mathbf{D}\mathbf{U}^{k-1,k,k+1}\mathbf{M}\mathbf{w}_E^k, \tag{5.7}$$

$$\mathbf{w}_E^{k+1} \leftarrow \mathbf{w}_E^k + \mu\mathbf{M}^T(\mathbf{U}^{k-1,k,k+1})^T\mathbf{D}^T\mathbf{e}^k, \tag{5.8}$$

where the taps of $\mathbf{w}_E$ and the elements of $\mathbf{U}^{k-1,k,k+1}$ are at the high rate and $\mathbf{y}^k$ is at the low rate. Note that due to the decimation, a factor κ has been gained in complexity.

TD-EC with decimation at the input (CO)

When the transmit IDFT is again κ times larger than the N-point receive DFT and when, in addition, it is assumed that the echo transfer function is band

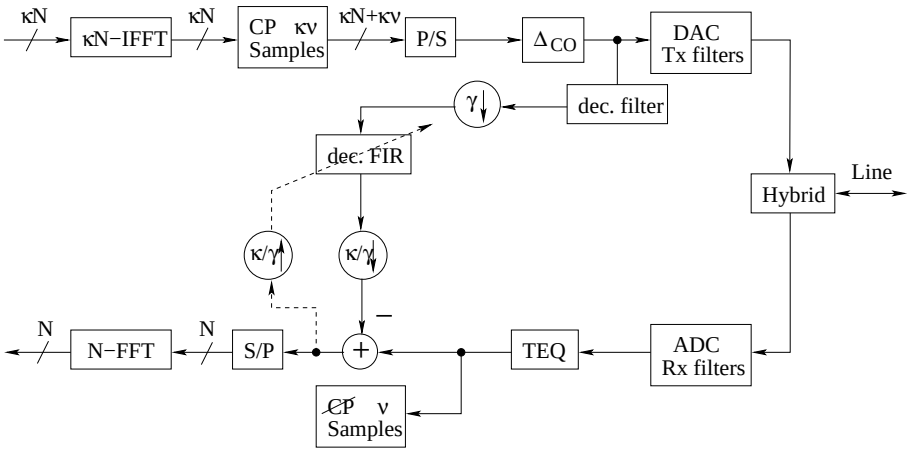

Figure 5.3: TD-EC with decimation at the input (CO).

limited to $\kappa N/2\gamma$ tones (which is valid in a typical ADSL scenario where the front end filters at the CO receive side include an anti-aliasing filter with a cut-off frequency at approximately 138 kHz), the echo cancelers complexity can be even further reduced. With a band limited echo channel, only a limited part of the transmitted echo signal spectrum will contribute to the received echo signal. Hence, it makes sense to decimate $\mathbf{w}_E^k$ and the transmitted echo signal with a factor γ before constructing $\mathbf{U}^{k-1,k,k+1}$ in (5.7). To avoid aliasing, an additional decimation filter in the echo path is required before decimating the echo reference symbols. The resulting TD-EC and the corresponding block LMS update are then obtained as

$$\mathbf{e}^k = \mathbf{y}^k - \mathbf{D}_{\gamma\downarrow}\mathbf{U}_{\gamma\downarrow}^{k-1,k,k+1}\mathbf{M}_{\gamma\downarrow}\mathbf{w}_{E,\gamma\downarrow}^k, \tag{5.9}$$

$$\mathbf{w}_{E,\gamma\downarrow}^{k+1} \leftarrow \mathbf{w}_{E,\gamma\downarrow}^k + \mu\mathbf{M}_{\gamma\downarrow}^T(\mathbf{U}_{\gamma\downarrow}^{k-1,k,k+1})^T\mathbf{e}_{\kappa/\gamma\uparrow}^k, \tag{5.10}$$

where $\mathbf{e}_{\kappa/\gamma\uparrow}^k = \mathbf{D}_{\gamma\downarrow}^T\mathbf{e}^k$, $\mathbf{D}_{\gamma\downarrow} = \mathbf{I}_{\kappa N/\gamma}[1:\kappa/\gamma:\kappa N/\gamma,:]$, $\mathbf{w}_{E,\gamma\downarrow} = \mathbf{w}_E^k[1:\gamma:\kappa N]$, $\mathbf{M}_{\gamma\downarrow} = [\mathbf{0}\ \ \mathbf{I}_{T_E/\gamma}\ \ \mathbf{0}]^T$ and where $\mathbf{U}_{\gamma\downarrow}^{k-1,k,k+1}$ is a Toeplitz matrix constructed with decimated echo samples. The resulting structure is depicted in **Fig. 5.3**. Hence, by resampling the echo path the complexity of the TD-EC is roughly reduced with a factor $\kappa \cdot \gamma$ compared to the symmetric rate case.

TD-EC with interpolation by zero padding the input (RT)

When the bandwidth of the transmitted echo signal is a factor κ smaller than the receive bandwidth, the transmit signal will be replicated over the entire receive bandwidth due to non-ideal front end filters. Typically, this is the case at RT. Therefore, the echo canceler has to interpolate the transmitted echo

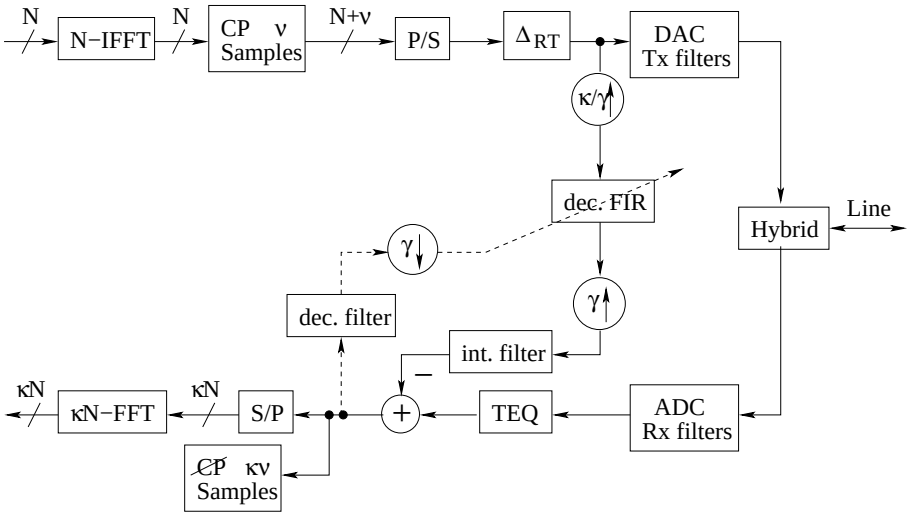

Figure 5.4: TD-EC with interpolated setup (RT).

signal. To obtain echo reference samples at high rate, $\kappa - 1$ zeroes are padded between the time domain echo samples. The echo canceled frequency domain received vector of length κN and the filter update are then given by

$$\mathbf{e}^k = \mathbf{y}^k - \mathbf{U}_{\kappa\uparrow}^{k-1,k,k+1}\mathbf{M}\mathbf{w}_E^k, \tag{5.11}$$

$$\mathbf{w}_E^{k+1} \leftarrow \mathbf{w}_E^k + \mu\mathbf{M}^T(\mathbf{U}_{\kappa\uparrow}^{k-1,k,k+1})^T\mathbf{e}^k, \tag{5.12}$$

where $\mathbf{M}$ and $\mathbf{w}_E^k$ are at the high rate and $\mathbf{U}_{\kappa\uparrow}^{k-1,k,k+1}$ is a Toeplitz matrix of size $\kappa N \times \kappa N$, based on an input sequence with $\kappa - 1$ zeroes inserted between two consecutive echo samples. When, in addition, it is assumed that the echo transfer function is band limited to $\kappa N/2\gamma$ tones ($\gamma \leqslant \kappa$), $\mathbf{w}_E^k$, which contains taps at the receive rate, could be downsampled by a factor γ. Since the transmitted echo signal only uses $N/2$ tones, the overall echo emulation could be performed at a rate that is γ times lower than the receive rate, provided that the time domain echo samples are upsampled with a factor κ/γ. Afterwards, the resulting echo estimate should be upsampled again with a factor γ to the receiver rate, which requires an additional interpolation filter, see **Fig. 5.4**. Hence, by resampling the echo path the complexity of the TD-EC is roughly reduced with a factor $\kappa \cdot \gamma$ compared to the symmetric rate case.

5.1.3 Complexity

The computational complexity of TD-EC is summarized in **Table 5.1**, where it is assumed that the echo channel is band limited to $\kappa N/2\gamma$ tones. The

TABLE 5.1
Complexity of TD-EC in real multiplications per symbol.

	Decimated EC (CO)	**Interpolated EC (RT)**
TD-EC	dec. filter$+\frac{\kappa N T_E}{\kappa\gamma}$	int. filter$+\frac{\kappa(N+\nu)T_E}{\kappa\gamma}$

complexity is expressed as the number of real multiplications required for echo emulation per symbol. Complexity figures for the decimation and interpolation filters are not given explicitly, since they highly depend on the actual implementation of the filters.

5.2 Circular echo synthesis (CES)

In [32], it was noted that TD-EC with block LMS exhibits slow convergence. Moreover, the complexity of TD-EC can be reduced substantially by exploiting the 'circular' aspects of the DMT line code. In [57], a more efficient mixed time/frequency domain (MTF) echo canceler based on circular echo synthesis (CES) was investigated. CES-based EC will be reviewed in this section. Symmetric rate and multi-rate structures will be treated in Subsection 5.2.1 and Subsection 5.2.2 respectively. Finally, complexity figures will be given in Subsection 5.2.3.

5.2.1 Symmetric rate CES-based EC

In [57], Ho et al. pointed out that the received echo signal has a circular and a non-circular echo component, where the non-circular part is caused by the head and tail of the echo channel. Hence, when canceling the non-circular part in the time domain – referred to as *circular echo synthesis* (CES) – the residual echo looks periodic (circular) before transformation to the frequency domain. In the frequency domain, the remaining echo can then be canceled efficiently by a complex multiplication per tone.

To describe CES, first assume a symmetric setup with equal DFT/IDFT size N for up- and downstream. The Toeplitz matrix $\mathbf{U}^{k-1,k,k+1}$ of (5.3) can be divided into a circulant matrix and a correction matrix:

$$\mathbf{U}^{k-1,k,k+1} = \mathbf{C}^k + \chi^{k-1,k,k+1}, \tag{5.13}$$

with $\mathbf{C}^k$ a circulant matrix containing only elements of symbol period k, defined

as

$$\mathbf{C}^k = \begin{bmatrix} u^k_{\Delta} & \dots & u^k_0 & u^k_{N-1} & \dots & u^k_{\Delta+1} \\ \vdots & \ddots & & & \ddots & \vdots \\ u^k_{N-1} & & & & & u^k_{N-1} \\ u^k_0 & & & & & u^k_0 \\ \vdots & \ddots & & & \ddots & \vdots \\ u^k_{\Delta-1} & \dots & u^k_0 & u^k_{N-1} & \dots & u^k_{\Delta} \end{bmatrix}, \tag{5.14}$$

and with $\chi^{k-1,k,k+1} = \mathbf{U}^{k-1,k,k+1} - \mathbf{C}^k$. The matrix $\chi^{k-1,k,k+1}$ is typically sparse and contains two triangles with non-zero elements, i.e.

$$\chi^{k-1,k,k+1} = \tag{5.15}$$
$$\begin{bmatrix} 0 & \dots & 0 & u^{k-1}_{N-1} - u^k_{N-\nu-1} & \dots & u^{k-1}_{\Delta+\nu+1} - u^k_{\Delta+1} \\ \vdots & \ddots & & & \ddots & \vdots \\ & & & & & u^{k-1}_{N-1} - u^k_{N-\nu-1} \\ \vdots & & & & & 0 \\ 0 & & & & & \vdots \\ u^{k+1}_{N-\nu} - u^k_0 & & & & & \\ \vdots & \ddots & & & \ddots & \vdots \\ u^{k+1}_{\Delta-\nu-1} - u^k_{\Delta-1} & \dots & u^{k+1}_{N-\nu} - u^k_0 & 0 & \dots & 0 \end{bmatrix}.$$

Using (5.5) and (5.13), one can write the echo cancellation error in the frequency domain as

$$E^k = \mathcal{F}_N(\mathbf{y}^k - \chi^{k-1,k,k+1}\mathbf{M}\mathbf{w}^k_E) - \mathcal{F}_N\mathbf{C}^k\mathbf{M}\mathbf{w}^k_E. \tag{5.16}$$

Since the circulant matrix $\mathbf{C}^k$ can be diagonalized by a DFT and an IDFT matrix (see Appendix A or [53]), i.e. $\mathbf{C}^k = \mathcal{I}_N \mathrm{diag}\{U^k \odot \mathbf{p}\}\mathcal{F}_N$, one has

$$E^k = \mathcal{F}_N(\underbrace{\mathbf{y}^k - \chi^{k-1,k,k+1}\mathbf{M}\mathbf{w}^k_E}_{\text{Time domain EC}}) - \underbrace{\mathrm{diag}\{U^k \odot \mathbf{p}\}W^k_E}_{\text{Frequency domain EC}}, \tag{5.17}$$

where $\mathbf{p} = \begin{bmatrix} 1 & \dots & e^{-j2\pi\Delta i/N} & \dots & e^{-j2\pi\Delta(N-1)/N} \end{bmatrix}^T$ is a phase rotation vector to account for the misalignment Δ, $W^k_E = \mathcal{F}_N\mathbf{M}\mathbf{w}^k_E$, $\odot$ denotes a component wise multiplication and where $\mathcal{F}_N$ is shared between the echo canceler and the far end signal demodulator. Hence, the received echo signal is cancelled partly in the time and partly in the frequency domain. The time domain part ensures that the residual echo behaves as a periodic signal before entering the DFT and is therefore called CES. Compared to TD-EC, a *complexity reduced* structure is obtained due to the *sparseness* of the $\chi^{k-1,k,k+1}$ matrix.

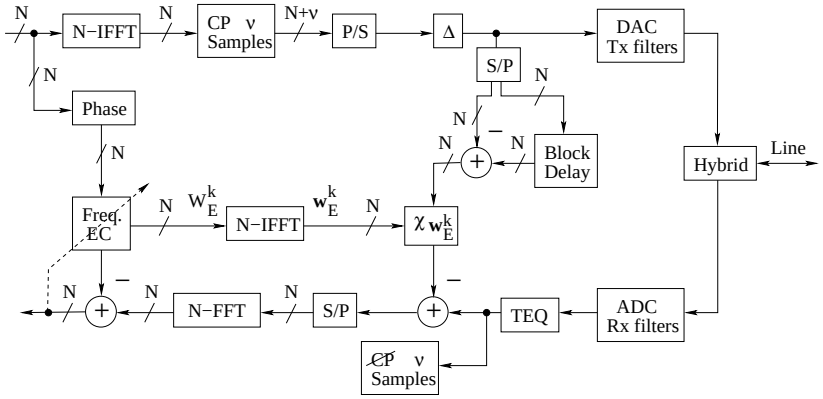

Figure 5.5: Symmetric rate CES-based EC.

Based on (5.6), the equivalent block LMS update in the frequency domain can be written as

$$W_E^{k+1} \leftarrow W_E^k + \mu \mathcal{F}_N \mathbf{M}\mathbf{M}^T (\mathbf{U}^{k-1,k,k+1})^T \mathcal{I}_N E^k. \tag{5.18}$$

With (5.13) this is completely equivalent to

$$W_E^{k+1} \leftarrow W_E^k + \mu (\mathcal{F}_N \chi^{k-1,k,k+1} \mathbf{M}\mathbf{M}^T \mathcal{I}_N + \mathrm{diag}\{U^k \odot \mathbf{p}\})^H E^k. \tag{5.19}$$

Ho et al. showed that (5.19) can be simplified to a *per tone update* of the frequency domain echo filter taps [57]

$$W_E^{k+1} \leftarrow W_E^k + \mu (U^k \odot \mathbf{p})^* \odot E^k. \tag{5.20}$$

The updated coefficients $\mathbf{w}_E^{k+1}$, as required to calculate E^{k+1} according to (5.17), can then be obtained as

$$\mathbf{w}_E^{k+1} \leftarrow \mathbf{M}^T \mathcal{I}_N W_E^{k+1}. \tag{5.21}$$

The IDFT operation in (5.21) can be executed *infrequently* compared to the update rate of W_E^k in (5.20) [57]. By this, the update complexity is further reduced. The resulting CES-based EC structure is shown in **Fig. 5.5**.

When $W_{E,i}^k$ denotes the component of W_E^k corresponding to the i-th tone, (5.20) clearly shows that $W_{E,i}^k$ will only be updated when U_i^k differs from zero with $i = 0, \ldots, N-1$. In ADSL, the available tones in U^k are assigned to upstream and/or to downstream. As a result, the elements of U^k will only be partially non-zero. As a consequence, *insufficient excitation* of U^k usually leads to poor echo rejection. Therefore, Cioffi and Bingham proposed to place

a small random excitation signal on the unused carriers to solve this problem [32]. This will be crucial in Subsection 5.5, where an alternative EC structure will be developed that does not need this extra excitation.

From (5.17), it is clear that the overall EC complexity is mainly determined by the time domain CES, i.e. $\chi^{k-1,k,k+1}\mathbf{M}\mathbf{w}_E^k$. Since the number of elements in $\chi^{k-1,k,k+1}$ is delay dependent, the authors in [65] and [129] investigate the CES complexity as a function of the frame misalignment Δ. The amount of operations to perform CES is directly proportional to the number of elements in $\chi^{k-1,k,k+1}\mathbf{M}$, which is minimal for $\Delta_{\text{opt}} = \delta + \frac{T_E-\nu}{2}$. In this way, an ADSL modem can set its misalignment between its transmit and receive path to obtain roughly a two-fold CES complexity reduction compared to the CES structure with $\Delta = 0$ as originally assumed in [57].

Due to the propagation delay of the channel, the choice of a specific, optimal misalignment at one end of the transmission system automatically dictates the alignment at the other end. Unfortunately, this imposed misalignment does not lead in general to minimal CES complexity in the second modem as well. To certify a minimal CES complexity, the second modem requires an extra DFT-IDFT pair. The EC is then described by

$$\begin{aligned} \mathbf{e}^k &= \mathbf{y}_{ext}^k - \chi_{ext}^{k-1,k,k+1}\mathbf{M}\mathbf{w}_E^k - \mathbf{P}\mathcal{I}_N(U^k \odot \mathbf{p} \odot W_E^k), \quad (5.22) \\ W_E^{k+1} &\leftarrow W_E^k + \mu \text{diag}\{(U^k \odot \mathbf{p})^*\}\mathcal{F}_N\mathbf{P}^T\mathbf{e}^k, \quad (5.23) \end{aligned}$$

where $\chi_{ext}^{k-1,k,k+1}$ is an extended Toeplitz matrix of size $(N+\nu) \times N$ instead of $N \times N$, $\mathbf{y}_{ext}^k$ is of length $N+\nu$ and $\mathbf{P}$ is given by (2.11). The echo canceling in (5.22) is completely performed in the time domain, hence the extra IDFT. The extra DFT operation in (5.23) is able to select any block of N echo samples out of the received data stream, independently of the far end demodulating DFT. Equations (5.22) and (5.23) imply that the modem can set the transmitter/EC misalignment independently of the symbol boundaries of the far end signal [65]. The receive DFT in CO is typically much smaller than in RT. Hence, in the overall transmission setup the modem at RT selects its optimal Δ, while the extra (I)DFT-processing is 'appointed' to CO, since this amounts to the lowest overall computational complexity.

5.2.2 Multi-rate CES-based EC

Similar to Subsection 5.1.2, the difference in sampling rate between the transmit and receive path in the modem can be exploited to reduce the CES complexity. In the following, decimated and interpolated CES-based echo cancelers will be discussed.

CES-based EC with decimation at the output (CO)

Again, assume a system where the transmit IDFT is κ times larger than the N-point DFT in the receive path. Similar to (5.7) and (5.8), the echo canceled symbol in the frequency domain and the corresponding filter update are given by

$$\begin{aligned} E^k &= \mathcal{F}_N(\mathbf{y}^k - \mathbf{D}\chi^{k-1,k,k+1}\mathbf{M}\mathbf{w}_E^k) - \frac{1}{\kappa}\mathbf{R}^T(U^k \odot \mathbf{p} \odot W_E^k), & (5.24)\\ W_E^{k+1} &\leftarrow W_E^k + \mu(U^k \odot \mathbf{p})^* \odot (\mathbf{R}E^k), & (5.25) \end{aligned}$$

with $\mathbf{R}^T = [\mathbf{I}_N \dots \mathbf{I}_N]$ and $\mathbf{w}_E^k = \mathbf{M}^T\mathcal{I}_{\kappa N}W_E^k$. In (5.24), the time domain part is downsampled with a factor κ after CES is performed at high rate. Since decimation in time corresponds to aliasing in the frequency domain, the frequency domain echo emulated symbols of size κN are blocked into symbols of length N and subsequently added (multiplication with $\mathbf{R}^T$). Since only every κ-th entry of the CES has to be computed, a factor κ has been gained in the CES complexity.

CES-based EC with decimation at the input (CO)

When the echo transfer function is again band limited to $\kappa N/2\gamma$ tones, one can use (5.9) to write the frequency domain error as

$$\begin{aligned} E^k &= \mathcal{F}_N(\mathbf{y}^k - \mathbf{D}_{\gamma\downarrow}\mathbf{U}_{\gamma\downarrow}^{k-1,k,k+1}\mathbf{M}_{\gamma\downarrow}\mathbf{w}_{E,\gamma\downarrow}^k), & (5.26)\\ &= \mathcal{F}_N(\mathbf{y}^k - \mathbf{D}_{\gamma\downarrow}(\chi_{\gamma\downarrow}^{k-1,k,k+1} + \mathbf{C}_{\gamma\downarrow}^k)\mathbf{M}_{\gamma\downarrow}\mathbf{w}_{E,\gamma\downarrow}^k), & (5.27) \end{aligned}$$

where $\chi_{\gamma\downarrow}^{k-1,k,k+1}$ and $\mathbf{C}_{\gamma\downarrow}^k$ are constructed from decimated echo reference samples, similar to $\mathbf{U}_{\gamma\downarrow}^{k-1,k,k+1}$. The $\kappa N/\gamma \times \kappa N/\gamma$ circulant matrix $\mathbf{C}_{\gamma\downarrow}^k$ can again be diagonalized by a DFT/IDFT matrix pair and the diagonal elements are determined by $\mathcal{F}_{\kappa N/\gamma}\mathbf{C}_{\gamma\downarrow}^k[:,1]$. Due to the additional decimation filter prior to downsampling, the DFT of the first column of $\mathbf{C}_{\gamma\downarrow}^k$ can not easily be derived from U^k. Hence, an extra $\kappa N/\gamma$-point DFT is effectively required to perform the echo emulation and filter update, i.e.

$$\begin{aligned} \tilde{U}^k &= \mathcal{F}_{\kappa N/\gamma}\mathbf{C}_{\gamma\downarrow}^k[:,1], & (5.28)\\ E^k &= \mathcal{F}_N(\mathbf{y}^k - \mathbf{D}_{\gamma\downarrow}\chi_{\gamma\downarrow}^{k-1,k,k+1}\mathbf{M}_{\gamma\downarrow}\mathbf{w}_{E,\gamma\downarrow}^k) - \frac{\gamma}{\kappa}\mathbf{R}_{\gamma\downarrow}^T(\tilde{U}^k \odot W_{E,\gamma\downarrow}^k), & (5.29)\\ W_{E,\gamma\downarrow}^{k+1} &\leftarrow W_{E,\gamma\downarrow}^k + \mu(\tilde{U}^k)^* \odot (\mathbf{R}_{\gamma\downarrow}E^k), & (5.30) \end{aligned}$$

where $\mathbf{R}_{\gamma\downarrow}^T = [\mathbf{I}_N \dots \mathbf{I}_N]$ contains only κ/γ identity matrices and $\mathbf{w}_{E,\gamma\downarrow}^k = \mathbf{M}_{\gamma\downarrow}^T\mathcal{I}_{\kappa N/\gamma}W_{E,\gamma\downarrow}^k$. The resulting structure is shown in **Fig. 5.6**. Depending on

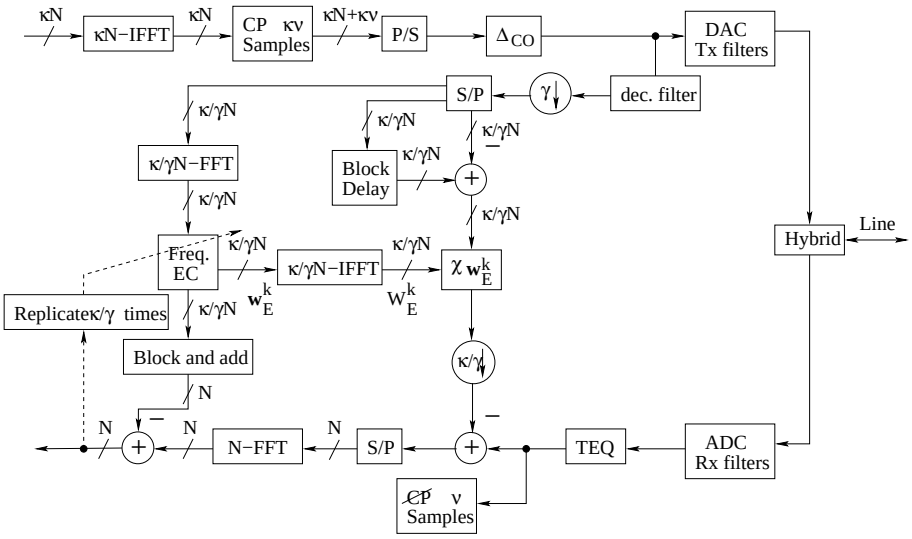

Figure 5.6: CES-based EC with decimation at the input (CO).

the values for κ, γ and T_E decimation at the input may lead to complexity savings.

CES-based EC with interpolation by zero padding the input (RT)

When the bandwidth of the transmitted echo signal is a factor κ smaller than the receive bandwidth, the transmit signal will be replicated over the entire receive bandwidth. The EC needs to interpolate the transmitted echo symbols in time and frequency domain. In the time domain $\kappa - 1$ zeroes are padded between two consecutive echo reference samples, while in the frequency domain, the symbols are replicated κ times. Mathematically, this leads to

$$E^k = \mathcal{F}_{\kappa N}(\mathbf{y}^k - \chi_{\kappa\uparrow}^{k-1,k,k+1}\mathbf{M}\mathbf{w}_E^k) - (\mathbf{R}(U^k \odot \mathbf{p})) \odot W_E^k, \quad (5.31)$$

$$W_E^{k+1} \leftarrow W_E^k + \mu(\mathbf{R}(U^k \odot \mathbf{p})^*) \odot E^k, \quad (5.32)$$

where $\mathbf{M}$ and $\mathbf{w}_E^k = \mathbf{M}^T\mathcal{I}_{\kappa N}W_E^k$ are at high rate and $\chi_{\kappa\uparrow}^{k-1,k,k+1}$ is based on a κ times upsampled input sequence. Clearly, a factor κ has been gained in the CES complexity, compared to the symmetric rate case. The resulting structure is shown in **Fig. 5.7**.

5.2.3 Complexity

The computational complexity of CES-based EC is summarized in **Table 5.2**, where it is assumed that the echo channel is band limited to $\kappa N/2\gamma$ tones. The

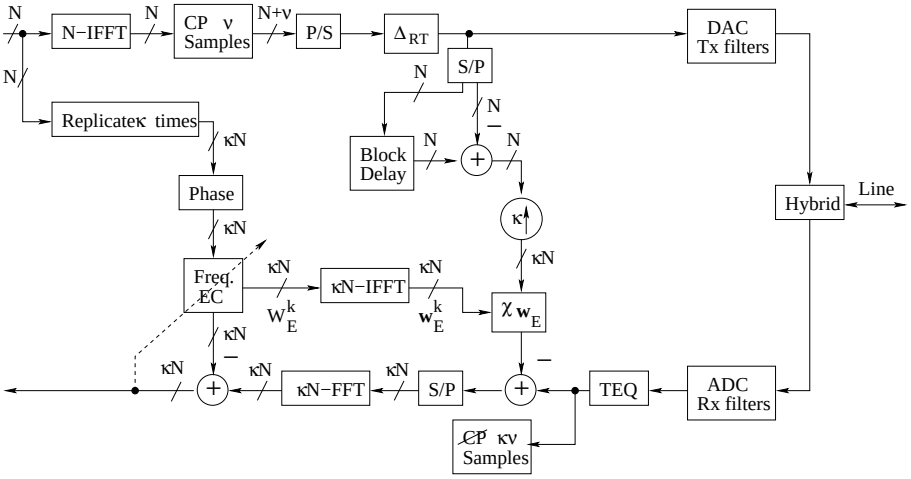

Figure 5.7: CES-based EC with interpolated setup (RT).

complexity of the multi-rate structures in Subsection 5.2.2 are misalignment dependent. Therefore, it is assumed that RT can choose its misalignment. Two cases are considered: in [57] Δ is equal to zero, while in [65][129] Δ is chosen in order to minimize the CES complexity. In both cases CO receives an additional DFT/IDFT pair, cf. (5.22) and (5.23). The complexity is again expressed as the number of real multiplications required for echo emulation per symbol. The multiplication with $\mathbf{p}$ is not counted since this phase vector in the frequency domain can also be modeled by a simple shift of the echo canceler coefficients in the time domain, see [129] for more details. Note that due to the complex conjugate symmetry in the frequency domain, only half of the frequency domain multiplications is effectively counted. For the (I)DFT complexity, the split-radix FFT algorithm was used for complex valued input data and real valued output data [117]. In **Table 5.2**, it can easily be seen that the CES complexity with optimal misalignment is approximately equal to half the complexity of the zero misalignment case. When decimation at the input is applied at CO, the CES complexity is roughly γ times lower at the expense of an additional decimation filter and a $\kappa N/\gamma$-point DFT.

5.3 Double talk cancellation (DTC)

Due to temperature variations of the line and the modem front end, the echo channel will slowly change over time. Hence, adaptive algorithms, as discussed in the previous sections, are used to track these channel variations [54]. However, when the far end signal is not silenced, which is e.g. the case during duplex

TABLE 5.2
Complexity of CES-based EC in real multiplications per symbol.

	Decimated EC (CO)	**Interpolated EC (RT)**
CES-based EC [65][129]	$\frac{1}{2\kappa}((\frac{T_E}{2})^2+(\frac{T_E-2}{2})^2)+4\frac{\kappa N}{2\gamma}$ $\frac{N}{2}\log_2 N-\frac{3N}{2}+2$	$\frac{1}{2\kappa}((\frac{T_E-\kappa\nu}{2})^2+(\frac{T_E-\kappa\nu-2}{2})^2)$ $+4\frac{\kappa N}{2\gamma}$
CES-based EC [57]	$\frac{(T_E-1)^2}{2\kappa}+4\frac{\kappa N}{2\gamma}+$ $\frac{N}{2}\log_2 N-\frac{3N}{2}+2$	$\frac{(T_E-\kappa\nu-1)^2}{2\kappa}+4\frac{\kappa N}{2\gamma}$

transmission, the adaptive update may exhibit a large excess mean square error (MSE). Although the far end signal is uncorrelated with the transmitted echo reference signal, its energy is much higher than the background noise level, thereby preventing the echo canceler from converging to the Wiener solution. A misadjustment of the echo channel estimate leads to more residual echo and hence a degradation of the signal to noise ratio (SNR) of the desired far end signal at the receiver. As a result, the achieved bit rate will be reduced. This is commonly known as the *double talk* problem and has been extensively studied in literature, see [49][52][64][152] and references therein.

A well known solution to this problem is to increase the noise averaging by *lowering the step size* in the adaptation process. Unfortunately, in most cases the step size has to be reduced to such an extent that it leads to insufficient tracking and/or slow convergence. Moreover, a sharply reduced step size in a finite precision implementation of the echo canceler may lead to a cancellation error considerably larger than predicted by the used coefficient precision [54].

In this section, we will modify the updating part of existing echo canceler structures in order to have faster convergence and tracking in the presence of a far end signal. The energy of the double talker will be lowered to the level of the far end ISI/ICI noise, such that a larger step size can be applied. Without loss of generality, we will assume a *symmetric rate* setup with equal IDFT and DFT size in the transmit and receiver path of the modem. Extensions to multi-rate setups can easily be made.

5.3.1 Double talk cancellation for TD-EC

The optimal MMSE echo canceler minimizes the following cost function:

$$\min_{\mathbf{w}_E} \mathcal{E}\{(e^k)^2\} \approx \min_{\mathbf{w}_E} \|\mathbf{e}^k\|_2^2, \tag{5.33}$$

where $\mathcal{E}\{\cdot\}$ denotes the expectation operator and $\mathbf{e}^k$ is given by (5.4). Applying Parseval's theorem [101], the equivalent cost function in the frequency domain can be stated as:

$$\min_{\mathbf{w}_E} \|E^k\|_2^2 = \min_{\mathbf{w}_E} \sum_{i=0}^{N-1} |E_i^k|^2, \tag{5.34}$$

where $E^k = \mathcal{F}_N \mathbf{e}^k$ and E_i^k is the entry of E^k corresponding to the i-th tone. In DMT systems a one-tap complex frequency domain equalizer (FEQ) for each tone i is used to compensate for magnitude and phase distortions introduced by the overall far end channel, cf. Chapter 2. When considering the frequency domain error of (5.5) after the one-tap FEQ, denoted by D_i for tone i, the cost function in (5.34) is equivalent to

$$\min_{\mathbf{w}_E} \sum_{i=0}^{N-1} \frac{|D_i E_i^k|^2}{|D_i|^2} = \min_{\mathbf{w}_E} \sum_{i=0}^{N-1} \frac{\left|D_i \mathcal{F}_N[i,:](\mathbf{y}^k - \mathbf{U}^{k-1,k,k+1}\mathbf{M}\mathbf{w}_E)\right|^2}{|D_i|^2}. \tag{5.35}$$

In case of perfect EC, the numerator contains only far end information and background noise. Moreover, the FEQ and TEQ are designed in such a way that the numerator is as close as possible to the transmitted far end symbol on tone i, X_i^k, cf. Chapter 3. Since the transmitted symbols, X_i^k, are available at the decision device[2] after the FEQ outputs (assuming that no or a limited number of decision errors are made), the energy of the far end signal can be reduced by subtracting X_i^k, i.e.

$$\begin{aligned}
&\min_{\mathbf{w}_E} \sum_{i=0}^{N-1} \frac{\left|D_i \mathcal{F}_N[i,:](\mathbf{y}^k - \mathbf{U}^{k-1,k,k+1}\mathbf{M}\mathbf{w}_E) - X_i^k\right|^2}{|D_i|^2} \\
&= \min_{\mathbf{w}_E} \left\|\mathrm{diag}\{D\}^{-1}(\mathrm{diag}\{D\}\mathcal{F}_N(\mathbf{y}^k - \mathbf{U}^{k-1,k,k+1}\mathbf{M}\mathbf{w}_E) - X_{0:N-1}^k)\right\|_2^2,
\end{aligned} \tag{5.36}$$

where $D = [D_0 \ \ldots \ D_{N-1}]^T$ is a vector of length N containing the FEQs for all the tones. Formula (5.36) effectively corresponds to (5.35) supplemented with *double talk cancellation (DTC)*. In this way, the level of the far end signal ('double talker') in (5.35) will be reduced to the level of the residual (far end) ISI/ICI, which remains present due to imperfect equalization.

The block LMS update for TD-EC can be readily obtained by calculating the gradient of (5.36) with respect to $\mathbf{w}_E$, resulting in

$$\begin{aligned}
\mathbf{w}_E^{k+1} \quad \leftarrow \quad & \mathbf{w}_E^k + \mu \mathbf{M}^T (\mathbf{U}^{k-1,k,k+1})^T \mathcal{I}_N \mathrm{diag}\{D\}^{-1} \cdot \\
& \left(\mathrm{diag}\{D\}\mathcal{F}_N \mathbf{e}^k - X_{0:N-1}^k\right),
\end{aligned} \tag{5.37}$$

where $\mathbf{e}^k$ is given by (5.4). The resulting algorithm is very similar to (5.6), but now $\mathbf{e}^k$ is first transformed to the frequency domain. After rotating and scaling the frequency domain error by the FEQs, the far end signal, $X_{0:N-1}^k$, is removed. Finally, the inverse FEQ operation is applied and the error is transformed back to the time domain. Observe that DTC for TD-EC is fairly simple but introduces extra computational complexity.

[2] W.l.o.g. an unbiased decision rule is assumed, see Chapter 3 for more details.

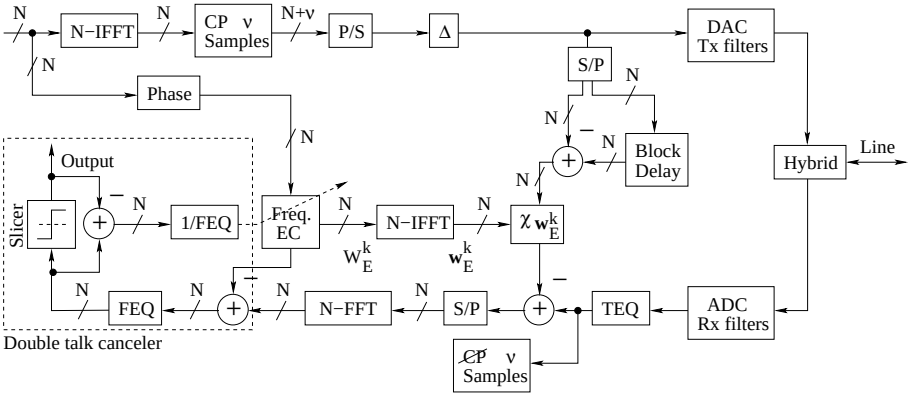

Figure 5.8: CES-based EC with double talk cancellation.

5.3.2 Double talk cancellation for CES-based EC

Also for CES-based EC double talk cancellation can be applied, be it at a much lower cost than for TD-EC. Adding DTC to (5.20), according to the same principles as in (5.37), leads to

$$W_E^{k+1} \leftarrow W_E^k + \mu(U^k \odot \mathbf{p})^* \odot D^{-1} \odot (D \odot E^k - X_{0:N-1}^k), \quad (5.38)$$

where E^k is given by (5.17). **Fig. 5.8** depicts the double talk principle for a CES-based echo canceler. The update error is constructed by taking the difference between input and output of the decision device. The updating of the echo transfer function estimate is done in the frequency domain, while the filtering part is partially in the time and partially in the frequency domain.

The goal of the receiver is to detect the transmitted far end symbols as accurately as possible. This detection process will be distorted by background noise, far end ISI/ICI and residual echo. A simple design criterion for the echo canceler is to ensure that the residual echo after echo canceler convergence remains far beneath the background noise plus ISI/ICI level. In this case, residual echo will not be the dominant noise source. The residual echo, as observed by the receiver, can be expressed as the excess MSE of the EC in (5.17). Under the assumption that all tones are excited, Cioffi et al. showed in [32] that the excess MSE for tone i is given by

$$\xi_{excess,i} = \lim_{k\to\infty} \mathcal{E}\left\{\mathcal{F}_N[i,:](\mathbf{U}^{k-1,k,k+1}\mathbf{h}_E - \mathbf{U}^{k-1,k,k+1}\mathbf{M}\mathbf{w}_E^k)\right\}, \quad (5.39)$$

$$= \frac{\mu\sqrt{\frac{T_E}{N}}}{2}\frac{1}{1-\gamma_i}\sigma_{u,i}^2\sigma_{n,i}^2, \quad (5.40)$$

TABLE 5.3
Complexity of DTC in real multiplications per symbol.

	DTC TD-EC	**DTC CES-based EC**
computation D^{-1}	$2\frac{N}{2}$	$2\frac{N}{2}$
multiplication with D^{-1}	$4\frac{N}{2}$	$4\frac{N}{2}$
complex-to-real IDFT	$\frac{N}{2}\log_2 N - \frac{3N}{2} + 2$	/

with γ_i a tone dependent constant (typically close to zero), $\sigma^2_{u,i}$ and $\sigma^2_{n,i}$ the echo transmit power and noise power per subchannel. Hence, when the noise power is increased due to double talk, the step size should be lowered to reach the same excess MSE as in the case when the far end signal is silenced. With double talk cancellation, however, the step size can be increased, resulting in better tracking performance of the echo channel.

5.3.3 Complexity

In this subsection the computational complexity of DTC is calculated. Only the additional complexity introduced by the double talk canceler is given. The complexity is expressed in the number of *real* multiplications per symbol period. It should be noted that in DMT-based DSL-systems tones appear in complex conjugate pairs. Therefore, only half of the tones are considered in the complexity calculations. The results for TD-EC and CES-based EC are given in **Table 5.3** and are based on the formulas (5.37) and (5.38).

The multiplication with the one tap FEQs is not taken into account, since this operation belongs to the equalization part of the modem. For the IDFT complexity, the split-radix FFT algorithm was used for complex valued input data and real valued output data [117]. The overall complexity of DTC for TD-EC becomes $(3\frac{N}{2} + \frac{N}{2}\log_2 N + 2)\frac{F_s}{N+\nu}$ real multiplications per second, with F_s the sampling rate and ν the size of the cyclic prefix. Similarly, for CES-based EC, the total number of operations is equal to $3N\frac{F_s}{N+\nu}$ real multiplications per second. Since these complexity figures are small compared to the complexity of the echo canceler itself (typically $2-4\%$), DTC comes at almost no extra cost.

5.4 Improved time/frequency domain echo canceling (ITF-EC)

The goal of this section is to introduce an EC algorithm that minimizes the CES complexity without imposing a specific temporal misalignment. In Sub-

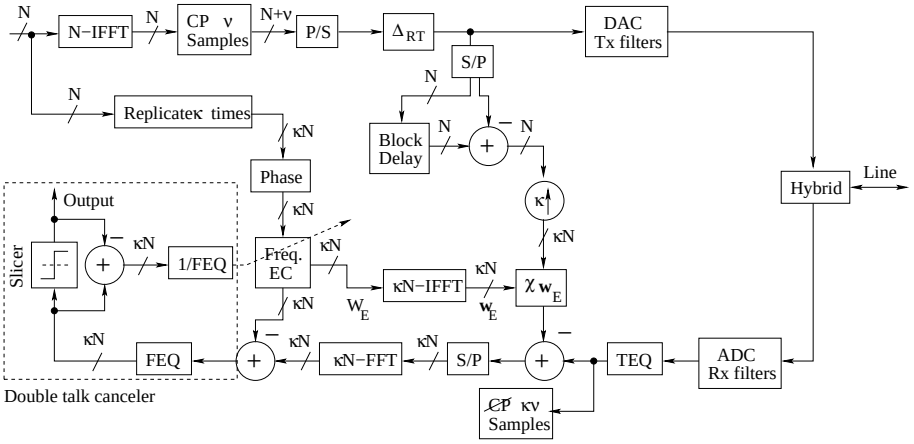

Figure 5.9: Echo cancellation at RT with alternative alignment. The misalignment at RT is determined to minimize the CES complexity. Typical values are $\kappa = 8$, $N = 64$ and $\nu = 4$.

section 5.4.1, we start the discussion with a motivation of our approach. Then, an outline of the algorithm will be given for a symmetric rate and a multi-rate setup in Subsections 5.4.2 and 5.4.3 respectively. Finally, the computational complexity of the resulting algorithm will be addressed in Subsection 5.4.4.

5.4.1 Motivation

In [57], Ho et al. describe an efficient method to cancel the received echo noise partially in the time domain (CES) and partially in the frequency domain. As discussed in Section 5.2, the complexity of the time domain processing can be minimized by optimizing the temporal misalignment Δ between the echo and far end symbols in the modem. Unfortunately, the choice of a specific misalignment at one end of the loop completely determines the misalignment at the other end. In general, the second modem does not have a misalignment that leads to minimal CES complexity, such that an extra DFT-IDFT pair is required in the receive path to set the transmitter/EC misalignment independently of the symbol boundaries of the far end signal [65]. Since the second modem does not share its receive DFT for far end signal demodulation and EC, the modem structure is not practical for simple DTC, cf. Section 5.3.

To illustrate the previous discussion, **Fig. 5.9** and **Fig. 5.10** depict the signal flow graphs for CES-based EC at RT and CO with minimal CES complexity. Compared to the EC structures presented in Section 5.2, DTC has been added to ensure fast convergence when the far end signal is not silenced. Whereas EC at RT is optimally split into a frequency domain and a time domain part,

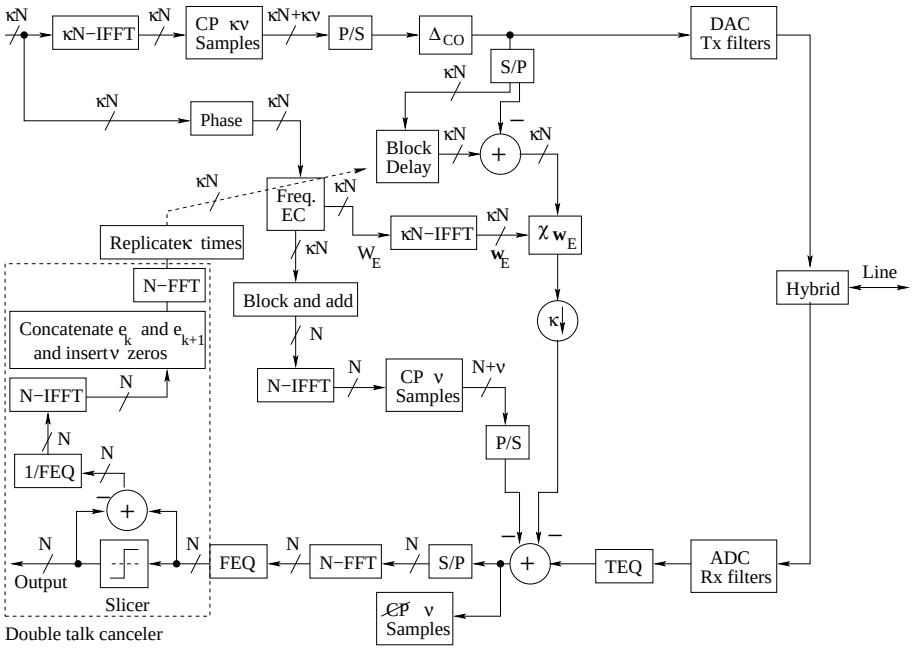

Figure 5.10: Echo cancellation at CO with alternative alignment. The misalignment can not be chosen at CO such that extra FFT processing is required. Typical values are $\kappa = 8$, $N = 64$ and $\nu = 4$.

the emulated echo at CO is completely subtracted in the time domain to allow an independent misalignment between the emulated echo sequence and the received far end symbol, cf. (5.22). At RT, DTC is fairly simple and obtained by replacing the original update error E^k by the slicer error to remove the far end component. Since the slicer error is computed after FEQ processing, a derotation with the inverse FEQ coefficients is required prior to the coefficient update. At CO, however, DTC is much more complex and suboptimal due to the requirement that the CES complexity has to be minimized. In general, DTC requires a frequency domain representation of the time domain echo estimation error. Since the cyclic prefix of the received signal is discarded, the corresponding samples of the time domain estimation error can not be recovered due to the misalignment. Therefore, in the frequency domain these estimation error samples can not be computed and are simply put to zero. Due to the independent misalignment between the emulated echo and the far end symbol, EC at CO requires one extra DFT for echo emulation and an additional DFT/IDFT pair for coefficient adaptation.

In this section, we present a new technique to *minimize the CES complexity without imposing a specific temporal misalignment*. The proposed scheme re-

quires only one extra DFT instead of the DFT/IDFT pair of [65]. This time, the extra DFT is at the *transmit* side of one of the modems such that the DFT in the receive path can still be used for both far end signal demodulation and EC, thereby enabling inexpensive DTC. The obtained structure, referred to as *improved time frequency domain EC (ITF-EC)*, will lead to a less expensive implementation of the overall system, which includes echo canceling in the modems at both sides of the loop.

5.4.2 Symmetric rate ITF-EC

First, assume a symmetric rate setup with equal transmit and receive (I)DFT sizes. Consider a different split of $\mathbf{U}^{k-1,k,k+1}$ (similar to (5.13)), i.e.

$$\mathbf{U}^{k-1,k,k+1} = \tilde{\chi}^{k-1,k,k+1} + \tilde{\mathbf{C}}, \tag{5.41}$$

where $\tilde{\mathbf{C}}$ is an $N \times N$ circulant matrix constructed with $N_b + 1$ samples from the first row and $N - N_b$ samples ($0 \leqslant N_b \leqslant N-1$) from the first column of $\mathbf{U}^{k-1,k,k+1}$. As illustrated in **Fig. 5.11**, $\tilde{\mathbf{C}}$ is defined as

$$\tilde{\mathbf{C}} = \begin{bmatrix} u^k_{\Delta} & \dots & u^k_0 & u^k_{N-1} & \dots & u^k_{N-\nu} & u^{k-1}_{N-1} & \dots & u^k_{\Delta+1} \\ \vdots & \ddots & & & & & & \ddots & \vdots \\ u^k_{N-N_b+\Delta-1} & & & & & & & & u^{k-1}_{N-1} \\ u^{k-1}_{N-N_b+\nu+\Delta} & & & & & & & & \vdots \\ \vdots & & & & & & & & \\ u^{k-1}_{N-1} & & & & & & & & \\ u^k_{N-\nu} & & & & & & & & \\ \vdots & & & & & & & & \\ u^k_{N-1} & & & & & & & & \\ u^k_0 & & & & & & & & \\ \vdots & \ddots & & & & & & \ddots & \vdots \\ u^k_{\Delta-1} & \dots & u^k_0 & \dots & & & & \dots & u^k_{\Delta} \end{bmatrix}. \tag{5.42}$$

Hence, $\tilde{\mathbf{C}}$ is formed by N elements located in the upper left corner of $\mathbf{U}^{k-1,k,k+1}$. As opposed to (5.14) and [57][65], $\tilde{\mathbf{C}}$ includes elements of two different echo reference symbols. Since $\tilde{\mathbf{C}}$ is circulant, it can be diagonalized by a DFT and IDFT matrix (see Appendix A):

$$\tilde{\mathbf{C}} = \mathcal{I}_N \mathrm{diag}\{\tilde{U}^k\}\mathcal{F}_N, \tag{5.43}$$

with $\tilde{U}^k = \mathcal{F}_N \tilde{\mathbf{C}}[:,1]$. Clearly, to obtain $\tilde{U}^k$, an extra DFT of the echo reference symbols is required at the *transmit* side of the modem. Similar to (5.17), the echo canceled frequency domain output can now be written as

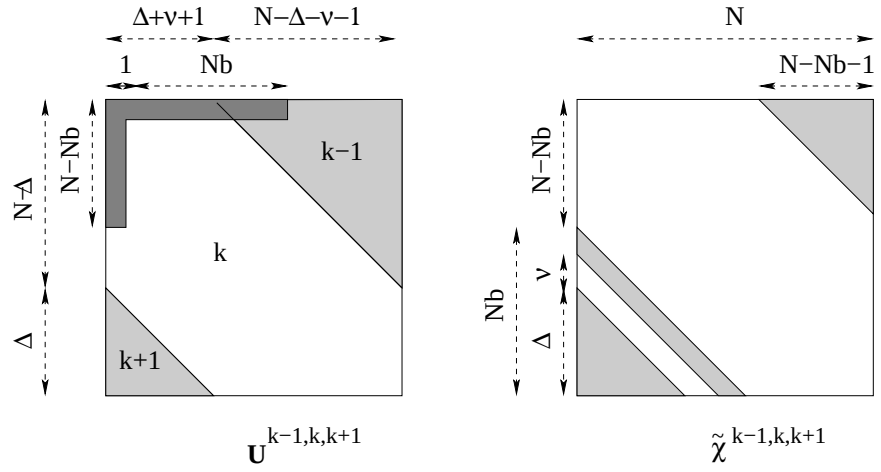

Figure 5.11: Illustration of the $N \times N$ Toeplitz matrices $\mathbf{U}^{k-1,k,k+1}$ and $\tilde{\chi}^{k-1,k,k+1}$ with the choice of N_b.

$$E^k = \mathcal{F}_N(\mathbf{y}^k - \tilde{\chi}^{k-1,k,k+1}\mathbf{M}\mathbf{w}_E^k) - \text{diag}\{\tilde{U}^k\}W_E^k \tag{5.44}$$

with $\tilde{\chi}^{k-1,k,k+1} = \mathbf{U}^{k-1,k,k+1} - \tilde{\mathbf{C}}$ and where $\mathbf{w}_E^k$ is obtained by taking (infrequently) the IDFT of W_E^k. The matrix $\tilde{\chi}^{k-1,k,k+1}$ is sparse (similar to (5.15)) and the number of non-zero elements is determined by N_b. Observe that N_b can be chosen such that the number of elements in $\tilde{\chi}^{k-1,k,k+1}$ is minimal, which evidently leads to the minimum number of operations to compute $\tilde{\chi}^{k-1,k,k+1}\mathbf{M}\mathbf{w}_E^k$. Hence, the value of N_b determines the the time domain EC complexity.

As in (5.20), an LMS-like procedure can be developed to update the EC coefficients in the frequency domain, i.e.

$$W_E^{k+1} \leftarrow W_E^k + \mu(\tilde{U}^k)^* \odot E^k. \tag{5.45}$$

Under the same assumptions as used to prove the convergence of (5.20) [57], it is shown in Appendix D.1 that (5.45) is convergent in the mean if the step size μ satisfies the following condition:

$$0 < \mu < \frac{2}{\sigma_u^2}, \tag{5.46}$$

where $\sigma_u^2 = \sigma_{u,i}^2$ denotes the transmitted echo energy on each tone. The assumptions in Appendix D.1 imply that all the available echo tones should be used and transmitted with equal power, which is rarely valid in practice. Henceforth, a *reduced power is allocated to unused echo tones* to guarantee

convergence, similar to [32].

Advantages of ITF-EC are:

- an optimal N_b exists which minimizes the number of operations in the computation of $\tilde{\chi}^{k-1,k,k+1}\mathbf{M}\mathbf{w}_E^k$ *without choosing a specific misalignment.* Minimizing the number of non-zero elements in $\tilde{\chi}^{k-1,k,k+1}\mathbf{M}$ yields the optimal N_b, i.e.

$$\begin{aligned} N_{b,opt} = \arg\min_{N_b} & \frac{(T_E+\delta-N_b-1)(T_E+\delta-N_b)}{2} + \frac{(N_b-\delta)(N_b-\delta+1)}{2} - \\ & \frac{(\Delta+\nu-\delta)(\Delta+\nu-\delta+1)}{2} + \frac{(\Delta-\delta)(\Delta-\delta+1)}{2}, \\ = \delta + & \frac{T_E-1}{2}, \end{aligned} \tag{5.47}$$

  where the value of δ originates from the definition of $\mathbf{M}$. When T_E is even, the optimal value for N_b is not an integer and will be approximated by $\delta + T_E/2$. Given the optimal value of N_b, the number of real multiplications in $\tilde{\chi}^{k-1,k,k+1}\mathbf{M}\mathbf{w}_E^k$ is readily obtained and upper bounded by $T_E^2/4$, which is alignment independent.

- The DFT in the receive path (for RT as well as CO) is always shared between the EC and the far end signal demodulator leading to a straightforward application of DTC:

$$W_E^{k+1} \quad \leftarrow \quad W_E^k + \mu(\tilde{U}^k)^* \odot D^{-1} \odot (D \odot E^k - X_{0:N-1}^k), \tag{5.48}$$

  where E^k is given by (5.44). Again, the far end signal is efficiently removed by using the slicer error (difference between slicer input and slicer output) instead of the DFT output in the echo canceler update. Equation (5.48) is valid for RT as well as for CO and therefore DTC at CO is as simple as at RT, as opposed to DTC at CO in **Fig. 5.10**.

- The ITF-EC of (5.44) can be reduced to the CES-based EC of (5.17): if a modem minimizes its CES complexity by choosing a specific misalignment and a specific N_b such that $\tilde{\mathbf{C}}$ is only a function of the k-th transmitted echo symbol, then the extra DFT (to calculate $\tilde{U}^k$) is obsolete at that side. The modem at the other side of the loop still has to compute $\tilde{U}^k$ by means of an extra DFT, since its misalignment is imposed by the first modem. The RT-transmitter is typically operating at the lowest rate ($N = 64$), hence the extra DFT should be executed at RT to yield the lowest overall complexity.

5.4.3 Multi-rate ITF-EC

Extending the symmetric rate ITF-EC to a multi-rate structure, i.e. where a different transmit and receive rate is used, is straightforward and is similar to Subsection 5.2.2. Here, for conciseness, multi-rate structures will mainly be treated graphically.

Decimated ITF-EC (CO)

At CO, the bandwidth of the transmitted echo signal is a factor κ larger than the receive bandwidth and aliasing occurs when going from the high transmit rate to the lower receive rate. To include these aliasing effects in the EC, the time domain part of the emulated echo will be decimated at the output of the echo canceler by computing only every κ-th sample. In the frequency domain, the echo emulated symbols of size κN are blocked into symbols of length N and subsequently added. Similar to (5.24) and (5.25), the corresponding EC and update equations are given by

$$\tilde{U}^k = \mathcal{F}_{\kappa N}\tilde{\mathbf{C}}[:,1], \tag{5.49}$$

$$E^k = \mathcal{F}_N(\mathbf{y}^k - \mathbf{D}\tilde{\chi}^{k-1,k,k+1}\mathbf{M}\mathbf{w}_E^k) - \frac{1}{\kappa}\mathbf{R}^T(\tilde{U}^k \odot W_E^k), \tag{5.50}$$

$$W_E^{k+1} \leftarrow W_E^k + \mu(\tilde{U}^k)^* \odot (\mathbf{R}(D^{-1} \odot (D \odot E^k - X_{0:N-1}^k))), \tag{5.51}$$

with DTC included and $\mathbf{w}_E^k = \mathbf{M}^T\mathcal{I}_{\kappa N}W_E^k$. The ITF-EC for CO is depicted in **Fig. 5.12**. In the figure, two options are depicted:

1. The κN-point DFT to obtain $\tilde{U}^k$ is obsolete when the misalignment Δ_{CO} and N_b are chosen such that $\tilde{\mathbf{C}}[:,1]$ is only a function of the k-th transmitted echo symbol. Similar to (5.17), an additional phase rotation, $\mathbf{p}$, per tone is then required.
2. When the misalignment Δ_{CO} can not be altered to optimize the CES complexity, a κN-point DFT effectively has to be executed to obtain $\tilde{U}^k$.

In Subsection 5.4.4, only the first option will be considered. As opposed to **Fig. 5.10**, it is clear from **Fig. 5.12** that DTC for ITF-EC at CO remains fairly simple.

Interpolated ITF-EC (RT)

At RT, the transmitted echo signal has to be interpolated, since its sampling rate is a factor κ smaller than the receive rate. In time domain, $\kappa - 1$ zeroes are padded between the time domain echo data samples. By this, the calculation of $\tilde{U}^k$ only requires the computation of one N-point DFT (instead of a

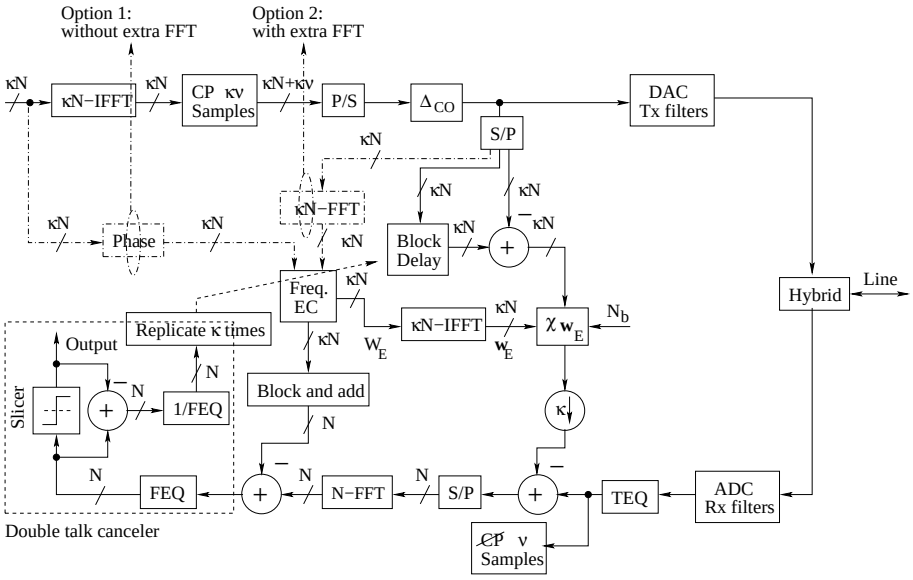

Figure 5.12: ITF-EC at CO, where typical values are $\kappa = 8$, $N = 64$ and $\nu = 4$.

κN-point DFT). $\tilde{U}^k$ will then be repeated κ times in the frequency domain. Mathematically, this comes down to

$$\tilde{U}^k = \mathcal{F}_N \tilde{\mathbf{C}}_{\kappa\uparrow}[1:\kappa:\kappa N, 1], \tag{5.52}$$

$$E^k = \mathcal{F}_{\kappa N}(\mathbf{y}^k - \tilde{\chi}_{\kappa\uparrow}^{k-1,k,k+1}\mathbf{M}\mathbf{w}_E^k) - (\mathbf{R}\tilde{U}^k) \odot W_E^k, \tag{5.53}$$

$$W_E^{k+1} \leftarrow W_E^k + \mu(\mathbf{R}(U^k \odot \mathbf{p})^*) \odot D^{-1} \odot (D \odot E^k - X_{0:\kappa N-1}^k), \tag{5.54}$$

where DTC is included and $\tilde{\chi}_{\kappa\uparrow}^{k-1,k,k+1}$ and $\tilde{\mathbf{C}}_{\kappa\uparrow}$ are based on a κ times upsampled echo reference sequence. The ITF-EC for RT is depicted in **Fig. 5.13**. Since the proposed EC shares the receive DFT for EC and far end signal demodulation, the DTC comes at almost no extra complexity.

5.4.4 Complexity

Table 5.4 summarizes the complexity of three different schemes for CO and RT. Scheme I represents CES-based EC as depicted in **Fig. 5.9** and **Fig. 5.10** according to [57] where the misalignment is assumed to be zero; scheme II represents CES-based EC (also depicted in **Fig. 5.9** and **Fig. 5.10**) but with optimal misalignment to minimize the CES complexity [65][129] and scheme III is the proposed ITF-EC, with the assumption that CO has chosen its alignment and N_b to avoid an extra DFT at the transmit side of the modem.

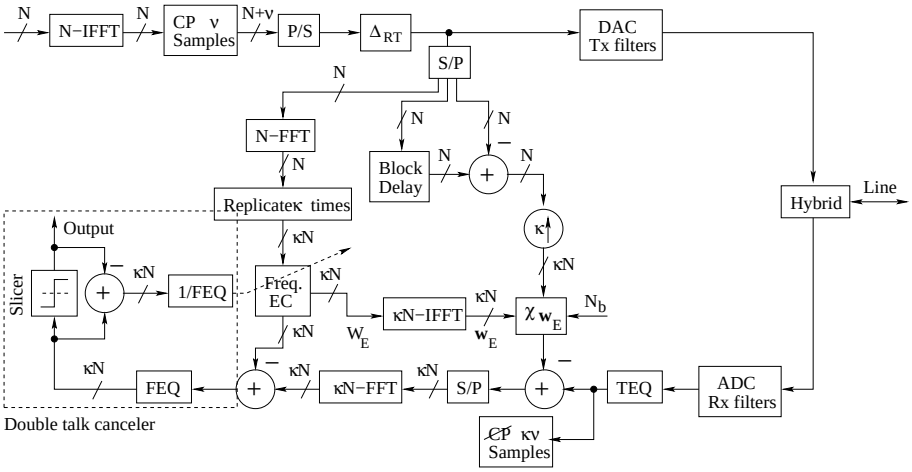

Figure 5.13: ITF-EC at RT, where typical values are $\kappa = 8$, $N = 64$ and $\nu = 4$.

The computational complexity of the algorithms is approximated by the number of real multiplications per iteration. A distinction has been made between the *echo emulation* and the *adaptation process*. For the emulation complexity of scheme I and scheme II, we refer to **Table 5.2**. For the adaptation process, the complexity of DTC is included.

For the double talk canceler it is assumed that no extra DFT processing is required at RT since the receiver DFT is shared between far end demodulation and EC. In schemes I and II CO requires two extra IDFTs and one extra DFT for DTC. The two IDFTs are needed to transform two consecutive blocks of slicer errors to the time domain and the extra DFT calculates the correctly aligned E^k for the EC adaptation. The complexity of the real to complex (I)DFTs is based on the split-radix FFT algorithm [117].

In the table, T_E is the number of time domain EC taps at high rate, N and ν are the IDFT size and cyclic prefix length at the low rate, κ is the up- or down sampling factor due to the multi-rate structure of the modem, γ denotes the bandlimited character of the echo transfer function and ϕ indicates that the frequency domain EC taps are infrequently transformed to the time domain by an IDFT [57]. Note that the CES of scheme II requires approximately half the complexity of the CES of scheme I.

The overall adaptation and emulation complexity of CO plus RT is depicted in **Fig. 5.14** as a function of T_E, with $\nu = 4$, $N = 64$, $\kappa = 8$ and $\phi = 30$. Scheme I is represented by plus-marks, scheme II by cross-marks and scheme III by circles. Observe that *the proposed ITF-EC has roughly the same complexity for echo emulation as CES-based EC with optimal misalignment*

TABLE 5.4
Complexity figures for the echo emulation and EC adaptation at CO and RT.

		Scheme I	**Scheme II**	**Scheme III**
RT	**Em.**	$\frac{(T_E-\kappa\nu-1)^2}{2\kappa}+$ $4\frac{\kappa N}{2\gamma}$	$\frac{1}{2\kappa}(\frac{T_E-\kappa\nu-2}{2})^2+$ $\frac{1}{2\kappa}(\frac{T_E-\kappa\nu}{2})^2+4\frac{\kappa N}{2\gamma}$	$\frac{T_E^2}{4\kappa}+4\frac{\kappa N}{2\gamma}+$ $\frac{N}{2}\log_2 N-\frac{3N}{2}+2$
	Ad.	$\frac{5\kappa N}{\gamma}+$ $\frac{\frac{\kappa N}{2}\log_2\kappa N-\frac{3\kappa N}{2}+2}{\phi}$	$\frac{5\kappa N}{\gamma}+$ $\frac{\frac{\kappa N}{2}\log_2\kappa N-\frac{3\kappa N}{2}+2}{\phi}$	$\frac{5\kappa N}{\gamma}+$ $\frac{\frac{\kappa N}{2}\log_2\kappa N-\frac{3\kappa N}{2}+2}{\phi}$
CO	**Em.**	$\frac{(T_E-1)^2}{2\kappa}+4\frac{\kappa N}{2\gamma}+$ $\frac{N}{2}\log_2 N-\frac{3N}{2}+2$	$\frac{1}{2\kappa}(\frac{T_E-2}{2})^2+$ $\frac{1}{2\kappa}(\frac{T_E}{2})^2+4\frac{\kappa N}{2\gamma}+$ $\frac{N}{2}\log_2 N-\frac{3N}{2}+2$	$\frac{1}{2\kappa}(\frac{T_E-\kappa\nu-2}{2})^2+$ $\frac{1}{2\kappa}(\frac{T_E-\kappa\nu}{2})^2+$ $4\frac{\kappa N}{2\gamma}$
	Ad.	$4\frac{\kappa N}{2\gamma}+3N+$ $\frac{3N}{2}\log_2 N-\frac{9N}{2}+6$ $+\frac{\frac{\kappa N}{2}\log_2\kappa N-\frac{3\kappa N}{2}+2}{\phi}$	$4\frac{\kappa N}{2\gamma}+3N+$ $\frac{3N}{2}\log_2 N-\frac{9N}{2}+6$ $+\frac{\frac{\kappa N}{2}\log_2\kappa N-\frac{3\kappa N}{2}+2}{\phi}$	$4\frac{\kappa N}{2\gamma}+3N+$ $\frac{\frac{\kappa N}{2}\log_2\kappa N-\frac{3\kappa N}{2}+2}{\phi}$

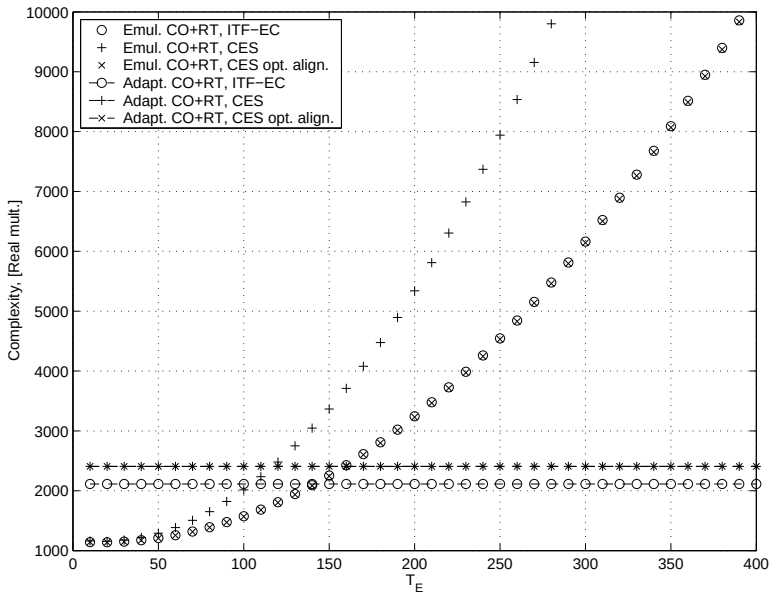

Figure 5.14: Complexity in real multiplications per iteration for echo emulation and coefficient adaptation as a function of the number of echo canceler taps T_E.

[65], while the overall update complexity is lower. Although the overall update complexity is lowered, *the convergence speed remains roughly the same*, as will be demonstrated in Section 5.6.

5.5 Circulant decomposition canceler (CDC)

In the previous sections it was assumed that *all* transmitted echo subcarriers were excited with a certain amount of power. In this section, we will develop an alternative EC scheme, referred to as circulant decomposition canceler (CDC), that works without the extra power requirements. In Subsection 5.5.1, we give a motivation of our approach. Similar to Section 5.4, we start with the symmetric rate CDC algorithm in Subsection 5.5.2. Multi-rate CDC structures are treated in Subsection 5.5.3. In Subsection 5.5.4 the CDC is integrated in a combined scheme with per tone equalization (PTEQ) and double talk cancellation (DTC). Finally, the complexity of the proposed structure is analyzed in Subsection 5.5.5.

5.5.1 Motivation

In (5.20), the echo filter is adapted in the frequency domain by means of a single-tap LMS procedure per tone, using the transmitted echo frequency domain symbols U^k as 'update direction'. Since the carriers of U^k are assigned to up- and/or downstream some of the modes of U^k are not excited, leaving the corresponding echo filter coefficients unaltered. This effect was also noticed in [32], where the authors proposed to transmit *dummy data with a reduced power level* on extra tones to circumvent this problem. Besides the increased transmit power, drawbacks of this solution are that front end filters have to be designed such that the resulting transmit signal remains below the standardized power masks [63]. A higher order of the front end filters results in a longer overall echo channel, resulting in an increased complexity of the echo canceler. In addition, the dummy data is located near the band edges of the front end filters, thereby causing extra inter-carrier-interference (ICI) at the other side of the loop. The extra ICI has to be mitigated by a more complex equalizer to avoid a reduction in achievable bit rates. Hence, it is clear that the transmission of extra power on additional tones is undesired.

In this section, we propose a new echo canceler structure that *does not require such extra transmit power* on unused tones for EC updating purposes. This structure will be referred to as Circulant Decomposition Canceler (CDC). The proposed scheme is based on a split of a Toeplitz matrix into a circulant and a skew-circulant part. The circulant part will lead to efficient frequency domain echo canceling, while the skew-circulant part will correspond to a partial time domain echo canceling. Hence, the obtained structure still belongs to the

class of mixed time/frequency domain echo cancelers. We will show that the proposed method has a complexity and convergence behaviour comparable to existing EC schemes. Moreover, it will be shown that the resulting structure can be combined cheaply with PTEQ and DTC.

5.5.2 Symmetric rate CDC

Echo emulation

First, a symmetric rate setup is assumed, where the IDFT and DFT in the transmit and receive path have the same size N. The derivation is based on the techniques used in frequency domain adaptive filtering (FDAF) to translate the block LMS update of (5.6) to the frequency domain. The correlation (filter update) and convolution (filtering) in (5.6) can indeed be implemented more efficiently in the frequency domain, using DFTs. Since DFTs perform circular convolutions/correlations, overlap-save or overlap-add operations are required. When applying the *overlap-save* procedure to convert a circular convolution into a linear convolution [110], the echo estimate in (5.4) can be written as

$$\hat{\mathbf{y}}_E^k = \left[\, \mathbf{I}_N \;\middle|\; \mathbf{0}_N \,\right] \underbrace{\left[\begin{array}{c|c} \mathbf{U}^{k-1,k,k+1} & \mathbf{S}^{k-1,k,k+1} \\ \hline \mathbf{S}^{k-1,k,k+1} & \mathbf{U}^{k-1,k,k+1} \end{array}\right]}_{\hat{\mathbf{C}}^{k-1,k,k+1}} \left[\begin{array}{c} \mathbf{M}\mathbf{w}_E^k \\ \hline \mathbf{0}_N \end{array}\right], \quad (5.55)$$

where $\mathbf{U}^{k-1,k,k+1}$ is defined in (5.3) and where $\mathbf{S}^{k-1,k,k+1}$ is an $N \times N$ Toeplitz matrix, given by

$$\mathbf{S}^{k-1,k,k+1} = \quad (5.56)$$

	sym. k+1				CP k+1			sym. k		
sym. k-1	$u_{\Delta+\nu}^{k-1}$	$u_{\Delta-\nu-2}^{k+1}$	$\cdots$	u_0^{k+1}	u_{N-1}^{k+1}	$\cdots$	$u_{N-\nu}^{k+1}$	u_{N-1}^{k}	$\cdots$	$u_{\Delta+1}^{k}$
	$\vdots$	$\ddots$							$\ddots$	$\vdots$
	u_{N-1}^{k-1}									u_{N-1}^{k}
CP k	$u_{N-\nu}^{k}$									$u_{N-\nu}^{k+1}$
	$\vdots$									$\vdots$
	u_{N-1}^{k}									u_{N-1}^{k+1}
sym. k	u_0^k									u_0^{k+1}
	$\vdots$	$\ddots$							$\ddots$	$\vdots$
	$u_{\Delta-1}^{k}$	$\cdots$	u_0^k	u_{N-1}^{k}	$\cdots$	$\cdots$	$u_{N-\nu}^{k}$	u_{N-1}^{k-1}	$\cdots$	$u_{\Delta+\nu}^{k-1}$

The matrix $\mathbf{S}^{k-1,k,k+1}$ is constructed in such a way that $\hat{\mathbf{C}}^{k-1,k,k+1}$ is a $2N \times 2N$ circulant matrix. Note that the element on the diagonal of $\mathbf{S}^{k-1,k,k+1}$ can be chosen arbitrarily. The circulant matrix $\hat{\mathbf{C}}^{k-1,k,k+1}$ is completely determined

by $2N$ different elements, while $\mathbf{U}^{k-1,k,k+1}$ contains only $2N-1$ different entries. Hence, when extending $\mathbf{U}^{k-1,k,k+1}$ (by means of $\mathbf{S}^{k-1,k,k+1}$) to a circulant matrix, one element of $\mathbf{S}^{k-1,k,k+1}$ is effectively undetermined. This is exactly the element on the diagonal of $\mathbf{S}^{k-1,k,k+1}$.

In (5.55) it was again assumed that the echo channel can be modeled with $T_E \leqslant N$ taps, which is true for most practical ADSL systems. When this assumption does not hold, the uncanceled echo taps will cause additional residual echo or a more complex echo canceler is required.

The circulant matrix $\hat{\mathbf{C}}^{k-1,k,k+1}$ can be diagonalized by means of a $2N$-point DFT/IDFT pair (see Appendix A), where the diagonal elements are given by the DFT of its first column, i.e.

$$\Lambda^k = \mathcal{F}_{2N}\hat{\mathbf{C}}^{k-1,k,k+1}[:,1], \tag{5.57}$$

$$\hat{\mathbf{C}}^{k-1,k,k+1} = \mathcal{I}_{2N}\mathrm{diag}\{\Lambda^k\}\mathcal{F}_{2N}. \tag{5.58}$$

With (5.58), equation (5.55) can be modified to

$$\hat{\mathbf{y}}_E^k = \left[\begin{array}{c|c} \mathbf{I}_N & \mathbf{0}_N \end{array}\right]\mathcal{I}_{2N}\mathrm{diag}\{\Lambda^k\}\mathcal{F}_{2N}\left[\frac{\mathbf{M}\mathbf{w}_E^k}{\mathbf{0}_N}\right], \tag{5.59}$$

$$= \mathcal{I}_{2N}[1\!:\!N, 1\!:\!2\!:\!2N]\mathrm{diag}\{\Lambda_{even}^k\}\mathcal{F}_{2N}[1\!:\!2\!:\!2N, 1\!:\!N]\mathbf{M}\mathbf{w}_E^k + \mathcal{I}_{2N}[1\!:\!N, 2\!:\!2\!:\!2N]\mathrm{diag}\{\Lambda_{odd}^k\}\mathcal{F}_{2N}[2\!:\!2\!:\!2N, 1\!:\!N]\mathbf{M}\mathbf{w}_E^k, \tag{5.60}$$

$$= \frac{1}{2}\left(\mathcal{I}_N\mathrm{diag}\{\Lambda_{even}^k\}\mathcal{F}_N\mathbf{M}\mathbf{w}_E^k + \mathbf{Q}^*\mathcal{I}_N\mathrm{diag}\{\Lambda_{odd}^k\}\mathcal{F}_N\mathbf{Q}\mathbf{M}\mathbf{w}_E^k\right), \tag{5.61}$$

where Λ_{even}^k and Λ_{odd}^k consist of the even and odd numbered elements of Λ^k respectively, i.e.

$$\Lambda_{even}^k = [\Lambda_0^k\ \Lambda_2^k\ \ldots\ \Lambda_{2N-2}^k]^T, \qquad \Lambda_{odd}^k = [\Lambda_1^k\ \Lambda_3^k\ \ldots\ \Lambda_{2N-1}^k]^T, \tag{5.62}$$

and

$$\mathbf{Q} = \mathrm{diag}\left\{\left[1\ \ldots\ e^{-j\pi i/N}\ \ldots\ e^{-j\pi(N-1)/N}\right]^T\right\}. \tag{5.63}$$

In Appendix D.2 it is shown that the first term in (5.61) in fact represents a convolution of $\mathbf{M}\mathbf{w}_E^k$ with the circulant matrix $(\mathbf{U}^{k-1,k,k+1} + \mathbf{S}^{k-1,k,k+1})$, while the second term represents a convolution of $\mathbf{M}\mathbf{w}_E^k$ with the skew-circulant matrix $(\mathbf{U}^{k-1,k,k+1} - \mathbf{S}^{k-1,k,k+1})$. Hence, as opposed to (5.13), $\mathbf{U}^{k-1,k,k+1}$ is now split into a *circulant* and a *skew-circulant* matrix, i.e.

$$\mathbf{U}^{k-1,k,k+1} = \frac{1}{2}(\mathbf{U}^{k-1,k,k+1} + \mathbf{S}^{k-1,k,k+1}) + \frac{1}{2}(\mathbf{U}^{k-1,k,k+1} - \mathbf{S}^{k-1,k,k+1}). \tag{5.64}$$

According to (5.4), the echo canceled DMT-symbol in the frequency domain is given by

$$E^k = \mathcal{F}_N(\mathbf{y}^k - \hat{\mathbf{y}}_E^k), \tag{5.65}$$

$$= \mathcal{F}_N \left(\mathbf{y}^k - \frac{1}{2}\mathbf{Q}^* \mathcal{I}_N \mathrm{diag}\{\Lambda_{odd}^k\} \mathcal{F}_N \mathbf{Q}\mathbf{M}\mathbf{w}_E^k \right) - \frac{1}{2}\mathrm{diag}\{\Lambda_{even}^k\} W_E^k. \quad (5.66)$$

With $\tilde{W}_E^k$ equal to $\mathcal{F}_N \mathbf{Q}\mathbf{M}\mathbf{M}^T \mathcal{I}_N W_E^k$, one obtains:

$$E^k = \mathcal{F}_N(\underbrace{\mathbf{y}^k - \frac{1}{2}\mathbf{Q}^* \mathcal{I}_N(\Lambda_{odd}^k \odot \tilde{W}_E^k)}_{\text{Time domain EC}}) - \underbrace{\frac{1}{2}(\Lambda_{even}^k \odot W_E^k)}_{\text{Frequency domain EC}} . \quad (5.67)$$

From now on, this EC scheme will be referred to as the *Circulant Decomposition Canceler (CDC)*. Notice that (5.67) is very similar to (5.17): echo cancellation is performed partly in the time, partly in the frequency domain.

Echo filter update

Starting from the definition of $\hat{\mathbf{C}}^{k-1,k,k+1}$, the block LMS update equation in (5.6) can be modified to

$$\mathbf{w}_E^{k+1} \leftarrow \mathbf{w}_E^k + \mu \mathbf{M}^T \left[\begin{array}{c|c} \mathbf{I}_N & \mathbf{0}_N \end{array} \right] (\hat{\mathbf{C}}^{k-1,k,k+1})^T \left[\frac{\mathbf{I}_N}{\mathbf{0}_N} \right] \mathbf{e}^k, \quad (5.68)$$

$$\leftarrow \mathbf{w}_E^k + \mu \mathbf{M}^T \left[\begin{array}{c|c} \mathbf{I}_N & \mathbf{0}_N \end{array} \right] \mathcal{I}_{2N} \mathrm{diag}\{(\Lambda^k)^*\} \mathcal{F}_{2N} \left[\frac{\mathbf{I}_N}{\mathbf{0}_N} \right] \mathbf{e}^k, \quad (5.69)$$

where (5.58) was used in the second step. In the frequency domain, this leads to

$$W_E^{k+1} \leftarrow W_E^k + \mu \mathcal{F}_N \mathbf{M}\mathbf{M}^T \left[\begin{array}{c|c} \mathbf{I}_N & \mathbf{0}_N \end{array} \right] \mathcal{I}_{2N} \mathrm{diag}\{(\Lambda^k)^*\} \mathcal{F}_{2N} \left[\frac{\mathbf{I}_N}{\mathbf{0}_N} \right] \mathbf{e}^k, \quad (5.70)$$

$$\leftarrow W_E^k + \mu \mathcal{F}_N \mathbf{M}\mathbf{M}^T \mathcal{I}_N \mathrm{diag}\{(\Lambda_{even}^k)^*\} E^k + \mu \mathcal{F}_N \mathbf{M}\mathbf{M}^T \mathbf{Q}^* \mathcal{I}_N \mathrm{diag}\{(\Lambda_{odd}^k)^*\} \mathcal{F}_N \mathbf{Q}\mathbf{e}^k, \quad (5.71)$$

which is still completely equivalent to the block LMS update of (5.6). Similar to the modification from (5.19) to (5.20) the second term in (5.71) will be neglected, leading to a much simpler update rule

$$W_E^{k+1} \leftarrow W_E^k + \mu \mathbf{G}((\Lambda_{even}^k)^* \odot E^k), \quad (5.72)$$

where $\mathbf{G} = \mathcal{F}_N \mathbf{M}\mathbf{M}^T \mathcal{I}_N$ is a gradient constraint, which takes into account that the time domain coefficients of $\mathbf{w}_E^k$ should be limited to T_E taps. Finally, also the gradient constraint will be removed such that the resulting update algorithm is given by

$$W_E^{k+1} \leftarrow W_E^k + \mu(\Lambda_{even}^k)^* \odot E^k, \quad (5.73)$$

$$\tilde{W}_E^{k+1} \leftarrow \mathcal{F}_N \mathbf{Q}\mathbf{M}\mathbf{M}^T \mathcal{I}_N W_E^{k+1}. \quad (5.74)$$

Notice that (5.73)-(5.74) is very similar to (5.20)-(5.21) and also here, the extra operations in (5.74) to obtain $\tilde{W}_E^{k+1}$, which is required in the computation of E^k, can be executed *infrequently*. The gradient of (5.73) no longer corresponds to a linear correlation, but represents a circular correlation. Looking at (5.73) from a different perspective, one might say that (5.73) is a steepest descent method applied to (5.67) assuming W_E^k and $\tilde{W}_E^k$ are independent variables. This reasoning will also be applied further on.

The *convergence* of (5.73) is proven in Appendix D.3 using the same assumptions as in [57] to prove the convergence of the CES-based EC of (5.20). It is shown that (5.73) is convergent in the mean if the step size μ satisfies the following condition:

$$0 < \mu < \frac{2N}{(N+\nu)\sigma_u^2}, \tag{5.75}$$

where σ_u^2 denotes the transmitted echo energy on each tone. The assumptions in Appendix D.3 imply that *all* the available echo tones should be transmitted with an equal amount of power. When not all carriers are equally excited, which is typically the case in an ADSL scenario, convergence is more difficult to prove (which also holds for the convergence proof given in [57]) and simulations have to show the actual performance (see Section 5.6).

When some echo carriers are not excited at all, (5.20) will not be able to converge to the true echo path, unless extra power is transmitted on unused echo tones. On the other hand, simulations will show that the update rule in (5.73) does not suffer from insufficient excitation since Λ_{even}^k in general does not have zero entries. Hence, in this case, *no extra power needs to be transmitted to obtain convergence.*

Remark 5.1 For one specific misalignment Δ the insufficient excitation problem is not automatically solved. When $\Delta = -\nu$, it is easy to see that the first column of $\mathbf{U}^{k-1,k,k+1}$ in (5.3) is completely determined by the elements of $\mathbf{u}^k$ only, whereas the first column of $\mathbf{S}^{k-1,k,k+1}$ in (5.56) only consists of samples from $\mathbf{u}^{k-1}$. Since Λ_{even}^k is equal to $\mathcal{F}_N(\mathbf{U}^{k-1,k,k+1}[:,1] + \mathbf{S}^{k-1,k,k+1}[:,1])$, the entries in Λ_{even}^k corresponding to unused echo tones will be perfectly zero and hence the problem of insufficient excitation is reintroduced. To solve this shortcoming, a small change in timing can be made when computing Λ_{even}^k. When $T_E < N$, one can write

$$\mathbf{U}^{k-1,k,k+1}\mathbf{M}\mathbf{w}_E^k = \tilde{\mathbf{U}}^{k-1,k,k+1}\tilde{\mathbf{M}}\mathbf{w}_E^k, \tag{5.76}$$

where $\tilde{\mathbf{U}}^{k-1,k,k+1}$ is constructed with a slightly different value for Δ compared to $\mathbf{U}^{k-1,k,k+1}$. The matrix $\tilde{\mathbf{M}}$ selects columns out of $\tilde{\mathbf{U}}^{k-1,k,k+1}$, such that $\mathbf{U}^{k-1,k,k+1}\mathbf{M} = \tilde{\mathbf{U}}^{k-1,k,k+1}\tilde{\mathbf{M}}$. As long as one selects columns with the same data in either matrix, the echo canceling performance will not change, but

Λ^k_{even} will. With the alternative timing, Λ^k_{even} will be non-zero again on entries corresponding to unused echo tones and by this the transmission of extra power is avoided. □

Double talk cancellation

Similar to ITF-EC in Subsection 5.4.2, it is possible to add DTC to the CDC update. Since the DFT in (5.67) is shared between CDC EC and demodulation of the far end signal, the slicer error (difference between the frequency domain equalizer (FEQ) output and the final decision on the received echo canceled symbol) could be used instead of E^k to update the echo canceler coefficients, i.e.

$$W_E^{k+1} \quad \leftarrow \quad W_E^k + \mu(\Lambda^k_{even})^* \odot D^{-1} \odot (D \odot E^k - X^k_{0:N-1}), \qquad (5.77)$$

where D denotes the vector with all the FEQ coefficients and E^k is given by (5.67). Also here, one may conclude that (5.77) is valid for both RT and CO. In contrast to the CES-based EC of Section 5.2, DTC at CO is as inexpensive as at RT and hence CDC is highly suitable for cheaply removing the far end signal in the coefficient update.

Physical interpretation

To obtain further insight into the CDC scheme, the CDC equations can be interpreted in a physical way. The $2N$-point DFT of the echo reference signal in (5.57) will generate odd and even frequencies (Λ^k_{even} and Λ^k_{odd}), where the even frequency points are located on the original DMT frequency grid, while the odd frequencies yield information in between this grid. The echo canceler coefficients can exploit this extra information when they are first modulated in time by half the carrier spacing. This corresponds to the multiplication with $\mathbf{Q}$ in (5.74). In this way, the coefficients are shifted to the other grid, leading to $\tilde{W}^k_E$. These coefficients are then used to filter Λ^k_{odd}. The filter output has to be demodulated back to the original DMT grid, by means of $\mathbf{Q}^*$, see (5.73). The final scheme is shown in **Fig. 5.15**. In other words, the insufficient excitation problem of CES-based EC is solved in the CDC update equations by taking DFT sidelobe information into account. This extra sidelobe information is obtained by increasing the frequency resolution of the original DMT grid, which is done by considering more time domain samples in the DFT window. As a result, the CDC update converges without transmitting extra power on unused tones.

5.5.3 Multi-rate CDC

An extension of the symmetric rate CDC scheme to a multi-rate structure can easily be made and is similar to Subsection 5.1.2 and Subsection 5.4.3.

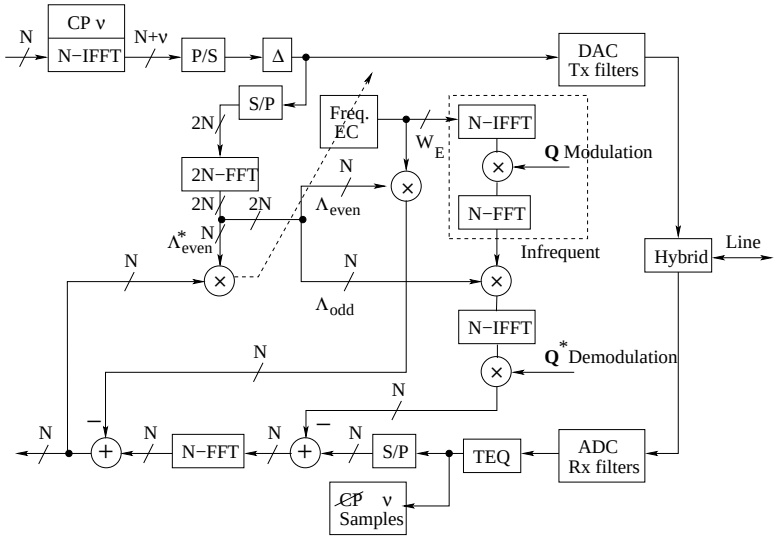

Figure 5.15: Circulant decomposition canceler for the symmetric case.

When properly designed, the complexity of echo cancellation can be reduced substantially in a multi-rate environment. In this subsection, several paths will be followed to incorporate decimation or interpolation in the CDC structure.

Decimation at the output (CO)

Similar to Subsection 5.4.3, the emulated echo can be decimated at the output of the echo canceler by computing only every κth sample, which is represented mathematically by the $N \times \kappa N$ decimation matrix $\mathbf{D} = \mathbf{I}_{\kappa N}[1 : \kappa : \kappa N, :]$. From (5.55) at the high rate, one obtains

$$\hat{\mathbf{y}}_E^k \;=\; \mathbf{D} \left[\begin{array}{c|c} \mathbf{I}_{\kappa N} & \mathbf{0}_{\kappa N} \end{array} \right] \hat{\mathbf{C}}^{k-1,k,k+1} \left[\frac{\mathbf{M}\mathbf{w}_E^k}{\mathbf{0}_{\kappa N}} \right], \tag{5.78}$$

where $\mathbf{w}_E$ now has T_E taps at the high rate. When combining (5.61) and (5.78) the echo canceled frequency domain received vector and the filter update can easily be derived:

$$\Lambda^k \;=\; \mathcal{F}_{2\kappa N} \hat{\mathbf{C}}^{k-1,k,k+1}[:, 1], \tag{5.79}$$

$$E^k \;=\; \mathcal{F}_N(\mathbf{y}^k - \frac{1}{2}\mathbf{D}\mathbf{Q}^* \mathcal{I}_{\kappa N}(\Lambda_{odd}^k \odot \tilde{W}_E^k)) - \frac{1}{2\kappa}\mathbf{R}^T(\Lambda_{even}^k \odot W_E^k), \tag{5.80}$$

$$W_E^{k+1} \leftarrow W_E^k + \mu(\Lambda_{even}^k)^* \odot (\mathbf{R}E^k), \tag{5.81}$$

where $\mathbf{R}^T = [\mathbf{I}_N \;\ldots\; \mathbf{I}_N]$. In (5.80), the time domain part is decimated after echo emulation at the high rate. In the frequency domain, the echo emulated

symbols of size κN are blocked into symbols of length N and then added (multiplication with $\mathbf{R}^T$).

Decimation by polyphase decomposition (CO)

Starting again from (5.55) at the high rate one can also write the decimated version of the emulated echo as

$$\hat{\mathbf{y}}_E^k = \left[\begin{array}{c|c} \mathbf{I}_N & \mathbf{0}_N \end{array}\right] \overbrace{\left[\begin{array}{cc} \mathbf{DU}^{k-1,k,k+1} & \mathbf{DS}^{k-1,k,k+1} \\ \mathbf{DS}^{k-1,k,k+1} & \mathbf{DU}^{k-1,k,k+1} \end{array}\right]}^{\hat{\mathbf{C}}_{dec}^{k-1,k,k+1}} \overbrace{\left[\begin{array}{c} \mathbf{Mw}_E^k \\ \hline \mathbf{0}_{\kappa N} \end{array}\right]}^{\hat{\mathbf{w}}_E^k}, \quad (5.82)$$

where $\hat{\mathbf{C}}_{dec}^{k-1,k,k+1}$ is now of size $2N \times 2\kappa N$. One can modify (5.82) by observing that every submatrix $\hat{\mathbf{C}}_{dec}^{k-1,k,k+1}[:, l\!:\!\kappa\!:\!2\kappa N]$ for $l = 1, \ldots, \kappa$ forms a circulant matrix. As a result, one may split the vector $\hat{\mathbf{w}}_E^k$ in its polyphase components $\hat{\mathbf{w}}_E^k[l\!:\!\kappa\!:\!2\kappa N]$, $l = 1, \ldots, \kappa$ and write (5.82) as a sum of κ terms:

$$\hat{\mathbf{y}}_E^k = \left[\begin{array}{c|c} \mathbf{I}_N & \mathbf{0}_N \end{array}\right] \sum_{l=1}^{\kappa} \hat{\mathbf{C}}_{dec}^{k-1,k,k+1}[:, l\!:\!\kappa\!:\!2\kappa N] \hat{\mathbf{w}}_E^k[l\!:\!\kappa\!:\!2\kappa N], \quad (5.83)$$

$$= \frac{1}{2}\mathcal{I}_N \left(\sum_{l=1}^{\kappa} \Lambda_{even,l}^k \odot W_{E,l}^k \right) + \frac{1}{2}\mathbf{Q}^* \mathcal{I}_N \left(\sum_{l=1}^{\kappa} \Lambda_{odd,l}^k \odot \tilde{W}_{E,l}^k \right), \quad (5.84)$$

where the same mathematical tricks were used as in the derivation of (5.61). The vectors $\Lambda_{even,l}^k$ and $\Lambda_{odd,l}^k$ are obtained from $\Lambda_l^k = \mathcal{F}_{2N} \hat{\mathbf{C}}_{dec}^{k-1,k,k+1}[:, l\!:\!\kappa\!:\!\kappa]$. Hence, instead of one $2\kappa N$-point DFT as in (5.79), the computation of κ times a $2N$-point DFT is required. Furthermore, the echo canceler coefficients are defined as $W_{E,l}^k = \mathcal{F}_N \hat{\mathbf{w}}_E^k[l\!:\!\kappa\!:\!\kappa N]$ and $\tilde{W}_{E,l}^k = \mathcal{F}_N \mathbf{QMM}^T \mathcal{I}_N W_{E,l}^k$. The echo canceled vector and the filter update equations are now given by

$$\Lambda_l^k = \mathcal{F}_{2N} \hat{\mathbf{C}}_{dec,1}^{k-1,k,k+1}[:, l\!:\!\kappa\!:\!\kappa], \quad l = 1, \ldots, \kappa, \quad (5.85)$$

$$E^k = \mathcal{F}_N \left(\mathbf{y}^k - \frac{1}{2}\mathbf{Q}^* \mathcal{I}_N \left(\sum_{l=1}^{\kappa} \Lambda_{odd,l}^k \odot \tilde{W}_{E,l}^k \right) \right) - \frac{1}{2} \left(\sum_{l=1}^{\kappa} \Lambda_{even,l}^k \odot W_{E,l}^k \right), \quad (5.86)$$

$$W_{E,l}^{k+1} \leftarrow W_{E,l}^k + \mu (\Lambda_{even,l}^k)^* \odot E^k, \quad l = 1, \ldots, \kappa, \quad (5.87)$$

where $\tilde{W}_{E,l}^k$ can again be updated infrequently.

Decimation at the input (CO)

If it is additionally assumed that the echo transfer function is band limited to $\kappa N/2\gamma$ tones, this information may be incorporated in the echo canceler

to reduce complexity. With a band limited echo channel, only a limited part of the transmitted echo signal spectrum will contribute to the received echo signal. Hence, it makes sense to decimate the transmitted echo signal with a factor γ before constructing $\mathbf{U}^{k-1,k,k+1}$ and $\mathbf{S}^{k-1,k,k+1}$ in (5.82) (see also Subsection 5.1.2). The resulting filtering and update equations are similar to (5.85)-(5.87), where κ is replaced by κ/γ, i.e.

$$\Lambda_l^k = \mathcal{F}_{2N}\hat{\mathbf{C}}_{\gamma\downarrow}^{k-1,k,k+1}[:, l:\kappa/\gamma:\kappa/\gamma], \quad l = 1, \ldots, \kappa/\gamma, \tag{5.88}$$

$$E^k = \mathcal{F}_N\left(\mathbf{y}^k - \frac{1}{2}\mathbf{Q}^*\mathcal{I}_N\left(\sum_{l=1}^{\kappa/\gamma}\Lambda_{odd,l}^k \odot \tilde{W}_{E,l}^k\right)\right) - \frac{1}{2}\left(\sum_{l=1}^{\kappa/\gamma}\Lambda_{even,l}^k \odot W_{E,l}^k\right), \tag{5.89}$$

$$W_{E,l}^{k+1} \leftarrow W_{E,l}^k + \mu(\Lambda_{even,l}^k)^* \odot E^k, \quad l = 1, \ldots, \kappa/\gamma, \tag{5.90}$$

where $\hat{\mathbf{C}}_{\gamma\downarrow}^{k-1,k,k+1}$ is now a $2N \times 2\kappa N/\gamma$ matrix constructed with time domain decimated samples. To avoid aliasing, an additional decimation filter in the echo path is required before decimating the echo reference symbols. The resulting decimated CDC structure is depicted in **Fig. 5.16**.

Interpolation by zero padding the input (RT)

When the bandwidth of the transmitted echo signal is a factor κ smaller than the receive bandwidth, the CDC scheme has to interpolate the transmitted echo signal in the time and in the frequency domain In the time domain $\kappa - 1$ zeroes are padded between the time domain echo data samples. By this, the calculation of Λ^k only requires the computation of one $2N$-point DFT (instead of a full $2\kappa N$-point DFT). The vector Λ^k will be repeated κ times in the frequency domain. The echo canceled frequency domain received vector and the filter update are then given by

$$\Lambda^k = \mathcal{F}_{2N}\hat{\mathbf{C}}^{k-1,k,k+1}[:, 1], \tag{5.91}$$

$$E^k = \mathcal{F}_{\kappa N}(\mathbf{y}^k - \frac{1}{2}\mathbf{Q}^*\mathcal{I}_{\kappa N}((\mathbf{R}\Lambda_{odd}^k) \odot \tilde{W}_E^k)) - \frac{1}{2}((\mathbf{R}\Lambda_{even}^k) \odot W_E^k), \tag{5.92}$$

$$W_E^{k+1} \leftarrow W_E^k + \mu(\mathbf{R}(\Lambda_{even}^k)^*) \odot E^k, \tag{5.93}$$

where $\hat{\mathbf{C}}^{k-1,k,k+1}$ is constructed with echo samples at the low rate. When it is again assumed that the echo channel is band limited, less multiplications are required in the component wise multiplications in (5.92). Note that a κN-point IDFT is still needed in (5.92).

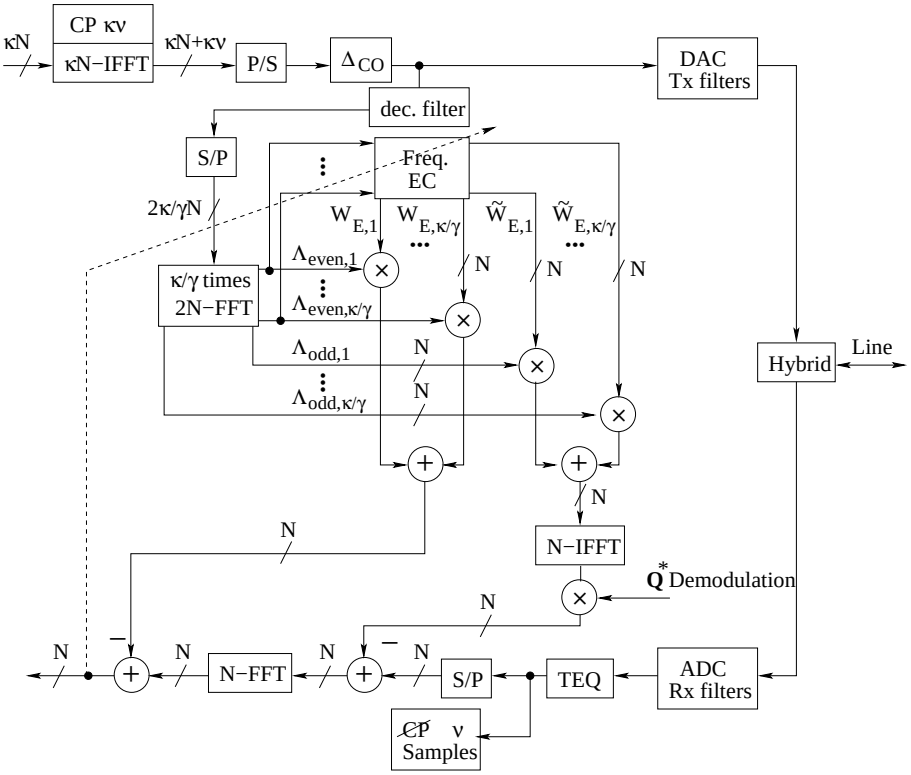

Figure 5.16: Decimated circulant decomposition canceler based on a polyphase decomposition of $\mathbf{w}_E$.

Interpolation by polyphase decomposition (RT)

From (5.55), one can write the interpolated echo estimate as

$$\hat{\mathbf{y}}_E^k \;=\; \left[\; \mathbf{I}_{\kappa N} \;\middle|\; \mathbf{0}_{\kappa N} \;\right] \hat{\mathbf{C}}_{\kappa\uparrow}^{k-1,k,k+1} \hat{\mathbf{w}}_E^k, \tag{5.94}$$

where $\hat{\mathbf{C}}_{\kappa\uparrow}^{k-1,k,k+1}$ is a circulant matrix of size $2\kappa N \times 2\kappa N$, based on an input sequence with $\kappa - 1$ zeroes inserted between two consecutive echo samples. Let $\hat{\mathbf{C}}^{k-1,k,k+1}$ be equal to $\hat{\mathbf{C}}_{\kappa\uparrow}^{k-1,k,k+1}[1:\kappa:2\kappa N, 1:\kappa:2\kappa N]$. Observe that the submatrices $\hat{\mathbf{C}}_{\kappa\uparrow}^{k-1,k,k+1}[l:\kappa:2\kappa N, l:\kappa:2\kappa N]$ for $l = 1,\ldots,\kappa$ are all circulant and equal to $\hat{\mathbf{C}}^{k-1,k,k+1}$. Hence, one can rewrite (5.94) in terms of the polyphase components of $\hat{\mathbf{w}}_E^k$:

$$\hat{\mathbf{y}}_E^k \;=\; \sum_{l=1}^{\kappa} \left[\; \mathbf{I}_{\kappa N} \;\middle|\; \mathbf{0}_{\kappa N} \;\right] \mathbf{D}_{2\kappa N,l} \hat{\mathbf{C}}^{k-1,k,k+1} \hat{\mathbf{w}}_E^k[l:\kappa:2\kappa N], \tag{5.95}$$

$$= \sum_{l=1}^{\kappa} \left[\begin{array}{c|c} \mathbf{I}_{\kappa N} & \mathbf{0}_{\kappa N} \end{array} \right] \mathbf{D}_{2\kappa N,l} \mathcal{I}_{2N} \mathrm{diag}\{\Lambda^k\} \mathcal{F}_{2N} \hat{\mathbf{w}}_E^k[l:\kappa:2\kappa N], \quad (5.96)$$

with $\mathbf{D}_{A,l} = \mathbf{I}_A[:, l:\kappa:A]$. Since $[\mathbf{I}_{\kappa N} \mid \mathbf{0}_{\kappa N}]\mathbf{D}_{2\kappa N,l} = \mathbf{D}_{\kappa N,l}[\mathbf{I}_N \mid \mathbf{0}_N]$, one obtains

$$\hat{\mathbf{y}}_E^k = \frac{1}{2} \sum_{l=1}^{\kappa} \mathbf{D}_{\kappa N,l} \left(\mathcal{I}_N(\Lambda_{even}^k \odot W_{E,l}^k) + \mathbf{Q}^* \mathcal{I}_N(\Lambda_{odd}^k \odot \tilde{W}_{E,l}^k) \right). \quad (5.97)$$

The echo canceled frequency domain received vector and the filter update are then given by

$$\Lambda^k = \mathcal{F}_{2N} \hat{\mathbf{C}}^{k-1,k,k+1}[:, 1], \quad (5.98)$$

$$E^k = \mathcal{F}_{\kappa N} \left(\mathbf{y}^k - \frac{1}{2} \sum_{l=1}^{\kappa} \mathbf{D}_{\kappa N,l} \mathbf{Q}^* \mathcal{I}_N(\Lambda_{odd}^k \odot \tilde{W}_{E,l}^k) \right) - \frac{1}{2}((\mathbf{R}\Lambda_{even}^k) \odot W_E^k), \quad (5.99)$$

$$W_E^{k+1} \leftarrow W_E^k + \mu(\mathbf{R}(\Lambda_{even}^k)^*) \odot E^k, \quad (5.100)$$

where $\tilde{W}_{E,l}^k$ can again be updated infrequently as

$$\tilde{W}_{E,l}^{k+1} = \mathcal{F}_N \mathbf{Q} \mathbf{w}_E^{k+1}[l:\kappa:\kappa N], \quad l = 1, \ldots, \kappa, \quad (5.101)$$

with $\mathbf{w}_E^{k+1} = \mathbf{M}\mathbf{M}^T \mathcal{I}_{\kappa N} W_E^k$. The time domain processing is nothing more than a multiplexer to obtain a high rate signal based on the low rate components $\mathbf{Q}^* \mathcal{I}_N(\Lambda_{odd}^k \odot \tilde{W}_{E,l}^k)$. The resulting interpolated CDC structure is depicted in **Fig. 5.17**.

5.5.4 CDC combined with PTEQ and DTC

In the previous sections, it was tacitly assumed that a time domain channel equalizer (TEQ) was included in the echo path. Hence, equalization is performed *prior* to EC and the echo canceler has to model the TEQ as well. When considering per tone equalization (PTEQ) as a more optimal equalizer structure (see Chapter 3), equalization will be executed *after* EC. The combined PTEQ-CDC enhanced with DTC will be discussed in this section. Without loss of generality, we will restrict ourselves to the symmetric rate CDC case. A similar scheme, where PTEQ and CES-based EC are combined, can be found in [129].

Based on the notation of Subsection 3.4.1, the difference between the PTEQ output and the transmitted far end symbol on tone i, X_i^k, can be written as

$$E_i^k = \bar{\mathbf{v}}_i^T \bar{\mathbf{F}}_i(\mathbf{y}_{ext}^k - \mathbf{U}_{ext}^{k-1,k,k+1} \mathbf{M} \mathbf{w}_E^k) - X_i^k, \quad (5.102)$$

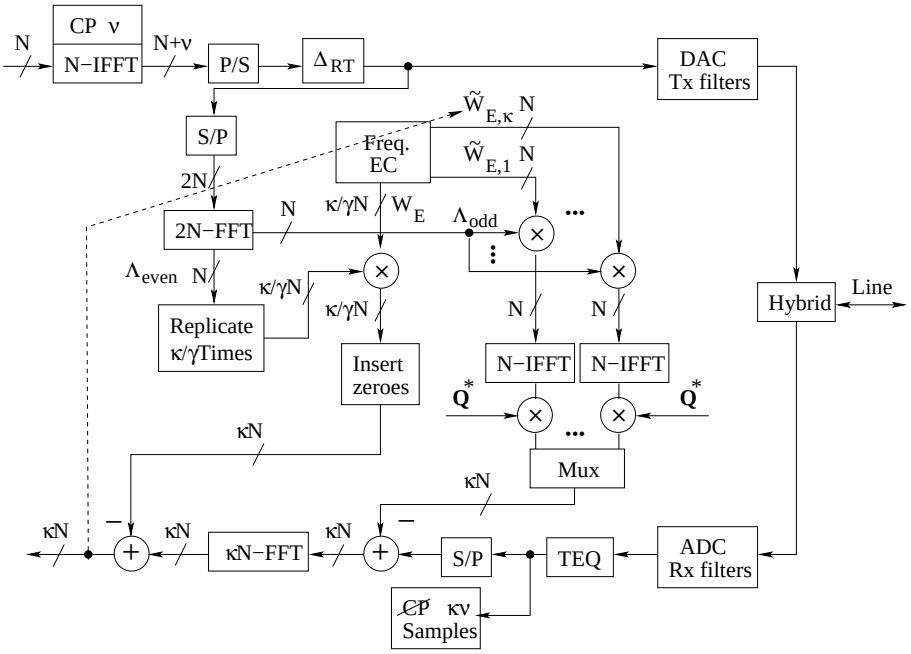

Figure 5.17: Interpolated circulant decomposition canceler based on a polyphase decomposition of $\mathbf{w}_E$.

where $\bar{\mathbf{v}}_i = [v_{T-1,i} \dots v_{0,i}]^T$ are the PTEQ coefficients for tone i and $\mathbf{y}^k_{ext}$ and $\mathbf{U}^{k-1,k,k+1}_{ext}$ are augmented with $T-1$ rows compared to $\mathbf{y}^k$ and $\mathbf{U}^{k-1,k,k+1}$ in (5.1) and (5.3). The matrix $\bar{\mathbf{F}}_i$ is equal to

$$\bar{\mathbf{F}}_i = \left[\begin{array}{c|c|c} \mathbf{I}_{T-1} & \mathbf{0} & -\mathbf{I}_{T-1} \\ \hline \mathbf{0} & \multicolumn{2}{c}{\mathcal{F}_N[i,:]} \end{array}\right]. \tag{5.103}$$

Define

$$\mathbf{P}_1 = \left[\begin{array}{c|c} \mathbf{0} & \mathbf{I}_{T-1} \\ \hline \multicolumn{2}{c}{\mathbf{I}_N} \end{array}\right], \qquad \mathbf{P}_2 = \left[\begin{array}{c|c} \mathbf{0} & -\mathbf{I}_{T-1} \\ \hline \multicolumn{2}{c}{\mathbf{I}_N} \end{array}\right], \tag{5.104}$$

then from the definitions of $\mathbf{U}^{k-1,k,k+1}$ and $\mathbf{S}^{k-1,k,k+1}$ one can write

$$\begin{aligned} 2\mathbf{U}^{k-1,k,k+1}_{ext} &= \mathbf{P}_1(\mathbf{U}^{k-1,k,k+1} + \mathbf{S}^{k-1,k,k+1}) + \\ &\quad \mathbf{P}_2(\mathbf{U}^{k-1,k,k+1} - \mathbf{S}^{k-1,k,k+1}). \end{aligned} \tag{5.105}$$

Since $\mathbf{U}^{k-1,k,k+1} + \mathbf{S}^{k-1,k,k+1}$ and $\mathbf{U}^{k-1,k,k+1} - \mathbf{S}^{k-1,k,k+1}$ can be diagonalized to $\text{diag}\{\Lambda^k_{even}\}$ and $\text{diag}\{\Lambda^k_{odd}\}$ respectively, (5.102) can be rewritten as

$$E^k_i = \tag{5.106}$$

$$\bar{\mathbf{v}}_i^T \bar{\mathbf{F}}_i \left(\mathbf{y}_{ext}^k - \frac{1}{2}\mathbf{P}_1 \mathcal{I}_N \mathrm{diag}\{\Lambda_{even}^k\} W_E^k - \frac{1}{2}\mathbf{P}_2 \mathbf{Q}^* \mathcal{I}_N \mathrm{diag}\{\Lambda_{odd}^k\} \tilde{W}_E^k \right) - X_i^k.$$

With the following equalities

$$\bar{\mathbf{F}}_i \mathbf{P}_1 = \left[\frac{\mathbf{0}_{(T-1)\times N}}{\mathcal{F}_N[i,:]} \right], \tag{5.107}$$

$$\bar{\mathbf{F}}_i \mathbf{P}_2 = \left[\frac{\mathbf{0}_{(T-1)\times N}}{\mathcal{F}_N[i,:]} \right] + \left[\frac{\mathbf{0}_{(T-1)\times (N-T+1)} \mid -2\mathbf{I}_{T-1}}{\mathbf{0}_{1\times N}} \right], \tag{5.108}$$

one may proceed as follows:

$$\begin{aligned} E_i^k = {} & v_{0,i} \mathcal{F}_N[i,:] \left(\mathbf{y}^k - \frac{1}{2}\mathbf{Q}^* \mathcal{I}_N (\Lambda_{odd}^k \odot \tilde{W}_{E,i}^k) \right) - \frac{v_{0,i}}{2} \Lambda_{even,i} W_{E,i}^k + \\ & [v_{T-1,i} \dots v_{1,i}] \left(\Delta \mathbf{y}^k + \left[\mathbf{0}_{(T-1)\times (N-T+1)} | \mathbf{I}_{T-1} \right] \mathbf{Q}^* \mathcal{I}_N (\Lambda_{odd}^k \odot \tilde{W}_{E,i}^k) \right) - \\ & X_i^k, \end{aligned} \tag{5.109}$$

where $\Delta \mathbf{y}^k = [\mathbf{I}_{T-1} | \mathbf{0}_{(T-1)\times (N-T+1)} | - \mathbf{I}_{T-1}] \mathbf{y}_{ext}^k$ are difference terms of the received symbol. If one considers a stochastic gradient update, where $W_{E,i}$ and $\tilde{W}_{E,i}$ are treated as independent variables (similar to (5.73)), the update equations become

$$W_E^{k+1} \leftarrow W_E^k + \mu \begin{bmatrix} v_{0,0} \\ \vdots \\ v_{0,N-1} \end{bmatrix}^* \odot (\Lambda_{even}^k)^* \odot E^k, \tag{5.110}$$

$$\tilde{W}_E^{k+1} \leftarrow \mathcal{F}_N \mathbf{Q} \mathbf{M} \mathbf{M}^T \mathcal{I}_N W_E^{k+1}. \tag{5.111}$$

where E^k is a vector of length N with entries given by (5.109). Remarkably, these equations still have low computational complexity and are very similar to (5.73) and (5.74). Apparently, only the PTEQ taps corresponding to the DFT outputs effectively play a role in the EC update equations. Moreover, since the slicer error is used in the update, (5.110) is effectively supplemented with DTC to improve convergence when the far end signal is not silenced.

5.5.5 Complexity

In this section, the overall complexity of the CDC is given and compared with other EC schemes. The complexity is expressed as the number of *real* multiplications at symbol rate. For the DFT complexity, the split-radix FFT algorithm is used, which requires the lowest number of operations of any known power of two FFT algorithm [117]. The split-radix (I)FFT for real or complex input data requires $\frac{N}{2}\log_2 N - \frac{3N}{2} + 2$ and $N \log_2 N - 3N + 4$ real multiplications

TABLE 5.5
Complexity of CDC for a symmetric setup in real multiplications per symbol.

Echo emulation		**Filter update**	
Operation	**Complexity**	**Operation**	**Complexity**
$\mathcal{F}_{2N}\hat{\mathbf{C}}^{k-1,k,k+1}[:,1]$	$N\log_2 2N-3N+2$	$\Lambda^{k^*}_{even}\odot E^k$	$4\frac{N}{2}$
$\Lambda^k_{even}\odot W^k_E$	$4\frac{N}{2}$	$\mathbf{M}\mathbf{M}^T\mathcal{I}_N W^k_E$	$\frac{\frac{N}{2}\log_2 N-\frac{3N}{2}+2}{\phi}$
$\Lambda^k_{odd}\odot \tilde{W}^k_E$	$4\frac{N}{2}$	$\mathbf{Q}$	$\frac{2N}{\phi}$
$\mathcal{I}_N(\Lambda^k_{odd}\odot \tilde{W}^k_E)$	$N\log_2 N-3N+4$	$\mathcal{F}_N$	$\frac{N\log_2 N-3N+4}{\phi}$
$\mathbf{Q}^*$	$2N$		

TABLE 5.6
Complexity of CDC for a multi-rate setup in real multiplications per symbol.

	Decimated EC (CO)	**Interpolated EC (RT)**
CDC	dec. filter$+2N+2\frac{\kappa}{\gamma}\frac{4N}{2}+$ $\frac{\kappa}{\gamma}(N\log_2 2N-3N+2)+$ $N\log_2 N-3N+4$	$N\log_2 2N-3N+2+$ $4\frac{\kappa N}{2\gamma}+2\kappa N+4\frac{\kappa N}{2}+$ $\kappa(N\log_2 N-3N+4)$

respectively. Multiplication with a factor 1/2 is not counted since this can be executed cheaply by a simple bit-shift.

A detailed complexity analysis of the *symmetric* rate CDC, based on (5.67), (5.73) and (5.74), is given in **Table 5.5**. Note that the last $N/2$ elements of $\Lambda^k_{odd}\odot\tilde{W}^k_E$ will be the complex conjugate of the first $N/2$ elements to obtain a real valued output after the IDFT and the multiplication with $\mathbf{Q}^*$. The parameter ϕ indicates the infrequent update of $\tilde{W}^k_E$.

A similar derivation can be made for the multi-rate structures of Subsection 5.5.3. The complexity of echo emulation is given in **Table 5.6**, where it is assumed that the echo channel is band limited to $\frac{\kappa N}{2\gamma}$ tones. In the table, EC at RT and CO is treated separately to make a distinction between a decimated (CO) and an interpolated (RT) setup.

In **Fig. 5.18** the emulation complexity of CDC is compared with CES-based EC and TD-EC for RT and CO, with $\nu=4$, $N=64$, $\kappa=8$, $\gamma=2$ and $\phi=30$. The complexity figures for TD-EC and CES-based EC can be found in **Table 5.1** and **Table 5.2** respectively. The complexity of additional decimation and interpolation filters is not taken into account. The ITF-EC scheme of Section 5.4 is not adopted in the figure, since its emulation complexity is approximately equal to the complexity of the CES-based EC with optimal misalignment [65][129].

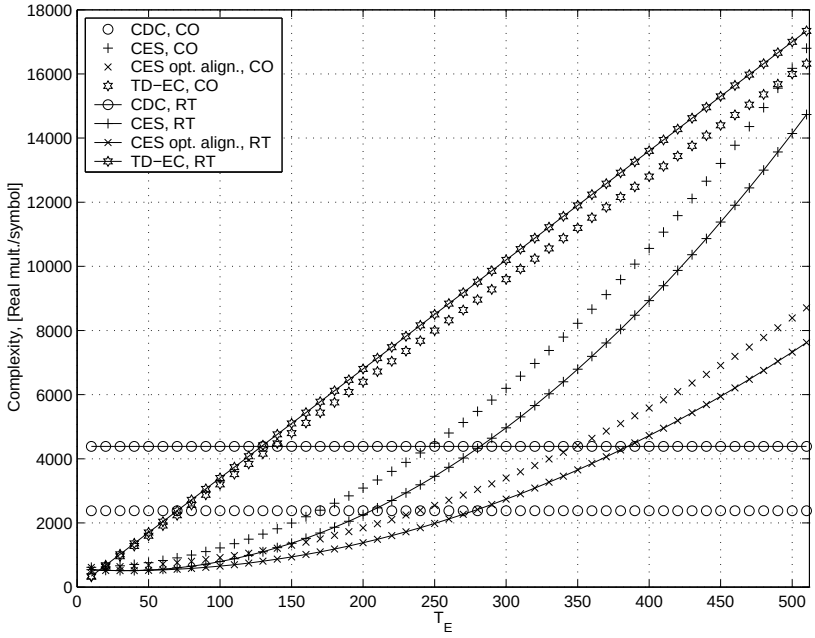

Figure 5.18: Complexity of echo emulation for different EC schemes.

In **Table 5.7** the complexity numbers are repeated for a typical echo channel length of $T_E = 256$ and a symbol rate equal to 4 kHz. Observe that TD-EC is the most complex of all. The remaining EC schemes all exhibit a complexity of the same order of magnitude[3]. However, the CES-based EC schemes require transmission of extra power on dummy tones and, furthermore, they are not very suitable for DTC, since the receive DFT is not shared between echo cancellation and far end demodulation, as discussed in Section 5.4.

5.6 Simulation results

5.6.1 Double talk cancellation

To verify the results of Section 5.3, simulations were performed for a central office (CO) modem and an ADSL 26 AWG (American Wire Gauge) inline, far end channel of 12 kft. The far end modem transmits the upstream tones

[3]To obtain an idea of the overall complexity of all the EC schemes, word lengths should be specified and 'bit true' simulations have to be performed. In addition, the amount of memory, the number of memory accesses and the number of gates effectively required to perform the computations have to be determined. This is, however, beyond the scope of this text.

TABLE 5.7
Complexity figures for different EC algorithms with $T_E = 256$, $\nu = 4$, $N = 64$, $\kappa = 8$, $\gamma = 2$, $\phi = 30$ and a symbol rate of 4 kHz.

	CO [Mmult./s]	**RT [Mmult./s]**
CDC	dec. filter+9.520	17.544
CES [65][129]	extra power+10.568	extra power+8.264
CES [57]	extra power+18.696	extra power+14.480
TD-EC	dec. filter+32.768	int. filter+34.816

$7 - 31$, while the echo reference signal is a downstream signal with tones $33 - 255$. In these simulations, each tone transmits a 4-QAM signal constellation. The downstream and upstream signal transmit with -40 dBm/Hz and -38 dBm/Hz respectively. The additive channel noise is white and Gaussian at -140 dBm/Hz. The transmit block length of the far end and echo IDFT are respectively 128 and 512. The receive DFT is of size 128. The true echo channel is modeled as an FIR of 512 samples at 2.2 MHz, while the number of used echo canceler taps is $T_E = 300$. In the echo path the modem front end filters, the hybrid and the TEQ are included. The CES-based EC of Subsection 5.2 is considered, where the echo reference symbols contain 20 extra tones (tones $13 - 32$) with 20 dB lower power to ensure convergence.

Fig. 5.19 illustrates the excess MSE after convergence of the CES-based EC in the presence of a double talker. The excess MSE summed over all the tones as a function of the step size is shown, with and without double talk canceler. The theoretical excess MSE for each tone is given by (5.40), while an estimate of the excess MSE after convergence in 10^4 symbols is obtained by

$$\hat{\xi}_{excess} = \frac{1}{K} \sum_{k=0}^{K-1} \sum_{i=0}^{N/2} |\mathcal{F}_N[i,:](\mathbf{U}^{k-1,k,k+1}\mathbf{h}_E - \mathbf{U}^{k-1,k,k+1}\mathbf{M}\mathbf{w}_E^{10^4})|^2, \quad (5.112)$$

with $K = 500$. The background noise (after TEQ and receiver front-end) together with the remaining ISI/ICI summed over all tones equals -118 dBm (relative to the tone bandwidth of 4.3125 kHz), while the received far end energy (after TEQ) is -69 dBm for this simulation. Hence, if the residual echo has to be 15 dB below the background noise floor, the step size can be 2^8 with DTC and much smaller than 2^1 (the optimal step size is not depicted on the figure) without DTC. Since a significantly larger step size can be used when DTC is present, also tracking performance will be substantially improved.

Also note that the curve represented by circles deviates from the theoretical curve for small step sizes. This error floor is due to the limited number of echo canceler taps ($T_E = 300$) for modeling the actual echo impulse response.

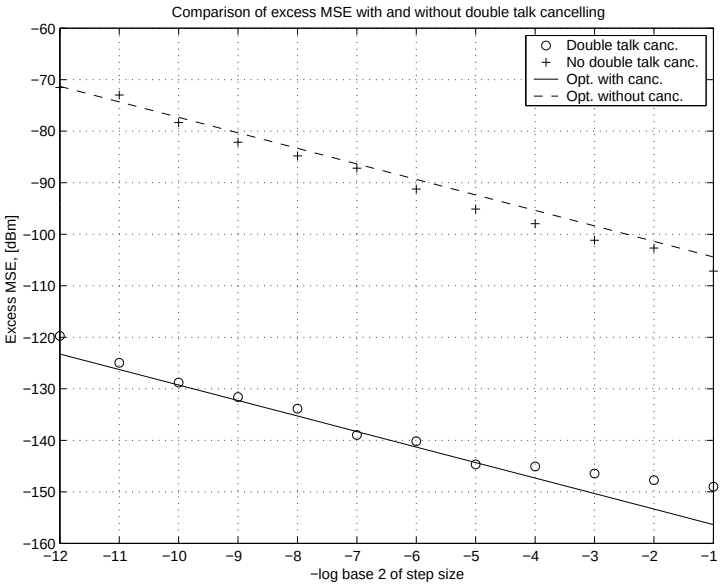

Figure 5.19: Excess MSE with and without DTC for CES-based EC.

However, since this model limitation leads to residual echo noise that is far below the background noise level, it will not alter the SNR at the receiver.

5.6.2 Performance of ITF-EC

Convergence

The convergence behaviour of ITF-EC is verified by simulations for an ADSL 26 AWG inline channel of 12 kft. The simulated loops for RT and CO are depicted in **Fig. 5.20** and **Fig. 5.21**. In upstream, tones $7-31$ are transmitted, while the downstream signal uses tones $33-255$. Convergence of the EC taps can only be guaranteed when all tones are transmitted with equal power. In ADSL these assumptions do not hold, hence a reduced power of 20 dB on the unused tones of the echo reference signal at RT and CO is added to ensure convergence, similar to [32]. The symbol size, the prefix length and the sampling rate at the low rate side of the modem are $N = 64$, $\nu = 4$ and $F_s = 276$ kHz respectively. For the asymmetric rate setup, κ is equal to 8: RT has a 64 point transmit IDFT and a 512 point receive DFT, while CO has a 512 point IDFT and a 64 point DFT. The echo channel is modeled with $T_E = 256$ at the high rate. Hence, with $\delta = 0$ the optimal N_b for ITF-EC, cf. (5.47), is equal to $\frac{T_E}{2} = 128$. The TEQ is assumed to be a single spike and the far end signal is silenced (half duplex). The EC coefficients are updated using a *normalized* LMS procedure [54], with a normalized step size of 0.05. The EC taps were initialized with all zeroes.

In **Fig. 5.22** ITF-EC is compared with the CES-based EC of [65] for RT and CO. The learning curves for two different misalignments, i.e. $\Delta = 0$ and $\Delta = 144$, are depicted for ITF-EC. The curves are calculated as $\text{MSE}^k = (E^k)^H E^k$. It can be observed that after convergence the white noise floor has been reached. From the simulation results, it can be seen that the convergence is weakly dependent on the misalignment, Δ, where $\Delta = 144$ corresponds to the worst case convergence rate. Furthermore, the convergence of ITF-EC is almost as fast as the CES-based EC of [65].

Fig. 5.23 depicts the residual echo after convergence with ITF-EC at RT. Observe the 20 dB lower power on unused echo tones. The figure clearly shows the effect of the DFT on the received echo: all tones are affected by echo due to the bad spectral containment of the DFT in the receive path of the modem. Similarly, **Fig. 5.24** shows the residual echo after convergence with ITF-EC at CO. Note that due to aliasing even the lowest tones are affected by echo noise.

Infrequent update of $\mathbf{w}_E^k$

As discussed in Section 5.4, $\mathbf{w}_E^k$ can be updated at a lower rate than W_E^k, similar to CES-based EC. To illustrate this infrequent update, ITF-EC convergence at RT is depicted in **Fig. 5.25** for different update rates of $\mathbf{w}_E^k$. While W_E^k is updated each time a new symbol is received, the update of $\mathbf{w}_E^k$ is decimated with a factor ϕ =1, 20, 30 and 40. For each decimation factor, the MSE is averaged over a range of misalignments, i.e. $\Delta = -50, -45, \ldots, 150$. Note that the convergence rate is still reasonably fast after decimating the update of $\mathbf{w}_E^k$.

Tracking

The goal of DTC is to track temperature variations in the echo channel. Therefore, the tracking behaviour of ITF-EC with DTC at CO will be investigated for a 12 kft 26 AWG loop. The temperature is increased from 25° C to 45° C, leading to a change in the echo transfer function, as depicted in **Fig. 5.26**. In the simulations it is assumed that the far end channel does not change due to the temperature increase. The TEQ is part of the echo channel and is computed by means of the BM-TEQ design criterion (see Chapter 3 for details). During the BM-TEQ design with $T = 40$ and $\delta_1 = 20$, the echo is perfectly canceled. In the frequency domain, ZF FEQs are used to remove the remaining phase and magnitude distortion of the far end channel. The echo channel is modeled with $T_E = 330$ taps at the high rate. Since δ is equal to 71, the optimal value for N_b is given by $N_b = \delta + T_E/2 = 236$. The frame misalignment is $\Delta = 144$.

Fig. 5.27 and **Fig. 5.28** show the SNR variation at the FEQ output due to a sudden temperature increase from 25° C to 45° C at iteration 3000. The SNR was averaged over 200 Monte Carlo simulations. **Fig. 5.27** clearly shows that the SNR is almost completely recovered from the step after 2000 symbols, with a normalized step size of $\mu = 0.05$ for the echo canceler.

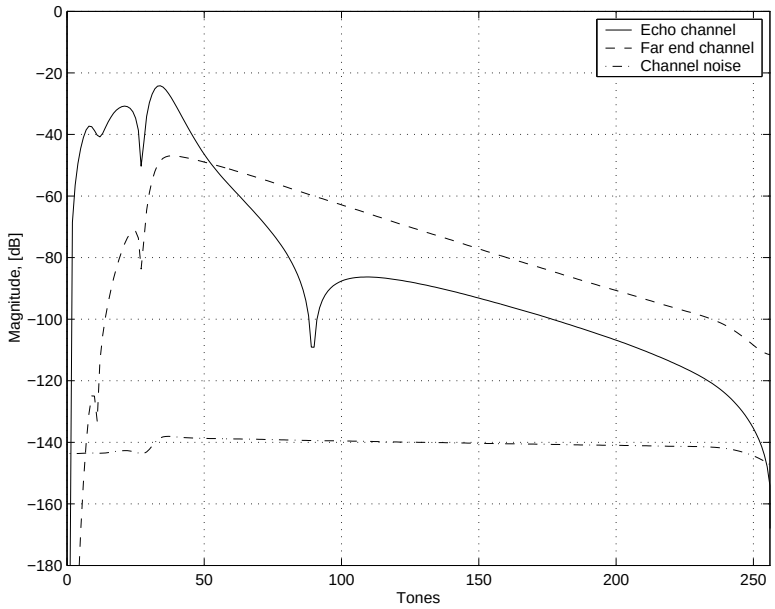

Figure 5.20: Channel and noise characteristics at RT.

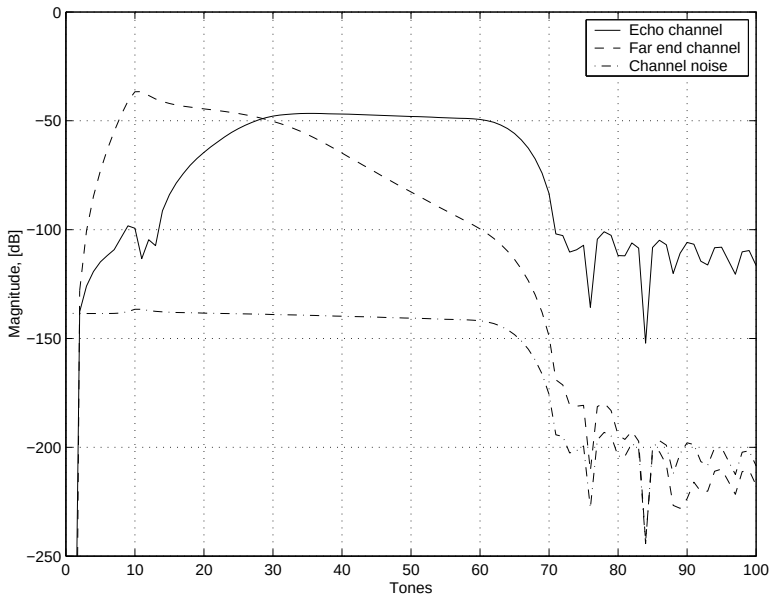

Figure 5.21: Channel and noise characteristics at CO.

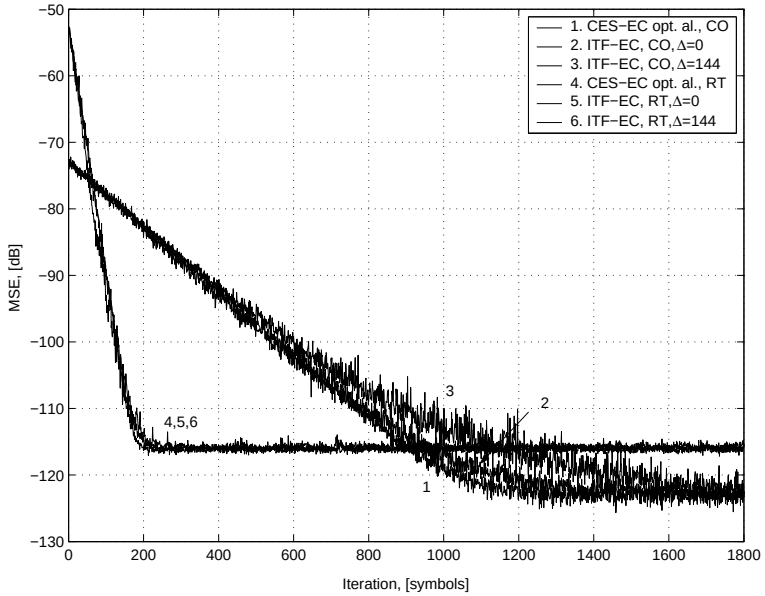

Figure 5.22: Learning curves for CES-based EC with optimal alignment and ITF-EC with optimal N_b at CO and RT.

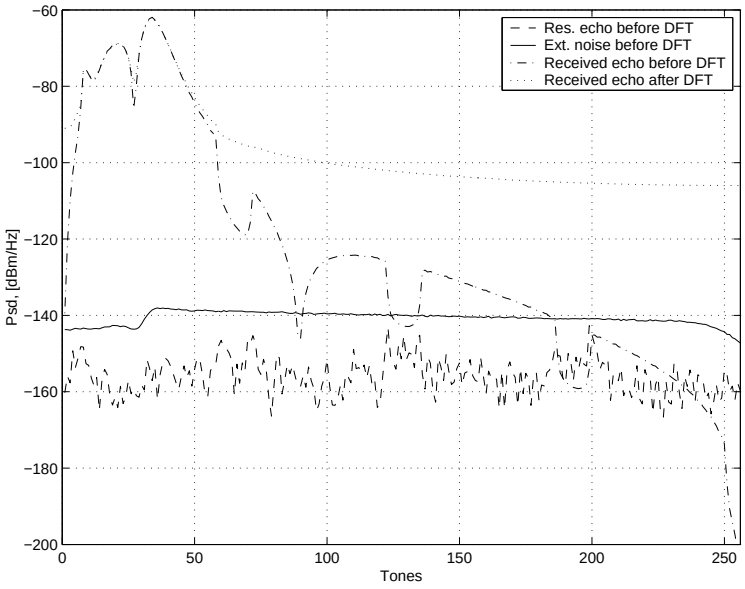

Figure 5.23: PSD of the received echo, the background noise and the residual echo before the receive DFT at RT. Also the received echo after the DFT is shown.

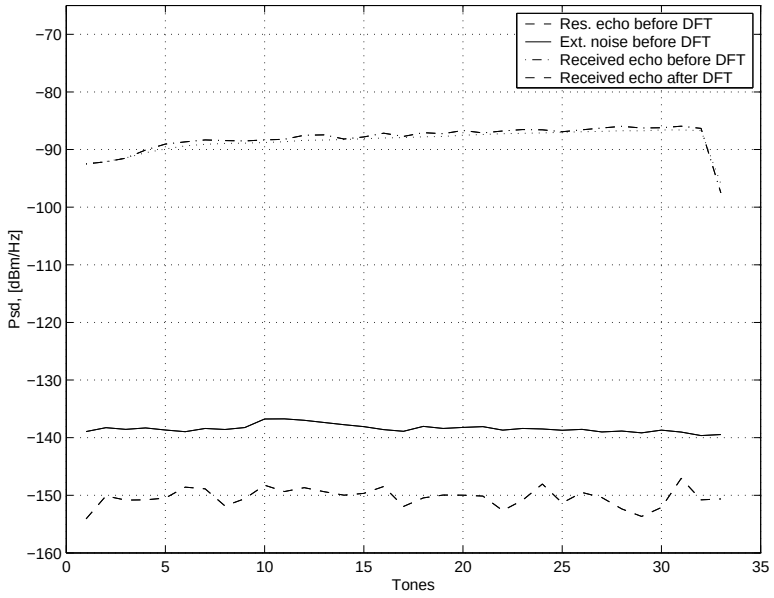

Figure 5.24: PSD of the received echo, the background noise and the residual echo before the receive DFT at CO. Also the received echo after the DFT is shown.

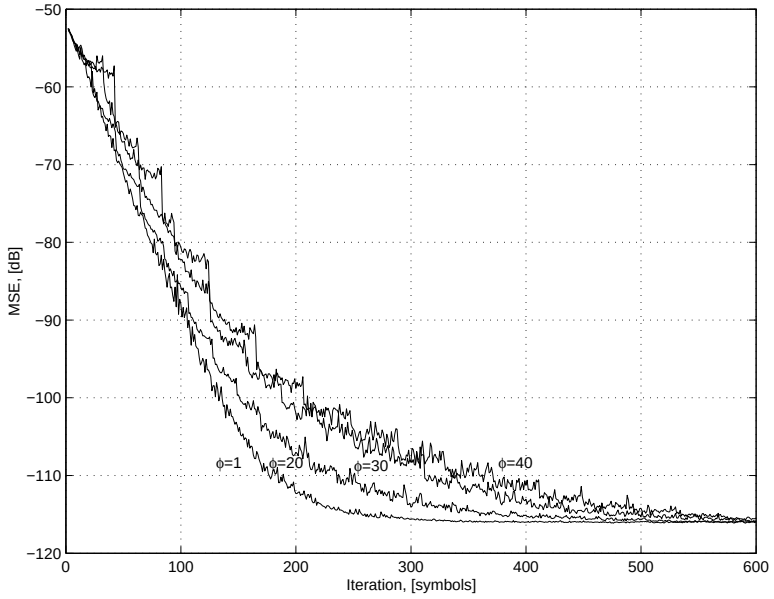

Figure 5.25: Infrequent update of $\mathbf{w}_E^k$ for ITF-EC at RT.

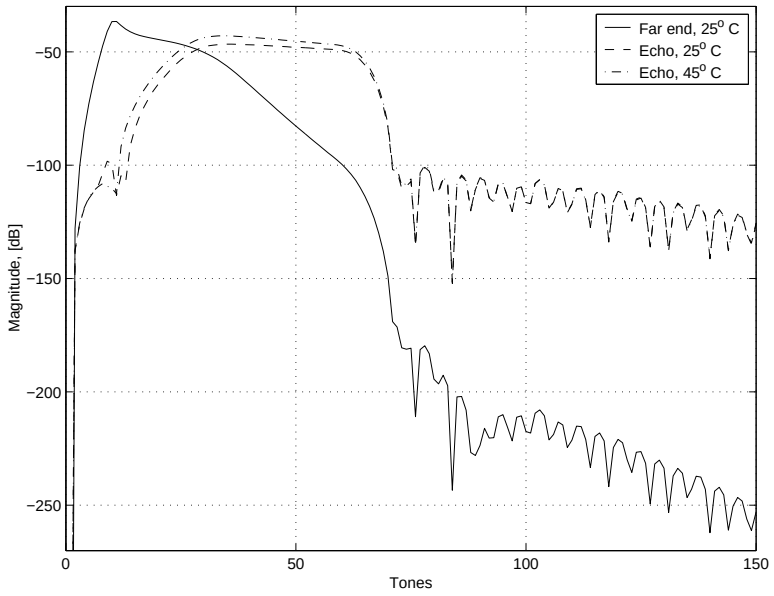

Figure 5.26: Far end transfer function at 25° C; echo transfer function at 25° C and 45° C.

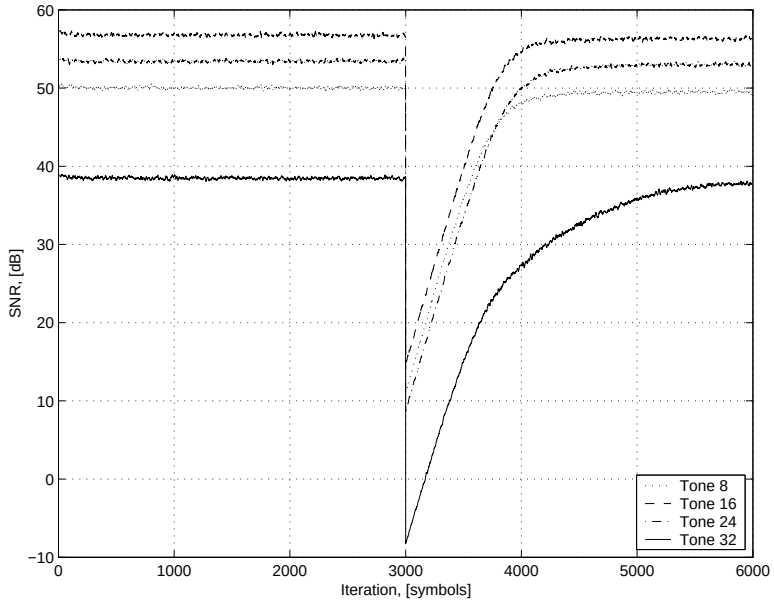

Figure 5.27: SNR variation as a function of the iteration index during full duplex data transmission.

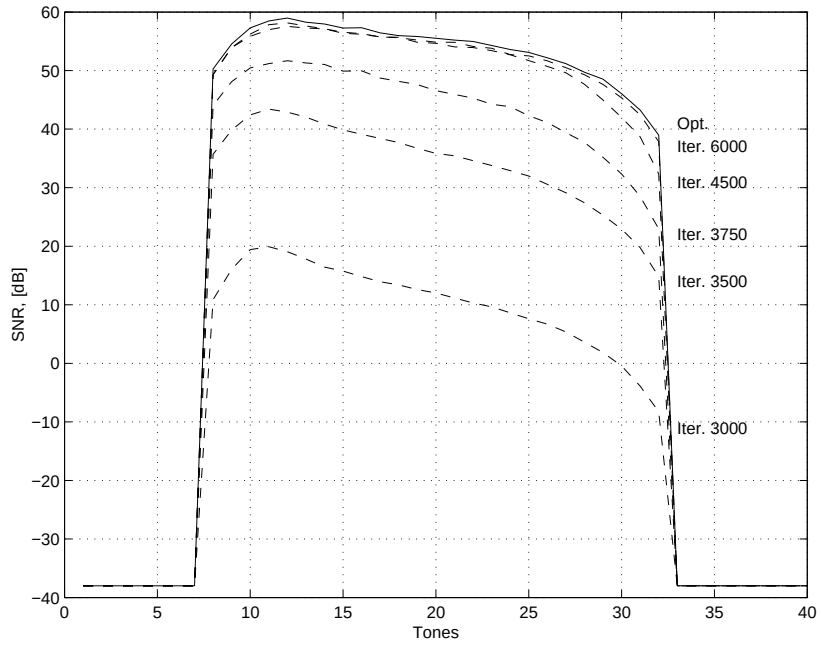

Figure 5.28: SNR variation during full duplex data transmission.

5.6.3 Performance of CDC

To demonstrate the performance of the CDC echo canceler, the 12 kft 26 AWG inline channel is again considered with -140 dBm/Hz additive white Gaussian noise (colored by the receiver front-end filters). Furthermore, the same ADSL setup was used as in Subsection 5.6.2.

Convergence

Fig. 5.29 shows typical learning curves for CDC and CES-based EC. The figure clearly demonstrates that the CES-based echo canceler only achieves convergence when also unused tones are excited with 20 dB lower power. Again, there was no equalizer and far end signal present in the obtained results. To compensate for slow modes, a *normalized* LMS algorithm is used in the adaptation process of the echo cancelers with a normalized step size of 0.05. The learning curves are averaged over a range of misalignments: $\Delta = 0, 5, 10, \ldots, 250$. For both RT and CO the convergence of CDC is roughly two times slower compared to CES-based EC due to the fact that the factor 1/2 of (5.67) was absorbed by the step size when computing the stochastic gradient update of (5.73). Important to note is that, as opposed to CES-based EC, the CDC does not require a power increase on extra tones to converge.

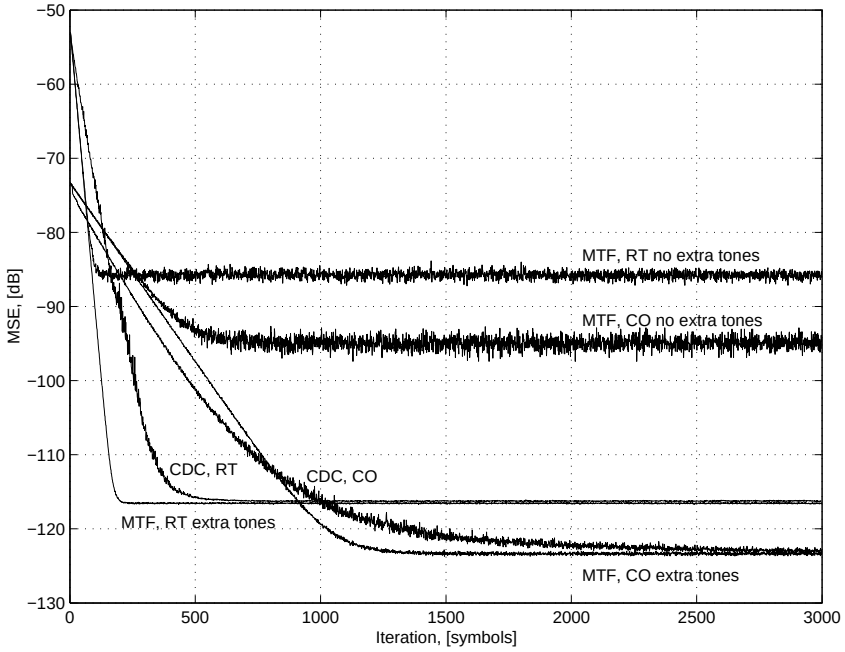

Figure 5.29: Learning curves of CDC compared with MTF EC (with and without the use of power on extra tones).

Infrequent update of $\tilde{W}_E^k$

To illustrate the infrequent update of $\tilde{W}_E^k$, the CDC convergence is depicted in **Fig. 5.30** for different update rates of $\tilde{W}_E^k$. Only once every ϕ symbols, $\tilde{W}_E^k$ is updated, which leads to a step-wise convergence behaviour. For each value of ϕ, the MSE is again averaged over a range of misalignments, i.e. $\Delta = -50, -45, \ldots, 200$. By decimating the update of $\tilde{W}_E^k$, substantial complexity savings can be achieved, while convergence remains fast.

CDC combined with PTEQ and DTC

The combination of CDC with PTEQ and DTC is demonstrated in **Fig. 5.31**. First, the PTEQ coefficients ($T = 24$) are initialized (without echo noise); then the CDC coefficients are adapted to remove the incoming echo, as described in Subsection 5.5.4. Since one is interested in maximizing bit rates (or SNRs) in ADSL, the figure shows the evolution of the SNR at the PTEQ output while the echo filter taps are converging. Notice that convergence remains fast in the presence of a far end signal due to the effective DTC.

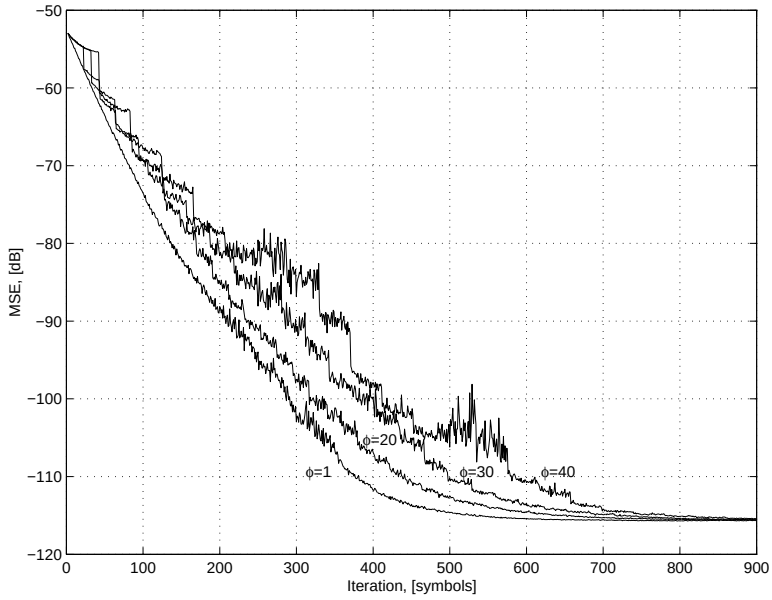

Figure 5.30: Infrequent update of $\tilde{W}_E^k$ for the CDC scheme at RT.

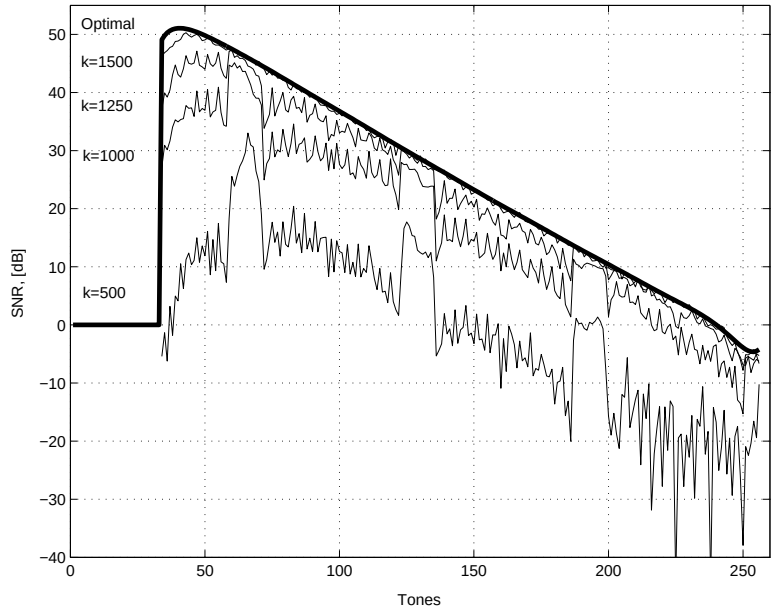

Figure 5.31: SNR after convergence of the CDC combined with PTEQ and DTC.

5.7 Conclusions

Compared to the performance of an FDD system, echo cancellation enables an improvement of the reach, bit rate and/or noise margin of an ADSL system. First, existing structures for EC in DMT-based systems were reviewed in this chapter. More in particular, TD-EC and CES-based EC for symmetric rate and multi-rate setups were discussed. The CES-based schemes lead to more efficient mixed time/frequency domain EC with faster convergence. A tone dependent step size can be adjusted for each tone separately to compensate for slow modes.

We then introduced a low complexity solution for double talk cancellation in ADSL echo canceled systems. The proposed method allows to use a larger step size in the adaptation process resulting in faster tracking and/or convergence in the presence of a far end signal, and hence, increased robustness against, e.g., temperature changes in the echo-path.

In addition, we presented a modification to the existing CES-based EC structures, referred to as ITF-EC. In contrast to currently known EC structures, the obtained echo canceler always achieves minimal CES complexity without choosing a specific alignment. Since the DFT in the receive path of the ADSL modem can be shared between ITF-EC and far end signal demodulation, DTC can easily be added. The resulting ITF-EC requires only one additional DFT at the transmit side of the RT modem and hence offers an inexpensive alternative to existing CES-based echo cancelers.

At present, CES-based echo cancelers are widely used in echo canceled DSL modems at the cost of transmitting extra power on unused echo reference tones to achieve convergence of the echo canceler coefficients. In addition, current DSL systems exhibit slow tracking capabilities of the echo channel since no DTC is present. In this chapter, an alternative EC scheme was proposed, referred to as CDC, that does not require this additional power transmission. We showed that the resulting CDC structure exhibits comparable complexity and convergence behaviour to existing EC schemes. Moreover, we outlined how the CDC can be combined with per tone equalization and low complexity double talk cancellation to optimize the system performance.

Chapter 6

Split SR-RLS for per tone equalizer and per tone echo canceler initialization

IN [129][137][138], Van Acker et al. presented a *joint per tone echo cancellation (PTEC) and per tone equalization (PTEQ)*, where an echo canceler and equalizer are designed for each tone separately. For a given number of equalizer and echo canceler taps per sub-carrier, this approach is able to optimize the signal-to-noise ratio (SNR) on each sub-carrier and hence to maximize the achievable bit rate.

The optimal PTEQ and PTEC coefficients can be obtained as the solution of a minimum mean square error (MMSE) problem per tone [129][137][138]. However, the direct computation of the MMSE solution, which requires the knowledge of the channel impulse response and the noise statistics, has a high computational complexity. Therefore, the goal of this chapter is to develop a cheap initialization method to initialize the PTEQ/PTEC coefficients based on an adaptive filtering algorithm with training symbols. Moreover, further coefficient adaptation during data transmission can then easily be done in a so-called 'decision directed' way.

In [129][133][134], it was shown that least mean square (LMS) adaptive filtering schemes exhibit slow convergence properties for the PTEQ-only (without PTEC) initialization problem. Alternatively, a recursive initialization based on the square-root recursive least square (SR-RLS) algorithm was proposed to overcome this slow convergence at the cost of extra computational complexity and memory requirement. Therefore, we will focus in this chapter on:

- the development of an adaptive filtering algorithm that exhibits fast convergence, low memory requirement and low computational complexity. Before introducing the combined PTEQ and PTEC initialization problem, some standard adaptive filtering algorithms will be reviewed in Section 6.1 and a new recursive initialization scheme, which will be referred to as the *split SR-RLS* method, will be proposed in Section 6.2. The resulting scheme is based on a modification of the split RLS algorithm of [151]. Our performance analysis will show that the proposed method converges in the mean and an upper bound for the step size will be given.
- the initialization of the PTEQ coefficients, where the split SR-RLS will be tuned to a PTEQ-only receiver structure. The resulting initialization algorithm will be a combination of SR-RLS and LMS, hence the name RLS-LMS. It will be shown in Section 6.3 how the algorithm improves upon previously published work [129][133][134] in terms of complexity and memory requirement, while keeping the convergence rate acceptably fast.
- the combined initialization of the PTEQ and PTEC coefficients. Also here, the initialization is based on the split SR-RLS of Section 6.2. The resulting algorithm will be outlined in Section 6.4. In addition, we will indicate how the presented initialization method can be reused in several other DSL design problems.

The chapter ends with simulation results and final conclusions in Section 6.5 and Section 6.6 respectively.

6.1 Standard adaptive filtering algorithms

Before introducing the PTEQ/PTEC initialization problem, several standard adaptive filtering algorithms will be discussed in this section to solve a general MMSE problem. After an introduction in Subsection 6.1.1, the LMS and the SR-RLS adaptive algorithms will be treated in more detail in Subsection 6.1.2 and Subsection 6.1.3 respectively.

6.1.1 Introduction

Consider the MMSE problem of the form

$$\min_{\mathbf{w}} \mathcal{E}\left\{\left(d^k - \mathbf{w}^T\mathbf{z}^k\right)^2\right\}, \tag{6.1}$$

where d^k is some desired signal at time k, $\mathbf{w} = [w_0 \ \ldots \ w_{T-1}]^T$ are the T unknown weight coefficients and $\mathbf{z}^k = [z_0^k \ \ldots \ z_{T-1}^k]^T$ is the input vector at

time k. The goal is to find the best $\mathbf{w}$ such that the filter output, $\mathbf{w}^T\mathbf{z}^k$, is as close as possible to some desired signal d^k in mean square sense. It is assumed that every variable can be complex valued and that the input data has no specific time structure, which is indeed the case for PTEQ and PTEC. In general, $\mathbf{w}$ just forms a linear combination of the input elements (components of $\mathbf{z}^k$) and is henceforth referred to as a *linear combiner*.

In the literature, several adaptive algorithms exist to solve (6.1). The most well known and extensively studied adaptive algorithm is certainly the least mean square (LMS) algorithm by Widrow and Hoff [54][149]. Although the algorithm is simple, a bad conditioning of the input autocorrelation matrix may lead to slow convergence. Since the 1970s, a lot of effort has been spent to find alternatives to LMS which exhibit faster convergence and this has led to a variety of algorithms:

- *LMS derivatives:* these algorithms are derived from the original LMS scheme and include algorithms such as normalized LMS (NLMS) [54] and looping LMS (LLMS) [8]. In NLMS the step size is normalized with the input signal power to avoid gradient noise amplification [54], resulting in slightly improved convergence. However, LMS and NLMS appear to converge too slowly for PTEQ and PTEC initialization. LLMS repeatedly applies LMS to a block of data, but still requires too many iterations and computations in case of the PTEQ/PTEC receiver.

- *Transform-domain LMS:* this type of adaptive filters refers to LMS filters, where blocks of input data are pre-processed with a (unitary) data-independent transformation [91][110]. The main purpose of this preprocessing step is to improve the eigenvalue distribution of the input autocorrelation matrix and hence to accelerate convergence. The choice of this transformation largely depends on the underlying problem. Time series filtering applications, where $\mathbf{z}^k$ is drawn from a tapped delay line, typically use the discrete Fourier transform (DFT), to obtain the so-called frequency domain LMS algorithm. However, the PTEQ/PTEC initialization in fact corresponds to a 'linear combiner' problem, where no shift structure in $\mathbf{z}^k$ is available. Hence, an optimal transformation is not straightforward to obtain.

- *Square-root recursive least squares (SR-RLS):* in general, the SR-RLS algorithm does not impose any restrictions on the input data structure $\mathbf{z}^k$ [54][96]. SR-RLS exhibits fast convergence, be it at the expense of extra computational complexity. Since the order of complexity increases with the square of the number of parameters in $\mathbf{w}$, complexity reductions are desired. To mitigate the high computational burden of RLS, the family of fast RLS algorithms such as fast transversal filters (FTF) [35] and QR-decomposition based lattice filters (QRD-LSL) have been proposed. Unfortunately, the complexity reductions attained in these algorithms

rely again on the signal shift nature of the filtering problem. Hence, these fast schemes are not suitable for our PTEQ/PTEC initialization problem in particular.

- *Split RLS*: this algorithm approximates the RLS algorithm with several lower dimensional RLS problems and is able to obtain a complexity that is linear in the number of parameters [151]. Although this method does not require any specific data structure, only the estimation error is computed without finding $\mathbf{w}$ directly. Moreover, the authors of [151] do not prove the convergence of the obtained algorithm and indicate that a high level of misadjustment is possible for highly correlated input signals.

In Section 6.2, we will derive a modified split RLS method for adaptively computing $\mathbf{w}$ without relying on any specific data structure in $\mathbf{z}^k$. The proposed method 'merges' the SR-RLS[1] and the split RLS algorithms to find the tap weight vector $\mathbf{w}$ directly. The resulting structure will be referred to as *split SR-RLS*. We will prove convergence, even for highly correlated input signals, and derive an upper bound for the step size.

In order to clearly understand the differences between NLMS, SR-RLS and split SR-RLS, the NLMS and SR-RLS adaptive structures will be reviewed in the remainder of this section.

6.1.2 Normalized least mean square (NLMS)

The (normalized) LMS algorithm was designed as a stochastic gradient descent method to solve (6.1) [54]. It approximates the MMSE solution by continuously updating the weight vector $\mathbf{w}$ as new data vectors are received, according to

$$\mathbf{w}^k \leftarrow \mathbf{w}^{k-1} + \frac{\mu}{\alpha^2 + (\mathbf{z}^k)^H \mathbf{z}^k} (\mathbf{z}^k)^* e^k, \tag{6.2}$$

where $e^k = d^k - (\mathbf{w}^{k-1})^T \mathbf{z}^k$, μ represents the step size to 'govern' the convergence rate and α is a regularization parameter that prevents overflow for signals with low energy. This algorithm is computationally simple, but a large eigenvalue spread of the input correlation matrix,

$$\mathbf{R}_{zz} = \mathcal{E}\left\{(\mathbf{z}^k)^* (\mathbf{z}^k)^T\right\}, \tag{6.3}$$

often leads to a convergence rate that is unacceptably slow [54].

[1] The SR-RLS algorithm is sometimes also referred to as the inverse QR-RLS algorithm [54].

6.1.3 Square-root recursive least square (SR-RLS)

To overcome the slow convergence of (normalized) LMS, (6.1) can be approximated by a least squares (LS) problem

$$\mathbf{w}^k = \arg\min_{\mathbf{w}} \left\| \mathbf{d}^k - \mathbf{Z}^k \mathbf{w} \right\|_2^2, \tag{6.4}$$

where $\mathbf{d}^k = [d^0 \ \ldots \ d^k]^T$ is a vector of training or desired symbols and $\mathbf{Z}^{k+1}$ contains a set of consecutive input signal vectors, i.e.

$$\mathbf{Z}^k = \begin{bmatrix} z_0^0 & \cdots & z_{T-1}^0 \\ \vdots & & \\ z_0^k & \cdots & z_{T-1}^k \end{bmatrix}. \tag{6.5}$$

Given $(\mathbf{Z}^k)^H \mathbf{Z}^k$ is full rank[2], the LS solution of (6.4) is given by

$$\mathbf{w}^k = \left((\mathbf{Z}^k)^H \mathbf{Z}^k \right)^{-1} (\mathbf{Z}^k)^H \mathbf{d}^k. \tag{6.6}$$

With $\mathbf{Q}^k \mathbf{L}^k$ the QR-decomposition of $\mathbf{Z}^k$ [53], one can rewrite (6.6) as

$$\mathbf{w}^k = (\mathbf{L}^k)^{-1} \mathbf{a}^k, \tag{6.7}$$

with $\mathbf{a}^k = (\mathbf{Q}^k)^H \mathbf{d}^k$. The SR-RLS algorithm is based on recursively updating the lower triangular matrix $\mathbf{S}^k = (\mathbf{L}^k)^{-T}$ by means of unitary Givens rotations [54]. For a definition of Givens rotations see (A.13). The matrix $\mathbf{L}^k$ is the (upper triangular) Cholesky factor of the sample covariance matrix

$$(\mathbf{Z}^k)^H \mathbf{Z}^k = (\mathbf{L}^k)^H \mathbf{L}^k = \sum_{j=0}^{k} (\mathbf{z}^j)^* (\mathbf{z}^j)^T \approx (k+1) \mathbf{R}_{zz}. \tag{6.8}$$

Often, an exponential weighting factor $0 < \epsilon < 1$ is included to ensure that data in the distant past is forgotten such that statistical variations of the input data can be tracked in a non-stationary environment. Correspondingly, one can write

$$(\mathbf{Z}^k)^H \mathbf{Z}^k = (\mathbf{L}^k)^H \mathbf{L}^k = \sum_{j=0}^{k} \epsilon^{2(k-j)} (\mathbf{z}^j)^* (\mathbf{z}^j)^T \approx \frac{1}{1-\epsilon^2} \mathbf{R}_{zz}. \tag{6.9}$$

where $\frac{1}{1-\epsilon^2}$ represents the effective memory of the system. The last equality only holds for large k and ϵ close to unity. SR-RLS uses an iterative update based on a transformed update direction

$$\mathbf{k}^k = (\mathbf{S}^k)^T (\mathbf{S}^k)^* (\mathbf{z}^k)^*, \tag{6.10}$$

which is called the Kalman gain vector. An efficient realization of updating $\mathbf{S}^k$ and $\mathbf{w}^k$ is described in **Table 6.1** [96].

[2] In practice, $k+1$ must at least be equal to T to satisfy this condition.

TABLE 6.1
Algorithm: SR-RLS[3] [96]

Initialize filter coefficients $\mathbf{w}^{-1}$ and $\mathbf{S}^{-1}$.
For $k = 0, \ldots, \infty$

1. Form the matrix-vector product:

$$\mathbf{b} = -\mathbf{S}^{k-1}\mathbf{z}^k. \tag{6.11}$$

2. For $m = 1, ..., T$ determine the Givens rotations $\mathbf{Q}_{m(T+1)}$, cf. (A.13), where $\mathbf{Q}_{m(T+1)}$ zeroes out the m-th element of $\mathbf{b}$:

$$\begin{bmatrix} \mathbf{0}_{T\times 1} \\ \hline \delta \end{bmatrix} = \mathbf{Q}_{T(T+1)} \cdots \mathbf{Q}_{1(T+1)} \begin{bmatrix} \mathbf{b} \\ \hline 1 \end{bmatrix}. \tag{6.12}$$

3. Update $\mathbf{S}^{k-1}$ and determine the Kalman gain vector, $\mathbf{k}^k$, using the previously obtained $\mathbf{Q}_{m(T+1)}$, $m = 1, ..., T$. Apply exponential weighting with ϵ:

$$\begin{bmatrix} \mathbf{S}^k \\ -\delta \cdot (\mathbf{k}^k)^T \end{bmatrix} \leftarrow \mathbf{Q}_{T(T+1)} \cdots \mathbf{Q}_{1(T+1)} \begin{bmatrix} \mathbf{S}^{k-1} \\ \mathbf{0}_{1\times T} \end{bmatrix}, \tag{6.13}$$

$$\mathbf{S}^k \leftarrow \mathbf{S}^k/\epsilon. \tag{6.14}$$

4. Update $\mathbf{w}^{k-1}$:

$$\mathbf{w}^k \leftarrow \mathbf{w}^{k-1} + \delta \cdot \mathbf{k}^k \left(\frac{d^k - (\mathbf{w}^{k-1})^T \mathbf{z}^k}{\delta} \right). \tag{6.15}$$

end

The convergence of SR-RLS is determined by the cross-correlation matrix of $\mathbf{k}^k$ and $\mathbf{z}^k$

$$\begin{aligned} \mathbf{R}_{kz} &= \mathcal{E}\left\{\mathbf{k}^k(\mathbf{z}^k)^T\right\}, && (6.16)\\ &= \mathcal{E}\left\{(\mathbf{S}^k)^T(\mathbf{S}^k)^*(\mathbf{z}^k)^*(\mathbf{z}^k)^T\right\}, && (6.17)\\ &= \mathcal{E}\left\{\left((\mathbf{L}^k)^H\mathbf{L}^k\right)^{-1}(\mathbf{z}^k)^*(\mathbf{z}^k)^T\right\}, && (6.18)\\ &\approx (1-\epsilon^2)\mathbf{R}_{zz}^{-1}\mathcal{E}\left\{(\mathbf{z}^k)^*(\mathbf{z}^k)^T\right\}, && (6.19)\\ &= (1-\epsilon^2)\mathbf{I}_T, && (6.20) \end{aligned}$$

[3]The term 'square-root' refers to the propagation of the square-root or Cholesky factor of $\mathbf{R}_{zz}^{-1}$ rather than $\mathbf{R}_{zz}^{-1}$ itself, as is done by the Riccati equation of the original RLS algorithm [54].

where (6.9) and (6.10) were used. It is observed that all the eigenvalues of $\mathbf{R}_{kz}$ are (approximately) equal. Hence, the Kalman gain update direction in a sense *removes the eigenvalue spread* and by this improves the convergence speed. This improvement in performance, however, is achieved at the expense of a large increase in computational complexity and memory requirement. Whereas the complexity of NLMS is on the order of $\mathcal{O}(T)$, the complexity and memory requirement of SR-RLS is on the order of $\mathcal{O}(T^2)$.

6.2 Split SR-RLS with reduced complexity

6.2.1 Algorithm outline

To alleviate the computational burden of a full-blown SR-RLS, the input elements of the 'linear combiner' $\mathbf{w}^{k-1}$ may be divided into smaller groups. This is also the idea behind the split RLS algorithm in [151]. In [151], the input elements $\mathbf{z}^k$ are divided into two or more groups. For each group, an upper triangular matrix $\mathbf{L}^{k-1}$ is updated, based on the original QR-RLS algorithm (without inverse updating) and the estimation error e^k is directly obtained, without computing $\mathbf{w}^k$.

For the PTEQ/PTEC initialization problem the combiner coefficients $\mathbf{w}^k$ are effectively required. Hence, our goal is to modify the split RLS principle in order to enable inverse updating and a recursive update of $\mathbf{w}^k$. The final algorithm will be a combination of the SR-RLS (cf. Subsection 6.1.3) and split RLS principles and will therefore be named the *split SR-RLS* algorithm. As will be motivated in the next sections, we are mainly interested in dividing the input vector into *two* (unequal) parts. The ultimate goal is to design a scheme maintaining a fast convergence rate but with lower computational complexity and lower memory requirement than a full SR-RLS.

Assume the input vector $\mathbf{z}^k$ is split into two parts of length T_1 and T_2 respectively, such that $T_1 + T_2 = T$ (a reordering of the inputs may be possible), i.e.

$$\mathbf{z}^k = \left[(\mathbf{z}_1^k)^T \;\; (\mathbf{z}_2^k)^T\right]^T, \tag{6.21}$$

with

$$\mathbf{z}_1^k = [z_0^k \;\ldots\; z_{T_1-1}^k]^T, \tag{6.22}$$

$$\mathbf{z}_2^k = [z_{T_1}^k \;\ldots\; z_{T-1}^k]^T. \tag{6.23}$$

Now, a separate SR-RLS problem can be solved for each set of inputs. This requires two lower triangular matrices $\mathbf{S}_1^{k-1}$ and $\mathbf{S}_2^{k-1}$ (of size $T_1 \times T_1$ and $T_2 \times T_2$ respectively) to be updated, see **Table 6.2**. The update direction is

now determined by $\mathbf{l}^k$, which consists of a concatenation of two Kalman gain type vectors, one for each input set. Similar to (6.10), one can write

$$\mathbf{l}^k = \underbrace{\left[\begin{array}{c|c} (\mathbf{S}_1^k)^T(\mathbf{S}_1^k)^* & \mathbf{0}_{T_1\times T_2} \\ \hline \mathbf{0}_{T_2\times T_1} & (\mathbf{S}_2^k)^T(\mathbf{S}_2^k)^* \end{array}\right]}_{\mathbf{T}^k} \underbrace{\left[\begin{array}{c} (\mathbf{z}_1^k)^* \\ (\mathbf{z}_2^k)^* \end{array}\right]}_{(\mathbf{z}^k)^*}. \tag{6.24}$$

Note that a step size μ has been added to tune the convergence rate.

6.2.2 Convergence

In appendix E.1, it is shown that the convergence of the proposed split SR-RLS scheme is determined by the maximum eigenvalue of the cross-correlation matrix between $\mathbf{l}^k$ and $\mathbf{z}^k$

$$\mathbf{R}_{lz} = \mathcal{E}\left\{\mathbf{l}^k(\mathbf{z}^k)^T\right\}. \tag{6.35}$$

Additionally, in appendix E.2 it is proven that $\mathbf{R}_{lz}$ has eigenvalues $1-\epsilon^2$ with multiplicity $T_1 - T_2$ and $2T_2$ eigenvalues equal to $(1-\epsilon^2)(1 \pm \sqrt{d_i})$, with the d_i's equal to the *cosines squared of the principal angles between the subspaces* $\mathcal{S}_1$ *and* $\mathcal{S}_2$ *spanned by the columns of* $\mathbf{Z}_1^k$ *and* $\mathbf{Z}_2^k$, where $\mathbf{Z}_1^k$ and $\mathbf{Z}_2^k$ are matrices containing the first T_1 and the last T_2 columns of $\mathbf{Z}^k$ respectively. Note that this result is in agreement with (6.20) when $T_1 = T$ and $T_2 = 0$. Apparently, the modified update direction is able to remove partially the eigenvalue spread and by this the convergence speed is expected to be intermediate between the convergence speed of SR-RLS and NLMS.

In appendix E.2, it is also shown that convergence in the mean is achieved when μ satisfies

$$0 < \mu < \frac{1}{1-\epsilon^2}. \tag{6.36}$$

Since the convergence rate depends on the eigenvalue spread of $\mathbf{R}_{lz}$, convergence will be faster when all eigenvalues tend to be equal, i.e. when the cosines of the principal angles between $\mathcal{S}_1$ and $\mathcal{S}_2$ go to zero. Hence, the convergence rate will be higher whenever $\mathcal{S}_1$ and $\mathcal{S}_2$ are more orthogonal or, in other words, when $\mathbf{z}_1^k$ and $\mathbf{z}_2^k$ are less correlated.

The proposed algorithm is straightforwardly obtained but can attain substantial complexity improvements and memory reductions, as will be illustrated in the following section. Similar to [151], the algorithm could be extended to more than two distinct parts, leading to higher misadjustment and slower convergence. In this case, an upper bound for the step size can not easily be derived. In the limit, an LMS-like update algorithm is obtained, where each input element is weighted with the averaged energy of this element.

TABLE 6.2
Algorithm: Split SR-RLS

Initialize filter coefficients $\mathbf{w}^{-1}$ and $\mathbf{S}_1^{-1}$, $\mathbf{S}_2^{-1}$.
For $k = 0, \ldots, \infty$

1. Form the matrix-vector products:

$$\mathbf{b}_1 = -\mathbf{S}_1^{k-1}\mathbf{z}_1^k, \tag{6.25}$$
$$\mathbf{b}_2 = -\mathbf{S}_2^{k-1}\mathbf{z}_2^k. \tag{6.26}$$

2. For $m_1 = 1, ..., T_1$ and $m_2 = 1, ..., T_2$ determine the Givens rotations $\mathbf{Q}_{m_1(T_1+1)}$ and $\mathbf{Q}_{m_2(T_2+1)}$, cf. (A.13), to zero out the elements of $\mathbf{b}_1$ and $\mathbf{b}_2$:

$$\left[\begin{array}{c} \mathbf{0}_{T_1\times 1} \\ \hline \delta_1 \end{array}\right] = \mathbf{Q}_{T_1(T_1+1)} \cdots \mathbf{Q}_{1(T_1+1)} \left[\begin{array}{c} \mathbf{b}_1 \\ \hline 1 \end{array}\right], \tag{6.27}$$
$$\left[\begin{array}{c} \mathbf{0}_{T_2\times 1} \\ \hline \delta_2 \end{array}\right] = \mathbf{Q}_{T_2(T_2+1)} \cdots \mathbf{Q}_{1(T_2+1)} \left[\begin{array}{c} \mathbf{b}_2 \\ \hline 1 \end{array}\right]. \tag{6.28}$$

3. Update $\mathbf{S}_1^{k-1}$ and $\mathbf{S}_2^{k-1}$ and determine the modified Kalman gain vector, $\mathbf{l}^k$, using the previously obtained $\mathbf{Q}_{m_1(T_1+1)}$ and $\mathbf{Q}_{m_2(T_2+1)}$. Apply exponential weighting with ϵ:

$$\left[\begin{array}{c} \mathbf{S}_1^k \\ \hline -\delta_1(\mathbf{k}_1^k)^T \end{array}\right] \leftarrow \mathbf{Q}_{T_1(T+1)} \cdots \mathbf{Q}_{1(T_1+1)} \left[\begin{array}{c} \mathbf{S}_1^{k-1} \\ \hline \mathbf{0}_{1\times T_1} \end{array}\right], \tag{6.29}$$
$$\left[\begin{array}{c} \mathbf{S}_2^k \\ \hline -\delta_2(\mathbf{k}_2^k)^T \end{array}\right] \leftarrow \mathbf{Q}_{T_2(T_2+1)} \cdots \mathbf{Q}_{1(T_2+1)} \left[\begin{array}{c} \mathbf{S}_2^{k-1} \\ \hline \mathbf{0}_{1\times T_2} \end{array}\right], \tag{6.30}$$
$$\mathbf{S}_1^k \leftarrow \mathbf{S}_1^k/\epsilon, \tag{6.31}$$
$$\mathbf{S}_2^k \leftarrow \mathbf{S}_2^k/\epsilon. \tag{6.32}$$

4. Update $\mathbf{w}^{k-1}$:

$$\mathbf{l}^k = \left[\begin{array}{c} \mathbf{k}_1^k \\ \hline \mathbf{k}_2^k \end{array}\right], \tag{6.33}$$
$$\mathbf{w}^k \leftarrow \mathbf{w}^{k-1} + \mu\mathbf{l}^k(d^k - (\mathbf{w}^{k-1})^T\mathbf{z}^k). \tag{6.34}$$

end

6.3 RLS-LMS for PTEQ initialization

In this section, the split SR-RLS algorithm will be applied to the PTEQ initialization problem. After a brief review of per tone equalization in Subsection 6.3.1, NLMS, SR-RLS and split SR-RLS (or RLS-LMS) for initializing the PTEQ coefficients will be treated in the Subsections 6.3.2, 6.3.3 and 6.3.4 respectively. Finally, complexity issues will be discussed in Subsection 6.3.5.

6.3.1 PTEQ revisited

As discussed in Chapter 3 and Chapter 4, Van Acker et al. proposed the PTEQ as an alternative to the TEQ-based receiver [129][136]. This structure is able to optimize the SNR for each tone separately and hence maximizes the achievable bit rate. Moreover, the PTEQ is a generalization of the TEQ such that its performance is always at least as good as, but in most cases significantly better than the performance of a single TEQ with the same number of taps.

The PTEQ structure consists of a bank of equalizers with T taps per tone, where equalization of tone i is accomplished by forming a *linear combination* of the i-th DFT output, Y_i^k, with $T-1$ *real valued difference terms*, $\Delta\mathbf{y}^k$. The output of the per tone equalizer for tone i at time k can be obtained as:

$$\hat{X}_i^k = \bar{\mathbf{v}}_i^T \left[\begin{array}{c|c|c} \mathbf{I}_{T-1} & \mathbf{0} & -\mathbf{I}_{T-1} \\ \hline \mathbf{0} & \multicolumn{2}{c}{\mathcal{F}_N[i,:]} \end{array}\right] \mathbf{y}^k = \bar{\mathbf{v}}_i^T \underbrace{\left[\begin{array}{c} \Delta\mathbf{y}^k \\ Y_i^k \end{array}\right]}_{\mathbf{z}_i^k}, \tag{6.37}$$

where $\bar{\mathbf{v}}_i$ contains the equalizer coefficients for tone i, see also (3.117). The unconstrained MMSE solution for $\bar{\mathbf{v}}_i$ is obtained as

$$\bar{\mathbf{v}}_{opt,i} = \arg\min_{\bar{\mathbf{v}}_i} \mathcal{E}\left\{\left|\hat{X}_i^k(\bar{\mathbf{v}}_i) - X_i^k\right|^2\right\}, \tag{6.38}$$

where X_i^k is the QAM symbol of interest, transmitted on tone i. Note that $\bar{\mathbf{v}}_i$ is a linear combiner that has to be initialized for each tone. The input vectors $\mathbf{z}_i^k$ can be separated into two parts:

- the elements of $\Delta\mathbf{y}^k$ are *real valued* since they are derived from a pre-DFT signal and hence are *common* for all tones,
- Y_i^k is *complex valued* and *tone-dependent*.

This distinct nature of the inputs will be exploited when applying the split SR-RLS to the PTEQ initialization, similar to [133][134].

Direct MMSE initialization of all the PTEQ coefficients, based on the knowledge of the channel impulse response and the signal and noise power spectral

TABLE 6.3
Algorithm: NLMS for PTEQ initialization

Initialize the PTEQ coefficients $\bar{\mathbf{v}}_i^{-1}$ for each tone $i \in \mathcal{S}$.
For $k = 0, \ldots, \infty$

- *Tone-independent part*

$$s = \|\Delta \mathbf{y}^k\|_2^2. \tag{6.41}$$

- *Tone-dependent part*

  For $i \in \mathcal{S}$

$$\|\mathbf{z}_i^k\|_2^2 = s + (Y_i^k)^* Y_i^k, \tag{6.42}$$

$$\bar{\mathbf{v}}_i^k \leftarrow \bar{\mathbf{v}}_i^{k-1} + \frac{\mu}{\alpha^2 + \|\mathbf{z}_i^k\|_2^2} (\mathbf{z}_i^k)^* \left(d_i^k - (\bar{\mathbf{v}}_i^{k-1})^T \mathbf{z}_i^k \right). \tag{6.43}$$

  end
end

densities, turns out to be computationally too expensive to implement in hardware. Therefore, in the following subsections, we will focus on initializing the equalizer coefficients based on adaptive algorithms with training symbols. During data transmission, further equalizer coefficient adaptation can be based on so-called 'decision directed operation'.

If an unbiased decision rule is used, recall that each PTEQ output has to be provided with an additional ZF FEQ to compensate for the bias, which is present, in general, with an unconstrained MMSE equalizer, see Subsection 3.4.1. W.l.o.g. the ZF FEQs will not be treated explicitly in this chapter. They can easily be obtained by estimating the statistics in

$$D_i = \frac{\sigma_{x,i}^2}{\mathcal{E}\{\hat{X}_i^k (X_i^k)^*\}}, \tag{6.39}$$

or by an additional LMS per tone

$$D_i^k \leftarrow D_i^{k-1} + \mu (X_i^k)^* (X_i^k - D_i^{k-1} \hat{X}_i^k), \tag{6.40}$$

where $\hat{X}_i^k$ denotes the PTEQ output for tone i at symbol period k.

6.3.2 NLMS-based PTEQ initialization

With the NLMS algorithm of Subsection 6.1.2, each equalizer can be updated according to **Table 6.3**. In the table, $\mathcal{S}$ denotes the set of used tones and d_i^k is either the decision on the filter output (decision directed mode) or a training

symbol X_i^k (training mode). A signal flow graph (SFG) is shown in **Fig. 6.2** and the functionality of the SFG building blocks is explained in **Fig. 6.1**.

The convergence rate of NLMS for PTEQ initialization is determined by the eigenvalue spread of

$$\mathbf{R}_{z_i z_i} = \mathcal{E}\left\{(\mathbf{z}_i^k)^*(\mathbf{z}_i^k)^T\right\}. \tag{6.44}$$

Simulations will show that $\mathbf{R}_{z_i z_i}$ typically has a large eigenvalue spread and as a consequence convergence is slow. Iterative initialization based on NLMS have low complexity but require, unfortunately, an excessively large number of training symbols. The low cost can easily be understood from **Fig. 6.2**.

6.3.3 SR-RLS-based PTEQ initialization

To overcome the slow convergence of NLMS, the SR-RLS of Subsection 6.1.3 can be used. In the PTEQ initialization problem several parallel least squares problems (LS), one LS problem for each tone, have to be solved. A straightforward implementation of the SR-RLS algorithm of **Table 6.1** would require the update of a lower triangular matrix $\mathbf{S}_i^k$ for each tone separately. Fortunately, due to the tone-independent difference terms, each submatrix $\mathbf{S}^k = \mathbf{S}_i^k[1:T-1, 1:T-1]$ with $i \in \mathcal{S}$ is equal and can be treated as common for all the used tones. Only the last row of $\mathbf{S}_i^k$, i.e. $\mathbf{s}_i^k = \mathbf{S}_i^k[T, 1:T]$, will be tone-specific and has to be updated separately [133][134]. The resulting SR-RLS algorithm for the PTEQ initialization problem is described in **Table 6.4**. Note that the proper ordering of the inputs is extremely important here, since it leads to this simplified SR-RLS algorithm. When, e.g., the DFT output Y_i^k is taken as the first input, $\mathbf{S}_i^k$ would be completely tone-dependent, resulting in an overwhelming computational complexity.

The overall algorithm is depicted in **Fig. 6.3**. The Givens rotations are represented by hexagons. Linear combinations are constructed by means of rectangular multiply-add cells. One can see that every used tone has a T-taps PTEQ with as its inputs the complex DFT output for this tone and $T-1$ real difference terms. One can clearly see that the $T-1$ real difference terms give rise to a $(T-1) \times (T-1)$ real valued triangular part $\mathbf{S}^k$, which is common for all the tones. The DFT output is used to update the complex valued and tone dependent $\mathbf{s}_i^k$. The figure also shows that the algorithm can work in two modes, namely 'training data based' during initialization or 'decision directed' during data transmission.

6.3.4 RLS-LMS-based PTEQ initialization

In **Fig. 6.3**, one can see that a large part of the computational cost is still caused by the per tone RLS-part $\mathbf{s}_i^k$, while the common part with $\mathbf{S}^k$ is reason-

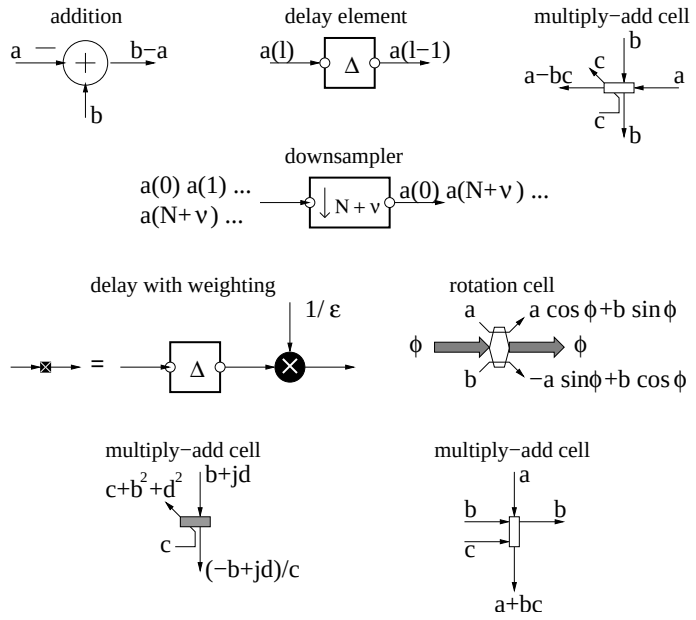

Figure 6.1: Building blocks for signal flow graphs (SFG).

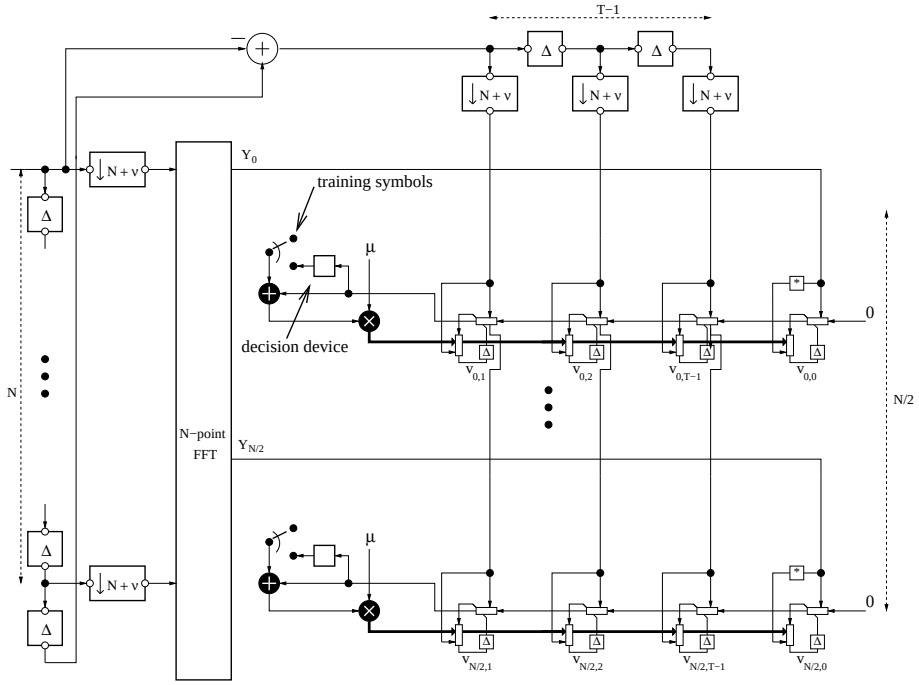

Figure 6.2: Signal flow graph of NLMS for PTEQ initialization.

TABLE 6.4
Algorithm: SR-RLS for PTEQ initialization

Initialize $\mathbf{S}^{-1}$ and $\bar{\mathbf{v}}_i^{-1}$, $\mathbf{s}_i^{-1}$ for each tone $i \in \mathcal{S}$.
For $k = 0, \ldots, \infty$

- *Tone-independent part*

  1. Form the matrix-vector product:

$$\mathbf{b} = -\mathbf{S}^{k-1}\Delta\mathbf{y}^k. \tag{6.45}$$

  2. For $m = 1, ..., T-1$ determine the Givens rotations $\mathbf{Q}_{mT}$, cf. (A.13), where $\mathbf{Q}_{mT}$ zeroes out the m-th element of $\mathbf{b}$:

$$\begin{bmatrix} \mathbf{0}_{(T-1)\times 1} \\ \delta \end{bmatrix} = \mathbf{Q}_{(T-1)T} \cdots \mathbf{Q}_{1T} \begin{bmatrix} \mathbf{b} \\ 1 \end{bmatrix}. \tag{6.46}$$

  3. Update $\mathbf{S}^{k-1}$ and apply exponential weighting with ϵ:

$$\begin{bmatrix} \mathbf{S}^k \\ -\delta\mathbf{k}^T \end{bmatrix} \leftarrow \mathbf{Q}_{(T-1)T} \cdots \mathbf{Q}_{1T} \begin{bmatrix} \mathbf{S}^{k-1} \\ \mathbf{0}_{1\times(T-1)} \end{bmatrix}, \tag{6.47}$$

$$\mathbf{S}^k \leftarrow \mathbf{S}^k/\epsilon. \tag{6.48}$$

- *Tone-dependent part*

  For $i \in \mathcal{S}$

  1. Form the product:

$$b_i = -\mathbf{s}_i^{k-1}\mathbf{z}_i^k. \tag{6.49}$$

  2. Determine the Givens rotation $\mathbf{Q}_{12,i}$ such that:

$$\begin{bmatrix} 0 \\ \delta_i \end{bmatrix} = \mathbf{Q}_{12,i} \begin{bmatrix} b_i \\ \delta \end{bmatrix}. \tag{6.50}$$

  3. Update $\mathbf{s}_i^{k-1}$ and apply exponential weighting with ϵ:

$$\begin{bmatrix} \mathbf{s}_i^k \\ -\delta_i(\mathbf{k}_i^k)^T \end{bmatrix} \leftarrow \mathbf{Q}_{12,i} \begin{bmatrix} \mathbf{s}_i^{k-1} \\ \begin{bmatrix} -\delta\mathbf{k}^T & 0 \end{bmatrix} \end{bmatrix}, \tag{6.51}$$

$$\mathbf{s}_i^k \leftarrow \mathbf{s}_i^k/\epsilon. \tag{6.52}$$

  4. Update $\bar{\mathbf{v}}_i^{k-1}$:

$$\bar{\mathbf{v}}_i^k \leftarrow \bar{\mathbf{v}}_i^{k-1} + \mathbf{k}_i^k \left(d_i^k - (\bar{\mathbf{v}}_i^{k-1})^T\mathbf{z}_i^k\right). \tag{6.53}$$

  end
end

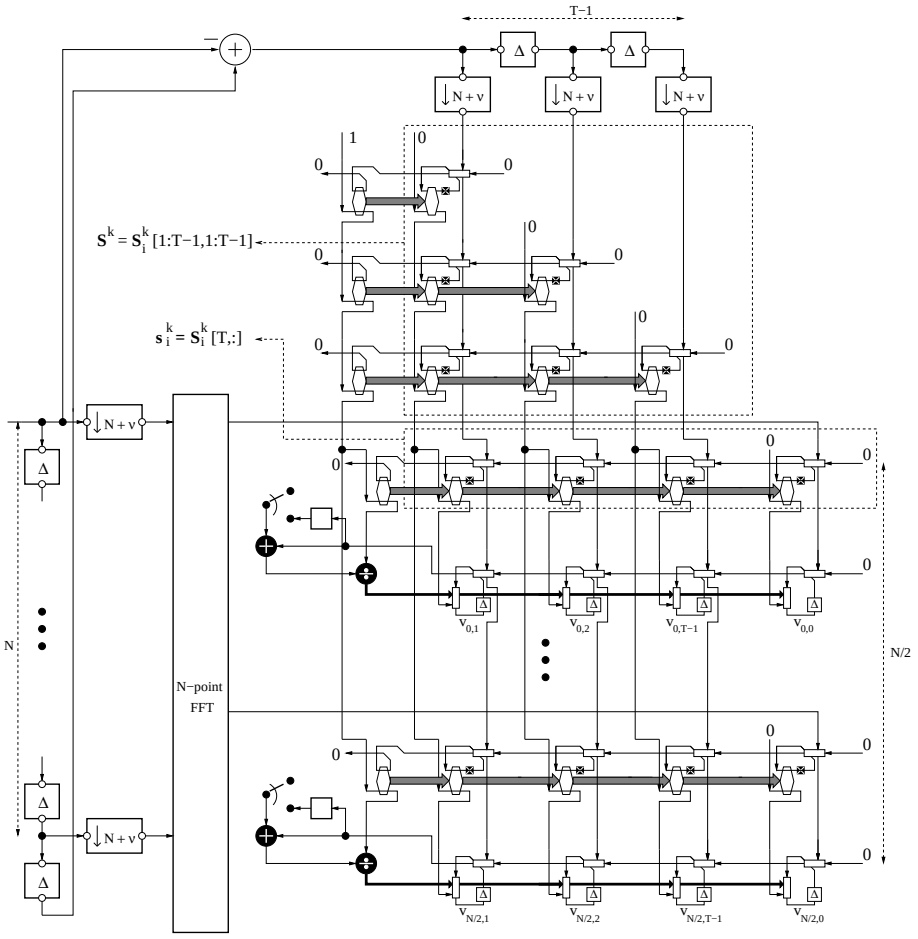

Figure 6.3: Signal flow graph of SR-RLS for PTEQ initialization.

ably inexpensive. It would be interesting if the per tone part could be simplified while preserving the fast convergence of SR-RLS.

A solution exists in applying the split SR-RLS of Subsection 6.2. Again, several parallel split SR-RLS problems have to be solved: one for each PTEQ. The distinct nature of the PTEQ inputs leads to a straightforward separation of the inputs into $T_1 = T - 1$ tone-independent difference terms and $T_2 = 1$ tone-dependent DFT output. Using the same terminology as in Subsection 6.2, a $(T-1)$-dimensional matrix $\mathbf{S}_{1,i}^k$ and a 1-dimensional matrix $\mathbf{S}_{2,i}^k$ have to be updated for each tone. Also here, $\mathbf{S}_{1,i}^k$ will be real valued and common for all the tones, whereas $\mathbf{S}_{2,i}^k = s_i^k$ will be a complex valued, tone-dependent scalar. In fact, $\mathbf{S}_{1,i}^k$ is exactly equal to $\mathbf{S}^k$ of the SR-RLS algorithm in **Table 6.4**.

TABLE 6.5
Algorithm: RLS-LMS for PTEQ initialization

Initialize $\mathbf{S}^{-1}$ and $\bar{\mathbf{v}}_i^{-1}$, e_i^{-1} for each tone $i \in \mathcal{S}$.
For $k = 0, \ldots, \infty$

- *Tone-independent part:* See **Table 6.4**.
- *Tone-dependent part*

  For $i \in \mathcal{S}$

  1. Accumulate the energy of the DFT output of tone i in order to scale the DFT output in a similar way as the difference terms

$$e_i^k \leftarrow \epsilon^2 e_i^{k-1} + (Y_i^k)^* Y_i^k. \tag{6.56}$$

  2. Update $\bar{\mathbf{v}}_i^{k-1}$:

$$\bar{\mathbf{v}}_i^k \leftarrow \bar{\mathbf{v}}_i^{k-1} + \mu \underbrace{\begin{bmatrix} \mathbf{k} \\ \frac{(Y_i^k)^*}{e_i^k} \end{bmatrix}}_{\mathbf{l}_i^k} \left(d_i^k - (\bar{\mathbf{v}}_i^{k-1})^T \mathbf{z}_i^k\right). \tag{6.57}$$

  end
end

According to (6.24), the PTEQ coefficients for tone i will now be updated in the direction determined by the Kalman gain type vector

$$\mathbf{l}_i^k = \left[\begin{array}{c|c} (\mathbf{S}^k)^T \mathbf{S}^k & \mathbf{0}_{(T-1)\times 1} \\ \hline \mathbf{0}_{1\times(T-1)} & s_i^k (s_i^k)^* \end{array}\right] (\mathbf{z}_i^k)^*. \tag{6.54}$$

The last element of $\mathbf{l}_i^k$ (6.54) is merely a scaled version of the DFT output for tone i. Similar to (6.9), it is possible to rewrite $s_i^k (s_i^k)^*$ as

$$\left(s_i^k (s_i^k)^*\right)^{-1} = \sum_{j=0}^{k} \epsilon^{2(k-j)} Y_i^k (Y_i^k)^*. \tag{6.55}$$

Hence, the scale factor $s_i^k (s_i^k)^*$ in (6.54) is just the inverse of the averaged DFT output energy for tone i. Stated differently: to obtain the update vector of (6.54), the difference terms are treated in RLS sense, while the DFT output is treated in NLMS sense. Therefore, the split SR-RLS for PTEQ initialization will be referred to as *RLS-LMS*. The resulting algorithm is given in **Table 6.5**. Note that e_i^k, $\mathbf{S}^k$ and the first $T-1$ elements of $\mathbf{l}_i^k$ have real values.

In a sense, the RLS part is used to improve the eigenvalue spread of the difference terms, while NLMS is applied to the DFT output. According to Appendix E.2, the resulting eigenvalue spread of the proposed RLS-LMS scheme

only depends on three unequal eigenvalues. Hence, one can state that RLS-LMS solves an LMS problem with 3 distinct eigenvalues. In general, LMS algorithms do not experience significant convergence problems in the case of an ill conditioned 3-dimensional problem.

As a second argument for the favorable convergence of the combined RLS-LMS approach, one can observe that the noise is averaged due to the exponential weighting. A pure LMS update is characterized by a large eigenvalue spread as well as a noisy version of the true gradient, leading both to slow convergence [54]. In the proposed algorithm the noise is averaged resulting in a more reliable update direction.

The RLS-LMS SFG is depicted in **Fig. 6.4**, which clearly illustrates the reduced per tone complexity compared to **Fig. 6.3** .

6.3.5 Complexity

In this subsection, the computational complexity for the different PTEQ initialization algorithms will be computed. In the complexity calculations, only the number of *real multiplications* and *real additions* per iteration will be considered, e.g. a multiplication of 2 complex numbers is counted as 4 real multiplications. Divisions and square-roots are not counted. Note again that the difference terms are real and the PTEQ coefficients are complex valued. The complexity associated with the construction of the difference terms and the product $(\bar{\mathbf{v}}_i^{k-1})^T \mathbf{z}_i^k$ is not counted, since this belongs to the 'filtering' complexity[4].

1. The complexity of NLMS is summarized in **Table 6.6**. Note that the per tone part should be multiplied by the number of used tones N_u to obtain the overall complexity.
2. Referring to **Fig. 6.3**, SR-RLS contains a real valued common part, due to the $T-1$ real valued common difference terms, as well as a complex valued per tone part. The complexity of the common part and the per tone part is given in **Table 6.7** and **Table 6.8** respectively. Since the common part is the same for SR-RLS as well as RLS-LMS, it can be described by equations (6.45) through (6.48). With SR-RLS, the Kalman gain vector in the per tone part is complex valued, resulting in extra complexity for the filter update compared to NLMS.
3. The combined RLS-LMS contains the same common part as SR-RLS, but has a significantly lower number of per tone computations. Comparing **Table 6.8** and **Table 6.9**, one can see that a substantial per tone complexity reduction is achieved.

[4]The 'filtering' complexity has to performed at symbol rate, while the 'initialization' complexity can be performed at a much lower rate.

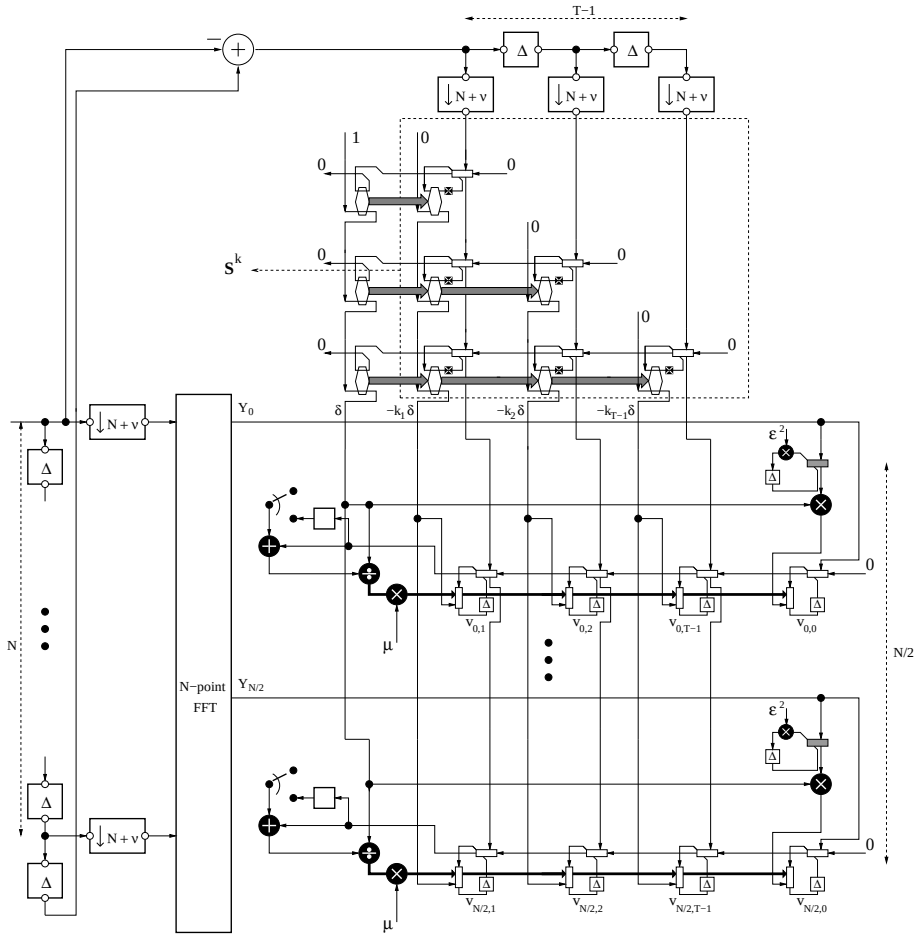

Figure 6.4: Signal flow graph of RLS-LMS for PTEQ initialization.

For a typical downstream ADSL setup with $N = 512$, $T = 16$ and approximately $N_u = N/2$ used tones, the number of real multiplications per iteration is depicted in **Fig. 6.5**. For a typical value of $T = 16$, a roughly 7-fold complexity reduction per iteration is obtained with RLS-LMS compared to SR-RLS. Also note that the RLS-LMS complexity is roughly equal to the NLMS complexity. Apart from the reduced complexity, the memory requirement for the per tone part are reduced as well. In the SR-RLS scheme the main part of the memory is assigned to store the T complex filter coefficients $\bar{\mathbf{v}}_i^k$ and the elements of the lower triangular matrix $\mathbf{S}_i^k$ for each tone i. Due to the real valued common difference terms $\mathbf{S}_i^k[1:T-1, 1:T-1]$ is real and common for all tones, while T complex numbers of $\mathbf{S}_i^k[T, 1:T]$ remain to be stored for each tone. For RLS-LMS the latter part disappears and instead only the real values e_i^k need

TABLE 6.6
Complexity of the tone-independent and tone-dependent part of NLMS for PTEQ initialization.

Common part	# add's	# mult's
$s = \|\Delta \mathbf{y}^k\|_2^2$	$T-2$	$T-1$
Total	$T-2$	$T-1$
Per tone part	# add's	# mult's
(1)= β^2	0	0
(2)= $s + (Y_i^k)^* Y_i^k$	2	2
(3)= $\frac{\mu}{\beta^2+(2)}$	1	0
(4)= $(d_i^k - (\bar{\mathbf{v}}_i^{k-1})^T \mathbf{z}_i^k)$	2	0
(5)=(3)·(4)	0	2
(6)=(5)·$(\mathbf{z}_i^k)^*$	2	$2(T-1)+4$
$\bar{\mathbf{v}}_i^k$=$\bar{\mathbf{v}}_i^{k-1}$+(6)	$2T$	0
Total	$2T+7$	$2T+6$

TABLE 6.7
Complexity of the common part of SR-RLS and RLS-LMS for PTEQ initialization.

Common part	# add's	# mult's
(1)=$-\mathbf{S}^{k-1}\Delta\mathbf{y}^k$	$\frac{(T-1)(T-2)}{2}$	$\frac{T(T-1)}{2}$
(2)=Givens $\tau = \frac{x}{y}$, $s = \frac{1}{\sqrt{1+\tau^2}}$, $c = s\tau$	$T-1$	$2(T-1)$
(3)=δ	$T-1$	$2(T-1)$
(4)=$-\delta\mathbf{k}$ & $\mathbf{S}^k$ update	$T(T-1)$	$2T(T-1)$
(5)=$\mathbf{S}^k/\epsilon$	0	$\frac{T(T-1)}{2}$
Total	$\frac{(T-1)(3T+2)}{2}$	$\frac{(T-1)(6T+8)}{2}$

TABLE 6.8
Complexity of the tone-dependent part of SR-RLS for PTEQ initialization.

Per tone part	# add's	# mult's
(1)=$-\mathbf{s}_i^{k-1}\mathbf{z}_i^k$	$2T$	$2(T+1)$
(2)=Givens, δ_i, $-\delta_i\mathbf{k}_i^k$, $\mathbf{s}_i^k$	$5T+1$	$9T+5$
(3)=$\mathbf{s}_i^k/\epsilon$	0	$2T$
(4)=$(d_i^k - (\bar{\mathbf{v}}_i^{k-1})^T\mathbf{z}_i^k)/\delta_i$	2	0
(5)=$(-\delta_i\mathbf{k}_i^k)$·(4)	$2T$	$4T$
$\mathbf{v}_i^k$=$\mathbf{v}_i^{k-1}$−(5)	$2T$	0
Total	$11T+3$	$17T+7$

TABLE 6.9
Complexity of the tone-dependent part of RLS-LMS for PTEQ initialization.

Per tone part	# add's	# mult's
$e_i^k = \epsilon^2 e_i^{k-1} + (Y_i^k)^* Y_i^k$	2	3
(1)=$\mu(d_i^k - (\bar{\mathbf{v}}_i^{k-1})^T \mathbf{z}_i^k)$	2	2
(2)=(1)$\cdot \mathbf{l}_i^k$	2	$2(T+1)$
$\mathbf{v}_i^k$=$\mathbf{v}_i^{k-1}$+(2)	$2T$	0
Total	$2T+6$	$2T+7$

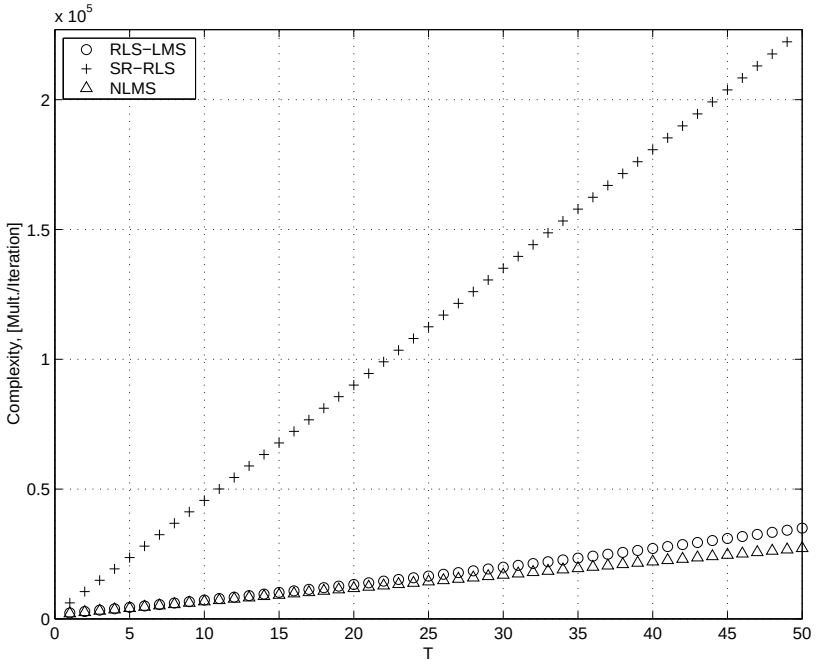

Figure 6.5: Initialization complexity for the downstream PTEQs.

to be stored. Hence, when T is small compared to the number of used tones, the common part is almost negligible and approximately a 2-fold reduction in memory is obtained with RLS-LMS compared to SR-RLS.

In the upstream case, the reduction in computational complexity is roughly by a factor 3, since less tones are used ($T = 40, N_u = 25$). However, the 2-fold reduction for the memory requirement of the per tone part still holds. Hence, RLS-LMS is also favorable for upstream initialization.

In this subsection, the computational complexity was expressed only in terms of additions and multiplications per iteration. A more detailed study with finite word lengths is required to obtain the overall complexity for implementation in hardware. This is, however, beyond the scope of this text.

6.4 Split SR-RLS for PTEQ/PTEC initialization

In this section, the split SR-RLS algorithm will be applied to the combined initialization of the PTEQ and PTEC-based receiver. First, per tone echo cancellation combined with per tone equalization will be briefly reviewed in Subsection 6.4.1. Then, the initialization algorithms based on NLMS, SR-RLS and split SR-RLS will be discussed in Subsections 6.4.2, 6.4.3 and 6.4.4. The section concludes with complexity calculations in Subsection 6.4.5.

6.4.1 Joint per tone echo cancellation and per tone equalization

In Chapter 5, it was explained that the available sub-channels in ADSL are assigned to either the up- or downstream transmission direction, or to both. When transmitted signals leak into the receive side of the modem, *echo* occurs. To allow efficient bidirectional communication over one twisted-pair *echo cancellation* is required to separate up- and downstream channels.

In the previous chapter, one of the underlying assumptions was that the equalizer and the echo canceler coefficients are designed independently. However, as noted in [146], the equalizer can help the echo canceler to shorten, besides the far end channel, also the echo impulse response, thereby reducing the echo canceler's complexity. Therefore, we will focus in this subsection on the *per tone echo cancelers (PTEC)*, where the bank of per tone equalizers is extended with a bank of per tone echo cancelers [137][138]. The resulting structure can then jointly be optimized for each tone $i \in S$. Although a PTEC-based receiver structure is more complex than the echo canceling of Chapter 5, the PTEQ/PTEC approach is able *to maximize the achievable bit rate for a given number of equalizer and echo canceler taps per tone.*

Similar to (3.111) and (3.112), which describe the conversion of a TEQ to a PTEQ, one can write the receiver output for tone i as

$$\begin{aligned} \hat{X}_i^k &= D_i \mathcal{F}_N[i,:](\mathbf{Y}^k\mathbf{w} - \mathbf{U}^{k-1,k,k+1}\mathbf{M}\mathbf{w}_E), && (6.58)\\ &= \mathcal{F}_N[i,:](\mathbf{Y}^k\mathbf{w}_i - \mathbf{U}^{k-1,k,k+1}\mathbf{M}\mathbf{w}_{E,i}), && (6.59)\\ &= \mathrm{row}_i(\mathcal{F}_N\mathbf{Y}^k)\mathbf{w}_i - \mathrm{row}_i(\mathcal{F}_N\mathbf{U}^{k-1,k,k+1}\mathbf{M})\mathbf{w}_{E,i}, && (6.60) \end{aligned}$$

where D_i is the FEQ for tone i, $\mathbf{Y}^k$ is an $N \times T$ Toeplitz matrix with received time domain samples and $\mathbf{U}^{k-1,k,k+1}\mathbf{M}$ is an $N \times T_E$ Toeplitz matrix with transmitted echo samples (cf. (6.5)). The matrix-vector products $\mathbf{Y}^k\mathbf{w}$ and $\mathbf{U}^{k-1,k,k+1}\mathbf{M}\mathbf{w}_E$ represent the T-taps TEQ filtering and T_E-taps TD-EC respectively. By incorporating D_i into $\mathbf{w}$ and $\mathbf{w}_E$, one obtains a complex valued PTEQ $\mathbf{w}_i$ and PTEC $\mathbf{w}_{E,i}$ for each tone separately.

The DFTs of the Toeplitz matrices $\mathbf{Y}^k$ and $\mathbf{U}^{k-1,k,k+1}$ in (6.60) can again be expressed in terms of difference terms. Let $\mathbf{y}^k$ denote the overall received signal vector of length $N+T-1$ and $\tilde{\mathbf{u}}^k$ the $N+T_E-1$-dimensional input vector for the echo canceler (see Subsection 2.3.2 for a definition of $\mathbf{y}^k$ and $\tilde{\mathbf{u}}^k$), then the output of the joint PTEQ/PTEC for tone i can be written as:

$$\hat{X}_i^k = \bar{\mathbf{v}}_i^T \left[\begin{array}{c|c|c} \mathbf{I}_{T-1} & \mathbf{0} & -\mathbf{I}_{T-1} \\ \hline \mathbf{0} & \multicolumn{2}{c}{\mathcal{F}_N[i,:]} \end{array}\right] \mathbf{y}^k + \bar{\mathbf{v}}_{E,i}^T \left[\begin{array}{c|c|c} \mathbf{I}_{T_E-1} & \mathbf{0} & -\mathbf{I}_{T_E-1} \\ \hline \mathbf{0} & \multicolumn{2}{c}{\mathcal{F}_N[i,:]} \end{array}\right] \tilde{\mathbf{u}}^k, \quad (6.61)$$

$$= \left[\begin{array}{cc} \bar{\mathbf{v}}_i^T & \bar{\mathbf{v}}_{E,i}^T \end{array}\right] \left[\begin{array}{c} \Delta\mathbf{y}^k \\ Y_i^k \\ \Delta\tilde{\mathbf{u}}^k \\ \tilde{U}_i^k \end{array}\right], \quad (6.62)$$

where $\bar{\mathbf{v}}_i$ and $\bar{\mathbf{v}}_{E,i}$ are the modified PTEQ and PTEC for tone i and $\Delta\mathbf{y}^k$, $\Delta\tilde{\mathbf{u}}^k$, Y_i^k and $\tilde{U}_i^k$ are the $T-1$ difference terms of the received signal, the T_E-1 difference terms of the echo reference signal and the corresponding DFT outputs for tone i respectively. The (unconstrained) MMSE solution for $\bar{\mathbf{v}}_i$ and $\bar{\mathbf{v}}_{E,i}$ can be obtained as

$$\left[\begin{array}{c} \bar{\mathbf{v}}_{opt,i} \\ \bar{\mathbf{v}}_{opt,E,i} \end{array}\right] = \arg \min_{\bar{\mathbf{v}}_i, \bar{\mathbf{v}}_{E,i}} \mathcal{E}\left\{\left(\hat{X}_i^k(\bar{\mathbf{v}}_i, \bar{\mathbf{v}}_{E,i}) - X_i^k\right)^2\right\}. \quad (6.63)$$

Also here, the *linear combiners*, $\bar{\mathbf{v}}_i$ and $\bar{\mathbf{v}}_{E,i}$, have to be initialized for each tone $i \in \mathcal{S}$. The input vector in (6.62) has similar properties as the PTEQ-only problem:

- $\Delta\mathbf{y}^k$ and $\Delta\tilde{\mathbf{u}}^k$ are $(T-1)+(T_E-1)$ *real valued* difference terms, common for all the frequency bins,
- Y_i^k and $\tilde{U}_i^k$ are 2 *complex valued* DFT outputs for each tone i.

By reordering the inputs, it is possible to separate the common part and the per tone part, i.e.

$$\hat{X}_i^k = \underbrace{\left[\begin{array}{cccc} \bar{\mathbf{v}}_i^T[1\!:\!T-1] & \bar{\mathbf{v}}_{E,i}^T[1\!:\!T_E-1] & \bar{\mathbf{v}}_i[T-1] & \bar{\mathbf{v}}_{E,i}[T_E-1] \end{array}\right]}_{\mathbf{v}_{tot,i}^T} \underbrace{\left[\begin{array}{c} \Delta\mathbf{y}^k \\ \Delta\tilde{\mathbf{u}}^k \\ Y_i^k \\ \tilde{U}_i^k \end{array}\right]}_{\mathbf{z}_{tot,i}^k}. \quad (6.64)$$

TABLE 6.10
Algorithm: NLMS for PTEQ/PTEC initialization

Initialize the PTEQ and PTEC coefficients $\bar{\mathbf{v}}_i^{-1}$, $\bar{\mathbf{v}}_{E,i}^{-1}$ for each tone $i \in \mathcal{S}$.
For $k = 0, \ldots, \infty$

- *Tone-independent part*

$$s = \|\Delta \mathbf{y}^k\|_2^2 + \|\Delta \tilde{\mathbf{u}}^k\|_2^2. \tag{6.65}$$

- *Tone-dependent part*

  For $i \in \mathcal{S}$

$$\begin{aligned} \|\mathbf{z}_{tot,i}^k\|_2^2 &= s + (Y_i^k)^* Y_i^k + (\tilde{U}_i^k)^* \tilde{U}_i^k, \qquad (6.66)\\ \mathbf{v}_{tot,i}^k &\leftarrow \mathbf{v}_{tot,i}^{k-1} + \frac{\mu}{\alpha^2 + \|\mathbf{z}_{tot,i}^k\|_2^2} (\mathbf{z}_{tot,i}^k)^* \left(d_i^k - (\mathbf{v}_{tot,i}^{k-1})^T \mathbf{z}_{tot,i}^k\right). \end{aligned}$$

  end
end

In the following, the initialization of $\mathbf{v}_{tot,i}$ by means of the NLMS, SR-RLS and split SR-RLS adaptive algorithms will be discussed.

6.4.2 NLMS-based PTEQ/PTEC initialization

Each PTEQ and PTEC can be updated jointly by means of the NLMS algorithm. An outline of the resulting algorithm is given in **Table 6.10**. Simulations showed that NLMS convergence is extremely slow for this particular problem. Hence, more advanced initialization algorithms based on SR-RLS or split SR-RLS are required.

6.4.3 SR-RLS-based PTEQ/PTEC initialization

The application of SR-RLS to initialize the PTEQ/PTEC coefficients requires the update and storage of a $(T + T_E - 2) \times (T + T_E - 2)$ real valued, upper triangular matrix $\mathbf{S}^k$, which is *common* for all the tones. In addition, since the DFT outputs are taken as the last inputs to the SR-RLS-structure, a $2 \times (T+T_E)$-dimensional *tone-dependent* part $\mathbf{S}_i^k$ has to be updated (and stored) for each tone $i \in \mathcal{S}$. This is similar to the PTEQ-only initialization problem, except that there are now two tone-dependent inputs per linear combiner. Again, it has to be stressed that the separation into a common and a tone-dependent part is due to the reordering of the inputs. The resulting algorithm is outlined in **Table 6.11**. The convergence rate of SR-RLS will be much higher than

TABLE 6.11
Algorithm: SR-RLS for PTEQ/PTEC initialization

Initialize $\mathbf{S}^{-1}$ and $\mathbf{v}_{tot,i}^{-1}$, $\mathbf{S}_i^{-1}$ for each tone $i \in \mathcal{S}$.
For $k = 0, \ldots, \infty$

- *Tone-independent part*

  1. Form the matrix-vector product:

$$\mathbf{b} = -\mathbf{S}^{k-1} \left[(\Delta \mathbf{y}^k)^T \quad (\Delta \tilde{\mathbf{u}}^k)^T \right]^T . \tag{6.67}$$

  2. For $m = 1, ..., T + T_E - 2$ determine the Givens rotations $\mathbf{Q}_{m(T+T_E-1)}$, cf. (A.13), where $\mathbf{Q}_{m(T+T_E-1)}$ zeroes out the m-th element of $\mathbf{b}$:

$$\begin{bmatrix} \mathbf{0}_{(T+T_E-2)\times 1} \\ \delta \end{bmatrix} = \mathbf{Q}_{(T+T_E-2)(T+T_E-1)} \cdots \mathbf{Q}_{1(T+T_E-1)} \begin{bmatrix} \mathbf{b} \\ 1 \end{bmatrix} . \tag{6.68}$$

  3. Update $\mathbf{S}^{k-1}$ and apply exponential weighting with ϵ:

$$\begin{bmatrix} \mathbf{S}^k \\ -\delta \mathbf{k}^T \end{bmatrix} \leftarrow \mathbf{Q}_{(T+T_E-2)(T+T_E-1)} \cdots \mathbf{Q}_{1(T+T_E-1)} \begin{bmatrix} \mathbf{S}^{k-1} \\ \mathbf{0} \end{bmatrix} , \tag{6.69}$$

$$\mathbf{S}^k \leftarrow \mathbf{S}^k / \epsilon. \tag{6.70}$$

- *Tone-dependent part*

  For $i \in \mathcal{S}$

  1. Form the product:

$$\mathbf{b}_i = -\mathbf{S}_i^{k-1} \mathbf{z}_{tot,i}^k . \tag{6.71}$$

  2. Determine the Givens rotations $\mathbf{Q}_{13,i}$ and $\mathbf{Q}_{23,i}$ such that:

$$\begin{bmatrix} \mathbf{0}_{2\times 1} \\ \delta_i \end{bmatrix} = \mathbf{Q}_{23,i} \mathbf{Q}_{13,i} \begin{bmatrix} \mathbf{b}_i \\ \delta \end{bmatrix} . \tag{6.72}$$

  3. Update $\mathbf{S}_i^{k-1}$ and apply exponential weighting with ϵ:

$$\begin{bmatrix} \mathbf{S}_i^k \\ -\delta_i (\mathbf{k}_i^k)^T \end{bmatrix} \leftarrow \mathbf{Q}_{23,i} \mathbf{Q}_{13,i} \begin{bmatrix} \mathbf{S}_i^{k-1} \\ \left[-\delta \mathbf{k}^T \quad \mathbf{0}_{1\times 2} \right] \end{bmatrix} , \tag{6.73}$$

$$\mathbf{S}_i^k \leftarrow \mathbf{S}_i^k / \epsilon. \tag{6.74}$$

  4. Update $\mathbf{v}_{tot,i}^{k-1}$:

$$\mathbf{v}_{tot,i}^k \leftarrow \mathbf{v}_{tot,i}^{k-1} + \mathbf{k}_i^k \left(d_i^k - (\mathbf{v}_{tot,i}^{k-1})^T \mathbf{z}_{tot,i}^k \right) . \tag{6.75}$$

  end
end

TABLE 6.12
Algorithm: Split SR-RLS for PTEQ/PTEC initialization

Initialize $\mathbf{S}_1^{-1} = \mathbf{S}^{-1}$ and $\bar{\mathbf{v}}_{tot,i}^{-1}$, $\mathbf{S}_{2,i}^{-1}$ for each tone $i \in \mathcal{S}$.
For $k = 0, \ldots, \infty$

- *Tone-independent part:* See **Table 6.11**.
- *Tone-dependent part*

  For $i \in \mathcal{S}$

  1. Form the matrix-vector product:

$$\mathbf{b}_{2,i} = -\mathbf{S}_{2,i}^{k-1} \left[Y_i^k \quad \tilde{U}_i^k \right]^T . \tag{6.76}$$

  2. Determine the Givens rotations $\mathbf{Q}_{13,i}$ and $\mathbf{Q}_{23,i}$ to zero out $\mathbf{b}_{2,i}$:

$$\begin{bmatrix} \mathbf{0}_{2\times 1} \\ \delta_{2,i} \end{bmatrix} = \mathbf{Q}_{23,i}\mathbf{Q}_{13,i} \begin{bmatrix} \mathbf{b}_{2,i} \\ 1 \end{bmatrix} . \tag{6.77}$$

  3. Update $\mathbf{S}_{2,i}^{k-1}$, determine the second part of the modified Kalman gain vector and apply exponential weighting with ϵ:

$$\begin{aligned} \begin{bmatrix} \mathbf{S}_{2,i}^k \\ -\delta_{2,i}\mathbf{k}_{2,i}^T \end{bmatrix} &\leftarrow \mathbf{Q}_{23,i}\mathbf{Q}_{13,i} \begin{bmatrix} \mathbf{S}_{2,i}^{k-1} \\ \mathbf{0}_{1\times 2} \end{bmatrix}, \\ \mathbf{S}_{2,i}^k &\leftarrow \mathbf{S}_{2,i}^k/\epsilon. \end{aligned} \tag{6.78}$$

  4. Update $\bar{\mathbf{v}}_i^{k-1}$:

$$\mathbf{v}_{tot,i}^k \leftarrow \mathbf{v}_{tot,i}^{k-1} + \mu \underbrace{\begin{bmatrix} \mathbf{k} \\ \mathbf{k}_{2,i} \end{bmatrix}}_{\mathbf{l}_i^k} \left(d_i^k - (\mathbf{v}_{tot,i}^{k-1})^T \mathbf{z}_{tot,i}^k \right) . \tag{6.79}$$

  end
end

NLMS, at the expense of a higher computational complexity and a higher memory requirement, mainly due to the tone dependent part.

6.4.4 Split SR-RLS-based PTEQ/PTEC initialization

To reduce the tone-dependent complexity and memory requirement of a full SR-RLS, the split SR-RLS (cf. **Table 6.2**) can be applied with $T_1 = T + T_E - 2$ and $T_2 = 2$. The matrix $\mathbf{S}_1^k$ will be constructed by means of $\Delta\mathbf{y}^k$ and $\Delta\tilde{\mathbf{u}}^k$ and is therefore equal to $\mathbf{S}^k$ of the full SR-RLS algorithm of Subsection 6.4.3. The second matrix $\mathbf{S}_{2,i}^k$ will be lower triangular of dimension 2×2, complex

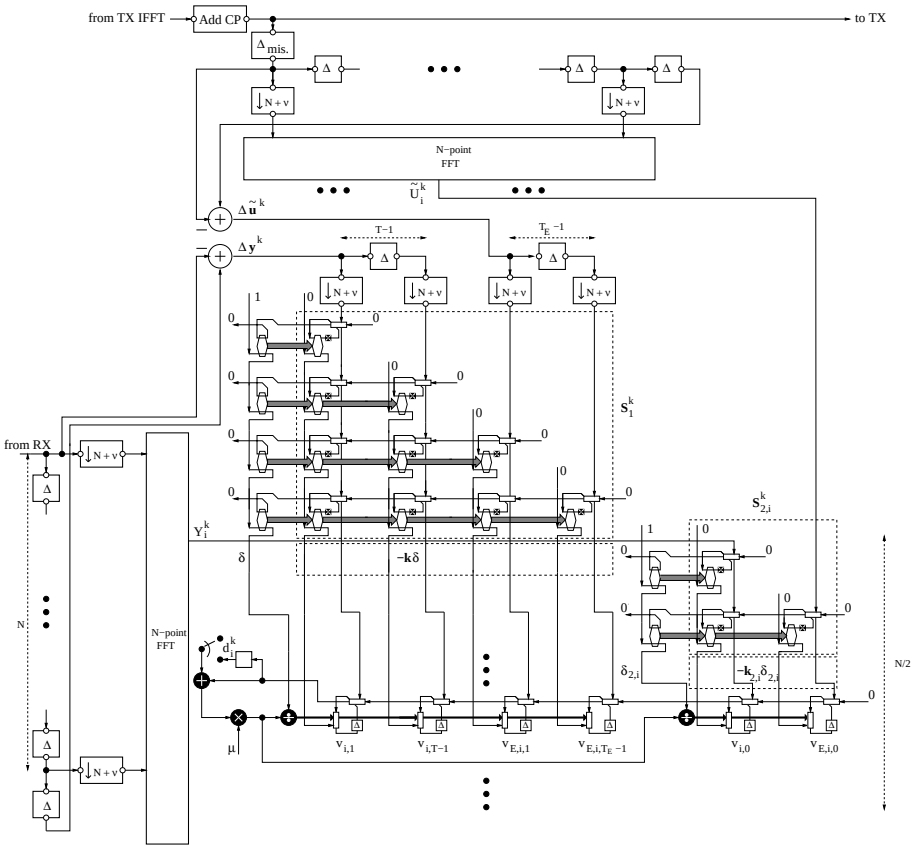

Figure 6.6: Signal flow graph of the split SR-RLS algorithm to initialize the joint PTEQ/PTEC problem.

valued and *tone-dependent*, since it receives Y_i^k and $\tilde{U}_i^k$ as inputs. The resulting initialization algorithm is given in **Table 6.12**.

Fig. 6.6 shows a SFG for the initialization of the PTEQ/PTEC receiver. Observe that $\mathbf{S}_1^k$ is common for all the tones and $\mathbf{S}_{2,i}^k$ has to be computed for each tone separately. Note that when considering only the first $T-1$ difference terms and Y_i^k as inputs in **Fig. 6.6**, the SFG for PTEQ-only initialization is obtained. It is clear that the smaller dimensions of $\mathbf{S}_{2,i}^k$ compared to $\mathbf{S}_i^k$ in the full SR-RLS algorithm lead to the desired complexity and memory savings.

6.4.5 Complexity

Based on **Table 6.10**, **Table 6.11** and **Table 6.12**, the computational complexity of NLMS, SR-RLS and split SR-RLS for PTEQ/PTEC initialization can

be computed. These computations are completely similar to Subsection 6.3.5 and therefore only the final results will be given. Note that due to the asymmetric character of ADSL data transmission, the upstream signal will typically be generated and demodulated by an (I)DFT size that is κ times smaller than the corresponding (I)DFT size for the downstream signal. This has some implications on the complexity and memory requirement:

- In a *downstream* ADSL scenario (modem at the customer premises), the echo transmit IDFT (upstream signal) is κ times *smaller* than the receive DFT. Van Acker et al. showed that due to this asymmetry, the number of PTEC taps can be reduced by a factor κ [129][137][138]. By this, the split SR-RLS scheme is able to save $2 \cdot (2 \cdot (T + T_E/\kappa - 2)) \cdot N_u$ memory places compared to full SR-RLS, where N_u is the number of used tones and the additional factor 2 is due to the complex valued elements.
- In the *upstream* case (modem at the central office), the echo transmit IDFT is κ times *larger* than the receive DFT size and, as a result, κ DFTs are required for the PTEC [129][137][138]. The matrix $\mathbf{S}_{2,i}^k$ in the split SR-RLS scheme will be of size $(\kappa + 1) \times (\kappa + 1)$ instead of the $(\kappa+1) \times (T+T_E)$-dimensional matrix $\mathbf{S}_i^k$ of the original SR-RLS. Hence, approximately $2 \cdot ((\kappa+1) \cdot (T+T_E-\kappa-1)) \cdot N_u$ memory places are saved.

With $T = 16$, $T_E = 200$, $\kappa = 8$ and $N_u = 223$ as typical values for downstream ADSL and $T = 40$, $T_E = 200$, $\kappa = 8$ and $N_u = 25$ for upstream ADSL, it is clear that substantial memory savings can be achieved with the split SR-RLS algorithm. In addition, the complexity (expressed in real valued operations per iteration) for the combined PTEQ/PTEC initialization can be computed. For *downstream* transmission, the overall complexity for the respective initialization algorithms becomes:

1. NLMS:
   $T + T_E/\kappa - 3 + N_u(2T + 2T_E/\kappa + 11)$ add./it.,
   $T + T_E/\kappa - 2 + N_u(2T + 2T_E/\kappa + 10)$ mult./it.,
2. SR-RLS:
   $\frac{(T+T_E/\kappa-2)(3T+3T_E/\kappa-1)}{2} + N_u(21T + 21T_E/\kappa + 5)$ add./it.,
   $\frac{(T+T_E/\kappa-2)(6T+6T_E/\kappa+2)}{2} + N_u(33T + 33T_E/\kappa + 9)$ mult./it.,
3. Split SR-RLS:
   $\frac{(T+T_E/\kappa-2)(3T+3T_E/\kappa-1)}{2} + N_u(2T + 2T_E/\kappa + 24)$ add./it.,
   $\frac{(T+T_E/\kappa-2)(6T+6T_E/\kappa+2)}{2} + N_u(2T + 2T_E/\kappa + 57)$ mult./it.

For *upstream* transmission, one has:

1. NLMS:
   $T + T_E - \kappa - 2 + N_u(2T + 2T_E + 4\kappa + 7)$ add./it.,
   $T + T_E - \kappa - 1 + N_u(2T + 2T_E + 4\kappa + 6)$ mult./it.,

TABLE 6.13
Complexity figures for the joint PTEQ/PTEC initialization, expressed in real additions and real multiplications per iteration with $T = 16$, $T_E = 200$, $\kappa = 8$ and $N_u = 223$ for downstream transmission and $T = 40$, $T_E = 200$, $\kappa = 8$ and $N_u = 25$ for upstream transmission.

		# add's/it.	# mult's/it.
Down	NLMS	$20.8 \cdot 10^3$	$20.6 \cdot 10^3$
	SR-RLS	$195.5 \cdot 10^3$	$308.6 \cdot 10^3$
	Split SR-RLS	$26.0 \cdot 10^3$	$35.8 \cdot 10^3$
Up	NLMS	$13.2 \cdot 10^3$	$13.2 \cdot 10^3$
	SR-RLS	$618.3 \cdot 10^3$	$1020.7 \cdot 10^3$
	Split SR-RLS	$105.7 \cdot 10^3$	$194.9 \cdot 10^3$

2. SR-RLS:
$\frac{(T+T_E-\kappa-1)(3T+3T_E-3\kappa+2)}{2} + N_u((10\kappa+11)(T+T_E)-5\kappa^2-2\kappa+3)$ add./it.,
$\frac{(T+T_E-\kappa-1)(6T+6T_E-6\kappa+8)}{2} + N_u((16\kappa+17)(T+T_E)-7(\kappa^2-1))$ mult./it.,

3. Split SR-RLS:
$\frac{(T+T_E-\kappa-1)(3T+3T_E-3\kappa+2)}{2} + N_u(2(T+T_E)+6\kappa^2+16\kappa+12)$ add./it.,
$\frac{(T+T_E-\kappa-1)(6T+6T_E-6\kappa+8)}{2} + N_u(2(T+T_E)+9\kappa^2+31\kappa+24)$ mult./it.

Based on the previously given ADSL parameter values, the overall computational complexity is summarized in **Table 6.13**. For downstream transmission, the split SR-RLS is roughly 9 times less expensive per iteration than SR-RLS, while in upstream, the split SR-RLS introduces a 5-fold complexity reduction. Simulations will show that the convergence rate of NLMS is too slow for ADSL applications, since the time to convergence exceeds the number of training symbols foreseen in the start-up phase of an ADSL modem.

6.4.6 Similar applications

Finally, we want to mention briefly some other ADSL initialization problems, where a similar split SR-RLS approach could be followed.

- In [38], a PTEQ-based receiver structure with a fixed window is described, which requires the initialization of T coefficients for each tone. The fixed window is added in front of the demodulating DFT to mitigate narrowband radio frequency interference (RFI). When e.g. a trapezoidal window is used, the split SR-RLS algorithm could be applied (similar to

Section 6.4) with $T_1 = 2(T-2)$ (tone-independent) and $T_2 = 2$ (tone-dependent). For a raised cosine window, the following values are required: $T_1 = 2(T-2)$ and $T_2 = 3$.

- In [145], per tone equalization in combination with the mitigation of a dominant alien near-end cross-talker such as HDSL, SDSL or HPNA is addressed. Again, initialization of T coefficients with the split SR-RLS is possible with $T_1 = 2(T-2)$ (tone-independent) and $T_2 = 2$ (tone-dependent).

For further details on these applications, we refer to the corresponding papers.

6.5 Simulation results

As a performance measure for the simulations, the overall bit rate and the SNR for tone i, as defined in Chapter 4, will be used. The convergence rate is expressed in terms of the bit rate, since it captures the convergence of the SNRs of the different tones in a uniquely determined way. Moreover, it is the only relevant way to combine the tone dependent SNRs into one measure representing all the tones. The bit rate is computed according to

$$r = F_{sym} \sum_{i \in \mathcal{S}} b_i, \tag{6.80}$$

$$b_i = \left\lfloor \log_2 \left(1 + 10^{((\mathrm{SNR}_i - \Gamma - \gamma_m + \gamma_c)/10)} \right) \right\rfloor, \tag{6.81}$$

where b_i is the number of bits assigned to tone i, $\mathcal{S}$ is the set of used tones, F_{sym} is the symbol rate, Γ is the SNR gap, γ_m the noise margin and γ_c the coding gain. In the simulations the following values will be used: $F_{sym} = 4.0588$ kHz, $\Gamma = 9.8$ dB, $\gamma_m = 6$ dB and $\gamma_c = 3$ dB. The SNR for tone i is given by

$$\mathrm{SNR}_i = \frac{\mathcal{E}\{|X_i^k|^2\}}{\mathcal{E}\{|X_i^k - \hat{X}_i^k|^2\}}, \tag{6.82}$$

where $\hat{X}_i^k$ denotes the PTEQ output for tone i. A ZF FEQ was included in the PTEQ coefficients to remove the bias that is present due to the unconstrained MMSE cost function, as discussed in Subsection 6.3.1.

In Subsection 6.5.1, simulation results for the PTEQ-only initialization problem are presented. The PTEQ-based receiver is then extended with PTEC for which simulation results can be found in Subsection 6.5.2.

6.5.1 PTEQ initialization

Convergence behaviour

Simulations were performed on a standard downstream CSA #4 loop with additive white Gaussian noise of -140 dBm/Hz and 24 DSL NEXT disturbers.

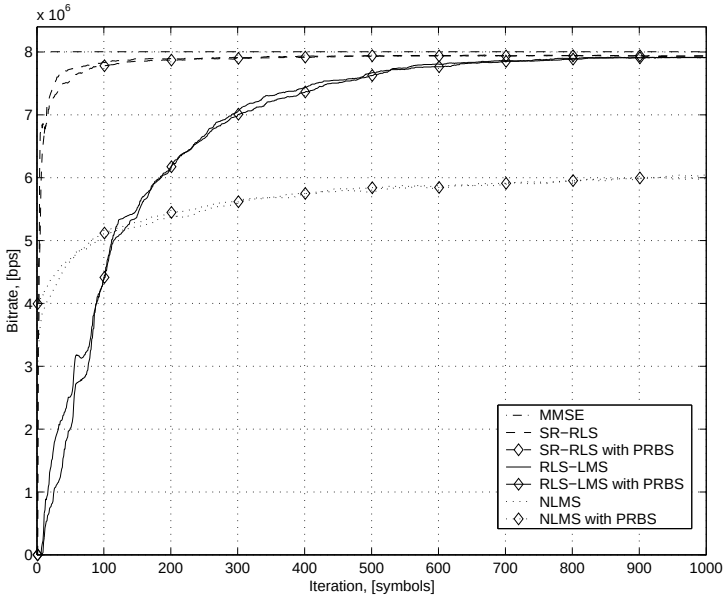

Figure 6.7: Comparison of different initialization procedures for the per tone equalizers with $T = 24$ for CSA #4 with 24 DSL NEXT disturbers (downstream).

Front end filters to separate up- and downstream transmission are included in the channel. It is assumed that echo is perfectly cancelled. The used tones range from 33 up to tone 255. Other parameters are: the number of PTEQ taps $T = 24$, the step size for NLMS $\mu = 0.1$, the step size for RLS-LMS $\mu = 1$ and the exponential weighting $\epsilon = 0.998$.

In **Fig. 6.7**, the learning curves of SR-RLS, NLMS and RLS-LMS for PTEQ-only initialization are shown, where the initial values for the PTEQ coefficients are equal to $[0\ 0 \ldots\ 1]^T$ and where $\mathbf{S}^k$ is initialized with $10^5 \cdot \mathbf{I}_{T-1}$. The curves are compared with the bit rate corresponding to the MMSE PTEQ. For the adaptive algorithms, two types of training sequences are used:

- a white training sequence, where data on different tones and different symbols are uncorrelated,
- a pseudo random binary sequence (PRBS), as defined in the ADSL standard, used during the start-up phase of the ADSL modem [63].

In the figure, one can clearly see the fast convergence of RLS-LMS, which is in between SR-RLS and NLMS. SR-RLS initialization needs approximately 200 symbols to converge, while the combination of RLS and LMS reaches the

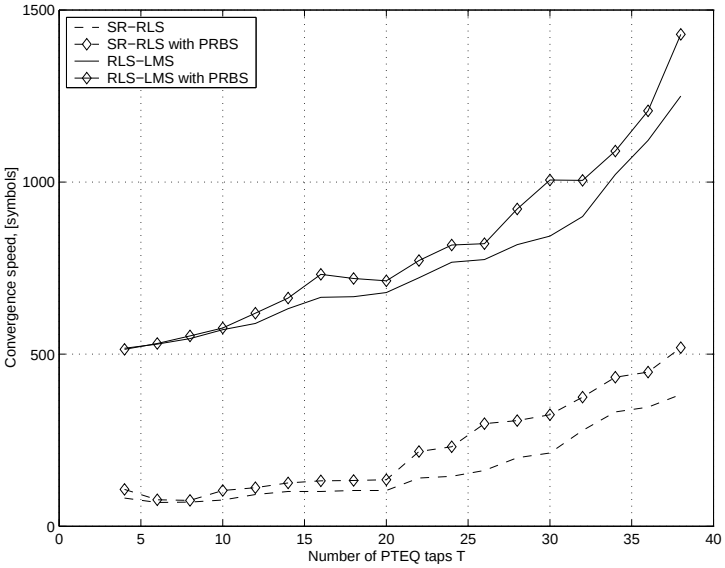

Figure 6.8: Convergence speed of SR-RLS and RLS-LMS for CSA #4 with 24 DSL NEXT disturbers.

optimal value after roughly 1000 symbols. Notice that after 1000 symbols NLMS has still not converged. Even after 16384 training symbols as foreseen in the ADSL standard for modem initialization [63], the PTEQ obtained with NLMS has a performance far below the performance of the MMSE PTEQ. The learning curves obtained with the PRBS show almost no performance difference compared to the completely random training signal.

Convergence versus equalizer taps

Fig. 6.8 shows the number of iterations required to reach 98.5% of the bit rate corresponding to the MMSE PTEQ as a function of the number of equalizer taps T per tone. SR-RLS and RLS-LMS are considered with a random training signal or a PRBS for loop CSA #4 with additive white Gaussian noise of -140 dBm/Hz and 24 DSL NEXT disturbers. The figure suggests that the convergence speed decreases with the number of taps. However, this is an observation which is valid for SR-RLS as well. The PRBS training sequence shows a slightly slower convergence behaviour.

Different channel models

To illustrate the performance of the proposed algorithm for a wide range of channel models, simulations were performed for the downstream CSA #1-#8

TABLE 6.14
Convergence behaviour of SR-RLS and RLS-LMS for the CSA #1-#8 loops.

	# symbols to reach 99% of MMSE bit rate		bit rate
CSA loop	SR-RLS	RLS-LMS	MMSE
1	212	867	8.552 Mbps
2	534	943	8.816 Mbps
3	497	1244	7.882 Mbps
4	325	1127	8.001 Mbps
5	281	1111	8.808 Mbps
6	204	884	7.570 Mbps
7	375	965	6.945 Mbps
8	246	1085	6.864 Mbps

channels (for a loop configuration, see **Fig. 3.5**) with additive white Gaussian noise of -140 dBm/Hz and 24 DSL NEXT disturbers. **Table 6.14** indicates the number of iterations required to reach 99% of the bit rate obtained with the MMSE PTEQ for $T = 24$, $\epsilon = 0.998$, $\mu = 1$. The worst case convergence difference between SR-RLS and RLS-LMS is obtained for loop CSA #8, where RLS-LMS is approximately 4.4 times slower than SR-RLS.

Eigenvalues of $\mathbf{R}_{lz}$

Fig. 6.9 depicts the eigenvalue spread of $\mathbf{R}_{lz}$ on a logarithmic scale for RLS-LMS with $T = 16$ and $\epsilon = 0.999$ for a standard loop T1.601 #13 [63]. Here, $\mathbf{R}_{lz}$ is determined based on 3000 symbols. It can be seen that $T-2$ eigenvalues are equal and that 2 eigenvalues are clearly different. This is in accordance with the derivation in Appendix E.2. In the appendix, it was also shown that the $T-2$ eigenvalues will be equal to $\frac{1}{1-\epsilon^2}$. With $\epsilon = 0.999$, the $T-2$ equal eigenvalues are expected to be equal to $\log_{10} 1/500 = -2.7$. This is approximately equal to the value obtained with the simulation. In Appendix E.2, it was shown that the largest eigenvalue of $\mathbf{R}_{lz}$ is upper bounded by $2(1-\epsilon^2)$, which is equal to $\log_{10} 2(1-0.999^2) = -2.4$ in our simulation. Also this value is approximately confirmed by **Fig. 6.9**.

6.5.2 Joint PTEQ/PTEC initialization

The joint initialization of the PTEQ and PTEC will again be demonstrated for the 8 CSA standard loops with additive white Gaussian noise of -140 dBm/Hz

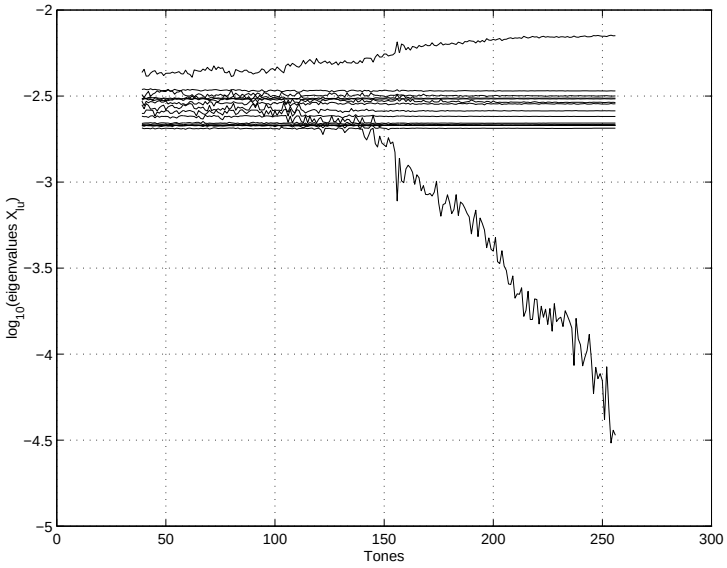

Figure 6.9: Eigenvalues of $\mathbf{R}_{lz}$ with $T = 16$ for standard channel T1.601 #13 with 24 DSL NEXT disturbers (downstream).

and 24 DSL NEXT disturbers. For downstream transmission, the used tones range from 33 to 255, while upstream transmission was simulated with tones 7 to 31.

Convergence behaviour

Fig. 6.10 shows typical power spectral densities of the received far-end, echo and channel noise signals before and after DFT demodulation for the CSA #1 loop. In this scenario, the upstream signal is modulated by a 64-point IDFT which causes echo due to aliasing and DFT leakage at the downstream receiver. For downstream transmission a 512-point transmit IDFT and received DFT are used, hence $\kappa = 8$. The PSD on the transmitted upstream and downstream tones are -38 dBm/Hz and -40 dBm/Hz respectively. The echo and far end channels include the transmission loop together with all the transmit and receive front end filters. Although the tones are 'separated' in frequency, one can clearly see that all the tones at the receiver are affected by echo. Hence, echo canceling on all sub-carriers is required.

Fig. 6.11 depicts the SNR evolution during convergence of the PTEQ and PTEC coefficients for the split SR-RLS scheme with $T = 16$, $T_E/\kappa = 25$, $\epsilon = 0.997$ and $\mu = 1$. The simulation was again performed for a downstream CSA #1 loop. The training and echo sequence where constructed using 4-

QAM modulation on all the tones. Notice that especially low frequency and high frequency tones have a relatively slow convergence due to the high ISI and ICI present in this region.

Different channel models

To illustrate the convergence rate of the split SR-RLS versus the original SR-RLS, simulations were performed on several CSA loops for PTEQ/PTEC initialization. Downstream and upstream bit rates as a function of the number of training symbols are depicted in **Fig. 6.12** and **Fig. 6.13** respectively. In the simulations, a 64-point DFT and IDFT and a 512-point DFT and IDFT were used for upstream and downstream transmission respectively. The downstream learning curves are simulated with $T = 16$, $T_E/\kappa = 25$, $\epsilon = 0.997$ and $\mu = 1$, while the upstream learning curves used $T = 40$, $T_E = 200$, $\epsilon = 0.999$ and $\mu = 1$. During the first $T + T_E$ training symbols, the coefficients of $\mathbf{v}_{tot,i}^k$ were not updated in order to initialize $\mathbf{S}_1$ and $\mathbf{S}_{2,i}$. The vector $\mathbf{v}_{tot,i}^k$ was initialized with all zeros and a one on the tap corresponding to Y_i^k. For this design problem, one observes that the split SR-RLS converges approximately 9 to 10 times slower than full SR-RLS, which still fits into the available ADSL training sequence.

6.6 Conclusions

In this chapter, we presented an efficient way to initialize the bank of per tone equalizers (PTEQ) and per tone echo cancelers (PTEC). The PTEQ/PTEC initialization problem is a linear combiner problem, where a set of unknown coefficients has to be found for each used tone. For each tone-dependent linear combiner, two distinct types of inputs can be distinguished, namely a set of tone-independent and a set of tone-dependent inputs.

Since direct MMSE initialization of the PTEQ and/or PTEC coefficients is computationally too complex to implement in hardware, adaptive initialization algorithms were reviewed at the beginning of this chapter. Based on SR-RLS and the split RLS algorithm, we developed the *split SR-RLS* scheme to obtain a convergence rate, complexity and memory requirement in between NLMS and full SR-RLS. The split SR-RLS essentially splits the inputs into two (or more) parts and executes the SR-RLS on each set of inputs. We showed that the method is convergent in the mean and that the convergence rate depends on the principal angles between the subspaces spanned by the first and the second input set. In addition, an upper bound for the step size was derived.

The split SR-RLS was successfully applied for the recursive initialization of the PTEQ-only. The difference terms were taken as the first set of inputs making

the first part in the split SR-RLS common for all the tones. The second set of inputs just included the DFT output for a particular tone and, as such, the second part in the split SR-RLS is tone-dependent and equivalent to NLMS on this input. Hence, the split SR-RLS for the PTEQ-only initialization problem was referred to as *RLS-LMS*. Due to a badly conditioned input correlation matrix, NLMS does not lead to convergence within the available number of ADSL training symbols. Fortunately, simulations clearly demonstrated an acceptably fast convergence of RLS-LMS, while keeping computational complexity close to NLMS. In addition, the memory requirement for RLS-LMS is substantially lower than for full SR-RLS.

Similarly, the split SR-RLS was used to initialize the PTEQ and PTEC in a joint way. Again, the nature of the inputs resulted in a common part and a tone-dependent part in the split SR-RLS scheme. While the convergence and the complexity was in between NLMS and SR-RLS, the split SR-RLS especially led to substantial memory savings. Finally, we briefly indicated how the presented algorithm could be applied to other DSL applications as well.

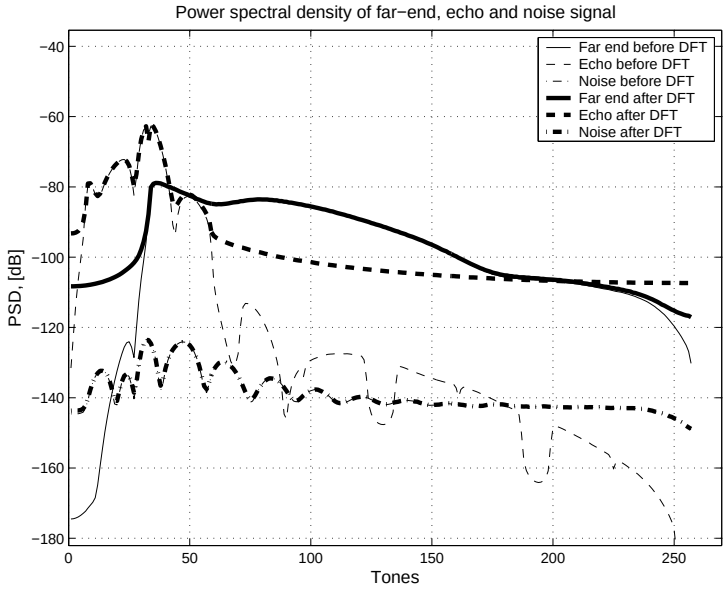

Figure 6.10: Power spectral densities (PSD) of received far end signal, echo and channel noise before and after DFT demodulation for CSA #1.

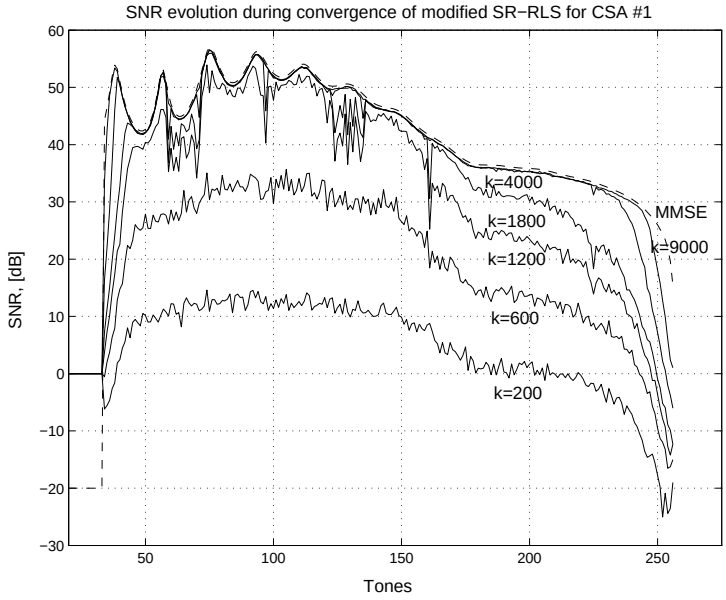

Figure 6.11: Evolution of the downstream SNR (CSA #1) during convergence for the split SR-RLS scheme. The upper curve indicates the maximal achievable SNR obtained by the MMSE solution for $\mathbf{v}_{tot,i}$.

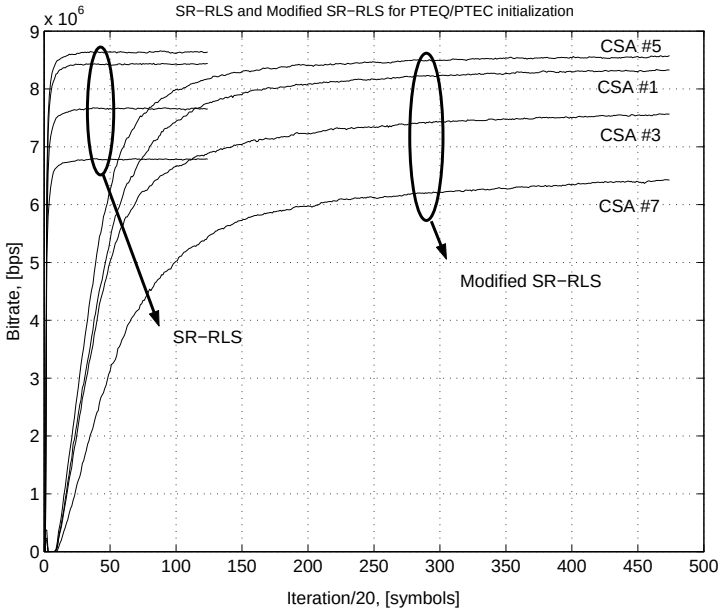

Figure 6.12: Downstream learning curves for the joint PTEQ/PTEC initialization using SR-RLS and split SR-RLS.

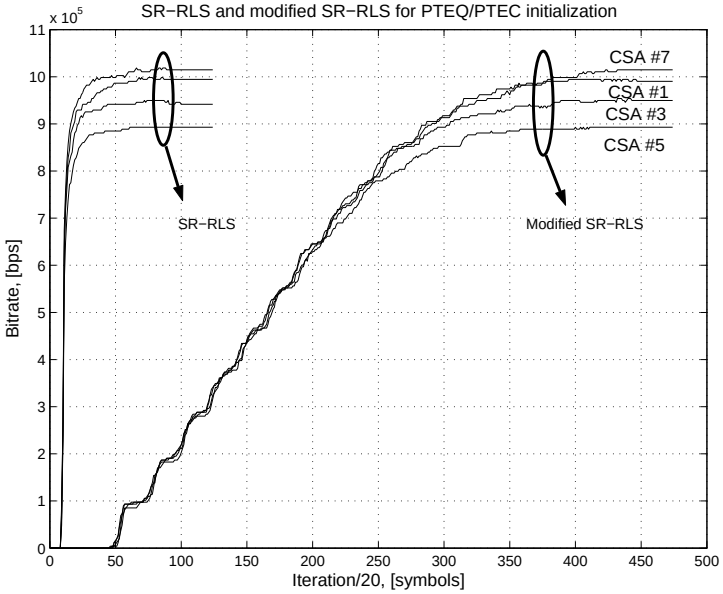

Figure 6.13: Upstream learning curves for the joint PTEQ/PTEC initialization using SR-RLS and split SR-RLS.

Chapter 7

Conclusions and further research

TO finalize this thesis, conclusions are drawn in Section 7.1 and some suggestions for further research are listed in Section 7.2.

7.1 Conclusions

With the arrival of the Internet, the demand of broadband communication has grown exponentially. DSL allows to achieve higher bit rates over the existing copper wire telephone network. In this thesis advanced digital signal processing algorithms were proposed to support these high bit rate requirements. More in particular, the thesis has focused on equalization and echo cancellation issues.

ADSL, ADSL2+ and VDSL use DMT modulation as the transmission format. In DMT a CP is inserted between consecutive transmitted symbols to ease equalization. When the duration of the channel impulse response is limited to the CP length, the phase and magnitude distortion introduced by the channel can easily be compensated by a one-tap FEQ per used tone. However, in e.g. ADSL, the time span of the channel impulse response exceeds the CP duration and an additional TEQ has to be inserted before DFT demodulation at the receiver. The task of the TEQ is to shorten the channel to the length of the CP, while, at the same time, avoiding noise enhancement. In DSL the ultimate TEQ design criterion is to maximize the bit rate of the communication system, which leads, however, to a non-linear optimization problem. As a consequence, many TEQ design algorithms have appeared in the literature. In Chapter 3, a unified mathematical framework and a unified notation was presented to

formulate the different TEQ designs as the maximization of a product of generalized Rayleigh quotients. The goal of this unified framework is to clarify the subtle differences between the different approaches. Within the common formulation, a distinction was made between three specific design cases: the maximization of a single generalized Rayleigh quotient, the maximization of a product of multiple generalized Rayleigh quotients and the maximization of a single generalized Rayleigh quotient for each tone separately. We showed that the first case comprises TEQ design methods with suboptimal performance, while the second case is required to truly maximize the bit rate with a single TEQ. Finally, by interchanging the order of TEQ filtering and the DFT demodulation, we end up with the design of an equalizer for each tone separately, i.e. the so-called per tone equalization.

In Chapter 3, we also treated the MMSE TEQ design criterion in more detail. The MMSE method minimizes the mean squared error between the TEQ output and the target impulse response. To avoid the trivial all zero solution an additional constraint has to be imposed. We showed that the MMSE TEQs with three different unit-energy constraints are essentially identical (up to a scale factor), resulting in the same performance in terms of bit rate. Moreover, an iterative initialization method, based on the power method or inverse iterations, was devised to obtain the TEQ solution for the three constraints. In addition, a geometrical interpretation revealed that the MMSE TEQ design subjected to unit-energy constraints is closely related to the principal angles between the subspaces spanned by the transmitted and received signals respectively.

Due to its large bandwidth occupation, DSL transmission is distorted by several narrowband RFIs. Due to the block based transmission, the DFT at the receiver will only process samples within a rectangular window of finite length. In the frequency domain, this leads to sinc shaped filtering characteristics with high sidelobes, leading to a bad spectral containment of the DFT filters. As a consequence, a narrowband interferer with high energy will be spread over almost all received DMT carriers. In Chapter 4, the sensitivity to RFI and the equalization problem is solved jointly by a combined equalizer and window design. We showed how to design a single TEQ and a single window, referred to as BM-WinTEQ, in order to maximize the bit rate of the overall system. The resulting cost function is non-linear and exhibits multiple local optima. Although no theoretical proof was given, simulations showed that the different local optima introduce almost no performance loss. Furthermore, the BM-WinTEQ design was placed in a broader framework, where a separate window and equalizer can be designed per group of used tones. In addition, we linked the per group design for a single tone to the constrained (unbiased) MMSE PTEQ, where the window operation is completely absorbed by additional PTEQ taps. Several special cases were addressed within this general framework: the bit rate maximizing design of a TEQ without windowing (BM-

TEQ), optimal TEQ design in the presence of a fixed window (BM-FWinTEQ), optimal window design without TEQ (BM-Win), ... Simulations showed that receiver windowing can help to solve the equalization problem and can reduce the sensitivity to RFI. Equalizer taps can be interchanged for some windowing coefficients, leading to a complexity reduced receiver. Furthermore, we noticed that the equalizer (preceding the demodulating DFT) is able to notch out stationary RFIs, while receiver windowing will improve the performance when non-stationary interferers are present.

Besides equalization and RFI mitigation, echo cancellation was investigated in this thesis. In DSL, the available bandwidth is assigned to the up- and/or downstream transmission direction. When the signals traveling in opposite directions of the loop occupy the same frequency band, the transmitted signal may leak into the receive side of the modem. This undesired leakage is called echo. In Chapter 5, several echo cancellation schemes were investigated and special attention was paid to cost efficient mixed time/frequency structures. In first instance, CES-based EC was reviewed, where echo emulation is partly executed in the time domain (CES) and partly in the frequency domain. We extended the CES-based echo canceler with a low complexity solution for DTC to cancel the far end signal in the update error of the coefficient adaptation process. Without DTC, the far end signal acts as an additional noise source for the echo canceler, which requires a small step size for a reasonably small misadjustment of the EC coefficients. DTC enables the use of a larger step size and hence results in improved tracking performance.

Secondly, the complexity of the CES-based EC as a function of the misalignment was reexamined. In the literature, it was shown that by choosing a specific misalignment between the echo and far end symbols, the complexity of the CES can be minimized. Unfortunately, the misalignment can only be chosen at one end of the loop leading to more complex EC at the other side. Here, we presented a modification to the existing CES-based EC (ITF-EC) to obtain minimal CES complexity irrespective of the alignment. Hence, both ends of the loop can minimize the complexity of their echo cancelers. In addition, we showed how the resulting structure can be supplemented with inexpensive DTC.

Finally, we pointed out in Chapter 5 that the previously discussed CES-based echo cancelers require extra power on unused echo reference tones to achieve convergence. We proposed an alternative EC scheme (CDC), which converges without additional transmitted power. The final scheme exhibits a comparable complexity as existing EC schemes and can easily be combined with per tone equalization and DTC to optimize the systems performance.

In Chapter 6, the recursive initialization of the PTEQ and the combined PTEQ/PTEC was discussed. As opposed to a direct initialization by means of an MMSE problem per tone, a recursive initialization based on training se-

quences has an acceptable computational cost. Due to the bad conditioning of the problem, convergence with simple LMS-based initialization algorithms is too slow. Existing recursive initialization algorithms for the PTEQ are based on solving a SR-RLS problem for each tone separately, where parts of the SR-RLS structures can be shared by all the tones. In this chapter, we introduced the split SR-RLS method, where two separate SR-RLS problems have to be solved, each on a different part of the inputs. Since the inputs of the PTEQ and PTEQ/PTEC problem can be separated into tone-independent and tone-dependent inputs, the split SR-RLS can easily be applied. The tone-independent part gives rise to the update of a lower triangular matrix, common for all the tones, while the tone-dependent part has typically a much smaller dimension and introduces almost no extra cost. By this, the computational complexity per iteration and the memory requirements are substantially reduced, compared to full SR-RLS. Although the convergence of the split SR-RLS is slower than full SR-RLS, simulations showed that the convergence rate remains within the available number of ADSL training symbols, while keeping the complexity per iteration close to NLMS.

7.2 Further research

BM-WinTEQ cost function

In Chapter 4, it was shown that BM-TEQ and BM-WinTEQ design lead to non-linear optimization problems, which require non-linear optimization techniques. In extensive simulations, it was observed that both the BM-TEQ and BM-WinTEQ cost functions exhibit multiple local optima, but apparently all optima have close to optimal performance. Further research is required in order to explore the shape of the BM-TEQ and BM-WinTEQ cost functions and to explain the behaviour of the minima. If all local optima truly lead to near-optimal data rates, the BM-TEQ and BM-WinTEQ can effectively be used as practical design methods. In addition, inexpensive adaptive procedures could be devised to initialize the BM-TEQ and BM-WinTEQ coefficients.

Split SR-RLS for other applications

In Chapter 6, the recursive initialization of the PTEQ/PTEC-based receiver was addressed. To accomplish this goal, the split SR-RLS scheme was developed and its advantages in terms of convergence rate, computational complexity and memory requirements were highlighted. Apart from the PTEQ/PTEC receiver structure, some other ADSL applications exist that could potentially benefit from an initialization with the split SR-RLS algorithm. These applications were briefly mentioned in Subsection 6.4.6 and further research is required to determine the computational complexity, convergence rate and memory savings of split SR-RLS for these applications.

Finite precision analysis

The favorable computational complexity of RLS-LMS or split SR-RLS makes both algorithms suitable for implementation in hardware. However, a detailed finite precision analysis still has to be performed to determine how many bits are effectively needed to represent the different variables. It is expected that due to the large eigenvalue spread of the input correlation matrix associated with the PTEQ-only or the PTEQ/PTEC problem, relatively high precision is required. However, a detailed study has to provide a decisive answer to this statement.

Crosstalk cancellation and MIMO equalization

Next generation DSL systems, like ADSL2+ and VDSL, allow increased data rates for broadband communication. These high rates are possible by using wider frequency bands (up to 2.208 MHz for ADSL2+ and 17.66 MHz for VDSL) and shorter telephone lines. Since copper wires are bundled in so-called binders, the short distances between twisted pairs combined with the high frequency ranges result in strong crosstalk interference (NEXT and FEXT). In this thesis, it was assumed that a DSL-binder is a set of individual users, where crosstalk was modeled as an extra additive noise source. Often some kind of coordination is possible between individual DSL-systems, which is called Multiple-Input Multiple-Output DSL (MIMO-DSL). At CO for instance all modems of a binder are co-located. Consequently, the detection of all received upstream signals can be executed jointly. Since NEXT can be seen as 'echo from a different user', the echo canceling schemes presented in Chapter 5 could be used to suppress NEXT. This is a topic for further research.

Due to the high frequency ranges in ADSL2+ and VDSL, FEXT severely limits the performance of these systems. In a MIMO-DSL system, one is able to mitigate downstream FEXT by pre-compensation at the CO transmitter. This is called MIMO crosstalk cancellation [21][22][51][122]. For MIMO crosstalk cancellation it is assumed that the order of all the crosstalk channels is limited to the length of the CP such that all tones can be processed independently. FEXT cancellation is then applied on a per tone basis. These assumptions are typically met for VDSL but not necessarily for ADSL2+. When the far end and crosstalk channels are longer than the CP, channel shortening, as discussed in Chapter 3 and Chapter 4, should be extended to the MIMO case. Hence, further research could be done on a combined MIMO equalization and MIMO crosstalk cancellation.

Alien crosstalk cancellation

Crosstalk in DSL systems can be classified into self-crosstalk and alien crosstalk. Self-crosstalk is crosstalk by systems using the same xDSL transmission format

and technology. Alien crosstalk, on the other hand, is crosstalk caused by systems with a different transmission scheme and overlapping frequency bands: e.g. HDSL and SDSL are both single carrier schemes that cause alien crosstalk in an ADSL system. In [145], the problem of alien crosstalk cancellation was addressed. The main signal processing difficulties arise due to the different symbol rates of the crosstalker and signal of interest, which makes the crosstalk signal non-stationary with respect to the impaired receiver. To tackle this non-stationarity, the authors in [145] use time invariant filtering techniques. Although these methods improve the achieved bit rates, only a fraction of the performance loss due to the crosstalker is regained. Hence, more advanced schemes for complete alien crosstalk cancellation are a topic for further research.

Bibliography

[1] M. Abdulrahman and D. Falconer. Cyclostationary crosstalk suppression by decision feedback equalization on digital subscriber loops. *IEEE Journal on Selected Areas in Commun.*, 10(3):640–649, April 1992.

[2] N. Al-Dhahir. FIR channel-shortening equalizers for MIMO ISI channels. *IEEE Trans. on Commun.*, 49(2):213–218, February 2001.

[3] N. Al-Dhahir and J.M. Cioffi. Optimum finite-length equalization for multicarrier transceivers. In *Proc. IEEE Global Telecommun. Conf. (GLOBECOM)*, pages 1884–1888, San Francisco, California, November 1994.

[4] N. Al-Dhahir and J.M. Cioffi. The combination of finite-length geometric equalization and bandwidth optimization for multicarrier transceivers. In *Proc. IEEE Int. Conf. on Acoustics, Speech and Signal Proc. (ICASSP)*, volume 2, pages 1201–1204, Detroit, Michigan, May 1995.

[5] N. Al-Dhahir and J.M. Cioffi. Efficiently computed reduced-parameter input-aided MMSE equalizers for ml detection: A unified approach. *IEEE Trans. on Information Theory*, 42(3):903–915, May 1996.

[6] N. Al-Dhahir and J.M. Cioffi. Optimum finite-length equalization for multicarrier transceivers. *IEEE Trans. on Commun.*, 44(1):56–64, January 1996.

[7] N. Al-Dhahir and J.M. Cioffi. A bandwidth-optimized reduced-complexity equalized multicarier transceiver. *IEEE Trans. on Commun.*, 45(8):948–956, August 1997.

[8] M.-L. Alberi, R.A. Casas, I. Fijalkow, and C.R. Johnson, Jr. Looping LMS versus fast least squares algorithms: Who gets there first ? In *Proc. of the 2nd IEEE Workshop on Sig. Proc. Advances in Wireless Commun. (SPAWC '99)*, pages 296–299, 1999.

[9] G. Arslan. *Equalization for Discrete Multitone Transceivers*. PhD thesis, The University of Texas at Austin, 2000.

[10] G. Arslan, B. Evans, and S. Kiaei. Equalization for discrete multitone transceivers to maximize bit rate. *IEEE Trans. on Signal Proc.*, 49(12):3123–3135, December 2001.

[11] G. Arslan, B.L. Evans, and S. Kiaei. Optimum channel shortening for discrete multitone transceivers. In *Proc. IEEE Int. Conf. on Acoustics, Speech and Signal Proc. (ICASSP)*, volume 5, pages 2965–2968, 2000.

[12] Aware. White paper: ADSL2 and ADSL2+ the new ADSL standards, revision 2. `http://support.aware.com/data/cgi-bin/adsl2_put.idc`.

[13] J. Balakrishnan, R.K. Martin, and C.R. Johnson, Jr. Blind, adaptive channel shortening by sum-squared auto-correlation minimization (SAM). In *Proc. of the Asilomar Conf. on Signals, Systems and Computers*, volume 1, pages 398–402, Pacific Grove, California, November 2002.

[14] S. Barbarossa, G. Scutari, and A. Swami. MUI-free CDMA systems incorporating space-time coding and channel shortening. In *Proc. IEEE Int. Conf. on Acoustics, Speech and Signal Proc. (ICASSP)*, volume 3, pages 2213–2216, May 2002.

[15] R. Baüml, R. Fischer, and J. Huber. Reducing the peak-to-average power ratio of multicarrier modulation by selected mapping. *Electronics Letters*, 32(22):2056–2057, October 1996.

[16] J.A.C. Bingham. Multicarrier modulation for data transmission: An idea whose time has come. *IEEE Commun. Mag.*, 28(5):5–14, May 1990.

[17] J.A.C. Bingham. *ADSL, VDSL, and Multicarrier Modulation.* Wiley-Interscience, 2000.

[18] K. Bong Song, S. Taek Chung, G. Ginis, and J.M. Cioffi. Dynamic spectrum management for next-generation DSL systems. *IEEE Commun. Mag.*, 40(10):101–109, October 2002.

[19] J. Campello. Optimal discrete bit loading for multicarrier modulation systems. In *Proc. IEEE Int. Symp. on Information Theory*, page 193, Cambridge, MA, USA, August 1998.

[20] J. Campello. Practical bit loading for DMT. In *Proc. IEEE Int. Conf. on Commun. (ICC)*, volume 2, pages 801–805, Vancouver, Canada, June 1999.

[21] R. Cendrillon, M. Moonen, G. Ginis, K. Van Acker, T. Bostoen, and P. Vandaele. Partial crosstalk cancellation exploiting line and tone selection in upstream DMT-VDSL. To appear in EURASIP Journal on Applied Signal Processing, Special Issue on Multicarrier Communications and Signal Processing, 2004.

[22] R. Cendrillon, M. Moonen, D. Gore, and A. Paulraj. Low complexity crosstalk cancellation with line selection in upstream VDSL. In *Proc. IEEE Int. Conf. on Acoustics, Speech and Signal Proc. (ICASSP)*, volume 4, pages 692–695, Hong Kong SAR, China, April 2003.

[23] IEEE History Center. `http://www.ieee.org/organizations/history_center/comsoc/techhist.html`.

[24] R.W. Chang. Synthesis of band-limited orthogonal signals for multichannel data transmission. *Bell System Tech. Journal*, 45:1775–1796, December 1966.

[25] W.Y. Chen, J.L. Dixon, and D.L. Waring. High bit rate digital subscriber line echo cancellation. *IEEE Journal on Selected Areas in Commun.*, 9(6):848–860, January 1991.

[26] S.M. Cherry. The wireless last mile. *IEEE Spectrum*, 40(9):18–22, September 2003.

[27] W. Chiu, W.K. Tsai, T.C. Liau, and M. Troulis. Time-domain channel equalizer design using the inverse power method. In *Proc. IEEE Int. Conf. on Commun. (ICC)*, volume 2, pages 973–977, Vancouver, Canada, June 1999.

[28] J.S. Chow and J.M. Cioffi. A cost-effective maximum likelihood receiver for multicarrier systems. In *Proc. IEEE Int. Conf. on Commun. (ICC)*, volume 2, pages 948–952, June 1992.

[29] J.S. Chow, J.C. Tu, and J.M. Cioffi. A discrete multitone transceiver system for HDSL applications. *IEEE Journal on Selected Areas in Commun.*, 9(6):895–908, August 1991.

[30] P.S. Chow, J.M. Cioffi, and J.A.C. Bingham. A practical discrete multitone transceiver loading algorithm for data transmission over spectrally shaped channels. *IEEE Trans. on Commun.*, 43(2/3/4):773–775, February/March/April 1995.

[31] J.M. Cioffi. Course notes of class EE379C, advanced digital communication. `http://www.stanford.edu/class/ee379c/`.

[32] J.M. Cioffi and J.A.C. Bingham. A data-driven multitone echo canceller. *IEEE Trans. on Commun.*, 42(10):2853–2869, October 1994.

[33] J.M. Cioffi, J.A.C. Bingham, and M. Ho. Recommendation for vendor-discretionary echo canceller use with DMT ADSL. Technical Report T1E1.4/93-116, ANSI, May 1993.

[34] J.M. Cioffi, G.P. Dudevoir, M.V. Eyuboglu, and G.D. Forney. MMSE decision-feedback equalizers and coding – part I: Equalization results. *IEEE Trans. on Commun.*, 43(10):2582–2594, October 1995.

[35] J.M. Cioffi and T. Kailath. Fast, recursive-least-squares transversal filters for adaptive filtering. *IEEE Trans. on Acoustics, Speech and Signal Proc.*, ASSP-32(2):304–337, April 1984.

[36] International Engineering Consortium. Cable modems. `http://www.iec.org/online/tutorials/cable_mod/index.html`.

[37] The MITRE Corporation. Semi-automatic ground environment (SAGE), `http://www.mitre.org/about/sage.html`.

[38] G. Cuypers, G. Ysebaert, M. Moonen, and P. Vandaele. Combining per tone equalization and windowing in DMT receivers. In *Proc. IEEE Int. Conf. on Acoustics, Speech and Signal Proc. (ICASSP)*, volume 3, pages 2341–2344, 2002.

[39] D. Daly, C. Heneghan, and A.D. Fagan. A minimum mean-squared error interpretation of residual ISI channel shortening for discrete multitone transceivers. In *Proc. IEEE Int. Conf. on Acoustics, Speech and Signal Proc. (ICASSP)*, volume 4, pages 2065–2068, Salt Lake City, Utah, May 2001.

[40] L. de Clercq, M. Peeters, S. Schelstraete, and T. Pollet. Mitigation of radio interference in xDSL transmission. *IEEE Commun. Mag.*, 38(3):168–173, March 2000.

[41] M. de Courville, P. Duhamel, P. Madec, and J. Palicot. Blind equalization of OFDM systems based on the minimization of a quadratic criterion. In *Proc. IEEE Int. Conf. on Commun. (ICC)*, volume 3, pages 1318–1322, Dallas, Texas, June 1996.

[42] B. De Moor. Angles between subspaces. Internal Report ESAT-SISTA/TR 00-129, K.U.Leuven, Belgium, pp. 155-182.

[43] B. De Moor. A note on constrained quadratic optimization and its representation in linear model estimation. Internal report.

[44] D.D. Falconer and F.R. Magee. Adaptive channel memory truncation for maximum likelihood sequence estimation. *Bell System Technical Journal*, pages 1541–1562, November 1973.

[45] B. Farhang-Boroujeny and Y.C. Lim. A comment on the computational complexity of sliding FFT. *IEEE Trans. on Circuits and Systems*, 39(12):875–876, December 1992.

[46] Alliance for Telecommunications Industry Solutions (ATIS). ATIS' T1E1 announces specification of DMT line coding in new VDSL American national standard. `http://www.atis.org/PRESS/pressreleases2003/062003.htm`.

[47] DSL Forum. `http://www.adsl.com/adsl_forum.html`.

[48] M. Friese. Multicarrier modulation with low peak-to-average power ratio. *Electronics Letters*, 32(8):713–714, April 1996.

[49] T. Gansler, S.L. Gay, M.M. Sondhi, and J. Benesty. Double-talk robust fast converging algorithms for network echo cancellation. *IEEE Trans. on Speech and Audio Proc.*, 8(6):656–663, November 2000.

[50] A. Gatherer, M.O. Polley, and A.J. Redfern. PAR reduction for DMT systems with unloaded subchannels. In *Proc. of the Asilomar Conf. on Signals, Systems and Computers*, volume 2, pages 1847–1851, Pacific Grove, California, November 2002.

[51] G. Ginis and J. Cioffi. Vectored transmission for digital subscriber line systems. *IEEE Journal on Selected Areas in Commun.*, 20(5):1085–1104, June 2002.

[52] R.D. Gitlin and S.B. Weinstein. The effects of large interference on the tracking capability of digitally implemented echo cancellers. *IEEE Trans. on Commun.*, COM-26(6):833–839, June 1978.

[53] G.H. Golub and C.F. Van Loan. *Matrix Computations*. The John Hopkins University Press, third edition, 1996.

[54] S. Haykin. *Adaptive Filter Theory*. Prentice Hall, third edition, 1996.

[55] W. Henkel and T. Kessler. Maximizing the channel capacity of multicarrier transmission by suitable adaptation of the time-domain equalizer. *IEEE Trans. on Commun.*, 48(12):2000–2004, December 2000.

[56] W. Henkel, S. Olcer, K.S. Jacobsen, B.R. Saltzberg, and A.M. Bush. Guest editorial: Twisted pair transmission – ever increasing performances on ancient telephone wires. *IEEE Journal on Selected Areas in Commun.*, 20(5):877–880, June 2002.

[57] M. Ho, J.M. Cioffi, and J.A.C. Bingham. Discrete multitone echo cancelation. *IEEE Trans. on Commun.*, 44(7):817–825, July 1996.

[58] D. Hughes-Hartogs. Ensemble modem structure for imperfect transmission media. U.S. Patents Nos. 4,679,227 (July 1987), 4,731,816 (March 1988) and 4,833,706 (May 1989).

[59] The European Telecomm. Standards Inst. Broadband radio access networks (BRAN); high performance radio local area networks (HIPERLAN) type 2; system overview. ETSI 101 683 V1.1.1, 2000.

[60] The European Telecomm. Standards Inst. Digital video broadcasting (DVB); framing structure, channel coding and modulation for digital terrestrial television. ETSI EN 300 744 V1.4.1, 2001.

[61] The European Telecomm. Standards Inst. Radio broadcasting systems; digital audio broadcasting (DAB) to mobile, portable and fixed receivers. ETSI EN 300 401 V1.3.3, 2001-2005.

[62] S. Ismail and I. Wu. Broadband internet access in OECD countries: A comparative analysis. *A Staff Report of the Office of Strategic Planning and Policy Analysis and International Bureau*, October 2002.

[63] International Telecommunications Union (ITU). Draft new recommendation G.992.1: ADSL transceivers. 1999.

[64] J.-C. Jenq and S.-F. Hsieh. Acoustic echo cancellation using iterative-maximal-length correlation and double-talk detection. *IEEE Trans. on Speech and Audio Proc.*, 9(8):932–942, November 2001.

[65] D.C. Jones. Frequency domain echo cancellation for discrete multitone asymmetric digital subscriber line transceivers. *IEEE Trans. on Commun.*, 43(2/3/4):1663–1672, February/March/April 1995.

[66] S. Kapoor and S. Nedic. Interference suppression in DMT receiver. In *Proc. IEEE Int. Conf. on Commun. (ICC)*, volume 2, pages 778–782, New Orleans, USA, June 2000.

[67] K.J. Kerpez and A.M. Gottlieb. The error performance of digital subscriber lines in the presence of impulse noise. *IEEE Trans. on Commun.*, 43(5):1902–1905, May 1995.

[68] P.J. Kyees, R.C. McConnell, and K. Sistanizadeh. ADSL: A new twisted-pair access to the information highway. *IEEE Commun. Mag.*, 33(4):52–60, April 1995.

[69] N. Lashkarian and S. Kiaei. Fast algorithm for finite-length MMSE equalizers with application to discrete multitone systems. In *Proc. IEEE Int. Conf. on Acoustics, Speech and Signal Proc. (ICASSP)*, volume 5, pages 2753–2756, Phoenix, Arizona, March 1999.

[70] N. Lashkarian and S. Kiaei. Optimum equalization of multicarrier systems: A unified geometric approach. *IEEE Trans. on Commun.*, 49(10):1762–1769, October 2001.

[71] E.A. Lee and D.G. Messerschmitt. *Digital Communication*. Kluwer Academic Publishers, second edition, 1994.

[72] I. Lee, J.S. Chow, and J.M. Cioffi. Performance evaluation of a fast-computation algorithm for the DMT in high-speed subscriber loop. *IEEE Journal on Selected Areas in Commun.*, 13(9):1564–1570, December 1995.

[73] A. Leke and J.M. Cioffi. A maximum rate loading algorithm for discrete multitone modulations systems. In *Proc. IEEE Global Telecommun. Conf. (GLOBECOM)*, pages 1514–1518, Phoenix, Arizona, November 1997.

[74] G. Leus, I. Barhumi, and M. Moonen. Per-tone equalization for MIMO-OFDM systems. In *Proc. IEEE Int. Conf. on Commun. (ICC)*, volume 4, pages 2345–2349, Anchorage, Alaska, May 2003.

[75] G. Leus and M. Moonen. Per-tone equalization for MIMO OFDM systems. *IEEE Trans. on Signal Proc.*, 51(11):2965–2975, November 2003.

[76] V.C. Liu. Circulant and skew-circulant matrices as new normal-form realization of IIR digital filters. *IEEE Trans. on Circuits and Systems*, 35(6):625–635, June 1988. Map 7 GY.

[77] R.K. Martin, J. Balakrishnan, W.A. Sethares, and C.R. Johnson, Jr. Blind, adaptive channel shortening for multicarrier systems. In *Proc. of the Asilomar Conf. on Signals, Systems and Computers*, Pacific Grove, California, November 2002.

[78] R.K. Martin, J. Balakrishnan, W.A. Sethares, and C.R. Johnson, Jr. A blind, adaptive TEQ for multicarrier systems. *IEEE Signal Proc. Letters*, 9(11):341–343, November 2002.

[79] R.K. Martin, M. Ding, B.L. Evans, and C.R. Johnson, Jr. Efficient channel shortening equalizer design. *EURASIP Journal on Applied Signal Processing, Special Issue on Signal Processing for Broadband Access Systems: Techniques and Implemenations*, (13):1279–1290, December 2003.

[80] R.K. Martin, C.R. Johnson, Jr., M. Ding, and B.L. Evans. Exploiting symmetry in channel shortening equalizers. In *Proc. IEEE Int. Conf. on Acoustics, Speech and Signal Proc. (ICASSP)*, Hong Kong SAR, China, April 2003.

[81] R.K. Martin, K. Vanbleu, M. Ding, G. Ysebaert, M. Milosevic, B.L. Evans, M. Moonen, and C.R. Johnson, Jr. Multicarrier equalization: Unification and evaluation. part I: Optimal designs. Internal Report ESAT-SISTA/TR 03-51, K.U.Leuven, Belgium, Submitted to *IEEE Trans. on Signal Proc.*, December 2003.

[82] R.K. Martin, K. Vanbleu, M. Ding, G. Ysebaert, M. Milosevic, B.L. Evans, M. Moonen, and C.R. Johnson, Jr. Multicarrier equalization: Unification and evaluation. part II: Complexity reduction, adaptation, and performance evaluation. Internal Report ESAT-SISTA/TR 03-52, K.U.Leuven, Belgium, Submitted to *IEEE Trans. on Signal Proc.*, December 2003.

[83] P.J.W. Melsa, R.C. Younce, and C.E. Rohrs. Impulse response shortening for discrete multitone transceivers. *IEEE Trans. on Commun.*, 44(12):1662–1672, December 1996.

[84] D.G. Mestdagh, M.R. Isaksson, and P. Ödling. Zipper VDSL: a solution for robust duplex communication over telephone lines. *IEEE Commun. Mag.*, 38(5):90–96, May 2000.

[85] D.J. Mestdagh and P.M. Spruyt. A method to reduce the probability of clipping in DMT-based transceivers. *IEEE Trans. on Commun.*, 44(10):1234–1238, October 1996.

[86] D.J.G. Mestdagh, P.M.P. Spruyt, B. Biran, and H. Verbueken. Echo cancellation versus fdm for DMT-based ADSL: a comparative study of system performance and implementation complexity. Technical Report T1E1.4/93-131, ANSI, May 1993.

[87] M. Milosevic, L.F.C. Pessoa, B.L. Evans, and R. Baldick. DMT bit rate maximization with optimal time domain equalizer filter bank architecture. In *Proc. of the Asilomar Conf. on Signals, Systems and Computers*, volume 1, pages 377–382, Pacific Grove, California, November 2002.

[88] M. Milosevic, L.F.C. Pessoa, B.L. Evans, and R. Baldick. Optimal time domain equalization design for maximizing data rate of discrete multi-tone systems. *IEEE Trans. on Signal Proc., Under Revision*, 2002.

[89] S. Müller and J. Huber. OFDM with reduced peak-to-average power ratio by optimum combination of partial transmit sequences. *Electronics Letters*, 33(5):368–369, February 1997.

[90] K. Murano, S. Unagami, and F. Amano. Echo cancellation and applications. *IEEE Commun. Mag.*, 28(1):49–55, January 1990.

[91] S.S. Narayan, A.M. Peterson, and M.J. Narasimha. Transform domain LMS algorithm. *IEEE Trans. on Acoustics, Speech and Signal Proc.*, ASSP-31(3):609–615, June 1983.

[92] S. Nedic and N. Popovic. Per tone adaptive equalization in DMT receivers with selective windowing. In *Proc. IEEE Int. Conf. on Commun. (ICC)*, volume 1, pages 179–183, Helsinki, Finland, June 2001.

[93] The Institute of Electrical and Electronics Engineers. Wireless LAN medium access control (MAC) and physical layer (PHY) specifications. IEEE std. 802.11a. 1999.

[94] F. Ouyang, P. Duvaut, O. Moreno, and L. Pierrugues. The first step of long-reach ADSL: smart DSL technology, READSL. *IEEE Commun. Mag.*, 41(9):124–131, September 2003.

[95] K. Pahlavan and J.L. Holsinger. Voice-band data communication modems – a historical review: 1919-1988. *IEEE Commun. Mag.*, 26(1):16–27, January 1988.

[96] C.T. Pan and R.J. Plemmons. Least squares modifications with inverse factorisations: Parallel implications. *Journal Comp. and Appl. Math.*, 27:109–127, 1989.

[97] Z. Papir and A. Simmonds. Competing for throughput in the local loop. *IEEE Commun. Mag.*, 37(5):61–66, May 1999.

[98] A. Peled and A. Ruiz. Frequency domain data transmission using reduced computational complexity algorithms. In *Proc. IEEE Int. Conf. on Acoustics, Speech and Signal Proc. (ICASSP)*, pages 964–967, Denver, Colorado, April 1980.

[99] B.R. Petersen and D.D. Falconer. Minimum mean square equalization in cyclostationary and stationary interference-analysis and subscriber line calculations. *IEEE Journal on Selected Areas in Commun.*, 9(6):931–940, August 1991.

[100] T. Pollet, H. Steendam, and M. Moeneclaey. Performance degradation of multicarrier systems caused by an insufficient guard interval duration. In *Proc. Int. Workshop on Copper Wire Access Systems 'Bridging the Last Copper Drop' (CWAS '97)*, pages 265–270, 1997.

[101] J.G. Proakis and D.G. Manolakis. *Digital Signal Processing.* Prentice Hall, third edition, 1996.

[102] A.J. Redfern. Receiver window design for multicarrier communication systems. *IEEE Journal on Selected Areas in Commun.*, 20(5):1029–1036, June 2002.

[103] B.R. Saltzberg. Performance of an efficient parallel data transmission system. *IEEE Trans. on Commun. Technology*, 15(6):805–811, December 1967.

[104] A. Scaglione, G.B. Giannakis, and S. Barbarossa. Redundant filterbank precoders and equalizers, part I: Unification and optimal designs. *IEEE Trans. on Signal Proc.*, 47:1988–2006, July 1999.

[105] A. Scaglione, G.B. Giannakis, and S. Barbarossa. Redundant filterbank precoders and equalizers, part II: Blind channel estimation, synchronization, and direct equalization. *IEEE Trans. on Signal Proc.*, 47:2007–2022, July 1999.

[106] R. Schur and J. Speidel. An efficient equalization method to minimize delay spread in OFDM/DMT systems. In *Proc. IEEE Int. Conf. on Commun. (ICC)*, volume 5, pages 1481–1485, Helsinki, Finland, June 2001.

[107] R. Schur, J. Speidel, and R. Angerbauer. Reduction of guard interval by impulse compression for DMT modulation on twisted pair cables. In *Proc. IEEE Global Telecommun. Conf. (GLOBECOM)*, pages 1632–1636, San Francisco, California, November 2000.

[108] J.L. Seoane, S.K. Wilson, and S. Gelfand. Analysis of intertone and interblock interference in OFDM when the length of the cyclic prefix is shorter than the length of the impulse response of the channel. In *Proc. IEEE Global Telecommun. Conf. (GLOBECOM)*, pages 32–36, Phoenix, Arizona, November 1997.

[109] C. Shannon. A mathematical theory of communication. *Bell System Technical Journal*, 27(5):379–423 and 623–656, July and October 1948.

[110] J.J. Shynk. Frequency-domain and multirate adaptive filtering. *IEEE Signal Proc. Mag.*, 9(1):14–37, January 1992.

[111] The Samuel Morse Historic Site. `http://www.morsehistoricsite.org/morse/morse.html`.

[112] F. Sjöberg. *The Zipper Duplex Method in Very High-Speed Digital Subscriber Lines*. PhD thesis, Luleå University of Technology, 2000.

[113] F. Sjöberg, M. Isaksson, R. Nilsson, P. Ödling, S.K. Wilson, and P.A. Börjesson. Zipper: A duplex method for VDSL based on DMT. *IEEE Trans. on Commun.*, 47(8):1245–1252, August 1999.

[114] F. Sjöberg, R. Nilsson, M. Isaksson, P. Ödling, and P.O. Börjesson. Asynchronous zipper. In *Proc. IEEE Int. Conf. on Commun. (ICC)*, volume 1, pages 231–235, Vancouver, Canada, June 1999.

[115] N.J.A. Sloane and A.D. Wyner, editors. *Claude Elwood Shannon: Collected Papers*. IEEE Press, USA, 1993.

[116] Internet Society. A brief history of the internet, `http://www.isoc.org/internet/history/brief.shtml`.

[117] H.V. Sorensen and C.S. Burrus. Efficient computation of the DFT with only a subset of input or output points. *IEEE Trans. on Signal Proc.*, 41(3):1184–1200, March 1993.

[118] P. Spruyt, P. Reusens, and S. Braet. Performance of improved DMT transceiver for VDSL. Technical Report T1E1.4/96-104, ANSI, April 1996.

[119] T. Starr, J.M. Cioffi, and P.J. Silverman. *Understanding Digital Subscriber Line Technology*. Prentice Hall, 1999.

[120] T. Starr, M. Sorbara, J.M. Cioffi, and P.J. Silverman. *DSL Advances*. Prentice Hall, 2003.

[121] R. Stolle. Electromagnetic coupling of twisted pair cables. *IEEE Journal on Selected Areas in Commun.*, 20(5):883–892, June 2002.

[122] G. Taubock and W. Henkel. MIMO systems in the subscriber-line network. In *Proc. of the fifth Int. OFDM-Workshop*, pages 18.1–18.3, Hamburg, Germany, September 2000.

[123] Tyco Telecommunications. `http://www.tycotelecom.com/aboutus/HistoryTelecom.asp`.

[124] J. Tellado. *Multicarrier Transmission with Low PAR*. PhD thesis, Stanford University, 1998.

[125] J. Tellado and J.M. Cioffi. Efficient algorithms for reducing PAR in multicarrier systems. In *Proc. IEEE Int. Symp. on Information Theory (ISIT)*, page 191, Boston, August 1998.

[126] The MathWorks, Inc. *Optimization Toolbox User's Guide*. 2002.

[127] What You Need to Know about Inventors. The history of the telephone, `http://inventors.about.com/library/inventors/bltelephone.htm`.

[128] What You Need to Know about Inventors. Inventors of the modern computer, `http://inventors.about.com/library/weekly/aa061698.htm`.

[129] K. Van Acker. *Equalization and Echo Cancellation for DMT-Based DSL Modems*. PhD thesis, K.U.Leuven, Belgium, 2001.

[130] K. Van Acker, G. Leus, M. Moonen, S. Claes, and O. van de Wiel. An improved optimization algorithm for time domain equalizer design in ADSL modems. In *Proc. of the Int. Workshop on Copper Wire Access Systems 'Bridging the last copper drop'*, pages 117–123, Budapest, Hungary, October 1997.

[131] K. Van Acker, G. Leus, M. Moonen, S. Claes, and O. van de Wiel. Improved time domain equalization for ADSL. In *Proc. of the ProRISC Workshop on Circuits Systems and Signal Proc. (CSSP)*, pages 615–620, Mierlo, The Netherlands, November 1997.

[132] K. Van Acker, G. Leus, M. Moonen, and T. Pollet. Frequency domain equalization with tone grouping in DMT/ADSL-receivers. In *Proc. of the Asilomar Conf. on Signals, Systems and Computers*, Pacific Grove, California, October 1999.

[133] K. Van Acker, G. Leus, M. Moonen, and T. Pollet. RLS-based initialization for per tone equalizers in DMT-receivers. In *Proc. European Signal Proc. Conf. (EUSIPCO)*, Tampere, Finland, September 2000.

[134] K. Van Acker, G. Leus, M. Moonen, and T. Pollet. RLS-based initialization for per-tone equalizers in DMT receivers. *IEEE Trans. on Commun.*, 51(6):885–889, June 2003.

[135] K. Van Acker, G. Leus, M. Moonen, O. van de Wiel, and T. Pollet. Per tone equalization for DMT receivers. In *Proc. IEEE Global Telecommun. Conf. (GLOBECOM)*, volume 5, pages 2311–2315, 1999.

[136] K. Van Acker, G. Leus, M. Moonen, O. van de Wiel, and T. Pollet. Per tone equalization for DMT-based systems. *IEEE Trans. on Commun.*, 49(1):109–119, January 2001.

[137] K. Van Acker, M. Moonen, and T. Pollet. Per tone echo cancellation for DMT-based systems. In *Proc. IEEE Int. Conf. on Acoustics, Speech and Signal Proc. (ICASSP)*, volume 4, pages 2365–2368, 2001.

[138] K. Van Acker, M. Moonen, and T. Pollet. Per-tone echo cancellation for DMT-based systems. *IEEE Trans. on Commun.*, 51(9):1582–1590, September 2003.

[139] K. Van Acker, T. Pollet, G. Leus, and M. Moonen. Combination of per tone equalization and windowing in DMT-receivers. *Signal Processing*, 81:1571–1579, 2001.

[140] M. Van Bladel and M. Moeneclaey. Time-domain equalization for multicarrier communication. In *Proc. IEEE Global Telecommun. Conf. (GLOBECOM)*, pages 167–171, 1995.

[141] J.-F. Van Kerckhove and P. Spruyt. Adapted optimization criterion for FDM-based DMT-ADSL equalization. In *Proc. IEEE Int. Conf. on Commun. (ICC)*, volume 3, pages 1328–1334, 1996.

[142] K. Vanbleu, G. Leus, and M. Moonen. Per-tone equalization for DMT-based transmission over IIR channels. In *Proc. IEEE Global Telecommun. Conf. (GLOBECOM)*, volume 1, pages 405–409, San Antonio, Texas, November 2001.

[143] K. Vanbleu, G. Ysebaert, G. Cuypers, and M. Moonen. Bitrate maximizing per-group equalization for DMT-based systems. Internal Report ESAT-SISTA/TR 03-48, K.U.Leuven, Belgium, Submitted for publication, 2003.

[144] K. Vanbleu, G. Ysebaert, G. Cuypers, M. Moonen, and K. Van Acker. Bitrate maximizing time-domain equalizer design for DMT-based systems. In *Proc. IEEE Int. Conf. on Commun. (ICC)*, volume 4, pages 2360–2364, Anchorage, Alaska, May 2003.

[145] K. Vanbleu, G. Ysebaert, M. Moonen, and P. Vandaele. Combined equalization and alien crosstalk cancellation in ADSL receivers. In *Proc. European Signal Proc. Conf. (EUSIPCO)*, Toulouse, France, September 2002.

[146] B. Wang and T. Adali. Joint impulse response shortening for discrete multitone systems. In *Proc. IEEE Global Telecommun. Conf. (GLOBECOM)*, pages 2508–2512, Rio de Janeiro, Brazil, December 1999.

[147] Z. Wang and G.B. Giannakis. Wireless multicarrier communications. *IEEE Signal Proc. Mag.*, 17:29–48, May 2000.

[148] S.B. Weinstein and P.M. Ebert. Data transmission by frequency-division multiplexing using the discrete fourier transform. *IEEE Trans. on Commun. Technology*, 19(5):628–634, October 1971.

[149] B. Widrow and M.E. Hoff. Adaptive switching circuits. In *IRE WESCON, Convention Record*, pages 96–104, New York, 1960.

[150] B.R. Wiese and J.S. Chow. Programmable implementations of xDSL transceiver systems. *IEEE Commun. Mag.*, 38(5):114–119, May 2000.

[151] A.-Y. Wu and K.J. Ray Liu. Split recursive least-squares: Algorithms, architectures, and applications. *IEEE Trans. on Circuits and Systems-II: Analog and Digital Sig. Proc.*, 43(9):645–658, September 1996.

[152] H. Ye and B.-X. Wu. A new double-talk detection algorithm based on the orthogonality theorem. *IEEE Trans. on Commun.*, 39(11):1542–1545, November 1991.

[153] A. Yeredor and B. De Moor. On homogeneous least-squares problems and the inconsistency introduced by mis-constraining. In *3rd workshop of the ERCIM Working Group on Matrix Computations and Statistics*, Neuchatel, Switzerland, November 2002.

[154] C. Yin and G. Yue. Optimal impulse response shortening for discrete multitone transceivers. *Electronics Letters*, 34:35–36, January 1998.

[155] G. Ysebaert, G. Cuypers, K. Vanbleu, K. Van Acker, and M. Moonen. Double talk cancellation in echo cancelled DMT-systems. In *Book of abstracts of the K.U.Leuven Faculty of Engineering PhD Symposium*, page 41, December 2002.

[156] G. Ysebaert, M. Moonen, and T. Pollet. Combined RLS-LMS initialization for per tone equalizers in DMT-receivers. In *Proc. IEEE Int. Conf. on Acoustics, Speech and Signal Proc. (ICASSP)*, volume III, pages 2537–2540, Orlando, Florida, May 2002.

[157] G. Ysebaert, F. Pisoni, M. Bonaventura, R. Hug, and M. Moonen. Circulant decomposition canceler for echo cancellation in DMT-based receivers. To appear in Proc. of IEEE Int. Conf. on Commun. (ICC).

[158] G. Ysebaert, F. Pisoni, M. Bonaventura, R. Hug, and M. Moonen. Echo cancellation in DMT-receivers: Circulant decomposition canceler. To appear in IEEE Trans. on Signal Proc., 2004.

[159] G. Ysebaert, K. Van Acker, M. Moonen, and B. De Moor. Constraints in channel shortening equalizer design for DMT-based systems. *Signal Processing*, 83(3):641–648, March 2003.

[160] G. Ysebaert, K. Vanbleu, G. Cuypers, and M. Moonen. ADSL per-tone/per-group optimal equalizer and windowing design. In *Proc. of the Asilomar Conf. on Signals, Systems and Computers*, Pacific Grove, California, November 2002.

[161] G. Ysebaert, K. Vanbleu, G. Cuypers, and M. Moonen. Bit rate maximizing window and equalizer design for dmt-systems. Internal Report ESAT-SISTA/TR 04-11a, K.U.Leuven, Belgium, Submitted to *European Signal Proc. Conf. (EUSIPCO)*, 2004.

[162] G. Ysebaert, K. Vanbleu, G. Cuypers, and M. Moonen. Joint window and time domain equalizer design for bit rate maximization in DMT-receivers. To appear in IEEE Trans. on Signal Proc., 2004.

[163] G. Ysebaert, K. Vanbleu, G. Cuypers, and M. Moonen. Split SR-RLS for the joint initialization of the per-tone equalizers and per-tone echo cancelers in DMT-based receivers. To appear in EURASIP Journal on Applied Signal Processing, Special Issue on Multicarrier Communications and Signal Processing, 2004.

[164] G. Ysebaert, K. Vanbleu, G. Cuypers, M. Moonen, and T. Pollet. Combined RLS-LMS initialization for per tone equalizers in DMT-receivers. *IEEE Trans. on Signal Proc.*, 51(7):1916–1927, July 2003.

[165] G. Ysebaert, K. Vanbleu, G. Cuypers, M. Moonen, and K. Van Acker. Double talk cancellation in echo cancelled DMT-systems. In *Proc. of Signal Processing Symposium (SPS)*, pages 169–172, Leuven, Belgium, March 2002.

[166] G. Ysebaert, K. Vanbleu, G. Cuypers, M. Moonen, and K. Van Acker. Double talk cancellation in echo cancelled DMT-systems. In *Proc. European Signal Proc. Conf. (EUSIPCO)*, volume II, pages 381–384, Toulouse, France, September 2002.

[167] G. Ysebaert, K. Vanbleu, G. Cuypers, M. Moonen, and J. Verlinden. Echo cancellation for discrete multitone frame-asynchronous ADSL transceivers. Internal Report ESAT-SISTA/TR 02-186, K.U.Leuven, Belgium, Submitted to *IEEE Trans. on Commun.*, December 2002.

[168] G. Ysebaert, K. Vanbleu, G. Cuypers, M. Moonen, and J. Verlinden. Echo cancellation for discrete multitone frame-asynchronous ADSL transmission. In *Proc. IEEE Int. Conf. on Commun. (ICC)*, volume 4, pages 2421–2425, Anchorage, Alaska, May 2003.

[169] W. Yu, G. Ginis, and J.M. Cioffi. Distributed multiuser power control for digital subscriber lines. *IEEE Journal on Selected Areas in Commun.*, 20(5):1105–1115, June 2002.

Appendix

A Basic linear algebra definitions

In this appendix some linear algebra definitions are briefly reviewed. In addition, some frequently used matrix properties will be reviewed. For further reading on matrix decompositions and implementation issues we refer to [53].

A.1 Structured matrices

Consider the $M \times M$ matrix $\mathbf{A}$ and the length-M vector $\mathbf{x}$,

$$\mathbf{A} = [a_{ij}] = \begin{bmatrix} a_{11} & a_{12} & \dots & a_{1M} \\ a_{21} & a_{22} & & a_{2M} \\ \vdots & & & \vdots \\ a_{M1} & a_{M2} & \dots & a_{MM} \end{bmatrix}, \tag{A.1}$$

$$\mathbf{x} = [x_i] = [x_1 \;\; x_2 \;\; \dots \;\; x_M]^T, \tag{A.2}$$

where $()^T$ denotes the transpose operation and indices i and j are used to indicate the i-th row and the j-th column of a matrix/vector respectively.

Definition A.1 The matrix $\mathbf{A}$ is *sparse* iff (if and only if) it has relatively few non-zero elements. □

Definition A.2 The matrix $\mathbf{A}$ is *symmetric* iff $a_{ij} = a_{ji}$,

$$\mathbf{A} \text{ is symmetric } \iff \mathbf{A} = \mathbf{A}^T. \tag{A.3}$$

□

Definition A.3 The matrix $\mathbf{A}$ is *hermitian* iff $a_{ij} = a_{ji}^*$,

$$\mathbf{A} \text{ is hermitian } \iff \mathbf{A} = (\mathbf{A}^*)^T = \mathbf{A}^H, \tag{A.4}$$

where $()^*$ denotes complex conjugation. □

Definition A.4 The matrix $\mathbf{A}$ is *skew-symmetric* (or anti-symmetric) iff $a_{ij} = -a_{ji}$,

$$\mathbf{A} \text{ is skew} - \text{symmetric } \iff \mathbf{A} = -\mathbf{A}^T. \tag{A.5}$$

□

Definition A.5 The matrix $\mathbf{A} \in \mathbb{R}^{M \times M}$ is *orthogonal* iff

$$\mathbf{A}\mathbf{A}^T = \mathbf{A}^T\mathbf{A} = \mathbf{I}_M, \tag{A.6}$$

where $\mathbf{I}_M$ denotes the $M \times M$ identity matrix. Hence, the inverse of an orthogonal matrix is equal to its transpose, i.e. $\mathbf{A}^{-1} = \mathbf{A}^T$. □

Definition A.6 The matrix $\mathbf{A} \in \mathbb{C}^{M \times M}$ is *unitary* iff

$$\mathbf{A}\mathbf{A}^H = \mathbf{A}^H\mathbf{A} = \mathbf{I}_M, \tag{A.7}$$

where $\mathbf{I}_M$ denotes the $M \times M$ identity matrix. Hence, the inverse of a unitary matrix is equal to its complex conjugate transpose, i.e. $\mathbf{A}^{-1} = \mathbf{A}^H$. □

Definition A.7 The matrix $\mathbf{A}$ is *positive definite* iff all its eigenvalues are strictly positive,

$$\mathbf{A} \text{ is positive definite } \iff \mathbf{x}^H\mathbf{A}\mathbf{x} > 0, \quad \forall \mathbf{x} \in \mathbb{C}^M. \tag{A.8}$$

□

Definition A.8 The matrix $\mathbf{A}$ is a *Toeplitz matrix* iff the elements along the diagonals of $\mathbf{A}$ are equal, i.e.

$$\mathbf{A} = \begin{bmatrix} a_{11} & a_{12} & a_{13} & \dots & a_{1M} \\ a_{21} & a_{11} & a_{12} & & a_{1(M-1)} \\ a_{31} & a_{21} & a_{11} & & a_{1(M-2)} \\ \vdots & & & \ddots & \vdots \\ a_{M1} & a_{(M-1)1} & a_{(M-2)1} & \dots & a_{11} \end{bmatrix}. \tag{A.9}$$

As can be readily verified, a Toeplitz matrix is completely determined by the elements of its first row and its first column. □

Definition A.9 The matrix $\mathbf{A}$ is a *circulant matrix* iff it is Toeplitz and each column is equal to the previous column rotated downwards by one element.

$$\mathbf{A} = \begin{bmatrix} a_{11} & a_{M1} & a_{(M-1)1} & \dots & a_{21} \\ a_{21} & a_{11} & a_{M1} & & a_{31} \\ a_{31} & a_{21} & a_{11} & & a_{41} \\ \vdots & & & \ddots & \vdots \\ a_{M1} & a_{(M-1)1} & a_{(M-2)1} & \dots & a_{11} \end{bmatrix}. \tag{A.10}$$

As can be readily verified, a circulant matrix is completely determined by the elements of its first column. □

Definition A.10 The matrix $\mathbf{A}$ is a *skew-circulant matrix* iff it is both circulant and skew-symmetric. It can be shown that every $M \times M$-dimensional Toeplitz matrix $\mathbf{A}$ can be written as the sum of a circulant and a skew-circulant matrix, i.e.

$$\mathbf{A} = \frac{1}{2}(\mathbf{A} + \mathbf{B}) + \frac{1}{2}(\mathbf{A} - \mathbf{B}), \tag{A.11}$$

where $\mathbf{A} + \mathbf{B}$ is an $M \times M$-dimensional circulant matrix and $\mathbf{A} - \mathbf{B}$ is an $M \times M$-dimensional skew-circulant matrix. □

Definition A.11 Let α be a primitive M-th root of unity, i.e. $\alpha = e^{-j2\pi/M}$, then the *M-point DFT matrix* is defined as

$$\mathcal{F}_M = \begin{bmatrix} 1 & 1 & 1 & \dots & 1 \\ 1 & \alpha & \alpha^2 & & \alpha^{M-1} \\ 1 & \alpha^2 & \alpha^4 & & \alpha^{2(M-1)} \\ \vdots & & & & \vdots \\ 1 & \alpha^{M-1} & \alpha^{2(M-1)} & \dots & \alpha^{(M-1)(M-1)} \end{bmatrix}. \tag{A.12}$$

The corresponding *M-point IDFT matrix* is given by $\mathcal{I}_M = \frac{\mathcal{F}_M^H}{M}$, such that $\mathcal{F}_M \mathcal{I}_M = \mathbf{I}_M$, where $\mathbf{I}_M$ denotes the $M \times M$ identity matrix. Notice that $\mathcal{F}_M$ and $\mathcal{I}_M$ are symmetric, i.e. $\mathcal{F}_M = \mathcal{F}_M^T$ and $\mathcal{I}_M = \mathcal{I}_M^T$. □

Definition A.12 The $M \times M$-dimensional matrix $\mathbf{Q}_{kl}$ is called a (complex) *Givens rotation* if it has the following structure

$$\mathbf{Q}_{kl} = \begin{array}{c} \\ \\ \\ \rightarrow^k \\ \\ \\ \rightarrow^l \\ \\ \\ \end{array} \begin{array}{c} \begin{array}{ccccccccc} & & & & \downarrow_k & & & \downarrow_l & \\ \end{array} \\ \begin{bmatrix} 1 & \dots & & & \dots & & & \dots & 0 \\ \vdots & \ddots & & & & & & & \vdots \\ & & 1 & & & & & & \\ & & & \cos\theta & \dots & e^{j\psi}\sin\theta & & & \\ & & & & 1 & & & & \\ \vdots & & & & \ddots & & & & \vdots \\ & & & & & 1 & & & \\ & & & -e^{-j\psi}\sin\theta & \dots & \cos\theta & & & \\ & & & & & & 1 & & \\ \vdots & & & & & & & \ddots & \vdots \\ 0 & \dots & & & \dots & & & \dots & 1 \end{bmatrix} \end{array}. \tag{A.13}$$

A complex Givens rotation is skew-hermitian and unitary. Pre-multiplication of a vector by $\mathbf{Q}$ amounts to a (complex) rotation in the (k, l)-th coordinate

plane. By using a Givens rotation a specified entry in a vector can be zeroed: given the vectors $\mathbf{x} \in \mathbb{C}^M$ and $\mathbf{y} = [y_i] = \mathbf{Q}\mathbf{x}$, then

$$y_i = \begin{cases} x_k \cos\theta + x_l e^{j\psi} \sin\theta, & i = k, \\ -x_k e^{-j\psi} \sin\theta + x_l \cos\theta, & i = l, \\ x_i, & i \neq k, l. \end{cases} \tag{A.14}$$

It is clear that y_l can be forced to zero by setting

$$\cos\theta = \frac{|x_k|}{\sqrt{|x_k|^2 + |x_l|^2}}, \qquad e^{j\psi} \sin\theta = \frac{x_k}{|x_k|} \frac{x_l^*}{\sqrt{|x_k|^2 + |x_l|^2}}. \tag{A.15}$$

Note that θ and ψ do not need to be computed explicitly and hence no inverse trigonometric functions are involved. □

A.2 Subspace related definitions

Definition A.13 The *range* of a matrix $\mathbf{A}$ is the subspace spanned by the vectors $\mathbf{A}\mathbf{x}$ for some $\mathbf{x}$. The dimension of this subspace is the rank of $\mathbf{A}$. □

Definition A.14 A matrix $\mathbf{P} \in \mathbb{C}^{M \times M}$ is called a *projector* iff $\mathbf{P}^2 = \mathbf{P}$. The *projection* of a vector $\mathbf{x} \in \mathbb{C}^M$ on the subspace range($\mathbf{P}$) is given by $\mathbf{P}\mathbf{x}$. Since $\mathbf{P}\mathbf{x}$ already lies in range($\mathbf{P}$), we have $\mathbf{P}(\mathbf{P}\mathbf{x}) = \mathbf{P}^2\mathbf{x} = \mathbf{P}\mathbf{x}$, $\forall \mathbf{x} \in \mathbb{C}^{M \times M}$. □

Definition A.15 Let $\mathbf{P}$ be a projector. The *complementary projector* to $\mathbf{P}$ is $\mathbf{I}_M - \mathbf{P}$. Clearly the complementary projector to $\mathbf{I}_M - \mathbf{P}$ is $\mathbf{P}$. □

Definition A.16 Let $\mathbf{a}_1, \ldots, \mathbf{a}_L$ be linearly independent columns in $\mathbb{C}^M$ spanning the subspace $\mathcal{S}_1$. Then the orthogonal projector onto $\mathcal{S}_1$ is given by

$$\mathbf{P} = \mathbf{A}(\mathbf{A}^H\mathbf{A})^{-1}\mathbf{A}^H, \tag{A.16}$$

where $\mathbf{A} = [\mathbf{a}_1 | \ldots | \mathbf{a}_L] \in \mathbb{C}^{M \times L}$ (with $M \geq L$). Notice that $\mathbf{P}^H = \mathbf{P}^2 = \mathbf{P}$. The orthogonal projector onto the orthogonal subspace of $\mathcal{S}_1$ is equal to $\mathbf{I}_M - \mathbf{P}$. □

A.3 Matrix decompositions

Definition A.17 The *QR-decomposition* of a matrix $\mathbf{A} \in \mathbb{C}^{M \times L}$ (with $M \geq L$) is defined as

$$\mathbf{A} = \mathbf{Q}\mathbf{R}, \tag{A.17}$$

where $\mathbf{Q}$ is an $M \times L$ unitary matrix and $\mathbf{R}$ is an $L \times L$ upper-triangular matrix. The QR-decomposition can be computed by means of Givens rotations. □

Definition A.18 The *Cholesky decomposition* of a hermitian positive definite matrix $\mathbf{A} \in \mathbb{C}^{M \times M}$ is defined as

$$\mathbf{A} = \mathbf{R}^H \mathbf{R}, \tag{A.18}$$

where $\mathbf{R}$ is an $M \times M$ non-singular upper-triangular matrix with positive real diagonal entries. □

Definition A.19 Given the square $M \times M$-dimensional matrix $\mathbf{A}$, we call λ_i an *eigenvalue* of $\mathbf{A}$ iff for some non-zero $\mathbf{v}_i \in \mathbb{C}^M$, $\mathbf{A}\mathbf{v}_i = \lambda_i \mathbf{v}_i$. The vector $\mathbf{v}_i$ is then called an *eigenvector* of $\mathbf{A}$ corresponding to λ_i. The eigenvalues of $\mathbf{A}$ can be found as the roots of its characteristic polynomial $\mathbf{p}(\lambda) = \det\{\mathbf{A} - \lambda \mathbf{I}_\mathrm{M}\}$. An eigenvector defines a one-dimensional subspace that is invariant to a pre-multiplication with $\mathbf{A}$. □

Definition A.20 If the $M \times M$-dimensional matrix $\mathbf{A} \in \mathbb{C}^{M \times M}$ has M linearly independent eigenvectors, then the *eigenvalue decomposition (EVD)* of $\mathbf{A}$ is given by

$$\mathbf{A} = \mathbf{V}\mathbf{\Lambda}\mathbf{V}^{-1}, \tag{A.19}$$

where $\mathbf{V}$ is an $M \times M$-dimensional matrix containing the eigenvectors $\mathbf{v}_i$ as columns and $\mathbf{\Lambda}$ is a diagonal matrix containing the eigenvalues λ_i, $i = 1, \ldots, M$ of $\mathbf{A}$. Typically, the eigenvectors are normalized such that $\|\mathbf{v}_i\|_2^2 = 1$, $i = 1, \ldots, M$. Some special cases can be distinguished:

- It can be shown that the EVD of a *hermitian* matrix $\mathbf{A}$ is equal to

  $$\mathbf{A} = \mathbf{V}\mathbf{\Lambda}\mathbf{V}^H, \tag{A.20}$$

  where $\mathbf{V}$ is a unitary matrix and all eigenvalues are real valued scalars.

- It can be shown that the EVD of a *circulant* matrix $\mathbf{A}$ can be written as

  $$\mathbf{A} = \mathcal{F}_M^{-1} \mathbf{\Lambda} \mathcal{F}_M, \tag{A.21}$$

  where the diagonal entries of $\mathbf{\Lambda}$ are obtained as $\mathcal{F}_M \mathbf{A}[:, 1]$. In other words, the eigenvectors of a circulant matrix $\mathbf{A}$ are equal to the DFT basis vectors and the eigenvalues are computed by taking the DFT of the first column of $\mathbf{A}$. Since DFTs can be implemented by means of the efficient FFT-algorithm, a product of the form $\mathbf{y} = \mathbf{A}\mathbf{x}$ can be solved at 'FFT-speed'.

□

Definition A.21 Given the $M \times M$-dimensional matrices $\mathbf{A}$ and $\mathbf{B}$, all non-zero (complex) M-dimensional vectors $\mathbf{v}_i \in \mathbb{C}^M$ and (complex) scalars λ_i that satisfy

$$\mathbf{A}\mathbf{v}_i = \lambda_i \mathbf{B}\mathbf{v}_i, \tag{A.22}$$

are called the *generalized eigenvectors* and *generalized eigenvalues* of the matrix pair ($\mathbf{A}$, $\mathbf{B}$). □

Definition A.22 If the $M \times M$-dimensional matrices $\mathbf{A}$ and $\mathbf{B}$ have M linearly independent generalized eigenvectors, then the generalized eigenvalue decomposition (GEVD) of $\mathbf{A}$ and $\mathbf{B}$ is given by

$$\mathbf{A}\mathbf{V} = \mathbf{B}\mathbf{V}\mathbf{\Lambda}, \tag{A.23}$$

where $\mathbf{V}$ is an $M \times M$-dimensional (invertible) matrix containing the generalized eigenvectors $\mathbf{v}_i$ as columns and $\mathbf{\Lambda}$ a diagonal matrix containing the generalized eigenvalues λ_i. When $\mathbf{B}$ is non-singular, hence $\mathbf{B}^{-1}$ exists, the generalized eigenvalues can be computed as the eigenvalues of the matrix $\mathbf{B}^{-1}\mathbf{A}$. □

Definition A.23 Let $\mathbf{A} \in \mathbb{C}^{M \times M}$ be a square hermitian matrix and $\mathbf{x} \in \mathbb{C}^M$ a non-zero vector, then the real valued scalar

$$r(\mathbf{x}) = \frac{\mathbf{x}^H \mathbf{A}\mathbf{x}}{\mathbf{x}^H \mathbf{x}}, \tag{A.24}$$

is called the *Rayleigh quotient* of $\mathbf{x}$. Note that if $\mathbf{x}$ is an eigenvector of $\mathbf{A}$, then $r(\mathbf{x})$ determines the corresponding eigenvalue. □

Definition A.24 Let $\mathbf{A} \in \mathbb{C}^{M \times M}$ and $\mathbf{B} \in \mathbb{C}^{M \times M}$ be two square hermitian matrices and $\mathbf{x} \in \mathbb{C}^M$ a non-zero vector, then the real valued scalar

$$r(\mathbf{x}) = \frac{\mathbf{x}^H \mathbf{A}\mathbf{x}}{\mathbf{x}^H \mathbf{B}\mathbf{x}}, \tag{A.25}$$

is called the *generalized Rayleigh quotient* of $\mathbf{x}$. Note that if $\mathbf{x}$ is a generalized eigenvector of $\mathbf{A}$ and $\mathbf{B}$, then $r(\mathbf{x})$ determines the corresponding generalized eigenvalue. □

Definition A.25 Every $M \times L$-dimensional matrix $\mathbf{A}$ (with $M \geq L$) can be decomposed as

$$\mathbf{A} = \mathbf{U}\Sigma\mathbf{V}^H, \tag{A.26}$$

where $\mathbf{U} \in \mathbb{C}^{M \times M}$ and $\mathbf{V} \in \mathbb{C}^{L \times L}$ are unitary matrices containing the left singular vectors $\mathbf{u}_i$ and the right singular vectors $\mathbf{v}_i$ respectively. The matrix

$\Sigma \in \mathbb{R}^{M \times L}$ is real, non-negative and diagonal with its diagonal elements arranged in non-increasing order (i.e. $\sigma_1 \geq \sigma_2 \geq \ldots \geq \sigma_M \geq 0$). The *singular values* of $\mathbf{A}$ are the diagonal elements, σ_i of Σ. The decomposition in (A.26) is called the *singular value decomposition (SVD)* of the matrix $\mathbf{A}$. If the matrix $\mathbf{A}$ has rank $R < M$, then $M - R$ singular values are equal to zero. □

Definition A.26 Given the matrices $\mathbf{A} \in \mathbb{C}^{M \times L}$ with $M \geq L$ and $\mathbf{B} \in \mathbb{C}^{P \times L}$ with $P \geq L$, then the *generalized singular value decomposition (GSVD)* of $\mathbf{A}$ and $\mathbf{B}$ is defined as

$$\mathbf{A} = \mathbf{U}_A \mathbf{\Sigma}_A \mathbf{V}^H, \tag{A.27}$$

$$\mathbf{B} = \mathbf{U}_B \mathbf{\Sigma}_B \mathbf{V}^H, \tag{A.28}$$

where $\mathbf{U}_A \in \mathbb{C}^{M \times L}$ is a unitary matrix, $\mathbf{U}_B \in \mathbb{C}^{P \times L}$ is a unitary matrix, $\mathbf{V}$ is an $L \times L$-dimensional invertible, but not necessarily unitary, matrix containing the (right) generalized singular vectors $\mathbf{v}_i$ and where $\mathbf{\Sigma}_A$ and $\mathbf{\Sigma}_B$ are $L \times L$-dimensional diagonal matrices containing $\sigma_{A,i}$ and $\sigma_{B,i}$, with $\sigma_{A,1} \geq \sigma_{A,2} \geq \ldots \geq \sigma_{A,L} \geq 0$ and $0 \leq \sigma_{B,1} \leq \sigma_{B,2} \leq \ldots \leq \sigma_{B,L}$. The generalized singular values are equal to $\sigma_{A,i}/\sigma_{B,i}$, $i = 1, \ldots, L$. □

A.4 Iterative eigensolvers

In several optimization problems an eigenvalue problem has to be solved where one is only interested in the eigenvector belonging to the largest (or smallest) eigenvalue. Here, we review two techniques to find the most dominant eigenvector of a matrix $\mathbf{A} \in \mathbb{C}^{M \times M}$: the power method and the inverse iteration method.

Power method

Definition A.27 Given the eigenvalue decomposition of a matrix $\mathbf{A} \in \mathbb{C}^{M \times M}$, $\mathbf{A} = \mathbf{V}\text{diag}\{\lambda_1, \ldots, \lambda_M\}\mathbf{V}^{-1}$ with $|\lambda_1| > |\lambda_2| \geqslant \ldots \geqslant |\lambda_M|$, the most dominant eigenvector of $\mathbf{A}$ can be obtained iteratively with the *power method* as follows:

$$\begin{array}{ll} \mathbf{v}^0 = \mathbf{v}_{init}, & \\ \text{for} \quad k = 1, 2, \ldots, N_{iter} & \\ \qquad \mathbf{v}^k = \mathbf{A}\mathbf{v}^{k-1}, & \\ \qquad \mathbf{v}^k = \mathbf{v}^k / \sqrt{(\mathbf{v}^k)^T \mathbf{v}^k}, & \\ \text{end.} & \end{array} \tag{A.29}$$

where $\mathbf{v}_{init}$ represents an M-dimensional initial vector and N_{iter} is the number of power iterations. When $\mathbf{v}^0$ has a component in the direction of the most dominant eigenvector, one can prove that the convergence speed is

$$\mathcal{O}\left(\left|\frac{\lambda_2}{\lambda_1}\right|^k\right). \tag{A.30}$$

In other words, the power method converges more easily when λ_1 is dominant with respect to the second largest eigenvalue λ_2. □

Inverse iteration

Definition A.28 Given the eigenvalue decomposition of a matrix $\mathbf{A} \in \mathbb{C}^{M \times M}$, $\mathbf{A} = \mathbf{V}\text{diag}\{\lambda_1, \ldots, \lambda_M\}\mathbf{V}^{-1}$ and a scalar μ such that $(\mathbf{A} - \mu\mathbf{I}_M) \in \mathbb{C}^{M \times M}$ is invertible, then the following is called *inverse iteration* or the *inverse power method*:

$$\begin{array}{ll} \mathbf{v}^0 = \mathbf{v}_{init}, & \\ \text{for} \quad k = 1, 2, \ldots, N_{iter} & \\ \qquad \text{solve}\{(\mathbf{A} - \mu\mathbf{I}_M)\mathbf{w}^k = \mathbf{v}^{k-1}\}, & \\ \qquad \mathbf{v}^k = \mathbf{w}^k / \sqrt{(\mathbf{w}^k)^T \mathbf{w}^k}, & \\ \text{end.} & \end{array} \tag{A.31}$$

where $\mathbf{v}_{init}$ represents an M-dimensional initial and N_{iter} is the number of iterations. Inverse iteration is equivalent to the power method applied to $(\mathbf{A} - \mu\mathbf{I}_M)^{-1}$ and hence converges to the most dominant eigenvector of $(\mathbf{A} - \mu\mathbf{I}_M)^{-1}$. Assume that λ_i and $\mathbf{v}_i$ are an eigenvalue and eigenvector pair of $\mathbf{A}$ such that $|\lambda_i - \mu|^{-1}$ is the largest eigenvalue of $(\mathbf{A} - \mu\mathbf{I}_M)^{-1}$ in magnitude. The inverse iteration converges if $\mathbf{v}_0$ is not perpendicular to $\mathbf{v}_i$ and one can prove that the convergence speed depends on

$$\mathcal{O}\left(\left|\frac{(\lambda_i - \mu)}{(\lambda_j - \mu)}\right|\right), \tag{A.32}$$

where λ_j is an eigenvalue of $\mathbf{A}$ such that $|\lambda_j - \mu|^{-1}$ is the second largest eigenvalue of $(\mathbf{A} - \mu\mathbf{I}_M)^{-1}$ in magnitude. Inverse iteration has the ability to converge to any desired eigenvector (the one with a corresponding eigenvalue nearest to μ). This method is particularly effective when a good approximation of a desired eigenvalue is known and only the computation of the corresponding eigenvector is required. □

A.5 Differentiation with respect to a parameter vector

In many optimization problems a cost function has to be differentiated with respect to an unknown parameter vector. In this subsection, the definition of the gradient and the Hessian of a cost function will be briefly addressed. In addition, some useful properties will be given. Since these differentiation issues will especially prove useful in Chapter 4, where the unknown parameter vector is real valued, we will restrict ourselves to the real valued case. Extensions to the complex valued case can easily be made.

Definition A.29 Given the parameter vector $\mathbf{x} \in \mathbb{R}^M$ and a real valued cost function $J(\mathbf{x})$ depending on $\mathbf{x}$. The vector $\nabla_{\mathbf{x}} J \in \mathbb{R}^M$ is called the *gradient*

vector of $J(\mathbf{x})$ and is defined as

$$\nabla_{\mathbf{x}} J = \left[\frac{\partial J}{\partial x_1} \ \cdots \ \frac{\partial J}{\partial x_M} \right]^T, \tag{A.33}$$

where $\frac{\partial J}{\partial x_i}$ denotes the partial derivative of J with respect to x_i. □

Definition A.30 Given the parameter vector $\mathbf{x} \in \mathbb{R}^M$ and a real valued cost function $J(\mathbf{x})$ depending on $\mathbf{x}$. The matrix $\nabla^2_{\mathbf{x}} J \in \mathbb{R}^{M \times M}$ is called the *Hessian* of $J(\mathbf{x})$ and is defined as

$$\begin{aligned} \nabla^2_{\mathbf{x}} J &= \begin{bmatrix} \frac{\partial^2 J}{\partial x_1 \partial x_1} & \frac{\partial^2 J}{\partial x_1 \partial x_2} & \cdots & \frac{\partial^2 J}{\partial x_1 \partial x_M} \\ \frac{\partial^2 J}{\partial x_2 \partial x_1} & \frac{\partial^2 J}{\partial x_2 \partial x_2} & & \\ \vdots & & \ddots & \vdots \\ \frac{\partial^2 J}{\partial x_M \partial x_1} & & \cdots & \frac{\partial^2 J}{\partial x_M \partial x_M} \end{bmatrix}, & \text{(A.34)} \\ &= \begin{bmatrix} \frac{\partial}{\partial x_1} \\ \vdots \\ \frac{\partial}{\partial x_M} \end{bmatrix} \begin{bmatrix} \frac{\partial J}{\partial x_1} & \cdots & \frac{\partial J}{\partial x_M} \end{bmatrix} = \nabla_{\mathbf{x}} (\nabla_{\mathbf{x}} J)^T. & \text{(A.35)} \end{aligned}$$

From this definition, it is clear that the Hessian is symmetric and can be obtained by differentiating the transposed gradient of $J(\mathbf{x})$. □

Property A.31 With the real valued variable $\mathbf{x} \in \mathbb{R}^M$ and the complex valued matrix $\mathbf{A} \in \mathbb{C}^{M \times M}$ and vector $\mathbf{a} \in \mathbb{C}^M$, the following gradient rules apply

$$\begin{aligned} \nabla_{\mathbf{x}} \mathbf{x}^T \mathbf{A} \mathbf{x} &= (\mathbf{A} + \mathbf{A}^T)\mathbf{x}, & \text{(A.36)} \\ \nabla_{\mathbf{x}} \mathbf{a}^T \mathbf{x} &= \mathbf{a}, & \text{(A.37)} \\ \nabla_{\mathbf{x}} \mathbf{a}^H \mathbf{x} &= \mathbf{a}^*, & \text{(A.38)} \\ \nabla_{\mathbf{x}} \mathcal{R}e\{\mathbf{a}^H\}\mathbf{x} &= \mathcal{R}e\{\mathbf{a}\}, & \text{(A.39)} \end{aligned}$$

which can easily be proven by element-wise computation of the elements in the gradient. □

B Appendix to Chapter 3

B.1 MMSE TEQ design with unit-norm constraint on TEQ

Property B.1 MMSE TEQ design according to (3.9) with a unit-norm constraint on the TEQ, i.e. $\mathbf{w}^T\mathbf{w} = 1$, is equivalent to solving (3.2) with

$$\mathbf{A} = \mathbf{R}_{yy} - \mathbf{R}_{yx}\mathbf{R}_{xx}^{-1}\mathbf{R}_{xy}, \tag{B.1}$$

$$\mathbf{B} = \mathbf{I}_T. \tag{B.2}$$

□

Proof : When subjected to a unit-norm constraint on $\mathbf{w}$, (3.9) comes down to

$$\min_{\mathbf{w},\mathbf{b}} \mathbf{w}^T\mathbf{R}_{yy}\mathbf{w} + \mathbf{b}^T\mathbf{R}_{xx}\mathbf{b} - 2\mathbf{b}^T\mathbf{R}_{xy}\mathbf{w} \quad \text{subject to} \quad \mathbf{w}^T\mathbf{w} = 1. \tag{B.3}$$

With the method of the Lagrange multipliers, the constraint can be incorporated into the cost function

$$\min_{\mathbf{w},\mathbf{b}} \mathcal{L}, \tag{B.4}$$

$$\min_{\mathbf{w},\mathbf{b}} \mathbf{w}^T\mathbf{R}_{yy}\mathbf{w} + \mathbf{b}^T\mathbf{R}_{xx}\mathbf{b} - 2\mathbf{b}^T\mathbf{R}_{xy}\mathbf{w} + \lambda(1 - \mathbf{w}^T\mathbf{w}), \tag{B.5}$$

where $\mathcal{L}$ is the Lagrangian and λ is a Lagrange multiplier. The minimum is obtained by setting the gradients of $\mathcal{L}$ with respect to $\mathbf{w}$, $\mathbf{b}$ and λ equal to zero

$$\nabla_{\mathbf{w}}\mathcal{L} = \mathbf{R}_{yy}\mathbf{w} - \mathbf{R}_{yx}\mathbf{b} - \lambda\mathbf{w} = \mathbf{0}, \tag{B.6}$$

$$\nabla_{\mathbf{b}}\mathcal{L} = \mathbf{R}_{xx}\mathbf{b} - \mathbf{R}_{xy}\mathbf{w} = \mathbf{0}, \tag{B.7}$$

$$\nabla_{\lambda}\mathcal{L} = \mathbf{w}^T\mathbf{w} - 1 = 0. \tag{B.8}$$

From (B.7), we obtain

$$\mathbf{b} = \mathbf{R}_{xx}^{-1}\mathbf{R}_{xy}\mathbf{w}, \tag{B.9}$$

which we use to simplify (B.6) as

$$(\mathbf{R}_{yy} - \mathbf{R}_{yx}\mathbf{R}_{xx}^{-1}\mathbf{R}_{xy})\mathbf{w} = \lambda\mathbf{w}. \tag{B.10}$$

This is an ordinary eigenvalue problem. Since $\mathcal{L}$ reduces to λ with (B.7) and (B.10), the optimal $\mathbf{w}$ is obtained as the eigenvector of $\mathbf{R}_{yy} - \mathbf{R}_{yx}\mathbf{R}_{xx}^{-1}\mathbf{R}_{xy}$ associated with the smallest eigenvalue. According to (3.3) or (3.4) this solution is equivalent to (3.2) with

$$\mathbf{A} = \mathbf{R}_{yy} - \mathbf{R}_{yx}\mathbf{R}_{xx}^{-1}\mathbf{R}_{xy}, \tag{B.11}$$

$$\mathbf{B} = \mathbf{I}_T, \tag{B.12}$$

which completes the proof. □

B.2 MMSE TEQ design with unit-tap constraint on TEQ

Property B.2 MMSE TEQ design according to (3.9) with a unit-tap constraint on the TEQ, i.e. $\mathbf{e}_p^T\mathbf{w} = 1$, is equivalent to solving (3.2) with

$$\mathbf{A} = \mathbf{R}_{yy} - \mathbf{R}_{yx}\mathbf{R}_{xx}^{-1}\mathbf{R}_{xy}, \tag{B.13}$$

$$\mathbf{B} = \mathbf{e}_p\mathbf{e}_p^T. \tag{B.14}$$

□

Proof: When subjected to a unit-tap constraint on $\mathbf{w}$, (3.9) comes down to

$$\min_{\mathbf{w},\mathbf{b}} \mathbf{w}^T\mathbf{R}_{yy}\mathbf{w} + \mathbf{b}^T\mathbf{R}_{xx}\mathbf{b} - 2\mathbf{b}^T\mathbf{R}_{xy}\mathbf{w} \quad \text{subject to} \quad \mathbf{e}_p^T\mathbf{w} = 1. \tag{B.15}$$

Since the constraint only involves $\mathbf{w}$, the gradient of J with respect to $\mathbf{b}$ will be equal to zero at the optimum, i.e.

$$\nabla_{\mathbf{b}} J = \mathbf{R}_{xx}\mathbf{b} - \mathbf{R}_{xy}\mathbf{w} = \mathbf{0}, \tag{B.16}$$

or equivalently

$$\mathbf{b} = \mathbf{R}_{xx}^{-1}\mathbf{R}_{xy}\mathbf{w}. \tag{B.17}$$

With (B.17), we simplify (B.15) to a cost function in the variable $\mathbf{w}$ only

$$\min_{\mathbf{w}} \mathbf{w}^T(\mathbf{R}_{yy} - \mathbf{R}_{yx}\mathbf{R}_{xx}^{-1}\mathbf{R}_{xy})\mathbf{w} \quad \text{subject to} \quad \mathbf{e}_p^T\mathbf{w} = 1. \tag{B.18}$$

Since the sign of the TEQ does not influence the performance (the sign is compensated by the FEQs), we might as well optimize

$$\min_{\mathbf{w}} \mathbf{w}^T(\mathbf{R}_{yy} - \mathbf{R}_{yx}\mathbf{R}_{xx}^{-1}\mathbf{R}_{xy})\mathbf{w} \quad \text{subject to} \quad \mathbf{w}^T\mathbf{e}_p\mathbf{e}_p^T\mathbf{w} = 1. \tag{B.19}$$

This is equivalent to the problem in (3.3) with

$$\mathbf{A} = \mathbf{R}_{yy} - \mathbf{R}_{yx}\mathbf{R}_{xx}^{-1}\mathbf{R}_{xy}, \tag{B.20}$$

$$\mathbf{B} = \mathbf{e}_p\mathbf{e}_p^T, \tag{B.21}$$

which completes the proof. □

B.3 MMSE TEQ design with unit-energy constraints

Property B.3 MMSE TEQ design according to (3.9) with the following unit-energy constraints

- case 1: $\min_{\mathbf{w}_1,\mathbf{b}_1} J(\mathbf{w}_1, \mathbf{b}_1)$ subject to $\mathbf{b}_1^T\mathbf{R}_{xx}\mathbf{b}_1 = 1$,

- case 2: $\min_{\mathbf{w}_2,\mathbf{b}_2} J(\mathbf{w}_2,\mathbf{b}_2)$ subject to $\mathbf{w}_2^T\mathbf{R}_{yy}\mathbf{w}_2 = 1$,
- case 3: $\min_{\mathbf{w}_3,\mathbf{b}_3} J(\mathbf{w}_3,\mathbf{b}_3)$ subject to $\mathbf{w}_3^T\mathbf{R}_{yy}\mathbf{w}_3 = 1$ and $\mathbf{b}_3^T\mathbf{R}_{xx}\mathbf{b}_3 = 1$,

have the following remarkable properties for the optimal solutions:

$$\begin{aligned} \mathbf{w}_1 &= \sigma\mathbf{w}_2, && \text{(B.22)}\\ \mathbf{b}_1 &= \sigma^{-1}\mathbf{b}_2, && \text{(B.23)}\\ \mathbf{w}_2 &= \mathbf{w}_3, && \text{(B.24)}\\ \mathbf{b}_1 &= \mathbf{b}_3, && \text{(B.25)}\\ J_{min}(\mathbf{w}_1,\mathbf{b}_1) = J_{min}(\mathbf{w}_2,\mathbf{b}_2) &\leq J_{min}(\mathbf{w}_3,\mathbf{b}_3), && \text{(B.26)} \end{aligned}$$

□

Proof: In case 1, the gradient with respect to $\mathbf{w}_1$ is equal to zero at the optimum of J, i.e.

$$\begin{aligned} \nabla_{\mathbf{w}_1} J &= \mathbf{R}_{yy}\mathbf{w}_1 - \mathbf{R}_{yx}\mathbf{b}_1 = \mathbf{0}, && \text{(B.27)}\\ \Rightarrow \mathbf{w}_1 &= \mathbf{R}_{yy}^{-1}\mathbf{R}_{yx}\mathbf{b}_1, && \text{(B.28)} \end{aligned}$$

where J is defined in (3.9). With this relation, $\mathbf{w}_1$ can be eliminated from the expression for J

$$\begin{aligned} \min_{\mathbf{b}_1} J &= \min_{\mathbf{b}_1} \mathbf{b}_1^T(\mathbf{R}_{xx} - \mathbf{R}_{xy}\mathbf{R}_{yy}^{-1}\mathbf{R}_{yx})\mathbf{b}_1 \quad \text{subject to} \quad \mathbf{b}_1^T\mathbf{R}_{xx}\mathbf{b}_1 = 1, && \text{(B.29)}\\ &= 1 - \max_{\tilde{\mathbf{b}}_1} \tilde{\mathbf{b}}_1^T(\mathbf{R}_{xx}^{-T/2}\mathbf{R}_{xy}\mathbf{R}_{yy}^{-1}\mathbf{R}_{yx}\mathbf{R}_{xx}^{-1/2})\tilde{\mathbf{b}}_1, && \text{(B.30)}\\ &= 1 - \max_{\tilde{\mathbf{b}}_1} \tilde{\mathbf{b}}_1^T(\mathbf{P}^T\mathbf{P})\tilde{\mathbf{b}}_1 \qquad \text{subject to} \quad \tilde{\mathbf{b}}_1^T\tilde{\mathbf{b}}_1 = 1, && \text{(B.31)} \end{aligned}$$

where $\tilde{\mathbf{b}}_1$ is a transformed version of $\mathbf{b}_1$,

$$\tilde{\mathbf{b}}_1 = \mathbf{R}_{xx}^{1/2}\mathbf{b}_1, \qquad \text{(B.32)}$$

and where $\mathbf{P}$ is given by $\mathbf{P} = \mathbf{R}_{yy}^{-T/2}\mathbf{R}_{yx}\mathbf{R}_{xx}^{-1/2}$. Hence, the optimal $\tilde{\mathbf{b}}_1$ can be found as the eigenvector corresponding to the maximum eigenvalue of $\mathbf{P}^T\mathbf{P}$. Using (B.32) results in the optimal TIR.

For case 2, one can prove (similarly to case 1) that $\mathbf{w}_2$ is the solution of

$$\min_{\mathbf{w}_2} J = 1 - \max_{\tilde{\mathbf{w}}_2} \tilde{\mathbf{w}}_2^T(\mathbf{P}\mathbf{P}^T)\tilde{\mathbf{w}}_2 \text{ subject to } \tilde{\mathbf{w}}_2^T\tilde{\mathbf{w}}_2 = 1, \qquad \text{(B.33)}$$

where $\tilde{\mathbf{w}}_2 = \mathbf{R}_{yy}^{1/2}\mathbf{w}_2$. This time, the optimal TEQ can be obtained from the eigenvector corresponding to the maximum eigenvalue of $\mathbf{P}\mathbf{P}^T$. Since the

eigenvalues of $\mathbf{P}^T\mathbf{P}$ and $\mathbf{P}\mathbf{P}^T$ are equal, both unit-energy constraints result in the same MMSE, i.e.

$$J_{min}(\mathbf{w}_1, \mathbf{b}_1) = J_{min}(\mathbf{w}_2, \mathbf{b}_2) = 1 - \lambda_{max}, \tag{B.34}$$

where λ_{max} is the largest eigenvalue of $\mathbf{P}^T\mathbf{P}$.

If λ_{max} is the largest eigenvalue of $\mathbf{P}^T\mathbf{P}$ and $\tilde{\mathbf{b}}_1$ the corresponding eigenvector then the following holds

$$\mathbf{P}^T\mathbf{P}\tilde{\mathbf{b}}_1 = \lambda_{max}\tilde{\mathbf{b}}_1. \tag{B.35}$$

By multiplying each side with $\mathbf{R}_{yy}^{-1}\mathbf{R}_{yx}\mathbf{R}_{xx}^{-1/2}$ and by using (B.32) and (B.28), we obtain

$$\underbrace{\mathbf{R}_{yy}^{-1}\mathbf{R}_{yx}\mathbf{R}_{xx}^{-1}\mathbf{R}_{xy}}_{\mathbf{Q}}\mathbf{w}_1 = \lambda_{max}\mathbf{w}_1. \tag{B.36}$$

In a similar way, vector $\tilde{\mathbf{w}}_2$ is such that

$$\mathbf{P}\mathbf{P}^T\tilde{\mathbf{w}}_2 = \lambda_{max}\tilde{\mathbf{w}}_2, \tag{B.37}$$

$$\underbrace{\mathbf{R}_{yy}^{-1}\mathbf{R}_{yx}\mathbf{R}_{xx}^{-1}\mathbf{R}_{xy}}_{\mathbf{Q}}\mathbf{w}_2 = \lambda_{max}\mathbf{w}_2, \tag{B.38}$$

with the same value of λ_{max} as in formulas (B.35) and (B.36). From (B.36) and (B.38), it is seen that the TEQs of the two different optimization problems are eigenvectors of the same matrix $\mathbf{Q}$ corresponding to the same eigenvalue[1] λ_{max}.

In case 3, it is easy to show by using Lagrange multipliers that the optimal TEQ and TIR can be obtained from the generalized eigenvalue problem

$$\begin{bmatrix} \mathbf{0} & \mathbf{R}_{yx} \\ \mathbf{R}_{xy} & \mathbf{0} \end{bmatrix}\begin{bmatrix} \mathbf{w}_3 \\ \mathbf{b}_3 \end{bmatrix} = \begin{bmatrix} \mathbf{R}_{yy} & \mathbf{0} \\ \mathbf{0} & \mathbf{R}_{xx} \end{bmatrix}\begin{bmatrix} \mathbf{w}_3 \\ \mathbf{b}_3 \end{bmatrix}(1-\alpha), \tag{B.39}$$

where $(1-\alpha)$ is a generalized eigenvalue. Since the cost function in (3.9) with $\mathbf{w}_3^T\mathbf{R}_{yy}\mathbf{w}_3 = 1$ and $\mathbf{b}_3^T\mathbf{R}_{xx}\mathbf{b}_3 = 1$ can be simplified to

$$J(\mathbf{w}_3, \mathbf{b}_3) = 2 - 2\mathbf{b}_3^T\mathbf{R}_{xy}\mathbf{w}_3 = 2\alpha, \tag{B.40}$$

the minimum is reached for the smallest possible α or the optimal solution corresponds to the generalized eigenvector belonging to the largest generalized eigenvalue of (B.39).

The scaling factor between $\mathbf{w}_1$ and $\mathbf{w}_2$ can be computed as follows. Consider first the singular value decomposition of $\mathbf{P}$

$$\mathbf{P} = \mathbf{U}\mathbf{\Sigma}\mathbf{V}^T. \tag{B.41}$$

[1] The contrived case of an algebraic multiplicity larger than one is not considered here.

Then we know from (B.35) and (B.37) that $\tilde{\mathbf{b}}_1 = \mathbf{V}(:,1)$ and $\tilde{\mathbf{w}}_2 = \mathbf{U}(:,1)$. By applying (B.28) and (B.32), the norm of $\mathbf{w}_1$ is equal to

$$\begin{aligned}
\mathbf{w}_1^T\mathbf{w}_1 &= \tilde{\mathbf{b}}_1^T\mathbf{R}_{xx}^{-T/2}\mathbf{R}_{xy}\mathbf{R}_{yy}^{-T}\mathbf{R}_{yy}^{-1}\mathbf{R}_{yx}\mathbf{R}_{xx}^{-1/2}\tilde{\mathbf{b}}_1, && \text{(B.42)}\\
&= \sigma_{max}\mathbf{U}(:,1)^T\mathbf{R}_{yy}^{-T/2}\mathbf{R}_{yy}^{-1/2}\mathbf{U}(:,1)\sigma_{max}, && \text{(B.43)}\\
&= \sigma_{max}^2\mathbf{w}_2^T\mathbf{w}_2, && \text{(B.44)}
\end{aligned}$$

where σ_{max} is the largest singular value of $\mathbf{P}$. In conclusion, $\mathbf{w}_1 = \pm\sigma_{max}\mathbf{w}_2$, i.e. the scaling factor between the TEQs is the largest singular value of $\mathbf{P}$.

A similar derivation can be given for the TIRs. It can be proven that $\mathbf{b}_1$ and $\mathbf{b}_2$ are eigenvectors belonging to the largest eigenvalue of matrix $\mathbf{R}_{xx}^{-1}\mathbf{R}_{xy}\mathbf{R}_{yy}^{-1}\mathbf{R}_{yx}$ and that $\mathbf{b}_2^T\mathbf{b}_2 = \sigma_{max}^2\mathbf{b}_1^T\mathbf{b}_1$, so that $\mathbf{b}_1 = \pm\sigma_{max}^{-1}\mathbf{b}_2$.

It is also possible to relate the solution obtained in case 3, with the solutions computed in cases 1 and 2. With the Cholesky decomposition of $\mathbf{R}_{yy}$ and $\mathbf{R}_{xx}$, i.e. $\mathbf{R}_{yy} = \mathbf{R}_{yy}^{T/2}\mathbf{R}_{yy}^{1/2}$ and $\mathbf{R}_{xx} = \mathbf{R}_{xx}^{T/2}\mathbf{R}_{xx}^{1/2}$, we can turn the generalized eigenvalue problem into an ordinary eigenvalue problem

$$\begin{bmatrix} \mathbf{0} & \mathbf{R}_{yy}^{-T/2}\mathbf{R}_{yx}\mathbf{R}_{xx}^{-1/2} \\ \mathbf{R}_{xx}^{-T/2}\mathbf{R}_{xy}\mathbf{R}_{yy}^{-1/2} & \mathbf{0} \end{bmatrix}\begin{bmatrix} \mathbf{R}_{yy}^{1/2}\mathbf{w}_3 \\ \mathbf{R}_{xx}^{1/2}\mathbf{b}_3 \end{bmatrix} = \begin{bmatrix} \mathbf{R}_{yy}^{1/2}\mathbf{w}_3 \\ \mathbf{R}_{xx}^{1/2}\mathbf{b}_3 \end{bmatrix}(1-\alpha), \quad \text{(B.45)}$$

$$\begin{bmatrix} \mathbf{0} & \mathbf{P} \\ \mathbf{P}^T & \mathbf{0} \end{bmatrix}\begin{bmatrix} \tilde{\mathbf{w}}_3 \\ \tilde{\mathbf{b}}_3 \end{bmatrix} = \begin{bmatrix} \tilde{\mathbf{w}}_3 \\ \tilde{\mathbf{b}}_3 \end{bmatrix}(1-\alpha), \quad \text{(B.46)}$$

where $\tilde{\mathbf{w}}_3$ and $\tilde{\mathbf{b}}_3$ are defined in the same way as $\tilde{\mathbf{b}}_1$ and $\tilde{\mathbf{w}}_2$. With the singular value decomposition of $\mathbf{P}$, cf. (B.41), the optimal solution becomes $\tilde{\mathbf{w}}_3 = \mathbf{V}(:,1)$ and $\tilde{\mathbf{b}}_3 = \mathbf{U}(:,1)$, which means that $\mathbf{w}_3 = \mathbf{w}_2$ and $\mathbf{b}_3 = \mathbf{b}_1$. It can easily be seen that the MMSE from (B.40) can be redefined in terms of the largest singular value of $\mathbf{P}$

$$J_{min}(\mathbf{w}_3, \mathbf{b}_3) = 2(1 - \sigma_{max}). \quad \text{(B.47)}$$

Since $J_{min}(\mathbf{w}_1, \mathbf{b}_1) = J_{min}(\mathbf{w}_2, \mathbf{b}_2) = 1 - \sigma_{max}^2 \geqslant 0$, $J_{min}(\mathbf{w}_3, \mathbf{b}_3)$ is always greater than or equal to $J_{min}(\mathbf{w}_1, \mathbf{b}_1)$, which completes the proof. □

Property B.4 MMSE TEQ design according to (3.9) with the following unit-energy constraints

- case 1: $\min_{\mathbf{w}_1,\mathbf{b}_1} J(\mathbf{w}_1, \mathbf{b}_1)$ subject to $\mathbf{b}_1^T\mathbf{R}_{xx}\mathbf{b}_1 = 1$,
- case 2: $\min_{\mathbf{w}_2,\mathbf{b}_2} J(\mathbf{w}_2, \mathbf{b}_2)$ subject to $\mathbf{w}_2^T\mathbf{R}_{yy}\mathbf{w}_2 = 1$,
- case 3: $\min_{\mathbf{w}_3,\mathbf{b}_3} J(\mathbf{w}_3, \mathbf{b}_3)$ subject to $\mathbf{w}_3^T\mathbf{R}_{yy}\mathbf{w}_3 = 1$ and $\mathbf{b}_3^T\mathbf{R}_{xx}\mathbf{b}_3 = 1$,

is equivalent to solving (3.9) with

$$\mathbf{A} = \mathbf{I}_T, \tag{B.48}$$
$$\mathbf{B} = \mathbf{R}_{yy}^{-1}\mathbf{R}_{yx}\mathbf{R}_{xx}^{-1}\mathbf{R}_{xy}. \tag{B.49}$$

□

Proof : Since we are only interested in the TEQ up to a scale factor, Property (B.3) indicates that it is sufficient to consider only one unit-energy constraint, e.g. case 2. From (B.38), we observe that $\mathbf{w}_2$ is the eigenvector associated with the largest eigenvalue of $\mathbf{R}_{yy}^{-1}\mathbf{R}_{yx}\mathbf{R}_{xx}^{-1}\mathbf{R}_{xy}$, i.e.

$$\mathbf{R}_{yy}^{-1}\mathbf{R}_{yx}\mathbf{R}_{xx}^{-1}\mathbf{R}_{xy}\mathbf{w}_2 = \lambda_{max}\mathbf{w}_2. \tag{B.50}$$

According to (3.4), this is equivalent to solving (3.2) with

$$\mathbf{A} = \mathbf{I}_T, \tag{B.51}$$
$$\mathbf{B} = \mathbf{R}_{yy}^{-1}\mathbf{R}_{yx}\mathbf{R}_{xx}^{-1}\mathbf{R}_{xy}, \tag{B.52}$$

which completes the proof. □

It is easy to show that other combinations of $\mathbf{A}$ and $\mathbf{B}$ lead to the same TEQ (up to a scale factor), e.g.

$$\mathbf{A} = \mathbf{R}_{yy}, \tag{B.53}$$
$$\mathbf{B} = \mathbf{R}_{yx}\mathbf{R}_{xx}^{-1}\mathbf{R}_{xy}. \tag{B.54}$$

or even

$$\mathbf{A} = \mathbf{R}_{yy}^{-1} - \mathbf{R}_{yx}\mathbf{R}_{xx}^{-1}\mathbf{R}_{xy}, \tag{B.55}$$
$$\mathbf{B} = \mathbf{R}_{yy}. \tag{B.56}$$

B.4 The unconstrained MMSE PTEQ

Property B.5 PTEQ design according to an unconstrained MMSE optimization, as in (3.121), leads to a biased solution, i.e. $\mathcal{E}\{E_i^k|X_i^k\} \neq 0$, with $E_i^k = \bar{\mathbf{v}}_{opt,i}^T\mathbf{z}_i^k - X_i^k$. □

Proof : The proof is based on the following assumptions:

- the symbols $X_{0:N-1}^k$ transmitted during symbol period k are uncorrelated with the symbols $X_{0:N-1}^l$ transmitted during symbol period l with $l \neq k$,

- the frequency domain symbols X_i^k transmitted during a certain symbol period on tone i are zero mean and independent of the frequency domain symbols X_j^k transmitted during the same symbol period on tone j with $i \neq j$,
- the external noise is zero mean and independent of the transmitted DMT symbols.

Starting from (3.121), which is repeated here for convenience,

$$\bar{\mathbf{v}}_{opt,i} = \arg\min_{\bar{\mathbf{v}}_i} \mathcal{E}\left\{\left|\bar{\mathbf{v}}_i^T \mathbf{z}_i^k - X_i^k\right|^2\right\}, \tag{B.57}$$

the Wiener solution for $\bar{\mathbf{v}}_i$ is given by

$$\bar{\mathbf{v}}_{opt,i} = (\mathcal{E}\{(\mathbf{z}_i^k)^*(\mathbf{z}_i^k)^T\})^{-1}\mathcal{E}\{(\mathbf{z}_i^k)^* X_i^k\}. \tag{B.58}$$

Let $\bar{\mathbf{F}}_i$ be equal to

$$\bar{\mathbf{F}}_i = \left[\begin{array}{c|c|c} \mathbf{I}_{T-1} & \mathbf{0} & -\mathbf{I}_{T-1} \\ \hline \mathbf{0} & \multicolumn{2}{c}{\mathcal{F}_N[i,:]} \end{array}\right], \tag{B.59}$$

then the PTEQ input elements for tone i can be obtained as

$$\begin{aligned} \mathbf{z}_i^k &= \bar{\mathbf{F}}_i \mathbf{y}^k, & \text{(B.60)} \\ &= \bar{\mathbf{F}}_i(\mathbf{H}_{N+i} X_i^k + \bar{\mathbf{H}}\bar{\mathbf{X}}^k + \mathbf{n}^k), & \text{(B.61)} \end{aligned}$$

where we used the data model for $\mathbf{y}^k$, given in (2.32). The Wiener solution for the PTEQ in (B.58) can now be written explicitly in terms of the channel and noise model

$$\bar{\mathbf{v}}_{opt,i} = \left(\bar{\mathbf{F}}_i^*(\sigma_{x,i}^2 \mathbf{H}_{N+i}^* \mathbf{H}_{N+i}^T + \bar{\mathbf{H}}^* \mathbf{R}_{XX} \bar{\mathbf{H}}^T + \mathbf{R}_{nn})\bar{\mathbf{F}}_i^T\right)^{-1} \bar{\mathbf{F}}_i^* \mathbf{H}_{N+i}^* \sigma_{x,i}^2 \tag{B.62}$$

where the assumptions given at the beginning of this proof were used and where $\sigma_{x,i}^2 = \mathcal{E}\{(X_i^k)^* X_i^k\}$, $\mathbf{R}_{XX} = \mathcal{E}\{(\bar{\mathbf{X}}^k)^*(\bar{\mathbf{X}}^k)^T\}$ and $\mathbf{R}_{nn} = \mathcal{E}\{\mathbf{n}^k(\mathbf{n}^k)^T\}$. Before determining the value of $\mathcal{E}\{E_i^k | X_i^k\}$, note that E_i^k can be written as

$$\begin{aligned} E_i^k &= \bar{\mathbf{v}}_{opt,i}^T \mathbf{z}_i^k - X_i^k, & \text{(B.63)} \\ &= \bar{\mathbf{v}}_{opt,i}^T \bar{\mathbf{F}}_i(\mathbf{H}_{N+i} X_i^k + \bar{\mathbf{H}}\bar{\mathbf{X}}^k + \mathbf{n}^k) - X_i^k, & \text{(B.64)} \end{aligned}$$

where (B.61) was used. The conditional probability $\mathcal{E}\{E_i^k | X_i^k\}$ is now equal to

$$\mathcal{E}\{E_i^k | X_i^k\} = \bar{\mathbf{v}}_{opt,i}^T \bar{\mathbf{F}}_i \mathbf{H}_{N+i} X_i^k - X_i^k, \tag{B.65}$$

where it is assumed that the noise is zero mean and independent of X_i^k, i.e $\mathcal{E}\{\mathbf{n}^k | X_i^k\} = \mathcal{E}\{\mathbf{n}^k\} = \mathbf{0}$, and that $\bar{\mathbf{X}}^k$ is zero mean and independent of X_i^k, i.e. $\mathcal{E}\{\bar{\mathbf{X}}^k | X_i^k\} = \mathcal{E}\{\bar{\mathbf{X}}^k\} = \mathbf{0}$. Equation (B.65) is not equal to zero, since

$$\bar{\mathbf{v}}_{opt,i}^T \bar{\mathbf{F}}_i \mathbf{H}_{N+i} \neq 1. \tag{B.66}$$

Consequently, the unconstrained MMSE PTEQ is biased, which completes the proof. □

The bias can be removed by adding the constraint

$$\bar{\mathbf{v}}_i^T \mathcal{E}\{\mathbf{z}_i^k (X_i^k)^*\} = \mathcal{E}\{X_i^k (X_i^k)^*\}, \tag{B.67}$$

to (B.57). Since $\bar{\mathbf{v}}_i^T \mathcal{E}\{\mathbf{z}_i^k (X_i^k)^*\}$ is given by

$$\bar{\mathbf{v}}_i^T \mathcal{E}\{\mathbf{z}_i^k (X_i^k)^*\} = \bar{\mathbf{v}}_i^T \bar{\mathbf{F}}_i \mathbf{H}_{N+i} \mathcal{E}\{X_i^k (X_i^k)^*\} \tag{B.68}$$

the constraint in (B.67) forces $\bar{\mathbf{v}}_{opt,i}^T \bar{\mathbf{F}}_i \mathbf{H}_{N+i}$ to be equal to one and hence leads to an unbiased solution.

Property B.6 MMSE PTEQ design according to (3.123) is equivalent to solving (3.7) with

$$\begin{aligned} \mathbf{A}_i &= \mathcal{E}\{(\mathbf{z}_i^k)^* (\mathbf{z}_i^k)^T\}), & \text{(B.69)} \\ \mathbf{B}_i &= \mathcal{E}\{(\mathbf{z}_i^k)^* X_i^k\} \mathcal{E}\{(X_i^k)^* (\mathbf{z}_i^k)^T\}. & \text{(B.70)} \end{aligned}$$

and with an additional one tap FEQ per tone to compensate for bias. □

Proof: Given the optimization problem (3.7) with $\mathbf{A}_i$ and $\mathbf{B}_i$ as in (B.69) and (B.70)

$$\mathbf{w}_{i,opt} = \arg\max_{\mathbf{w}_i} \frac{\mathbf{w}_i^T \mathcal{E}\{(\mathbf{z}_i^k)^* X_i^k\} \mathcal{E}\{(X_i^k)^* (\mathbf{z}_i^k)^T\} \mathbf{w}_i}{\mathbf{w}_i^T \mathcal{E}\{(\mathbf{z}_i^k)^* (\mathbf{z}_i^k)^T\} \mathbf{w}_i} \quad \text{for} \quad i \in \mathcal{S}, \tag{B.71}$$

the solution is obtained as the generalized eigenvector corresponding to the maximum generalized eigenvalue λ of the following generalized eigenvalue problem

$$\mathcal{E}\{(\mathbf{z}_i^k)^* X_i^k\} \mathcal{E}\{(X_i^k)^* (\mathbf{z}_i^k)^T\} \mathbf{w}_i = \lambda \mathcal{E}\{(\mathbf{z}_i^k)^* (\mathbf{z}_i^k)^T\} \mathbf{w}_i. \tag{B.72}$$

Since $\mathcal{E}\{(\mathbf{z}_i^k)^* (\mathbf{z}_i^k)^T\})$ is in general positive definite and hence invertible, (B.72) can be turned into an ordinary eigenvalue problem

$$\left(\mathcal{E}\{(\mathbf{z}_i^k)^* (\mathbf{z}_i^k)^T\}\right)^{-1} \mathcal{E}\{(\mathbf{z}_i^k)^* X_i^k\} \mathcal{E}\{(X_i^k)^* (\mathbf{z}_i^k)^T\} \mathbf{w}_i = \lambda \mathbf{w}_i. \tag{B.73}$$

Here, the positive semi definite matrix $\mathcal{E}\{(\mathbf{z}_i^k)^* X_i^k\} \mathcal{E}\{(X_i^k)^* (\mathbf{z}_i^k)^T\}$ is of rank one. As a consequence, only one eigenvalue is strictly positive and different from zero. The most dominant eigenvector and the corresponding eigenvalue are then given by

$$\begin{aligned} \mathbf{w}_{opt,i} &= \left(\mathcal{E}\{(\mathbf{z}_i^k)^* (\mathbf{z}_i^k)^T\}\right)^{-1} \mathcal{E}\{(\mathbf{z}_i^k)^* X_i^k\}, & \text{(B.74)} \\ \lambda_{max} &= \mathcal{E}\{(X_i^k)^* (\mathbf{z}_i^k)^T\} (\mathcal{E}\{(\mathbf{z}_i^k)^* (\mathbf{z}_i^k)^T\})^{-1} \mathcal{E}\{(\mathbf{z}_i^k)^* X_i^k\}. & \text{(B.75)} \end{aligned}$$

Note that $\mathbf{w}_{opt,i}$ corresponds to the Wiener solution of (3.122). Since (B.71) is scale invariant, $\mathbf{w}_{opt,i}$ has to be scaled by a one tap FEQ D_i to avoid bias. In other words, the optimal unbiased PTEQ is given by

$$\bar{\mathbf{v}}_{opt,i} = D_i \mathbf{w}_{opt,i}, \quad i \in \mathcal{S}, \tag{B.76}$$

with

$$D_i = \frac{\mathcal{E}\{|X_i^k|^2\}}{\mathcal{E}\{(X_i^k)^*(\mathbf{z}_i^k)^T\}(\mathcal{E}\{(\mathbf{z}_i^k)^*(\mathbf{z}_i^k)^T\})^{-1}\mathcal{E}\{(\mathbf{z}_i^k)^* X_i^k\}}, \tag{B.77}$$

which is completely equivalent to (3.124) and (3.125). □

C Appendix to Chapter 4

C.1 SNR for TEQ filtering combined with windowing

Property C.1 When TEQ filtering is combined with a single time domain window, the SNR for tone i can be simplified to

$$\begin{aligned} \mathrm{SNR}_i &= \frac{\mathcal{E}\{|X_i^k|^2\}}{\mathcal{E}\{|D_i Y_{dw,i}^k - X_i^k|^2\}}, && \text{(C.1)} \\ &= \frac{1}{\rho_i^{-2}(\mathbf{d},\mathbf{w}) - 1}, && \text{(C.2)} \end{aligned}$$

where $\rho_i^2(\mathbf{d},\mathbf{w})$ is a tone dependent, normalized correlation function, depending on the window taper $\mathbf{d}$ and the TEQ coefficients $\mathbf{w}$. □

Proof : Starting from (4.8), the noise component in the denominator can be written as

$$\begin{aligned} \mathcal{E}\{|D_i Y_{dw,i}^k - X_i^k|^2\} &= |D_i|^2 \mathcal{E}\{|Y_{dw,i}^k|^2\} - D_i \mathcal{E}\{Y_{dw,i}^k X_i^{k^*}\} - && \text{(C.3)} \\ & \quad D_i^* \mathcal{E}\{Y_{dw,i}^{k^*} X_i^k\} + \mathcal{E}\{|X_i^k|^2\}, && \text{(C.4)} \end{aligned}$$

where the FEQ was brought outside the statistical expectation, since it is not a statistical quantity. With the definition of the ZF FEQ in (4.26) and after some rearrangement of the terms, one arrives at

$$\mathcal{E}\{|D_i Y_{dw,i}^k - X_i^k|^2\} = \mathcal{E}\{|X_i^k|^2\} \left(\frac{\mathcal{E}\{|X_i^k|^2\}\mathcal{E}\{|Y_{dw,i}^k|^2\}}{\mathcal{E}\{Y_{dw,i}^k X_i^{k^*}\}} - 1 \right). \quad \text{(C.5)}$$

Combining the definition of $\rho_i^2(\mathbf{d},\mathbf{w})$ in (4.29) with (C.1) and (C.5) completes the proof. □

C.2 Gradient and Hessian of the BM-WinTEQ cost function

In this appendix we will derive expressions for the gradient and Hessian of the BM-WinTEQ cost function (4.30), which is repeated here for convenience

$$b_{DMT}(\mathbf{d},\mathbf{w}) = \sum_{i \in \mathcal{S}} \log_2 \left(1 + \frac{1}{\Gamma_i(\rho_i^{-2}(\mathbf{d},\mathbf{w}) - 1)} \right), \quad \text{(C.6)}$$

where $\rho_i^2(\mathbf{d},\mathbf{w})$ is defined as

$$\rho_i^2(\mathbf{d},\mathbf{w}) = \frac{|\mathbf{r}_{XY,i}\mathbf{w} + \mathbf{r}_{X\Delta,i}\mathbf{\Omega}_i\mathbf{w}|^2}{\left(\mathbf{w}^T(\mathbf{R}_{YY,i} + \mathbf{R}_{Y\Delta,i}\mathbf{\Omega}_i + \mathbf{\Omega}_i^H\mathbf{R}_{Y\Delta,i}^H + \mathbf{\Omega}_i^H\mathbf{R}_{\Delta\Delta}\mathbf{\Omega}_i)\mathbf{w} \right) \sigma_{x,i}^2}. \quad \text{(C.7)}$$

We refer to Appendix A.5 for a definition of the gradient operator and some useful properties related to differentiation of a real valued cost function.

Gradient

The gradient $\mathbf{g}(\mathbf{d},\mathbf{w})$ of (C.6) is defined as

$$\mathbf{g}(\mathbf{d},\mathbf{w}) = \begin{bmatrix} \nabla_{\mathbf{w}} b_{DMT} \\ \nabla_{\mathbf{d}} b_{DMT} \end{bmatrix}, \tag{C.8}$$

$$= \nabla_{\mathbf{d},\mathbf{w}} \sum_{i\in\mathcal{S}} \log_2\left(1+\frac{1}{\Gamma_i(\rho_i^{-2}-1)}\right), \tag{C.9}$$

where $\nabla_{\mathbf{x}}$ is the gradient operator with respect to the parameter vector $\mathbf{x}$ and where the dependencies on $\mathbf{d}$ and $\mathbf{w}$ are omitted for compact notation. After applying the chain rule, one obtains

$$\mathbf{g}(\mathbf{d},\mathbf{w}) = \sum_{i\in\mathcal{S}} \frac{\log_2 e}{(\Gamma_i(1-\rho_i^2)+\rho_i^2)(1-\rho_i^2)} \nabla_{\mathbf{d},\mathbf{w}}\rho_i^2, \tag{C.10}$$

where $\nabla_{\mathbf{d},\mathbf{w}}\rho_i^2$ is equivalent to

$$\nabla_{\mathbf{d},\mathbf{w}}\rho_i^2 = \begin{bmatrix} \nabla_{\mathbf{w}}\rho_i^2 \\ \nabla_{\mathbf{d}}\rho_i^2 \end{bmatrix}. \tag{C.11}$$

Define $\mathbf{A}_i$ and $\mathbf{B}_i$ as

$$\mathbf{A}_i = \left(\mathbf{r}_{XY,i} + \mathbf{r}_{X\Delta,i}\mathbf{\Omega}_i\right)^H \left(\mathbf{r}_{XY,i} + \mathbf{r}_{X\Delta,i}\mathbf{\Omega}_i\right), \tag{C.12}$$

$$\mathbf{B}_i = \left(\mathbf{R}_{YY,i} + \mathbf{R}_{Y\Delta,i}\mathbf{\Omega}_i + \mathbf{\Omega}_i^H\mathbf{R}_{Y\Delta,i}^H + \mathbf{\Omega}_i^H\mathbf{R}_{\Delta\Delta}\mathbf{\Omega}_i\right)\sigma_{x,i}^2. \tag{C.13}$$

Based on (C.7), the first component of (C.11) is equal to

$$\nabla_{\mathbf{w}}\rho_i^2 = 2\rho_i^2 \mathcal{R}e\left\{\frac{\mathbf{A}_i\mathbf{w}}{\mathbf{w}^T\mathbf{A}_i\mathbf{w}} - \frac{\mathbf{B}_i\mathbf{w}}{\mathbf{w}^T\mathbf{B}_i\mathbf{w}}\right\}, \tag{C.14}$$

where $\mathcal{R}e\{\cdot\}$ takes the real part of its argument. Similarly, define

$$\mathbf{c}_i = \mathcal{R}e\left\{\mathbf{W}_i^H\mathbf{r}_{X\Delta,i}^H\mathbf{r}_{XY,i}\mathbf{w}\right\}, \qquad \mathbf{D}_i = \left(\mathbf{r}_{X\Delta,i}\mathbf{W}_i\right)^H\left(\mathbf{r}_{X\Delta,i}\mathbf{W}_i\right), \tag{C.15}$$

$$\mathbf{e}_i = \mathcal{R}e\left\{\mathbf{W}_i^H\mathbf{R}_{Y\Delta,i}^H\mathbf{w}\right\}\sigma_{x,i}^2, \qquad \mathbf{F}_i = \mathbf{W}_i^H\mathbf{R}_{\Delta\Delta}\mathbf{W}_i\sigma_{x,i}^2. \tag{C.16}$$

The second component of (C.11) can now be computed as

$$\nabla_{\mathbf{d}}\rho_i^2 = 2\rho_i^2 \mathcal{R}e\left\{\frac{\mathbf{c}_i + \mathbf{D}_i\mathbf{d}}{\mathbf{w}^T\mathbf{A}_i\mathbf{w}} - \frac{\mathbf{e}_i + \mathbf{F}_i\mathbf{d}}{\mathbf{w}^T\mathbf{B}_i\mathbf{w}}\right\}. \tag{C.17}$$

Finally, combining (C.10), (C.11), (C.14) and (C.17) results in the complete expression for the gradient:

$$\mathbf{g}(\mathbf{d},\mathbf{w}) = \sum_{i\in\mathcal{S}} \beta_i \mathcal{R}e\left\{\begin{bmatrix} \frac{\mathbf{A}_i\mathbf{w}}{\mathbf{w}^T\mathbf{A}_i\mathbf{w}} - \frac{\mathbf{B}_i\mathbf{w}}{\mathbf{w}^T\mathbf{B}_i\mathbf{w}} \\ \frac{\mathbf{c}_i+\mathbf{D}_i\mathbf{d}}{\mathbf{w}^T\mathbf{A}_i\mathbf{w}} - \frac{\mathbf{e}_i+\mathbf{F}_i\mathbf{d}}{\mathbf{w}^T\mathbf{B}_i\mathbf{w}} \end{bmatrix}\right\}, \tag{C.18}$$

with $\beta_i = \frac{2\rho_i^2\log_2 e}{(\Gamma_i(1-\rho_i^2)+\rho_i^2)(1-\rho_i^2)}$ a tone dependent scalar.

Hessian

Since the windowing and TEQ coefficients are real valued, the Hessian matrix will be symmetric and real valued as well. Based on the expression of the gradient in (C.18), the Hessian of the BM-WinTEQ cost function in (C.6) is given by

$$\mathbf{H}(\mathbf{d},\mathbf{w}) = \nabla_{\mathbf{d},\mathbf{w}}\mathbf{g}(\mathbf{d},\mathbf{w})^T = \sum_{i\in\mathcal{S}} \nabla_{\mathbf{d},\mathbf{w}}\beta_i \tilde{\mathbf{g}}_i^T(\mathbf{d},\mathbf{w}), \tag{C.19}$$

where $\tilde{\mathbf{g}}_i(\mathbf{d},\mathbf{w})$ is defined as

$$\tilde{\mathbf{g}}_i(\mathbf{d},\mathbf{w}) = \begin{bmatrix} \tilde{\mathbf{g}}_{\mathbf{w},i} \\ \tilde{\mathbf{g}}_{\mathbf{d},i} \end{bmatrix} = \mathcal{R}e\left\{ \begin{bmatrix} \frac{\mathbf{A}_i\mathbf{w}}{\mathbf{w}^T\mathbf{A}_i\mathbf{w}} - \frac{\mathbf{B}_i\mathbf{w}}{\mathbf{w}^T\mathbf{B}_i\mathbf{w}} \\ \frac{\mathbf{c}_i+\mathbf{D}_i\mathbf{d}}{\mathbf{w}^T\mathbf{A}_i\mathbf{w}} - \frac{\mathbf{e}_i+\mathbf{F}_i\mathbf{d}}{\mathbf{w}^T\mathbf{B}_i\mathbf{w}} \end{bmatrix} \right\}. \tag{C.20}$$

With the gradient rules for products, (C.19) can be modified to

$$\mathbf{H}(\mathbf{d},\mathbf{w}) = \sum_{i\in\mathcal{S}} [\nabla_{\mathbf{d},\mathbf{w}}\beta_i] \left[\tilde{\mathbf{g}}_{\mathbf{w},i}^T \mid \tilde{\mathbf{g}}_{\mathbf{d},i}^T\right] + \sum_{i\in\mathcal{S}} \beta_i \begin{bmatrix} \nabla_{\mathbf{w}} \\ \nabla_{\mathbf{d}} \end{bmatrix} \left[\tilde{\mathbf{g}}_{\mathbf{w},i}^T \mid \tilde{\mathbf{g}}_{\mathbf{d},i}^T\right]. \tag{C.21}$$

In the following, an explicit expression for the unknown components of (C.21) will be derived.

- $$\nabla_{\mathbf{d},\mathbf{w}}\beta_i = \frac{-2\log_2 e(\Gamma_i(1-\rho_i^4)+\rho_i^4)}{(\Gamma_i(1-\rho_i^2)+\rho_i^2)^2(1-\rho_i^2)^2}\nabla_{\mathbf{d},\mathbf{w}}\rho_i^2, \tag{C.22}$$

where $\nabla_{\mathbf{d},\mathbf{w}}\rho_i^2$ is given by (C.11), combined with (C.14) and (C.17).

- $$\nabla_{\mathbf{w}}\tilde{\mathbf{g}}_{\mathbf{w},i}^T = \frac{\mathcal{R}e\{\mathbf{A}_i^H\}}{\mathbf{w}^T\mathbf{A}_i\mathbf{w}} - \frac{2\mathcal{R}e\{\mathbf{A}_i\}\mathbf{w}\mathbf{w}^T\mathcal{R}e\{\mathbf{A}_i^H\}}{(\mathbf{w}^T\mathbf{A}_i\mathbf{w})^2} - \frac{\mathcal{R}e\{\mathbf{B}_i^H\}}{\mathbf{w}^T\mathbf{B}_i\mathbf{w}} + \frac{2\mathcal{R}e\{\mathbf{B}_i\}\mathbf{w}\mathbf{w}^T\mathcal{R}e\{\mathbf{B}_i^H\}}{(\mathbf{w}^T\mathbf{B}_i\mathbf{w})^2}, \tag{C.23}$$

- $$\nabla_{\mathbf{d}}\tilde{\mathbf{g}}_{\mathbf{d},i}^T = \frac{\mathcal{R}e\{\mathbf{D}_i^H\}}{\mathbf{w}^T\mathbf{A}_i\mathbf{w}} - \frac{2\mathcal{R}e\{\mathbf{c}_i+\mathbf{D}_i\mathbf{d}\}\mathcal{R}e\{\mathbf{c}_i^H+\mathbf{d}^T\mathbf{D}_i^H\}}{(\mathbf{w}^T\mathbf{A}_i\mathbf{w})^2} - \frac{\mathcal{R}e\{\mathbf{F}_i^H\}}{\mathbf{w}^T\mathbf{B}_i\mathbf{w}} + \frac{2\mathcal{R}e\{\mathbf{e}_i+\mathbf{F}_i\mathbf{d}\}\mathcal{R}e\{\mathbf{e}_i^H+\mathbf{d}^T\mathbf{F}_i^H\}}{(\mathbf{w}^T\mathbf{B}_i\mathbf{w})^2}, \tag{C.24}$$

- $$\nabla_{\mathbf{d}}\tilde{\mathbf{g}}_{\mathbf{w},i}^T = \frac{\nabla_{\mathbf{d}}\mathcal{R}e\{\mathbf{w}^T\mathbf{A}_i^H\}}{\mathbf{w}^T\mathbf{A}_i\mathbf{w}} - \frac{2\mathcal{R}e\{\mathbf{c}_i+\mathbf{D}_i\mathbf{d}\}\mathbf{w}^T\mathcal{R}e\{\mathbf{A}_i^H\}}{(\mathbf{w}^T\mathbf{A}_i\mathbf{w})^2} - \frac{\nabla_{\mathbf{d}}\mathcal{R}e\{\mathbf{w}^T\mathbf{B}_i^H\}}{\mathbf{w}^T\mathbf{B}_i\mathbf{w}} + \frac{2\mathcal{R}e\{\mathbf{e}_i+\mathbf{F}_i\mathbf{d}\}\mathbf{w}^T\mathcal{R}e\{\mathbf{B}_i^H\}}{(\mathbf{w}^T\mathbf{B}_i\mathbf{w})^2}, \tag{C.25}$$

- $$\nabla_{\mathbf{d}}\mathcal{R}e\{\mathbf{w}^T\mathbf{B}_i^H\} = (\nabla_{\mathbf{d}}\tilde{\mathbf{g}}_{\mathbf{w},i}^T)^T, \tag{C.26}$$

where the last equation holds due to the symmetry property of the Hessian and where (C.25) is completely determined by considering

$$* \quad \nabla_{\mathbf{d}}\mathcal{R}e\{\mathbf{w}^T\mathbf{A}_i^H\} = \nabla_{\mathbf{d}}\mathcal{R}e\left\{\mathbf{w}^T\mathbf{r}_{XY,i}^H\mathbf{r}_{X\Delta,i}\mathbf{\Omega}_i\right\} + \mathcal{R}e\left\{\mathbf{W}_i^H\mathbf{r}_{X\Delta,i}^H\mathbf{r}_{XY,i}\right\} +$$

$$\nabla_{\mathbf{d}} \mathcal{R}e\left\{\mathbf{d}^T \mathbf{W}_i^H \mathbf{r}_{X\Delta,i}^H \mathbf{r}_{X\Delta,i} \mathbf{\Omega}_i\right\}, \tag{C.27}$$

$$* \quad \nabla_{\mathbf{d}} \mathcal{R}e\{\mathbf{w}^T \mathbf{B}_i^H\} = \mathcal{R}e\{\mathbf{W}_i^H \mathbf{R}_{Y\Delta,i}^H\}\sigma_{x,i}^2 + \nabla_{\mathbf{d}} \mathcal{R}e\{\mathbf{w}^T \mathbf{R}_{Y\Delta,i} \mathbf{\Omega}_i\} + \nabla_{\mathbf{d}} \mathcal{R}e\left\{\mathbf{d}^T \mathbf{W}_i^H \mathbf{R}_{\Delta\Delta} \mathbf{\Omega}_i\right\} \sigma_{x,i}^2. \tag{C.28}$$

In (C.27) and (C.28), two types of gradients still remain, i.e. $\mathbf{H}_1 = \nabla_{\mathbf{d}} \mathcal{R}e\left\{\mathbf{a}^T \mathbf{\Omega}_i\right\}$ and $\mathbf{H}_2 = \nabla_{\mathbf{d}} \mathcal{R}e\left\{\mathbf{d}^T \mathbf{A} \mathbf{\Omega}_i\right\}$, where $\mathbf{a} \in \mathbb{C}^{\mu+T-1}$ and $\mathbf{A} \in \mathbb{C}^{\mu \times \mu+T-1}$ are independent of the windowing coefficients. In the following, an expression will be derived for each of these specific gradients.

Starting with $\mathbf{H}_1 = [h_{1,pq}]$, it is easy to show that the element on the p-th row and the q-th column is equal to

$$h_{1,pq} = \frac{\partial}{\partial d_{p-1}} \sum_{k=0}^{\mu-1} \mathcal{R}e\left\{a_{T-(q-1)+k} \alpha^{i(N-\mu+k)}\right\} d_k, \tag{C.29}$$

$$= \mathcal{R}e\left\{a_{T-q+p} \alpha^{i(N-\mu+p-1)}\right\}, \tag{C.30}$$

with $\alpha = e^{-j2\pi/N}$ and where the definition of Ω_i in (4.24) was used to write $h_{1,pq}$ explicitly as a function of the windowing coefficients. In matrix notation, this results in

$$\mathbf{H}_1 = \mathcal{R}e\left\{\mathbf{D}_{\mathcal{F},i} \begin{bmatrix} a_T & a_{T-1} & \dots & a_1 \\ a_{T+1} & a_T & \dots & a_2 \\ \vdots & \ddots & & \vdots \\ a_{T+\mu-1} & \dots & \dots & a_\mu \end{bmatrix}\right\}. \tag{C.31}$$

For $\mathbf{H}_2 = [h_{2,pq}]$, it is easy to derive that the element on the p-th row and the q-th column is equal to

$$h_{2,pq} = \frac{\partial}{\partial d_{p-1}} \sum_{k=0}^{\mu-1} \sum_{l=0}^{\mu-1} \mathcal{R}e\left\{a_{(l+1)(T-q+k+1)} \alpha^{i(N-\mu+k)}\right\} d_k d_l, \tag{C.32}$$

$$= \frac{\partial}{\partial d_{p-1}} \left(\mathcal{R}e\left\{a_{p(T-q+p)} \alpha^{i(N-\mu+p-1)}\right\} d_{p-1}^2 + d_{p-1} \sum_{k=0, k\neq p-1}^{\mu-1} \mathcal{R}e\left\{a_{p(T-q+k+1)} \alpha^{i(N-\mu+k)}\right\} d_k + d_{p-1} \sum_{l=0, l\neq p-1}^{\mu-1} \mathcal{R}e\left\{a_{(l+1)(T-q+p)} \alpha^{i(N-\mu+p-1)}\right\} d_l \right), \tag{C.33}$$

$$= \sum_{k=0}^{\mu-1} \mathcal{R}e\left\{a_{p(T-q+k+1)} \alpha^{i(N-\mu+k)}\right\} d_k +$$

$$\sum_{l=0}^{\mu-1} \mathcal{R}e\left\{a_{(l+1)(T-q+p)}\alpha^{i(N-\mu+p-1)}\right\} d_l, \tag{C.34}$$

where the definition of Ω_i in (4.24) was again applied to simplify the equations in terms of the windowing coefficients. In matrix notation, one obtains

$$\mathbf{H}_2 = [h_{2,pq}] \tag{C.35}$$

$$= \left[\mathcal{R}e\left\{\mathbf{A}[p,:]\mathbf{\Omega}_i[:,q] + \alpha^{i(N-\mu+p-1)}\mathbf{d}^T\mathbf{A}[:,T-q+p]\right\}\right], \tag{C.36}$$

$$= \mathcal{R}e\left\{\mathbf{A}\mathbf{\Omega}_i + \mathbf{D}_{\mathcal{F},i}\begin{bmatrix}\mathbf{d}^T & \mathbf{0} & \dots\\ \mathbf{0} & \mathbf{d}^T & \\ \vdots & & \ddots\end{bmatrix}\begin{bmatrix}\mathbf{A}[:,T] & \mathbf{A}[:,T-1] & \dots\\ \mathbf{A}[:,T+1] & \mathbf{A}[:,T] & \\ \vdots & & \ddots\end{bmatrix}\right\}.$$

Using (C.31) and (C.36) to complete (C.27) and (C.28) finalizes the definition of the Hessian.

C.3 Efficient computation of the correlation matrices

Property C.2 Based on the computation of the auto- and cross-correlation matrices

$$\begin{aligned}\sigma_{x,i}^2 &= \mathcal{E}\{|X_i^k|^2\},\\ \mathbf{r}_{xy,i} &= \mathcal{E}\{(X_i^k)^*[(\Delta\mathbf{y}^{ext,k})^T \;\; Y_i^k]\},\\ \mathbf{R}_{yy,i} &= \mathcal{E}\left\{\begin{bmatrix}\Delta\mathbf{y}^{ext,k}\\ Y_i^k\end{bmatrix}[(\Delta\mathbf{y}^{ext,k})^T \;\; (Y_i^k)^*]\right\},\end{aligned} \tag{C.37}$$

all the statistical quantities in (4.25), which are required to evaluate the BM-WinTEQ cost function in (4.30), can be obtained efficiently. Furthermore, the quantities of (C.37) are easy to determine when an estimate of the channel and the noise statistics is available. □

Proof: With the definition of $\Delta\mathbf{y}^{ext,k}$ and Y_i^k in (4.22) and (4.32), one can write

$$\begin{bmatrix}\Delta\mathbf{y}^{ext,k}\\ Y_i^k\end{bmatrix} = \underbrace{\left[\begin{array}{c|c|c}\mathbf{I}_{\mu+T-1} & \mathbf{0} & -\mathbf{I}_{\mu+T-1}\\ \hline \mathbf{0} & \multicolumn{2}{c}{\mathcal{F}_N[i,:]}\end{array}\right]}_{\bar{\mathbf{F}}_i^{ext}}\mathbf{y}^{ext,k}, \tag{C.38}$$

which is similar to (3.116) and (3.117). In addition, recall that $\mathbf{y}^{ext,k}$ is the result of

$$\mathbf{y}^{ext,k} = \mathbf{H}^{ext}\mathbf{X}^k + \mathbf{n}^{ext,k}, \tag{C.39}$$

$$= \mathbf{H}_{N+i}^{ext}X_i^k + \bar{\mathbf{H}}^{ext}\bar{\mathbf{X}}^k + \mathbf{n}^{ext,k}, \tag{C.40}$$

as discussed in Subsection 2.3.3. With (C.38), (C.39) and (C.40), the cross- and auto-correlation matrices $\mathbf{r}_{xy,i}$ and $\mathbf{R}_{yy,i}$ can simply be determined in terms of the channel and noise statistics as follows

$$\mathbf{r}_{xy,i} = \mathcal{E}\{(X_i^k)^*[(\Delta\mathbf{y}^{ext,k})^T \;\; Y_i^k]\} = \mathcal{E}\{|X_i^k|^2\}(\mathbf{H}_{N+i}^{ext})^H(\bar{\mathbf{F}}_i^{ext})^H, \quad \text{(C.41)}$$

$$\begin{aligned}\mathbf{R}_{yy,i} &= \mathcal{E}\left\{\begin{bmatrix}\Delta\mathbf{y}^{ext,k}\\ Y_i^k\end{bmatrix}[(\Delta\mathbf{y}^{ext,k})^T \;\; (Y_i^k)^*]\right\},\\ &= \bar{\mathbf{F}}_i^{ext}\mathbf{H}^{ext}\mathcal{E}\{\mathbf{X}^k(\mathbf{X}^k)^H\}(\mathbf{H}^{ext})^H(\bar{\mathbf{F}}_i^{ext})^H + \\ &\quad \bar{\mathbf{F}}_i^{ext}\mathcal{E}\{\mathbf{n}^{ext,k}(\mathbf{n}^{ext,k})^T\}(\bar{\mathbf{F}}_i^{ext})^H, \quad \text{(C.42)}\end{aligned}$$

where it was assumed that the QAM-symbols transmitted on different tones and/or on different symbol intervals are uncorrelated. Note that this assumption also implies that $\mathcal{E}\{\mathbf{X}^k(\mathbf{X}^k)^H\}$ is a diagonal matrix with non-zero energy, i.e. with $\sigma_{x,i}^2 \neq 0$, on the entries corresponding to the used tones. Observe that $\mathbf{R}_{yy}$ is symmetric such that only the computation of half the number of elements is required. Moreover, the first $T-1$ rows and $T-1$ columns are tone independent and as such can be shared by all the used tones.

To express the statistics of (4.25) in terms of $\sigma_{x,i}^2$, $\mathbf{r}_{xy,i}$ and $\mathbf{R}_{yy,i}$, the sliding DFT $\mathbf{Y}_i^{sl,k}$ has to be written as a function of difference terms. Therefore, one can first derive $\mathbf{Y}_i^{sl,k}$ directly from $\mathbf{y}^k$ as

$$(\mathbf{Y}_i^{sl,k})^T = (\mathcal{F}_N[i,:]\mathbf{Y}^k)^T, \quad \text{(C.43)}$$

$$= \mathbf{P}\underbrace{\begin{bmatrix}\boxed{\mathcal{F}_N[i,:]} & \dots & 0\\ \ddots & \ddots & \\ 0 & \dots & \boxed{\mathcal{F}_N[i,:]}\end{bmatrix}}_{\mathbf{F}_i}\mathbf{y}^k, \quad \text{(C.44)}$$

where $\mathbf{P}$ is a zero matrix with ones on the anti-diagonal. The matrix $\mathbf{P}$ was added to stay in agreement with the sliding DFT definition of (3.113). Similar to (3.115), one can decompose $\mathbf{F}_i$ as

$$\mathbf{F}_i = \underbrace{\begin{bmatrix}1 & \alpha^i & \dots & \alpha^{i(T-1)}\\ & \ddots & & \vdots\\ & & 1 & \alpha^i\\ 0 & & & 1\end{bmatrix}}_{\mathbf{Q}}\underbrace{\left[\begin{array}{c|c|c}\mathbf{I}_{T-1} & \mathbf{0} & -\mathbf{I}_{T-1}\\ \hline \mathbf{0} & \multicolumn{2}{c}{\mathcal{F}_N[i,:]}\end{array}\right]}_{\bar{\mathbf{F}}_i}, \quad \text{(C.45)}$$

with $\alpha = e^{-j2\pi/N}$. After combining (C.44) and (C.45), one obtains

$$(\mathbf{Y}_i^{sl,k})^T = \mathbf{PQ}\begin{bmatrix}\Delta\mathbf{y}^k\\ Y_i^k\end{bmatrix}, \quad \text{(C.46)}$$

where $\Delta\mathbf{y}^k$ corresponds to a vector with the last $T-1$ difference terms of $\Delta\mathbf{y}^{ext,k}$.

The correlation matrices $\mathbf{r}_{xy,i}$ and $\mathbf{R}_{yy,i}$ can now effectively be used to derive the different statistical quantities of (4.25). With the matrices $\mathbf{P}_1$ and $\mathbf{P}_2$, defined as

$$\mathbf{P}_1 = \left[\frac{\mathbf{I}_{\mu+T-1}}{\mathbf{0}_{1\times(\mu+T-1)}}\right], \qquad \mathbf{P}_2 = \left[\frac{\mathbf{0}_{\mu\times T}}{\mathbf{Q}^T\mathbf{P}^T}\right], \tag{C.47}$$

one can write

$$\mathbf{r}_{X\Delta,i} = \mathbf{r}_{xy,i}\mathbf{P}_1, \quad \mathbf{r}_{XY,i} = \mathbf{r}_{xy,i}\mathbf{P}_2, \quad \mathbf{R}_{YY,i} = \mathbf{P}_2^H\mathbf{R}_{yy,i}\mathbf{P}_2, \tag{C.48}$$

$$\mathbf{R}_{Y\Delta,i} = \mathbf{P}_2^H\mathbf{R}_{yy,i}\mathbf{P}_1, \quad \mathbf{R}_{\Delta\Delta} = \mathbf{P}_1^T\mathbf{R}_{yy,i}\mathbf{P}_1. \tag{C.49}$$

Hence, based on (C.41) and (C.42) one is able to compute all the necessary statistics. Alternatively, the required statistics could be calculated recursively based on a training sequence. During data transmission the quantities could be updated in a decision directed way. □

D Appendix to Chapter 5

D.1 Convergence in the mean ITF-EC

Property D.1 Under the assumptions that

- the echo channel can be modeled as an FIR with zero mean, additive white Gaussian noise (AWGN),
- the external noise is uncorrelated with the transmitted echo symbols,
- the transmitted echo symbols U^k are uncorrelated with U^l with $l \neq k$ and the frequency domain elements within a vector U^l, denoted as U_i^l, are uncorrelated with each other, i.e. $\mathcal{E}\{(U_i^l)^* U_j^k\} = \sigma_u^2 \delta[i-j]\delta[k-l]$ with δ the Dirac delta function,

the ITF-EC update

$$W_E^{k+1} \leftarrow W_E^k + \mu(\tilde{U}^k)^* \odot E^k, \tag{D.1}$$

is convergent in the mean, if the step size satisfies the following bounds:

$$0 < \mu < \frac{2}{\sigma_u^2}. \tag{D.2}$$

□

Proof : First note that the above mentioned assumptions are exactly the same as the ones used in [57] to prove the convergence of CES-based EC. The third assumption is the most severe one, since it implies that the samples of the corresponding time domain vectors (excluding the prefix), i.e. $\mathcal{I}_N U^l = \mathbf{u}^l$ and $\mathcal{I}_N U^k = \mathbf{u}^k$, are independent from one time sample to the next. In addition, the third assumption also indicates that *all the echo symbols are transmitted with equal power on all the tones.*

When combining (5.45) with (5.43) and (5.44), one can write

$$\begin{aligned} W_E^{k+1} &\leftarrow W_E^k + \mu \mathcal{F}_N \tilde{\mathbf{C}}^T \mathcal{I}_N \left(\mathcal{F}_N(\mathbf{y}^k - \tilde{\chi}^{k-1,k,k+1} \mathbf{M} \mathbf{w}_E^k) - \mathrm{diag}(\tilde{U}^k) W_E^k \right), \\ &\leftarrow W_E^k + \mu \mathcal{F}_N \tilde{\mathbf{C}}^T \mathcal{I}_N \left(\mathcal{F}_N(\mathbf{y}^k - \mathbf{U}^{k-1,k,k+1} \mathbf{M}\mathbf{M}^T \mathcal{I}_N W_E^k) \right), \end{aligned} \tag{D.3}$$

where (5.41) was used to obtain the last equation. After some simple linear algebra, this leads to

$$W_E^{k+1} \leftarrow \left(\mathbf{I}_N - \mu \mathcal{F}_N \tilde{\mathbf{C}}^T \mathbf{U}^{k-1,k,k+1} \mathbf{M}\mathbf{M}^T \mathcal{I}_N \right) W_E^k + \mu \mathcal{F}_N \tilde{\mathbf{C}}^T \mathbf{y}^k, \tag{D.4}$$

with $\mathbf{I}_N$ the identity matrix of size N. When H_E denotes the frequency response of the echo channel, i.e. $H_E = \mathcal{F}_N \mathbf{h}_E$, one can specify $\mathbf{y}^k$ as

$$\mathbf{y}^k = \mathbf{U}^{k-1,k,k+1}\mathbf{M}\mathbf{M}^T\mathcal{I}_N H_E + \mathbf{n}^k. \tag{D.5}$$

Since the external noise is uncorrelated with the transmitted echo symbols, i.e. $\mathcal{E}\{\tilde{\mathbf{C}}^T\mathbf{n}^k\} = \mathbf{0}$, one modify (D.4) to

$$\mathcal{E}\left\{W_E^{k+1} - H_E\right\} = \mathcal{E}\left\{(\mathbf{I}_N - \mu\mathcal{F}_N\tilde{\mathbf{C}}^T\mathbf{U}^{k-1,k,k+1}\mathbf{M}\mathbf{M}^T\mathcal{I}_N)(W_E^k - H_E)\right\}. \tag{D.6}$$

After invoking the *independence assumption* [54], which states that the weight error vector is independent of the input sequence, one obtains

$$\mathcal{E}\left\{W_E^{k+1} - H_E\right\} = \mathcal{E}\{\mathbf{I}_N - \mu\mathcal{F}_N\tilde{\mathbf{C}}^T\mathbf{U}^{k-1,k,k+1}\mathbf{M}\mathbf{M}^T\mathcal{I}_N\}\mathcal{E}\left\{W_E^k - H_E\right\}. \tag{D.7}$$

Hence, the convergence behaviour is determined by the eigenvalue spread of the covariance matrix

$$\begin{aligned}\mathcal{X}_f &= \mathcal{E}\{\mathbf{I}_N - \mu\mathcal{F}_N\tilde{\mathbf{C}}^T\mathbf{U}^{k-1,k,k+1}\mathbf{M}\mathbf{M}^T\mathcal{I}_N\}, &\text{(D.8)}\\ &= \mathcal{F}_N\mathcal{E}\{\mathbf{I}_N - \mu\tilde{\mathbf{C}}^T\mathbf{U}^{k-1,k,k+1}\mathbf{M}\mathbf{M}^T\}\mathcal{I}_N. &\text{(D.9)}\end{aligned}$$

Since $\mathcal{F}_N$ and $\mathcal{I}_N$ do not alter the eigenvalues, one may as well look at the eigenvalues of the time domain covariance matrix

$$\mathcal{X}_t = \mathcal{E}\{\mathbf{I}_N - \mu\tilde{\mathbf{C}}^T\mathbf{U}^{k-1,k,k+1}\mathbf{M}\mathbf{M}^T\}. \tag{D.10}$$

Since all time domain samples are uncorrelated, $\tilde{\mathbf{C}}^T\mathbf{U}^{k-1,k,k+1}\mathbf{M}\mathbf{M}^T$ is a diagonal matrix with T_E non-zero elements

$$\begin{aligned}&\frac{c}{N}\sigma_u^2, \ldots, \frac{c+\Delta-1}{N}\sigma_u^2, \underbrace{\frac{c+\Delta}{N}\sigma_u^2, \ldots, \frac{c+\Delta}{N}\sigma_u^2}_{\nu+1},\\ &\frac{c+\Delta+1}{N}\sigma_u^2, \ldots, \sigma_u^2, \frac{N-1}{N}\sigma_u^2, \ldots,\end{aligned} \tag{D.11}$$

with $c = N - N_b + \nu$. Hence, all the eigenvalues λ of $\mathcal{X}_t$ are equal to the diagonal elements of (D.11). Moreover, all the eigenvalues are positive and smaller than or equal to σ_u^2. Now, convergence in the mean is guaranteed, if the step size μ satisfies the following condition

$$0 < \mu < \frac{2}{\lambda_{\max}} = \frac{2}{\sigma_u^2}. \tag{D.12}$$

□

When not all carriers are excited, convergence can not be guaranteed. This problem is also present in the CES-based EC of [32][57]. In [32], Cioffi et al. propose to put a small amount of power on unused echo tones to obtain convergence. The same heuristic could be applied for ITF-EC to guarantee convergence.

D.2 Circulant and skew-circulant decomposition

Property D.2 Given the emulated echo

$$\hat{\mathbf{y}}_E^k = \mathbf{U}^{k-1,k,k+1}\mathbf{M}\mathbf{w}_E^k, \tag{D.13}$$

$$= \frac{1}{2}\left(\mathcal{I}_N \text{diag}\{\Lambda_{even}^k\}\mathcal{F}_N\mathbf{M}\mathbf{w}_E^k + \mathbf{Q}^*\mathcal{I}_N\text{diag}\{\Lambda_{odd}^k\}\mathcal{F}_N\mathbf{Q}\mathbf{M}\mathbf{w}_E^k\right), \tag{D.14}$$

with Λ_{even}^k and Λ_{odd}^k defined in (5.62), then the first term represents the convolution of $\mathbf{M}\mathbf{w}_E^k$ with the circulant matrix $(\mathbf{U}^{k-1,k,k+1} + \mathbf{S}^{k-1,k,k+1})$, while the second term corresponds to the convolution of $\mathbf{M}\mathbf{w}_E^k$ with the skew-circulant matrix $(\mathbf{U}^{k-1,k,k+1} - \mathbf{S}^{k-1,k,k+1})$. □

Proof: The Toeplitz matrix $\mathbf{U}^{k-1,k,k+1}$ can be written as

$$\mathbf{U}^{k-1,k,k+1} = \frac{1}{2}(\mathbf{U}^{k-1,k,k+1} + \mathbf{S}^{k-1,k,k+1}) + \frac{1}{2}(\mathbf{U}^{k-1,k,k+1} - \mathbf{S}^{k-1,k,k+1}), \tag{D.15}$$

where $\mathbf{U}^{k-1,k,k+1}$ and $\mathbf{S}^{k-1,k,k+1}$ are defined in (5.3) and (5.56). The two components of (D.15) are now addressed individually:

- It is easy to see that $(\mathbf{U}^{k-1,k,k+1} + \mathbf{S}^{k-1,k,k+1})$ is a *circulant* matrix. Consequently, it can be diagonalized by a DFT/IDFT pair [53], i.e.

$$\mathbf{U}^{k-1,k,k+1} + \mathbf{S}^{k-1,k,k+1} = \mathcal{I}_N\text{diag}\{\Lambda_1^k\}\mathcal{F}_N, \tag{D.16}$$

  where Λ_1^k is the N-point DFT of the first column of $(\mathbf{U}^{k-1,k,k+1} + \mathbf{S}^{k-1,k,k+1})$:

$$\Lambda_1^k = \mathcal{F}_N\left(\mathbf{U}^{k-1,k,k+1}[:,1] + \mathbf{S}^{k-1,k,k+1}[:,1]\right). \tag{D.17}$$

  Since Λ_{even}^k is defined as

$$\Lambda_{even}^k = \mathcal{F}_{2N}[1\!:\!2\!:\!2N,:]\begin{bmatrix}\mathbf{U}^{k-1,k,k+1}[:,1] \\ \mathbf{S}^{k-1,k,k+1}[:,1]\end{bmatrix}, \tag{D.18}$$

$$= [\mathcal{F}_N|\mathcal{F}_N]\begin{bmatrix}\mathbf{U}^{k-1,k,k+1}[:,1] \\ \mathbf{S}^{k-1,k,k+1}[:,1]\end{bmatrix}, \tag{D.19}$$

  it is clear that Λ_1^k is equal to Λ_{even}^k. Hence, the first term of (D.14) effectively corresponds to the convolution of $\mathbf{M}\mathbf{w}_E^k$ with $(\mathbf{U}^{k-1,k,k+1} + \mathbf{S}^{k-1,k,k+1})$.

- It is easy to see that $(\mathbf{U}^{k-1,k,k+1} - \mathbf{S}^{k-1,k,k+1})$ is a *skew-circulant* matrix. Using the diagonal matrix

$$\mathbf{Q} = \text{diag}\left\{\begin{bmatrix}1 & \dots & e^{-j\pi i/N} & \dots & e^{-j\pi(N-1)/N}\end{bmatrix}^T\right\}, \tag{D.20}$$

the skew-circulant matrix can be transformed into the complex valued circulant matrix $\mathbf{Q}(\mathbf{U}^{k-1,k,k+1} - \mathbf{S}^{k-1,k,k+1})\mathbf{Q}^{-1}$ [76]. Since a circulant matrix can be diagonalized by a DFT/IDFT pair [53], one can write

$$\mathbf{Q}(\mathbf{U}^{k-1,k,k+1} - \mathbf{S}^{k-1,k,k+1})\mathbf{Q}^{-1} = \mathcal{I}_N \mathrm{diag}\{\Lambda_2^k\}\mathcal{F}_N, \tag{D.21}$$

where Λ_2^k is the N-point DFT of the first column of $\mathbf{Q}(\mathbf{U}^{k-1,k,k+1} - \mathbf{S}^{k-1,k,k+1})\mathbf{Q}^{-1}$, i.e.

$$\Lambda_2^k = \mathcal{F}_N \mathbf{Q}(\mathbf{U}^{k-1,k,k+1}[:,1] - \mathbf{S}^{k-1,k,k+1}[:,1]). \tag{D.22}$$

With Λ_{odd}^k defined as

$$\Lambda_{odd}^k = \mathcal{F}_{2N}[2\!:\!2\!:\!2N,:] \left[\frac{\mathbf{U}^{k-1,k,k+1}[:,1]}{\mathbf{S}^{k-1,k,k+1}[:,1]}\right], \tag{D.23}$$

$$= [\mathcal{F}_N\mathbf{Q}| - \mathcal{F}_N\mathbf{Q}] \left[\frac{\mathbf{U}^{k-1,k,k+1}[:,1]}{\mathbf{S}^{k-1,k,k+1}[:,1]}\right], \tag{D.24}$$

it is clear that Λ_2^k is equal to Λ_{odd}^k. Since $\mathbf{Q}$ is a unitary matrix, (D.21) is equivalent to

$$(\mathbf{U}^{k-1,k,k+1} - \mathbf{S}^{k-1,k,k+1}) = \mathbf{Q}^* \mathcal{I}_N \mathrm{diag}\{\Lambda_{odd}^k\}\mathcal{F}_N\mathbf{Q}. \tag{D.25}$$

Hence, the second term of (D.14) effectively corresponds to the convolution of $\mathbf{M}\mathbf{w}_E^k$ with $(\mathbf{U}^{k-1,k,k+1} - \mathbf{S}^{k-1,k,k+1})$, which completes the proof.

□

D.3 Convergence in the mean CDC

Property D.3 Under the assumptions that

- the echo channel can be modeled as an FIR with zero mean, additive white Gaussian noise (AWGN),
- the external noise is uncorrelated with the transmitted echo symbols,
- the transmitted echo symbols U^k are uncorrelated with U^l with $l \neq k$ and the frequency domain elements within a vector U^l, denoted as U_i^l, are uncorrelated with each other, i.e. $\mathcal{E}\{(U_i^l)^* U_j^k\} = \sigma_u^2 \delta[i-j]\delta[k-l]$ with δ the Dirac delta function,

the CDC update

$$W_E^{k+1} \leftarrow W_E^k + \mu(\Lambda_{even}^k)^* \odot E^k, \tag{D.26}$$

is convergent in the mean, if the step size satisfies the following bounds:

$$0 < \mu < \frac{2N}{(N+\nu)\sigma_u^2}. \tag{D.27}$$

□

Proof : Note that the above mentioned assumptions are exactly the same as the ones used in [57] to prove the convergence of CES-based EC. The same assumptions were also used in Appendix D.1 to prove the convergence of ITF EC. The third assumption is rarely valid in practice, but it greatly simplifies the convergence proof. This assumption implies that all the echo symbols are transmitted with equal power on *all* the tones and that the samples of the corresponding time domain vector (excluding the prefix), i.e. $\mathcal{I}_N U^l = \mathbf{u}^l$, are independent from one time sample to the next.

With (5.5), the LMS-like adaptive update (D.26) can be written as

$$W_E^{k+1} \leftarrow W_E^k + \mu \text{diag}\{(\Lambda^k)^*_{even}\}\mathcal{F}_N(\mathbf{y}^k - \mathbf{U}^{k-1,k,k+1}\mathcal{I}_N W_E^k). \tag{D.28}$$

Since one has

$$\text{diag}\{\Lambda^k_{even}\} = \mathcal{F}_N(\mathbf{U}^{k-1,k,k+1} + \mathbf{S}^{k-1,k,k+1})\mathcal{I}_N, \tag{D.29}$$

(D.28) can be rewritten as

$$\begin{aligned} W_E^{k+1} &\leftarrow W_E^k + \\ &\quad \mu\mathcal{F}_N(\mathbf{U}^{k-1,k,k+1} + \mathbf{S}^{k-1,k,k+1})^T(\mathbf{y}^k - \mathbf{U}^{k-1,k,k+1}\mathcal{I}_N W_E^k), \quad \text{(D.30)} \\ &\leftarrow \left(\mathbf{I}_N - \mu\mathcal{F}_N(\mathbf{U}^{k-1,k,k+1} + \mathbf{S}^{k-1,k,k+1})^T\mathbf{U}^{k-1,k,k+1}\mathcal{I}_N\right) W_E^k + \\ &\quad \mu\mathcal{F}_N(\mathbf{U}^{k-1,k,k+1} + \mathbf{S}^{k-1,k,k+1})^T\mathbf{y}^k. \quad \text{(D.31)} \end{aligned}$$

When H_E denotes the frequency response of the echo channel, i.e. $H_E = \mathcal{F}_N\mathbf{h}_E$, one can rearrange (D.31) to

$$\begin{aligned} & W_E^{k+1} - H_E \quad \text{(D.32)} \\ &= \left(\mathbf{I}_N - \mu\mathcal{F}_N(\mathbf{U}^{k-1,k,k+1} + \mathbf{S}^{k-1,k,k+1})^T\mathbf{U}^{k-1,k,k+1}\mathcal{I}_N\right)(W_E^k - H_E) + \\ &\quad \mu\mathcal{F}_N(\mathbf{U}^{k-1,k,k+1} + \mathbf{S}^{k-1,k,k+1})^T(\underbrace{\mathbf{y}^k - \mathbf{U}^{k-1,k,k+1}\mathbf{h}_E}_{\mathbf{n}^k}), \end{aligned}$$

where (5.1) was applied. If Δ^k denotes $W_E^k - H_E$, one observes that (D.32) is a stochastic difference equation in the weight error vector Δ^k. After invoking the *independence assumption*, which is often used to prove convergence of the LMS algorithm for small step sizes [54] and which states in our case that

$$\mathcal{E}\left\{\left(\mathbf{I}_N - \mu\mathcal{F}_N(\mathbf{U}^{k-1,k,k+1} + \mathbf{S}^{k-1,k,k+1})^T\mathbf{U}^{k-1,k,k+1}\mathcal{I}_N\right)\Delta^k\right\} \tag{D.33}$$

$$= \mathcal{E}\left\{\left(\mathbf{I}_N - \mu\mathcal{F}_N(\mathbf{U}^{k-1,k,k+1} + \mathbf{S}^{k-1,k,k+1})^T\mathbf{U}^{k-1,k,k+1}\mathcal{I}_N\right)\right\}\mathcal{E}\left\{\Delta^k\right\},$$

one obtains

$$\mathcal{E}\{\Delta^{k+1}\} = \mathcal{F}_N\mathcal{E}\left\{\mathbf{I}_N - \mu(\mathbf{U}^{k-1,k,k+1} + \mathbf{S}^{k-1,k,k+1})^T\mathbf{U}^{k-1,k,k+1}\right\}\mathcal{I}_N\mathcal{E}\{\Delta^k\}, \tag{D.34}$$

where it was assumed that $\mathbf{n}^k$ is zero mean and statistically uncorrelated with the transmitted echo signal. Hence, the convergence behaviour of CDC EC is determined by the eigenvalue spread of the covariance matrix

$$\mathcal{X}_f = \mathcal{F}_N\mathcal{E}\left\{(\mathbf{U}^{k-1,k,k+1} + \mathbf{S}^{k-1,k,k+1})^T\mathbf{U}^{k-1,k,k+1}\right\}\mathcal{I}_N. \tag{D.35}$$

Since the DFT and IDFT matrices do not alter the eigenvalues, one might as well look at the eigenvalues of the time domain covariance matrix

$$\mathcal{X}_t = \mathcal{E}\left\{(\mathbf{U}^{k-1,k,k+1} + \mathbf{S}^{k-1,k,k+1})^T\mathbf{U}^{k-1,k,k+1}\right\}. \tag{D.36}$$

When all the tones of the echo reference signal are transmitted and equipowered, i.e. $\mathcal{E}\{U_i^*U_i\} = \sigma_u^2,\ \forall i$, and when all the time domain samples are uncorrelated, then $\mathcal{X}_t$ is a diagonal matrix

$$\mathcal{X}_t = N\frac{\sigma_u^2}{N}\mathbf{I}_N + \nu\frac{\sigma_u^2}{N}\mathbf{I}_N. \tag{D.37}$$

Hence, all the eigenvalues λ of $\mathcal{X}_t$ are equal to the diagonal elements. Moreover, all the eigenvalues are equal and positive. Now, convergence in the mean is guaranteed, if the step size μ satisfies the following condition

$$0 < \mu < \frac{2N}{(N+\nu)\sigma_u^2}. \tag{D.38}$$

□

In practice, the convergence bounds might be tighter since the independence assumption will only be valid for small step sizes. When not all carriers are excited, convergence can not be guaranteed (which also holds for the convergence proof given in [57]) and simulations have to show the true performance.

E Appendix to Chapter 6

E.1 Convergence in the mean split SR-RLS

Property E.1 Given the update rule for the split SR-RLS algorithm

$$\mathbf{w}^k \leftarrow \mathbf{w}^{k-1} + \mu \mathbf{l}^k (d^k - (\mathbf{w}^{k-1})^T \mathbf{z}^k), \tag{E.1}$$

then convergence in the mean is achieved when

$$0 < \mu < \frac{2}{\lambda_{max}}, \tag{E.2}$$

with λ_{max} the most dominant eigenvalue of $\mathbf{R}_{lz} = \mathcal{E}\{\mathbf{l}^k (\mathbf{z}^k)^T\}$. □

Proof : Let d^k be equal to

$$d^k = (\mathbf{z}^k)^T \mathbf{w}_0 + n_0^k, \tag{E.3}$$

where n_0^k is the estimation error when applying the optimal Wiener solution $\mathbf{w}_0$. Now, define the weight error, using (E.1), as:

$$\begin{aligned}
\Delta^k &= \mathbf{w}^k - \mathbf{w}_0, && \text{(E.4)}\\
&= \mathbf{w}^{k-1} + \mu \mathbf{l}^k (d^k - (\mathbf{z}^k)^T \mathbf{w}^{k-1}) - \mathbf{w}_0, && \text{(E.5)}\\
&= (\mathbf{I}_T - \mu \mathbf{l}^k (\mathbf{z}^k)^T) \mathbf{w}^{k-1} + \mu \mathbf{l}^k d^k - \mathbf{w}_0, && \text{(E.6)}\\
&= (\mathbf{I}_T - \mu \mathbf{l}^k (\mathbf{z}^k)^T) \Delta^{k-1} + \mu \mathbf{l}^k (d^k - (\mathbf{z}^k)^T \mathbf{w}_0), && \text{(E.7)}
\end{aligned}$$

where $\mathbf{I}_T$ denotes the identity matrix of size T. With (E.3), this leads to

$$\Delta^k = (\mathbf{I}_T - \mu \mathbf{l}^k (\mathbf{z}^k)^T) \Delta^{k-1} + \mu \mathbf{l}^k n_0^k. \tag{E.8}$$

With the explicit definition of $\mathbf{l}^k = \mathbf{T}^k (\mathbf{z}^k)^*$ (cf. (6.24)), one has

$$\Delta^k = (\mathbf{I}_T - \mu \mathbf{l}^k (\mathbf{z}^k)^T) \Delta^{k-1} + \mu \mathbf{T}^k (\mathbf{z}^k)^* n_0^k. \tag{E.9}$$

Taking the statistical expectation of (E.9) yields

$$\mathcal{E}\{\Delta^k\} = \mathcal{E}\{(\mathbf{I}_T - \mu \mathbf{l}^k (\mathbf{z}^k)^T) \Delta^{k-1}\} + \mu \mathbf{T}^k \mathcal{E}\{(\mathbf{z}^k)^* n_0^k\}, \tag{E.10}$$

where it is assumed that $\mathbf{T}^k$ becomes independent of the time index (which holds for stationary inputs and $\epsilon < 1$). This relation will only hold approximately when varying $\mathbf{T}^k$ is slowly time-varying due to non-stationary inputs. Due to the orthogonality principle [54], the input vector $\mathbf{z}^k$ will be orthogonal to the estimation error when approaching the Wiener solution and hence zeroes the second term in (E.10). According to the traditional 'independence

assumption' [54] – standardly applied in LMS analyses – the input vector $\mathbf{z}^k$ is independent of Δ^{k-1}. Hence, one may write

$$\begin{aligned} \mathcal{E}\{\Delta^k\} &= (\mathbf{I}_T - \mu\mathcal{E}\{\mathbf{l}^k(\mathbf{z}^k)^T\})\mathcal{E}\{\Delta^{k-1}\} && \text{(E.11)} \\ &= (\mathbf{I}_T - \mu\mathbf{R}_{lz})\mathcal{E}\{\Delta^{k-1}\} && \text{(E.12)} \end{aligned}$$

The unknown coefficients $\mathbf{w}^k$ converge to the optimal Wiener solution $\mathbf{w}_0$ when $\mathcal{E}\{\Delta^k\} = \mathbf{0}$ or $\mathcal{E}\{\mathbf{w}^k\} = \mathbf{w}_0$. This occurs when all eigenmodes of $\mathbf{R}_{lz}$ decrease in time. Hence, when all eigenvalues λ_j, $j = 1, ..., T$ of $\mathbf{R}_{lz}$ satisfy:

$$-1 < (1 - \mu\lambda_j) < 1, \tag{E.13}$$

convergence is guaranteed. This relation is true for all j when

$$0 < \mu < \frac{2}{\lambda_{max}}, \tag{E.14}$$

and all λ_j's are positive. Hence, the split SR-RLS converges in the mean when (E.14) is satisfied, which completes the proof. □

E.2 Upper bound for the step size of split SR-RLS

Property E.2 The split SR-RLS update of (E.1) is convergent in the mean when the step size remains within the following bounds

$$0 < \mu < \frac{1}{1-\epsilon^2} \leq \frac{2}{\lambda_{max}}. \tag{E.15}$$

□

Proof: In the previous section, it was shown that the convergence of the split SR-RLS algorithm is determined by the most dominant eigenvalue of $\mathbf{R}_{lz}$. To derive more specific upper and lower bounds for the step size μ, the eigenvalues of $\mathbf{R}_{lz}$ will be computed explicitly.

With k approaching infinity, one can state approximately

$$\begin{aligned} \mathbf{R}_{11}^{-1} &= \left(\mathcal{E}\{(\mathbf{z}_1^k)^*(\mathbf{z}_1^k)^T\}\right)^{-1} \approx \frac{1}{1-\epsilon^2}(\mathbf{S}_1^k)^T(\mathbf{S}_1^k)^*, && \text{(E.16)} \\ \mathbf{R}_{22}^{-1} &= \left(\mathcal{E}\{(\mathbf{z}_2^k)^*(\mathbf{z}_2^k)^T\}\right)^{-1} \approx \frac{1}{1-\epsilon^2}(\mathbf{S}_2^k)^T(\mathbf{S}_2^k)^*, && \text{(E.17)} \end{aligned}$$

where the factor $\frac{1}{1-\epsilon^2}$ represents the effective window length. The matrix $\mathbf{R}_{lz}$ can now be written as:

$$\begin{aligned} \mathbf{R}_{lz} &= \mathcal{E}\{\mathbf{l}^k(\mathbf{z}^k)^T\}, && \text{(E.18)} \\ &= \mathcal{E}\left\{ \left[\begin{array}{c|c} (\mathbf{S}_1^k)^T(\mathbf{S}_1^k)^* & \mathbf{0}_{T_1\times T_2} \\ \hline \mathbf{0}_{T_2\times T_1} & (\mathbf{S}_2^k)^T(\mathbf{S}_2^k)^* \end{array}\right] \left[\begin{array}{c} (\mathbf{z}_1^k)^* \\ (\mathbf{z}_2^k)^* \end{array}\right] \left[\begin{array}{cc} (\mathbf{z}_1^k)^T & (\mathbf{z}_2^k)^T \end{array}\right] \right\}, \end{aligned}$$

$$\begin{aligned} &\approx \quad (1-\epsilon^2)\left[\begin{array}{c|c} \mathbf{R}_{11}^{-1} & \mathbf{0}_{T_1\times T_2} \\ \hline \mathbf{0}_{T_2\times T_1} & \mathbf{R}_{22}^{-1} \end{array}\right] \mathcal{E}\left\{\left[\begin{array}{c} (\mathbf{z}_1^k)^* \\ (\mathbf{z}_2^k)^* \end{array}\right]\left[\begin{array}{cc} (\mathbf{z}_1^k)^T & (\mathbf{z}_2^k)^T \end{array}\right]\right\}, \\ &= \quad (1-\epsilon^2)\left[\begin{array}{c|c} \mathbf{I}_{T_1} & \mathbf{R}_{11}^{-1}\mathbf{R}_{12} \\ \hline \mathbf{R}_{22}^{-1}\mathbf{R}_{21} & \mathbf{I}_{T_2} \end{array}\right], \end{aligned} \tag{E.19}$$

where the following correlation matrix definitions were applied:

$$\mathbf{R}_{12} = \mathcal{E}\{(\mathbf{z}_1^k)^*(\mathbf{z}_2^k)^T\}, \tag{E.20}$$

$$\mathbf{R}_{21} = \mathcal{E}\{(\mathbf{z}_2^k)^*(\mathbf{z}_1^k)^T\}. \tag{E.21}$$

Using the following relationship between determinants of block matrices

$$\left|\begin{array}{cc} \mathbf{A} & \mathbf{B} \\ \mathbf{C} & \mathbf{D} \end{array}\right| = |\mathbf{A}|\left|\mathbf{D}-\mathbf{C}\mathbf{A}^{-1}\mathbf{B}\right| = |\mathbf{D}|\left|\mathbf{A}-\mathbf{B}\mathbf{D}^{-1}\mathbf{C}\right|, \tag{E.22}$$

the eigenvalues λ of $\mathbf{R}_{lz}$ in (E.19) can easily be obtained as the T roots of the characteristic polynomial

$$\begin{aligned} &|\mathbf{R}_{lz}-\lambda\mathbf{I}_T| \\ &\quad = (1-\epsilon^2-\lambda)^{T_1}\left|(1-\epsilon^2-\lambda)\mathbf{I}_{T_2}-\frac{(1-\epsilon^2)^2}{1-\epsilon^2-\lambda}\mathbf{R}_{22}^{-1}\mathbf{R}_{21}\mathbf{R}_{11}^{-1}\mathbf{R}_{12}\right|, \\ &\quad = (1-\epsilon^2-\lambda)^{T_1-T_2}(-1)^{T_2}\left|(1-\epsilon^2)^2\mathbf{R}_{22}^{-1}\mathbf{R}_{21}\mathbf{R}_{11}^{-1}\mathbf{R}_{12}-(1-\epsilon^2-\lambda)^2\mathbf{I}_{T_2}\right|. \end{aligned} \tag{E.23}$$

One observes that $\mathbf{R}_{lz}$ has an eigenvalue $1-\epsilon^2$ with multiplicity T_1-T_2 where the remaining eigenvalues are obtained as $(1-\epsilon^2)(1\pm\sqrt{d_i})$, with d_i equal to the eigenvalues of the matrix $\mathbf{R}_{22}^{-1}\mathbf{R}_{21}\mathbf{R}_{11}^{-1}\mathbf{R}_{12}$. Due to the specific structure of $\mathbf{R}_{22}^{-1}\mathbf{R}_{21}\mathbf{R}_{11}^{-1}\mathbf{R}_{12}$, one can prove that the d_i's represent in fact the cosines squared of the principal angles [53] between the subspaces spanned by the columns of $\mathbf{Z}_1^k$ and $\mathbf{Z}_2^k$. Here, $\mathbf{Z}_1^k$ and $\mathbf{Z}_2^k$ are matrices containing the first T_1 and the last T_2 columns of $\mathbf{Z}^k$ (see (6.5)) respectively. Hence, all the d_i's are always positive and less than or equal to one. As a consequence, the maximum eigenvalue λ_{max} of $\mathbf{R}_{lz}$ is upper bounded by $2(1-\epsilon^2)$.

Since convergence in the mean is guaranteed when (E.14) is satisfied, one obtains the following bounds for the step size

$$\boxed{0<\mu<\tfrac{1}{1-\epsilon^2}\leqslant\tfrac{2}{\lambda_{max}}.} \tag{E.24}$$

This equation indicates that in order for (E.1) to converge, the step size must be smaller than the effective number of samples in the *memory* of the system, $\frac{1}{1-\epsilon^2}$, where ϵ is the forgetting factor. □

List of publications

All the papers below are available at `ftp://ftp.esat.kuleuven.ac.be/pub/sista`.

International journal papers

- G. Ysebaert, K. Van Acker, M. Moonen and B. De Moor. Constraints in channel shortening equalizer design for DMT-based systems. *Signal Processing*, 83(3):641–648, March 2003.

- G. Ysebaert, K. Vanbleu, G. Cuypers, M. Moonen and T. Pollet. Combined RLS-LMS initialization for per tone equalizers in DMT-receivers. *IEEE Trans. on Signal Proc.*, 51(7):1916–1927, July 2003.

- G. Ysebaert, F. Pisoni, M. Bonaventura, R. Hug, and M. Moonen. Echo cancellation in DMT-receivers: Circulant decomposition canceler. To appear in *IEEE Trans. on Signal Proc.*, 2004.

- G. Ysebaert, K. Vanbleu, G. Cuypers and M. Moonen. Split SR-RLS for the joint initialization of the per-tone equalizers and per-tone echo cancelers in DMT-based receivers. To appear in *EURASIP Journal on Applied Signal Processing, Special Issue on Multicarrier Communications and Signal Processing*, 2004.

- K. Vanbleu, G. Ysebaert, G. Cuypers, M. Moonen and K. Van Acker. Bitrate maximizing time-domain equalizer design for DMT-based systems. To appear in *IEEE Trans. on Commun.*, 2004.

- G. Ysebaert, K. Vanbleu, G. Cuypers and M. Moonen. Joint window and time domain equalizer design for bit rate maximization in DMT-receivers. To appear in *IEEE Trans. on Signal Proc.*, 2004.

International conference papers

- G. Cuypers, K. Vanbleu, G. Ysebaert and M. Moonen. Combining per tone equalization and windowing in DMT receivers. In *Proc. of Signal Processing Symposium (SPS)*, pages 173–176, Leuven, Belgium, March 2002.

- K. Vanbleu, G. Ysebaert, M. Moonen and P. Vandaele. Combined equalization and alien crosstalk cancellation in ADSL. In *Proc. of Signal Processing Symposium (SPS)*, pages 49–52, Leuven, Belgium, March 2002.

- G. Ysebaert, K. Vanbleu, G. Cuypers, M. Moonen and K. Van Acker. Double talk cancellation in echo cancelled DMT-systems. In *Proc. of Signal Processing Symposium (SPS)*, pages 169–172, Leuven, Belgium, March 2002.

- G. Cuypers, G. Ysebaert, P. Vandaele and M. Moonen. Combining per tone equalization and windowing in DMT receivers. In *Proc. IEEE Int. Conf. on Acoustics, Speech and Signal Proc. (ICASSP)*, volume III, pages 2341–2344, Orlando, Florida, May 2002.

- G. Ysebaert, M. Moonen and T. Pollet. Combined RLS-LMS initialization for per tone equalizers in DMT-receivers. In *Proc. IEEE Int. Conf. on Acoustics, Speech and Signal Proc. (ICASSP)*, volume III, pages 2537–2540, Orlando, Florida, May 2002.

- K. Vanbleu, G. Ysebaert, M. Moonen and P. Vandaele. Combined equalization and alien crosstalk cancellation in ADSL receivers. In *Proc. European Signal Proc. Conf. (EUSIPCO)*, pages 281-284, Toulouse, France, September 2002.

- G. Ysebaert, K. Vanbleu, G. Cuypers, M. Moonen and K. Van Acker. Double talk cancellation in echo cancelled DMT-systems. In *Proc. European Signal Proc. Conf. (EUSIPCO)*, volume II, pages 381–384, Toulouse, France, September 2002.

- G. Ysebaert, K. Vanbleu, G. Cuypers and M. Moonen. ADSL per-tone/per-group optimal equalizer and windowing design. In *Proc. of the Asilomar Conf. on Signals, Systems and Computers*, Pacific Grove, California, November 2002.

- G. Cuypers, K. Vanbleu, G. Ysebaert and M. Moonen. Egress reduction by intra-symbol windowing in DMT-based transmitters. In *Proc. IEEE Int. Conf. on Acoustics, Speech and Signal Proc. (ICASSP)*, volume IV, pages 532–535, Hong Kong, April 2003.

- G. Cuypers, K. Vanbleu, G. Ysebaert, M. Moonen and P. Vandaele. Combining raised cosine windowing and per tone equalization for RFI mitigation in DMT receivers. In *Proc. IEEE Int. Conf. on Commun. (ICC)*, volume 4, pages 2852–2856, Anchorage, Alaska, May 2003.
- K. Vanbleu, G. Ysebaert, G. Cuypers, M. Moonen and K. Van Acker. Bitrate maximizing time-domain equalizer design for DMT-based systems. In *Proc. IEEE Int. Conf. on Commun. (ICC)*, volume 5, pages 2360–2364, Anchorage, Alaska, May 2003.
- G. Ysebaert, K. Vanbleu, G. Cuypers, M. Moonen and J. Verlinden. Echo cancellation for discrete multitone frame-asynchronous ADSL transmission. In *Proc. IEEE Int. Conf. on Commun. (ICC)*, volume 4, pages 2421–2425, Anchorage, Alaska, May 2003.
- G. Ysebaert, F. Pisoni, M. Bonaventura, R. Hug and M. Moonen. Circulant decomposition canceler for echo cancellation in DMT-based receivers. To appear in *Proc. IEEE Int. Conf. on Commun. (ICC)*, 2004.
- K. Vanbleu, G. Ysebaert, G. Cuypers and M. Moonen. Adaptive bitrate maximizing TEQ design for DMT-based systems. To appear in *Proc. IEEE Int. Conf. on Acoustics, Speech and Signal Proc. (ICASSP)*, 2004.

Abstracts

- G. Ysebaert, G. Cuypers, K. Vanbleu, K. Van Acker, and M. Moonen. Double talk cancellation in echo cancelled DMT-systems. In *Book of abstracts of the K.U.Leuven Faculty of Engineering PhD Symposium*, December 2002.
- G. Ysebaert and M. Moonen. ADSL: Advanced Digital Signal Processing towards Higher Bit Rates. In *Book of abstracts of the 1st Flanders Engineering PhD Symposium*, December 2003.

Submitted papers

- G. Cuypers, K. Vanbleu, G. Ysebaert, M. Moonen and P. Vandaele. Combined per tone equalization and receiver windowing in DSL receivers: WiPTEQ. Internal Report ESAT-SISTA/TR 02-125, K.U.Leuven, Belgium. Submitted to *Signal Processing*, September 2002.
- G. Ysebaert, K. Vanbleu, G. Cuypers, M. Moonen and J. Verlinden. Echo cancellation for discrete multitone frame-asynchronous ADSL transceivers.

Internal Report ESAT-SISTA/TR 02-186, K.U.Leuven, Belgium. Submitted to *IEEE Trans. on Commun.*, December 2002.

- K. Vanbleu, G. Ysebaert, G. Cuypers and M. Moonen. Bitrate maximizing per group equalization for DMT-based systems. Internal Report ESAT-SISTA/TR 03-48, K.U.Leuven, Belgium. Submitted to *Signal Processing*, August 2003.

- R.K. Martin, K. Vanbleu, M. Ding, G. Ysebaert, M. Milosevic, B.L. Evans, M. Moonen and C.R. Johnson, Jr. Multicarrier equalization: Unification and evaluation. Part I: Optimal designs. Internal Report ESAT-SISTA/TR 03-51, K.U.Leuven, Belgium. Submitted to *IEEE Trans. on Signal Proc.*, December 2003.

- R.K. Martin, K. Vanbleu, M. Ding, G. Ysebaert, M. Milosevic, B.L. Evans, M. Moonen and C.R. Johnson, Jr. Multicarrier equalization: Unification and evaluation. Part II: Complexity reduction, adaptation, and performance evaluation. Internal Report ESAT-SISTA/TR 03-52, K.U.Leuven, Belgium. Submitted to *IEEE Trans. on Signal Proc.*, December 2003.

- K. Vanbleu, G. Ysebaert, G. Cuypers and M. Moonen. On time-domain and frequency-domain MMSE-based TEQ design for DMT transmission. Internal Report ESAT-SISTA/TR 04-02, K.U.Leuven, Belgium. Submitted to *IEEE Trans. on Signal Proc.*, January 2004.

Curriculum vitae

Geert Ysebaert was born in Leuven, Belgium, in 1976. In 1999, he received the degree in electrical engineering from the Katholieke Universiteit Leuven, Belgium. For his Master thesis, entitled *Covariance Matching for Blind Channel Estimation in MIMO and SIMO Communication Systems*, he visited KTH - the Royal Institute of Technology, Stockholm, Sweden (prof. B. Ottersten). In September 1999, he started his PhD under the supervision of prof. Marc Moonen at the signal processing laboratory (SCD-SISTA) of the electrical engineering department ESAT, KU Leuven. His research interests are in the area of digital signal processing techniques for telecommunications.

From 2000 up to 2003 he was funded by the I.W.T. (Flemish Institute for Scientific and Technological Research in Industry). He was involved in several research projects in cooperation with Alcatel Bell, Antwerp and Alcatel Microelectronics (now ST Microelectronics), Belgium. During the fall of 2002, he visited prof. C.R. Johnson, Jr. to initiate a collaboration with the BARD research group at Cornell University, NY, USA.